U.S.NRC
United States Nuclear Regulatory Commission
Protecting People and the Environment

NUREG/CR-6975

Rod Bundle Heat Transfer Test Facility Test Plan and Design

Office of Nuclear Regulatory Research

U.S.NRC
United States Nuclear Regulatory Commission
Protecting People and the Environment

NUREG/CR-6975

Rod Bundle Heat Transfer Test Facility Test Plan and Design

Manuscript Completed: October 2008
Date Published: July 2010

Prepared by
L.E. Hochreiter, F-B Cheung, T.F. Lin, C. Frepoli, A. Sridharan,
D.R. Todd, E.R. Rosal

The Pennsylvania State University
University Park, PA 16802

K. Tien, NRC Project Manager

NRC Job Code W6855

Office of Nuclear Regulatory Research

ABSTRACT

This report describes the program objectives of the Rod Bundle Heat Transfer (RBHT) Program as well as the proposed test design, scaling efforts and the integration of the program into the analysis efforts for improving the best-estimate thermal-hydraulic computer codes. The primary area of investigation is the dispersed flow film boiling processes associated with the reflood portion of a large-break Loss of Coolant Accident. A detailed Phenomena Identification Ranking Table was developed for the reflood process in which the phenomena were subdivided into the individual component phenomena, which a best-estimate computer code models or represents. The individual component models are added in the computer code to provide a prediction of the overall wall heat flux as a function of time during the transient. Since the best-estimate computer codes are modeling individual phenomena on a component level, the experiments and the test instrumentation were developed to provide the detailed information such that the modeling could be confirmed. In this manner, the effects of compensating errors in the modeling will be minimized.

A comprehensive review of other experimental programs has been performed as well as the open literature such that the facility design benefits from the previous experimental work. In addition, a detailed scaling analysis was performed of the facility to determine what, if any, distortion effects could be present which could influence the quality of the experimental data. Both a top down and bottom up scaling analysis was performed using the Zuber-Wulff scaling approach which is state-of-the-art for thermal-hydraulic scaling. The Pi groups were calculated for the facility and for a pressurized water reactor (PWR) and a boiling water reactor (BWR) plant reflood transient and compared. It was found that there is some distortion in the test facility due to material differences of the heater rods relative to nuclear fuel rods, and the radiation heat sink effects of the housing which surround the heater rod bundle. The result was to increase the bundle size, and to investigate the different material types in a separate effects test.

The instrumentation requirements for the facility were driven by the phenomena modeling needs identified in the PIRT. There will be ample instrumentation, as compared to previous tests, to obtain data on void fraction, vapor superheat temperatures in addition to heater rod wall temperatures. In addition, a laser illuminated digital system will be used to measure the entrained droplet size and velocity distributions within the rod bundle. Also, a gamma densitometer may be used to measure the void fraction at fixed locations to compare with the void fraction data from the differential pressure cells. A conceptual design for the test facility has been developed along with a detailed instrumentation plan which addresses the phenomena which was identified in the PIRT. There are over 400 channels of instrumentation for the facility.

The RBHT facility is a unique facility which will provide new data for the fundamental development of best-estimate computer code models. This effort will reduce the uncertainty in the NRC's thermal-hydraulic computer codes which will enhance the understanding of the complex two-phase phenomena which is modeled for the reflood transient.

FOREWORD

Reflood thermal-hydraulics represents an important set of phenomena during a hypothetical loss-of-coolant-accident (LOCA) that results in core uncovery. These phenomena must be accurately simulated by systems codes in determining plant response to a LOCA. In spite of significant research into reflood thermal-hydraulics, there still exists a large uncertainty in these calculations. As a result, the Nuclear Regulatory Commission (NRC) conducts experimental investigations of reflood thermal-hydraulics in order to provide data for model development and to more thoroughly assess its systems codes.

The NRC is currently assessing and improving the TRAC/RELAP Computational Engine (TRACE) code for best estimate analysis of light water reactors. While calculation of reflood by TRACE appears to be reasonable, higher accuracy is beneficial as the code is applied to power uprates and new plant designs to ensure acceptable margin between expected plant performance and the regulatory limits. Accurate prediction of the consequences of a LOCA is important because it is one of the postulated accident scenarios that determine the licensed core power and several other operational parameters. As the NRC places greater emphasis on risk-informed regulation, a more accurate and reliable systems code will be useful to obtain realistic rather than conservative predictions.

To acquire detailed, fundamental data for use in developing models for a LOCA, the NRC sponsored the design and construction of a Rod Bundle Heat Transfer (RBHT) Test Facility. Some of these detailed data have only recently become possible because of recent advances in instrumentation technology for two-phase flow measurements.

This report describes the program objectives of the RBHT Program as well as the proposed test design, scaling efforts and the integration of the program into the analysis efforts for improving the best-estimate thermal-hydraulic computer codes. A detailed Phenomena Identification Ranking Table was developed for the reflood process in which the phenomena were subdivided into the individual component phenomena, which a best-estimate computer code models or represents. As such, this report will prove useful in understanding the detailed scaling analysis which was performed for the RBHT Test Facility to determine what, if any, distortion effects could be present which could influence the quality of the experimental data.

With improved data and code models for simulating LOCAs, we can more accurately predict the consequences of these scenarios and provide better technical bases for regulations associated with such accidents. As a result, this study will help to ensure the agency's regulations are effective and efficient.

CONTENTS

FIGURES

TABLES

EXECUTIVE SUMMARY

A research program entitled “Rod Bundle Heat Transfer (RBHT),” funded by the U.S. Nuclear Regulatory Commission, was initiated at The Pennsylvania State University (PSU) on November 3, 1997, to develop a RBHT Test Facility and to conduct experiments to aid in the development of reflood heat transfer models which could be used in the NRC’s thermal-hydraulics computer codes. The RBHT program consists of the following 16 major tasks:

- Task 1 - Development of a Preliminary Phenomena Identification and Ranking Table
- Task 2 - Critical Review of Existing Experimental Data Base
- Task 3 - Defining Information Needed for New Code Modeling Capabilities, Validation, and Assessment
- Task 4 - Defining the Program Objectives and Facility Mission
- Task 5 - First Tier Scaling for the Experimental Facility
- Task 6 - Second Tier Scaling Analysis for the Local Phenomena
- Task 7 - Defining the Instrumentation Requirements
- Task 8 - Developing Facility Input Model
- Task 9 - Drafting a Test Matrix
- Task 10 - Test Facility Design
- Task 11 - Construction and Characterization of the RBHT Facility
- Task 12 - Definition of Test Initial and Boundary Conditions
- Task 13 - Performing Tests and Qualifying the Test Data
- Task 14 - Analyzing the Test Data
- Task 15 - Assessing New or Modified Models
- Task 16 - Final Model Description, Implementation, and Scaling Report

This report describes the results obtained in the initial phase of the program; i.e., Tasks 1 through 10. It is written for NRC review purpose to insure that the course of the program is properly directed and that the RBHT Facility is adequately designed, consistent with the NRC model development and improvement efforts which are underway.

This report (i.e., the program objectives, test design, and the test and analysis approach) was also peer reviewed by individuals who are very knowledgeable and have significant expertise in the heat transfer and two-phase flow area. The individuals were selected by the Nuclear Regulatory Commission. The comments made by the different individuals were incorporated into the report as well as into the planning, design, and analysis plans for the RBHT program. In addition, there was also a specific Instrumentation Peer Review Meeting in which the facility instrumentation plan was reviewed with specialists in two-phase flow testing and instrumentation to provide guidance, comments, and critique of the proposed instrumentation for the RBHT program. Again, the comments and ideas provided by the Peer Review Panel were factored into the instrumentation design, testing methods and the resulting data analysis.

An introduction, providing the pertinent background information to justify the needs for and the significance of conducting the RBHT program, is given in Section 1 of the report.

Section 2 presents a preliminary reflood-heat-transfer specific Phenomena Identification and Ranking Table (PIRT) developed under Task 1 using the same ranking methodology as that employed by Los Alamos, Brookhaven and Idaho National Laboratories, and the NRC.

Separate preliminary PIRTs are provided for each of the important reflood regions such that the particular reflood phenomena for a given region could be subdivided into specific component models and phenomena for which a computer code would be used to perform the calculation. The relative rankings listed in these PIRTs clearly indicate the most important reflood phenomena which a best-estimate computer code should simulate with high accuracy. They also serve as a guide in the execution of the subsequent Tasks set forth in the program.

Section 3 describes the results of a comprehensive review of the literature on reflood heat transfer performed under Task 2. Unique information from the available rod bundle data and selective tube data useful to address the phenomena identified in the PIRTs is gathered and then subdivided into several different classifications to indicate which information can be used for each specific type of phenomena. A master cross-reference table is constructed identifying the data source for the highly ranked PIRT phenomena and indicating the applicability and major deficiencies (if any) of the data to determine and quantify the particular phenomena of interest. Based on the results of Task 2, new or improved data that will contribute to reducing the large uncertainties associated with some of the highly ranked phenomena, have been identified.

Using the PIRTs developed in Task 1 and the master reference tables in Task 2, the modeling capabilities of the current best-estimate computer codes including RELAP5/MOD3, TRAC-B, TRAC-P, and COBRA-TF have been examined under Task 3 to determine how well the current models in these codes can represent the highly ranked phenomena in the PIRTs. The past code validation has also been reviewed to determine the state of the validation of the codes. These are discussed in Section 4 of the report. Based on the results of Tasks 1, 2, and 3, the data needed to either help develop specific models or validate specific models for the highly ranked reflood phenomena calculated in a best-estimate code have been identified. These data needs were used to define the mission for the RBHT facility and then translated into the program objectives which have been established under Task 4, as described in Section 5. Separate-effect component experiments will be performed to meet the program objectives by isolating each highly ranked PIRT phenomenon as best as possible so as to permit specific model development for that particular phenomenon and to minimize the risk of introducing compensating errors into the advanced reflood model package. The proposed experiments will provide new data as well as supplement existing reflood heat transfer data.

Section 6 presents a first tier “top-down” systems scaling on the RBHT test facility performed under Task 5 using the combined Zuber-Wulff scaling approach which is the current state-of-the-art methodology for scaling thermal-hydraulic systems. The fluid energy equation, the rod energy equation and the bundle fluid momentum equations have been developed and made dimensionless such that the various dimensionless Pi groups are derived to examine the similitude between the proposed RBHT test facility and prototypical pressurized water reactor (PWR) and boiling water reactor (BWR) fuel assemblies. Comparisons of the derived Pi groups indicate that if prototypical fluid conditions are used in the tests, and the bundle geometry is retained, including using the prototypical spacer grids, there is a very strong similarity between the RBHT test bundle and the PWR and BWR fuel assemblies, and the data should be applicable to either reactor fuel assembly type. However, the presence of a test housing in the proposed RBHT facility does lead to extra Pi groups for this structure relative to modeling of a PWR fuel assembly, indicating that distortion in the test is possible. The RBHT facility is actually a closer representation to a BWR fuel assembly which also has a Zircaloy can or

channel surrounding the fuel rod bundle. For code modeling and validation purposes, the effects of the test housing need to be accounted for. In addition to the first tier scaling, a "bottom-up" second tier scaling has also been performed under Task 6 as described in Section 7.

The second tier scaling, which focuses on the Pi groups in the system of equations governing the particular phenomena of interest, is used to characterize the transport terms and to establish relationships for calculating them when comparing the terms of the scaled facility to those of the full size prototype. As mentioned above, the main distortion of the RBHT facility when compared to a PWR situation is the presence of the housing. Thus the housing effects have been studied using the MOXY computer program. The housing represents a heat sink for the radiative heat transfer from the rods and, subsequently, a heat source because of the stored energy during the quench period. Another possible distortion is that due to rod material differences which may alter the heat capacity, thermal time constants, surface emissivity, and surface rewetting characteristics. A detailed analysis is made to account for the fact that Inconel-600 is used in the electrical rods instead of Zircaloy for the clad, while Boron Nitride is used instead of Uranium Dioxide. The gap conductance is 96.875 kW/m^2-K (5000 $Btu/hr\text{-}ft^2$-F) for the electrical rods as compared to approximately 19.375 kW/m^2-K (1000 $Btu/hr\text{-}ft^2$-F) for nuclear fuel rods. The effects of gap conductance and material differences are found to be moderately small with the possible exception of the minimum film boiling temperature.

Section 8 describes the instrumentation requirements for the proposed RBHT facility, developed under Task 7, using the PIRTs as a guide for the important phenomena for the different types of tests which the experiments must capture for model development and code validation. There will be ample instrumentation, proven to perform in previous rod bundle experiments, which will be used in the proposed RBHT experiments. There will also be state-of-the-art instrumentation which will be used to measure the details of the two-phase flow field to determine, for example, void fraction, droplet size, droplet velocity, and droplet number density at and above the quench front. The instrumentation requirements described in Section 8 represent a robust instrumentation plan that allow most of the highly ranked phenomena to be either directly measured or directly calculated from the experimental data.

Two facility input models were developed under Task 8 using COBRA-TF as the source code as presented in Section 9. A two-channel model was used to estimate the fluid conditions for a given reflood transient and to help set test conditions. A more detailed model considered a 1/8 sector of the 7x7 bundle comprised of 45 heater rods, four unheated corner rods, and the surrounding housing. A fine nodal structure is adopted so as to resolve, in more detail, the housing and rod temperature distribution at and just above the quench front where the droplet entrainment occurs, as well as the flow behavior downstream of spacer grids where local heat transfer enhancement occurs in both single and two-phase flows.

A test matrix for the planned tests has been developed under Task 9 as presented in Section 10. A "building block" approach has been used in developing the test types and the test matrix such that simpler experiments will first be performed to quantify a particular reflood heat transfer mechanism alone and then add the additional complications of the two-phase dispersed flow film boiling behavior of the test facility.

The planned test types include single phase pressure drop, heat loss, subcooled and saturated boiling, radiation only tests with an evacuated rod bundle, single-phase steam convective heat transfer, two-phase droplet-injection convective heat transfer, forced reflood, and variable

reflood experiments. The range of conditions has been chosen for each type of experiments so as to overlap those conditions currently calculated with best estimate and Appendix K safety analysis codes, to compliment the existing data base, and to provide new data for model development and code validation. The ranges to be examined will cover the expected ranges that best-estimate codes are expected to calculate with accuracy.

Based upon the results of Tasks 1 through 9, the RBHT test facility was successfully designed under Task 10 as a flexible rod bundle separate-effects test facility which can be used to perform single and two-phase experiments under well-controlled laboratory conditions to generate fundamental reflood heat transfer data. The facility is capable of operating in both forced and gravity reflood modes covering wide ranges of flow and heat transfer conditions at pressures up to 0.402 MPa (60 psia). It has five major components: (i) a test section consisting of a 7x7 electrically heated rod bundle contained in a low mass flow housing with windows, a lower plenum, and an upper plenum, (ii) a coolant injection and steam injection system, (iii) a phase separation and liquid collection system, (iv) a downcomer and crossover leg system, and (v) a system pressure oscillation damping tank and steam exhaust piping. A detailed description of the component design is given in Section 11. The test facility has instrumentation that meets all the instrumentation requirements developed under Task 7 (see Section 8). The heater rods have been designed using prototypical spacer grids such that they can be used in two bundle builds to conduct all types of the planned experiments according to the test matrix developed under Task 9 (see Section 10).

The RBHT facility, with its robust instrumentation, is a unique facility that can be used to provide new data for the fundamental assessment of the physical relationships upon which the code constitutive models are based. It will aid in reflood model development and uncertainty reduction for the NRC's thermal-hydraulics computer code. Preliminary conclusions drawn from the results obtained in Tasks 1 through 10 are given in Section 12. An executive summary of the work performed and the major findings obtained in each of the first ten tasks of the RBHT program is given below.

Task 1 - Development of a Preliminary Phenomena Identification and Ranking Table

To aid in the development for the experimental requirements of the RBHT facility, a Preliminary PIRT was developed, focusing on the low pressure reflood portion of the PWR and BWR LOCA transients. The objective was to sub-divide the phenomena down to the lowest level by which a best-estimate computer code would calculate these phenomena. With the phenomena broken down, the capabilities of the proposed test facility were assessed to determine which could be measured with confidence, which could only be qualitatively measured, and what instrumentation would be needed.

The phenomenon in the core region is of most interest since the core thermal-hydraulic response determines the resulting peak cladding temperature (PCT). In PWR reflood calculations, the core is reflooded by the gravity head of water in the downcomer. This gravity head refloods and quenches the core, at a rate determined by the venting of steam and water which exits the top of the core. The core heat transfer response is a dependent parameter since it depends on the gravity flow into the core and, the ability of the reactor system to vent the two-phase mixture.

The approach for developing the Preliminary PIRT for the core region is based on examining the FLECHT-SEASET test data and analysis. Six regions of interest within the core during reflooding have been identified. These include:

1) the single-phase heat transfer region below the quench front,
2) the subcooled and saturated nucleate boiling region below the quench front,
3) the quench front region,
4) the froth region above the quench front,
5) the dispersed flow film boiling region above the froth region,
6) the topdown quench front.

At the bottom of the fuel rod (or heater rods in the experiment), the heat transfer is by single phase forced or natural convection. As the coolant temperature approaches the saturation temperature, subcooled nucleate boiling occurs and eventually saturated boiling. The quench front region is the next region of interest. At this point, the stored energy from the fuel/heater rods is released into the coolant which results in significant steam generation. The result of the steam generation at the quench front produces a two-phase froth mixture which entrains liquid flow. The froth region above the quench front is the location where the steam generated from the quench front acts to shear the liquid flow into liquid ligaments and eventually into a spectrum of droplets which are then entrained upward.

Above the froth region, the flow field consists of entrained droplets in a superheated steam flow. This is the heat transfer regime where the calculated PCT typically occurs. It is a region of low heat transfer since the vapor sink temperature is superheated and can approach the rod surface temperature. Since cladding temperatures are high, radiation heat transfer to surfaces, droplets and vapor must be accounted for.

At the very top of the rod bundle, there can be a top quench front which moves down the fuel/heater rod. The movement of the top quench front depends on the amount of liquid entrainment in the flow and the power profile of the fuel/heater rod as well as the previous blowdown heat transfer history. The top quench occurs at elevations which are significantly above the location of the PCT so its behavior does not influence the PCT value. However, the top quench front is related to the amount of liquid which leaves the core and may affect the overall reflood system behavior.

Separate preliminary PIRTs were developed for each of these six regions such that the particular phenomena for a particular region could be subdivided into specific component models which a computer code would be used to perform the calculation. The same ranking method as that employed by Los Alamos National Laboratory is used to denote the relative importance of the "High", "Medium", and "Low" phenomena. The highly ranked phenomena that were identified for the PWR transient are listed in six separate PIRT tables, one for each of the six regions of interest. To be complete, the tables also contain medium and low-ranked phenomena. These PIRT tables were used to develop and guide the design of the RBHT facility and to structure the instrumentation plan for the single phase convection tests, radiation-only tests, dispersed flow heat transfer tests (i.e., droplet injection tests), and the forced reflood tests. A separate PIRT table is also presented for the gravity or variable flow reflood transients.

Nearly all the phenomena identified with rod bundle heat transfer for PWRs are applicable to the hot assembly in a BWR since it refloods in a similar manner. However, one difference between the reflooding behavior of the high power BWR assemblies and a PWR assembly is the

presence of the fuel assembly shroud in the BWR design. The shroud is calculated to quench from the liquid in the bypass region such that there is additional surface-to-surface radiation heat transfer occurring in the BWR fuel assembly as compared to a PWR fuel assembly. The additional surface-to-surface radiation can be simulated in the RBHT experiments since the test facility will have a shroud around the test bundle. There is also surface-to-surface radiation within a PWR fuel bundle, due to colder guide tube thimbles. The RBHT bundle simulates a Westinghouse or Framatome fuel assembly with smaller thimbles. A Combustion Engineering fuel assembly design would have larger guide tube thimbles. The difference in the radiation heat transfer can be calculated. Since the high power BWR fuel assemblies are in co-current upflow, similar to PWR fuel assemblies, the key thermal-hydraulic phenomena identified as being highly ranked for PWR are also highly ranked for the BWR design. (The one factor which would change is the surface-to-surface radiation heat transfer in the dispersed flow film boiling regime is a higher ranked phenomenon for the BWR application as compared to the PWR application.)

The ability of the proposed RBHT facility to simulate the highly ranked PWR and BWR PIRT items has also been assessed and it has been found that the test facility can represent nearly all the phenomena of interest. The areas where the simulation is the weakest is in the materials used for the cladding, heater rods and the housing, as compared to nuclear fuel rods and a BWR Zircaloy channel box. Scaling studies have been performed as part of the program to select the materials such that the deviation from the true plant design is minimized.

Task 2 - Critical Review of Existing Experimental Data Base

A number of important rod bundle experiments have been reviewed to determine the availability of data, test facility design, types of tests, instrumentation, and data from tests. These rod bundle experiments include FLECHT Cosine Tests (NRC/Westinghouse), FLECHT Skewed Axial Power Shape Tests (NRC/Westinghouse), FLECHT-SEASET 21 Rod Bundle Tests (NRC/Westinghouse), FLECHT-SEASET 161 Unblocked Bundle Tests (NRC/Westinghouse), FEBA Reflood Tests (Germany), THTF Rod Bundle Tests (NRC/Oak Ridge National Lab), FRIGG Rod Loop Tests (Sweden), GE 9-Rod Bundle Tests (General Electric), NRC/NRU Rod Bundle Tests (Canada), ACHILLES Reflood Tests (Great Britain), NRC/Lehigh 9-Rod Bundle Tests (Lehigh University), and PERICLES Reflood Tests (France). In addition to the above rod bundle tests that are included in the first portion of the review, more than three hundred articles on single tube tests and related studies have been included in the second portion of the review. The relevant information is sub-divided into 10 different classifications. These include:

1) liquid entrainment and breakup,
2) drop size distribution and droplet number density,
3) interfacial shear and droplet acceleration,
4) droplet-enhanced convective heat transfer,
5) droplet evaporative heat transfer,
6) direct contact heat transfer,
7) total wall heat transfer,
8) effects of spacer grids,
9) effects of variable inlet flow, and
10) thermal non-equilibrium, and other factors.

From the literature survey, it was found that there are large differences between the data obtained from the rod bundle tests and those from the single tube tests. The RBHT test facility

is designed specifically to address this data deficiency. The RBHT program will aim at obtaining not only wall-to-fluid heat transfer correlations but also models for interfacial heat transfer. To develop and assess models for interfacial phenomena with the goal of significantly improved accuracy and to minimize the potential for compensating errors will require a new or improved database that includes more detailed information than is currently available. The specific needs for new or improved data are described below:

1. In dispersed flow film boiling, the primary heat transfer mechanism is convective heat transfer to superheated steam. It is now recognized that the steam convective heat transfer coefficient can be enhanced by up to 100 percent due to the presence of entrained droplets. No suitable models currently exist for this phenomenon. The combination of single-phase convection experiments and two-phase convection experiments with droplet injections (with known drop sizes and flow rates) to be performed in the RBHT test facility will provide important new data and result in the development of the needed model.

2. Once the uncertainty involving droplet-enhanced heat transfer is resolved, there still remains the difficulty in predicting the heat transfer rate for the dispersed flow film boiling (DFFB) regime due to the difficulty in calculating the steam superheat. The amount of steam superheat is governed by the interfacial heat transfer between the steam and the evaporating droplets. To correctly calculate the interfacial heat transfer requires the knowledge of both the entrained drop size and the droplet flow rate. There is very little data of this type currently available for quenching rod bundles. The RBHT program will generate the needed database through advanced instrumentation involving the use of a laser illuminated digital camera system to determine the entrained drop size and measure the droplet flow rate.

3. Although data showing the effects of spacer grids are available, the phenomenon is still not completely understood. In particular, the separate-effects of spacer grids for interfacial shear in rod bundles at low pressures, in dispersed flow film boiling, and in transition boiling heat transfer during reflood, are not known. It is necessary to determine the grid geometry effects. The RBHT program, which will explore two or more types of space grids and will perform heat transfer measurements in various flow regions at locations just before and after the spacer grids, will greatly augment the database needed for modeling the spacer grid effects.

4. There is insufficient data on transition boiling heat transfer during quenching in rod bundles. This is especially true regarding the minimum film boiling temperature. For reflood conditions where precursory cooling is important, the transition regime is responsible for the final quench which influences the quench front propagation. The emphasis of the RBHT program to measure the local values of the void fraction in the quench front region will provide the much needed database.

5. When the flow at the quench front is subcooled, an inverted annular film boiling (IAFB) regime would develop immediately downstream of the quench front. The liquid-rich region provides the precursory cooling that controls the quench front velocity and provides the source of vapor and entrained liquid for the DFFB region. It has been demonstrated that many of the apparent functional dependencies for the IAFB regime are primarily due to the axial profile of the void fraction in this region. Currently available data for this regime in rod bundles is insufficient for model development due to the coarse spacing used for the void fraction measurements. The RBHT program will address this data need through the use of

finely spaced differential pressure cells and by a local void fraction measurement provided by a low energy gamma-densitometer.

6. The heat transfer rate in the IAFB region increases rapidly with liquid subcooling. Higher subcooling promotes heat transfer to the liquid core and reduces vapor generation and the thickness of the vapor film, thus enhancing heat transfer. It is traditional to formulate reflood test matrices by fixing the inlet subcooling and then vary the inlet flow rate. This procedure does not provide a true single parameter variation needed for model development at the subcomponent levels. In the RBHT program, non-traditional procedures involving fixing either the local subcooling or the mass flux at constant values at the quench front will be done by choosing appropriate combinations of the inlet flow rate and subcooling in the planned experiments. This will provide important new data not available heretofore.

7. The database in the nucleate boiling regime for void fraction (i.e., interfacial shear) in rod bundles at low pressure conditions has been identified as a code deficiency during the AP600 code applicability program. Some data exist or can be calculated from other reflood test data after the bundle has quenched. The RBHT will be conveniently used to generate a database with systematic variation of parameters that would greatly aid model development and assessment.

The various technical issues discussed above provide clear justifications for the need for developing the RBHT facility. Separate-effects tests will be performed in this facility to obtained new or improved data for model development and code validation at the most fundamental subcomponent levels practicable.

Task 3 - Defining Information Needed for New Code Modeling Capabilities, Validation, and Assessment.

The modeling capabilities of the best-estimate codes including RELAP5/MOD3, TRAC-B, TRAC-P and COBRA-TF systems computer codes have been examined. All of these codes attempt to predict a transient boiling curve for a heated surface with internal heat generation for a given surface temperature and the fluid conditions adjacent to the surface such as the pressure, void fraction, vapor temperature and mass flow rate. The calculated boiling curve is generated by combining different individual heat transfer correlations which model one specific phenomenon such that a continuous calculation can be performed, as the fluid conditions change, the boiling curve predicted by the computer code also changes as some phenomena become larger and others become smaller such that the calculated surface heat transfer coefficient between the coolant and the heated surface may result in the surface heating-up to higher temperature, or the surface cooling down to a lower temperature.

Individual empirical or semi-empirical heat transfer correlations are used to calculate the local heat transfer behavior from the heated surface to the fluid. The difference between the empirical and semi-empirical correlations is meant to indicate the degree to which the true physical condition is modeled by the correlation. Most correlations are usually empirical, that is, derived from a specific set of data, and predict a single phenomenon, or several phenomena in parallel. These correlations are often applied to conditions and geometries which were not included in the original basis for the correlation when performing reactor safety analysis. The heat transfer correlations may also require some modifications to make the correlation consistent with the numerical solution scheme of the code such that rapid calculations can be performed in a reliable fashion. Such modifications can result in essentially a different

correlation than was originally developed. The process of combining different individual specific correlations can lead to compensating errors, in which one calculates the “right” answer for the wrong reason because there are multiple errors in the calculational scheme. The heat transfer correlations, which comprise the calculated boiling curve, are also usually based on test data which is scaled relative to the reactor system. The resulting reactor systems code is also validated against scaled systems experiments. Therefore, one must address the effects and uncertainties of applying the correlations which are developed from scaled data to the analysis of a full scale reactor system.

While each code had the basic models for a boiling curve, and thermal and mechanical non-equilibrium, as well as the use of particular sets of heat transfer correlations, the COBRA-TF thermal-hydraulic formulation and additional detailed component models makes this code an attractive choice to refine reflood development. COBRA-TF can be used on a sub-channel basis to model the limiting hot fuel pin in a rod bundle. COBRA-TF is also a three field formulation with an explicit entrained liquid field and a corresponding interfacial area transport equation which permits more accurate modeling of the entrained liquid phase, which is most important for calculating dispersed flow film boiling. Using the unique representation of the third field or entrained droplet field results in more accurate predictions of flow regimes, their transition, and the resulting heat transfer in the different regimes. There is also believed to be less of a chance of compensating error since one is not adjusting a two field model to represent the effects of three fields. Specific attention has been spent in the COBRA-TF dispersed flow heat transfer model to account for the different component models which represent "reflood" heat transfer. Fine mesh renodalization for the heated conductors is used to better represent the quench front, the two-phase convective enhancement is accounted for in the calculations and a subchannel radiation model is used to more accurately represent radiation within a rod bundle. COBRA-TF also models the effects of spacer grids in the dispersed two-phase flow in a mechanistic manner accounting for the convective effects of spacer grids, the spacer grid quenching behavior and the droplet breakup caused by spacer grids. In particular, a small droplet field has been added to COBRA-TF to model the heat transfer effects of the much smaller drops as they evaporate and provide additional cooling downstream of the grids.

Compensating errors, however, remain an important issue in using COBRA-TF to predict the large-break LOCA transient. In view of this, complete sets of valid test data and the associated data analysis are needed to improve the specific models in the computer code to insure that compensating errors are minimized, the heat transfer models are applicable at full scale with acceptable uncertainty, and the implementation of the correlations into the code do not change the nature or predictability of the original correlation.

The formulation of the COBRA-TF code, as developed as part of the FLECHT-SEASET 161 Blocked Bundle Program, has the desired basic structure to develop the improved component models needed for dispersed flow film boiling in reflood. The RBHT program will utilize COBRA-TF for modeling purposes, and predictions and model validation purposes in the development of improved reflood models.

Task 4 - Defining the Program Objectives and Facility Mission.

The results of Task 1, 2, and 3 have identified the phenomena of interest and the existing data base for reflood component model development and validation over the range of conditions of interest. Improved analysis models are the objective of the RBHT program. The needs define

the specific mission of the test program as well as the analysis efforts which will compliment the experiments.

The objectives of the RBHT program are to:

1. Develop a Phenomena Identification Ranking Table for reflood heat transfer on a component model level and estimate the relative importance of each phenomenon for predicting reflood heat transfer,

2. Develop a test facility design which has a minimum of distortion to represent reflood heat transfer in PWR and BWR cores,

3. Assess the needs of best-estimate computer codes on their modeling approaches for reflood heat transfer and the component models used in the computer codes,

4. Perform component experiments which isolate individual phenomena that influence reflood heat transfer,

5. Determine the effects of the fuel assembly spacer grids on the dispersed flow film boiling heat transfer of the grid,

6. Develop specific component models from these experiments,

7. Add the component models into a best-estimate computer code and compare to the forced reflood heat transfer data from this series of experiments as well as other sets of reflood heat transfer data,

8. Validate the new proposed component reflood heat transfer models over their range of application,

9. Document the results of the experiments and analysis in a form that it can be used by others.

The first three objectives have already been met by performing the tasks described in this report whereas the last six objectives will be achieved by the conduct of specifically directed experiments, development of physically based heat transfer models and implementation of these models into a best-estimate code.

The proposed experiments will be performed in a building block approach such that the more complex experiments occur after the more fundamental experiments. In this fashion, additional information and desired test conditions can be modified as needed to optimize the test matrix of the forced reflooding tests which are the most difficult tests to perform. The proposed experiments will provide new data as well as supplement existing reflood heat transfer data but they will focus on the improvements of specific best-estimate thermal-hydraulic models rather than identifying licensing margin.

To achieve the objectives of the experiments and to capture the important thermal-hydraulic phenomena which have been identified for reflood heat transfer, several new or novel approaches are proposed for the bundle instrumentation.

Experiments will be performed using new instrumentation to isolate a specific phenomenon as best as possible so as to permit specific model development for that phenomenon. In this fashion, the risk of introducing compensating error into the advanced reflood model package can be minimized.

Task 5 - First Tier Scaling Analysis for the Local Phenomena

The combined Zuber-Wulff scaling approach which is the current state-of-the-art methodology for scaling thermal-hydraulic systems, has been used to assess the ability of the RBHT facility to capture the phenomena of interest for the reflood phase of a LOCA transient such that the data can be used with confidence to verify and develop heat transfer and two-phase flow models for best-estimate thermal-hydraulic computer codes. In addition to verifying that the test facility can produce the desired data, the two-tiers scaling process also identifies possible distortions in the test facility relative to the nuclear reactor core and will provide a numerical assessment of the importance of the possible distortion.

There are three equations which are examined in the first-tier "top-down" systems scaling for the RBHT facility: these are the fluid energy equation, the solid energy (heater rod, fuel rod) equation and the fluid momentum equation. Each conservation equation is derived in the fashion as recommended by Zuber and Wulff, the equations are normalized and the terms are divided by the "driver term" such that the resulting Pi groups are dimensionless. This approach is applied to both the RBHT facility as well as to a PWR and a BWR fuel assembly to indicate the non-typical effects and distortions in the test facility relative to the actual plant component.

The fluid energy equation, which represents the energy balance for the fluid in the entire bundle at a given time, includes 23 Pi groups. These Pi groups can be categorized into quench energy terms, convective heat transfer terms, and radiative heat transfer terms. In general, the stored energy, the rod quench energy, the convection from rod to vapor, the interfacial heat transfer and the flow energy terms are of significance. On the other hand, the values of the radiation Pi groups are negligibly small, thereby indicating the predominance of convection over radiation heat transfer. Though the rod quench energy term is significant, the housing, grid and the guide tube thimble rod quench energy terms are small.

The rod energy equation includes 13 Pi groups, among which the significant terms are the convective heat transfer to the surrounding fluid, the radiation from hot rod to the cold rods and radiation to entrained drops. Property differences exist between the electrical rod and the nuclear rod exist and hence the Pi groups involving the properties of the rods are different.

The flow momentum equation Pi groups, which involved eight terms, are calculated using the given inlet conditions of 0.27 MPa (40 psia), 60 degrees C (140 degrees F) subcooling, and flooding rate of 0.0254 m/s (1 in/s) with the known value of flow area. The inlet is assumed to be single phase and the exit is dispersed two-phase mixture. The quench front is assumed to be at 1.22 m (4 ft) elevation and there are two grids that are covered with water, therefore there are six grids in the two phase region. Hydraulic diameter is calculated based on the wetted perimeter and flow area. Based on this hydraulic diameter, the Reynolds number and the single phase friction factor are calculated. Results indicate that the only important Pi group is the term representing the liquid gravity head.

In summary, it is found that the presence of a test housing leads to extra Pi groups for this structure relative to modeling of a PWR fuel assembly, thereby indicating that distortion in the

test is possible. The test facility is actually a closer representation to a BWR fuel assembly which also has a Zircaloy shroud surrounding the fuel rods. Therefore, for code modeling and validation purposes, the effect of the test housing will have to be modeled including the rod-to-rod and rod-to-housing radiation heat transfer. The housing effects will also have to be considered in the analysis of the test data such that the radiation effects can be determined.

The housing had a less important effect on the fluid momentum equation since it only affected the hydraulic diameter and resulting fluid Reynolds number and friction factor such that the frictional component of the fluid pressure drop would be somewhat larger than a PWR fuel assembly. Since the majority of the pressure drop in the bundle is due to the spacer grid form losses and the elevation head, and since prototypical grids are used in the test bundle, the hydraulic distortion is negligible.

There also can be some difference in the PWR/BWR Pi groups relative to the test due to the material differences. These effects are believed to be relatively small and can be accounted for in the analysis of the data. Comparisons of the derived Pi groups for the test and a PWR and a BWR fuel assembly indicate that if prototypical fluid conditions are used in the tests, and the bundle geometry is retained, there is a very strong similarity between the bundle and the PWR and BWR fuel assemblies and the data should be applicable to either reactor fuel assembly type.

Task 6 - Second Tier Scaling Analysis for the Local Phenomena.

In the second-tier "bottom-up" scaling approach, analysis was performed to determine the radiation heat transfer effects of the test section housing relative to an infinite size rod bundle. These calculations would tend to over-emphasize the distortion of the test relative to a PWR fuel assembly. For a BWR fuel assembly, the BWR fuel assembly channel is very similar to that of the RBHT facility such that the distortion would be less.

Calculations were also performed modeling a fuel rod, with its properties and the fuel-pellet gap as well as the electrical heater rod, to determine the heat released at quench as well as the stored energy effects and maximum temperatures and radial temperature distributions. A step-change transient in the fluid temperature was combined with the rod power being kept constant during the transient.

The effect of difference in the cladding material on the value of Tmin was assessed by comparing Inconel and Zircaloy cladding quench data from different tests. These comparisons indicate that there is a bias in which the Zircaloy cladding would be expected to quench at a higher temperature relative to stainless steel or Inconel cladding.

One of the main distortions of the RBHT facility, when compared to a PWR fuel assembly, is the presence of the housing which represents a heat sink for the radiative heat transfer from the rods. The housing can also be a heat source for the fluid later into the transient because of the release of its stored energy during the quenching period at a given elevation. In order to address housing behavior in more detail, a rod-to-rod, rod-to-housing radiation heat transfer model based on the MOXY computer program was developed.

Another issue which arose from the scaling analysis is the rod material differences. The electrical heater rods use Inconel-600 instead of Zircaloy for the clad, and Boron Nitride is used instead of Uranium Dioxide. The electric power is generated only in an annulus area inside the

rod made of Monel K-500 coil. Another difference is the gap conductance which is assumed to be 5.678 kW/m^2-K (1000 Btu/hr-ft^2-F) for a nuclear rod and 28.39 kW/m^2-K (5000 Btu/hr-ft^2-F) for the electrical rod. A detailed analysis was performed to quantify the transient temperature response distortion of an electrical rod when compared with a nuclear rod.

Results of the second-tier scaling indicate that the housing acts as a radiation and convection heat sink for the fluid and heater rods, as well as a heat source to the fluid as the housing quenches. The presence of the housing induces a radial temperature distribution across the bundle, which in turn causes energy to flow from the inner portion of the bundle to the housing. As a result, during the transient the temperature in the inner region of the RBHT bundle is lower than the temperature in an ideal case where the housing is not present such as in a PWR bundle. The effect of the housing is less important for a large bundle since the inner region is shielded by the outer region of the bundle. Sensitivity analyses have been carried out to quantify the housing distortion for different bundle sizes starting from a 5x5 bundle up to a 11x11 bundle. The distortion decreases significantly when the bundle size is increased from 5x5 to 7x7 while for further increases the distortion reduction becomes less and less significant. A 7x7 bundle size appears to be a good compromise in the attempt to reduce costs and scaling distortions at the same time. In this case the maximum temperature distortion in the inner 3x3 rods array respect to an infinite (no-housing) bundle is about 121 degrees C (250 degrees F).

The second-tier scaling analysis shows the sensitivity of other parameters such as housing thickness, housing initial temperature, surfaces emissivity, radial power distribution and dummy rods contribution. These are generally second order effects and the temperature in the center region of the bundle changes by 10 degrees C (50 degrees F) at most. The material differences between the electrical heater rods and the nuclear rods, which also include a gap between the fuel pellet and the cladding, is the second major facility distortion. The analysis shows that the quench time can be affected by these parameters especially by the material difference. Starting from the same temperature, the nuclear rod is expected to quench almost in the same time interval since the average thermal inertia of the electrical heater rod is very close to the corresponding value for the nuclear rod. The separate effect of the gap heat transfer coefficient is small. In addition, differences of the cladding material on the value of T_{min} were assessed by comparing Inconel and Zircaloy cladding quench data from different tests. These comparisons indicate that there is a bias in which the Zircaloy cladding would be expected to quench at a higher temperature relative to stainless steel or Inconel cladding.

Task 7 - Defining the Instrumentation Requirements.

The objective of the RBHT program is to provide data on the key thermal-hydraulic phenomena of interest for dispersed flow film boiling and reflood heat transfer. To accomplish this objective, specific instrumentation requirements have been developed such that the experiments will provide the data needed. One major requirement is the detailed measurements of the void fraction, droplet size, droplet velocity, as well as the local heat transfer from the heater rods. The liquid entrainment at the quench front and the resulting droplet field downstream are responsible for the improved cooling at the upper elevations in the rod bundle where the peak cladding temperature occurs. Most computer codes have difficulty predicting the correct amount of liquid entrainment as well as the timing of the entrainment. The instrumentation used in the RBHT program should help resolve this modeling issue for best-estimate computer codes.

The guideline for the RBHT tests is that the instrumentation should allow transient mass and energy balances be performed on the test facility. The inlet flow, pressures, and coolant

temperatures will be measured for each type of experiment. The outlet vapor flow, pressure, and liquid flows will also be measured. Since the reflood tests are transients, there will be mass accumulation within the bundle. The mass accumulation will be measured using sensitive differential pressure cells with fine axial spacing.

Using the inlet and exit measurements as well as the measured axial heat flux distribution into the coolant, the actual quality distribution along the bundle, can be obtained above the quench front and the amount of liquid evaporation can be calculated from the data. In a similar fashion, the void distribution along the heated bundle can also be determined to indicate the flow and heat transfer regimes in the bundle and will be used to correlate the measured heat transfer data. The differential pressure drop measurements will have to be corrected for the frictional pressure drop as well as any acceleration pressure drop to infer the local void fraction. Since the actual quality is non-equilibrium, measurements of the true vapor temperature are needed as well as the wall heat flux into the fluid. There will also be ample miniature thermocouples placed into the different subchannels along the axial length of the bundle. In addition, since the spacer grids can promote improved cooling downstream of the spacer, fluid thermocouples will also be placed in these locations. A local quality can be calculated wherever a local vapor temperature is measured in the bundle.

The fuel rods will be simulated using electrical heater rods which will have the power capability of simulating the reactor decay power at 20 seconds following reactor scram. These rods will have an internal heating coil with a prescribed axial power shape which is representative of those shapes calculated in Best-Estimate LOCA analyzes. There will be eight thermocouples placed in the rod such that all the rods will fully cover the complete axial length of the bundle. There will be thermocouples at specific elevations to obtain the radial temperature profile in the bundle. The total measured heat flux will be calculated from an inverse conduction calculation using the measured thermocouple data. In addition, these experiments are designed for computer code validation purposes. Therefore, there will be a specific arrangement of the thermocouples and the differential pressure cells within the bundle, such that the heat transfer data can be correlated with the local void fraction.

In addition to the heat transfer behavior and the vapor and structure temperatures, direct data is needed on the flow behavior in the test bundle. In the froth or transition region, data on the local void fraction distribution, interfacial area, droplet/liquid ligament size are lacking. Also in the dispersed flow regime, data are needed on the droplet size, velocity, and number density is also needed for the wall-to-drop radiation heat transfer, and the vapor-to-drop radiation and convective heat transfer. The facility will characterize the flow regime in the froth region where the liquid changes from a continuous liquid flow into a dispersed droplet flow. Therefore, the test section has windows which will permit viewing and photographing the flow at important time periods in the transient.

In addition to the fine axial mesh of the differential pressure cells along the length of the bundle and across the spacer grids for void fraction measurements, a soft gamma ray measuring devise will also be used at selected fixed elevations along the lower portion of the bundle. The gamma densitometer will give chordal average densities of the two-phase flow mixture as the flow regime changes from a dispersed droplet flow to the froth region and finally to solid water. In the RBHT program, a pulsed laser technique will be used in conjunction with a fine grid digital camera to obtain drop sizes and droplet velocities. The pulsed laser will provide the backlighting as well as the focus volume for pictures in the center subchannels of the rod bundle. This measurement technique has software which will allow the determination of the

droplet spectrum, Sauter mean drop size, droplet velocities, and an estimate of the droplet number density. These data can be used to calculate the interfacial area of the entrained droplet phase. The pulsed laser and digital camera technique has not been applied to reflood experiments before. Therefore, to verify the performance of the system and confirm the accuracy of the measurements, a series of "bench-top" experiments have been performed with the new instrumentation and to develop the data reduction and analysis programs to analyze the droplet data.

With the proposed instrumentation plan, nearly all the highly ranked phenomena will be directly measured or directly calculated from the experimental data. When a parameter is directly calculated from the experimental data, the calculation uses the transient mass and energy balance on the test section to calculate the fluid properties, there is no use of a best-estimate computer code at this stage of the analysis such that the data analysis is independent of any computer code which may be validated by the experiments. The use of the various techniques described above provides a robust instrumentation plan for the RBHT program.

Task 8 - Developing Facility Input Model.

The COBRA-TF computer code was used to model the RBHT facility. The purpose of this analysis is to perform pre-test calculations to obtain information about the range of the parameters to expect during reflood transient. This analysis will also provide basis to develop the test matrix and will indicate the maximum temperature conditions reached in the bundle for a given set of conditions.

The COBRA-TF code was developed at the Pacific Northwest Laboratory under the sponsorship of NRC to provide the best-estimate thermal-hydraulic analyses of LWR vessel during LOCA accidents. The two-phase flow is described with a two-fluid, three-field model. Thermal radiation and grid spacer effects are also included in the code as well as a more detailed dispersed flow film boiling model as given in Section 4 of this report. The code was developed for use with either rectangular Cartesian or sub-channel coordinates. Herein the sub-channel scheme is adopted since it is more suitable for complex and irregular geometries.

Two COBRA-TF models of the RBHT test facility were developed including a two-channel model and a more detailed individual sub-channel model. The two-channel model is being used to examine the local fluid conditions within the test facility so as to compare them to those conditions which are typically predicted in safety analysis calculations for a plant. This model does not account for the rod-to-rod or the rod-to-housing radiation heat transfer from the inner channel which exists in the test bundle. The model does account for the test section housing and calculates the convection heat transfer to the housing as well as the energy released from the housing as it quenches.

The two-channel analysis considered a 7x7 rod array comprised of 45 heater rods, four unheated rods, and the surrounding housing. The facility modeling approach was to divide the test facility into four sections and five fluid regions, representing the lower and upper plenums, the initial unheated length of the rod bundle, the actual heated length of the rod bundle, which contains two fluid channels. The inner channel encompasses a total of sixteen ‘hot’ rods; this includes the nine center rods and summation of the fractional parts of the rods that lie on the channel’s boundary. The second channel is comprised of the remaining twenty-nine heater rods, the four unheated rods and the housing.

Three flooding transients have been considered in the analysis with different flooding rates: 0.0203, 0.0254 and 0.0381 m/s (0.8, 1.0 and 1.5 in/s). A constant pressure, 0.27 MPa (40 psia), is set in the upper plenum and the water inlet subcooling is 49 degrees C (120 degrees F). Results of the analysis show that the vapor Reynolds number can be in the laminar, transition and turbulent flow regimes. In addition, the Weber number could vary from 7.4 just above the quench front to 3.9 at the top of the bundle.

A more detailed, 1/8th sector of the test facility has been modeled on a sub-channel basis with each sub-channel uniquely modeled along with each individual surface on the heater rod and the gap between rods. The subchannel capability of the COBRA-TF code allows more accurate representation of smaller rod bundle arrays since each individual rod can be modeled, each with different surfaces for radiation heat transfer, such that the rod-to-rod and rod-to-housing radiation heat transfer can be more accurately modeled. In this fashion, the radial temperature gradient which develops due to the radiation heat losses to the test section housing can be simulated. There are specific experiments planned in the RBHT program which will examine the radiation only heat transfer within the rod bundle and to the test section housing.

The sub-channel model uses the same power profile and linear power densities as the two-channel model, the peak linear power being at 2.743m (108 in) and 2.3 kW/m (0.7 kW/ft). The axial noding of the test section is identical to the two-channel model. A plenum is modeled at the top and bottom of the test section to provide the inlet and exit boundary conditions. An intermediate section with three channels is used to link the test section to the plena because COBRA-TF does not allow more then six channels to be directly linked to one channel.

To determine the effect of the housing on the bundle temperature distribution, the sub-channel model was run with and without the ten radiation channels. The inlet conditions were set to zero such that the bundle was heated in an adiabatic manner in a stagnant steam environment. However, as the bundle was heated, steam convective current developed and steam was released from the top pressure boundary to maintain the system pressure at 40 psia. Also, the bundle underwent convective heat transfer from the hot rods to the unheated surfaces because natural circulation paths were set in motion between grid spans. Results show that the outermost row of the rod bundle is quite effective in shielding the remainder of the rods. The temperature of the central 5x5 array of rods is practically uniform with the maximum temperature difference less than 200 degrees C.

Task 9 - Drafting a Test Matrix.

A test matrix for the planned RBHT tests has been developed for each type of planned tests. The range of conditions is given and the objectives for the proposed tests are described in detail. Some of the proposed tests have been compared to the conditions and types of previous rod bundle tests to show how the proposed tests overlap and complement the existing data base. The strategy in developing the test types and test matrix will be to use a "building block" approach in which simpler experiments are performed first to quantify a particular heat transfer mechanism alone and then the additional complications of the two-phase flow film boiling behavior of the test facility are added in later experiments. The proposed test conditions and fluid conditions also bracket those conditions which would be calculated for a postulated LOCA. The types of tests which are proposed for this program include:

1. Steady-state liquid flow characterization tests to determine the rod bundle frictional pressure drop and the spacer grid loss coefficients.

2. Heat loss experiments which characterize the facility heat loss to the environment.

3. Radiation only tests with an evacuated rod bundle. These tests will be performed over a range of rod bundle powers to achieve a wide range of heater rod surface temperatures, characteristic of those expected for dispersed flow film boiling. The objective of these experiments will be to confirm the proper emissivities to be used to characterize the rod bundle and housing surfaces as well as to verify that the outer row of heater rods effectively shields the inner 5x5 rows of rods.

4. Subcooled and saturated boiling experiments at low flows and low pressure to validate existing boiling correlations for these conditions for rod bundles. The experiments will be conducted in a steady-state manner and the heat transfer and void distributions will be measured along the rod bundle.

5. Convective steam cooling tests over a wide range of Reynolds numbers to determine the single phase convective heat transfer in superheated steam. These tests will be to characterize the single phase convective heat transfer cooling separately without the complications of a dispersed droplet field.

6. Steam cooling tests with injected droplets of known initial sizes and velocities at the entrance of the test bundle. The objective of these experiments will be to examine the heat transfer effects of a highly dispersed phase of entrained liquid droplets, on the convective heat transfer within the rod bundle. These tests will be performed under quasi-steady conditions such that the Laser-Illuminated Digital Camera Systems (LIDCS) can be used at carefully selected elevations to track the droplets and measure their size and velocity distributions, such that the change of the droplet interfacial area can be measured and compared to predictions. These tests represent a unique contribution to the rod bundle dispersed flow film boiling literature.

7. Forced reflooding experiments will be performed which will overlap and compliment with the existing data base. The forced reflooding tests will also overlap the steam cooling and the droplet injection two-phase experiments. The forced reflooding experiments will contain all the elements of the experiments performed earlier with the additional complications of the heater rod quench front movement, quench heat release, and the generation of the entrainment heat transfer effects expected for reactor conditions for a prescribed set of initial and boundary conditions. The focus of these experiments is to examine the generation of the entrainment at the quench front and within the transition region.

8. Simple gravity reflood experiments or variable inlet injection experiments will also be performed. These experiments will examine the system response on the inlet flooding rate into the test bundle and the resulting heat transfer within the bundle.

The ranges of conditions for the experiments will cover the current ranges of conditions which best-estimate and Appendix K reflood models are required to calculate. The precise test conditions are not given since there is a need to perform pre-test predictions so as to select the range of rod powers and initial temperatures to provide the data needed while at the same time, to minimize the duty on the heater rods. However, the facility design envelope is sufficiently broad such that the tests can be performed over a wide range of initial and boundary conditions.

Rather than the usual approach of marching blindly through a pre-determined matrix to meet the program's milestones, the test matrix for the RBHT program will remain flexible so that it can be responsive to model development needs. Although the proposed test matrix is somewhat non-specific, the various types of tests have been carefully structured. These include a well-defined progression from bundle characterization (pressure drop and heat loss experiments) to radiation-only tests, single-phase heat transfer tests, quasi-steady dispersed flow heat transfer tests (i.e., droplet injection tests), to forced reflood and gravity reflood tests. It is decided that flexibility in the test matrix be maintained so that as the model development progresses and needs are better identified, the matrix can be adjusted accordingly to make the program most cost effective.

Task 10 - Test Facility Design.

The RBHT facility is designed to conduct systematic separate-effects tests under well-controlled laboratory conditions in order to generate fundamental rod bundle heat transfer data including single phase steam cooling tests, low flow boiling tests, steam flow tests with injected droplets and inverted annular film boiling and dispersed flow film boiling heat transfer in rod bundles. The facility is capable of operating in both forced and variable reflood modes covering wide ranges of flow and heat transfer conditions at pressures from 0.233 to 0.501 MPa (20 to 60 psig).

The test facility consists of five major components. These are:

1) test section consisting of a lower plenum, a low-mass flow housing containing the heater rod bundle, and an upper plenum,
2) coolant injection and steam injection systems,
3) phase separation and liquid collection systems,
4) downcomer and crossover leg system, and
5) system pressure oscillation damping tank and steam exhaust piping.

All components are well insulated to minimize heat losses to the environment, and to minimize errors in the overall heat balances calculations around the system.

The heater rod bundle simulates a portion of a 17x17 reactor fuel assembly. The electrically powered heater rods have a diameter of 9.5 mm (0.374 in) arranged in a 7x7 array with a prototypical 12.6 mm (0.496 in) pitch. The bundle has 45 heater rods and four unheated corner rods. The corner rods are used to support the bundle grids and the grid and fluid thermocouple leads. The support rods are made out of Inconel 600 tubing having a diameter of 9.5 mm (0.374 in), a wall thickness of 2.11 mm (0.083 in), and are 3.96 m (156 in) long.

The heater rods are single ended and consist of a Monel 500 electrical resistance element filled and surrounded by hot pressed boron nitride (BN) insulation, and enclosed in an Inconel 600 cladding. This material was chosen for its high strength and low thermal expansion coefficient at high temperatures, which minimizes rod bowing and failure at high temperature operating conditions since it was desired to reuse the heater rods for a second bundle build.

The heater rods have a 3.66 m (12 ft) heated length with a skewed axial power profile, with the peak power located at the 2.74 m (9 ft) elevation. The maximum-to-average power ratio (P_{max}/P_{avg}) is 1.5 and the minimum-to-average power ratio (P_{min}/P_{avg}) is 0.5 at both ends of the heated length. The bundle has a uniform radial power distribution.

Power to each rod is provided by a 60 volt, 12,600 amp, 750 kW DC power supply. Each rod is rated for 10 kW, and designed to operate at 1.44 MPa (200 psig) at a maximum temperature of 1200 degrees C (2200 degrees F), but because of its solid construction can be operated at up to 10.16 MPa (1500 psig). Each rod is instrumented with eight 20 mil diameter ungrounded thermocouples attached to the inside surface of the Inconel sheath at various locations. All of the thermocouple leads exit at the bottom end of the heater rod. The rod bundle has eight grids located about 0.522 m (20.55 in) apart except for the spacing between the first and second grids, which are 0.588 m (23.16 in) apart.

The flow housing provides the pressure and flow boundary for the heater rod bundle. It has a square geometry with rounded corners, with nominal inside dimensions of 0.09x0.09 m (3.55x3.55 in) and a wall thickness of 6.35 mm (0.25 in). The low mass housing is made out of Inconel 600 material, which is the same material used for the heater rod cladding and thermocouple sheath. As pointed out previously, the high strength of Inconel 600 at elevated temperatures will minimize housing distortion during testing. The 6.35 mm (0.25 in) wall thickness is the minimum allowable wall thickness needed for operating this vessel at 0.501 MPa (60 psig) and 538 degrees C (1000 degrees F), taking into consideration the cutouts to accommodate the large windows and the numerous pressure and temperature penetrations through the walls.

The test facility instrumentation is designed to measure temperatures, power, flows, liquid levels, pressures, void fractions, and droplet sizes, distribution, and velocities. Using these measurements initial test boundaries can be established. Overall and transient mass and energy balances, mass inventories, carryover liquid and steam flows as a function of time can be calculated. Heater rod power , temperature, and fluid temperature are used to calculate heat fluxes and heat transfer coefficients, quench times, rod bundle energy losses, convective and radiation heat transfer to steam, droplets, grids, support rods, and housing. Effects of grids, support rods and housing behavior during reflood can be determined. Void fraction measurements below the quench front and in the froth level above the quench front, in conjunction with the laser illuminated digital camera measurements are used to determine droplet entrainment behavior droplet effects on heat transfer, and steam desuperheating. The laser illuminated digital camera system measurements provide droplet size distribution and velocities during reflood.

Loop instrumentation has 61 instrumentation channels which are assigned to the measurement of electrical power, fluid and wall temperatures, levels, flows, differential pressures, and static pressure. The injection water supply tank has three fluid and three wall thermocouples to monitor water and wall temperatures during heat-up prior to testing. It has a differential pressure transmitter used as a level meter to determine water mass in the tank and mass depletion during reflood testing. It also has a static pressure transmitter which monitors the nitrogen overpressure and controls the nitrogen flow needed to maintain a constant pressure during forced injection reflood tests.

The Data Acquisition System consists of a digital computer and several analog conversion subsystems. It uses a Ziatech ZT-8910 digital processor capable of collecting, storing, and retrieving data from power, pressure, temperature, level and flow instrumentation. It can also provide control functions, and display critical operating parameters during testing. It is to be designed to process up to 412 instrumentation channels at a maximum sampling rate of 10 Hz.

This system, in conjunction with panel mounted strip chart recorders, gauges, and controllers, is used to establish test boundary conditions prior to starting a test.

In summary, the RBHT facility is designed as a flexible rod bundle separate-effects test facility which can be used to perform single-phase and two-phase experiments under well-controlled laboratory conditions to generate fundamental reflood heat transfer data. The facility is capable of operating in both forced and variable reflood modes covering wide ranges of flow and heat transfer conditions at pressures up to 0.402 MPa (60 psia). It has extensive instrumentation that meets all the instrumentation requirements developed under Task 7. It can be used to conduct all types of the planned experiments according to the test matrix developed under Task 9. The present design also allows future upgrading of the facility for the performance of high-pressure transient film boiling tests. It is felt that the RBHT facility with its robust instrumentation represents a unique NRC facility for the in-depth studies of the highly ranked reflood phenomena identified in the PIRT table developed under Task 1.

Concluding Remarks

The RBHT program will be of considerable benefit to the NRC effort to improve the TRACE reflood model. The effort will of necessity include not only wall-to-fluid heat transfer correlations but also models for interfacial shear and interfacial heat transfer. To develop and assess models for these phenomena with the goal of significantly improved accuracy (to provide a better estimate of margin) and to minimize the potential for compensating errors will require a database that includes more detailed information than is currently available. In addition, this detailed data base needs to be for prototypic rod bundle geometry as large differences exist between the data obtained from heated tubes and rod bundles. It is exactly this data deficiency for which the Rod Bundle Heat Transfer program is designed. The successful completion of this experimental program will make a fundamental contribution to the database for reflood model development and is a key component of the NRC's code improvement program.

Specifically, the RBHT program will generate detailed data for model development that are either unique or of higher quality than currently available data in the following areas:

- Two-Phase Convective Enhancement. In dispersed flow film boiling, the primary heat transfer mechanism is convective heat transfer to superheated steam. It is known that the steam heat transfer coefficient can be enhanced by up to 100 percent due to the presence of entrained droplets. No suitable models currently exist for this phenomenon. The combination of single-phase vapor heat transfer tests with the forced droplet injection tests (where drop size and flow rate are known) will result in the development of the much needed model.

- "Inverted Annular" Film Boiling. The liquid rich region just downstream of the quench front (void fraction of 20 to 60 percent) provides the precursory cooling that controls the quench front velocity and provides the source of vapor and entrained liquid for the dispersed flow film boiling region. It has been demonstrated that many of the apparent functional dependencies (i.e., mass flux, subcooling, and distance from the quench front) for this heat transfer regime are primarily due to the axial profile of the void fraction in this region. Currently available data for this regime in rod bundles is insufficient for model development due to the coarse spacing (from one to two feet) used for the delta-P cells to measure the void fraction. The RBHT program will redress this data deficiency through the use of finely spaced differential pressure cells (three inches apart over a

distance of two feet) and by a local void fraction measurement provided by a low energy gamma-densitometer.

- Dispersed Flow Film Boiling. Once the uncertainty involving convective enhancement is resolved, there still remains the difficulty in calculating the heat transfer rate for this regime due to the difficulty in calculating the steam superheat. The amount of steam superheat is governed by the interfacial heat transfer between the steam and the evaporating drops. To correctly calculate the interfacial heat transfer requires the knowledge of both the entrained droplet flow rate and diameter. There is very little data of this type currently available for quenching rod bundles. The RBHT program will generate the needed database through the use of advanced instrumentation, specifically through the use of the Laser Illuminated Digital Camera System (LIDCS).

This program will also augment the database needed for model development in the areas of grid spacer effects in dispersed flow film boiling, transition boiling heat transfer during reflood, and for interfacial heat transfer and shear in rod bundles at low pressure. The RBHT program will complement NRC's efforts in improving the TRACE reflood models.

NOMENCLATURE

A	area (m^2)
Bi	Biot number (dimensionless)
c	specific heat (J/kg-K)
D	diameter (m)
e	specific internal energy (J/kg)
f	friction factor (dimensionless)
Fo	Fourier number (dimensionless)
g	acceleration due to gravity (m/s^2)
g_c	gravitational constant (32.17 lbm-ft/lbf-s^2)
h	enthalpy (J/kg)
h	heat transfer coefficient (W/m^2-K)
J	radiosity (W/m^2)
k	thermal conductivity (W/m-K)
K	loss coefficient (dimensionless)
L	length (m)
m	number of grids in two phase region (Equation 6-78)
n	number of grids in single phase region (Equation 6-78)
Nu	Nusselt number (dimensionless)
p	rod pitch (m)
P	pressure (N/m^2)
Q	heat energy (W)
R	radius (m)
R	resistance (used in radiation network) (Equation 6-102)
Re	Reynolds number (dimensionless)
t	time (s)
T	temperature (degrees K)
u	velocity (m/s)
V	volume (m^3)
W	mass flow rate (kg/s)
z	elevation (m)

Greek

α	void fraction
α	thermal diffusivity
μ	kinematic viscosity
π	non dimensional ‘Pi’ group
ρ	density
τ	time constant
Δ	increment

Subscripts

B	bundle
c	cladding
ci	cladding inside surface

co	cladding outside surface
cr	cold rod
c	convection (usually with heat transfer coefficient)
CL	centerline
d	drops
dcht	direct contact heat transfer
DP	decay power
DR	dead rods
DR/d	dead rods to drops
DR/v	dead rods to vapor
e	exit
f	fluid
f	saturated liquid
f	fuel
FB	film boiling
g	grid
g	saturated vapor
gap	gap in the nuclear fuel rod
g/d	grid to drops
g/v	grid to vapor
hr	hot rod
H	housing
H/d	housing to drops
H/v	housing to vapor
i	reference case
i	inlet
I	Interfacial liquid
lw	liquid-wall contact
m	mixture
min	minimum
max	maximum
o	outlet
p	constant pressure
q	quench
r	rod
r/d	rod to drops
r/v	rod to vapor
s	surface
s	superheated
sat	saturated
t	test
T	total
v	superheated vapor
v/d	vapor to drops
1φ	single phase
2φ	two phase

Superscripts

$'$	per unit length
$''$	per unit volume
$*$	non dimensional variable
$\bar{}$	average
$\overline{\varphi_{fo}^2}$	two phase flow multiplier
D_e	equivalent diameter
R_f	total frictional and form resistance
E_b	black body emissive power

ACKNOWLEDGEMENTS

There were several individuals who made significant contributions to this report which the authors would like to acknowledge. The technical efforts of Ernest Miklavic, Andrew Ireland, Christina D'Arrigo and James Apple are gratefully acknowledged. The editing, correcting, and typing efforts of Mrs. Christine Wilson, Kristie Kalvin, Donna Gensimore, and Michelle Alterio are also gratefully acknowledged and without their effort this report would not have been completed as scheduled. The technical comments and insights by the two independent Nuclear Regulatory Commission sponsored peer review panels for the program objectives and approach, and for the instrumentation design are also gratefully acknowledged. The authors also acknowledge the guidance, review, and active participation that William Macon, Dr. Steve Bajorek, Joseph Kelly, Gene Rhee and David Bessette and of the Nuclear Regulatory Commission have played in the Rod Bundle Heat Transfer Program. The comments which were received were integrated into the test design and analysis and will improve the quality of the work performed in the program.

We also acknowledge the continuing support of Drs. R. C. Benson and K. Thole, former and current Head of the Mechanical and Nuclear Engineering Department, respectively. The Rod Bundle Heat Transfer Program is a cost shared program between The Pennsylvania State University and the Nuclear Regulatory Commission. The authors acknowledge the financial support provided by the University for the equipment match and the new building annex for the test facility. In particular, the authors acknowledge the support of Drs. D. N. Wormley, L. C. Burton, L. R. Hettche, and R. A. Erickson. The experiments will be performed at the Thermal Propulsion Research Facility (Test Site) of Applied Research Laboratory, Pennsylvania State University. The authors acknowledge the continuing support and help of Dr. D. H. Kiely, R. A. Grove, I. S. McClellan, R. A. Peters, C. P. Jones, D. M. Adams, and J. R. Bischof from the Applied Research Laboratory.

1. INTRODUCTION

1.1 Background

Safety analysis is performed on Nuclear Reactor power plants to ensure the health and safety of the public, for accidents which are postulated to occur. Accidents are analyzed which are anticipated to occur over the life time of the plant as well as hypothetical accidents which are not expected to occur but are postulated to determine the mitigating features of the particular reactor design. Each reactor design has Engineered Safeguard Systems which are safety systems designed to mitigate accident scenarios.

Within the reactor design basis, the most challenging accident which is examined is a large-break Loss of Coolant Accident (LOCA). Analysis of this particular accident can result in limits in the reactor total core power as well as the allowable peak linear fuel rod power in the hottest rods. For this type of accident, the initial coolant in the reactor core is expelled out the broken piping and the core cooling is dependent on the Engineered Safeguards Systems. Analysis of the particular accident verifies that the design of the Engineered Safeguards Systems will mitigate the accident. In a large-break LOCA, the fuel rod cladding is calculated to rupture at high temperatures, and the primary piping is assumed to have failed so as to generate the LOCA. Without adequate core cooling the reactor core will continue to overheat and can lead to failure thereby releasing fission products from the fuel.

The Nuclear Regulatory Commission developed the requirements of Title 10 of the *Code of Federal Regulations*, Part 50, Appendix K (Appendix K), in 1973 for acceptable analytical methods used to predict the safety performance of the Engineered Safeguards System for reactor designs. The requirements were acknowledged to be conservative to account for the uncertainties in the calculation and the database at that time. A significant research effort was performed by the NRC, Electrical Power Research Institute (EPRI), and the reactor vendors from 1973 to 1988 to determine the degree of conservatism in the Appendix K requirements. During the same time period, the American Physical Society urged the NRC to develop improved, more realistic “Best-Estimate” analytical computer models for the reactor systems such that realistic calculations could be performed. In 1988, the Appendix K rule was revised and Best-Estimate thermal-hydraulic methods were allowed to be used to evaluate the reactor system and the Engineering Safeguards System response to a postulated LOCA.

With the approval of the Appendix K rule revisions, vendors are starting to utilize “Best-Estimate” safety analysis thermal-hydraulic methods to perform large-break LOCA analysis to evaluate the allowable core thermal limits. Even with the application of best-estimate methods, the large-break LOCA still is generally the most limiting transient and results in establishing the maximum allowable fuel rod linear power level (kW/ft). Typically what has occurred is that as Best-Estimate analysis methods have identified peak linear heat rate margin; this margin has been used by the utility or the vendor for power up-ratings, longer fuel cycles, low leakage core loadings and advanced fuel designs to improve the economics of the nuclear power plant. All of these economic improvements result in the need for higher operating linear heat generation rates. This is true for both BWR and PWR designs. When the best-estimate methods are applied with the higher linear heat rates, the resulting calculated peak cladding temperatures are nearly the same as those previously calculated using the original Appendix K requirements. However, the difference is that the allowable linear heat rate (kW/ft) is now higher.

The best-estimate calculations indicate that for nearly all PWR designs the peak cladding temperatures are reached during the reflood portion of the transient at low pressures, typically 0.1 to 0.3 MPa. A similar situation also occurs in the hot channel for the more modern BWR designs (BWR5 and 6), as well. The flow pattern in the BWR hot channel is co-current up flow during reflood similar to a PWR.

There are two basic flow regimes for reflooding in a rod bundle. For high flooding rates, typically 0.15 m/s (6 in/s), the dominant flow regime for the post-CHF regions in the bundle is an inverted annular regime in which a thin layer of vapor separates the heated wall from the sub cooled liquid flow which nearly fills the channel. Since the inlet flow is larger than the quench rate of the fuel rods, a long region of inverted film boiling can exist above the quench front. As one proceeds upward along the bundle, the liquid becomes saturated and begins to break into chunks or liquid slugs. The length of the inverted annular and the liquid chunk regimes depends on the flooding rate into the heated bundle, the initial sub cooling of the liquid, the system pressure, and the rod bundle initial temperature and power level. The heat transfer in this regime is very high and results in immediate clad temperature turnover such that lower peak cladding temperatures are calculated for this reflood regime. Figure 1.1 shows an example of the high flooding rate reflood heat transfer and flow regime.

For low flooding rates, there is no sub cooled inverted annular film boiling region. Because of the low injection flow rate, the liquid quickly reaches saturation and there is bulk boiling of the fluid below the quench front. In the quench front region, and above the quench front, there is a froth region which has a void fraction which transitions between a low void fraction, below the quench front, to the much higher void fraction in the dispersed flow regions above the quench front. This behavior is shown in Figure 1.2. The dominant flow regime for the low flooding rates is a highly dispersed flow film-boiling region in which the heat transfer rates are very low. The heat transfer in this region occurs between the heated wall and the superheated steam. The liquid droplets in the superheated steam evaporate reducing the steam temperature as well as increasing the flow rate of the steam. As a result, the calculated peak cladding temperature usually occurs in this region. In most reactor reflood calculations, after the initial surge into the core, the flooding rates are very low, typically 0.0254 m/s (1 in/s) or less, such that the dispersed flow film boiling region is the dominant flow regime of interest and is the heat transfer regime in which the peak cladding temperature occurs.

In either case and for all designs, the thermal-hydraulic heat transfer phenomenon which dominates the reflood portion of the transient is dispersed flow film boiling. The heat transfer rates during this period are very low and several different mechanisms are responsible for the total wall heat flux. No single mechanism dominates the heat transfer process such that several different mechanisms must be predicted by the best-estimate calculational tool with roughly equal precession. Those mechanisms include:

- Convection to superheated vapor,
- Surface radiation to vapor and droplets,
- Interfacial heat transfer between droplets and superheated vapor,
- Direct contact heat transfer between the wall and entrained liquid,
- Convective enhancement of the vapor by the entrained droplets
- Impact of structures (grids) in the rod bundle causing flow acceleration and droplet break-up,
- Quench fronts at the top and bottoms of the rods.

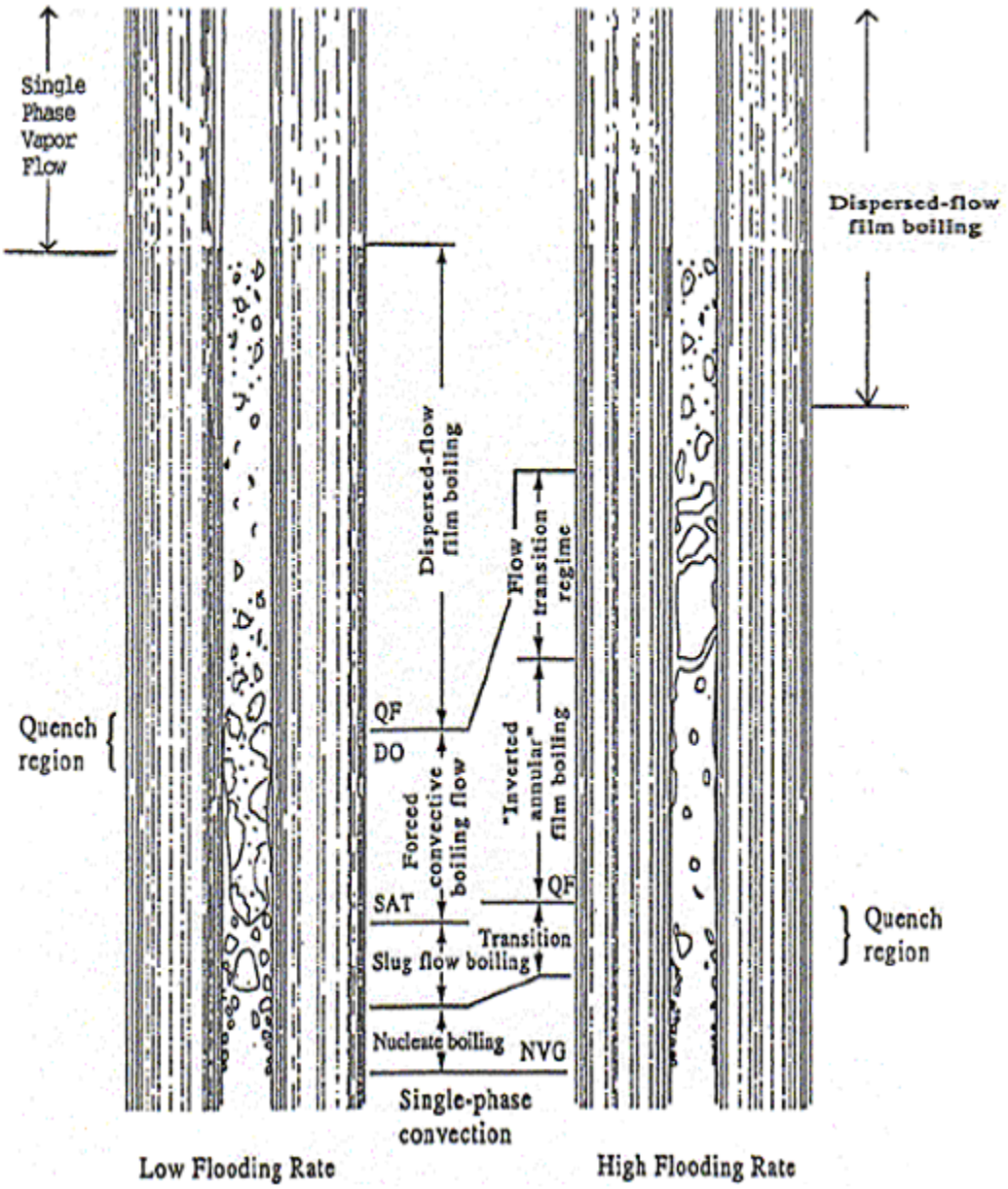

Figure 1.1 Reflood Flow Regimes for High and Low Reflood Rates.

Also, since the different mechanisms are of comparable magnitude, improving one particular model is difficult since very little data is available to isolate its particular contribution to the total wall heat flux. Therefore, compensating errors can result as the code's predictive capabilities are improved.

Dispersed flow film boiling also dominates the down flow period of the PWR blow down transient as well as the reflood transient. Similar heat transfer mechanisms are present for the blow down flow period as well as the reflood period. The primary difference is that the vapor

convection term is more dominate for the blow down situation as compared to the reflood phase, and the vapor has less superheat.

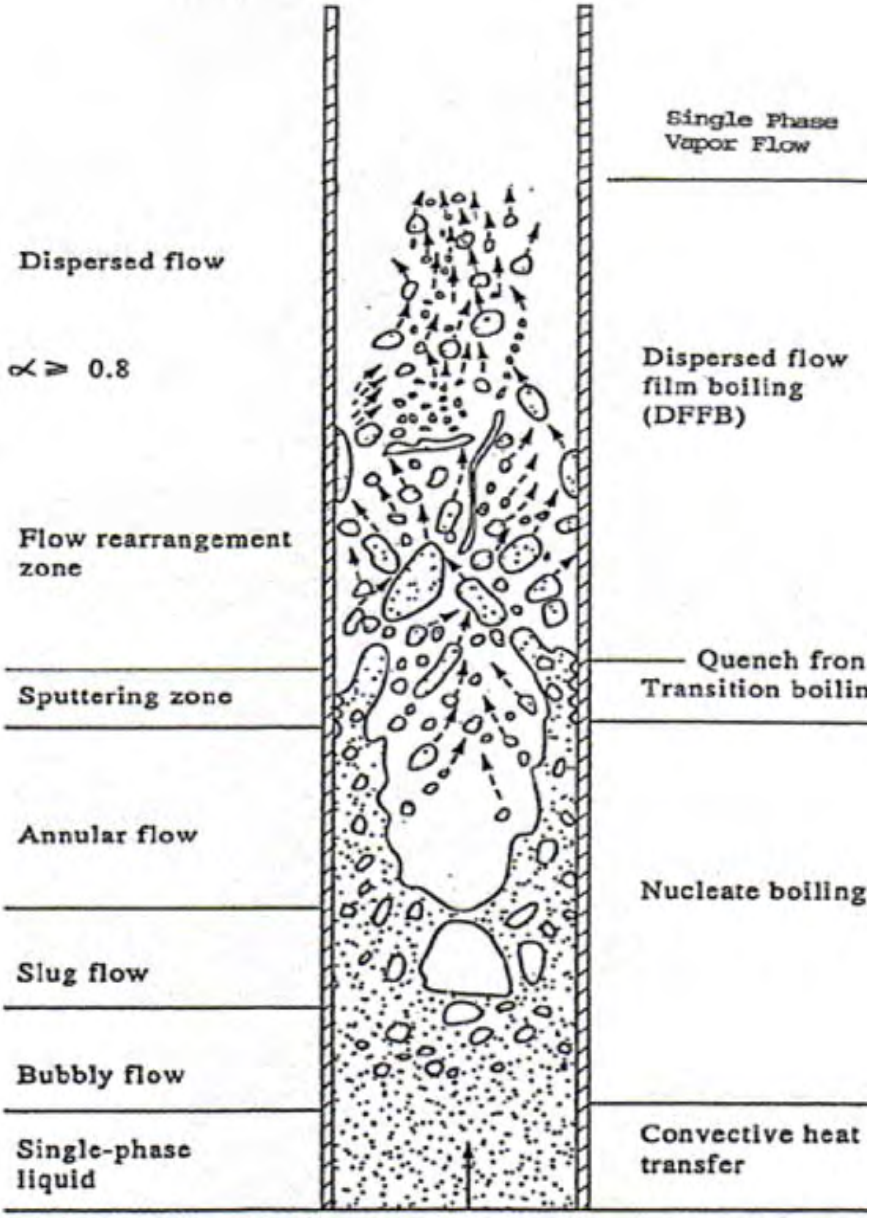

Figure 1.2 Detailed Low Flooding Rate Reflood Flow Regimes.

The single largest uncertainty in predicting the dispersed flow film boiling heat transfer in reflooding rod bundles is the liquid entrainment at the top of the froth region just above the quench front. The froth region is a region at and above the quench front in which the void fraction changes from low values typical of the boiling below the quench front, to the very high values in the dispersed flow film-boiling regime. The froth regime is a liquid rich regime while the dispersed flow regime is very liquid deficient. Figure 1.3 shows the quench front data from a low flooding rate FLECHT-SEASET test (Ref. 1) with the froth region location indicated. Figure

1.4 indicates a schematic of the flow regime just above the quench front within the froth region of the flow. In this region, the steam generation from the quenching of the fuel rods results in

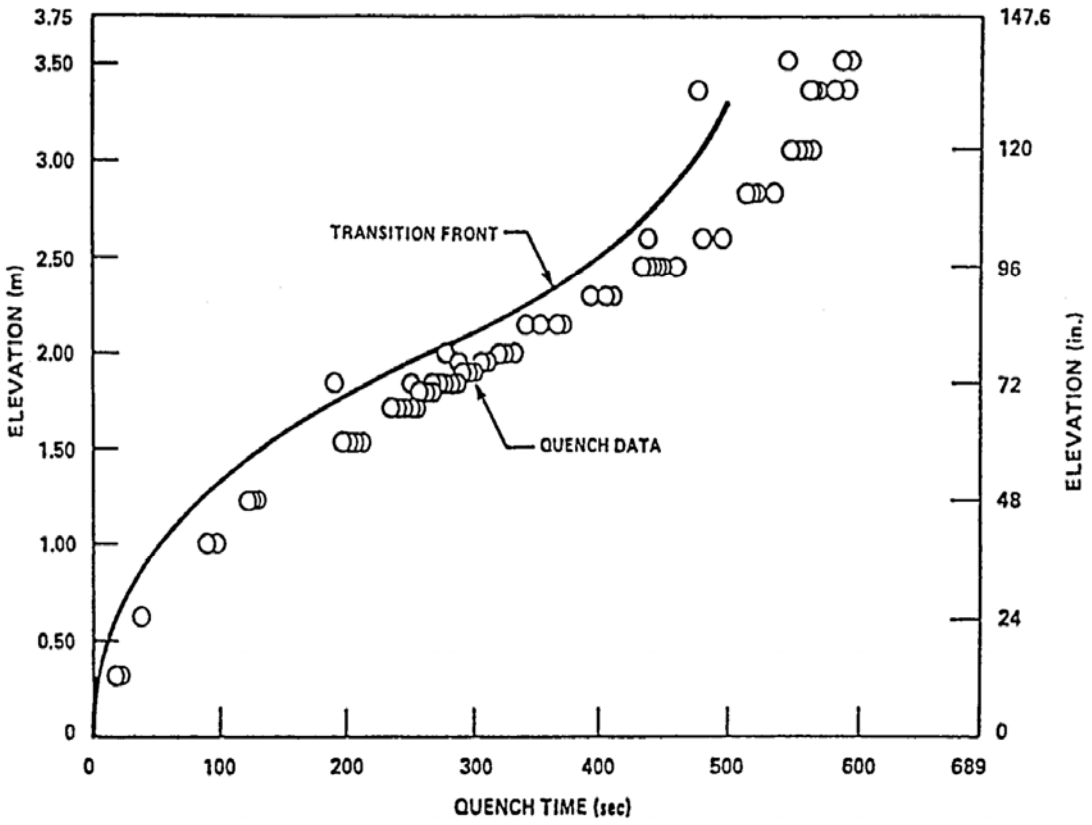

Figure 1.3 Transition and Quench Fronts for FLECHT-SEASET Test 31504.

very large vapor velocities which entrain and shear liquid filaments into droplets which are then swept into the upper regions of the rod bundle. The entrained droplets provide cooling by several different mechanisms in the upper regions of the rod bundle where the resulting peak clad temperatures are calculated.

Figure 1.5 shows the different heat transfer mechanisms which are present in the high temperature portions of the rod bundle where the peak cladding temperatures are calculated (Refs. 1 and 2). The heat transfer process is a combination of a “two-step” and “three-step” dispersed flow film boiling process. A “two-step” dispersed flow film boiling process consists of heat transfer from the wall to the vapor flow by convection as well as by radiation. There is also wall-to-wall radiation heat transfer and wall-to-entrained droplet heat transfer. The vapor is the heat sink and quickly reaches superheated conditions as it receives energy from the wall. The second step of the “two-step” process is the heat transfer between the superheated vapor and the entrained droplets. The interfacial heat transfer between the drops and the vapor lowers the vapor temperature which is the fluid heat sink for the wall heat transfer. The “two-step” film boiling process becomes a “three-step” process as the wall temperature decreases such that there can be intermittent direct (or near direct) droplet-wall contact heat transfer. It is believed that the direct wall contact heat transfer component occurs within and just above the froth region

which results in improved heat transfer. The improved heat transfer in this region can be seen from the FLECHT-SEASET test data.

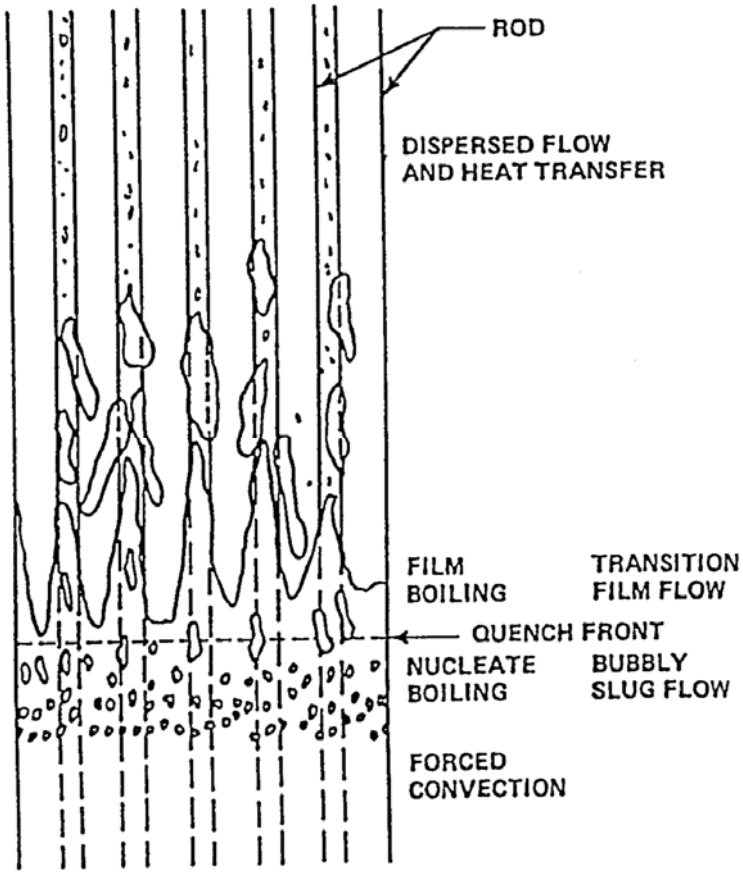

Figure 1.4 Entrainment Behavior for Rod Bundle Reflooding.

The ability of a best-estimate computer code to accurately predict the integrated effects of the individual phenomena for the dispersed flow film-boiling region is a challenge. The uncertainty in the individual models is large and the integrated effects of the uncertainties will accumulate as the calculation progresses upward along the heated channel. The error or uncertainty accumulation is one reason that the code predictions of temperatures above the mid-plane of the FLECHT-SEASET rod bundle or the Japanese Cylindrical Core Test Facility have always been worse than predictions lower in the bundle, closer to the froth region. Also, code calculations for lower flooding rates which are reflected in a slower quench front velocity and a longer transient time show poorer predictions relative to the test data.

1.2 Program Objectives

Reflood Heat Transfer experiments have been performed since the original Full Length Emergency Core Heat Transfer (FLECHT) program began in 1967. These experiments were designed to examine the total heat transfer for a heated rod bundle subjected to reflood bottom or top spray effects. At this time no data existed for rod bundles in the literature, therefore, the

initial tests were more scoping and were designed to provide data on the overall heat transfer rather than the phenomena which were responsible for the heat transfer. The initial FLECHT tests were more sparsely instrumented and one could not perform a mass balance on the tests.

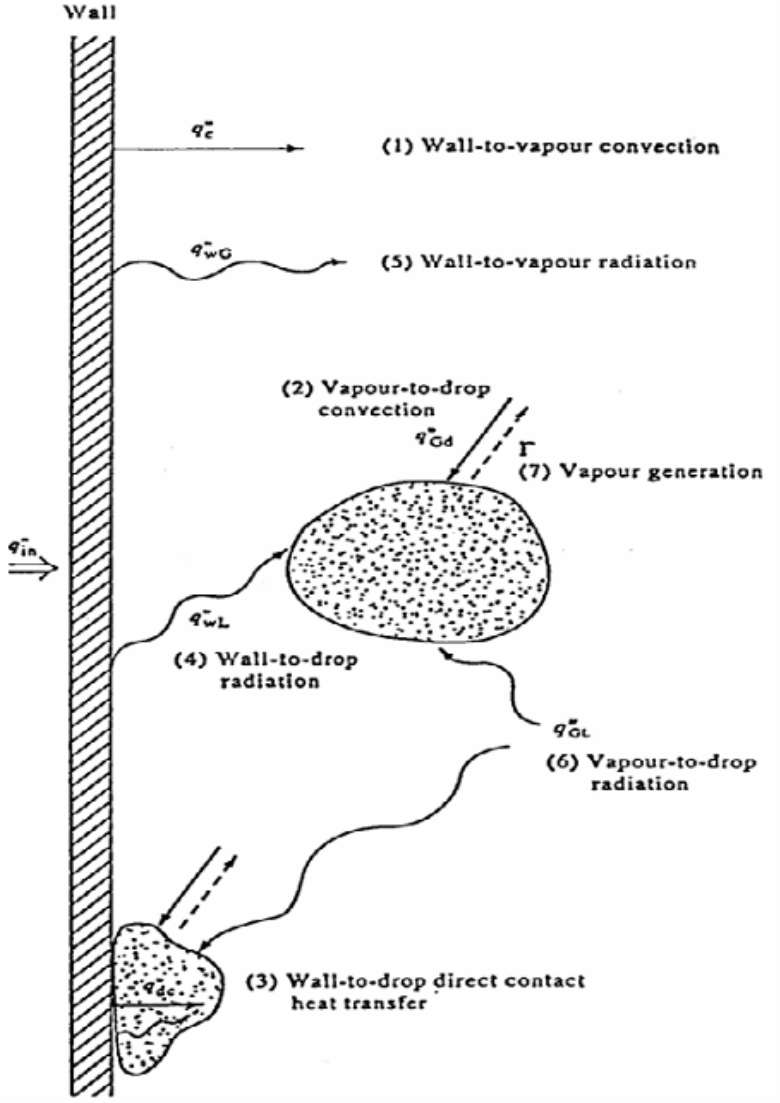

Figure 1.5 Heat and Mass Transfer Mechanism in Dispersed Flow Film Boiling.

The test conditions in the original FLECHT series did not reflect the effects of steam binding and hence the flooding rates are much larger than current plants. The rod peak powers were also higher. Other FLECHT test series were also performed in which the flooding rates were reduced to better cover the plant calculated conditions. However, the objective remained the same, to determine the total heat transfer over a wider range of conditions. A very highly empirical heat transfer correlation was developed, which was a function of the reactor system parameters (not local thermal-hydraulic conditions) and was used in the Appendix K models by the vendors and the NRC. Because the heat transfer correlation was empirical and not based on any physical model, the application for different rod bundle arrays, conditions, axial power shapes, and geometries was suspect.

Improved reflood experiments were performed in the FLECHT-SEASET program which was initiated in the mid 1970's. The FLECHT-SEASET tests represent the first attempt to understand the reflood phenomena. Additional instrumentation was added to examine the thermal-hydraulic conditions within the test bundle. However, the tests were conducted in the same manner as the previous FLECHT tests and the primary result of these tests was the overall reflood heat transfer for a different rod bundle array which was correlated in a similar manner as the previous FLECHT experiments. There was additional analysis performed on the FLECHT-SEASET tests to attempt to divide the measured total heat transfer into the individual heat transfer components, however, the uncertainties were very large such that the phenomena could be identified but not quantified with sufficient confidence. The ACHILLES and PERICLES experiments were similar to the FLECHT-SEASET tests in size and types of test performed. Both of these test series used prototypical spacer grids, which were found to enhance heat transfer. However, no local data was obtained to explain the reflood heat transfer phenomena. There were also systems reflood tests such as the FLECHT-SET tests, the 2D/3D program Cylindrical Core Test Facility (CCTF), the Slab Core Test Facility (SCTF); and the KWU 340 rod systems tests. These experiments primarily examined the effects of the reactor system effects on the core reflooding rate and the resulting heat transfer within the core. No attempts were made to instrument these experiments to determine the local heat transfer phenomena within the rod bundle, rather, the determination of the system response during reflood was the test objective. The overall heat transfer in the rod bundle was measured as well as the heater rod temperatures.

All of these experiments made important contributions to the total understanding of the reflood process for a PWR or a BWR and the data is useful, in varying degrees, for safety analysis computer code validation. However, none of these experiments were designed with the objective of model development and validation based on the local thermal-hydraulic conditions. The experiments which have been conducted were primarily to provide data over a wide range of system conditions for an Appendix K reactor safety analysis and not to examine the details of the local two-phase flow and heat transfer effects which could occur in a rod bundle during reflooding. Therefore, when this data is used for computer code validation and the predictions do not agree with the data, the analyst does not have sufficient experimental information to determine which of the many models is causing the mis-prediction. As a result, as models are “improved”, compensating errors can enter into the calculations which tend to make the computer code suspect when extrapolating the results to the full scale PWR or BWR.

One important feature of the RBHT program is that the experiments and the instrumentation are designed from a model development and validation point of view, rather than an Appendix K margin approach. Much of the instrumentation will be unique and will be used to determine local conditions. The data can be used to validate specific models in a manner such that the effects of compensating error can be identified and corrected. The program will also break the dispersed flow film boiling phenomena into its individual contributions such as:

- Single phase pressure drop experiments to characterize the spacer grids and the rod bundle,
- Surface-to-surface, surface to liquid, and surface to vapor radiation heat transfer,
- Convection of superheated steam over a wide range of Reynolds numbers.

- The effects of entrained droplets within a superheated steam flow, and the effects of the droplets on convection enhancement, as well as evaporation,

- Forced reflood tests which will cover a wide range of reflood flow regimes and heat transfer state,

- Variable reflood tests in which the interaction of the injected flow and the quench front can be assessed.

The instrumentation is designed to provide data on the local void fraction within the froth regions, the steam superheating that occurs along the bundle, the liquid entrainment within the bundle, entrained drop sizes, distributions, velocities and droplet velocity distributions.

The RBHT program is needed to provide detailed data which can be used to improve the NRC's safety analysis prediction capabilities for the large break LOCA transient. The NRC needs a large break LOCA analysis tool that can be applied with a high degree of confidence to assure the public safety without unduly penalizing the utilities. Initial validation of the TRAC-PF1/MOD1 code was performed and the code and model uncertainty was determined as part of the Code Scaling Applicability and Uncertainty (CSAU) (Ref. 3) effort which also provided an initial estimate the 95th percentile peak cladding temperature. However, these calculations were performed at approximately 30.68 kW/m (9.35 kW/ft) while today, plants are being licensed at 49-59 kW/m (15-18 kW/ft). Figure 1.6 shows the peak cladding temperatures for the original CSAU study and a more recent safety analysis calculation performed at 49.54 kW/m (15.1 peak kW/ft).

A complex reflood heat transfer package has been rewritten as part of TRAC-PF1/MOD2 (Ref. 4) using primarily single tube and Winfrith "Hot Patch" tests as a basis for the models. Initial calculations for separate effects tests indicate the new models significantly under-predict the cooling at low flooding rates and can exhibit large oscillations which make the interpretation of the results difficult at best. Before the code and model uncertainty can be determined for TRAC-PF1/MOD2, there is the need for significant reflood heat transfer model improvement.

The approach which has been used in the past has been to try different correlations, tune coefficients of the correlations, try smoothing relationships for the correlations, and developing an "ad hoc" model or correlation which has no physical basis but allows to the code to continue to perform calculations. These approaches can lead to codes with large biases and uncertainty when compared to a comprehensive data set. Also, adjusting coefficients on correlations to match data can result in compensating errors which may not scale properly from the test configuration to the full size reactor.

The RBHT program is designed to provide detailed data on local conditions which can be used for model development. Models will be developed and selected based on fundamental assessments such that the correct heat transfer is predicted for the given local fluid conditions. The tests in the RBHT program are structured so as to decompose the complex nature of dispersed flow film boiling into the component models that a computer code would calculate. In this fashion, compensating errors in the models will be reduced. The result will be a more accurate analysis tool for the NRC for best-estimate audit calculations.

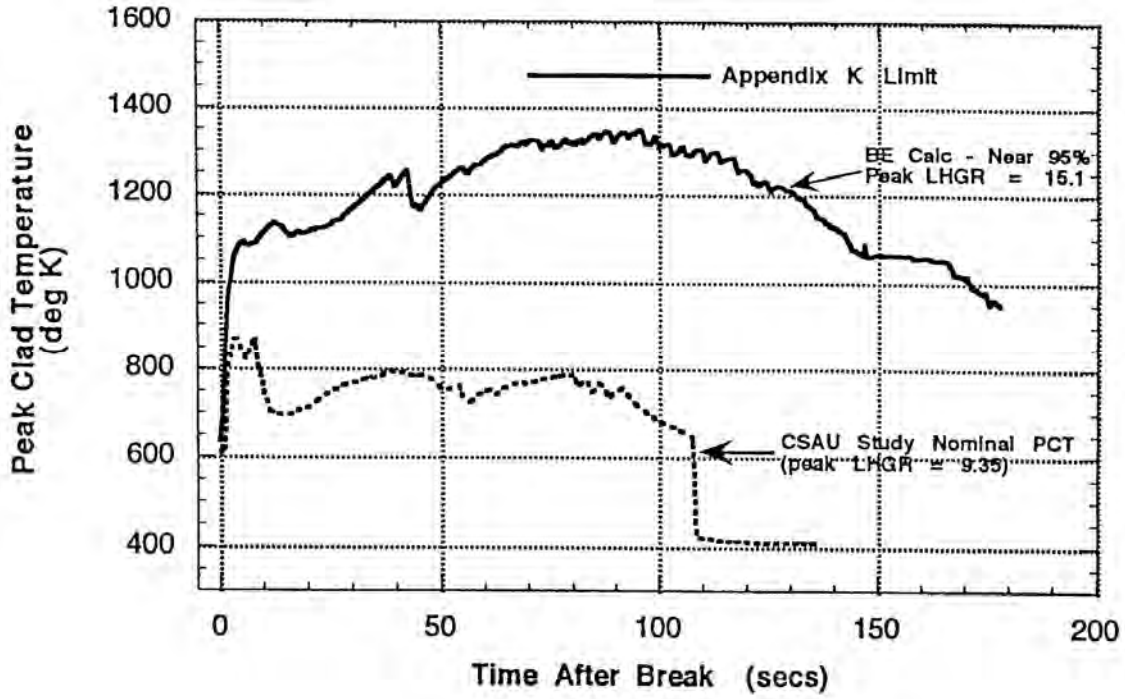

Figure 1.6 Comparison of Current Best Estimate Calculated PCTs with CSAU Study.

1.3 Products from the Rod Bundle Heat Transfer Program

The detailed experimental data and the associated model development will provide the NRC with an improved analytical capability to be applied for Risk Informed Regulation for the large break LOCA. Improved models will reduce the code uncertainty which must be assessed as part of the best-estimate methodology using CSAU. The resulting analysis method will be more accurate, credible, and robust.

The RBHT program will significantly expand the existing database which can be used to develop and validate reflood heat transfer models. It should be noted that the RBHT program is specifically developed to support best-estimate Safety Analysis model development methods, not as a demonstration of the Appendix K margin. The database will be expanded with detailed measurements of local conditions which are targeted to address existing code modeling issues. The data will be provided in a format which will be user friendly such that it can be used for code validation purposes.
The RBHT facility is being designed as a flexible rod bundle separate effects test facility which can be used to perform single and two-phase experiments. Development of the RBHT facility will help maintain the NRC's leadership in the reactor thermal-hydraulics safety analysis area in the world. Placing the test facility in a university setting also provides educational opportunities for students who will become the next generation of reactor engineers in the United States.

1.4 Technical Approach

A reflood heat transfer specific Phenomena Identification and Ranking Table (PIRT) has been developed which indicates the individual component models which constitute "reflood heat

transfer." The PIRT and its relative rankings indicate the important phenomena which a best-estimate computer code should simulate with a high degree of accuracy. The PIRT will also be used as a guide when reviewing the reflood heat transfer logic for the different best-estimate computer codes. This will indicate the state-of-the-art in reflood modeling.

Using the PIRT, the available rod bundle data and selective tube data will be examined to see whether they can address the important PIRT phenomena. The PIRT also serves as a guide in developing the RBHT facility since it will indicate what type of data is needed and which measurements should be made, if possible. The PIRT provides guidance on the types and number of instrumentation, types of tests to be run and the test conditions to be simulated. The result will be data developed specifically for two-fluid, best-estimate computer code development and validation.

The RBHT program will use a full-length, smaller, but well instrumented rod bundle which will provide data for the fundamental assessment of the physical relationships upon which the code constitutive models are based. This effort will provide new, needed data which is specifically targeted at the best-estimate two-fluid code modeling needs.

1.5 References

1. Lee, N., Wong, S., Yeh, H.C., and Hochreiter, L.E., "PWR FLECHT-SEASET Unblocked Bundle, Forced and Gravity Reflood Task Data Evaluation & Analysis Report," NRC/EPRI/Westinghouse Report No. 10, WCAP-9891, NUREG/CR-2256, EPRI NP-2013, November, 1981.

2. Andreani, M., and Yadigaroglu, G., "Prediction Methods for Dispersed Flow Film Boiling," Int. J. Multiphase Flow, Vol. 20, Suppl., 1-51, 1994.

3. U.S. Nuclear Regulatory Commission, "Quantifying Reactor Safety Margins", NUREG/CR-5249, 1989.

4. Nelson, R.A., Pimental, D.A., Jolly-Woodruff, S., and J. Spore, "A Phenomenological Thermal-Hydraulic Model of Hot Rod Bundles Experiencing Simultaneous Bottom and Top Quenching and an Optimization Methodology for Closure Development," Los Alamos, Draft Report, 1998.

5. Kelly, J.M., Presentation to Advisory Committee on Reactor Safety (ACRS), Rockville, MD, February 18, 1998.

2. ROD BUNDLE HEAT TRANSFER PROGRAM PHENOMENA IDENTIFICATION AND RANKING TABLE (PIRT)

2.1 Introduction/Background

The concept of a Phenomena Identification Ranking Table (PIRT) was first developed as part of the Nuclear Regulatory Commission program for assessing safety margins in operating reactors as given in the quantifying Reactor Safety Margins report, called; Code Scaling, Applicability and Uncertainty or CSAU (Ref. 1). The idea behind the CSAU effort was to provide a rational and documented method of determining the applicability and accuracy of a specific safety analysis computer code for analysis of a specific Nuclear Power Plant Design for a given accident scenario. The accident scenario which was examined in the CSAU effort was the large-break Loss Of Coolant Accident (LOCA) which is the limiting accident for most light water reactor designs. There are three elements to the CSAU methodology:

a) Requirements and Code Capabilities
b) Assessment and Ranging of Parameters
c) Sensitivity and Uncertainty Analysis

The accident scenario was first specified then the specific nuclear power plant was selected. Plants could be grouped if they had sufficient common features. Given the accident and the plant design, a Phenomena Identification and Ranking Table was then developed as a basis for judging the capabilities of the safety analysis computer code which would be used for the transient. The full CSAU flow chart for the code scaling, applicability and uncertainty from Reference 1 is shown in Figure 2.1.

A PIRT is developed by an independent group of experts to rank the most important phenomena that need to be simulated for a particular accident scenario. This table and the individual ranking can be reviewed by a second set of independent experts (i.e., peer reviewed) for completeness and proper ranking of the most important phenomena. Such a procedure was followed for the CSAU PIRT, and the Los Alamos PIRT which was developed for the AP600 (Ref. 2). A similar approach was used for the PIRTs developed at Westinghouse for LOCA analysis of three and four loop plants as well as for the AP600 different transient types such as Small Break LOCA, Large Break LOCA, Long Term Cooling, Transient Analysis and Containment Analysis. Similar PIRT tables have been generated for BWR Transient Analysis and LOCA Analysis (Ref. 3).

The scenarios of interest for the RBHT program are the transients or postulated accidents which can lead to core uncovery and recovery at low pressure. In most cases this is a result of a large break loss of coolant accident (LOCA) in which nearly the entire initial coolant inventory is lost and the core experiences a heat-up. The calculated Peak Cladding Temperature (PCT) occurs for a calculated large-break LOCA such that the core limits, reactor power capability, and fuel loading patterns are affected by the calculated performance of the plant for a postulated LOCA. The component of interest is the response of the core and fuel rods for these transients.

The objective of the RBHT program is to define the source and nature of the limitations and uncertainty in the current thermal-hydraulic models used in best-estimate thermal hydraulic codes for reflood heat transfer. The Program will generate fundamental data and information to

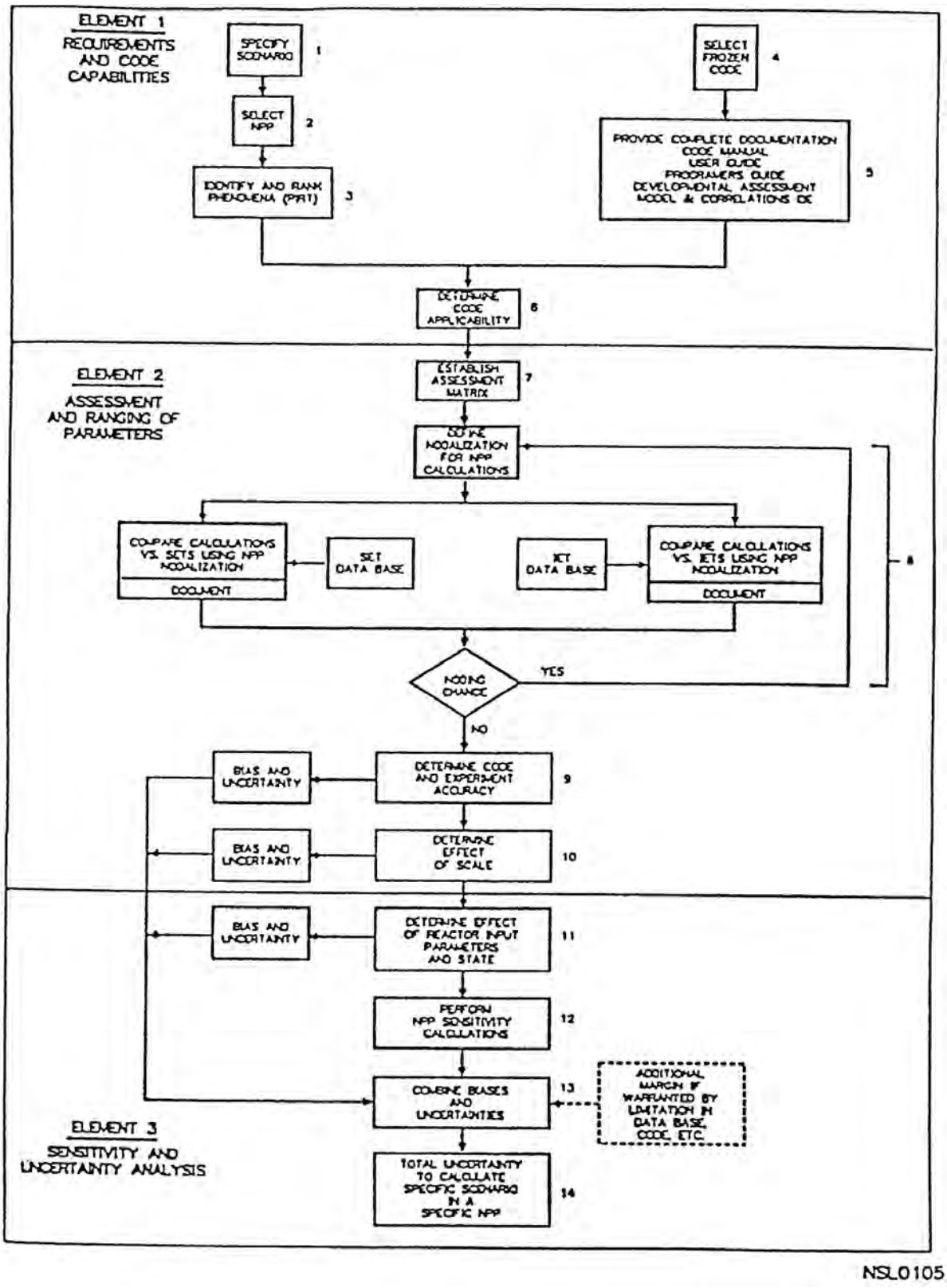

Figure 2.1 Code Scaling, Applicability and Uncertainty (CSAU) Evaluation Methodology.

support development of improved multi-field models that will allow more physical and accurate modeling of low pressure post Critical Heat Flux (CHF) heat transfer, axial void distribution, interfacial area and interfacial drag for reflooding of rod bundles.

To aid in the development for the experimental requirements of the RBHT facility, a Preliminary PIRT was developed which focused on the low pressure reflood portion of the PWR and BWR transients. The objective was to sub-divide processes down to the lowest level by which a best-estimate computer code would calculate these phenomena. With the phenomena broken down, the capabilities of the proposed test facility were assessed to determine which phenomena could be measured with confidence, which phenomena could only be qualitatively measured, and what instrumentation would be needed.

2.2 Preliminary PIRT for the Rod Bundle Heat Transfer Tests - PWR Phenomena

2.2.1 Introduction

Phenomena occurring in the core region are of most interest for the RBHT program since the core thermal-hydraulic response determines the resulting PCT. In PWRs, the core is reflooded by the gravity head of water in the downcomer. The core heat transfer response is a dependent parameter since it depends on the gravity flow into the core and the ability of the reactor system to vent the two-phase mixture generated in the core. The Emergency Core Cooling (ECC) System design, break size and location, and the containment pressure influences the flooding rate into the core and hence the core cooling. Calculations indicate that there can be an initial surge of water into the reactor core which is then reversed due to the steam generation and resulting increase in pressure drop downstream of the core. The flooding rate will quickly stabilize at a near constant value which slowly decreases over time as the effective driving head of the downcomer is decreased. The RBHT program will investigate the reflood heat transfer processes by performing separate effects tests to examine the different components of the heat transfer phenomena for reflood.

The experiments and the instrumentation will be designed to complement existing rod bundle data and to provide unique data and insights into the thermal-hydraulic phenomena such that the existing data and the new data to be gathered in the program can be more effectively utilized for computer code validation. In this fashion, the existing rod bundle database will become more valuable and can be integrated with the new data. The experiments will be structured so as to separate out the individual phenomena which have been identified in the preliminary Phenomena Identification and Ranking Table. The experiments will include:

- Heat loss experiments to characterize the facility for mass and energy balances;
- Single phase pressure drop experiments to characterize rod bundle and spacer grid pressure losses;
- Radiation heat transfer tests in an evacuated bundle to characterize the rod-to-rod radiation heat transfer, surface emissivity, and the rod-to-housing heat transfer;
- Convection to superheated steam to examine the rod bundle convective heat transfer over a wide range of Reynolds numbers and single phase heat transfer for enhancement by spacer grids;

- Convection to superheated steam with droplet injection to examine the effects of the entrained drops on vapor temperatures due to evaporation, the development and change of the interfacial area for heat and mass transfer along the length of the bundle, effects of the drops on the convective heat transfer, radiation heat transfer to the drops on vapor, spacer grid effects on droplet breakup, vapor de-superheating and grid quenching;

- Forced reflooding experiments over a wide range of conditions of flow, pressure, inlet subcooling, initial rod temperature, and rod powers to overlap with existing forced reflood data, with the emphasis on the entrainment mechanisms at the quench front;

- Variable reflooding experiments over a range of conditions of flow, pressure, inlet subcooling, initial rod temperatures, rod powers, and outlet liquid and vapor flows to overlap with existing reflood data.

2.2.2 Development of the Classifications for the Different Regions for the Rod Bundle Heat Transfer Program Preliminary PIRT

The Preliminary PIRT for the RBHT program was developed by examining the different components in the reactor system for a PWR to identify the key phenomena. The core region is the focus of this program to obtain data to improve heat transfer models. The remainder of the reactor system components will also be discussed and the phenomena will be identified.

The approach for developing the Preliminary PIRT for the core region is based on examining the FLECHT-SEASET (Ref. 4) test data and analysis. Figures 2.2 to 2.4 show the quench front curve and the two-phase froth region, which is above the quench front, for different flooding rates at the same pressure and bundle power. A schematic of the flow regimes at and above the quench front is shown in Figure 2.5. This figure gives a clearer indication of the flow behavior for the region above the quench front and below the dispersed flow film-boiling region.

Using Figures 2.2 to 2.5 as guides, six regions of interest are identified within the core during reflooding. At the bottom of the fuel rod (or heater rods in the experiment), the heat transfer is by single phase forced or natural convection. As the coolant temperature approaches the saturation temperature, subcooled nucleate boiling begins, and eventually saturated boiling.

The quench front is the next region of interest. At this point, the stored energy in the fuel or heater rods is released into the coolant resulting in significant steam generation. The local rod temperature decreases from the minimum film boiling point to the critical heat flux temperature and into nucleate boiling. Local temperature decreases in this region are several hundred degrees over a short distance such that a substantial volume of steam is generated. The steam generated near the quench front entrains liquid.

The froth region above the quench front is the location where the steam generated near the quench front shears the liquid flow into liquid ligaments and eventually into a spectrum of droplets which are entrained upwards. Above the froth region, the flow field consists of the entrained droplets in a superheated steam flow. This is the heat transfer regime where the calculated PCT typically occurs. It is a region of low heat transfer since the vapor sink temperature becomes superheated and approaches the rod surface temperature. Since

temperatures are high, radiation heat transfer to surfaces, droplets, and vapor must be accounted for, as indicated by the FLECHT-SEASET experiments.

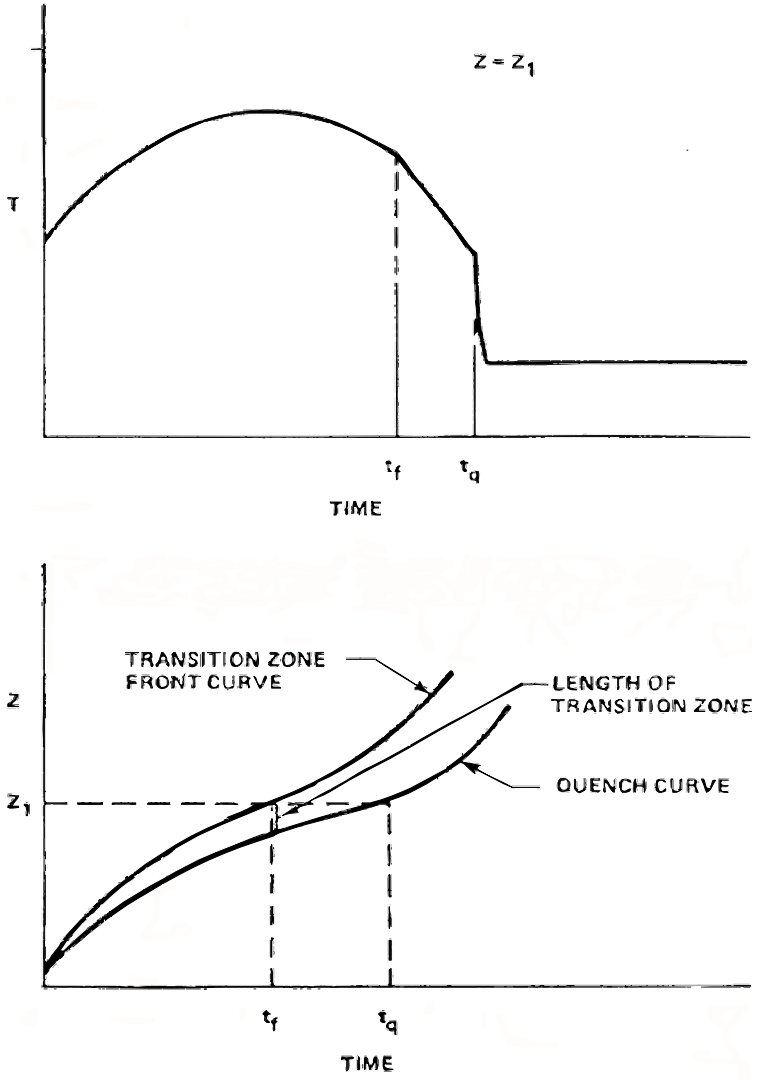

Figure 2.2 Froth Region and Quench Front Locations for Reflood.

At the very top of the rod bundle, there can be a second quench front which moves down the fuel/heater rod. The movement of the top quench front depends on the amount of liquid entrainment in the flow and the power profile of the fuel/heater rod as well as the previous blowdown heat transfer history. Assuming that there is sufficient entrained liquid in the flow which can be deposited, the top quench front is an axial conduction progression down the fuel/heater rod. The excess liquid flow from the downward liquid film flow is sputtered-off into the up flowing steam and is re-entrained with droplets from below. The top quench occurs at elevations significantly above the location of the PCT so its behavior does not influence the PCT value directly. However, the top quench front will affect the amount of liquid which leaves the core and affects the system reflood behavior.

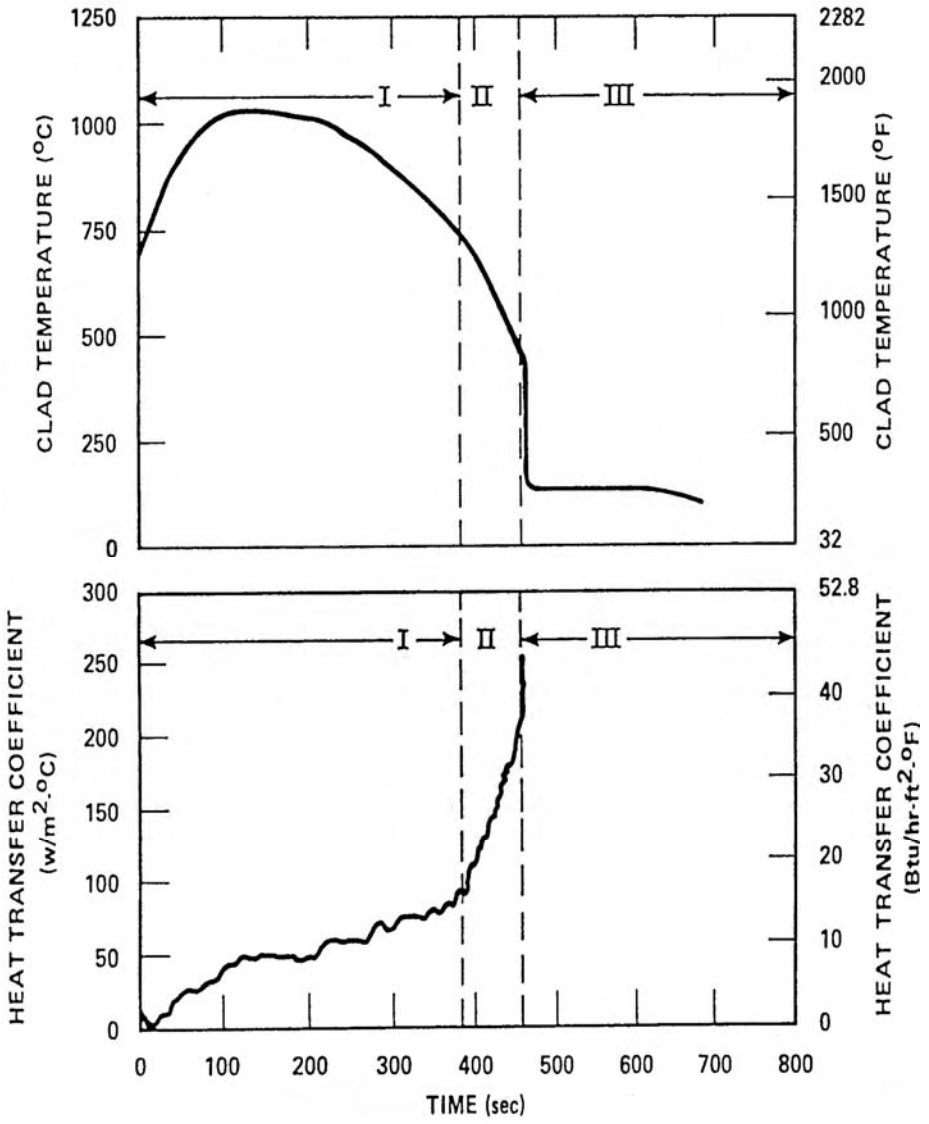

Figure 2.3 Froth Front and Quench Front Curves for FLECHT-SEASET Run 31203, 1.5 in/s, 40 psia Test.

The exact nature of the six regions are a function of the flooding rate into the core, system pressure, core power level, inlet subcooling and the rod bundle initial temperature. As the flooding rate increases, the single-phase convection region increases; there is reduced subcooled nucleate boiling and no saturated boiling. The height of the froth region above the quench front increases with increased flooding rates into the bundle as shown in Figures 2.2 to 2.5. As the froth region increases in size, the dispersed flow film-boiling region decreases and the resulting vapor superheat in this region is reduced and higher heat transfer rates result. Also, the top down quench front is enhanced because of the additional liquid in the entrained flow.

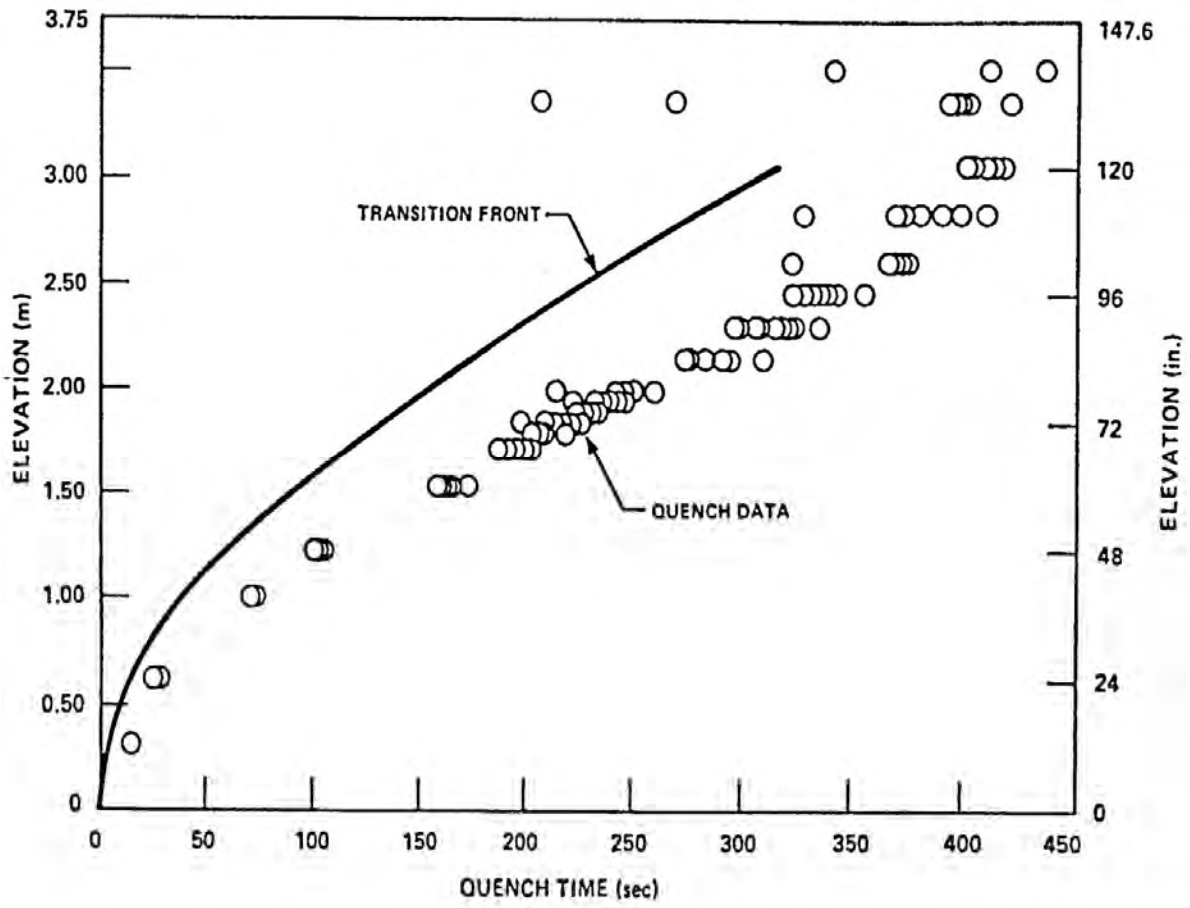

Figure 2.4 Froth Front and Quench Front Curves for FLECHT-SEASET Run 31504, 1.0 in/s, 40 psia Test.

Since there are different regions in the core during reflooding, with perhaps different phenomena which are important, the core was subdivided into six regions for the preliminary PIRT and phenomena identified for each. There may be overlap in the phenomena; however, different phenomena can have a different weighting for the different regions. The six regions identified are:

a) single phase heat transfer region below the quench front;

b) subcooled nucleate boiling and saturated boiling region below the quench front;

c) quench front region where the heat is released from the quenching fuel rods;

d) froth region where the entrained liquid is sheared into droplets;

e) dispersed flow film boiling region above the froth region where the PCT occurs; and

f) top down quench front.

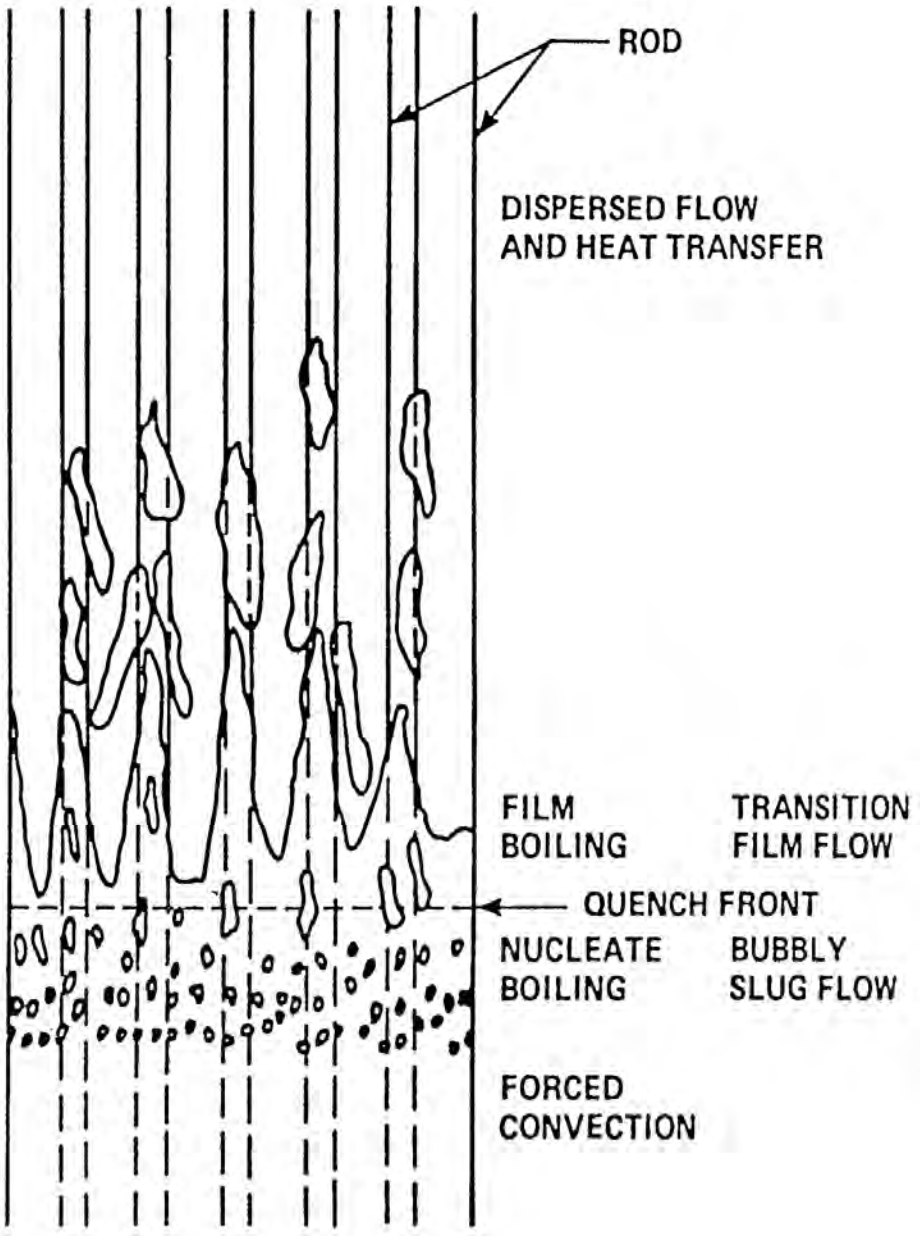

Figure 2.5 Typical Conditions in Rod Bundle During Reflood.

Separate preliminary PIRTs were developed for each of these core regions such that the particular phenomena for a particular region could be subdivided into specific component models which a computer code uses to perform the reflood calculation. The same ranking method as that employed by Los Alamos will be used to denote the relative importance of the "High", "Medium" and "Low" phenomena. The preliminary PIRTs for the core for each region are given in Tables 2.1 to 2.6. These PIRTs will be used to develop and guide the design of the RBHT facility for the single phase convection, radiation heat transfer, single phase steam with droplet injection, and the forced reflooding tests.

Table 2.1 Single Phase Liquid Convective Heat Transfer

Process/Phenomena	Ranking	Basis	RBHT Program
Effects of geometry	L	Limited data exists which can be used as a guide, should have little uncertainty on PCT	There is little data for natural convection in rod bundles, usually $Gr/Re^2<<1$.
Convective heat transfer	M	1Φ convective heat transfer data has been correlated for rod bundles, uncertainty will not affect PCT, can affect point of boiling.	Will Measure T_s, T_f and power below quench front so forced convective heat transfer or natural convection heat transfer can be calculated.
Effects of geometry	L	De has been shown to be acceptable for P/D of 1.3 (Ref. 5). Limited data exists which can be used as a guide, should have little uncertainty on PCT	There is little data for natural convection in rod bundles, usually $Gr/Re^2<<1$.
Effects of spacers	L	Effects of spacers in 1Φ convective heat transfer is known, see Reference 7. No impact on PCT uncertainty. Effect unknown for natural convection, but enhances heat transfer. No impact on PCT uncertainty.	Effects will be measured, with proper placement of heater rod T/C's and fluid T/C's.
Effects of properties	L	Property effects are accounted for in analysis for 1Φ heat transfer, little uncertainty.	Property effects can be calculated from T_s and T_b.
Liquid velocity (Reynolds number)	M	Determine convective heat transfer, onset of boiling	Will measure total flow T_w, T_f, can calculate heat transfer from data and correlate.
Liquid subcooling	M	Liquid is heat sink, determine point of boiling	Fluid temperatures will be measured with miniature steam probes, selected T/C's can traverse.
Decay power	H	Source of energy for rods, boundary condition for test.	Will be simulated.

Table 2.2 Subcooled and Saturated Boiling - The Core Component Below the Quench Front

Process/Phenomena	Ranking	Basis	RBHT Program
Subcooled boiling heat transfer (BHT) and heat flux, split of energy between liquid and vapor production	M	A significant variation in the subcooled boiling heat transfer coefficient will not affect the PCT uncertainty since rod is quenched. Will effect energy partition to sensible heat and vapor generation.	Will measure rod temperature (surface) local fluid temperatures (selectively) and power such that total wall heat flux can be calculated. Bundle average quality can be calculated from an energy balance. Codes that use the Chen Model (Ref. 8) which has a superposition of convection and boiling. The BHT can be used to test this type of correlation since both T_s and q" are measured. However, it will be difficult, if not impossible, to directly determine the heat flux split between convection and boiling without using the correlation.
Effects of geometry, P/D, De heater and properties	L	Boiling effects in rod bundles have been correlated for our P/D, De range with acceptable uncertainty (Refs. 5 and 6).	The void fraction will be measured along the test section using DP cells, and at fixed locations with a soft gamma ray detector.
Effects of spacers	M	Locally enhances heat transfer; correlations/models are available, acceptable uncertainty (Ref. 7).	Effects of spacer grids can be measured with the proper T/C placement.
Effects of fluid properties	L	Data exists for our range of conditions, little uncertainty.	
Local void fraction	M	Data does exist for tubes and rod bundles	The void fraction will be measured along the test section using DP cells, and at fixed location with a low energy gamma ray detector.
Liquid subcooling	M	Determines the near wall condensation of vapor, energy split between sensible, and net vapor production.	Subcooling will be measured with miniatures T/C's and Traversing T/C's.

Table 2.2 Subcooled and Saturated Boiling - The Core Component Below the Quench Front (Continued)

Process/Phenomena	Ranking	Basis	RBHT Program
Interfacial heat transfer area	M	Determines net vapor generation, near wall condensation	Movies can be taken at different positions but very difficult to obtain interfacial area. May be able to see bubbles with laser.
Decay power	H	Energy source for heat transfer	Will be simulated over a range of conditions.
Saturated boiling heat transfer and heat flux	M	Similar to subcooled boiling, data is available for our P/D, De range. The uncertainty of Saturated boiling heat transfer coefficient will not significantly impact the PCT since rod is quenched. Can determine and T_{CHF}.	Rod wall temperature and heat flux will be measured as well as the fluid temperature (saturation).
Effects of geometry, P/D, De	L	Data exists in the range of P/D, De with acceptable uncertainties (Refs. 5 and 6).	
Effects of spacers	L	Locally enhances heat transfer, correlations/models are available (Ref. 7), with acceptable uncertainty.	
Effects of properties	L	Data exists for our range of conditions, little uncertainty.	
Local void fraction	H	Provide the fluid conditions as the flow enters the quench front region and total steam flow which effects the liquid entrainment which directly impacts PCT.	The void fraction will be measured along the test section using DP cells.

Table 2.3 Quench Front Behavior in the Core Component

Process/Phenomena	Ranking	Basis	RBHT Program
Fuel/heater rod materials, and thickness ℓ, C_p, k, rod diameter	H	These properties effect the stored energy in the fuel/heater rod and its quench rate, uncertainty directly impacts PCT.	Inconel Heater Rods will be used. Scaling and sensitivity studies will be performed to help design the heater rods to be as similar to fuel rods as possible. Inconel will be used for the BHT program which has conductivity close to both Zircaloy and Stainless Steel. Separate effects tests planned to address properties.
Gap heat transfer coefficient	M	Second largest resistance in fuel rod. Can limit heat release rate from fuel pellet. Gap heat transfer coefficient has large uncertainty, but its impact on PCT is smaller since all stored energy will be released, timing may change however.	Heater rods will not have a gap like fuel rods since they are swagged. Very high gap resistance is used for heater rods (5000 Btu/hr-ft-F since rods are swagged. Gap effects cannot be directly simulated with conventional heaters.
Cladding surface effects • Oxides • Roughness • Materials • T_{min} • T_{CHF}	M	Since Zircaloy can oxidize, the oxide layer will quench sooner due to its low conductivity, versus Inconel or unoxidized Zircaloy. Also roughness from oxide promotes easier quenching. The surface condition affects T_{min} (Refs. 9 and 10). Quenching is a quasi-steady two dimensional process; values of T_{min} and T_{CHF} can be estimated. Large uncertainty and impact on PCT.	Inconel will be used for the cladding since repeated tests will be performed. Other data on Zircaloy quench will be sought and compared to Inconel and specific T_{min} models, such that a simple model can treat both materials (Refs. 9 and 10). Separate effects tests planned to address properties.

Table 2.3 Quench Front Behavior in the Core Component (Continued)

Process/Phenomena	Ranking	Basis	RBHT Program
Transition boiling heat transfer (surface-intermittent liquid contact heat transfer)	H	Determines the rate of heat release at quench front directly impacts PCT, large uncertainty.	Depends on wall super heat: low super heats give high values: high super heats give low values. Quasi-steady, two-dimensional process. Estimates can be made using the closely spaced heater rod T/C's to obtain the axial conduction effects and using a two dimensional analysis of the heat rod.
Decay power	M	Stored energy is the primary source of energy for rods.	Will be simulated in tests.
Void fraction/flow regime	H	Determines the wall heat transfer since large α results in dispersed flow, low α is film boiling. Directly impacts PCT.	Void fraction will be measured (estimated) using DP cells, and gamma densitometers.
Interfacial area	H	Determines the initial configuration of the liquid as it enters the froth region directly impacts liquid/vapor heat transfer and resulting PCT downstream.	Interfacial area can be estimated from high-speed photography (if windows remain dry) and the void measurements.
Fluid temperature	H	Influences the quench rate and net vapor generation. Note: this is important for high flooding rates, with high subcooling.	Local miniature fluid temperatures will measure fluid temperature at many axial positions. Void fraction will also be measured with DP cells and gamma densitometer.

Table 2.4 Two-Phase Froth (Transition) Region for Core Component

Process/Phenomena	Ranking	Basis	RBHT Program
Void fraction/flow regime	H	Void fraction/flow regime helps determine the amount of vapor-liquid heat transfer which affects the downstream vapor temperature at PCT, large uncertainty.	The average void fraction will be measured with DP cells, the vapor superheat will be estimated from miniature fluid T/C's
Liquid entrainment	H	Significant generation of steam in the froth and quench regions helps to create the liquid entrainment.	Can be calculated from the rod bundle energy balance, however, assumption must be made on vapor temperature. Mass stored in froth region is measured by DP cells, and gamma measurements.
Liquid ligaments, drop sizes, interfacial area, droplet number density	H	Liquid surface characteristics determine the interfacial heat transfer in the transition region as well as the dispersed flow region, large uncertainty	The flow regime, interfacial area droplet size and velocities will be estimated by high speed photography, and laser measurements, if possible.
Film boiling heat transfer at low void fraction: classical film boiling (Bromley)	H	Film boiling heat transfer is the sum of the effects listed below in the adjacent column. Each effect is calculated separately and is added together in a code calculation, large uncertainty.	The test will measure the total heat transfer and the vapor heat transfer will be estimated from the bundle energy balance. The difference is the film boiling and direct contact heat transfer.
Droplet contact heat transfer	H	Wall temperature is low enough that some direct wall-to-liquid heat transfer is possible with a high heat transfer rate; large uncertainty.	Some data exists (Ref. 11). However we cannot separate this component from total heat flux.
Convective vapor heat transfer	M	Vapor convective heat transfer is not quite as important since the liquid content in the flow is large and the vapor velocities are low; but large uncertainty.	Calculate from bundle energy balance using measured vapor temperatures, if possible.

Table 2.4 Two-Phase Froth (Transition) Region for Core Component (Continued)

Process/Phenomena	Ranking	Basis	RBHT Program
Interfacial heat transfer	M	Interfacial heat transfer effects are expected to be small since the steam temperature is low, large uncertainty exists.	The effects of the interfacial heat transfer will be inferred from the vapor temperature measurements and flow as calculated from bundle energy balance and high speed movies and void fraction data.
Radiation heat transfer to liquid/vapor	M	The radiation heat transfer effects are also small since the rod temperatures are low.	Radiation tests will help isolate the different components, can calculate from data.
Effects of spacers	M	The velocities and Reynolds numbers are low in this region such that droplet breakup and mixing are not as important. Drop deposition could occur.	Heater rod T/C's will measure the effects of spacers, spacer T/C's will indicate if spacers wet.
Decay power	H	Source of power for rods.	Will be simulated.

Table 2.5 Dispersed Flow Region for Core Component

Process/Phenomena	Ranking	Basis	RBHT Program
Decay power	H	Energy source which determines the temperature of the heater rods, and energy to be removed by the coolant.	Power is a controllable parameter in the experiment.
Fuel rod/heater properties ρ, C_p, k	L	The exact properties can be modeled and stored energy released is not as important.	
Dispersed flow film boiling (components are given below)	H	Dispersed flow film boiling modeling has a high uncertainty which directly effects the PCT.	Current plan for tests is to perform a bundle energy balance to get the local quality. The convective heat transfer will be calculated using the steam only tests such that a 1Φ convective correlation for BHT facility will be available. Specific tests will also be run to determine the affects of enhancement and radiation heat transfer such that the different heat transfer effects should be separable from the total heat transfer measured in a reflood test.
Convection to superheated vapor	H	Principle mode of heat transfer as indicated in FLECHT-SEASET experiments (Ref. 4).	Similar behavior is expected in the BHT tests, will have specific tests to measure, can estimate from energy balance.
Dispersed phase enhancement of convective flow	H	Preliminary models indicate that the enhancement can be over 50 percent in source cases (Ref. 13).	A series of separate tests will be performed to examine this heat transfer effect.
Direct wall contact heat transfer	L	Wall temperatures are significantly above T_{min} such that no contact is expected.	Will verify no contact from the literature. This component cannot be directly measured in the BHT tests; can estimate its effects. Separate small scale tests are needed.

Table 2.5 Dispersed Flow Region for Core Component (Continued)

Process/Phenomena	Ranking	Basis	RBHT Program
Dry wall contact	M	Iloeje (Ref. 12) indicated this heat transfer mechanism is less important than vapor convection.	This component cannot be separated out of the total heat flux data in the BHT tests. Separate smaller scale tests are needed.
Vapor interfacial to droplet heat transfer.	H	The interfacial heat transfer reduces the vapor temperature which is the heat sink for the wall heat flux.	The axial vapor temperature distribution will be measured, and the bundle average quality will be calculated to obtain the evaporation. Also, drop sizes, velocities will be measured.
Radiation heat transfer to: • surfaces • vapor • droplets	 H/M H/M H/M	This is important at higher bundle elevations (h) where the convective heat transfer is small since the vapor is so highly superheated. Very important for BWR reflood with sprays, and colder surrounding can. Large uncertainty.	Separate tests will be used to characterize the radiation behavior of the BHT test facility. Radiation heat transfer will be calculated for the forced flooding tests.
Gap heat transfer	L	Controlling thermal resistance is the dispersed flow film boiling heat transfer resistance. The large gap heat transfer uncertainties can be accepted, but fuel center line temperature will be impacted.	Heater rods will not simulate the gap heat transfer, but not needed for this regime.
Cladding material	L	Cladding material in the tests is Inconel which has the same conductivity as Zircaloy nearly the same temperature drop will occur.	Test will use Inconel.
Reaction rate	M	Inconel will not react while Zircaloy will react and create a secondary heat source at very high PCTs, Zirc reaction can be significant.	Reaction rate not simulated in tests since cladding is proposed to be Inconel.

Table 2.5 Dispersed Flow Region for Core Component (Continued)

Process/Phenomena	Ranking	Basis	RBHT Program
Fuel clad swelling/ballooning	L	Ballooning can divert flow from the PCT location above the ballooning region. The ballooned cladding usually is not the PCT location.	Flow blockage is not simulated but was modeled in FLECHT-SEASET test (Ref. 13), heat transfer was improved at PCT location.

Table 2.6 Top Down Quench in Core Component

Process/Phenomena	Ranking	Basis	RBHT Program
De-entrainment of film flow	L[1]	The film flow is the heat sink needed to quench the heater rod. This has high uncertainty.	The top quench front will be measured but the de-entrainment onto the liquid film will not be measured.
Sputtering droplet size and velocity	L	The droplets are sputtered off at the quench front and are then re-entrained upward. Since the sputtering front is above PCT location, no direct impact. The entrained sputtered drops do effect the total liquid entrainment into the reactor system, as well as the steam production in the steam generators.	If the top quench front progresses downward such that it is within a viewing location then droplet size and velocity can be estimated from high speed movies and laser measurements.
Fuel rod/heater rod properties for stored energy ρ, C_p, k.	L[1]	These properties are important since they determine the heat release into the coolant. However, since this occurs above PCT level, no impact.	Heater rod properties approximately the same as fuel rods will be used to obtain the correct stored energy release.
Gap heat transfer	L[1]	Affects the rate of energy release from fuel/heater rod.	No gap heat transfer simulated.

[1]Some of these individual items can be ranked as high (H) within the top-down quenching process; however, the entire list is ranked as low for a PWR/BWR since it occurs downstream of the PCT location.

Table 2.7 Preliminary PIRT for Gravity Reflood Systems Effects Tests

Process/Phenomena	Ranking	Basis	RBHT Program
Upper plenum - entrainment/de-entrainment	M	The plenum will fill to a given void fraction after which the remaining flow will be entrained unto the hot leg, large uncertainty.	A non-scaled plenum will be simulated in the tests, it should be easier to entrain relative to a plant.
Hot leg - entrainment/de-entrainment	L	The hot legs have a small volume and any liquid swept with the hot leg will be entrained into the steam generator plenums, medium uncertainty.	Hot leg entrainment can be simulated up to the separator which will separate the liquid flow.
Pressurizer	L	Pressurizer is filled with steam and is not an active component- small uncertainty.	Pressurizer will not be simulated.
Steam generators	H	The generators evaporate entrained droplets and superheat the steam such that the volume flow releases (particularly at low pressure). The result is a higher steam flow downstream of the generators-high uncertainty since a good model is needed. FLECHT-SEASET data exists for reflood.	The steam generators will not be simulated, but the aspects of the higher steam flow will be accounted for when specifying the inlet flooding rates.
Reactor coolant pumps	H	Largest resistance in the reactor coolant system; directly affects the core flooding rate; low uncertainty.	The resistance in the test will be considered to give approximate inlet flooding rate response observed in the system calculations.
Cold leg accumulator injection	H	Initial ECC flow into the bundle.	Accumulator flow rates will be scaled and simulated.
Cold leg pumped injection	H	Pumped injection maintains core cooling for the majority of the reflood transient.	Pumped injection will be simulated

Table 2.7 Preliminary PIRT for Gravity Reflood Systems Effects Tests (Continued)

Process/Phenomena	Ranking	Basis	RBHT Program
Pressure	H	Low pressure (~35 psia) significantly impacts the increased vapor volume flow rate, which decreases the bundle flooding rate	Pressure range will be simulated.
Injection subcooling	M/H	Lower subcooling will result in more boiling below the quench front such that there is additional vapor to vent.	Subcooling range will be simulated.
Downcomer wall heat transfer	H	The heat transfer from the downcomer walls can raise the ECC fluid temperature as it enters the core, resulting in less subcooling and more steam generation.	Simulate effect by varying the inlet temperature.
Lower plenum wall heat transfer	M	Same effect as downcomer but less severe.	Simulate the metal heat effect by varying the inlet temperature.
Break	L	Excess ECC injection spills from system; break ΔP helps pressurize reactor system.	Simulate break ΔP.

In addition to the forced reflood, experiments will be performed to simulate the effects of the gravity reflood. Previous large-break LOCA PIRTs were reviewed to determine the most important system components which can affect the core thermal response during reflood. Table 2.7 lists those components designated as having a HIGH ranking by the Los Alamos and the Westinghouse PIRTs, along with the ranking as developed in this program. Many of the components listed in Table 2.7 will not be simulated in the RBHT facility since the primary focus is for separate-effects tests. However, variable reflood tests can be performed in which the effects of the most important system parameters can be assessed as discussed in Table 2.7. The injection flows, system pressure and the effects of the different core inlet ECC temperatures can be simulated. Steam binding due to additional evaporation of liquid carried to the generators, which are not modeled in the test facility, can be simulated with the selected variable inlet flooding rate. In this table, it is already assumed that the core component is a highly ranked parameter and the focus will be on the reactor system components.

2.3 PIRT for Rod Bundle Heat Transfer Tests - BWR Phenomena

2.3.1 Introduction

Best estimate calculations for a BWR-6 plant were reviewed (Ref. 14). The calculations indicated that once the vessel was depressurized, a three-dimensional flow pattern would be established in which there was downflow at the core edge through the low powered assemblies since the counter current flow was less limiting at these locations, and upflow in the hotter high power fuel assemblies. The bypass region also helped direct the spray flow down from the upper plenum to the lower plenum. The highest powered assemblies were calculated to be in co-current upflow for the majority of the transient such that they reflooded in a very similar manner as a PWR hot assembly. The high power assemblies generated sufficient steam flow such that they remained above the flooding limit at the top of the fuel assembly and very little, if any, water penetrated into the assembly from the upper plenum.

2.3.2 BWR Reflood Phenomena of Interest

Nearly all the phenomena identified with rod bundle heat transfer for PWRs are applicable to the hot assembly in a BWR since it refloods in a similar manner. However, one difference between the reflooding behavior of the high power BWR assemblies and a PWR assembly is the presence of the fuel assembly shroud or channel in the BWR design. The shroud is calculated to quench from the liquid in the bypass region so there is more surface-to-surface radiation heat transfer occurring in the BWR fuel assembly compared to a PWR fuel assembly. The additional surface-to-surface radiation can be simulated in the RBHT experiments since the test facility will have a shroud around the test bundle.

Since the high power BWR fuel assemblies are in co-current upflow, similar to PWR fuel assemblies, the key thermal-hydraulic phenomena identified as being highly ranked in Tables 2.1 to 2.6 are also highly ranked for the BWR. The one factor which changes is the surface-to-surface radiation heat transfer in the dispersed flow film boiling regime. It is a higher ranked phenomenon for BWRs than PWRs.

Table 2.8 High Ranked BWR Core Phenomena

Process/Phenomena	Basis	RBHT Program
Core • Film boiling	PCT is determined in film boiling period.	Film boiling components will be measured.
• Upper tie plate CCFL	Hot assembly is in co-current up flow above CCFL	Similar behavior to PWR reflooding.
• Channel-bypass flow	Flow bypass will help cool the BWR fuel assembly core.	The housing in the RBHT test will approximately simulate a BWR channel.
• Steam cooling	A portion of the dispersed flow film boiling heat	Simulated in RBHT tests.
• Dryout	Transition from nucleate boiling and film boiling	Simulated in RBHT tests, but hot assembly is calculated to be in upflow.
• Natural circulation flow	Flow into the core and system pressure drops.	Flow range can be simulated in RBHT.
• Fluid mixing	Determines the liquid temperature in the upper plenum for CCFL break down.	Not simulated in RBHT, but hot assembly is calculated to be in upflow.
• Fuel rod quench front	Heat release from quench front will determine entrainment to the upper region of the bundle.	Scaling analysis will be performed to determine the heat release rate relative to nuclear fuel rods.
• Decay heat	Energy source for heat transfer	Simulated in RBHT.
• Interfacial shear	Affects the void fraction and resulting droplet and liquid velocity in the entrained flow.	Since pressure, temperature, geometry, and power are simulated in RBHT, interfacial shear should be simulated.
• Rewet: bottom Reflood	BWR hot assembly refloods like PWR.	Simulated in RBHT.
• Rewet temperature	Determines the quench front point on the fuel rod.	RBHT will use different materials than fuel rod; other data will be used to support the RBHT data.

Table 2.8 High Ranked BWR Core Phenomena (Continued)

Process/Phenomena	Basis	RBHT Program
• Top down rewet	Top of the hot assembly fuel will rewet in a similar manner to PWR.	Will be simulated in RBHT.
• Void distribution	Liquid distribution in the bundle.	Should be same/similar for PWR in RBHT.
• Two-phase level	Similar to quench front location, indicates location of nucleate and film boiling.	Two-phase level should be simulated since the power, temperature, and pressure are simulated.

The highest ranked phenomena for the reflood period are summarized in Table 2.8. Comparing those ranked as HIGH in Tables 2.1 to 2.6 shows that the BWR hot assembly phenomena are captured.

2.4 Conclusions

Preliminary PIRTs were developed in which the components of the heat transfer models were identified on a sub-component level in the same fashion as a best-estimate computer code would calculate the phenomena for both a PWR and a BWR hot assembly. For either design, the hot assembly thermal-hydraulic behavior is very similar so there is substantial over-lap in the PIRTs for the large-break LOCA.

The ability of the RBHT facility to simulate the highly ranked PWR and BWR PIRT items was assessed and the test facility can represent nearly all the phenomena of interest. The area where the simulation is the weakest is in the materials used for the cladding, heater rods and the housing, as compared to nuclear fuel rods and a BWR Zircaloy channel box. Scaling studies will be performed as part of the program to select the materials to minimize the deviation from the true plant design. Another area where the exact separation of different phenomena is difficult is the direct measurement and separation of certain boiling heat transfer mechanisms such as the effects of forced convection in convective boiling, direct droplet contact heat transfer from film boiling, and dry contact heat transfer from film boiling. The total heat flux will be measured, and estimates of these effects will be made.

Another area of limited simulation is the modeling of system effects behavior using an oscillatory injection flow to simulate the effects of gravity refloods. Several of the primary system components are not simulated in the proposed facility; however, these effects will be reflected in the range of flows simulated in the oscillatory mode.

2.5 References

1. US Nuclear Regulatory Commission, “Quantifying Reactor Safety Margins”, NUREG/CR-5249, 1989.

2. Boyack, B., “AP600 Large-Break Loss-of-Coolant Accident Phenomena Identification and Ranking Tabulation,” LA-UR-95-2718, 1995.

3. Letter from L. W. Ward to Dr. D. Ebert, “Draft of BWR PIRT Tables and Preliminary Assessment Matrix,” September 30, 1997.

4. Lee, N., Wong, S., Yeh, H. C. and Hochreiter, L. E., “PWR FLECHT-SEASET Unblocked Bundle Forced and Gravity Reflood Task Data Evaluation and Analysis Report,” NUREG/CR-2256, 1981.

5. Todreas, N. E. and Kazimi, M. S., Nuclear Systems I, Thermal Hydraulic Fundamentals, Hemisphere Pub., 1990.

6. Tong, L. S. and Tang, Y. S., Boiling Heat Transfer and Two-Phase Flow, Second Edition, Taylor & Francis Pub., 1997.

7. Yao, S-C., Hochreiter, L. E. and Leech, W. J., “Heat Transfer Augmentation in Rod Bundles Near Spacer Grids,” J. of Heat Transfer, Trans. ASME, Vol 104, No. 1, pg 76-81, 1982.

8. Chen, J. C. “A Correlation for Boiling Heat Transfer to Saturated Fluids in Convective Flows,” Ind. & Eng. Chem., Process Design and Dev., Vol 5, pg 322, 1963.

9. Henry, R.E., “A Correlation for the Minimum Film Boiling Temperature,” AIChE Symposium, 138, Vol 70, pg 81, 1974.

10. Shumway, R.W., “Return to Nucleate Boiling,” Presented at the National Heat Transfer Conference, Denver, ANS Proc., CONF-850810 (EGG-M-03985), 1985.

11. Petersen, C. O. “The Dynamics and Heat Transfer Characteristics of Water Droplets Impinging on a Heated Surface,” PhD Thesis, Carnegie-Mellon University, 1967.

12. Iloeje, O. C., Rohsenow, W. M. and Griffith, P., “Three-Step Model of Dispersed Flow Heat Transfer (Post CHF Vertical Flow),” ASME Publication, 75-WA-HT-1, Presentation at Winter Annual Meeting, Houston, 1975.

13. Paik, C. Y., Hochreiter, L.E., Kelly, J.M. and Kohrt, R.J., “Analysis of FLECHT-SEASET 163-Rod Blocked Bundle Data using COBRA-TF,” NUREG/CR-4166, 1985.

14. Wheatly, P. D., “Analysis of a BWR/6-218 During a Large Break Loss of Coolant Accident Using Evaluation Type Boundary Conditions,” EGG-SAAM-6519, 1984.

3. LITERATURE REVIEW

3.1 Introduction

A number of important rod bundle experiments were reviewed to determine the availability of data, test facility design, types of tests, instrumentation, and data from tests. These rod bundle experiments include:

- FLECHT Cosine Tests (NRC/Westinghouse)
- FLECHT Skewed Axial Power Shape Tests (NRC/Westinghouse)
- FLECHT-SEASET 21 Rod Bundle Tests (NRC/Westinghouse)
- FLECHT-SEASET 161 Unblocked Bundle Tests (NRC/Westinghouse)
- FEBA Reflood Tests (Germany)
- THTF Rod Bundle Tests (NRC/Oak Ridge National Lab)
- FRIGG Rod Loop Tests (Sweden)
- GE 9-Rod Bundle Tests (NRC/General Electric)
- NRU Rod Bundle Tests (Canada)
- ACHILLES Reflood Tests (United Kingdom)
- Lehigh 9-Rod Bundle Tests (NRC/Lehigh University)
- PERICLES Reflood Tests (France)

In addition to the above rod bundle tests comprising the first portion of the review, more than three hundred articles on single tube tests and related studies were included in the second portion. The relevant information is sub-divided into 10 different classifications, including liquid entrainment and breakup; drop size distribution and droplet number density; interfacial shear and droplet velocity; droplet-enhanced heat transfer; droplet evaporative heat transfer; direct contact heat transfer; total wall heat transfer; effects of spacer grids; effects of inlet flow oscillation and thermal non-equilibrium; and other factors.

A comprehensive review of the literature on reflood heat transfer was performed; it included two major portions. The first portion focused on the rod bundle tests whereas the second portion focused on single tube tests and related studies. Unique information useful to address the phenomena identified in the PIRT is gathered from both. This information is then sub-divided into several different classifications indicating which information can be used for which phenomena. A master cross-reference table is constructed identifying the data source for the highly ranked phenomena. The applicability of the data to determine and quantify the particular phenomena of interest is discussed along with their major deficiencies, if any.

3.2 Rod Bundle Tests

The dispersed flow film boiling reflood period is the most limiting heat transfer period for the large break LOCA. Several experimental programs were performed over the years to provide the data needed to develop models for this portion of the LOCA transient. For PWRs, the most significant program was sponsored by the Nuclear Regulatory Commission and Westinghouse, the Full Length Emergency Core Heat Transfer (FLECHT) Program which was completed in 1973 (Refs. R1-R4). This initial program, including FLECHT Cosine tests and FLECHT Skewed Power Shape tests, provided experimental data used to develop empirical correlations to

calculate heat transfer and entrainment using simple thermal-hydraulic models which would conform to the Appendix K rules, as given in 1974.

The FLECHT Cosine tests produced some data which is of interest for improved reflood modeling. In particular, the vapor temperature data at the 2.1, 3.05, 3.81m (7, 10, and 12.5 ft) elevations could be useful since these data indicate the degree of non-equilibrium within the flow. The pressure drop measurements, however, were too coarse to be used as an indicator of the void fraction within the bundle. A more detailed review of the FLECHT Cosine tests is given in Appendix A-1.

The FLECHT Skewed Power Shape tests also produced data of interest. In particular, the different axial power shape used in these tests is quite useful for assessing computer codes for a cosine power shape. The pressure drop measurements were improved in the skewed bundle tests to provide better measurement of local void fraction. In addition, the low flooding rate tests provided information on the overall heat transfer process and some of the individual models and phenomena which comprise the reflood heat transfer process. However, there was insufficient information on the vapor temperature distribution in the test bundle to accurately determine the local non-equilibrium. A more detailed review of the FLECHT Skewed Power Shape tests is given in Appendix A-2.

More recently, the Nuclear Regulatory Commission, Westinghouse and Electrical Power Research Institute sponsored the FLECHT-Separate Effects and Systems Effects Tests FLECHT-SEASET program, which was completed in 1985 (Refs. R5-R8). A total of 16 reports were produced. The objectives of this program were to quantify the conservatism in the Appendix K rule for the reflood portion of the transient and to provide experimental data which could be used to validate a PWR best-estimate thermal-hydraulic computer code. The FLECHT-SEASET program provided a portion of the database used by the NRC to revise 10CFR50.46.

A detailed review of the FLECHT-SEASET 21-Rod Bundle tests is given in Appendix A-3 while a review of the FLECHT-SEASET 161 Unblocked Bundle tests is given in Appendix A-4. The 21-Rod Bundle tests provided information on single-phase friction factors and grid pressure loss coefficients. However, no attempt was made to determine the void fraction, droplet size, and droplet velocity since there were no windows in the test bundle. The 161 Unblocked Bundle tests did provide data on void fraction, drop size, and droplet velocity as well as local quality, vapor temperature, rod surface temperature, and heat flux split between radiation heat transfer and convective Dispersed Flow Film Boiling heat transfer. The analysis of the test data was the most complete of all the FLECHT series. It is recommended that the 161 Unblocked Bundle Tests data be screened and used to validate the NRC consolidated code.

One of the more interesting rod bundle reflood experiments was the FEBA (Refs. R9-R11) program performed at the Karlsruhe Research Center. FEBA examined the effects of spacer grids on dispersed flow film boiling by performing tests with and without a spacer grid located at the center of the bundle. The data clearly shows the beneficial effects of spacer grids in promoting improved heat transfer downstream of the spacer by shattering entrained droplets, enhancing convective heat transfer, and quenching of the grid. Current vendor fuel assembly designs use mixing vane spacer grids. These types of grids have a higher rod bundle subchannel flow area reduction and provide greater heat transfer improvement downstream of the spacer grid. The FEBA data, however, provided very little information on the individual

thermal-hydraulic processes during the reflood stage. A more detailed review of the FEBA tests is given in Appendix A-5.

The Nuclear Regulatory Commission has sponsored higher pressure rod bundle film boiling, steam cooling, and level swell experiments at the Oak Ridge National Laboratory on a full length 8x8 rod bundle (Refs. R12 and R13) in the Thermal Hydraulics Test Facility (THTF). The THTF tests also examined dispersed flow film boiling conditions. However, the pressure was much higher, more characteristic of a PWR or BWR blowdown situation. These experiments also confirmed the beneficial heat transfer effects of spacer grids for higher-pressure blowdown situations as well as for reflood heat transfer. However, the effect of non-equilibrium was not accounted for because the fluid conditions were determined from mass and energy conservation by assuming thermodynamic equilibrium. A more detailed review of the THTF tests is given in Appendix A-6.

Earlier bundle data include the FRIGG facility performed in Sweden (Refs. R14-R16) and the GE 9-Rod Bundle tests performed by General Electric (Refs. R17 and R18). FRIGG employed a uniform power shape, improved our understanding of the burnout limits and the natural circulation flow inside a simulated Marviken core. The GE 9-Rod Bundle tests improved our understanding of the subchannel flow and energy diversions under typical BWR conditions. Neither tests, however, addressed the heat transfer phenomena associated with post-LOCA reflood conditions. More detailed reviews of FRIGG and the GE 9-Rod Bundle tests are given in Appendices A-7 and A-8, respectively.

NRU rod bundle tests were performed in Chalk River, Canada (Refs. R19 and R20). These nuclear fuel rod reflood experiments provide data on cladding temperature, coolant temperature, and shroud temperature during the preconditioning, pre-transient, and transient phases. However, only the total wall heat transfer was measured so their usefulness in validating models is limited. A more detailed review of the NRU Rod Bundle tests is given in Appendix A-9.

Most recently, the ACHILLES reflood tests (Refs. R21-R26) sponsored by the Central Electricity Generating Board (CEGB), were performed by the United Kingdom Atomic Energy Agency (UKAEA) at the Winfrith Laboratories as part of the safety case for PWRs in the United Kingdom. These tests covered a wide range of conditions and included inlet flow oscillations, stepped forced flooding rates, and gravity reflood. They provide some of the best reflood data available for computer code validation. Unique data include subchannel droplet distribution, spacer grid loss coefficients, instrumented spacer grid and local fluid temperatures, and finely spaced heater rod thermocouple data which shows the heat transfer effects of the spacer grids and the quench front. The differential pressure data was taken using small spans both between grids and across spacer grids. This data must be corrected for frictional and acceleration pressure drop to infer the local void fraction. Once this is performed, local heat transfer can then be correlated with void fraction. The ACHILLES data should be screened and used to validate the NRC consolidated code. A more detailed review of the ACHILLES Reflood tests is given in Appendix A-10.

Finally, there were smaller rod bundle tests performed at Lehigh University (Refs. R27 and R28). These tests employed a 9-rod bundle having a four foot test section with one spacer grid located at 30 inches from the bottom. The rods had a linear power profile to provide a constant heat flux over the length of the test section. Traversing stream probes were used to measure the thermodynamic non-equilibrium near the quench front. A more detailed review of these tests is given in Appendix A-11.

Only the FLECHT-SEASET experiments attempted to measure the details of the heat transfer and non-equilibrium flow such that a best-estimate computer code could be assessed against the data. In these experiments, vapor superheat was measured at several axial locations. Wall temperatures were measured for the housing, and guide tube thimbles and the heater rods. Limited data of droplet diameters and velocities were obtained for a few selected tests using high-speed photography. The heater rod total heat flux was calculated from an inverse conduction technique using the heater rod thermocouples and measured power. With these measurements, the heat transfer due to radiation could be calculated and separated from the total wall heat transfer, as shown in Reference 7. Convective heat transfer, droplet evaporation, and droplet enhancement of the convection heat transfer were also calculated. Mass and energy balances could be calculated for the test bundle such that the axial behavior of the flow quality could be calculated. Void fraction was measured along the bundle, with the most accurate measurements at or near the quench front. The calculated radiation heat transfer was subtracted from the total measured heat flux to obtain the convective portion. The FLECHT-SEASET data are useful for code validation.

Table 3.1 compares the data from the various rod bundle tests indicating the specific data source applicable to particular phenomena of interest and the major deficiencies of the data source.

3.3 Single-Tube Tests and Related Studies

3.3.1 Liquid Entrainment and Breakup

The physical mechanisms that lend to liquid entrainment and breakup are of paramount importance in that they affect the drop size distribution and the number density. These two quantities together with the droplet velocity determine the interfacial surface area and interfacial heat transport. In addition to the interfacial surface area, the presence of droplets in the vapor flow directly influences the convective heat transfer by modifying the turbulence structure in the flow field, by evaporation of the droplets, and by direct contact heat transfer at the wall. In fact, liquid entrainment from the froth region just above the quench front is the single largest uncertainty in predicting the DFFB behavior in reflooding the rod bundle.

This section focuses on the topic of liquid entrainment and breakup. The topics of drop size distribution and number density will be discussed in 3.3.2, droplet velocity, drag, and interactions in 3.3.3, droplet-enhanced heat transfer in 3.3.4, droplet evaporative heat transfer in 3.3.5, and direct contact heat transfer in 3.3.6. In addition, total wall heat transfer will be discussed in 3.3.7, effects of spacer grids in 3.3.8, the effects of inlet flow oscillation and non-equilibrium in 3.3.9, and other factors in 3.3.10.

The subject of liquid entrainment and breakup has been studied by Adams and Clare [1, 2], Almenas and Lee [6], Binder and Hanratty [22], Clare and Fairbain [46-48], Cousins and Hewitt [52], Dallman et al. [55, 56], El Kassaby and Ganic [72], Faeth [79], Ganic et al. [83, 85], Hanratty and Engen [98], Hay et al. [106], Hewitt [108], Hughmark [116], Hutchinson [117], Ishii [130], Ishii and Grolmes [131], Ishii and Mishima [125, 126], Jensen [132], Kataoka et al. [139], Kline et al. [154], Kocamustafaogullari [155], Krzeczkowski [157], Kuo and Cheung [158], Kutateladze [159], Lee and Ryley [163], Levy [175, 176], Lindsted et al. [177], Lopes and Dukler [180-182], Lopez de Bertodano and Jan [183], Mastanajak [187], Minh and Huyghe [190], Newitt et al. [203], Nigmatulin [206], Paras and Karabelas [219], Petrovichev et al. [223],

Table 3.1 Comparison of the Data from Various Rod Bundle Tests

Rod Bundle Tests	Specific Data Source Applicable to Particular Phenomena of Interest	Major Deficiencies of the Data Source	Recommendations
FLECHT Cosine Tests	Vapor temperature data at the 7, 10, and 12.5 foot elevations could be useful since these data indicate the degree of non-equilibrium within the flow.	Pressure drop measurements too coarse to be used as an indicator of void fraction within the bundle.	May be worth considering.
FLECHT Skewed Power Shape Tests	The different axial power shape used in these tests and the low flooding rate data could be useful in determining some of the individual models and phenomena.	Lack of detailed information on the vapor temperature distribution in the test bundle to determine the local non-equilibrium.	May be worth considering.
FLECHT-SEASET 21-Rod Bundle Tests	Useful information on single-phase friction factors and grid pressure loss coefficients.	No attempt made to determine the void fraction, droplet velocity, and drop size, no windows in the test bundle.	May be worth considering.
FLECHT-SEASET 161 Unblocked Bundle Tests	Measured details of non-equilibrium DFFB heat transfer, provided useful data on void fraction, drop size, droplet velocity, local quality, vapor temperature, rod surface temperature, and heat flux split between radiation and convective DFFB.	Some of the steam probes used in these tests did not function as desired. Also, the bundle was rebuilt due to heater rod problems, so that channel designation may have changed.	Should be used.
FEBA Reflood Tests	Data show effects of spacer grids in promoting mixing downstream of the spacer by shattering entrained droplets, enhanced convective heat transfer, and the quenching effect of the grid.	Very little information on individual processes such as the droplet behavior was reported.	Data on effects of the spacer grid should be considered.
THTF Rod Bundle Tests	DFFB behavior under high-pressure conditions, more characteristic of a blowdown situation. Useful data were obtained on the effect of spacer grid.	Applicable to high-pressure blowdown situations rather than the reflood stage. Fluid conditions were determined by assuming thermodynamic equilibrium.	To be considered in the future phase for high-pressure tests.

Table 3.1 Comparison of the Data from Various Rod Bundle Tests (Continued)

Rod Bundle Tests	Specific Data Source Applicable to Particular Phenomena of Interest	Major Deficiencies of the Data Source	Recommendations
FRIGG Loop Tests	Data on burnout limits and the natural circulation flow inside the test core may be useful.	Uniform power shape. Reflood heat transfer phenomena were not addressed.	May not be worth considering.
GE 9-Rod Bundle Tests	Provide some data on the subchannel flow and the energy diversions under typical BWR conditions.	Very little information was reported for the phenomena associated with post-LOCA reflood conditions.	May not be worth considering.
NRU Rod Bundle Tests	Nuclear fuel rod reflood experiments. Provide some data on the cladding temperature, coolant temperature and shroud temperature during the pre-transient and transient phases.	Only the total wall heat transfer was measured. No fluid conditions were determined in the experiments. May involve compensating errors.	Should be considered.
ACHILLES Reflood Tests	Included inlet flow oscillations, stepped forced flooding, and gravity reflood. Provide some unique data on subchannel droplet distribution, spacer grid loss coefficient, instrumented spacer grid and local fluid temperature, and finely spaced heater rod thermocouple data showing the heat transfer effects of the spacer grids and the quench front.	The differential pressure data was taken using small spans both between grids and across spacer grids. This data needs to be corrected for frictional pressure drop and acceleration pressure drop in order to be used for inferring the local void fraction.	Should definitely be considered.
Lehigh 9-Rod Bundle Tests	Employed a traversing steam probe in a 4-foot test section with a spacer grid located at the 30-inch elevation to measure the non-equilibrium reflood heat transfer.	The test section was only 4 feet in length with only one spacer grid.	May not be worth considering.

Podvysotsky and Shrayber [226], Ramirez [228], Richter [233], Sarjeant [235], Schadel et al. [238], Sekoguchi and Takeishi [242], Smith [247], Soliman and Sims [249], Sugawara [256], Van der Molen [278], Wicks and Dukler [288], Wilkes et al. [290], Williams et al. [294], Woodmansee and Hanratty [297], Yadigaroglu [301], Yao [304, 305, 308], Yoshioka and Hasegawa [315] and Zuber [321].

Depending on the flow situation, entrainment may take place in a number of different ways. Physically, when two fluids flow over each other, the interface of the two fluids is inherently unstable. As the relative velocity between the two fluids exceeds a certain critical value, instabilities set in and grow in the interfacial region, resulting in the formation of wavy interface and large amplitude roll waves (Hanratty and Hershmen [97] and Ishii and Grohmes [131]). This so-called Kelvin-Helmholtz instability is responsible for the entrainment of liquid droplets from a wavy film into a gas flow. Hydrodynamic and surface tension forces govern the motion and deformation of the wave crests. Under certain conditions, these forces lead to extreme deformation of the interface resulting in the breakup of a portion of the wave into several fluid droplets.

The forces acting on the wave crests depend on the flow pattern around them as well as the shape of the interface. In the reflood phase of LOCA, liquid droplets are likely to be generated by shearing off of roll waves. The drag force acting on the wave tops deforms the interface against the retaining force of the liquid surface tension. At vapor velocities beyond the inception of entrainment, the tops of large amplitude roll waves are sheared off from the wave crests by the vapor flow and then broken into small droplets.

A clear physical understanding of the droplet generation mechanisms is crucial in modeling reflood. The initial sizes and velocities of the droplets depend on how they were generated above the quench front in the froth region. The onset of entrainment is believed to occur when the deforming forces (i.e., the interfacial shear forces or the hydrodynamic drag forces) become greater than the retaining forces (i.e., the surface tension forces) [131, 139]. Under some special circumstances, however, large liquid globules can be generated above the quench front by disintegration of waves formed in the wetted position of a flow channel [2].

Inception criteria for the onset of entrainment in annular two-phase flow have been based largely on experimental data, as reported by Ardron and Hall [11], Ishii and Grolmes [131], Jensen [132], Kataoka et al. [139], Kocamustafaogullari et al. [155], Kutateladze [159], Newitt et al. [203], Nigmatulin [206], Richter [233], Sekoguchi and Takeishi [242], Wallis [280], and Zuber [321]. Thus far, no dynamic models have been implemented in existing transient analysis codes to describe the functional dependence of the initial drop sizes and velocities on the droplet generation mechanisms. The key controlling parameters that need to be considered include the film Reynolds number, the viscosity numbers of the fluids, the critical Weber number, the critical mass flux and the Kutateladze number.

The rate of entrainment has been correlated by a number of investigators based upon measured data. Entrainment measurements in annular gas-liquid flow have been interpreted by Dallman et al. [56]. There are two widely used techniques for measuring the fraction of liquid flux that is entrained into the gas phase as droplets. The first is based on local measurements using a sampling probe to determine the liquid mass flux at the axial location of the probe. Usually, measurement is made only along the centerline with the assumption that the mass flux is uniform radially. This technique has been used with limited success [52, 289, 299]. The second technique is based on the measurement of the liquid film flow by removing it from the

test section. In so doing, it eliminates those uncertainties associated with the local probe measurement technique. This liquid film removal method is thought to be more accurate [52, 126, 218, 223].

In general, the entrainment rate, which governs the rate of droplet formation, is measured in terms of the so-called entrained fraction. This quantity is defined as the fraction of the liquid flux flowing as droplets in the two-phase flow system. Correlations of the entrainment data have been made by a number of investigators with limited success. The most widely used entrainment correlations include those reported by Dallman et al. [55, 56], Hutchinson and Whalley [117], Ishii and Mishima [125], Ishii [130], Minh and Hugghe [190], Nigmatulin [206], Paleev and Filipovich [218], Paras and Karabelas [219], Wicks and Dukler [289], and Williams et al. [294].

An important quantity that needs to be considered along with the rate of liquid entrainment is the rate of deposition of droplets carried by the vapor core to the liquid film. Whereas the entrainment of liquid from the film will cause an increase in the fraction of liquid entrained in the vapor core, the deposition of droplet onto the liquid film will cause a decrease in the fraction of liquid in the vapor core. Although the initial drop sizes and velocities are dictated by the mechanisms of liquid entrainment, the droplet number density and the drop sizes downstream of the point of droplets generation depend on both the rates of entrainment and deposition. Specifically, the rate of deposition has direct influence on the evolution of the liquid droplets in the downstream locations of the vapor core.

The process of droplet deposition has been studied by Almenas and Lee [6], Binder and Hanratty [22], Cousins and Hewitt [52], Dallman and Kirchner [55], El Kassaby and Ganic [72], Ganic et al. [83, 85], Hanratty [99], Hay et al. [106], Langevin [161], Lee and Almenas [164], Lopes and Dukler [182], Mastanajah [187], Nishio and Hirata [208], Paras and Karabelas [219], Pedersen [221], Schadel et al. [238], Sugawara [256], Wilkes et al. [290] and Williams et al. [294]. In general, the rate of deposition of droplets from the vapor core onto the liquid film is a function of the fluid properties, the droplet concentration in the vapor core, and the radial velocities of the droplets. Experimental observations have indicated that the rate of deposition is dependent linearly on the droplet concentration in the vapor core. Useful correlations have been obtained by Binder and Hewitt [22], Nigmatulin [206], Schadel et al. [238], and Williams et al. [294].

3.3.2 Drop Size Distribution and Number Density

The interfacial area and thus the interfacial heat and mass transfer depend not only on the drop size distribution but also on the volumetric concentration of the droplets, i.e., the number density. As mentioned in 3.3.1, these two quantities (drop size distribution and number density) are functions of the droplet generation mechanisms and their previous history (i.e., time evolution of the droplets) in the flow field. The latter requires the consideration of droplet entrainment, droplet evaporation, droplet breakup induced by spacer grids, drop coalescence, and droplet deposition upon impingement on the wall. The topics of drop size distribution and number density have been studied extensively by many investigators in the past, notably among which are Adams and Clare [2], Ardron and Hall [11], Claire and Fairbain [46], Coulaloglou and Tavlarides [51], Cousins and Hewitt [52], Cumo et al. [54], De Jarlias [58], Hagiwara et al. [96], Hay et al. [106], Jepson et al. [133], Juhel [135], Kataoka et al. [139], Kocamustafaogullari et al. [155], Kuo and Cheung [158], Lee et al. [165], Mugele and Evans [199], Nukiyama and

Tanazawa [212], Podvysotsky and Shrayber [226], Sarjeant [235], Seban et al. [239, 241], Wick and Dukler [289], Wilkes et al. [290], Wong and Hochreiter [295] and Zuber et al. [319, 320].

Owing to the difficulty in defining the drop size distribution, many investigators have characterized the droplets by an average diameter. This simplification, however, can be justified only if the axial velocity of the droplets and the droplet concentration are independent of the drop size and do not vary in the radial direction. Whereas the droplet velocities can be assumed independent of the drop size in some cases [11, 290], the droplet concentration cannot be assumed uniform in the radial direction (Zuber et al. [319, 320]). The data of Hagiwara et al. [96] showed that the droplet concentration decreases from the turbulent core to zero near the wall. Thus, the use of an average diameter in the expression for the interfacial area is questionable.

Most of the proposed drop size distribution functions are derived from experiments [54, 58, 139, 155, 165, 212, 295]. The maximum drop size is usually calculated using a critical Weber number. However, the standard droplet disintegration mechanism overestimates the observed droplet sizes. Most droplets are produced by entrainment at the gas-liquid interface rather than generated during their evolution downstream of the points of entrainment above the quench front. Experimental data indicate that the droplets downstream of the quench front are too small to have been generated by fragmentation (i.e., by the secondary breakup mechanism during their flight as droplets in the gas or vapor flow). In other words, the critical Weber number based upon the relative velocity between the droplets and the gas flow gives rise to much larger droplet sizes than experimentally observed. Sarjeant [235] found that the breakup time and number of fragments depend on the Weber number. However, the critical Weber number is essentially independent of the droplet Reynolds number. Note that coalescence of droplets may take place immediately downstream of the quench front, owing to the chaotic motion of the droplets. Whereas the secondary breakup due to fragmentation or disintegration would increase the droplet number density (Juhel [135]), coalescence due to collisions of droplets could increase the Sauter mean diameter (Clare and Fairbaim [46]).

3.3.3 Droplet Velocity, Interfacial Shear, and Interactions

Owing to mechanical non-equilibrium [11, 166], the liquid droplets, once entrained, are accelerated by the aerodynamic drag forces exerted by the vapor flow. Thus, the relative velocity between the liquid and vapor phases may vary continuously in the flow field. Since all the transfer mechanisms at the liquid/vapor interface are affected by the relative velocity, the droplet velocity and interfacial drag as well as droplet-droplet interactions need to be taken into account in modeling the reflood heat transfer. The concentration of the droplets, i.e., the number density, at different elevations above the quench front, depends largely on the velocities of the droplets. The topics of droplet velocity, drag and interaction have been studied by a number of investigators, including Ardron and Hall [11], Brauner and Maron [26], Chuchottaworn and Asano [41], Harmathy [101], Hassan [104, 105], Ishii et al. [127, 128, 129], Kataoka et al. [139], Lee et al. [166-174], Lindsted et al. [177], Nigmatulin and Kukharenko [205], Temkin and Mehta [263], Tsuji et al. [269], Wilkes et al. [290] and Williams and Crane [292].

If the motion of the droplets can be described by a single momentum equation applied to the center of mass of the dispersed phase, i.e., the liquid droplets, the drag force per unit volume can be expressed in terms of the interfacial area concentration, the droplet velocity, and the ratio between the Sauter mean diameter and the mean drag diameter [127]. For spherical particles, the ratio of the Sauter mean diameter and the mean drag diameter is essentially equal

to unity regardless of the drop size distribution [139]. For non-spherical particles or distorted droplets, the drag force should be better calculated using the drag coefficient. According to Ishii and Zuber [128], the distorted droplet regime is characterized by the viscosity number.

It should be noted that the drag coefficient calculated by the standard laws does not account for the effect of mass flux and the droplet-droplet interactions. Chuchottaworn and Assano [41] calculated the drag coefficient on an evaporating or condensing droplet and found that the effect of mass flux due to phase change can influence the resulting drag coefficient. The experimental data of Lee and Durst [166] and Tsuji et al. [269] as well as the analysis of Lee [168], on the other hand, indicated a significant effect of droplet-droplet interactions on the drag coefficient. The dependency of the drag coefficient on the Reynolds number is modified appreciably in the highly dispersed gas-particle viscous regime. For small particles and low concentrations, the drag coefficient becomes smaller whereas for large particles and high concentrations, the reverse is found to be the case.

As mentioned above, the droplet motion is usually described by a single momentum equation for the center of mass of the droplets. This approach requires that the droplet velocities to be independent of the drop sizes. Since the droplets are accelerated by the vapor flow as soon as they are generated, one may expect that there are considerable differences in the velocities among droplets of different sizes. Small droplets, being entrained readily by the vapor flow, should move faster than large droplets. This expectation, however, may not be the case. Experimental data for dispersed flow above the quench front [11] and for annular mist flow in tubes [290] have shown that droplets of various sizes move axially at nearly the same velocity, close to the terminal velocity of the droplets of average size. This behavior may due in part to the droplet-droplet interactions and in part to the different radial migration of small and large droplets. In the former case, momentum exchange during droplet-droplet interactions tends to render the velocities of the droplets uniform. In the latter case, the small droplets are being slow down as they are carried by the turbulent eddies toward the wall. On the other hand, the large droplets, being less affected by turbulent eddies, continue to be accelerated by the vapor flow. As a result, the droplet velocities may not vary considerably with the droplet sizes.

3.3.4 Droplet-Enhanced Heat Transfer

The presence of liquid droplets in the dispersed flow region has significant effects on the total heat transfer in the reflood phase. First, the droplets are not at thermal equilibrium with the vapor flow and there is convective heat transfer between the droplets and the vapor. Second, the droplet temperatures are different than those of the wall and there is wall to droplet radiation heat transfer. Third, vaporization of the droplets may take place during their flight and the phase change process may result in de-superheating of the vapor flow. The rates of convective heat transfer between the droplets and the vapor, wall to droplet radiation heat transfer and droplet evaporation depend on the total interfacial area which is a function of the drop size distribution and number density. Fourth, the liquid droplets may impinge upon the wall which results in direct contact heat transfer. Fifth, the droplets are hydrodynamically coupled to the vapor flow. Whereas the droplet motion depends strongly on the flow characteristics of the continuous vapor phase, the turbulence intensity and transport properties of the vapor flow can be substantially modified by the presence of the liquid droplets. In most cases, the liquid droplets may induce higher turbulence in the vapor phase, which would enhance convective heat transfer of the vapor flow at the wall.

The topic of droplet-enhanced heat transfer (i.e., the fifth item mentioned above) has been studied by many investigators, including Aihara [4], Boothroyd and Hague [23], Boothroyd [24], Briller and Peskir [27], Chu [40], Danziger [57], Depew and Kramer [61], Drucker et al. [67], Evans et al. [77], Farbar and Depew [80], Farbar and Morley [81], Hasegawa et al. [103], Holman et al. [114], Kianjah et al. [150], Kiger and Lasheras [151, 152], Koizumi et al. [156], Shrayber [245, 246], Spokoynyy [251], Sukomel et al. [261], Theofanous and Sullivan [264], Tien and Quan [265], Tsuji et al. [269], and Wilkinson and Norman [291]. In most of these studies, solid particles are used to simulate the liquid droplets, excluding the effect of evaporation. The modification of the convective heat transfer coefficient is determined by comparing the case of an upward gas-particle flow to the case of a pure gas flow.

In general, a dispersed phase may alter the convective heat transfer to and from the continuous gas phase in several ways. First, the presence of particles may strongly modify the turbulence structure of the gas phase. Second, the slip between phases may enhance the mixing of the carrier gas. Third, the radial motion of the particles may promote energy exchange between the laminar sublayer and the turbulent core. Fourth, owing to the penetration of the particles in the viscous sublayer, the thickness of the sublayer may be reduced. All these factors tend to flatten the gas velocity profile in the core and reduce the viscous sublayer thickness, resulting in a steeper temperature gradient at the wall and thus a higher rate of convection.

Under certain conditions (large particles at small loading ratios), however, the presence of particles could dampen the eddy motion in the turbulent flow field and may reduce the convective heat transfer due to the transition from turbulent to laminar flow [103, 246]. The key parameters that need to be considered include the loading ratio (i.e., the quality), the particle size, Reynolds number of the flow, the hydraulic diameter and the wall temperature. Thus far, no correlation is available that properly accounts for the effects of all these parameters.

3.3.5 Droplet Evaporative Heat Transfer

One characteristic feature of dispersed flow is the presence of very high temperature gradients in the continuous vapor phase. Thus, the distribution of the evaporating liquid droplets plays an important role in the heat transfer process. The topic of droplet evaporative heat transfer has been studied by Bellan and Harstad [18], Duncan and Leonard [70], Faeth [79], Gaugler [86], Ghazanfari [87], Harpole [102] Hoffman and Ross [113, 114], Iloeje et al. [123], Kiger and Lasheras [151], Labowsky [160], Lee and Ryley [163], Mostinshiy and Lamden [198], O'Rourke [216], Rane and Yao [231], Sawan and Carbon [237], Toknoka et al. [266], Unal et al. [274, 277], Yamanuchi [302], Yao et al. [308], and Yuen and Chen [317]. Perhaps the most important effects of droplet evaporation are vapor de-superheating near the wall. Droplets can be transported towards the wall by turbulent diffusion. The migration of droplets towards the wall and subsequent evaporation of the droplets greatly reduces the vapor temperature near the wall. This vapor de-superheating effect increases the driving temperature difference between the wall and the vapor and thus enhances the convective heat transfer at the wall. The rate of droplet migration, however, depends on the radial droplet concentration distribution and the ability of the droplets to penetrate the viscous sublayer at the wall.

The evaporation of droplets also affects the convective heat transfer from the vapor to the droplets. In the range of high Reynolds numbers and high evaporation rates, a shielding effect is observed as a result of droplet evaporation [113, 317]. This shielding effect, caused by the mass efflux associated with droplet evaporation, reduces convective heat transfer from the

superheated vapor to the liquid droplets. The total evaporation rate for a cloud of droplets can be quite different than that predicted by the single-drop model [160].

At high droplet concentrations, i.e., for a dense cluster of droplets, there could be an appreciable reduction of the droplet evaporation rate. This is probably due to the difficulty of the outer flow to penetrate through the dense cluster. Owing to overlapping boundary layers around the droplets, the outer flow tends to by pass the cluster of drops. Thus, only those droplets at the periphery of the cluster are affected by the outer flow. The droplets inside the cluster evaporate at the rate typical of that for droplet evaporation in a quiescent fluid. This cluster effect of droplets, however, is somewhat controversial. Bellan and Harstad [18] found that the evaporation time for a dense cluster of drops is only weakly dependent on the relative velocity between the cloud of droplets and the vapor flow. On the other hand, Faeth [79] found that for evaporating sprays, there is very little effect of adjacent droplets on the vaporization rate.

3.3.6 Direct Contact Heat Transfer

The topic of direct contact heat transfer has been investigated by Carbajo and Siegal [30]. Cokmez-Tuzla et al. [50], Dua and Tien [68], Duffey and Porthouse [69], Elias and Yadigaroglu [74], Groeneveld and Stewart [92], Henry [107], Iloeje et al, [123], Kendall [146], Lin and Yao [178], Nishio and Hirata [208], Pedersen [221, 222], Piggot et al. [224], Styrikovich et al. [253], Yao and Cai [303] and Yao and Henry [307]. A comprehensive review of the subject was recently made by Ayyaswamy [13]. In general, droplet impingement onto the wall is capable of removing a significant amount of heat from the wall either by direct contact with the hot wall or by evaporation in the superheated thermal boundary layer at the wall. The latter case results in de-superheating of the vapor phase and thus increasing the driving temperature difference between the wall and the vapor, as discussed previously in item V. The former case (i.e., direct contact heat transfer) is a very effective cooling mechanism and may lead to a significant enhancement of the heat transfer rate above the quench front. However, direct contact heat transfer is possible only if the wall is lower than a limiting temperature, i.e., the Leidenfrost temperature. It is possible, though, to achieve direct liquid-wall contact momentarily on a very small time scale at higher temperatures [92, 107, 303, 307]. Above the limiting temperature, the wall is not wettable continuously.

The wettability of a hot wall is an important issue that has been studied by Duffey and Porthouse [69], Groeneveld and Stewart [92], Iloeje et al. [121-123], Kervinen et al. [147], Nishio and Hirata [208], Piggot et al. [224] and Yao and Cai [303]. The wettability is a rather complicated issue and there is no reliable criterion for the wettability of a hot wall. The limiting temperature is not well known, the highest value being the one reported by Nishio and Hirata [208]. Yao and Cai [303] found that the wettability of a hot surface depends not only on the radial velocity normal to the wall but also on the axial velocity in the tangential direction.

Iloeje et al. [123] identified the direct contact heat transfer as “wet” contacts so as to distinguish it from that of “dry” contacts for which the droplets do not have enough transverse momentum to penetrate through the thermal boundary layer. In general, the importance of wet contacts diminishes, relative to that of dry contact, with increasing wall temperature. Evidently, the relative importance of the wet and dry contacts depends on the probability that a droplet reaches the hot surface. One widely used approach is to divide the contact area between the wall and the two phases based on the average void fraction. Unfortunately, this approach is not physically realistic, though it is convenient to use. A general, reliable criterion for the wettability of a hot wall by impacting droplets of various sizes and velocities is needed.

3.3.7 Total Wall Heat Transfer

In modeling the dispersed flow film-boiling (DFFB) regime, the most complete models are the so-called three-step models which consider wall-to-liquid, wall-to-vapor and vapor-to-liquid heat transfer. These are mechanistic models as the phenomenon is fully taken into account. The only element of empiricism is due to the use of correlations for describing the various mechanisms of momentum, heat and mass transfer. As discussed in items IV and V above, the turbulence structure of the continuous vapor phase may be significantly modified by the dispersed phase whereas droplet evaporation may result in enhanced convective heat transfer due to vapor de-superheating near the wall. Thus the vapor-to-liquid heat transfer needs to be considered in modeling the DFFB phenomenon. The Dougal-Rohsenow correlation [64], for example, fails to predict the wall-to-vapor heat transfer, as it does not account for the effect of dispersed droplets.

The wall-to-liquid heat transfer includes the convective heat transfer from the wall to the droplets (i.e., direct contact heat transfer discussed in section 3.3.6 above) and the radiation heat transfer from the wall to the droplets. The later has been studied by Chung and Olafsson [44], Deruaz and Petitpain [62], and Sun et al. [262]. The liquid droplets are treated as distributed heat sinks and the heat transfer from the wall to the fluid is determined by calculating the combined radiation and convection from the wall to the two-phase mixture. The total heat transfer and the prediction methods for DFFB have been discussed by Afifi [3], Akimoto and Murao [5], Andreani and Yadigaroglu [7-10], Arrieta and Yadigaroglu [12], Axford [13], Chen [34], Chiou and Hochreiter [37], Choi et al. [39], Chung and Ohafsson [44], De Salve et al. [59], Ghiaasiaan [89], Hassan [105], Kaminaga et al. [136, 137], Kawaji and Banerjee [142, 143], Kirillov et al. [153], Mastanajah and Ganic [186], Majinger and Langner [188], Moose and Ganic [192], Murata et al. [201], Naitoh et al. [202], Ottesen [217], Paras and Karabelas [219], Plummer et al. [225], Spencer et al. [250], Sudo [255], Toman et al. [268], Varone and Rohsenow [279], Wong and Hochreiter [295, 296], Yadigaroglu [300, 301], Yao and Sun [306], Yoder and Rohsenow [310], and Zemlianoukhin et al. [318].

3.3.8 Effects of Spacer Grids

During the reflood phase of LOCA, the enhanced DFFB cooling downstream of spacer grids is an important heat transfer mechanism. According to Yao et al. [308, 309], the spacer grids can enhance cooling of the fuel rod by four mechanisms. These are the breakup of droplets into smaller fragments, flow restructuring associated with thermal boundary layer separation and reattachment, spacer grid early rewetting to allow direct contact heat transfer to take place and direct radiation from the fuel rods. Usually, overlooking the presence of spacer grids would result in under prediction of the cooling rate and over prediction of the cladding temperatures downstream of the grids. The effects of spacer grids has been investigated by Adams and Claire [2], Becker and Hernborg [17], Cha and Jun [32], Chiou et al. [38], Chung et al. [42, 43], Clement et al [49], Crecy [53], Groeneveld and Yousef [93], Hochreiter et al. [112], Ihle and Rust [119], Ihle et al. [120], Kanazawa et al. [138], Lee et al. [169-174], Rehme [232], Stosic [252], Sugimoto and Murao [257-259], Westinghouse Work [286], Yao et al. [308, 309], and Yoder et al. [312-314].

The spacer grid is a device that maintains uniform gap between fuel rods and minimizes rod vibration. In many cases, mixing vanes are attached to the spacer to enhance turbulent mixing and induce swirl flow. Recent experiments by Chung et al. [42, 43] clearly showed that the space grids or mixing vanes generally increase the critical heat flux. The presence of spacer

grids tend to breakup large bubbles, direct the entrained liquid droplets to the heated wall, improve subchannel mixing, and strip the liquid film off the unheated surface.

3.3.9 Effects of Inlet Flow Oscillation and Thermal Non-equilibrium

The effects of flow oscillations and transients on DFFB have been investigated by Cha et al. [33], Cheung and Griffith [36], Clement et al. [49], Ghazanfari et al. [88], Kawaji et al. [145], Ng and Banerjee [204], Oh [213], Oh et al. [214], and White and Duffey [287]. Cheung and Griffith [36] studied the phenomenon of gravity reflood oscillations, Ghazanfari et al. [88] studied the unsteady DFFB behavior, Kawaji et al. [145] investigated the flow and heat transfer with oscillatory coolant injection, Ng and Banerjee [204] investigated the two-phase flow characteristics during controlled oscillating reflooding, Oh et al. [214] determined the quench front and liquid carryover behavior during reflooding with oscillating injection, and White and Duffey [287] investigated unsteady flow and heat transfer in the reflooding of rod bundles. In general, large oscillations have been observed in void fractions and wall temperature for reflooding with oscillatory coolant injection. This observed phenomenon implies that there could be periodic changes in the flow regime near the quench front.

The effect of thermal non-equilibrium on reflood heat transfer has been reported by Chen et al. [35], Evans et al. [76, 78], Gottula [90, 91], Jones and Zuber [134], Kawaji [144], Loftus et al. [179], Morris et al. [193-197], Nijhawan et al. [207], Tuzla et al. [270, 271], Unal et al. [273-275], Webb and Chen [281-283], and Williams [293]. Experimental evidence has indicated that significant thermal non-equilibrium can be present in DFFB with vapor superheats of several hundred degrees.

3.3.10 Other Factors

The phenomena of quench front propagation and quench time have been studied by Afifi [3], Barnea and Elias [15], Chung et al. [45], De Salve et al. [59], Dhir and Catton [63], Era et al. [75], Juhel [135], Seban et al. [241], Ueda et al. [272], Webb and Chen [283], and Yu and Yadigaroglu [316]. The regime of film boiling during reflood has been described by Berenson [21], Hsu [115], Styrikovich et al. [254], Sudo [255], and Weisman [285], whereas the regime of subcooled boiling has been reported by Dowlati et al. [65], Maitra and Subba-Raju [184], Murao and Sugimoto [200], Savage et al. [236], and Shoukri et al. [244].

The subject of void distribution measurement and prediction has been discussed by Banerjee et al. [14], De Young et al. [60], Dowlati et al. [65], Maitra and Subba-Raju [184], Savage et al. [236], and Zuber and Findlay [319]. The subject of post-dryout heat transfer has been studied by Barnea [16], Chen et al. [34, 35], Evans et al. [76, 78], Gottula et al. [91], Hochreiter et al. [109-111], Ishii and De Jarlais [124], Ishii and Mishima [125], Jones and Zuber [134], Kendall [146], Mayinger and Langner [188], Obot and Ishii [215], Plummer et al. [225], Stosic [252], and Unal et al. [274, 276].

The issue of simulating a nuclear fuel pin by an electrically heated rod has been addressed by Broughton et al. [28], Carajilescov [29], Casal et al. [31], Malang and Rust [185], McPherson and Tolman [189], Raepple et al. [227], Soda [248], Sugimoto et al. [260], and Tolman and Gottula [267]. Evaluation of heater rod properties, clad swelling, and rupture behavior has been performed by Hanson [100], Larson [162], Mohr and Hesson [191], Nithianandan et al. [209-211], and Sugimoto et al. [260].

The heat transfer rate for single phase and two phase flows in tubes or around bundles have been discussed by Bennett et al. [19], Benodekar and Date [20], Drucker and Dhir [66], Dwyer and Berry [71], El-Genk et al. [73], Forslund and Rohsenow [82], and Groeneveld [94, 95], Hynek at al. [118], Kianjah [148-150], Ramm and Johannsen [229] and Rane and Yao [230].

Finally, phenomena identification and ranking table (PIRT) has been developed for thermal-hydraulic phenomena during large break LOCA by a number of researchers such as Boyack [25], Rohatgi et al. [234], Shaw et al. [243], and Wulff [298]. The RBHT PIRT presented in section 2 of this report was developed specifically for thermal-hydraulic phenomena during the reflood stage of a large break LOCA. The table is most up to date and is most appropriate for reflood heat transfer studies.

3.4 Master Table: Previous Studies Relevant to the High-Ranking Phenomena Identified in the PIRT for the RBHT Program

Based on the PIRT for the RBHT program described in section 2.0 and the results of the literature review presented in sections 3.2 and 3.3, Table 3.2 is developed which summarizes all the previous studies relevant to the highly ranked phenomena during the reflood stage of a large break LOCA. This master table identifies the data sources listed in section 3.5 that may be useful for addressing each type of phenomena taking place in various regions of the rod bundle during the reflood stage.

From the literature survey as highlighted in the master table, it was found that there are large differences between the data obtained from the rod bundle tests and those from the single tube tests. The RBHT test facility is designed specifically to address this data deficiency. The RBHT program will aim at obtaining not only wall-to-fluid heat transfer correlations but also models for interfacial heat transfer. To develop and assess models for interfacial phenomena with the goal of significantly improved accuracy and to minimize the potential for compensating errors will require a new or improved database that includes more detailed information than is currently available. The specific needs for new or improved data are described below:

1. In dispersed flow film boiling, the primary heat transfer mechanism is convective heat transfer to superheated steam. It is now recognized that the steam heat transfer coefficient can be enhanced by up to 100 percent due to the presence of entrained droplets. No suitable models currently exist for this phenomenon. The combination of single-phase convection experiments and two-phase convection experiments with droplet injections (with known drop sizes and flow rates) to be performed in the RBHT test facility will provide important new data and result in the development of the needed model.

2. Once the uncertainty involving droplet-enhanced heat transfer is resolved, there still remains the difficulty in predicting the heat transfer rate for the dispersed flow film-boiling (DFFB) regime due to the difficulty in calculating the steam superheat. The amount of steam superheat is governed by the interfacial heat transfer between the steam and the evaporating droplets. To correctly calculate the interfacial heat transfer requires the knowledge of both the entrained drop size and the droplet flow rate. There is very little data of this type currently available for quenching rod bundles. The RBHT program will generate the needed database through advanced instrumentation involving the use of a laser illuminated digital camera system to determine the entrained drop size and measure the droplet flow rate.

3. Although data showing the effects of spacer grids is available, the phenomenon is still not completely understood. In particular, the separate-effects of spacer grids for interfacial shear in rod bundles at low pressures, in dispersed flow film boiling, and in transition boiling heat transfer during reflood, are not known. It is necessary to determine the grid geometry effects. The RBHT program, which will explore two or more types of space grids and will perform heat transfer measurements in various flow regions at locations just before and after the spacer grids, will greatly augment the database needed for modeling the spacer grid effects.

4. There is insufficient data on transition boiling heat transfer during quenching in rod bundles. This is especially true regarding the minimum film boiling temperature. For reflood conditions where precursory cooling is important, the transition regime is responsible for the final quench and most likely controls the quench front propagation. The emphasis of the RBHT program to measure the local values of the void fraction in the quench front region will provide the much-needed database.

5. When the flow at the quench front is subcooled, an inverted annular film boiling (IAFB) regime would develop immediately downstream of the quench front. The liquid-rich region provides the precursory cooling that controls the quench front velocity and provides the source of vapor and entrained liquid for the DFFB region. It has been demonstrated that many of the apparent functional dependencies for the IAFB regime are primarily due to the axial profile of the void fraction in this region. Currently available data for this regime in rod bundles is insufficient for model development due to the coarse spacing used for the void fraction measurements. The RBHT program will address this data need through the use of finely spaced DP cells and by a local void fraction measurement provided by a low energy gamma-densitometer.

6. The heat transfer rate in the IAFB region increases rapidly with liquid subcooling. Higher subcooling promotes heat transfer to the liquid core and reduces vapor generation and the thickness of the vapor film, thus enhancing heat transfer. It is traditional to formulate reflood test matrices by fixing the inlet subcooling and then varying the inlet flow rate. This procedure does not provide a true single parameter variation needed for model development at the subcomponent levels. In the RBHT program, non-traditional procedures involving fixing either the local subcooling or the mass flux at constant values at the quench front will be done by choosing appropriate combinations of the inlet flow rate and subcooling in the planned experiments. This will provide important new data not available heretofore.

7. The database in the nucleate boiling regime for void fraction (i.e., interfacial shear) in rod bundles at low-pressure conditions has been identified as a code deficiency during the AP600 code applicability program. Some data exists or can be backed out of other reflood test data after the bundle has quenched. The RBHT can be conveniently used to generate, for negligible additional costs, a comprehensive database with systematic variation of parameters that would greatly aid model development and assessment.

The various technical issues discussed above provide clear justifications for the need for developing the RBHT facility. Separate-effects tests will be performed in this facility to obtain new or improved data for model development and code validation at the most fundamental subcomponent levels.

Table 3.2 Previous Studies Relevant to the High-Ranking Phenomena During the Reflood Stage of a Large Break LOCA

Region of Interest	High-Ranking Phenomena	Basis: Uncertainty and Impact on PCT	Citation of the Relevant Literature
Single-Phase Liquid HT Region	Decay Power	Source of Energy for Rods, Boundary Condition for Tests. Minimum Uncertainty.	N/A. Known Measured Initial Condition.
Subcooled and Saturated Boiling Region	Decay Power	Source of Energy for Rods, Boundary Condition for Tests. Minimum Uncertainty.	N/A. Known Measured Initial Condition.
Quench Front	Fuel Rod Material Properties Effects on Rod Quench	Material Properties (r, c_p, k) Affect the Stored Energy in the Fuel/Heater Rod and Its Quench Rate, Uncertainty Directly Impacts PCT.	[28], [29], [31], [100], [162], [185], [189], [227], [248], [260], [267], R1, R2, R4-R7.
Quench Front	Cladding Surface Effects on Rod Quench	The Cladding Surface Effects (Oxides, Roughness, Material, T_{min} and T_{CHF}) have Large Uncertainty and Impact on PCT. Oxide Layer Quenches Sooner Due to Low k. In addition, Roughness from Oxide Promotes Easier Quenching. Needs to Estimate T_{min} and T_{CHF}. Large Uncertainty.	[28], [29], [31], [69], [71], [92], [95], [107], [121], [147], [185], [188], [189], [209], [224], [241], [260], [267], [272], [307], R1, R2, R4.
Quench Front	Transition Boiling Heat Transfer	The Rate of Heat Release at the Quench Front Directly Impacts PCT. Large Uncertainty.	[33], [59], [115], [116], [135], [193], [197], [224], [241], [250], [316], R1-R3, R27, R28.
Quench Front	Steam Generation at Quench Front	The Rapid Generation of Steam at the Quench Front Leads to the Onset of Liquid Entrainment, Important Impact on PCT with Large Uncertainty.	[19], [89], [116], [132], [135], [149], [155], [205], [223], [241], [250], [254], [277], [301], [316], R6-R8.
Quench Front	Decay Power	Source of Energy for Rods, Boundary Conditions for Tests. Minimum Uncertainty.	N/A. Known Measured Initial Condition.
Quench Front	Liquid Entrainment at Quench Front Which Includes the Initial Drop Size and Droplet Number Density	Liquid Entrainment Cools the PCT Location Downstream and Directly Impacts PCT. High Uncertainty.	[6], [15], [51], [52], [56], [108], [117], [125], [126], [132], [139], [155], [165], [180], [183], [203], [219], [223], [228], [249], [278], [297], [301], [321], R6-R8, R27, R28.

Table 3.2 Previous Studies Relevant to the High-Ranking Phenomena During the Reflood Stage of a Large Break LOCA (Continued)

Region of Interest	High-Ranking Phenomena	Basis: Uncertainty and Impact on PCT	Citation of the Relevant Literature
Quench Front	Rewet Temperature	Determine the Quench Front Point on the Fuel Rod. Large Uncertainty.	[69], [92], [121], [122], [147], [208], [224], [301], [303], R1, R2, R4.
Quench Front	Void Fraction / Flow Regime	Determines the Wall Heat Transfer Since Large Void Results in Dispersed Flow, Whereas Small Void Results in Film Boiling. Directly Impacts PCT. Large Uncertainty.	[14], [15], [61], [65], [139], [165], [184], [236], [316], R6-R8, R14-R18, R21-R28
Quench Front	Interfacial Area	Determines the Initial Configuration of the Liquid as It Enters the Transition Region. Directly Impacts Liquid/Vapor Heat Transfer and Resulting PCT Downstream. Large Uncertainty.	[7], [8-10], [46-48], [127], [129], [135], [141], [142], [153], [242], [293], R6, R7, R8.
Froth Region	Decay Power	Source of Energy for Rods, Boundary Conditions for Tests. Minimum Uncertainty.	N/A. Known Measured Initial Condition.
Froth Region	Void Fraction / Flow Regime	Helps Determine the Amount of Vapor-Liquid Heat Transfer Which Affects the Downstream Vapor Temperature at PCT. Large Uncertainty.	[14], [15], [18], [65], [115], [165], [184], [236], [244], [319], R6-R8, R14-R18.
Froth Region	Liquid Ligaments, Drop Sizes, Droplet Number Density, Interfacial Area	Determines the Interfacial Heat Transfer in the Transition Region. Large Uncertainty.	[2], [6], [11], [22], [46-48], [51], [52], [304], [305], [308], [315], [319-321], R6-R8.
Froth Region	Film Boiling Heat Transfer at Low Void Fractions	This Includes Convective Vapor Heat Transfer, Direct Contact Heat Transfer, Radiation Heat Transfer, etc. Large Uncertainty.	[21], [58], [92], [107], [115], [193], [195], [196], [217], [255], [283], [307], R1-R11.
Froth Region	Direct Contact Heat Transfer	Wall Temperature Is Low Enough to Allow Direct Droplet Contact Heat Transfer to the Wall with a Very High Heat Transfer Rate. Large Uncertainty.	[13], [30], [50], [68], [69], [74], [92], [107], [123], [146], [178], [208], [221], [222], [224], [253], [303], [307].

Table 3.2 Previous Studies Relevant to the High-Ranking Phenomena During the Reflood Stage of a Large Break LOCA (Continued)

Region of Interest	High-Ranking Phenomena	Basis: Uncertainty and Impact on PCT	Citation of the Relevant Literature
DFFB Region	Decay Power	Source of Energy for Rods, Boundary Conditions for Tests. Minimum Uncertainty.	N/A. Known Measured Initial Condition.
DFFB Region	Dispersed Flow Film Boiling	Directly Impacts PCT, High Uncertainty in Modeling	[3], [5], [7-10], [12], [34], [37], [39], [44], [59], [89], [105], [109-111], [136], [137], [142], [143], [153], [186], [188], [192], [201], [202], [217], [219], [225], [250], [255], [268], [279], [295], [296], [300], [301], [306]m [310], [318], R1-R13, R19-R26.
DFFB region	Convection to Superheated Vapor	Principal Mode of Heat Transfer, Directly Impacts PCT. Large Uncertainty.	[8-10], [19], [66], [77], [82], [89], [94], [105], [118], [136], [137], [143-145], [148], [149], [153], [186], [192], [201], [207], [230], [250], [268], [295], [296], [300], [306], [310], R1-R8, R12, R13.
DFFB Region	Drop Sizes, Droplet Number Density, Interfacial Area	Determines the Interfacial Heat Transfer in the DFFB Region. Large Uncertainty.	[54-56], [58], [72], [79], [83], [85], [96], [98], [106], [108], [116], [117], [125], [130], [131], [133], [135], [139], [154], [155], [157-159], [163], [165], [175-177], [180-183], [187], [190], [199], [203], [206], [212], [219], [223], [226], [228], [233], [235], [238], [239], [241], [242], [247], [249], [256], [278], [288-290], [293-295], [297], [301].

Table 3.2 Previous Studies Relevant to the High-Ranking Phenomena During the Reflood Stage of a Large Break LOCA (Continued)

Region of Interest	High-Ranking Phenomena	Basis: Uncertainty and Impact on PCT	Citation of the Relevant Literature
DFFB Region	Dispersed Phase Enhancement of Convective Heat Transfer	Important Impact on PCT as the Enhancement Can Be Over 50 Percent in Some Cases. Large Uncertainty.	[4], [23], [24], [27], [40], [57], [61], [67], [77], [80], [81], [103], [114], [150-152], [156], [245], [246], [251], [261], [264], [265], [269], [291], R1, R2, R4.
DFFB Region	Droplet to Vapor Interfacial Heat Transfer	The Interfacial Heat Transfer Reduces the Vapor Temperature (i.e., De-superheat) Which Is the Heat Sink for the Wall Heat Flux. Large Uncertainty.	[18], [70], [79], [86], [87], [102], [113], [114], [123], [151], [160], [163], [198], [216], [231], [237], [266], [274], [277], [302], [308], [317], R1, R2, R5-R8, R21, R23-R26.
DFFB Region	Radiation Heat Transfer Between Surfaces, Vapor, and Droplets	Very Important at High Bundle Elevations Where the Convective Heat Transfer Is Small Due to Large Vapor Superheat. Very Important for BWR Reflood with Sprays and Cold Surrounding Surfaces. Large Uncertainty.	[37], [44], [62], [89], [102], [109-111], [137], [188], [192], [251], [261], [262], R1-R8, R13, R19, R20, R25.
DFFB Region	Interfacial Shear and Droplet Velocity	Effects the Void Fraction Distribution and Resulting Droplet Velocity in the Entrained Flow. Large Uncertainty.	[11], [26], [41], [101], [104], [105], [127-129], [139], [166-174], [177], [205], [263], [269], [290], [292], R6-R8.
Spacer Grids	Effects of Spacer Grids on Droplet Deposition, Breakup, and Heat Transfer	Important Enhanced Cooling Mechanism Especially in the Froth and DFFB Regions Due to Their Effects in Droplet Evolution and Flow Restructuring. Large Uncertainty.	[2], [17], [32], [38], [42], [43], [49], [53], [93], [112], [119], [120], [138], [166-174], [232], [252], [257-259], [286], [308], [309], [312-314], R6-R8, R9-R11, R21-R26.
Inlet Region	Inlet Flow Oscillation	Directly Impacts the Flooding Behavior, Inducing Large Oscillations in Void Fraction and Wall Temperature, Increasing Entrainment and Initial Liquid Carryover, Altering the Speed of Quench Front Propagation. Large Uncertainty.	[33], [36], [49], [88], [145], [204], [213], [214], [287], R21-R26.

3.5 References

3.5.1 Rod Bundle Tests

1. Rosal, E. R., et al., “FLECHT Low Flooding Rate Cosine Test Series Data Report,” WCAP-8651, Dec. 1975.

2. Lilly, G. P., H. C. Yeh, L. E. Hochreiter, and N. Yamaguchi, “PWR FLECHT Cosine Low Flooding Rate Test Series Evaluation Report,” WCAP-8838, Mar. 1977.

3. Rosal, E. R., et al., “FLECHT Low Flooding Rate Skewed Test Series Data Report,” WCAP-9108, May 1977.

4. Lilly, G. P., H. C. Yeh, C. E. Dodge, and S. Wong, “PWR FLECHT Skewed Profile Low Flooding Rate Test Series Evaluation Report,” WCAP-9183, Nov. 1977.

5. Loftus, M. J., et al., “PWR FLECHT SEASET 21-Rod Bundle Flow Blockage Task Data and Analysis Report,” NUREG/CR-2444, EPRI NP-2014, WCAP-992, Vol. 1, Vol. 2, Sept. 1982.

6. Loftus, M. J., et al., “PWR FLECHT-SEASET Unblocked Bundle Forced and Gravity Reflood Task Data Report,” NUREG/CR- 1532, June 1980.

7. Lee, N., S. Wong, H. C. Yeh, and L. E. Hochreiter, “PWR FLECHT-SEASET Unblocked Bundle Forced and Gravity Reflood Task, Data Evaluation and Analysis Report,” Feb. 1982.

8. Wong, S. and L. E. Hochreiter, “PWR FLECHT-SEASET Analysis of Unblocked Bundle Steam-Cooling and Boil-off Tests,” NUREG/CR-1533, January 1981.

9. Ihle, P. and K. Rust, “FEBA – Flooding Experiments with Blocked Arrays Evaluation Report,” KFK 3657, Mar. 1984.

10. Ihle, P. and K. Rust, “FEBA – Flooding Experiments with Blocked Arrays Data Report 1, Test Series I through IV,” KFK 3658, Mar. 1984.

11. Ihle, P. and K. Rust, “FEBA – Flooding Experiments with Blocked Arrays Data Report 2, Test Series V through VIII,” KFK 3659, Mar. 1984.

12. Mullins, C. B., et al., “ORNL Rod Bundle Heat Transfer Test Data,” NUREG/CR-2525, Vol. 1 to Vol. 5, 1982.

13. Yoder, G. L., et al., “Dispersed Flow Film Boiling in Rod Bundle Geometry – Steady State Heat Transfer Data and Correlations Comparisons,” NUREG/CR-24351, 1982.

14. Becker, K. M., J. Flinta, and O. Nylund, “Dynamic and Static Burnout Studies for the Full Scale 36-Rod Marviken Fuel Element in the 8 MW Loop FRIGG,” Paper presented at the Symposium on Two-Phase Flow Dynamics, Eindhoven, Sept. 1967.

15. Nylund, O., et al., “Measurements of Hydrodynamic Characteristics, Instability Thresholds, and Burnout Limits for 6-Rod Clusters in Natural and Forced Circulation,” ASEA and AB Atomenergi Report FRIGG-1, 1967.

16. Nylund, O., K. M. Becker, R. Eklund, O. Gelium, I. Haga, G. Herngorg, Z. Rouhani, and F. Åkerhielm, “Hydrodynamic and Heat Transfer Measurements on a Full Scale Simulated 36-Rod Marviken Fuel Element with Uniform Heat Flux Distribution,” ASEA and AB Atomenergi Report FRIGG-2, 1968.

17. Lahey, R. T. and F. A. Schraub, “Mixing, Flow Regimes, and Void Fraction for Two-Phase Flow in Rod Bundles,” Two-Phase Flow and Heat Transfer in Rod Bundles, ASME, Nov. 1969.

18. Lahey, R. T., B. S. Shiralkar, and D. W. Radcliff, “Two-Phase Flow and Heat Transfer in Multirod Geometries: Subchannel and Pressure Drop Measurements in a Nine-rod Bundle for Diabatic and Adiabatic Conditions,” GEAP-13049, AEC.

19. Mohr, C. L., et al., “Data Report for Thermal-Hydraulic Experiment 2 (TH-2),” NUREG/CR-2526, PNL-4164, Nov. 1982.

20. Mohr, C. L., et al., “Data Report for Thermal-Hydraulic Experiment 3 (TH-3),” NUREG/CR-2527, PNL-4165, Mar. 1983.

21. Denham, M. K., D. Jowitt, and K. G. Pearson, “ACHILLES Unballooned Cluster Experiments, Part 1: Description of the ACHILLES Rig, Test Section, and Experimental Procedures,” AEEW-R2336, Winfrith Technology Centre (Commercial in Confidence), Nov. 1989.

22. Denham, M. K. and K. G. Pearson, “ACHILLES Unballooned Cluster Experiments, Part 2: Single Phase Flow Experiments,” AEEW-R2337, Winfrith Technology Centre (Commercial in Confidence), May 1989.

23. Pearson, K. G. and M. K. Denham, “ACHILLES Unballooned Cluster Experiments, Part 3: Low Flooding Rate Reflood Experiments,” AEEW-R2339, Winfrith Technology Centre (Commercial in Confidence), June 1989.

24. Pearson, K. G. and M. K. Denham, “ACHILLES Unballooned Cluster Experiments, Part 4: Low Pressure Level Swell Experiments,” AEEW-R2339, Winfrith Technology Centre (Commercial in Confidence), July 1989.

25. Dore, P. and M. K. Denham, “ACHILLES Unballooned Cluster Experiments, Part 5: Best Estimate Experiments,” AEEW-R2412, Winfrith Technology Centre (Commercial in Confidence), July 1990.

26. Dore, P. and D. S. Dhuga, “ACHILLES Unballooned Cluster Experiments, Part 6: Flow Distribution Experiments,” AEA-RS-1064, Winfrith Technology Centre (Commercial in Confidence), Dec. 1991.

27. Tuzla, K., C. Unal, O. Badr, S. Neti, and J. C. Chen, “Thermodynamic Non-equilibrium in Post-Critical-Heat-Flux Boiling in a Rod Bundle,” NUREG/CR-5095, Vol. 1-4, June 1988.

28. Unal, C., K. Tuzla, O. Badr, S. Neti, and J. C. Chen, “Convective Boiling in a Rod Bundle: Traverse Variation of Vapor Superheat Temperature Under Stabilized post-CHF Conditions,” Int. J. Heat and Mass Transfer, Vol. 34, No. 7, pp. 1695-1706, 1991.

3.5.2 Single Tube Tests and Related Studies

1. Adams, J. E. and A. J. Clare, “A Preliminary Study of Droplet Breakup at PWR Spacer Grids,” PWR/HTWG/P 130, 1983.

2. Adams, J. E. and A. J. Clare, “Droplet Break-up and Entrainment at PWR. Spacer Grids,” First Int. Workshop on Fundamental Aspects of Post-Dryout Heat Transfer, Salt Lake City, Utah, NUREG/CP-0060, April 2-4, 1984.

3. Afifi, J., “Evaluation of Some Large “Best Estimate” Computer Codes for the Prediction of Loss of Coolant Accidents in Light Water Reactors,” Ph.D. Thesis, University of London, 1985.

4. Aihara, T., “Augmentation of Convective Heat Transfer by Gas-Liquid Mist,” CONF-900803, pp. 445-462, 1990.

5. Akimoto, H. and Y. Murao, “Current Experiment Status and Future Plan for Reflood Tests at Japan Atomic Energy Research Institute,” paper presented at ICAP Post-CHF Meeting, Winfrith, England, June 22-25, 1987.

6. Almenas, K. and R. Lee, “Droplet Deposition Above a Quench Front During Reflood,” Trans. American Nuclear Society, Vol. 43, pp. 787-788, 1982.

7. Andreani, M. and G. Yadigaroglu, “A Mechanistic Eulerian-Lagrangian Model for Dispersed Flow Film Boiling,” CONF-9005311, pp. 423-432, 1991.

8. Andreani, M. and G. Yadigaroglu, “Difficulties in Modeling Dispersed-Flow Film Boiling,” Waeme- und Stoffuebertragung (Germany), Vol. 27:1, pp. 37-49, Oct. 1991.

9. Andreani, M. and G. Yadigaroglu, “Dispersed Flow Film Boiling: An Investigation of the Possibility to Improve the Models Implemented in the NRC Computer Codes for the Reflood Phase for the LOCA,” NUREG/IA-0042, Aug. 1992.

10. Andreani, M. and G. Yadigaroglu, “Prediction Methods for Dispersed Flow Film Boiling,” Int. Journal Multiphase Flow, Vol. 20, pp. 1-51, 1994.

11. Ardron, K. A. and P. C. Hall, “Droplet Hydrodynamics and Heat Transfer in the Dispersed Flow Regime in Bottom Flooding,” CEGB, RD/B/5007N81, University of California at Berkeley, 1981.

12. Arrieta, L. and G. Yadigaroglu, “An Analytical Model for Bottom Reflooding Heat Transfer in Light Water Reactors (UNFLOOD Code),” EPRI-NP-756, 1978.

13. Ayyaswamy, P. S., “Direct-Contact Transfer Precesses with Moving Liquid Droplets,” Advances in Heat Transfer, Vol. 26, pp. 1-105, 1995.

14. Banerjee, S., P. Yeun, and M. A. Vanderbroek, “Calibration of Fast Neutron Scattering Technique for Measurement of Void Fraction in Rod Bundles,” J. Heat Transfer, Vol. 101, May 1979.

15. Barnea, Y. and E. Elias, “Flow and Heat Transfer Regimes During Quenching of Hot Surfaces,” Int. Journal Heat Mass Transfer, Vol. 37, pp. 1441-1453, 1994.

16. Barzoni, G., “A Study on Postdryout Heat Transfer for Conditions of Interest in Loss of Coolant Accident Ananysis,” CISE-1616, P. 31, 1980.

17. Becker, K. H., and C. M. Hernborg, “Measurements of the Effects of Spacers on the Burnout Conditions for Flow Boiling Water in a Vertical Annulus and a Vertical 7-Rod Cluster,” AE-165, 1964.

18. Bellan, J. and K. Harstad, “Analysis of the Convective Evaporation of Nondilute Clusters of Drops,” Int. Journal Heat Mass Transfer, Vol. 30, No. 1, pp. 125-136, 1987.

19. Bennett, A. W., G. F. Hewitt, H. A. Kearsey and R. F. K. Keeys, “Heat Transfer to Steam-Water Mixtures Flowing in Uniformly Heated Tubes in Which the Critical Heat Flux Has Been Exceeded,” AERE-R-5373, 1967.

20. Benodekar, R. W., and A. W. Date, “Numerical Prediction of Heat-Transfer Characteristics of Fully Developed Laminar Flow Through a Circular Channel Containing Rod Clusters,” Int. Journal Heat Mass Transfer, Vol. 21, pp. 935-945, 1978.

21. Berenson, P. J., “Film Boiling Heat Transfer from a Horizontal Surface,” Journal Heat Transfer, Vol. 83, pp. 351-358, 1961.

22. Binder, J. L. and T. J. Hanratty, “A Diffusion Model for Droplet Deposition in Gas-Liquid Annular Flow,” Int. Journal multiphase Flow, Vol. 17, pp. 1-9, 1991.

23. Boothroyd, R. G. and H. Hague, “Fully Developed Heat Transfer to a Gaseous Suspension of Particles Flowing Turbulently in Ducts of Different Size,” Journal Mechanical Engineering Science, Vol. 12, No. 3, pp. 191-200, 1970.

24. Boothroyd, R. G., “Similarity in Gas-Born Flowing Particulate Suspensions,” ASME Paper No. 68-MH-11, 1968.

25. Boyack, B., “AP600 Large Break Loss-of-Coolant Accident Phenomena Identification and Ranking Tabulation,” LA-UR-95-2718, 1995.

26. Brauner, N. and D. M. Maron, “Dynamic Model for the Interfacial Shear as a Closure Law in Two-Fluid Models,” Nuclear Engineering and Design, Vol. 149, pp. 67-79, 1994.

27. Briller, R., and R. L. Peskin, “A Mechanistic Approach to Gas Solid Suspension Heat Transfer and Friction Factors,” Augmentations of Convective Heat & Mass Transfer, ASME, New York, pp. 124-133, 1970.

28. Broughton, J. M., D. W. Golden, and P. E. MacDonald, “Assessment of Nuclear Fuel Rod and Solid Electric Heater Thermal Behavior During the Heatup and Reflood Phases of a Large Break LOCA,” CONF-810802-23, P. 12, 1981.

29. Carajilescov, P., “Limits of the Simulation of a Nuclear Fuel Pin by an Electrically Heated Rod,” CONF-921234, P. 3, 1992.

30. Carbajo, J. J., and A. D. Siegel, “A Review and Comparison Among the Different Models for Rewetting in LWR’s,” Nucl. Engr. Design, Vol. 58, pp. 33-44, 1980.

31. Casal, V., S. Malang, and K. Rust, “Comparison of Thermal Behavior of Different PWR Fuel Rod Simulators for LOCA Experiments,” KFK-3416-B, P. 2, Oct. 1982.

32. Cha, J. H. and H. G. Jun, “Air-Water Flooding in Multirod Channels: Effects of Spacer Grids and Blockage,” Journal Korean Nucl. Soc., Vol. 30, pp. 381-393, 1993.

33. Cha, Y. S., R. E. Henry, and P. A. Lottes, “An Experimental Investigation of Quench Front Movement During Bottom Reflood of a Vertical Tube Under Forced-Oscillation Conditions,” ANL/RAS/LWR-80-1, Jan. 1980.

34. Chen, J. C., “A Short Review of Dispersed Flow Heat Transfer in Post-Dryout Boiling,” Nucl. Engr. Design, Vol. 95, pp. 375-383, 1984.

35. Chen, J. C., F. T. Ozkaynak and R. K. Sundaram, “Vapor Heat Transfer in Post-CHF Region Including the Effect of Thermodynamic Non-equilibrium,” Nucl. Engineering and Design, Vol. 59, pp. 143-155, 1979.

36. Cheung, Y. L. and P. Griffith, “Gravity Reflood Oscillations in a Pressurized Water Reactor,” NUREG/CR-1314, 1980.

37. Chiou, J. S. and L. E. Hochreiter, “Combined Radiation and Dispersed Flow Film Boiling in BWR Rod Bundles with Top Spray,” Proceedings of the 26th Natl. Heat Transfer Conference, Philadelphia, PA, Aug. 1989.

38. Chiou, J. S., L. E. Hochreiter, M. J. Lottus, M. Y. Young, J. Chao, C. Chui, “Effects of Spacer Grids on Thermal Hydraulic Performance During a Postulated Reflood Transient,” CONF-841075, 1984.

39. Choi, J. H., S. Y. Lee, and S. K. Kim, “Incorporation of Droplet Breakup Model at Spacer Grid into RELAP/MOD2,” J. Korean Nuclear Society, Vol. 22:4, pp. 326-336, Dec. 1990.

40. Chu, N. C., “Turbulent Heat Transfer of Gas-Solid Two-Phase Flow in Circular Tubes,” Ph.D. Thesis, Department of Mechanical Engineering, University of Washington, 1971.

41. Chuchottaworn, P. and K. Asano, “Calculation of Drag Coefficients on an Evaporating or Condensing Droplet,” Journal of Chem. Engineering of Japan, Vol. 18, pp. 91-94, 1985.

42. Chung, J. B., “An Experimental Study of the Effects of the Mixing Vane of the CHF in the Low-Pressure, Low-Flow Conditions,” M.S. Thesis, KAIST, Korea, 1995.

43. Chung, J. B., W. P. Baek and S. H Cheng, “Effects of Spacer and Mixing Vanes on Critical Heat Flux for Low-Pressure Water at Low-Velocities,” Int. Comm. Heat Mass Transfer, Vol. 23, pp. 757-765, 1996.

44. Chung, J. N. and S. I. Olafsson, “Two-Phase Droplet Flow Convective and Radiative Heat Transfer,” Int. Journal Heat Mass Transfer, Vol. 27, No. 6, pp. 901-910, 1984.

45. Chung, M. K., S. H. Lee, C. K. Park, and Y. W. Lee, “Reflood Experiments with Horizontal and Vertical Flow Channels,” Journal Korean Nucl. Soc., Vol. 12, pp. 153-162, 1980.

46. Clare, A. J. and S. A. Fairbairn, “Droplet Dynamics and Heat Transfer in Dispersed Two-Phase Flow,” The First Int. Workshop on Fundamental Aspects of Post-Dryout Heat Transfer, Salt Lake City, Utah, NUREG/CP-0060, April 2-4, 1984.

47. Clare, A. J., S. A. Fairbairn, and H. C. Simpson, “Droplet Dynamics and Heat Transfer in Dispersed Two-Phase Flow,” CONF-840709, pp. 49-71, 1984.

48. Clare, A. J., S. A. Fairbairn, E. Skupinski, B. Tolley, and J. Vilain, “Droplet Dynamics and Heat Transfer in Dispersed Two-Phase Flow,” CONF-8410331, pp. 51-62, 1985.

49. Clement, P., R. Deruazz, and J. M. Viteau, “Reflooding of a PWR Bundle Effect of Inlet Flow Rate Oscillations and Spacer Grids,” Jun. 1982.

50. Cokmez-Tuzla, A. F., K. Tuzla, and J. C. Chen, “Experimental Assessment of Liquid-Wall Contacts in Post-CHF Convective Boiling,” Nucl. Engr. Design, Vol. 139, pp. 97-103, 1993.

51. Coulaloglou, C. A. and L. L. Tavlarides, “Droplet Size Distribution and Coalescence Frequencies of Liquid-Liquid Dispersions in Flow Vessels,” AIChE Journal, Vol. 22, No. 2, pp. 289-296, Mar. 1976.

52. Cousins, L. B. and C. F. Hewitt, “Liquid Phase Mass Transfer in Annular Two-Phase Flow: Droplet Deposition and Liquid Entrainment,” UK AEA Report AERE-R5657, 1968.

53. Crecy, F. de., “The Effect of Grid Assembly Mixing Vanes on Critical Heat Flux Values and Azimuthal Location in Fuel Assemblies,” Sixth Int. Topical Mtg. Nuclear Reactor Thermal Hydraulics, Grenoble, France, 1993.

54. Cumo, M., G. E. Farello, G. Ferrari and G. Palazzi, “On Two-Phase Highly Dispersed Flows,” ASME Paper 73-HT-18, 1973.

55. Dallman, J. C. and W. L. Kirchner, “De-entrainment Phenomena on Vertical Tubes in Droplet Cross Flow,” NUREG/CR-1421, April 1980.

56. Dallman, J. C., B. E. Jones and T. J. Hanratty, “Interpretation of Entrainment Measurements in Annular Gas-Liquid Flow,” Two-Phase Momentum Heat Mass Transfer, Vol. 2, pp. 681-705, 1979.

57. Danziger, W. J., “Heat Transfer to Fluidized Gas-Solids Mixtures in Vertical Transport,” I&EC Process Design and Development, Vol. 2, No. 4, pp. 269-276, 1963.

58. De Jarlais, G., “An Experimental Study on Inverted Annular Flow Hydrodynamics Utilizing on Adiabatic Simulation,” NUREG/CR-3339, 1983.

59. De Salve, M., B. Panella, C. Chin and G. Brown, “Validation of a Bottom Flooding Model,” 3rd Int. Mtg. Nuclear Reactor Thermal Hydraulics, 1985.

60. De Young, T. L. and M. P. Plessinger, “Fist Bundle Void Fractions,” Idaho Natl. Engineering Laboratory, Oct. 1986.

61. Depew, C. A., and T. J. Kramer, “Heat Transfer to Flowing Gas-Solid Mixtures,” Advances on Heat Transfer, Vol. 9, pp. 113-180, 1973.

62. Deruaz, R. and B. Petitpain, “Modelling of Heat Transfer by Radiation During the Reflooding Phase of LWR,” Proc. of the Specialist Meet on the Behavior of the Fuel Elements under Accident Conditions, Spatind, Norway, September 13-16, 1976.

63. Dhir, V. K. and I. Catton, “Reflood Experiments with a 4-Rod Bundle,” EPRI-NP-1277, 1979.

64. Dougal, R. L. and W. M. Rohsenow, “Film Boiling on the Inside of Vertical Tubes with Upward Flow of the Fluid at Low Qualities,” MIT-TR-9079-26, 1963.

65. Dowlati, R., M. Kawaji, D. Chisholm, and A. Chen, “Void Fraction Predication on Two-Phase Flow Across a Tube Bundle,” AIChE Journal, Vol. 38, pp. 619-622, 1992.

66. Drucker, M. and V. K. Dhir, “Studies of Single- and Two-Phase Heat Transfer in a Blocked Four-Rod Bundle,” EPRI-NP-3485, Jun. 1984.

67. Drucker, M. I., V. K. Dhir and R. B. Duffey, “Two-Phase Heat Transfer for Flow in Tubes and Over Rod Bundles with Blockages,” Journal Heat Transfer, Vol. 106, pp. 856-864, 1984.

68. Dua, S. S., and C. L. Tien, “Two-Dimensional Analysis of Conduction Controlled Rewetting with Precursory Cooling,” Journal Heat Transfer, Vol. 98, pp. 407-413, 1976.

69. Duffey, R. B. and D. T. C. Porthouse, “The Physics of Rewetting in Water Reactor Emergency Core Cooling,” Nucl. Engr. Design, Vol. 25, pp. 379-394, 1973.

70. Duncan, J. D. and J. E. Leonard, “Heat Transfer in a Simulated BWR Fuel Bundle Cooled by Spray Under Loss of Coolant Conditions,” GEAP-13086, Paper II-2, 1972.

71. Dwyer, O. E. and H. C. Berry, “Effects of Cladding Thickness and Thermal Conductivity on Heat Transfer for Laminar In-line Flow Through Rod Bundles,” Nuclear Science & Engineering, Vol. 42, pp. 69-80, 1970.

72. El Kassaby, M. M. and E. N. Ganic, “A Further Study in Drop Deposition,” Multiphase Flow and Heat Transfer III, Part A, ed. Veziroglu and Bergles, Elsevier Science Publishers B. V., Amsterdam, 1984.

73. El-Genk, M. S., J. S. Philbin, and F. C. Foushee, “Research Program: The Investigation of Heat Transfer and Fluid Flow at Low Pressure,” CONF-8604117-3, 1986.

74. Elias, E. and G. Yadigaroglu, “A General One-Dimensional Model for Conduction Controlled Rewetting of a Surface,” Nucl. Engr. Design, Vol. 42, pp. 184-194, 1977.

75. Era, A., G. P. Gaspari, A. Hassid, A. Milani and R. Zavattarelli, “Heat Transfer Data in the Liquid Deficient Region for Steam-Water Mixtures at 70 kg/cm2 Flowing in Tubular and Annular Conduits,” CISE-R-184, June 1966.

76. Evans, D. G., S. W. Webb and J. C. Chen, “Measurement of Axially Varying Non-equilibrium in Post-Critical-Heat-Flux Boiling in a Vertical Tube,” NUREG/CR-3363, June 1983.

77. Evans, D. G., S. W. Webb, and J. C. Chen, “Axially Varying Superheats in Convective Film Boiling,” J. Heat Transfer, Vol. 107, Aug. 1985.

78. Evans, D., “Experimental Data for Non-equilibrium Post-CHF Heat Transfer in a Vertical Tube,” Proc. 10th Water Reactor Safety Information Meeting, Vol. 1, pp. 227-231, 1983.

79. Faeth, G. M., “Evaporation and Combustion of Sprays,” Prog. Energy Comb. Sci., Vol. 9, pp. 1-76, 1983.

80. Farbar, L. and C. A. Depew, “Heat Transfer Effects to Gas-Solids Mixtures Using Spherical Particles of Uniform Size,” Industrial and Engineering Chemistry-Fundamentals, Vol. 2, No. 2, pp. 130-135, 1963.

81. Farbar, L., and M. J. Morley, “Heat Transfer to Flowing Gas-Solids Mixtures in a Circular Tube,” Industrial and Engineering Chemistry, Vol. 49, No. 7, pp. 1143-1150, 1957.

82. Forslund, R. P. and W. M. Rohsenow, “Dispersed Flow Film Boiling,” Journal Heat Transfer, Vol. 90, pp. 399-407, 1968.

83. Ganic, E. N. and K. Mastanajah, “Investigation of Droplet Deposition from a Turbulent Gas Stream,” Int. Journal Multiphase Flow, Vol. 7, pp. 401-422, 1981.

84. Ganic, E. N. and W. M. Rohsenow, “Dispersed Flow Heat Transfer,” Int. Journal Heat Mass Transfer, Vol. 20, pp. 855-866, 1977.

85. Ganic, E. N. and W. M. Rohsenow, “On the Mechanism of Liquid Drop Deposition in Two-Phase Dispersed Flow,” Journal Heat Transfer, Vol. 101, pp. 288-294, 1979.

86. Gaugler, R. E., “An Experimental Study of Spray Cooling of High Temperature Surfaces,” Dept. of Mech. Eng., Carnegie Inst. Of Tech., Pittsburgh, PA, July 1966.

87. Ghazanfari, A., “Instationary Heat Transfer in a Droplet Flow After Exceeding of the Wetting Temperature,” CONF-780465, pp. 150-153, 1978.

88. Ghazanfari, A., E. F. Hicken and A. Ziegler, “Unsteady Dispersed Flow Heat Transfer Under Loss of Coolant Accident Related Conditions,” Nucl. Technology, Vol. 51, pp. 21-26, 1980.

89. Ghiaasiaan, S. M., “On Multi-Dimensional Thermal-Hydraulics and Two-Phase Phenomena During Reflooding of Nuclear Reactor Cores,” Ph.D. Dissertation, University of California at Los Angeles, 1983.

90. Gottula, R. C., R. A. Nelson, J. C. Chen, S. Neti, and R. K. Sandaram, “Forced Convective, Non-equilibrium, Post-CHF Heat Transfer Experiments in a Vertical Tube,” ASME-JSME Thermal Engineering Conference, Honolulu, Mar. 1983.

91. Gottula, R. C., R. G. Condie, R. K. Sandaram, S. Neti, J. C. Chen, and R. A. Nelson, “Forced Convective, Non-equilibrium, Post-CHF, Heat Transfer Experiment Data and Correlation Comparison Report,” Idaho Natl. Engineering Laboratory Report EGG-2245, NUREG/CR-3193, Mar. 1985.

92. Groeneveld, D. C. and J. C. Stewart, “The Minimum Film Boiling Temperature for Water During Film Boiling Collapse,” Proc. 7th Int. Heat Transfer Conf., Munich, Germany, Vol. 4, pp. 393-398, 1982.

93. Groeneveld, D. C. and W. W. Yousef, “Spacing Devices for Nuclear Fuel Bundles: A Survey of their Effect on CHF, Post-CHF Heat Transfer and Pressure Drop,” Proc. ANS/ASME Int. Top. Mtg. on Nuclear Reactor T/H, Saratoga Springs, New York, 1980.

94. Groeneveld, D. C., “Post-Dryout Heat Transfer: Physical Mechanisms and a Survey of Prediction Methods,” Nucl. Eng. Des., Vol. 32, pp. 283-294, 1975.

95. Groeneveld, D. C., “The Thermal Behavior of a Heated Surface at and Beyond Dryout,” AECL-4308, Nov. 1972.

96. Hagiwara, Y., K. Suzuki and T. Sato, “An Experimental Investigation on Liquid Droplets Diffusion in Annular-Mist Flow,” Multiphase Transport, Ed. Veziroglu, Hemisphere Publishing Corp., Washington, 1980.

97. Hanratty, T. J. and A. Hershman, “Initiation of Roll Wave,” AIChE Journal, Vol. 7, P. 488, 1961.

98. Hanratty, T. J. and J. M. Engen, “Interaction Between a Turbulent Air Stream and a Moving Water Surface,” AIChE Journal, Vol. 3, P. 299, 1957.

99. Hanratty, T., “Droplet Distribution and Deposition in Gas-Liquid Annular Flow,” CONF-9205147, pp. 1-8, Jul. 1992.

100. Hanson, R. G., “Semiscale Heater Rod Material Property Evaluation,” CONF-801091-2, 1980.

101. Harmathy, T. Z., “Velocity of Large Drops and Bubbles in Media of Infinite and Restricted Extent,” AIChE Journal, Vol. 6, P. 281, 1960.

102. Harpole, G. “Water Droplet Evaporation in High Temperature Surrounds,” ASME Paper 79-WA/HT-6, 1979.

103. Hasegawa, S., R. Echigo, K. Kanemaru, K. Ichimiya and M. Sanui, “Experimental Study of Forced Convective Heat Transfer of Flowing Gaseous Solid Suspension at High Temperature,” Int. Journal Multiphase Flow, Vol. 9, pp. 131-145, 1983.

104. Hassan, Y. A., “Assessment of a Modified Interfacial Drag Correlation in Two-Fluid Model Codes,” Trans. ANS, Vol. 54, P. 211, 1987.

105. Hassan, Y. A., “Dispersed-Flow Heat Transfer During Reflood in a Pressurized Water Reactor After a Large Break Loss-of-Coolant Accident,” Trans. ANS, Vol. 53, P. 326, 1986.

106. Hay, K. J., Z. Lu and T. J. Hanratty, “Relation of Deposition to Drop Size that the Rate Law is Nonlinear,” Int. Journal Multiphase Flow, Vol. 22, pp. 829-837, 1996.

107. Henry, R. E., “A Correlation for the Minimum Film Boiling Temperature,” AIChE Symposium, Vol. 70, No. 138, PP 81-90, 1974.

108. Hewitt, G. F., “Photographic and Entrainment Studies in Two-Phase Flow Systems, AERE-R 4683, 1965.

109. Hochreiter, L. E., A. C. Howards, and B. A. McIntyre, “Heat Transfer Uncertainty Analysis of Transient CHF and Post-CHF Rod Bundle Experiments,” Proceedings of the ASME, Paper 83-HT-106, 1983.

110. Hochreiter, L. E., J. M. Kelly, C. Y. Paik, and M. Y. Young, “Improved Analytical Models for PWR Safety Analysis,” Proceedings of the Transient Phenomena in Multiphase Meeting, Dubrovnik, Yugoslavia, 1987.

111. Hochreiter, L. E., J. M. Kelly, R. J. Kohrt, C. Y. Paik, and D. B. Utton, “Reflood Heat Transfer Models for Rod Bundles with Flow Blockage,” Proceedings of the 1987 ASME/AIChE National Heat Transfer Conference, Pittsburgh, PA, Aug. 1987.

112. Hochreiter, L. E., M. J. Loftus, F. J. Erbacher, P. Ihle, and K. Rust, “Post-CHF Effects of Spacer Grids and Blockages in Rod Bundles,” Private Communication, 1985.

113. Hoffmann, T. W. and L. L. Ross, “A Theoretical Investigation of the Effect of Mass Transfer on Heat Transfer to an Evaporating Droplet,” Int. Journal Heat Mass Transfer, Vol. 15, pp. 599-617, 1972.

114. Holmann, J. P., P. E. Jenkins and F. G. Sullivan, “Experiments on Individual Droplet Heat Transfer Rates,” Int. Journal Heat Mass Transfer, Vol. 15, pp. 1489-1495, 1972.

115. Hsu, Y. Y., “A Tentative Correlation for the Regime of Transition Boiling and Film Boiling During Reflood,” 3rd Water Reactor Safety Information Mtg., 1975.

116. Hughmark, G. A., “Film Thickness, Entrainment, and Pressure Drop in Upward Annular and Dispersed Flow,” AIChE Journal, Vol. 19, P. 1012, 1973.

117. Hutchinson P. and P. B. Whalley, “A Possible Characterization of Entrainment in Annular Flow,” Chem. Engr. Sci., Vol. 28, P. 974, 1973.

118. Hynek, S. J., W. M. Rohsenow, and Bergles, A. E., “Forced-Convective Dispersed-Flow Film Boiling,” MIT Report 70586-63, April 1969.

119. Ihle, P. and K. Rust, “Influence of Spacers on the Heat Transfer During the Flood Phase of a Pressurized Water Reactor Loss-of-Coolant Accident,” ISBN-0303-4003, 1982.

120. Ihle, P., K. Rust, and S. L. Lee, “Experimental Investigation of Reflood Heat Transfer in the Wake of Grid Spacers,” NUREG/CP-0043, Sept. 1982.

121. Iloeje, O. C., D. N. Plummer, W. M. Rohsenow, and P. Griffith, “A Study of Wall Rewet and Heat Transfer in Dispersed Vertical Flow,” MIT Report 72718-92, 1974.

122. Iloeje, O. C., D. N. Plummer, W. M. Rohsenow, and P. Griffith, “An Investigation of the Collapse and Surface Rewet in Film Boiling in Forced Vertical Flow,” J. Heat Transfer, Vol. 97, pp. 166-172, May 1975.

123. Iloeje, O. C., W. M. Rohsenow and P. Griffith, “Three-Step Model of Dispersed Flow Heat Transfer (Post CHF Vertical Flow),” ASME Paper 75-WA/HT-1, 1975.

124. Ishii, M. and G. De Jarlais, “Flow Visualization Study of Inverted Annular Flow of Postdryout Heat Transfer Region,” Nuclear Engineering and Design (Netherlands), Vol. 99, pp. 187-199, Feb. 1987.

125. Ishii, M. and K. Mishima, “Droplet Entrainment Correlation in Annular Two-Phase Flow,” Int. Journal Heat Mass Transfer, Vol. 32, No. 10, P. 1835, 1989.

126. Ishii, M. and K. Mishima, “Correlation for Liquid Entrainment in Annular Two-Phase Flow of Low Viscous Fluid,” NUREG/CR-2885, 1981.

127. Ishii, M. and K. Mishima, “Two-Fluid Models and Hydrodynamic Constitutive Relations,” Nucl. Engr. Design, Vol. 82, pp. 107-126, 1984.

128. Ishii, M. and N. Zuber, “Drag Coefficients and Relative Velocity in Bubbly, Droplet or Particulate Flows,” AIChE Journal, Vol. 25, pp. 843-855, 1979.

129. Ishii, M. and S. T. Revankar, “Measurements of Local Interfacial Area and Velocity in Bubbly Flow,” HTC-Vol. 5, P. 181, Best Paper Award, 27th National Heat Transfer Conference, 1992.

130. Ishii, M., “Droplet Entrainment Correlation in Annular Two-Phase Flow,” ANL/PPRNT-90-211, P. 38, 1990.

131. Ishii, M., and M. A. Grolmes, “Inception Criteria for Droplet Entrainment in Two-Phase Concurrent Film Flow,” AIChE Journal, Vol. 21, P. 308, 1975b.

132. Jensen, R. T., “Inception of Liquid Entrainment during Emergency Cooling of Pressurized Water Reactors.” Ph.D. Thesis, Utah State University, 1972.

133. Jepson, D. M., P. B. Whalley, and B. J. Azzopardi, “The Effect of Physical Properties on Drop Size in Annular Flow,” CONF-900803, pp. 95-100, 1990.

134. Jones, O. C. and N. Zuber, “Post-CHF Heat Transfer: A Non-equilibrium, Relaxation Model,” ASME Paper 77-HT-75, 1977.

135. Juhel, D. “A Study on Interfacial and Wall Heat Transfer Downstream of a Quench Front,” The First Int. Workshop on Fundamental Aspects of Post-Dryout Heat Transfer, Salt Lake City, Utah, NUREG/CP-0060, April 2-4, 1984.

136. Kaminaga, F., “Dispersed Flow Boiling in the Reflood Phase,” Nippon Dennetsu Shinpojiumu Koen Ronbunshu, Vol. 16, pp. 217-219, Jun. 1979.

137. Kaminaga, F., “Heat Transfer Model for Dispersed Flow Regime During Reflood,” J. Nuclear Science and Technology, Vol. 18:1, pp. 6-14, 1981.

138. Kanazawa, T., K. Nishida, T. Nagayoshi, T. Kawasaki, and O. Yokomizo, “Critical Power Evaluation with Consideration of Differences in Droplet Behavior Due to Spacer Shape Influence,” J. Nuclear Science and Technology, Vol. 32:4, pp. 301-312, Apr. 1995.

139. Kataoka, I., M. Ishii and K. Mishima, “Generation and Size Distribution of Droplet in Annular Two-Phase Flow,” Journal of Fluids Engineering, Vol. 105, pp. 230-238, 1983.

140. Kawaji, M., Y. S. Ng, S. Banerjee, and G. Yadigaroglu, “Reflooding with Steady and Oscillating Injection: Part 1 – Flow Regimes, Void Fraction, and Heat Transfer,” Journal of Heat Transfer, Vol. 107, pp. 670-678, 1985.

141. Kawaji, M. and S. Banerjee, “Application of a Multifield Model to Reflooding of a Hot Vertical Tube: Part 1 - Model Structure and Interfacial Phenomena,” Journal Heat Transfer, Vol. 109, pp. 204-211, 1987.

142. Kawaji, M. and S. Banerjee, “Application of a Multifield Model to Reflooding of a Hot Vertical Tube: Part 2 – Analysis of Experimental Results,” J. Heat Transfer, Vol. 110:3, pp. 710-720, Aug. 1988.

143. Kawaji, M. and S. Banerjee, “Two-Phase Flow Characteristics During Reflooding of a Hot Vertical Tube,” EPRI-NP-2820, March 1983.

144. Kawaji, M., “Transient Non-equilibrium Two-Phase Flow: Reflooding of a Vertical Flow Channel,” Ph.D. Thesis, University of California, Berkeley, 1984.

145. Kawaji, M., Y. S. Ng and S. Banerjee, “Flow Regime and Heat Transfer Measurements During Reflooding with Steady and Oscillatory Coolant Injection,” Thermal Hydraulics of Nuclear Reactors, M. Merilo ed., ANS, Vol. 1, PP 262-270 (2nd Int. Topical Mtg. on Nuclear Reactor Thermal-Hydraulics, Santa Barbara, CA, Jan 11-14), 1983.

146. Kendall, G. E., “Heat Transfer to Impacting Drops and Post-Critical Heat Flux Dispersed Flow,” Ph.D. Thesis, M. I. T., Cambridge, MA, 1978.

147. Kervinen, T., S. Jaakkola, and L. Mattila, “REWET-1 Single Pin Reflood Experiments,” VTT-YDI-49, P. 73, Jun. 1980.

148. Kianjah, H. and V. K. Dhir, “Experimental and Analytical Investigation of Dispersed Flow Heat Transfer,” Experimental Thermal and Fluid Science (USA), Vol. 2, pp. 410-424, Oct. 1989.

149. Kianjah, H., “Single Phase Flow and Two Phase Disperse Flow Around Rod Bundles,” Ph.D. Dissertation, University of California at Los Angeles, 1987.

150. Kianjah, H., V. J. Dhir and A. Singh, “An Experimental Study of Heat Transfer Enhancement in Disperse Flow in Rod Bundles,” The First Int. Workshop on Fundamental Aspects of Post-Dryout Heat Transfer, Salt Lake City, Utah, NUREG/CP-0060, April 2-4, 1984.

151. Kiger, K. T. and J. C. Lasheras, “Dissipation Due to Particle/Turbulence Interaction in a Two-Phase, Turbulent, Shear Layer,” Phys. Fluids, Vol. 9, pp. 3005-3023, Oct. 1997.

152. Kiger, K. T. and J. C. Lasheras, “Vortex Pairing and Droplet Dissipation in a Turbulent, Free Shear Layer,” 25th Symposium on Combustion, pp. 407-412, 1994.

153. Kirillov, P. L., V. M. Kashcheyev, Yu. V. Muranov and Yu. S. Yuriev, “A Two-Dimensional Mathematical Model of Annular Dispersed and Dispersed Flows,” Int. Journal Heat Mass Transfer, Vol. 30, pp. 791-806, 1987.

154. Kline, M., R. D. Woodward, R. L. Burch, F. B. Cheung, K. K. Kuo, and, “Experimental Observations of Imaging in Jet Breakup Utilizing Laser-Sheet Illumination Photography,” AIAA/NASA/OAI Conference on Advanced Set Technologies, Cleveland Ohio, 1991.

155. Kocamustafaogullari, E., G. De Jarlais and M. Ishi, “Droplet Generation During Core Reflood,” Trans. ANS, Vol. 45, pp. 804-805, 1983.

156. Koizumi, Y., T. Ueda and H. Tanaka, “Post-Dryout Heat Transfer to R-113. Upward Flow in a Vertical Tube,” Int. Journal. Heat Mass Transfer, Vol. 22, pp. 669-678, 1979.

157. Krzeczkowski, S. A., “Measurement of Liquid Droplet Disintegration Mechanisms,” Int. Journal Multiphase Flow, Vol. 11, pp. 227-239, 1980.

158. Kuo, K. K. and F. B. Cheung, “Droplet Entrainment and Breakup by Shear Flows,” Technology Efforts in ETC Gun Propulsion, ARL-SR-12, Vol. 6, Jun. 1994.

159. Kutateladze, S. S., “Elements of the Hydrodynamics of a Gas Liquid System,” Fluid Mech. - Sov. Res., Vol. 1, pp. 29-34, 1972.

160. Labowsky, M., “A Formalism for Calculating the Evaporation Rates of Rapidly Evaporating Interacting Particles,” Comb. Science and Technol., Vol. 18, pp. 145-151, 1978.

161. Langevin, C., “Droplet Deposition in Vertical Two-Phase Flow,” CFD-84/22, P. 177, Aug. 1984.

162. Larson, T. K., “Testing and Analysis of the Semiscale Mod-1 Heater Rod Design,” CONF-801091-3, P. 32, 1980.

163. Lee, K and D. J. Ryley, “The Evaporation of Water Droplets in Superheated Steam,” ASME Paper 68-HT-11, 1968.

164. Lee, R. and K. Almenas, “Droplet Deposition Above a Quench Front During Reflooding,” Trans. ANS, Vol. 39, pp. 787-788, 1982.

165. Lee, R., J. N. Reyes and K. Almenas, “Size and Number Density Change of Droplet Population Above a Quench Front During Reflooding,” Int. Journal Heat Mass Transfer, Vol. 27, pp. 573-585, 1984.

166. Lee, S. L. and F. Durst, “On the Motion of Particles in Turbulent Duct Flows,” Int. Journal Multiphase Flow, Vol. 8, pp. 125-146, 1982.

167. Lee, S. L. and J. Srinivasan, “An LDA Technique for In-Situ Simultaneous Velocity and Size Measurement of Large Spherical Particles in a Two-Phase Suspension Flow,” Int. J. Multiphase Flow, Vol. 8, pp. 47-57, 1982.

168. Lee, S. L., “Particle Drag in a Dilute Turbulent Two-Phase Suspension Flow,” Int. Journal Multiphase Flow, Vol. 13, pp. 247-256, 1987.

169. Lee, S. L., H. J Sheen, S. K. Cho and I. Issapour, “Measurement of Droplet Dynamics Across Grid Spacer in Mist Cooling of Subchannel of PWR,” The First Int. Workshop on Fundamental Aspects of Post-Dryout Heat Transfer, Salt Lake City, Utah, NUREG/CP-0060, April 2-4, 1984.

170. Lee, S. L., H. J. Sheen, I. Issapour, and S. K. Cho, “A Study of Grid Spacer’s Enhanced Droplet Cooling in LOCA Reflood of a PWR by LDA Measurements,” Private Communication, 1984.

171. Lee, S. L., H. J. Sheen, S. K. Cho, I. Issapour, S. Q. Hua, “Measurement of Grid Spacer’s Enhanced Droplet Cooling Under Reflood Conditions in a PWR by LDA,” 11th Water Reactor Safety Research Information Meeting, Gaithersburg, MD, Oct. 24-28, 1983.

172. Lee, S. L., J. Srinivasan, and Y. Y. Hsu, “Laser-Doppler Anemometry Technique Applied to Two-Phase Dispersed Flows,” NUREG-0375, pp. I.4.1-I.4.34, Sep. 1977.

173. Lee, S. L., P. Ihle and K. Rust, “On the Importance of Grid Spacer Induced Mist Cooling on the Suppression of Core Peak Cladding Temperature During Reflood of PWR,” Proc. ASME-JSME Thermal Eng. Joint Conf., Honolulu, Hawaii, Vol. 3, PP 381-385, 1983.

174. Lee, S. L., S. K. Cho, M. Aghill, and H. J. Sheen, “A Study of Droplet Hydrodynamics Across the Spacer Grid Geometry,” NUREG/CR-4034, 1981.

175. Levy, S. and J. M. Healzer, “Prediction of Annular Liquid-Gas Flow with Entrainment: Cocurrent Vertical Pipe Flow with Gravity,” EPRI-NP-1521, P. 67, Sept. 1980.

176. Levy, S., “Two-Phase Annular Flow With Liquid Entrainment,” Int. Journal Heat Mass Transfer, Vol. 9, P. 171, 1966.

177. Lindsted, R. D., D. L. Evans, J. Gass and R. V. Smith, “Droplet with Flow Pattern Data for Vertical Two-Phase Air-Water Flow Using Axial Photography,” Technical Report, Wichita State University, Department of Mechanical Engineering, 1978.

178. Liu, L. and S. C. Yao, “Heat Transfer Analysis of Droplet Flow Impinging on a Hot Surface,” 7th Int. Heat Transfer Conf., Munich, Germany, 1982.

179. Loftus, M. J., L. E. Hochreiter, C. E. Conway, E. R. Rosal, and A. H. Wenzel, “Nonequlibrium Vapor Temperature Measurements in Rod Bundle and Steam Generator Two-Phase Flows,” Proceedings of the Third CSNI Specialist Meeting of Transient Two-Phase Flow, Mar. 1981.

180. Lopes, J. C. B. and A. E. Dukler, “Droplet Entrainment in Vertical Annular Flow,” AIChE Journal, Vol. 32, pp. 1500-1517, 1986.

181. Lopes, J. C. B. and A. E. Dukler, “Droplet Entrainment in Vertical Annular Flow and Its Contribution to Momentum Transfer,” NUREG/CR-4729, P. 54, Sept. 1986.

182. Lopes, J. C. B. and A. E. Dukler, “Droplet Sizes, Dynamics and Deposition in Vertical Annular Flows,” NUREG/CR-4424, P. 315, Oct. 1985.

183. Lopez de Bertodano, M. A. and S. C. Jan, “Droplet Entrainment Correlation for High Pressure Annular Two-Phase Flow,” WAPD-T-3071, P. 52, 1996.

184. Maitra, D. and K. Subba-Raju, “Vapor Void Fraction in Subcooled Flow Boiling,” Nucl. Engr. Design, Vol. 32, pp. 20-38, 1975.

185. Malang, S. and K. Rust, “Simulation of Nuclear Fuel Rods by Electrically Heated Rods,” Nuclear Technology, Vol. 58:1, pp. 53-62, Jul. 1982.

186. Mastanajah, K. and E. N. Ganic, “Heat Transfer in Two-Component Dispersed Flow,” Journal Heat Transfer, Vol. 103, pp. 300-306, 1981.

187. Mastanajah, K., “Experimental and Theoretical Investigation of Droplet Deposition and Heat Transfer in Air-Water Dispersed Flow,” Ph.D. Thesis, University of Illinois at Chicago, 1980.

188. Mayinger, F. and H. Langner, “Post-Dryout Heat Transfer,” 6th Int. Heat Transfer Conf., Toronto, Canada, 1978.

189. McPherson, G. D. and E. L. Tolman, “Review of Experiments to Evaluate the Ability of Electrically Heated Rods to Simulate Nuclear Fuel Rod Behavior During Postulated Loss-of-Coolant Accidents in Light Water Reactors,” CONF-801091-10, P. 16, 1980.

190. Minh, T. Q. and J. D. Huyghe, “Some Hydrodynamical Aspects of Annular Dispersed Flow: Entrainment and Film Thickness,” Symp. On Two-Phase Flow, Vol. 1, Paper C2, Exeter, UK, 1965.

191. Mohr, C. L. and G. M. Hesson, “LOCA Rupture Strains and Coolability of Full-Length PWR Fuel Bundles,” CONF-830805-62, P. 26, Mar. 1983.

192. Moose, R. A. and E. N. Ganic, “On the Calculation of Wall Temperatures in the Post-Dryout Heat Transfer Region,” Int. Journal Muliphase Flow, Vol. 8, pp. 525-542, 1982.

193. Morris, D. G., C. B. Mullins, and G. L. Yoder, “Analysis of Transient Film Boiling of High-Pressure Water in a Rod Bundle (PWR),” NUREG/CR-2469, P. 231, Mar. 1982.

194. Morris, D. G., C. B. Mullins, and G. L. Yoder, “Dispersed-Flow Film Boiling of High Pressure Water in a Rod Bundle (PWR),” NUREG/CR-2183, P. 85, Aug. 1982.

195. Morris, D. G., C. B. Mullins, and G. L. Yoder, “Rod-Bundle Transient Film Boiling of High-Pressure Water in the Liquid-Deficient Regime (PWR),” CONF-820604-10, P. 13, 1982.

196. Morris, D. G., C. B. Mullins, G. L. Yoder, L. J. Ott, and D. A. Reed, “Steady-State Film-Boiling Data in Rod-Bundle Geometry and Non-equilibrium Correlation Assessment,” CONF-820604-9, P. 17, 1982.

197. Morris, D. G., C. R. Hyman, C. B. Mullins, and G. L. Yoder, “Transient Dispersed Flow Film Boiling of High Pressure Water in Rod Bundle Geometry,” AIChE Symposium Series, Vol. 77, pp. 282-289, 1981.

198. Mostinskiy, I. L. and D. I. Lamden, “Heat and Mass Transfer in Vaporization of Droplets of Solutions in a High-Temperature Gas Flow,” Heat Transfer – Soviet Research, Vol. 9, No. 2, Mar.-Apr. 1977.

199. Mugele, R. A. and H. D. Evans, “Droplet Size Distribution in Sprays,” Ind. Eng. Chem., Vol. 43, P. 1317, 1951.

200. Murao, Y. and J. Sugimoto, “Correlation of Heat Transfer Coefficient for Saturated Film Boiling During Reflood Phase Prior to Quenching,” Journal Nuc. Sci. Tech. Vol. 18, pp. 275-284, 1981.

201. Murata, S., A. Minato, and O. Yokomizo, “Development of Three-dimensional Analysis Code for Two-Phase Flow Using Two-Fluid Model,” J. Nuclear Science and Technology, Vol. 28[11], pp. 1029-1040, Nov. 1991.

202. Naitoh, M., K Chino and H. Ogasawara, “Cooling Mechanism During Transient Reflooding of a Reactor Fuel Bundle After Loss of Coolant,” Nucl. Engr. Design, Vol. 44, pp. 193-200, 1977.

203. Newitt, D. M., N. Dombrowski and F. H. Knelman, “Liquid Entrainment: The Mechanism of Drop Formation from Gas or Vapor Bubbles,” Trans. Inst. Chem Engr., Vol. 32, P. 244, 1954.

204. Ng, Y. S. and S. Banerjee, “Two-Phase Flow Characteristics During Controlled Oscillating Reflooding of a Hot Vertical Tube,” EPRI Report, NP-2821, 1983.

205. Nigmatulin, R. I. and V. N. Kukharenko, “Heat Transfer in the Over-Crisis Region in a Stream-Generating Channel with Stream-Droplet Flow,” Teplofizica Vysokikh Temperatur (USSR), Vol. 29:3, pp. 557-563, May-June 1991.

206. Nigmatulin, R. I., “Entrainment and Deposition Rates in a Dispersed Film Flow,” Int. Journal Multiphase Flow, Vol. 22, pp. 19-25, 1996.

207. Nijhawan, S., J. C. Chen, R. K. Sundaram and E. H. London, “Measurement of Vapor Superheat in Post-Critical-Heat-Flux Boiling,” Journal Heat Transfer, Vol. 102, pp. 465-470, 1980.

208. Nishio, S. and M. Hirata, “Direct Contact Phenomenon Between a Liquid Droplet and High Temperature Solid Surfaces,” 6th Int. Heat Transfer Conf., Toronto, Canada, 1978.

209. Nithianandan, C. K. and J. R. Biller, “Thermal-Hydraulic Effects of Clad Swelling and Rupture During Reflood,” Trans. American Nuclear Society, Vol. 62, pp. 720-721, 1990.

210. Nithianandan, C. K., R. J. Lowe, and J. R. Biller, “Thermal-Hydraulic Effect of Grid Spacers and Cladding Rupture During Reflood,” Trans. American Nuclear Society, Vol. 66, pp. 614-616, 1992.

211. Nithiandan, C. K., J. A. Klingenfus, and S. S. Reilly, “RELAP5 Model to Simulate the Thermal-Hydraulic Effects of Grid Spacers and Cladding Rupture During Reflood,” NUREG/CP-0142, Vol. 3, pp. 2410-2427, Sept. 1995.

212. Nukiyama, S. and Y. Tanazawa, “An Experiment on the Atomization of Liquid By Means of an Air Stream,” Trans. JSME, Vol. 4, P. 86, 1938.

213. Oh, S. J., “The Effect of Oscillation During Reflooding of a Tubular Test Section,” Ph.D. Dissertation, University of California, Berkeley, CA, 1982.

214. Oh, S. J., S. Banerjee, and G. Yadigaroglu, “Reflooding with Steady and Oscillating Injection: Part 2 – Quench Front and Liquid Carryover Behavior,” Journal of Heat Transfer, Vol. 108, pp. 448-456, 1986.

215. Obot, N. T. and M. Ishii, “Two-Phase Flow Regime Transition Criteria in Post-Dryout Region Based on Flow Visualization Experiments,” Int. J. Heat Mass Transfer (U. K.), Vol. 31:12, pp. 2559-2570, Dec. 1988.

216. O’Rourke, P. J., “Collective Drop Effects on Vaporizing Liquid Sprays,” Ph.D. Thesis, University of Princeton, 1981.

217. Ottosen, P., “Experimental and Theoretical Investigation of Inverse Annular Film Flow and Dispersed Droplet Flow, Important under LOCA Conditions,” DE83702327, P. 150, Jul. 1980.

218. Paleev, I. I. and B. S. Filipovich, “Phenomena of Liquid Transfer in Two-Phase Dispersed Flow,” Int. Journal Heat Mass Transfer, Vol. 9, P. 1089, 1966.

219. Paras, S. V. and A. J. Karabelas, “Properties of the Liquid Layer and Droplet Entrainment and Deposition in Horizontal Annular Flow,” Int. Journal Multiphase Flow, Vol. 17, pp. 439-454, 1991.

220. Peake, W. T., “Dispersed Flow Film Boiling During Reflooding,” Univ. of California, Berkeley, P. 217, 1979.

221. Pedersen, C. O., “An Experimental Study of the Dynamic Behavior and Heat Transfer Characteristics of Water Droplets Impinging Upon a Heated Surface,” Int. Journal Heat Mass Transfer, Vol. 13, pp. 369-381, 1970.

222. Pederson, C. O., “The Dynamics and Heat Transfer Characteristics of Water Droplets Impinging on a Heater Surface,” Ph.D. Thesis, Carnegie Inst. of Tech., 1967.

223. Petrovichev, V. I., L. S. Kokorev, A. Y. Didenko and J. Dubvroskiy, “Droplet Entrainment in Boiling of Thin Liquid Film,” Heat Transfer - Sov. Res., Vol. 3, P. 19, 1971.

224. Piggot, B. D. G., E. P. White and R. B. Duffey, “Wetting Delay Due to Film and Transient Boiling on Hot Surfaces,” Nucl. Engr. Design, Vol. 36, pp. 169-181, 1976.

225. Plummer, D. N., P. Griffith and W. M. Rohsenow, “Post-Critical Heat Transfer to Flowing Liquid in a Vertical Tube,” Trans. CSME, Vol. 3, pp. 151-158, 1977.

226. Podvysotsky, A. M. and A. A. Shrayber, “Coalescence and Break-Up of Drops in Two-Phase Flows,” Int. Journal Multiphase Flow, Vol. 10, pp. 195-209, 1984.

227. Raepple, B., J. Hauschild, M. Hespeler, W. Knappschneider, and M. Pressmann, “Reference Tests to In-Pile Experiments with Electrically Heater Fuel Rod Simulators (Single Rods),” Kernforschungszentrum Karlsruhe, pp. 334-338, Nov. 1976.

228. Ramirez de Santiago, M., “Study of Droplet Entrainment from Bubbling Surface in a Bubble Column,” DE92743657, P. 358, May 1991.

229. Ramm, H. and K. Johannsen, “A Phenomenological Turbulence Model and its Application to Heat Transport in Infinite Rod Arrays with Axial Turbulent Flow,” Journal Heat Transfer, Trans. ASME, Vol. 97, No. 2, pp. 231-237, 1975.

230. Rane, A. G. and S. Yao, “Convective Heat Transfer to Turbulent Droplet Flow in Circular Tubes,” Journal Heat Transfer, Vol. 103, pp. 679-684, 1981.

231. Rane, A. G. and S. Yao, “Heat Transfer of Evaporating Droplet Flow in Low Pressure Systems,” ASME Paper 79-WA/HT-10, 1980.

232. Rehme, K., “Pressure Drop of Spacer Grids in Smooth and Roughened Rod Bundles,” Nuclear Technology, Vol. 31, pp. 314-317, 1997.

233. Richter, H. J., “Separated Two-Phase Flow Model, Application to Critical Two Phase Flow, Int. Journal Multiphase Flow, Vol. 9, pp. 511-519, 1983.

234. Rohatgi, U. S., Cheng, H. S., H. Khan, and W. Wulff, “Preliminary Phenomena Identification and Ranking Tables (PIRT) for SBWR Start Up Stability,” Draft Report to NRC, May 31, 1995.

235. Sarjeant, M., “Drop Break-Up by Gas Streams,” CEGB, R/M/N1005, 1978.

236. Savage, R. A., D. Archer and D. Swinnerton, “Heat Transfer and Voidage Measurements in Steady State Post-Dryout at Low Quality and High Pressure,” 3rd UK National Heat Transfer Conf., Vol. 1, pp. 607-615, 1992.

237. Sawan, M. and M. W. Carbon, “A Review of Spray Cooling and Bottom-Flooding Work for LWR Cores,” Nucl. Engr. Design, Vol. 32, pp. 191-207, 1975.

238. Schadel, S. A., G. M. Lean and T. J. Hanratty, “Rate of Atomization and Deposition in Vertical Annular Flow,” Int. Journal Multiphase Flow, Vol. 16, pp. 363-374, 1990.

239. Seban, R. A. and A. Chariots, “Single-Tube Reflood with Subsequent Boiling Dry Because of Termination of the Feed,” EPRI-NP-80-4-LD, August 1980.

240. Seban, R. A., “Reflooding of a Vertical Tube at 1, 2, 3, Atmospheres,” EPRI-NP-3191, July 1983.

241. Seban, R. A., S. T. Wang, C. A. La Djinnis and A. Heydari, “Heat Transfer During Quench and Dryout in a Vertical Tube,” EPRI-NP-4157, July 1985.

242. Sekoguchi, K., and M. Takeiski, “Interfacial Structure in Vertical Upward Annular Flow,” Int. Journal Multiphase Flow, Vol. 15, pp. 295-301, 1989.

243. Shaw, R. A., S. Z. Ronhani, T. K. Larson, and R. A. Dimenna, “Development of a Phenomena Identification and Ranking Table (PIRT) for Thermal-Hydraulic Phenomena During a Large Break LOCA,” NUREG/CR-5074, Oct. 1988.

244. Shoukri, M., R. L. Judd and B. Donevski, “Experiments on Subcooled Flow Boiling and Condensation in Vertical Annular Channels,” Phase-Interface Phenomena in Multiphase Flow, pp. 413-422, Hemisphere, 1991.

245. Shrayber, A. A., “Model for Turbulent Heat Transfer by Gas-Solid Flows,” Heat Transfer – Soviet Research, Vol. 9, No. 3, May-Jun. 1977.

246. Shrayber, A. A., “Turbulent Heat Transfer in Pipe Flows of Gas Conveyed Solids,” Heat Transfer - Soviet Research, Vol. 8, No. 3, pp. 60-67, 1976.

247. Smith, T. A., “Heat Transfer and Carryover of Low Pressure Water in a Heated Vertical Tube,” NUREG-0105, P. 112, Jan. 1976.

248. Soda, K., “On-Line Simulation of Thermal Characteristics of Nuclear Fuel Rod by Electrically Heated Rod,” J. Nuclear Science and Technology, Vol. 13:9, pp. 523-526, Sep. 1976.

249. Soliman, H. M. and G. E. Sims, “Theoretical Analysis of the Onset of Liquid Entrainment for Slots of Finite Width,” Int. J. Heat and Fluid Flow (U.K.), Vol. 12:4, pp. 360-364, Dec. 1991.

250. Spencer, A. C., M. Y. Young, L. E. Hochreiter, G. L. Sozzi, “Mechanistic Model for the Best Estimate Analysis of Reflood Transients (the BART Code),” ASME, pp. 41-55, 1980.

251. Spokoynyy, F. Ye, Z. R. Gorbis, N. V. Svyatetskiy, and R. V. Zagaynova, “Investigation of Combined Radiant and Convective Heat Transfer to and from a Turbulent Gas Suspension Flow,” Heat Transfer – Soviet Research, Vol. 8, No. 5, Sept. 1976.

252. Stosic, Z. D., “Rod Bundle Spacer Grids Effects on Post-Dryout Heat Transfer Augmentation Analyzed by the Model HECHAN,” Private Communication, 1994.

253. Styrikovich, M. A. Yu. V. Baryshev, G. V. Tsiklauri and M. E. Grigorieva, “The Mechanism of Heat and Mass Transfer Between a Drop and a Heated Surface,” 6th Int. Heat Transfer Conf., Toronto, Canada, 1978.

254. Styrikovich, M. A., Yu. V. Baryshev, M. E. Grigorieva and G. V. Tsiklauri, “Investigation of Heat Transfer Processes During Film Boiling in Steam Generating Channel,” 7th Int. Heat Transfer Conf., Munich, Germany, 1982.

255. Sudo, Y., “Film Boiling Heat Transfer During Reflooding Phase in Postulated PWR Loss of Coolant Accident,” Journal Nuc. Sci. Tech., Vol. 17, pp. 516-530, 1980.

256. Sugawara, S., “Droplet Deposition and Entrainment Modeling Based on Three-Fluid Model,” Nuclear Engineering and Design, Vol. 122:1-3, pp. 67-84, Sep. 1990.

257. Sugimoto, J. and Y. Murao, “Effect of Grid Spacers on Reflood Heat Transfer in PWR-LOCA,” J. Nuclear Science and Technology, Vol. 21:2, pp. 103-114, Feb. 1984.

258. Sugimoto, J. and Y. Murao, “Report on Reflood Experiment of Grid Spacer Effect,” JAERI-M-84-131, P. 230, Jul. 1984.

259. Sugimoto, J., “Study on Thermo-Hydraulic Behavior During Reflood Phase of a PWR-LOCA,” JEARI-M-88-262, P. 139, Jan. 1989.

260. Sugimoto, J., T. Sudoh, and Y. Murao, “Analytical Study of Thermal Response Similarity Between Simulated Fuel Rods and Nuclear Fuel Rods During Reflood Phase of PWR-LOCA,” J. Nuclear Science and Technology, Vol. 23:4, pp. 315-325, Apr. 1986.

261. Sukomel, A. S., S. I. Koryukin, F. F. Tsvetkov, R. V. Kerimov and Z. N. Spirina, “Experimental Study of Heat Transfer to Aerosol Flows at High Wall Temperatures,” Heat Transfer - Soviet Research, Vol. 11, No. 4, pp. 137-141, 1979.

262. Sun, K. H., J. M. Gonzales and C. L. Tien, “Calculations of Combined Radiation and Convection Heat Transfer in Rod Bundles Under Emergency Cooling Conditions,” ASME Paper 75-HT-64, 1975.

263. Temkin, S. and H. K. Mehta, “Droplet Drag in An Accelerating and Decelerating Flow,” Journal Fluid Mech., Vol. 116, pp. 297-313, 1982.

264. Theofanous, T. G. and J. Sullivan “Turbulence in Two-Phase Dispersed Flows,” Journal Fluid Mech., Vol. 116, pp. 343-362, 1982.

265. Tien, C. L. and V. Quan, “Local Heat Transfer Characteristics of Air-Glass and Air-Lead Mixtures in Turbulent Pipe Flow,” ASME Paper No. 62-HT-15, 1962.

266. Toknoka, N., T. Kobayashi and G. T. Sato, “The Evaporation of a Small Droplet in a Hot Air Stream,” 2nd Int. Conf. on Liquid Atomization and Spray Systems, Madison, Wisconsin, 1982.

267. Tolman, E. L. and R. C. Gottula, “Evaluation of the Ability of Electrical Rods to Simulate Nuclear Rod Behavior During a Loss-of-Coolant Accident,” EGG-LOFT-5008, P. 61, Oct. 16, 1979.

268. Toman, W. I., I. Catton and R. B. Duffey, “Multidimensional Thermal-Hydraulic Reflood Phenomena in a 1692-Rod Slab Core,” EPRI-NP-2392, 1982.

269. Tsuji, Y., Y. Morikawa and H. Shiomi, “LDV Measurements of an Air-Solid Two-Phase Flow in a Vertical Pipe,” Journal Fluid Mech., Vol. 139, pp. 417-434, 1984.

270. Tuzla, K., C. Unal, O. Badr, S. Neti, and J. Chen, “Thermodynamic Non-equilibrium in Post-Critical-Heat-Flux Boiling in a Rod Bundle: Data for Advancing Quench Front Tests,” NUREG/CR-5095, Vol. 3, P. 563, June 1988.

271. Tuzla, K., C. Unal, O. Badr, S. Neti, and J. Chen, “Thermodynamic Non-equilibrium in Post-Critical-Heat-Flux Boiling in a Rod Bundle: Description of Experiments and Sample Results,” NUREG/CR-5095, Vol. 1, P. 151, June 1988.

272. Ueda, T., H. Tanaka and Y. Koizumi, “Dryout of Liquid Film in High Quality R-113 Upflow in a Heated Tube,” 6th Int. Heat Transfer Conf., Toronto, Canada, 1978.

273. Unal, C., “An Experimental Study of Thermal Non-equilibrium Convective Boiling in Post-Critical-Heat-Flux Region in Rod Bundles,” Ph.D. Dissertation, Lehigh Univ., 1985.

274. Unal, C., K. Tuzla, O. Badr, S. Neti, and J. Chen, “Convective Boiling in Rod Bundle: Transverse Variation of Vapor Superheat Temperature Under Stabilized Post-CHF Conditions,” Int. J. Heat Mass Transfer, Vol. 34, pp. 1695-1706, 1991.

275. Unal, C., K. Tuzla, O. Badr, S. Neti, and J. Chen, “Convective Film Boiling in Rod Bundle: Axial Variation of Non-equilibrium Evaporation Rates,” Int. J. Heat Mass Transfer, Vol. 31, pp. 2091-2100, 1988.

276. Unal, C., K. Tuzla, O. Badr, S. Neti, and J. Chen, “Parametric Trends for Post-CHF Heat Transfer in Rod Bundles,” J. Heat Transfer, Vol. 110:3, pp. 721-727, Aug. 1988.

277. Unal, C., Tuzla, K., A. F. Cokmez-Tuzla, and J. C. Chen, “Vapor Generation Rate Model for Dispersed Drop Flow,” Nuclear Engineering and Design (Netherlands), Vol. 125:2, pp. 161-173, Feb. 1991.

278. van der Molen, S. B., F. W. B. M. Galjee, and T. N. Veziroglu, “Entrainment of Droplets During the Reflood Phase of a LOCA and the Influence of the Channel Geometry,” CONF-790423, pp. 1461-1482, 1979.

279. Varone, A. F. and W. M. Rohsenow, “Post Dryout Heat Transfer Prediction,” The First Int. Workshop on Fundamental Aspects of Post-Dryout Heat Transfer, Salt Lake City, Utah, NUREG/CP-0060, April 2-4, 1984.

280. Wallis, G. B., “Phenomena of Liquid Transfer in Two-Phase Dispersed Annular Flow,” Int. J. Heat Mass Transfer, Vol. 11, pp. 783-785, 1968.

281. Webb, S. W. and J. C. Chen, “A Non-equilibrium Model for Post-CHF Heat Transfer,” 3rd CSNI Specialist Mtg. on Transient Two-Phase Flow, Pasadena, CA, March 23-25, 1981.

282. Webb, S. W. and J. C. Chen, “A Numerical Model for Turbulent Non-equilibrium Dispersed Flow Heat Transfer,” Int. Journal Heat Mass Transfer, Vol. 25, pp. 325-335, 1982.

283. Webb, S. W. and J. C. Chen, “A Two-Region Vapor Generation Rate Model for Convective Film Boiling,” The First Int. Workshop on Fundamental Aspects of Post-Dryout Heat Transfer, Salt Lake City, Utah, NUREG/CP-0060, April 2-4, 1984.

284. Webb, S. W., J. C. Chen and R. K. Sundaram, “Vapor Generation Rate in Non-equilibrium Convective Film Boiling,” 7th Int. Heat Transfer Conf., Munich, Germany, 1982.

285. Weisman, J., “Heat Transfer Flowing Parallel to Tube Bundles,” Nuclear Science and Engineering, Vol. 6, No. 1, pp. 78-79, 1959.

286. Westinghouse, “Grid Heat Transfer Enhancement Factor,” Westinghouse Proprietary Class 2, 1980.

287. White, P. E. and R. B. Duffey, “A Study of Unsteady Flow and Heat Transfer in the Reflooding of Water Reactor Cores,” Ann. Nuc. Energy, Vol. 3, pp. 197-210, 1976.

288. Wicks, M. and A. E. Dukler, “Entrainment and Pressure Drop in Concurrent Gas-Liquid Flow: Air-Water in Horizontal Flow,” AIChE Journal, Vol. 6, P. 463, 1960.

289. Wicks, M. and Dukler, A. E, “In Situ Measurements of Drop Size Distribution in Two-Phase Flow,” Int. Heat Transfer Conf., Chicago, Illinois, 1966.

290. Wilkes, N. S., B. J. Azzopardi and I. Willetts, “Drop Motion and Deposition in Annular Two-Phase Flow,” Thermal Hydraulics of Nuclear Reactors, M. Merilo ed., ANS, Vol. 1, pp. 202-209 (2nd Int. Topical Meeting on Nuclear Reactor Thermal-Hydraulics, Santa Barbara, CA, Jan. 11-14), 1983.

291. Wilkinson, G. T. and J. R. Norman, “Heat Transfer to a Suspension of Solids in a Gas,” Trans. Inst. Chem. Engrs., Vol. 45, pp. T314-T318, 1967.

292. Williams, J. J. and R. I. Crane, “Particle Collision Rate in Turbulent Flow,” Int. Journal of Multiphase Flow, Vol. 9, pp. 421-435, 1983.

293. Williams, K. A., “Numerical Fluid Dynamics of Non-equilibrium Steam-Water Flows with Droplets,” Ph.D. Dissertation, University of New Mexico, 1983.

294. Williams, L. R., L. A. Dykhno and T. J. Hanratty, “Droplet Flux Distribution and Entrainment in Horizontal Gas-Liquid Flows,” Int. Journal Multiphase Flow, Vol. 22, pp. 1-12, 1996.

295. Wong, S. and L. E. Hochreiter, “A Model for Dispersed Flow Heat Transfer During Reflood,” Proc. 19th Nat. Heat Transfer Conf., Orlando, FL, 1980.

296. Wong, S. and L. E. Hochreiter, “Analysis of Heat Transfer to Axial Dispersed Flow Between Rod Bundles Under Reactor Emergency Cooling Conditions,” J. Heat Transfer, Vol. 102:3, pp. 508-512, Aug. 1980.

297. Woodmansee, D. E. and T. J. Hanratty, “Mechanism for the Removal of Droplets from a Liquid Surface by a Parallel Air Flow,” Chem. Engr. Sci., Vol. 24, P. 299, 1969.

298. Wulff, W., “Scaling of Thermal Hydraulic Systems,” Nuclear Engineering and Design, Vol. 163, pp. 359-395, 1996.

299. Yablonik, R. M. and V. A. Khaimov, “Determination of the Velocity of Inception of Droplet Entrainment in Two-Phase Flow,” Fluid Mech. - Sov. Res., Vol. 1, P. 130, 1972.

300. Yadigaroglu, G., “The Reflooding Phase of LOCA in PWR’s. Part I: Core Heat Transfer and Fluid Flow,” Journal Nuc. Safety, Vol. 19, pp. 20-36, Jan-Feb 1978.

301. Yadigaroglu, G., “The Reflooding Phase of LOCA in PWR’s. Part II: Rewetting and Liquid Entrainment,” Journal Nuc. Safety, Vol. 19, pp. 60-75, Mar-Apr 1978.

302. Yamanuchi, A., “Effect of Core Spray Cooling in a Transient State After Loss of Coolant Accident,” Journal Nuc. Sci. Tech., Vol. 5, pp. 547-558, 1968.

303. Yao, S .C. and K. Y. Cai, “The Dynamics and Leidenfrost Temperature of Drops Impacting on a Hot Surface at Small Angles,” ASME Paper 87-WA/HT-39, 1985.

304. Yao, S. C, “Convective Heat Transfer of Laminar Droplet Flow in Thermal Entrance Region of Circular Tubes,” Journal Heat Transfer, Vol. 101, pp. 480-483, 1979.

305. Yao, S. C. and A. Rane, “Heat Transfer of Laminar Mist Flow in Tubes,” Journal Heat Transfer, Vol. 102, pp. 678-683, 1980.

306. Yao, S. C. and K. H. Sun, “A Dispersed Flow Heat Transfer Model for Low-Flow Bottom Reflooding Conditions,” Heat Transfer in Nuclear Reactor Safety, ed. Bankoff and Afgan, Hemisphere Publishing Corp., Washington, 1982.

307. Yao, S. C. and R. E. Henry, “An Investigation of the Minimum Film Boiling Temperature on Horizontal Surfaces,” Journal Heat Transfer, Vol. 100, pp. 260-267, 1978.

308. Yao, S. C., L. E. Hochreiter and K. Y. Cai, “Dynamics of Droplets Impacting on Thin Heated Strips,” Journal Heat Transfer, Vol. 110, pp. 214-220, 1988.

309. Yao, S. C., L. E. Hochreiter and W. J. Leech, “Heat Transfer Augmentation in Rod Bundles Near Grid Spacers,” Journal Heat Transfer, Trans. ASME, Vol. 104, No. 1, pp. 76-81, 1982.

310. Yoder, G. L. and W. M. Rohsenow, “A Solution for Dispersed Flow Heat Transfer Using Equilibrium Fluid Conditions,” Journal Heat Transfer, Vol. 105, pp. 10-17, 1983.

311. Yoder, G. L., “Dispersed Flow Film Boiling in Rod Bundle Geometry – Steady State Heat Transfer Data and Correlation Comparisons,” NUREG/CR-2435, Mar. 1982.

312. Yoder, G. L., “Heat Transfer Near Spacer Grids in Rod Bundles,” 1985 Natl. Heat Transfer Conference, Denver, Colorado, Aug. 1985.

313. Yoder, G. L., “Rod Bundle Spacer Grid Heat Transfer Data Base,” NUREG/CR-4421, Sep. 1985.

314. Yoder, G. L., D. G. Morris, C. B. Mullins, and L. J. Ott, “Dispersed Flow Film Boiling Heat Transfer Data Near Spacer Grids in a Rod Bundle,” Nuclear Technology, Vol. 60:2, pp. 304-313, Feb. 1983.

315. Yoshioka, K. and S. Hasegawa, “A Correlation in Displacement Velocity of Liquid Film Boundary Formed on a Heated Vertical Surface in Emergency Cooling,” Journal Nuc. Sci. Tech, Vol. 12, pp. 735-741, 1975.

316. Yu, K. P. and G. Yadigaroglu, “Heat Transfer Immediately Downstream of the Quench Front During Reflooding,” ASME Paper 79-HT-48, 1979.

317. Yuen, M. C. and L. W. Chen, “Heat Transfer Measurements of Evaporating Liquid Droplets,” Int. Journal Heat Mass Transfer, Vol. 21, pp. 537-542, 1978.

318. Zemlianoukhin, V. V., L. P. Kabanov, P. L. Makarovski, V. M. Mordashev, and Yu. V. Rybakov, “Reflooding Heat Transfer in Zirconium Alloy Rod Bundle of VVER Reactor,” CONF-891004, pp. 584-590, 1989.

319. Zuber, N and J. A. Findlay, “Average Volumetric Concentration in Two-Phase Flow System,” Journal Heat Trans., Vol. 87, pp. 453-368, 1965.

320. Zuber, N. and F. W. Staub, “An Analytical Investigation of the Transient Response of the Volumetric Concentration in a Boiling Forced Flow System,” Journal Nuc. Sci. Eng., Vol. 30, pp. 268-278, 1967.

321. Zuber, N., “On the Atomization and Entrainment of Liquid Films in Shear Flow,” 62GL513, General Electric, 1962.

4. DEFINE INFORMATION NEEDED FOR NEW CODE MODELING CAPABILITIES, VALIDATION, AND ASSESSMENT

4.1 Introduction

The large reactor safety analysis systems computer codes, such as the TRAC and RELAP, all attempt to predict a transient boiling curve for a heated surface with internal heat generation for a given surface temperature and fluid conditions adjacent to the surface such as the pressure, void fraction, vapor temperature and mass flow rate. The calculated boiling curve is generated by combining different individual heat transfer correlations such that a continuous calculation can be performed. As the fluid conditions change, the boiling curve predicted by the computer code also changes as some phenomena become larger and others become smaller such that the calculated surface heat transfer coefficient may result in the surface heating-up to higher temperature, or the surface cooling down to a lower temperature.

The computer codes use individual empirical or semi-empirical heat transfer correlations to calculate the local heat transfer behavior from the heated surface to the fluid. The difference between the empirical and semi-empirical correlations is meant to indicate the degree in which the true physical condition is modeled by the correlation. Most correlations are usually empirical, that is, derived from a specific set of data, and predict single phenomena, or several phenomena in parallel. These correlations are often applied to conditions and geometries which were not included in the original basis for the correlation when performing reactor safety analysis.

The heat transfer correlations may also require some modifications to make the correlation consistent with the numerical solution scheme of the code such that rapid calculations can be performed in a reliable fashion. Such modifications can result in essentially a different correlation than was originally developed by the author. The process of combining different individual specific correlations can lead to compensating errors, in which one calculates the right answer for the wrong reason because there are multiple errors in the calculational scheme.

The heat transfer correlations, which compromise the calculated boiling curve, are also usually based on test data which is scaled relative to the reactor system. Therefore, one must address the effects and uncertainties of applying the correlations which are developed from scaled data to the analysis of a full scale reactor system. The computer code must be validated against several sets of independent, complete, data at different scales, over the range of conditions that the code would calculate, for geometries which would be modeled by the computer code. The emphasis is on the data independence, that is, data not used in the original correlation development, and a complete set of data such that the effects of compensating error can be determined.

Therefore, complete sets of valid test data and the associated data analysis are one of the most needed items to validate the specific models in the computer codes to insure that compensating error is minimized, the heat transfer models are applicable at full scale with acceptable uncertainty and that the implementation of the correlations into the code do not change the nature or predictability of the original correlation.

The RBHT program is designed to specifically address the need for providing complete sets of valid data and data analysis for the low pressure film boiling regime which occurs during the reflood process.

The process which has been used in the RBHT program is to develop the modeling requirements by developing a specific reflood PIRT as given in Section 2 which identifies the phenomena and the interaction of the different phenomena which the code should be able to calculate, then designing the experiments to isolate, as best as possible, those phenomena which are most important for the code predictions such that individual component code models can be assessed. In this fashion, compensating errors are less likely since the component models will be validated over the ranges of interest before they are integrated into the final heat transfer correlation package which would be used to predict the boiling curve.

This Section of the report will provide a road map for the highly ranked phenomena developed from the PIRT given in Section 2 of this report, to the code models and finally to the instrumentation and methods of the data analysis. The objective is to indicate which code models interact to predict the important phenomena, and how the RBHT program will provide data and analysis to assess these models.

4.2 Brief Review of Heat Transfer Models Used in Best-Estimate Codes for Reflood

4.2.1 RELAP5/MOD3

4.2.1.1 *Introduction*

The RELAP5 code (Ref. 1) was developed for best-estimate transient simulation of light water reactor coolant systems during postulated accidents. The code was developed at Idaho National Engineering Laboratory (INEL) for the U.S. Nuclear Regulatory Commission (NRC). Code applications include analysis to support rulemaking, licensing audit calculations, evaluation of accident mitigation strategies, evaluation of operator guidelines, and experiment planning analysis. The MOD3 version has been developed jointly by the NRC and a consortium consisting of several countries and domestic organizations that were member of the International Code Assessment and Applications Program (ICAP) and its successor organization, Code Applications and Maintenance Program (CAMP).

The RELAP5/MOD3 code is based on a non-homogeneous and non-equilibrium model for the two-phase system that is solved by a fast partially implicit numerical scheme. The objective of RELAP5 development effort was to produce a code that included important first-order effects necessary for accurate prediction of system transients but that was sufficiently simple and cost effective so that parametric or sensitivity studies are possible. The code is one-dimensional and solves six basic field equations for six dependent variables (pressure, specific internal energies for liquid and vapor, void fraction, liquid and vapor velocities).

The constitutive relations include models for defining flow regimes and flow-regime-related models for interface drag and shear, the coefficient of virtual mass, wall friction, wall heat transfer, and interface heat and mass transfer. Volumes flow regimes are used for calculations of interfacial heat and mass transfer while junction flow regimes are used for interface drag. The junction properties are consistent with the state of the fluid being transported through the

junction. The same approach has been used successfully in the TRAC-B code. The wall heat transfer depends on volume flow regime maps in a less direct way. Generally, void fraction and mass flux are used to incorporate the effects of the flow-regime and because the wall heat transfer is calculated before the hydrodynamics, the flow information is taken from the previous time step.

The vertical volume flow regime map is shown in Figure 4.1. The schematic is three-dimensional to illustrate flow regime transitions as function of void fraction, average mixture velocity and boiling regime (pre-CHF, transition and post dryout). Heat and mass transfer and drag relations for the transition boiling region between pre-CHF and dryout are found by interpolating the correlations on either side. This means that for certain void fractions in the transition boiling region, two and sometimes three adjacent correlations are combined to obtain the necessary relations for heat/mass transfer and drag.

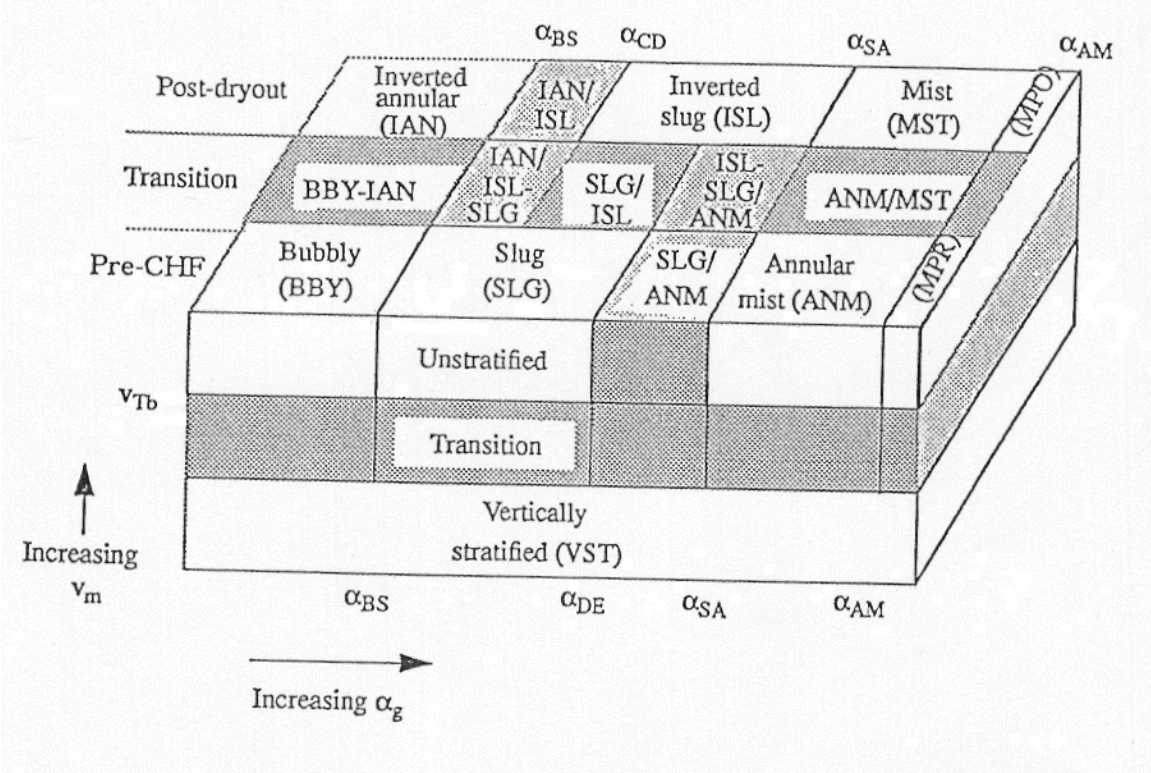

Figure 4.1 RELAP5/MOD3 Vertical Flow Regime Map.

4.2.1.2 *RELAP5/MOD3 Heat Transfer Package*

The heat transfer is viewed as a two-step mechanism: (1) a wall to fluid bulk heat transfer; and, (2) a bulk interfacial heat and mass transfer. In addition a separate, near-wall interfacial heat transfer is considered to account for the special case when the wall is communicating with a two-phase mixture, for then boiling or condensation can occur as direct result of the wall heat transfer.

A boiling curve is used in RELAP5/MOD3 to govern the selection of the wall to fluid heat transfer correlations. The RELAP5 boiling curve logic is based on the value of the heat slab

surface temperature. These correlations are based on fully developed steady-state flow while entrance effects are considered only for the calculation of Critical Heat Flux (CHF). Table 4.1 shows the heat transfer modes and corresponding correlations used while Figure 4.2 shows the wall heat transfer mode selection flow chart.

4.2.1.3 *Single Phase Liquid*

When the wall is subcooled and the void fraction is below 0.1, single-phase convection to liquid is assumed. For the vertical flow, depending on the value of the Re number, the heat transfer coefficient is calculated with either the Dittus-Boelter correlation (forced turbulent convection) (Ref. 2) or Churchill-Chu correlation (natural convection) (Ref. 3). A constant Nu number equal to 4.6 is assumed for the forced laminar convection case.

4.2.1.4 *Single Phase Vapor*

In a similar fashion, when the wall is superheated and the quality is greater than 0.99, depending on the Re number, the Dittus-Boelter (Ref. 2) and Churchill-Chu (Ref. 3) correlations are used for the single phase vapor convection.

4.2.1.5 *Nucleate Boiling*

When the wall is superheated the Chen correlation (Ref. 4) is used for both subcooled nucleate boiling and saturated nucleate boiling. Although the correlation was based on saturated liquid conditions, it is used for subcooled liquid conditions by using the bulk liquid temperature as the reference temperature for the convective part of the correlation. The wall is viewed as fully wetted by water except for vertically stratified conditions or, as the void fraction goes above 0.99, the heat transfer coefficient to liquid is ramped to zero at void fraction equal to 0.999 and the heat transfer to vapor is ramped up to the value obtained from the Dittus-Boelter correlation (Ref. 2). The standard deviation for all the data considered in the Chen correlation development is stated as 11.6 percent for the saturated nucleate boiling conditions. The correlation was tested by Moles and Shaw (Ref. 5) for the subcooled nucleate boiling regime where the data scatter is large (+180 to -60 percent). The data are generally underpredicted by the correlation.

4.2.1.6 *Critical Heat Flux*

RELAP5/MOD2 has been criticized for using the Biasi correlation (Refs. 6 and 7) for predicting the CHF in rod bundles because the correlation is based on tube data. MOD3 uses the 1986 AECL-UO Critical Heat Flux Lookup Table (Ref. 8) method by Groeneveld and co-workers. The table is made from tube data normalized to a tube inside diameter of 0.008 m but has factors that are applied to allow its use in other sized tubes or in rod bundles. In addition, it considers both forward and reverse flow, axial power shape, and the effect of boundary layer changes at both the bundle inlet and downstream of grid spacers. The root-mean-squared error at low pressure is generally below 20 percent. Its accuracy for rod bundles is uncertain.

4.2.1.7 *Minimum Stable Film Boiling Point*

The other point which is fixed on the boiling curve is the minimum film boiling point, T_{min}. In RELAP5 a constant T_{min} equal to 600 degrees K (620 degrees F) is used.

Table 4.1 RELAP5/MOD3 Heat Transfer Modes

Mode number	Heat transfer phenomena	Correlations
0	Noncondensable-steam-water	Kays,[4.2-1] Ditus-Boelter,[4.2-2] ESDU[a], Shah,[4.2-3] Churchill-Chu,[4.2-4] McAdams[4.2-5]
1	Supercritical or single-phase liquid	Same as mode 0
2	Single-phase liquid or subcooled wall with voidg<0.1	Same as mode 0
3	Subcooled nucleate boiling	Chen[4.2-6]
4	Saturated nucleate boiling	Same as mode 3
5	Subcooled transition boiling	Chen-Sundaram-Ozkaynak[4.2-7]
6	Saturated transition boiling	Same as mode 5
7	Subcooled film boiling	Bromley,[4.2-8] Sun-Gonzales-Tien,[4.2-9] and mode 0 Correlations
8	Saturated film boiling	Same as mode 7
9	Supercritical two-phase or single phase gas	Same as mode 0
10	Filmwise condensation	Nusselt,[4.2-10] Shah,[4.2-11] Colburn-Hougen[4.2-12]
11	Condensation in steam	Same as mode 10
3,4 for horizontal bundles	Nucleate boiling	Forster-Zuber,[4.2-13] Polley-Ralston-Grant,[4.2-14] ESDU[a]

a. ESDU (Engineering Science Data Unit, 73031, Nov 1973; ESDU International Plc, 27, Corsham Street, London, N1 6UA)

4.2.1.8 *Transition Boiling*

The Chen transition boiling model (Ref. 9) considers the total transition boiling heat transfer to be the sum of two individual components, one describing wall heat transfer to the liquid and a second describing the wall heat transfer to the vapor. Radiative heat transfer from the wall to the fluid is neglected. The model was compared to data (4167 points) with a standard deviation of 16 percent. The calculated heat flux value for transition boiling is applied to post-CHF heat transfer if it is larger than the value for film boiling.

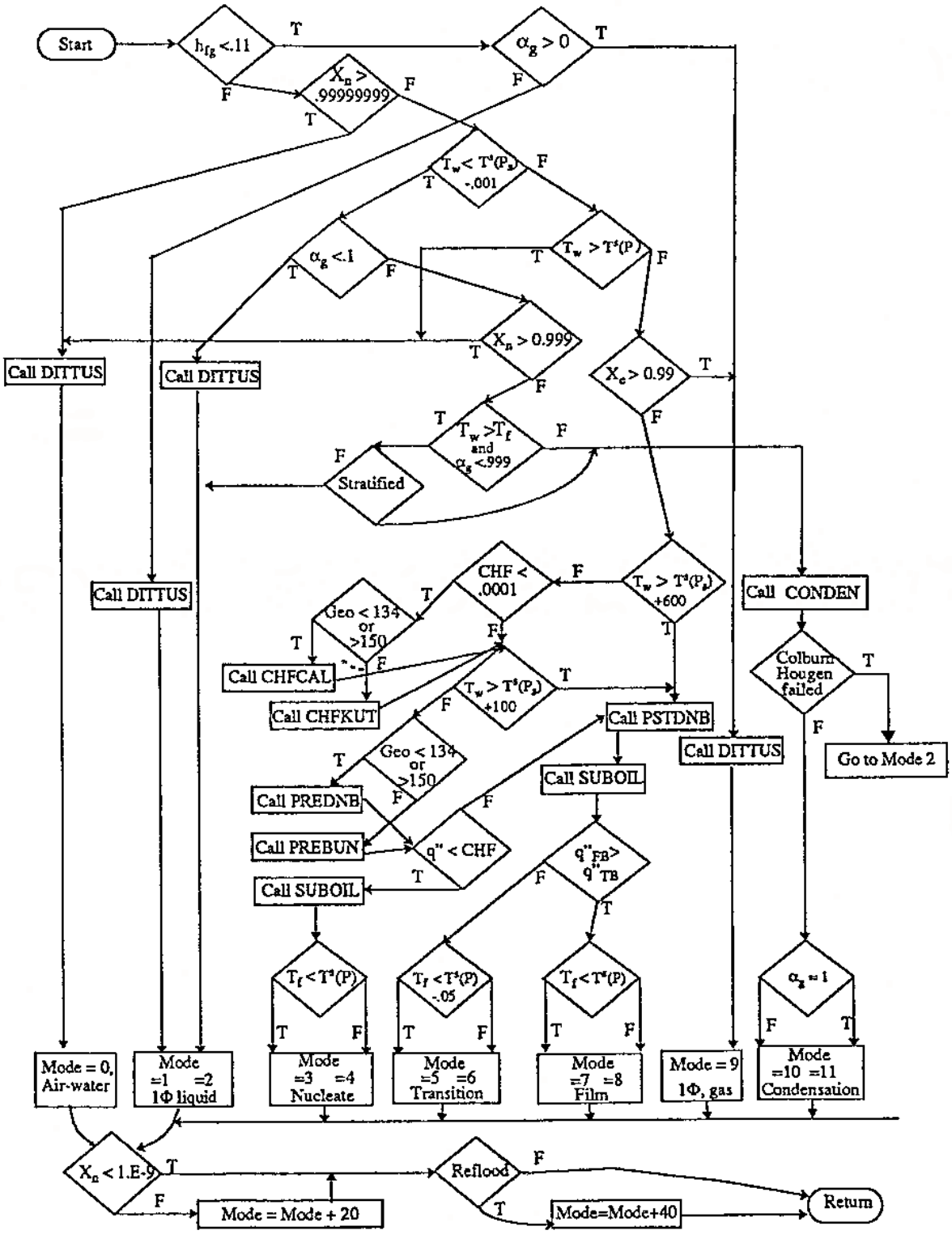

Figure 4.2 RELAP5 Wall Heat Transfer Flow Chart.

4.2.1.9 *Film Boiling*

Film boiling heat transfer is calculated with the Bromley correlation (Ref. 10). The data were correlated within +18 percent. In this case a radiation heat transfer model is included to calculate the radiation heat transfer from the wall to the fluid. This model is attributed to Sun (Ref. 11).

4.2.1.10 *Interfacial Heat Transfer*

The flow regime determines the bulk interfacial heat transfer correlation to be used. For each vertical flow regime (bubbly, slug, annular-mist, inverted annular, inverted slug and dispersed) a correlation is used to calculate the interfacial volumetric heat transfer coefficient for either superheated liquid, subcooled liquid, superheated gas or subcooled gas. These are generally semi-empirical and/or mechanistic models which have been modified from the original model in the literature (Refs. 12-17) to account for numerical stability concerns. The interfacial heat transfer is the product of the interfacial area based on the flow regime and the interfacial heat transfer coefficient.

For each flow regime the interfacial heat transfer coefficient is split into superheated-liquid (SHL), subcooled-liquid (SCL), superheated-gas (SHG) and subcooled-gas (SCG). In the code metastable states are generally driven rapidly to equilibrium by large empirical exponential functions. A summary of the interfacial areas and heat transfer coefficients is reported in Table 4.2 while the original interfacial heat transfer models are reported in References 12 to 17.

4.2.1.11 *Quench Front Model*

Besides the heat transfer to the fluid another important process during reflood transients is the rod axial conduction at the quench front. The rod axial conduction is considered in RELAP5/MOD3 by a specific reflood heat conduction model which is based on a mesh-rezoning scheme very similar to the one used in COBRA-TF.

4.2.1.12 *Liquid Entrainment*

The liquid droplet entrainment process is considered to occur only in the annular-mist flow regime where the Ishii and Mishima (Refs. 18 and 19) correlation is used to determine the fraction of liquid flux flowing as droplets. The model gives very accurate results at location where annular mist flow regime exists.

4.2.1.13 *Conclusions*

The heat transfer correlations are used to provide closure for the energy equations and are based on data which reflects only a subset of thermal-hydraulic conditions. Such correlations are very often applied outside their database. Moreover some of the correlations are based on engineering judgment, due partly to incompleteness of the science and partly to numerical stability requirements. From this perspective, by treating each correlation individually, the critical reviewer will conclude that the models are inadequate. In this case it is recognized that only an integral assessment is realistic where the global response of the code rather than the local response, becomes more meaningful.

Table 4.2 Summary of Interfacial Areas and Heat Transfer Coefficients

Flow Type	a_{gf}	$h_{if,SHL}$	$h_{if,SCL}$	$h_{ig,SHG}$	$h_{ig,SCG}$
Bubbly	$\frac{3.6\alpha_{bub}}{d_b}$	Lee-Ryley[M] Plesset-Zwick	Unal[M]	$10^4\, f(\Delta T_{sg})$	$10^4\, f(\Delta T_{sg})$
Slug:					
Bubbles	$\frac{3.6\alpha_{g,s}(1-\alpha_{TB})}{d_b}$	Lee-Ryley[M] Plesset-Zwick	Unal[M]	$10^4\, f(\Delta T_{sg})$	$10^4\, f(\Delta T_{sg})$
Taylor bubble	$\frac{4.5}{D}\alpha_{Tb}(2.0)$	$3\times10^6\, f(\Delta T_{sf})$	Sieder-Tate[M]	Lee-Ryley[M]	$10^4\, f(\Delta T_{sg})$
Annular mist:					
Drops	$\frac{3.6\alpha_{fd}(1-\alpha_{ff})}{d_d}$	$\frac{k_f}{d_d} f(\Delta T_{sf})$	Brown[M] $xf(\Delta T_{sf})$	Lee-Ryley[M]	$10^4\, f(\Delta T_{sg})$
Liquid film	$\frac{4}{D}(1-\alpha_{ff})^{1/2}(2.5)$	3×10^6	Theofanous[M]	Dittus-Boelter[M]	$10^4\, f(\Delta T_{sg})$
Inverted annular:					
Bubbles	$\frac{3.6\alpha_{bub}}{d_b}(1-\alpha_B)$	Lee-Ryley[M] Plesset-Zwick	Unal[M]	$10^4\, f(\Delta T_{sg})$	$10^4\, f(\Delta T_{sg})$
Vapor film	$\frac{4}{D}(1-\alpha_B)^{1/2}(2.5)$	3×10^6	Dittus-Boelter[M]	$\frac{k_g}{D} f(\Delta T_{sg})$	$\frac{k_g}{D} f(\Delta T_{sg})$
Inverted slug:					
Drops	$\frac{3.6\alpha_{drp}}{d_d}(1-\alpha_B)$	$\frac{k_f}{D} f(\Delta T_{sf})$	Brown[M] $xf(\Delta T_{sf})$	Lee-Ryley[M]	Lee-Ryley[M]
Taylor drop	$\frac{4.5}{D}(\alpha_B)(2.5)$	$\frac{k_f}{D} f(\Delta T_{sf})$	Brown[M] $xf(\Delta T_{sf})$	$\frac{k_g}{D} f(\Delta T_{sg})$	$\frac{k_g}{D} f(\Delta T_{sg})$
Dispersed (droplet, mist)	$\frac{3.6\alpha_{drp}}{d_d}$	$\frac{k_f}{D} f(\Delta T_{sf})$	Brown[M] $xf(\Delta T_{sf})$	Lee-Ryley[M] $xf(\Delta T_{sg})$	$10^4\, f(\Delta T_{sg})$
Horizontal stratified	$\frac{4\sin\theta}{\pi D}$	Dittus-Boelter $xf(\Delta T_{sf})$	Dittus-Boelter	Dittus-Boelter $10^4\, f(\Delta T_{sg})$	$10^4\, f(\Delta T_{sg})$
Vertical stratified	$\frac{A_c}{V}$	$h_{if,REG}$	McAdams	McAdams	$h_{ig,REG}$

a. SCL = subcooled liquid; SHL = superheated liquid; SHG = superheated gas; SCG = subcooled gas; M = modified; $f(\Delta T_{sg})$ = function of $\Delta T_{sg} = T^s - T_g$; $f(\Delta T_{sf})$ = function of $\Delta T_{sf} = T^s - T_f$; REG = flow regime when not vertically stratified.

For example, the correlation used to calculate the volumetric interfacial heat transfer coefficient in the annular mist flow between the liquid annular film and the gas core is based on the work of Brumfield et al. (Ref. 12). This is based on a falling liquid film surrounded by quiescent air, whereas annular-mist involves a turbulent, flowing vapor core. The correlation is also based on the liquid velocity.

The liquid velocity in the code is a single bulk value representing an average of both liquid annular film and the liquid droplets in the vapor core. As such, it is possible for the liquid velocity to be zero when the mass flow of droplets in one direction is balanced by the annular-film flow in the opposite direction. In such case, the code would incorrectly predicted zero for the interfacial heat transfer coefficient.

Another example of application of engineering judgment is the calculation of the droplet size in the inverted slug flow and dispersed flow regimes. The characteristic droplet size is calculated by assuming a critical Weber number equal to 6.0 and bounded by a minimum value for droplet diameter of 2.5 mm at low pressure, to allow more steam superheat during reflood. This is inconsistent with what observed during FLECHT-SEASET experiments where the Sauter mean diameter was estimated to be close to 1.0 mm.

A deficiency in RELAP5/MOD3 when compared to COBRA-TF is that there are not specific models to calculate the entrainment and/or deentrainment at spacer grids. In addition, entrainment and deentrainment are only calculated for annular flow or horizontal stratified flows.

Concerning the RELAP5/MOD3 capabilities to simulate accurately the phenomena involved in reflood transient, a big disadvantage is certainly the two field scheme where a single bulk value represents both the liquid in the continuous phase and droplets.

4.2.2 TRAC-BF1 Reflood Model

4.2.2.1 *Introduction*

The TRAC-BF1 model was developed specifically for BWRs and its development followed the development of the TRAC-PD2 PWR model. The heat transfer models are somewhat more simplified as compared to TRAC-PF1. However, a specific CHAN (channel) component was added to allow more accurate modeling of the BWR fuel channel during a LOCA. Surface-to-surface radiation heat transfer models were added with the CHAN component to calculate the radiation heat transfer expected in the canned assembly for LOCA conditions.

4.2.2.2 *Quench Front Model*

TRAC-BF1 uses a fine mesh renodalization model for modeling quench fronts. The fine mesh model inserts additional nodes into the heated wall if significant temperature gradients exist along the wall. In the case of reflood modeling, the use of the fine mesh option allows one to capture the rapid changes in temperature along a fuel rod due to the presence of the quench front. It increases both the accuracy and the robustness of the code. No special heat transfer model is employed in TRAC-BF1 to model the quench front. Instead, both the heat transfer and flow regime map used in all other wall heat transfer calculations is employed.

4.2.2.3 *Fine-Mesh Algorithm*

To model the advancing quench front, a numerical technique is employed which allows additional mesh points to be introduced within the structures (rods) around the quench front. The method allows the resolution of the high thermal gradients encountered near a quench front. The use of the fine mesh allows a more accurate representation of the heat transfer and energy content of the wall. The fine mesh heat transfer nodalization is superimposed on the coarse mesh usually used for the heat transfer analysis. Rows of transitory nodes are inserted whenever the temperature difference, DT_{max}, between adjacent nodes exceeds a user specified value. The number of nodes inserted is also user specified and remains during the entire reflood phase and move with the front. Multiple quench fronts may be modeled.

The model uses two values of DT_{max} , one for the quenching region that is in nucleate or transition boiling and the other to all other heat transfer regimes. The largest wall heat transfer occurs in the former regions.

4.2.3 TRAC-PF1 Reflood Model

4.2.3.1 *Introduction*

The TRAC-PF1 code series is the oldest best-estimate thermal-hydraulic codes developed for safety analysis purposes. The code formulation and interfacial heat, mass and momentum models have had several improvements over the years as the code has been used in a number of applications. TRAC-PF1 models the two-phase flow with two fields, liquid and vapor with three-dimensional capability within the vessel component. The coordinate systems used for the code are cylindrical such that the core region is modeled as a series of connected pie wedges. Specific models used in the code will be discussed below for this version of the code. A more recent version of the code, TRAC-PF1/MOD2 has a new reflood model. A brief review of this code will be added to this section at a later date.

4.2.3.2 *Quench Front Model*

TRAC-PF1 uses both fine mesh renodalization and a special heat transfer model for modeling quench fronts. The fine mesh model inserts additional nodes into the heated wall if significant axial temperature gradients exist along the wall. In the case of reflood modeling, the use of the fine mesh option allows one to capture the rapid changes in temperature along a fuel rod due to the presence of the quench front. It increases both the accuracy and the robustness of the code. The heat transfer model in MOD2 is based on Ishii and uses a special flow regime map which inserts additional regimes near the CHF point.

4.2.3.3 *Fine-Mesh Algorithm*

To model the advancing quench front, a numerical technique is employed which allows additional mesh points to be introduced within a region around the quench front. The method allows the resolution of the high thermal gradients encountered near a quench front. The use of the fine mesh allows a more accurate representation of the heat transfer and energy content of the wall. The fine mesh heat transfer nodalization is superimposed on the coarse mesh usually used for the heat transfer analysis. Rows of transitory nodes are inserted whenever the temperature difference, DT_{max}, between adjacent nodes exceeds a user specified value. The

number of nodes inserted is also user specified and remains during the entire reflood phase and move with the front. Multiple quench fronts may be modeled.

The model uses two values of DT_{max}, one for the quenching region that is in nucleate or transition boiling and the other to all other heat transfer regimes. The largest wall heat transfer occurs in the former regions.

4.2.3.4 *Heat Transfer Model During Reflood*

The model for calculating the heat transfer in TRAC-PF1 is based on the void-fraction wall-superheat plane shown in Figure 4.3, and consists of eight different heat transfer regimes, which are listed in Table 4.3. The primary basis for correlation selection in TRAC-PF1 is the void fraction and wall superheat. While some pressure dependence enters the correlations through the properties of the parameters used in the calculations, the choice of correlation for any one particular regime is not based primarily on pressure criteria. The same is true for phasic temperatures and phasic velocities, which are introduced into the correlations through the heat flux equations and the flow correlations, respectively. To avoid any discontinuities in the heat flux, the current version of TRAC-PF1/MOD 2 (Ref. 20) evaluates the heat transfer coefficient for both laminar and turbulent natural convection, as well as forced convection, and then chooses the maximum value of the heat transfer coefficient to use in calculations.

Table 4.3 TRAC-PF1/MOD2 Heat Transfer Regimes

Mode	Wall-to-Fluid Heat Transfer Regime
1	Forced Convection to Single-Phase Liquid
2	Nucleate Boiling
3	Transition Boiling
4	Film Boiling
6	Convection to Single-Phase Vapor
7	Convection to Two-Phase Mixture
11	Condensation
12	Liquid Natural Convection

In each of the heat transfer regimes, the heat transfer coefficients are calculated in the subroutines HTCOR and HTVSSL. HTVSSL is used during reflood. The correlations used in HTVSSL are summarized here in detail. With the exception of the film boiling regime and the transition boiling regime, many of the correlations used in HTVSSL are the same as HTCOR. The post-CHF flow-regimes in HTVSSL are based on the more recent work done by Ishii, which showed that there are four inverted annular flow regimes downstream of the transition boiling regime, as shown in Figure 4.4. The selection logic for HTVSSL is shown in detail in Figures 4.5 through 4.11.

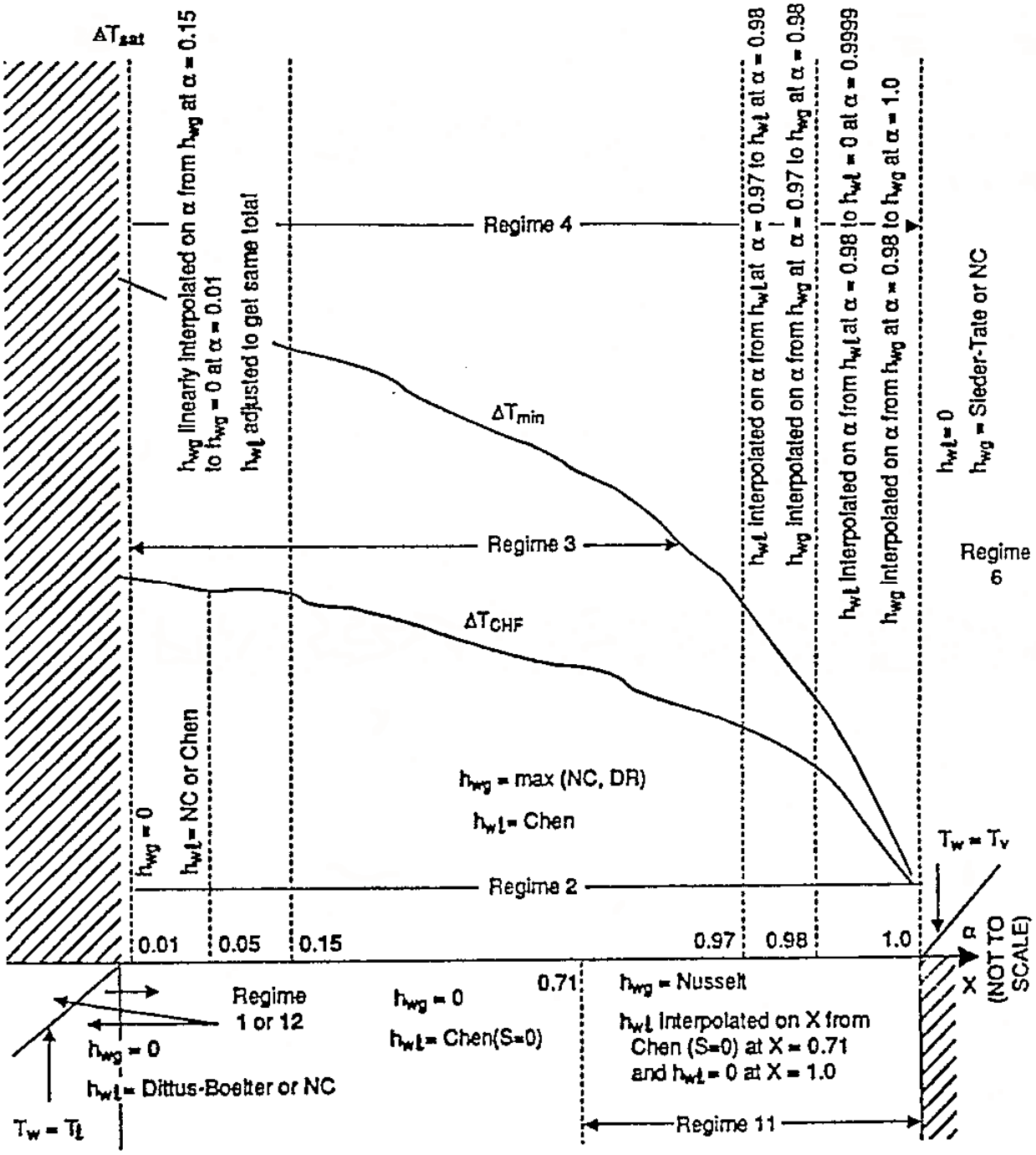

Figure 4.3 Void Fraction Superheat Plane.

During reflood, TRAC-PF1 employs a special flow-regime map based on the flow-regimes depicted in Figure 4.4. According to Ishii, along the flow channel various flow regimes occur beyond the point of CHF. These different flow regimes are characterized by different heat transfer conditions requiring different closure relations. The different closure relations are

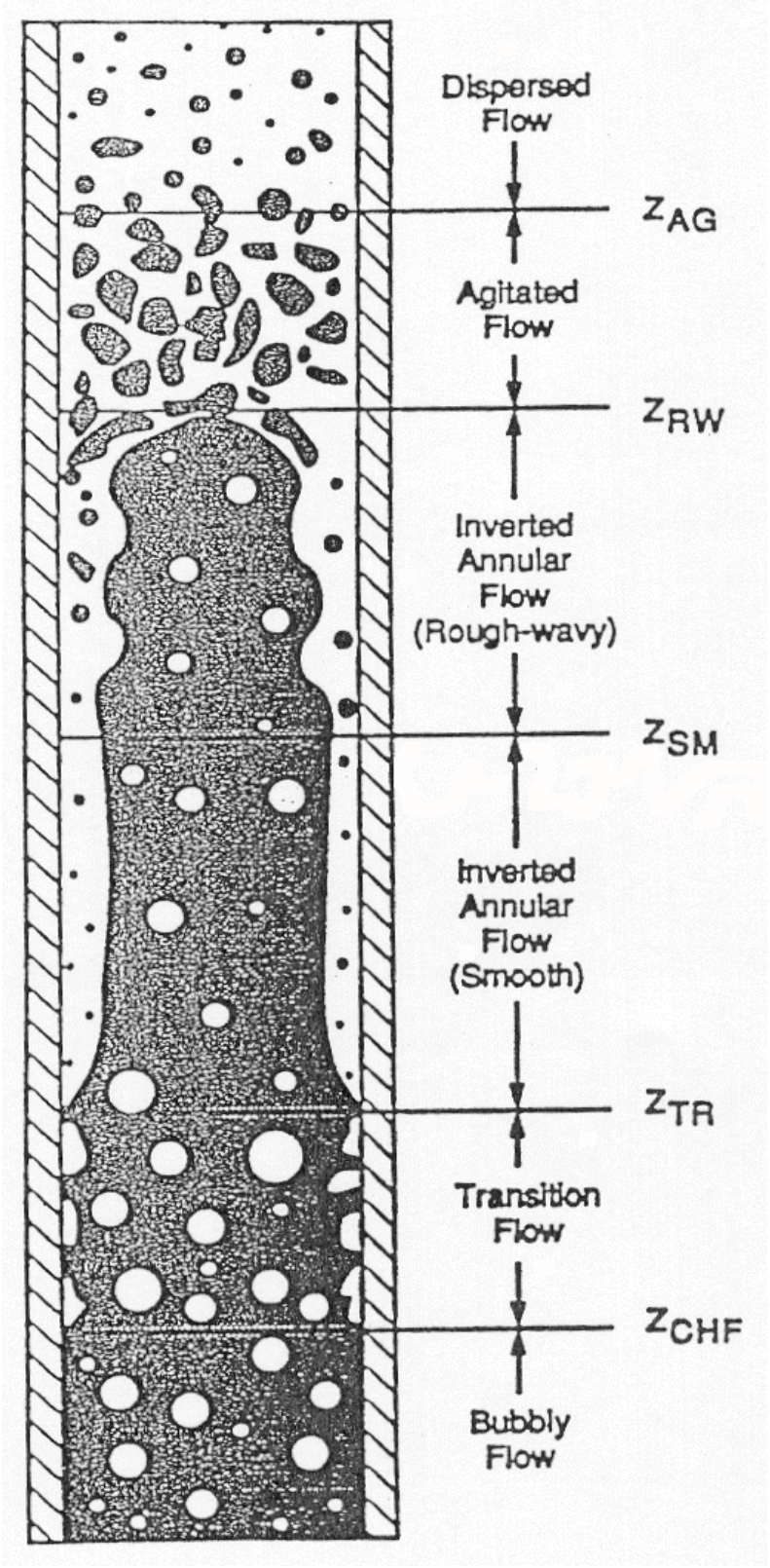

Figure 4.4 Flow Regime Map During Reflood.

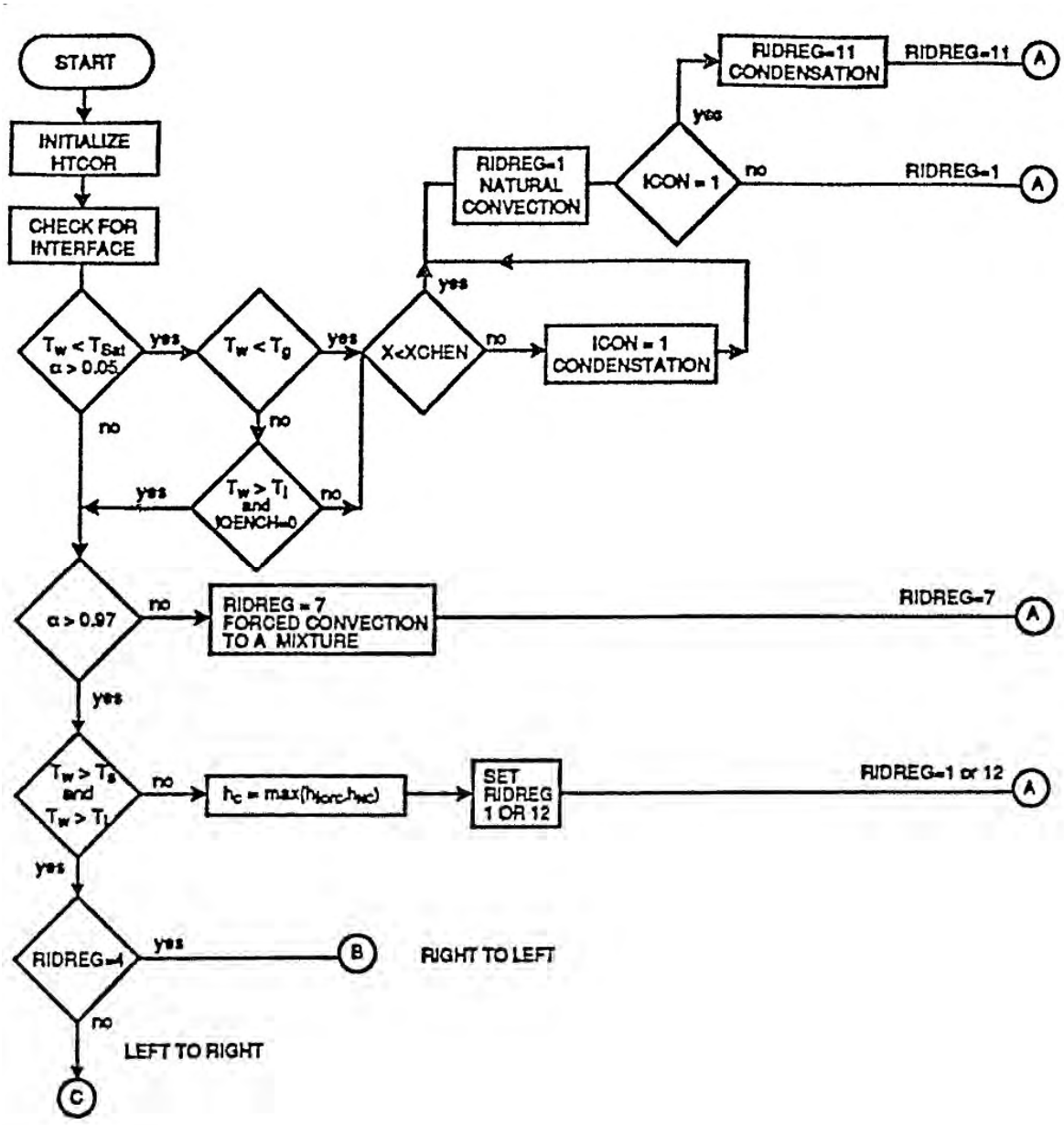

Figure 4.5 HTC Correlation Selection Logic.

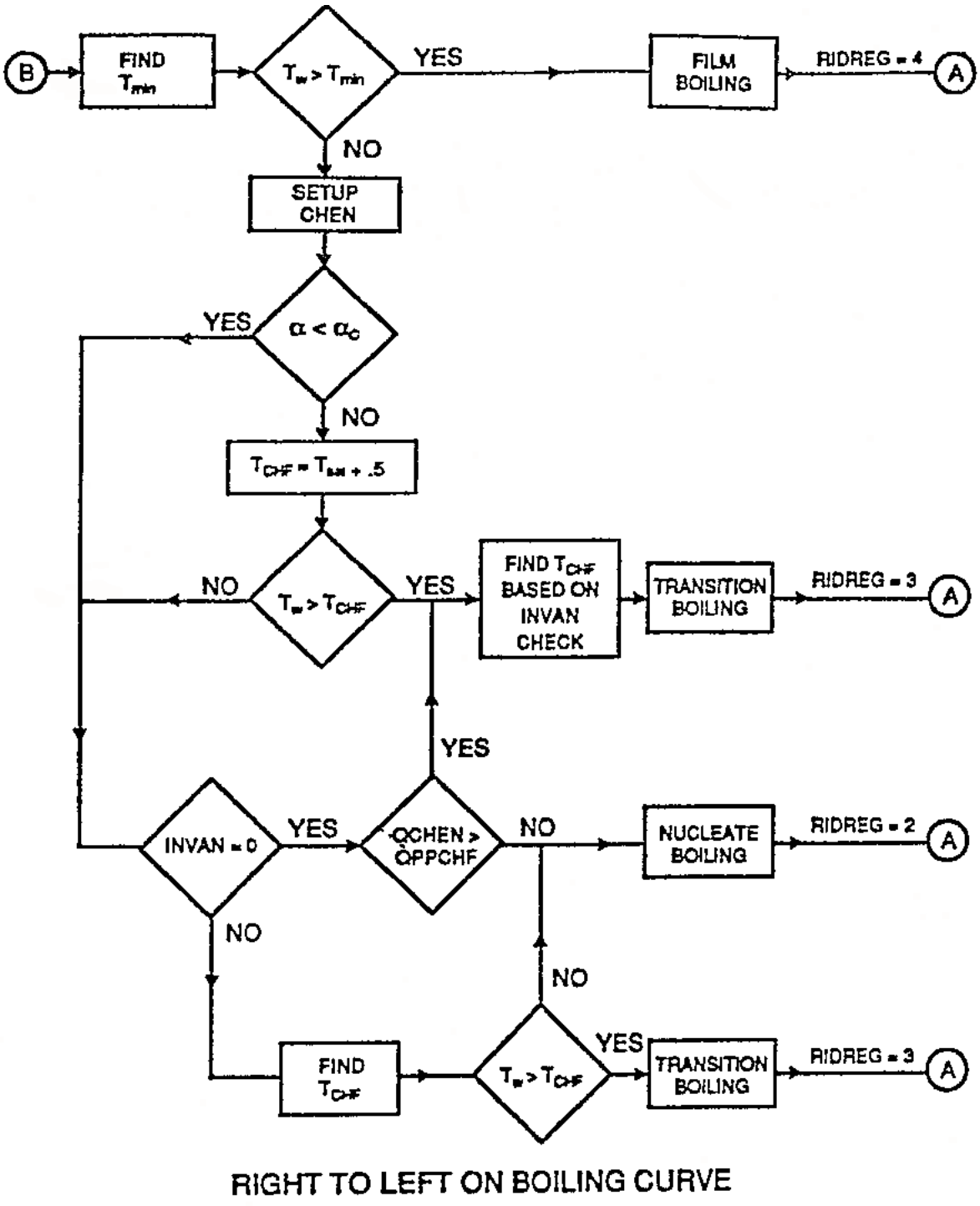

Figure 4.6 HTC Correlation Selection Logic.

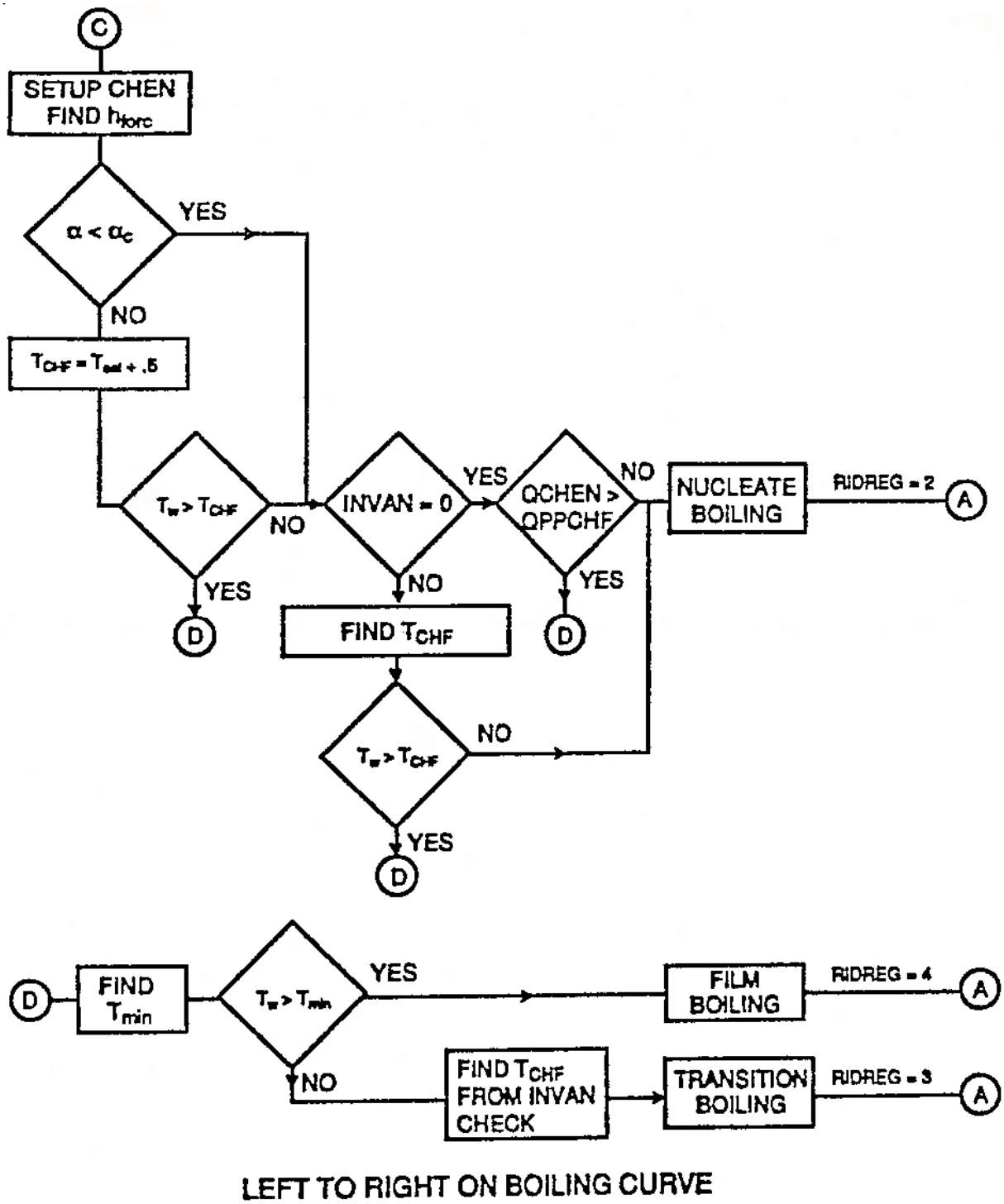

Figure 4.7 HTC Correlation Selection Logic.

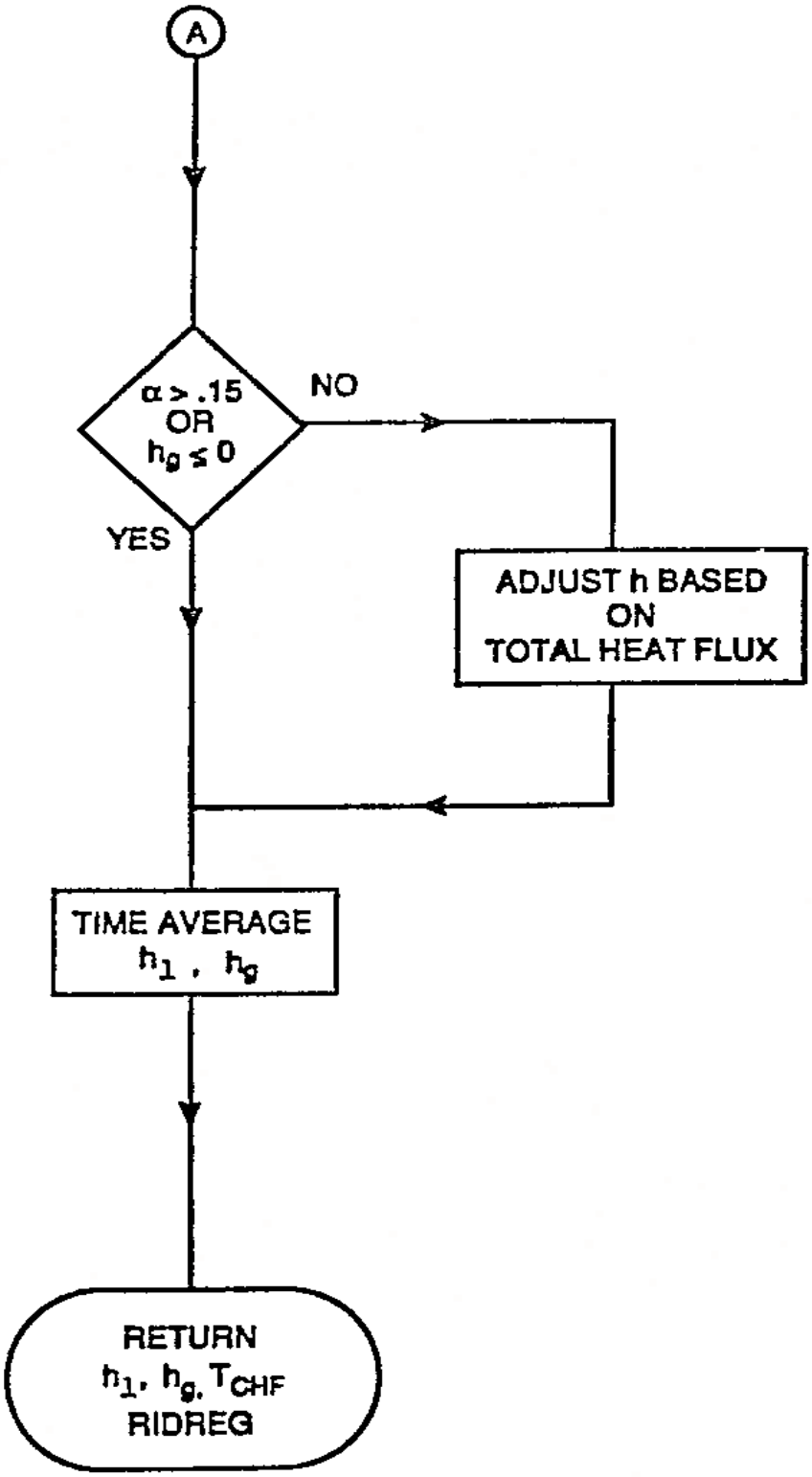

Figure 4.8 HTC Correlation Selection Logic.

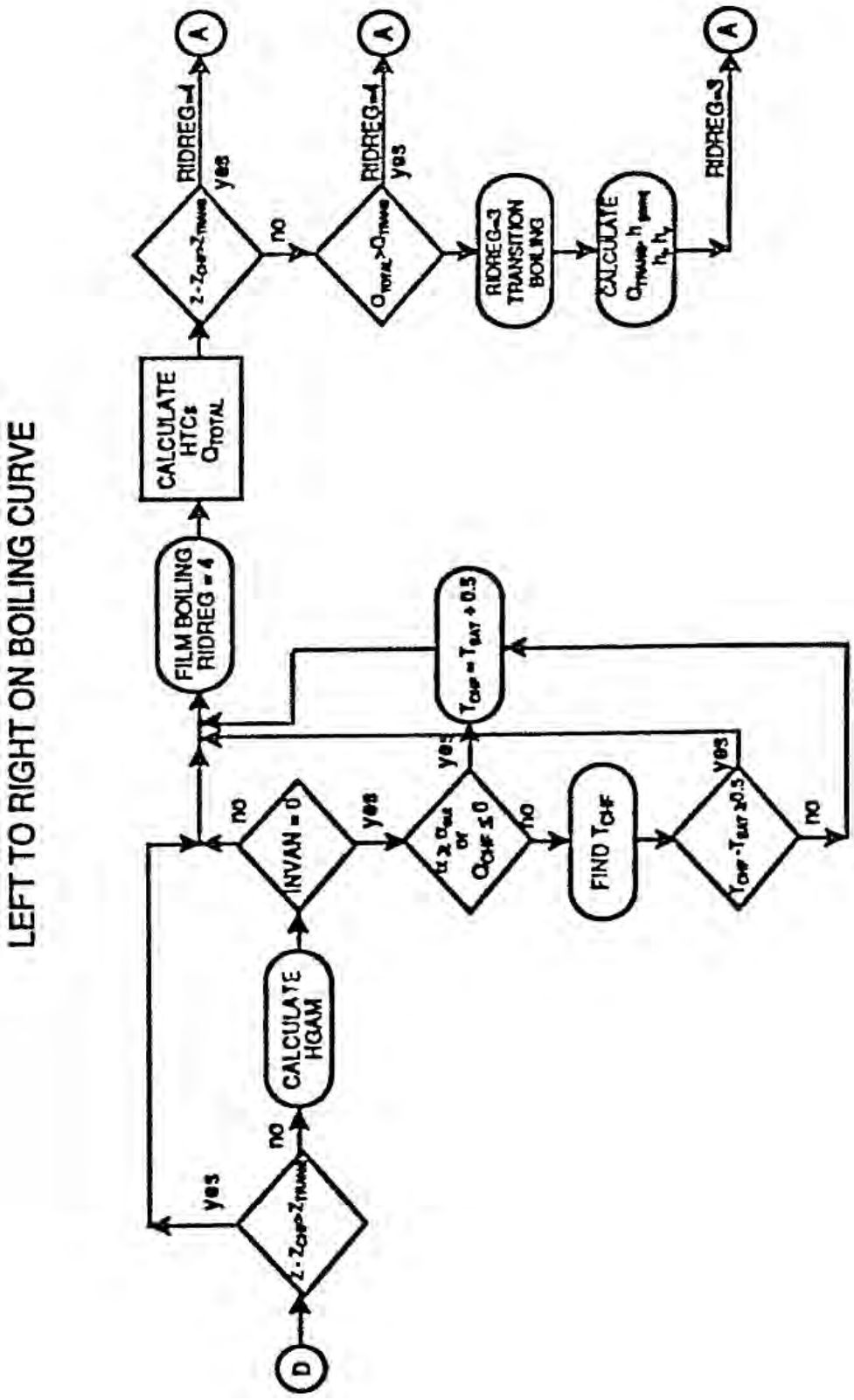

Figure 4.9 HTC Correlation Selection Logic for Reflood Model.

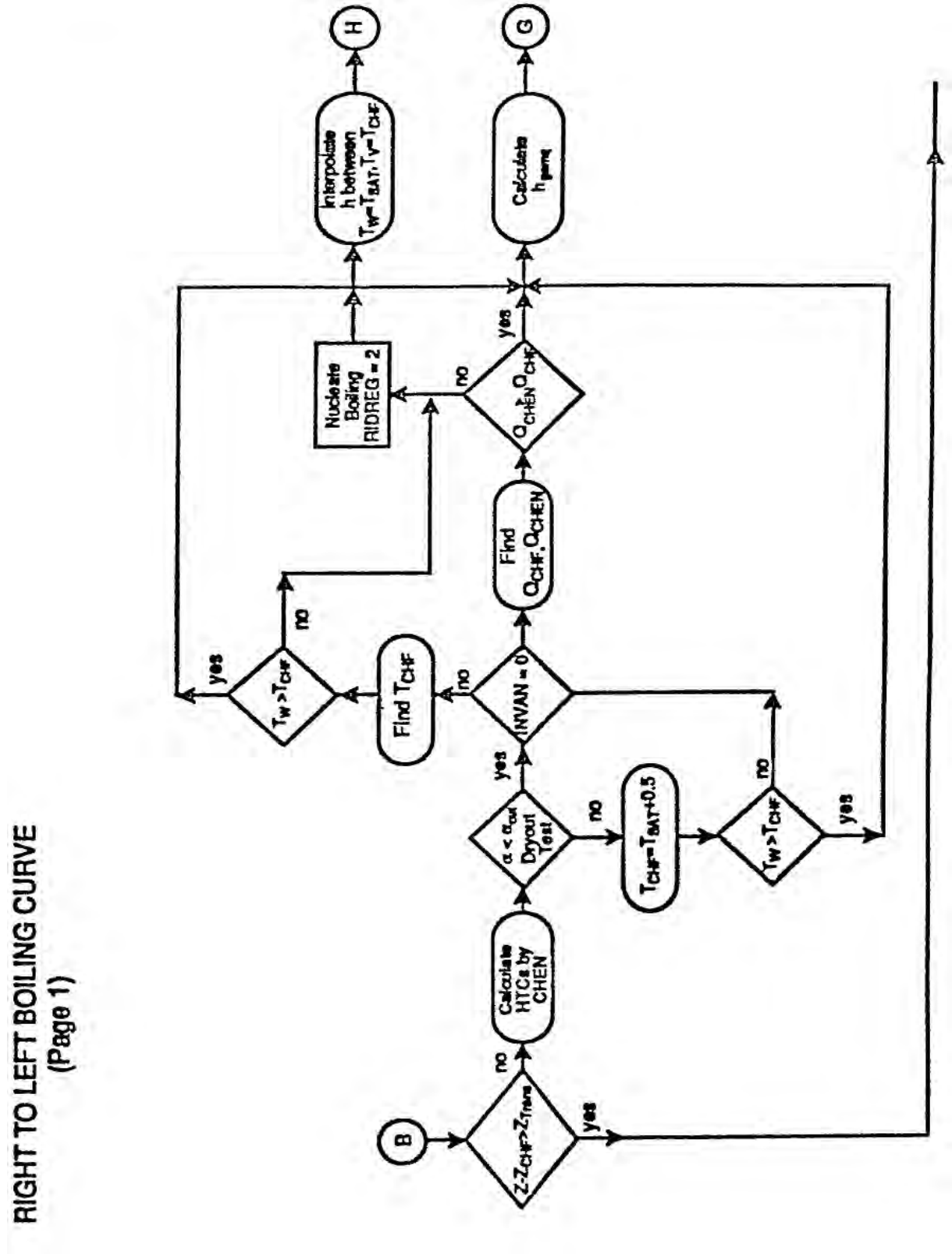

Figure 4.10 HTC Correlation Selection Logic for Reflood Model.

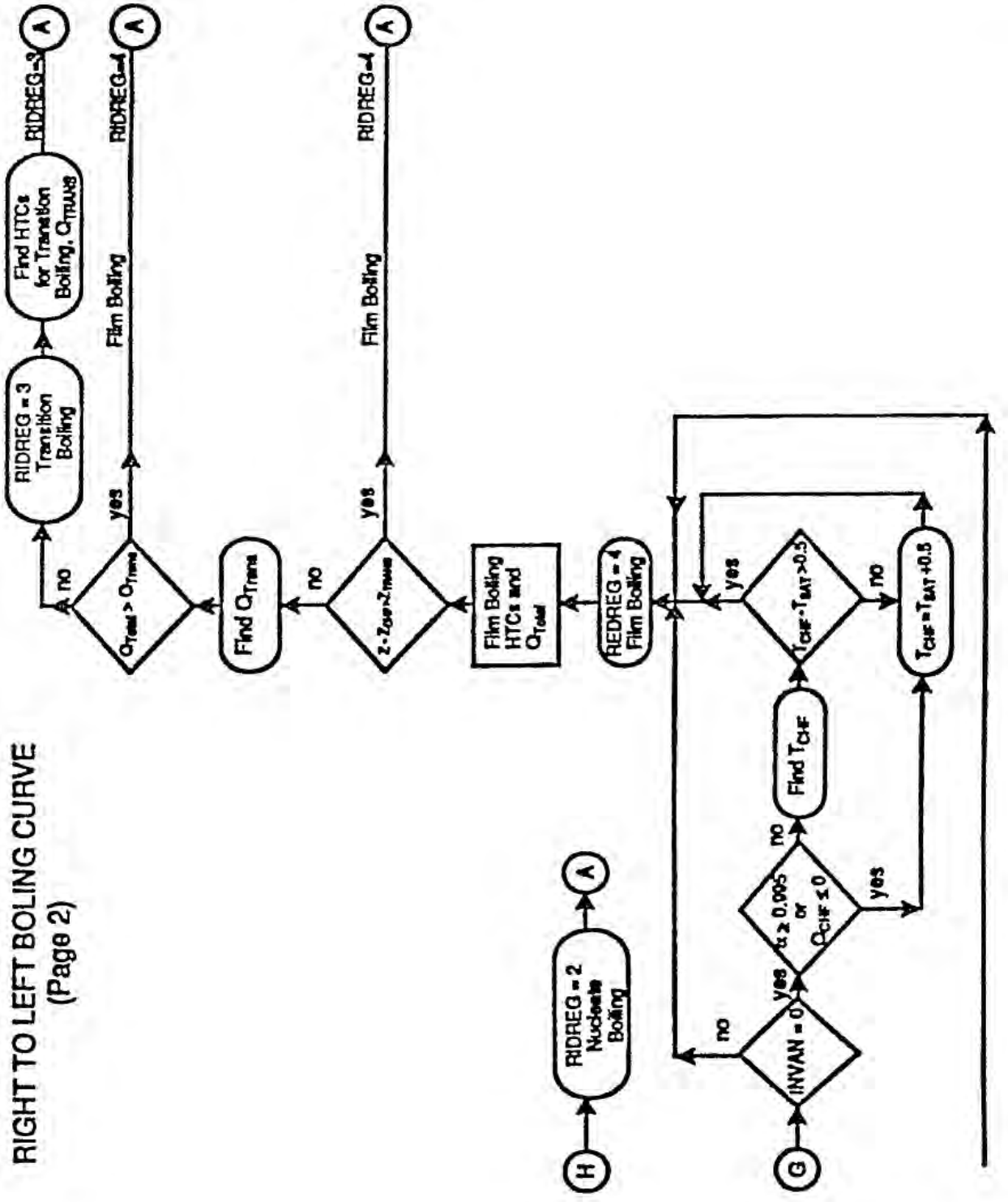

Figure 4.11 HTC Correlation Selection Logic for Reflood Model.

applied depending upon the location of the flow regime within the cell. A weighting factor is applied based on the cell length and the elevation within the cell at which the regime occurs. Table 4.4 shows how the weighting factors are calculated (Ref. 20).

Table 4.4 Weighting Factors of Reflood Interfacial Heat Transfer Models

z	W_{sb}	W_{sm}	W_{rw}	W_{ds}	W_{inv}
$z_t \le Z_{TR}$	1	0	0	0	0
$Z_{TR} < z_t < Z_{SM}$	Eq. (4 – 102)*	Eq. (4 – 103)	0	0	Eq. (4 – 103)
$Z_{SM} \le z_t < Z_{AG}$	Eq. (4 – 102)	Eq. (4 – 103)	Eq. (4 – 104)	0	Eq. (4 – 105)
$Z_{AG} \le z_t$	Eq. (4 – 102)	Eq. (4 – 103)	Eq. (4 – 104)	Eq. (4 – 106)	Eq. (4 – 105)
$z_b \le Z_{AG}$	0	0	0	1	0

*See Reference 20 for specific equations

$$W_{inv} = W_{rs} + W_{sm} \tag{4-1}$$

$$W_{ds} = 1 - W_{sb} - W_{rs} - W_{sm} \tag{4-2}$$

The closure relationship is then calculated according to

$$X_{reflood} = W_{sb} \cdot X_{bubbly} + W_{ds} \cdot X_{dispersed} + W_{inv} \cdot X_{inverted} \tag{4-3}$$

where X represents either A_i , H_{ALVE} , H_{CHTI} , or H_{CHTA}. For flashing, the maximum value of H_{ALVE} or a special model described in the next section is used. For the case of noncondensables, the value of H_{ALVE} is modified. The exact process is discussed in the references.

4.2.3.5 *Bubbly-Flow Models*

In bubbly CHF upstream of the quench front, the void fraction is restricted to be between 0.05 and 0.30. Slugs are not allowed to be formed. The interfacial area and heat transfer coefficient are identical to those used in HTCOR under similar conditions. If T_ℓ is greater than T_{sat} then the heat transfer coefficient is not calculated using this method. Instead, the reflood model uses a simple model based on the kinetic theory of evaporation from liquid surfaces. The theoretical maximum evaporation rate predicted by this theory was converted by the code authors to a Heat Transfer Coefficient (HTC). The coefficient of evaporation of 0.4 is modified to predict evaporation rate for each of the flow regimes in nucleate and film boiling. The HTC for flashing is given by:

$$H_{fls} = C_{eva} h_{fls,teo} = C_{eva} \times 0.1857 \left(\frac{q_v h_{fg}^2}{T_{sat}^{1.5}} \right) \tag{4-4}$$

The coefficient C_{eva} is defined for bubbly- and mist-annular-flow and is assumed to be void fraction dependent in the bubbly flow when the cell void fraction is between 0.3 and 0.5, otherwise it is a constant. The interfacial areas in bubbly flow are identical to those in HTCOR.

The liquid side heat transfer factor during flashing is then given by

$$H_{ALV} = h_{fls} A_{I,bubble} \tag{4-5}$$

For the mist annular regime, C_{eva} is equal to 0.0002.

If the flow regime is determined as the transition between the bubbly and mist annular flows, an interpolation is used according to

$$H_{ALV,trans} = W \cdot H_{ALV,mist} + (1 - W) \cdot H_{ALV,bubbly} \tag{4-6}$$

4.2.3.6 *Dispersed and Post-Agitated Inverted Annular Flows*

The flow regimes farthest from the quench front according to Ishii are the dispersed and post-agitated inverted annular flows. In the reflood model, the void fraction is restricted to be between 0.3 and 0.9995. If there is a cold wall in the hydro cell, a thin liquid film can form and is allowed by the model. To evaluate the interfacial area it is necessary to divide the liquid into a film and droplet phase. The liquid is divided by determining a liquid film thickness and equivalent liquid fraction for the film. Once this is determined, a liquid drop fraction may be obtained and the corresponding interfacial areas calculated.

The vapor to interface heat transfer is calculated in the dispersed flow regime by first calculating the mass fraction of liquid. The mass fraction is then used to determine a homogeneous void fraction. If the homogeneous void fraction is greater than 0.75 and the difference between $1-\alpha_{dd}$ is less than or equal to 0.95, then $H_{CHTI,dispersed}$ is set equal to 10^{-6} W/K. Otherwise a correlation is used according to Unal et al (Ref. 21). The correlation was modified to allow its use as a heat transfer coefficient instead of a vapor generation rate. Changes were also made to the constants which appear in the correlation.

If the cell void fraction is less than 0.98, then the flow regime is assumed to be post-agitated inverted annular flow. In that case, the value of H_{CHTI} is calculated using the value for dispersed inverted annular flow with a void fraction weighting according to

$$H_{CHTI,post-ag} = H_{CHTI,DP}\left[\frac{\alpha - \alpha_{SM}}{\alpha_{DP} - \alpha_{SM}}\right]^{-0.01} \tag{4-7}$$

The liquid heat transfer in the reflood model is not calculated using subroutine HTIF when T_ℓ is less then T_{sat}. Rather, the sensible heat that goes to the sub-cooled liquid is calculated in HTVSSL in the wall-to-liquid HTC. If the liquid is superheated, then the coefficient in the flashing model is set equal to 0.002. The value of H_{ALV} for the dispersed or post-agitated inverted annular flow is calculated as

$$H_{ALV,\text{dispersed (or post-agitated)}} = h_{fls} A_{I,\text{dispersed (or post-agitated)}} \tag{4-8}$$

where h_{fls} is calculated according to the flashing model discussed earlier.

4.2.3.7 *Inverted Annular Flow*

In inverted annular flow, the void fraction is limited to between 0.05 and 0.95. In this region, the interfacial area and the heat transfer coefficients are calculated according to the following:

The hydraulic area of the liquid core is calculated by adjusting the hydraulic diameter of the channel by multiplying by 1-α. The interfacial area is computed as the product of the core hydraulic diameter and the length $\pi D \cdot x$. If flashing is occurring, then the interfacial area is recalculated using an expression for the film thickness developed by Ishii (Ref. 22). This is then used to calculate the wall void fraction and the interfacial surface area near the walls. The void fraction for bubbles may then be determined using the interfacial area near the walls and the void fraction. The total interfacial area is then the sum of the wall and bubble interfacial area.

The vapor heat transfer model is a simple product of constant times the interfacial area for inverted flow calculated using the method in the previous paragraph. The liquid side heat transfer coefficient is not calculated in subroutine HTIF for the inverted annular flow regime when T_ℓ is less than T_{sat}. The sensible heat is calculated in HTVSSL in the wall-to-liquid heat transfer coefficient. As is the case for post-agitated flow, the coefficient for evaporation is set equal to 0.002. The $H_{ALV,}$ uses the same formula as used in dispersed and post-agitated flow.

4.2.3.8 *Spacer Grid Model*

If grid spacers are present, an attempt is made to correct for the cooling effect of the grid spacers. The vapor-to-liquid heat transfer coefficient is modified to account for the temperature of the grid spacer.

4.2.3.9 *Noncondensables*

An attempt to account for the presence of noncondensables is also made.

4.2.4 COBRA-TF Code

4.2.4.1 *Introduction*

The COBRA-TF code was developed by Pacific Northwest Laboratory under the sponsorship of the Nuclear Regulatory Commission to provide a best-estimate calculational capability for transient and accident analysis. The version of the COBRA-TF code (Ref. 24) which is being used in the RBHT program was refined from the original version of the COBRA-TRAC code Ref. 25) as part of the FLECHT-SEASET 163-Rod Blocked Bundle Test and analysis program.

COBRA-TF has several differences as compared to the TRAC and RELAP codes which make it more suitable for analyzing rod bundle reflood tests. COBRA-TF uses a separated flow model for the two-phase region conservation equations which model three distinct fields. The three fields which are modeled include: the continuous liquid field for low void fraction flow and falling or climbing films; vapor field for the steam flow, and the entrained droplet field. Using two liquid fields is a more accurate and convenient method of representing the liquid phase over a wide range of two-phase situations which would occur during reflood of a hot bundle. Flow regimes such as inverted annular, churn-turbulent, and droplet flow can be modeled more accurately. One can also model the flow regime transitions more accurately as well as countercurrent flow in which a liquid film falls and the entrained droplets are carried upward. In addition in the

FLECHT-SEASET version of the COBRA-TF code, a fourth field exists which models the effects of a non-condensable gas.

Mass conservation equations are written for each field, continuous liquid, vapor, entrained liquid, and non-condensable gas. The energy equations are more simplified in that the continuous liquid and the entrained liquid are assumed to have the same liquid temperature within the same computational cell. Also, a combined energy equation is used for the vapor and non-condensable gas. There are three momentum equations solved for the vapor, continuous liquid, and the entrained liquid. The momentum equations are three dimensional such that they can represent a rod bundle array with the smallest computational cell being a single subchannel. When the code is used in the subchannel formulation, some of the higher order momentum flux terms which represent the cross products of the lateral velocities are ignored.

In the FLECHT-SEASET flow blockage program (Ref. 24), the capabilities of COBRA-TF were expanded to include a small droplet field which is used to model the smaller micro-droplets which are generated as larger drops shatter when they impact structures in the rod bundles such as spacer grids and flow blockages. There were some simplifications used for the small droplet field model. The small droplet field was not directly coupled to the hydrodynamic solution matrix, the interface of the small droplet field occurred as source and sink terms in the equation such that the mass of the entrained liquid was preserved. It was also assumed that there was no lateral flow of the small droplets, and the model was not valid for negative top down flow.

COBRA-TF is also unique in that in addition to the conservation equations, the code uses a interfacial area transport equation which calculates the total droplet interfacial area in a computational cell considering the sources and sinks of interfacial area such as entrainment and deposition of the drops on to a liquid film.

One of the differences of COBRA-TF from the other systems codes is that it has both "hot" wall and "cold" wall flow regimes. The hot wall regime is used when the wall temperature exceeds T_{sat} + 42 degrees C (75 degrees F). The hot wall regimes include subcooled inverted annular flow, saturated liquid churn or slug flow, dispersed droplet-vapor flow, falling film flow, and top-down liquid deluge flow. The hot wall flow regimes and logic selection are shown in Figures 4.12 and 4.13. For bottom reflood when the reflood flow is subcooled, an inverted annular flow regime is assumed. If the liquid is saturated, the liquid churn or slug flow regime is assumed and the liquid is treated as very large droplets surrounded by vapor.

4.2.4.2 *COBRA-TF Heat Transfer Package*

The heat transfer package in COBRA-TF consists of a library of correlations and a selection logic which allows the code to predict a boiling curve as a function of the computational cell void fraction, pressure, mass flow and the heated surface temperature. Figure 4.14 shows the boiling curve and regions of interest and Figure 4.15 shows the heat transfer regime selection logic in a simplified fashion. The heat transfer package which is used by the code calculates both the wall-to-fluid heat transfer as well as the interfacial heat transfer between the phases (Table 4.5). Since separate energy equations are used for the phases, a non-equilibrium flow will be calculated in some cases. Therefore, the interfacial heat transfer and the interfacial heat transfer area are calculated to determine the temperature of each phase. Both will be discussed below with the emphasis on reflood heat transfer.

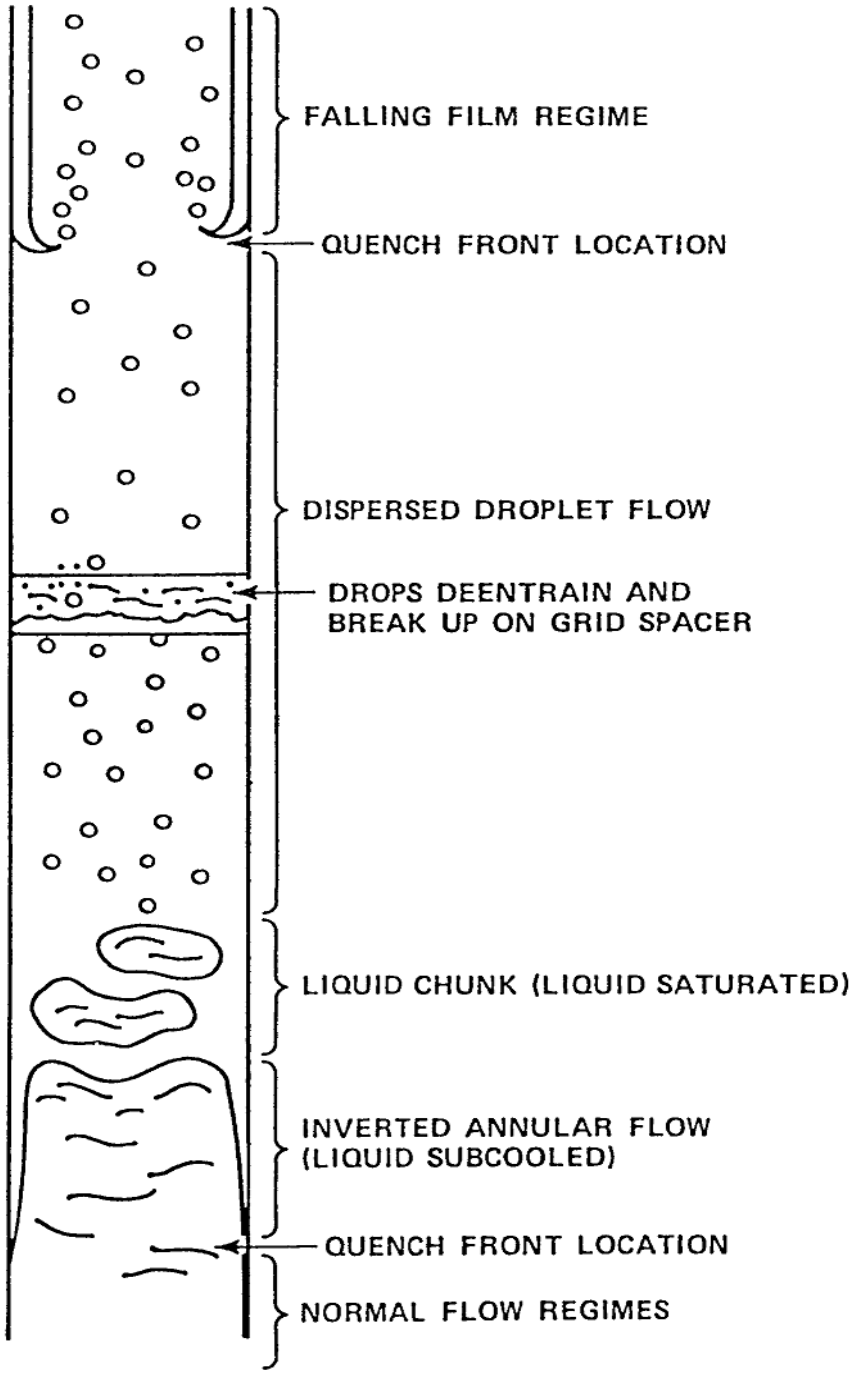

Figure 4.12 Hot Wall Flow Regimes.

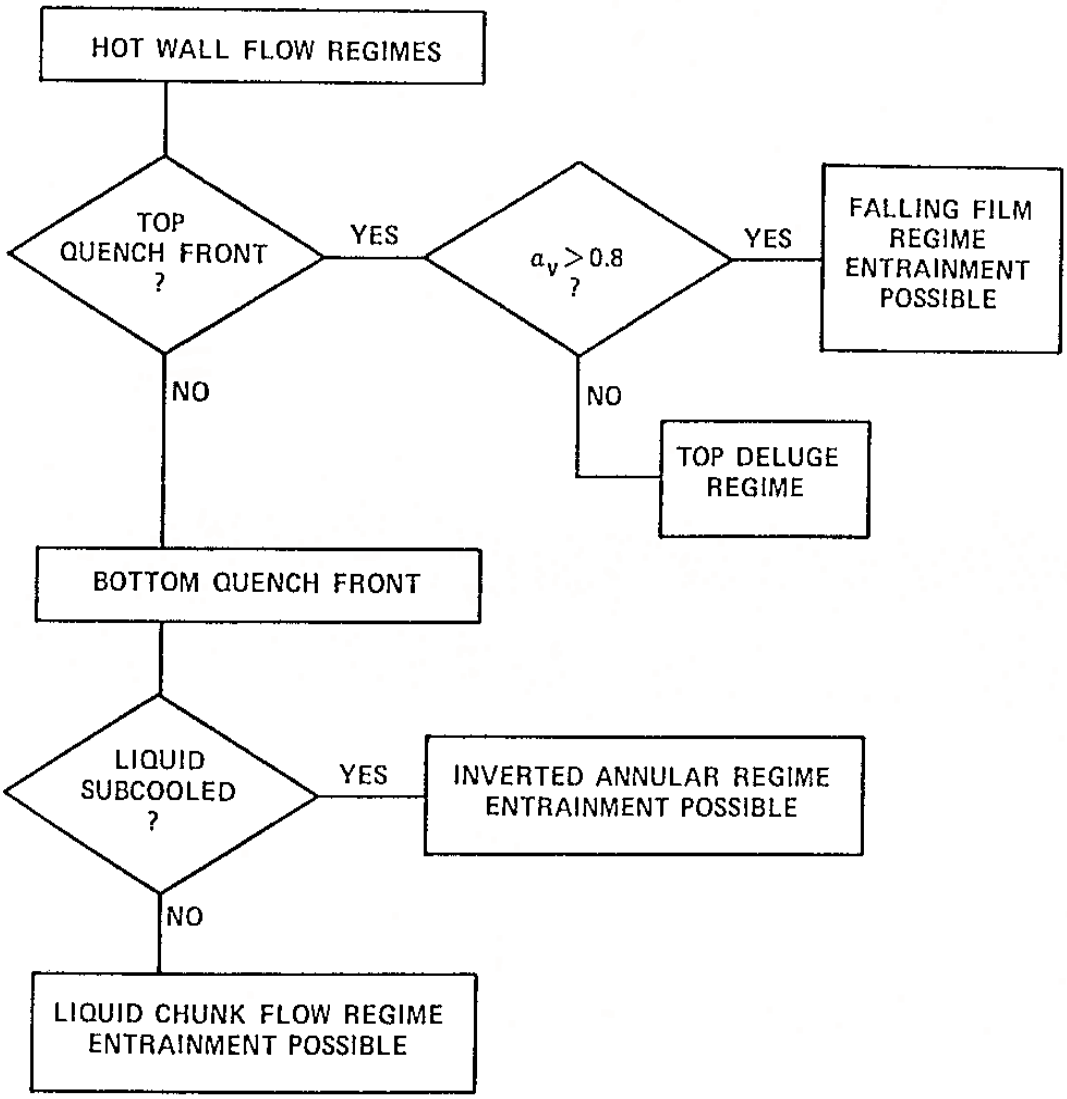

Figure 4.13 Hot Wall Flow Regime Selection Logic.

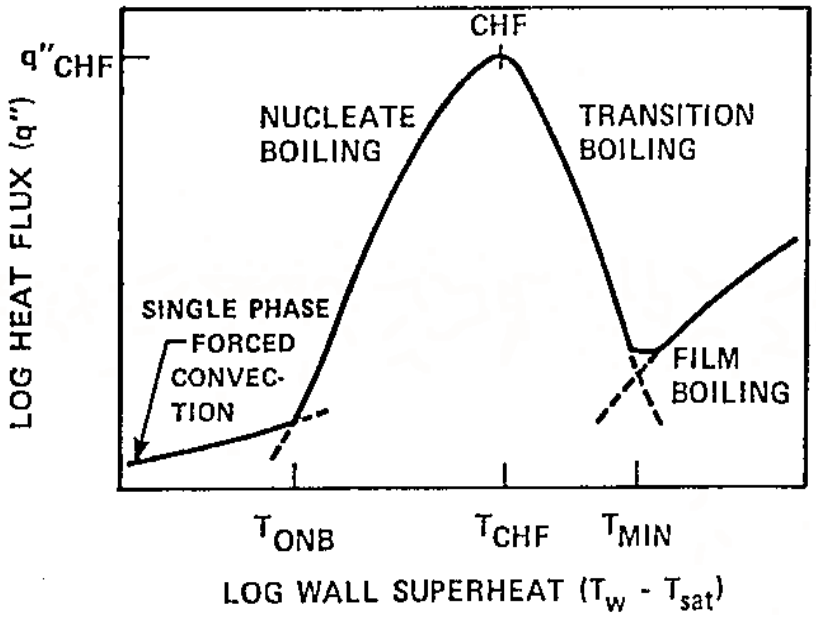

Figure 4.14 Schematic Representation of Boiling Curve.

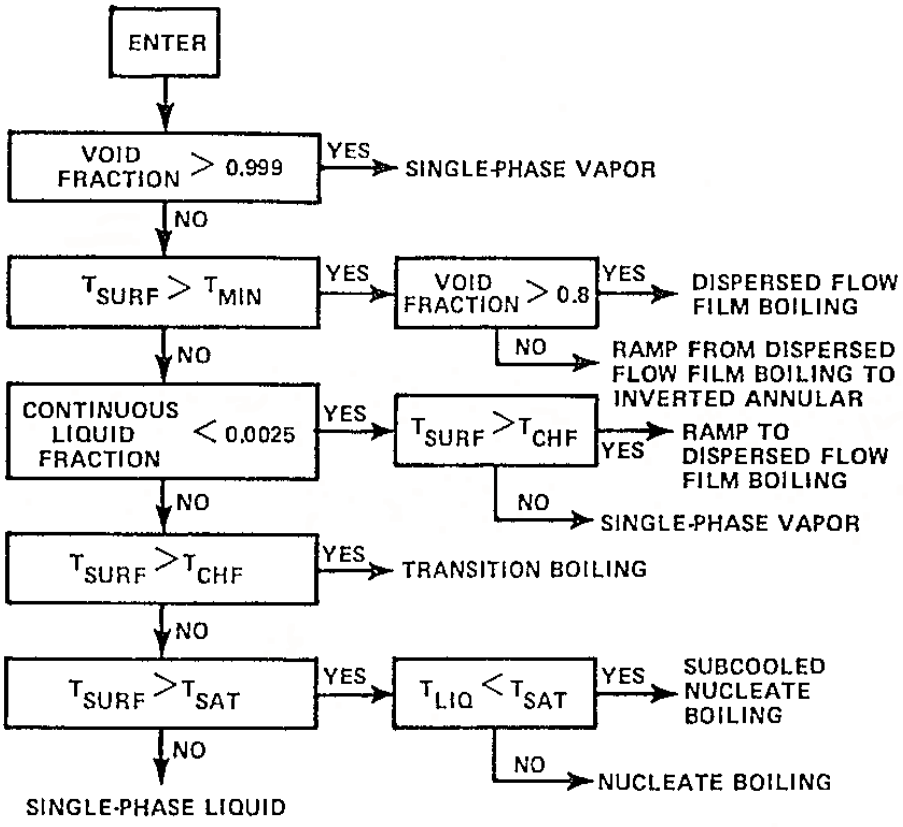

Figure 4.15 Heat Transfer Regime Selection Logic.

Table 4.5 Interfacial Heat Transfer Area Per Unit Volume

Mode of Heat Transfer	Correlation (Btu/hr-ft^2-°F)	Flow Regime
H_{SHV}	$\frac{f_I}{2} \rho_v C_{p_v} \lvert U_{v\ell} \rvert Pr_v^{-2/3}$	Film
	$\frac{(2.0 + 0.55\ Re_d^{0.5}\ Pr_v^{1/3})\ \frac{k_v}{2r_d}}{1 + 0.5\ (h_v - h_g)/h_{fg}}$	Drop(a)
	$\frac{(2.0 + 0.55\ Re_v^{0.5}\ Pr_v^{1/3})\ \frac{k_v}{D_H}}{1 + 0.5\ (h_v - h_g)/h_{fg}}$	Liquid chunk, inverted annular
H_{SCV}	1.0×10^4 (b)	All regimes
H_{SHL}	1.0×10^5 (b)	Large bubble, liquid chunk and inverted annular
H_{SHL}	The maximum of $1.925\ \rho_\ell\ C_{p_\ell} \lvert U_\ell \rvert / [Re_f^{2/3}\ Pr_\ell^{2/3}]$ for $Re_f \leq 1000$	Film(c)

a. Rowe, P. N., et al., "Heat Transfer From a Single Sphere in an Extensive Flowing Fluid," Trans. Inst. Chem. Engin. 43, 1965, T14-T31.

b. A constant large value is used to drive toward phase equilibrium.

c. From Colburn analogy using friction factors of Hughmark(e)

Table 4.5 Interfacial Heat Transfer Area Per Unit Volume (Continued)

Mode of Heat Transfer	Correlation (Btu/hr-ft^2-°F)	Flow Regime
H_{SCL}	$0.2701 \rho_\ell C_{p_\ell} \mid U_\ell \mid / [Re_f^{0.38} Pr_\ell^{2/3}]$ for $1000 \leq Re_f$ and $2.0\ k_\ell/\delta$	
	$C \frac{\pi^2}{3} \frac{k_\ell}{r_d}$ $(C = 2.7)$	Drop[d]
	$1.925\ \rho_\ell\ C_{p_\ell} \mid U_\ell \mid / [Re_f^{2/3}\ Pr_\ell^{2/3}]$ for $Re_f < 1000$ $0.2701\ \rho_\ell\ C_{p_\ell} \mid U_\ell \mid / [Re_f^{0.38}\ Pr_\ell^{2/3}]$ for $1000 \leq Re_f$	Film[c]
	$C \frac{\pi^2}{3} \frac{k_P}{r_d}$ $(C = 2.7)$	Drop, liquid chunk, inverted annular[d]

d. Andersen, J. G. M., REMI/HEAT COOL, A Model for Evaluation of Core Heatup and Emergency Core Spray Cooling System Performance for Light-Water Cooled Nuclear Power Reactors, "Heat Transfer in a Spherical Droplet," Report 296, Riso National Laboratory, Denmark, September 1973.

e. Hughmark, G. A., "Film Thickness, Entrainment, and Pressure Drop in Upward Annular and Dispersed Flow," J. Amer. Inst. Chem. Engin. 14, 1973, 1062.

Table 4.5 Interfacial Heat Transfer Area Per Unit Volume (Continued)

Flow Regime	Interfacial Area, A'''_I
Film	$\alpha_v P_w/A$
Liquid chunk	$N_d \pi D_H^2$ (a)
Inverted annular	$\alpha_\ell P_w/A$
Drop	Drop interfacial area transport equation
a. $N_d = \frac{\alpha_\ell}{\frac{\pi D_H^3}{6}}$	

4.2.4.3 *Single Phase Vapor*

COBRA-TF calculates the local Reynolds number within the computational cell and determines if the flow is laminar or turbulent. If the flow is turbulent, it uses the maximum of the Dittus-Boelter correlation (Ref. 2) or the correlation developed from the FLECHT-SEASET 161-rod bundle tests (Ref. 26). If the flow is calculated to be laminar, the code uses a Nusselt number of 10, which is based on the FLECHT-SEASET data.

4.2.4.4 *Single Phase Liquid*

In a similar fashion, the code calculates the Reynolds number of the cell and if the flow is turbulent, the code uses the Dittus-Boelter correlation for the convective heat transfer. If the

flow is calculated to be laminar, the heat transfer correlation by Sparrow et al (Ref. 27) is used which has a maximum Nusselt number equal to 7.86.

4.2.4.5 *Nucleate Boiling*

When the wall temperature exceeds the saturation temperature but is less than the wall temperature at the critical heat flux point, the Chen correlation (Ref. 4) is used to calculate the wall heat transfer. The Chen correlation applies to both saturated nucleate boiling and forced convection evaporation and will automatically transition into single phase convection at low wall superheats and into pool boiling at low mass flow rates. The Chen correlation regards the wall heat transfer as consisting of a combination of forced convection heat transfer as well as pool boiling heat transfer. In this fashion both extreme limits of forced convection and pool boiling are preserved.

4.2.4.6 *Subcooled Nucleate Boiling*

The Chen correlation can also be extended into the non-equilibrium regime of subcooled nucleate boiling. Again, the Chen correlation combines a forced convective heat transfer contribution and a boiling contribution to calculate the total wall heat transfer. For the subcooled case, the "F" factor used in the Chen correlation is set to unity but the remainder of the correlation is applied as in the nucleate boiling case.

In subcooled nucleate boiling, there exists thermodynamic non-equilibrium between the voids which are formed and the bulk liquid temperature which is subcooled. Therefore, there is heat transfer between the vapor and the liquid such that the vapor condenses and the liquid temperature increases along the channel. The heat transfer processes of interest include:

- Forced convection to the liquid,
- Vapor generation at the wall,
- Condensation near the wall, and
- Bulk condensation in the liquid core.

The partition of the vapor generation and the forced convection portions of the wall heat flux are calculated by the Chen correlation for the given set of conditions. The interfacial heat transfer processes are directly calculated in the fluid energy equations as part of the fluid conditions for the cell. The near wall condensation was calculated using the Hancox-Nicoll correlation (Ref. 28) which was then subtracted from the nucleate boiling heat transfer to obtain the net vapor generation. There were further refinements which accounted for the fraction of the subcooled liquid which would penetrate the saturated liquid layer on the wall using the Rouhani and Axelsson correlation (Ref. 29). Using this approach, the net amount of vapor generation at the wall can be calculated and the remainder of the vapor will then be mixed in to the bulk flow through the liquid energy equation and will condense.

4.2.4.7 *Critical Heat Flux*

COBRA-TF calculates the critical heat flux and the wall temperature superheat at the CHF point to fix this location on the boiling curve as shown in Figure 4.14. For reflood heat transfer, the Zuber (Ref. 30) pool boiling correlation is chosen for the critical heat flux since the liquid flow velocities are small.

4.2.4.8 *Minimum Stable Film Boiling Point*

The other point which is fixed on the boiling curve is the minimum film boiling point, T_{min}. This location denotes the boundary between stable film boiling and transition boiling. COBRA-TF uses the larger of a modified version of the homogeneous nucleation temperature which is curve-fit as a function of the difference between the critical pressure and the local pressure, and which has also been modified to account for wall properties and the Henry modification (Ref. 31) of the Berenson correlation. In addition, for reflood, COBRA-TF limits the value of T_{min} to be 426 degrees C (800 degrees F) < T_{min} < 650 degrees C (1200 degrees F).

4.2.4.9 *Transition Boiling*

The transition region is viewed as a mixture of film boiling with a vapor layer contacting the wall and nucleate boiling or wetted wall in which liquid contact with the wall is possible. The wetted wall portion of the wall heat flux is calculated using Ganic and Rohsenow (Ref. 32) which uses the McCoy and Hanratty model (Ref. 33) for determining the droplet migration to the wall. Once the droplet contacts the wall a droplet efficiency is calculated which is a function of the wall temperature and the liquid temperature. At high wall temperatures, the efficiency becomes very small as the drops will not contact the hot wall. The wetted wall portion of the heat flux is added to the dry wall film boiling heat flux calculation to give the total transition boiling wall heat flux.

There are separate models for top down quench in which the heat transfer is enhanced below the top down quench front location which is used as a multiplier on the critical heat flux.

4.2.4.10 *Inverted Annular Film Boiling*

COBRA-TF assumes the wall heat transfer is in inverted annular film boiling if the wall temperature is greater than T_{min}, and the void fraction is less than 0.4. The modified Bromley correlation (Ref. 10) is used for the film-boiling portion of the wall heat flux. The radiation heat transfer from the wall to the liquid is also accounted for as well as the droplet contact heat transfer using the Ganic and Rohsenow correlation as described earlier. Therefore:

$$q''_{IAFB} = q''_{Brom} + q''_{R} + q''_{W-D} \tag{4-9}$$

When the cell void fraction is greater than 0.4 and less than 0.9, the wall heat flux is linearly interpolated between the value for inverted annular film boiling and dispersed flow film boiling. There are also interfacial heat and mass transfer models in the inverted annular film-boiling regime which include estimates of the interfacial area between the vapor and the liquid such that the proper liquid and vapor temperatures can be calculated. The heat flux behavior as a function of void fraction is shown in Figure 4.16.

4.2.4.11 *Dispersed Flow Film Boiling*

The dispersed flow film boiling is assumed to occur when the wall temperature exceeds T_{min} and the void fraction is greater than 0.9. The dispersed flow film boiling heat transfer mode received the greatest amount of attention and refinement as part of the FLECHT-SEASET program. The wall heat flux in dispersed flow film boiling is comprised of three different heat transfer mechanisms which are summed to give the total wall heat flux:

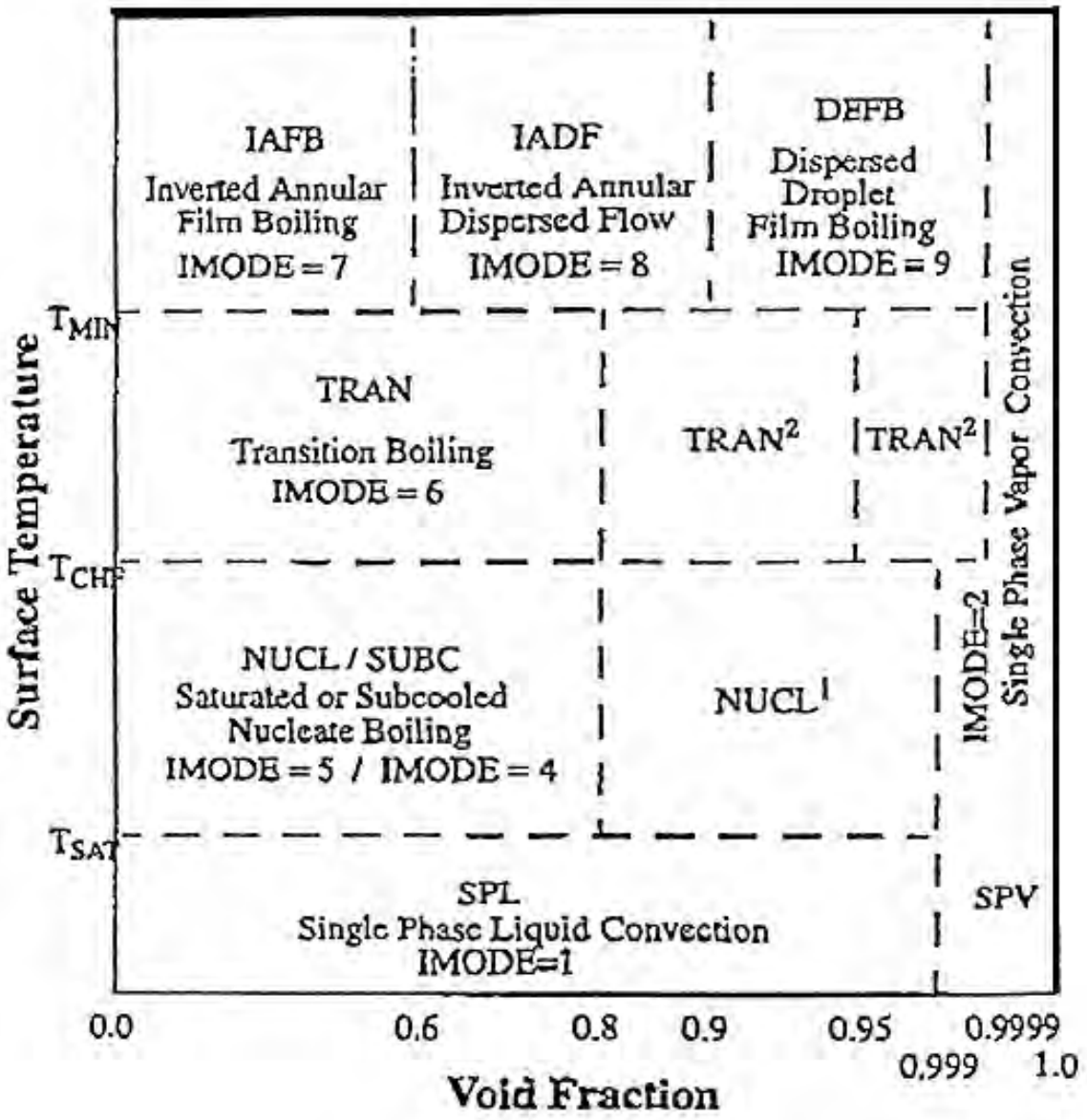

Figure 4.16 WCOBRA/TRAC Heat Transfer Regime Map.

$$q''_{DFFB} = q''_{FC} + q''_{R} + q''_{W-D} \qquad (4\text{-}10)$$

where

q''_{FC} vapor convective heat flux (either laminar of turbulent)

q''_{R} radiation heat flux

q''_{W-D} droplet impinging heat flux or droplet contact heat flux

The vapor convective heat flux is enhanced by a factor Ψ which experimentally accounts for the effect of the entrained droplets increasing the convective heat transfer. Data for the

enhancement factor was obtained from the FLECHT and FLECHT-SEASET programs and has been compared to data obtained by Drucker and Dhir (Ref. 34). The two-phase enhancement factor can be shown to be an extension of the basic analogy theory between heat transfer and momentum transfer as given in Kays (Ref. 35). Figure 4.17 shows the scatter of the data for the enhancement value Ψ. Note the scale on the plot. It is relatively easy for value for the single-phase convective heat transfer to be enhanced by 100 percent in a two-phase dispersed flow.

The radiation heat transfer q''_R, consists of two separate models. The surface-to-surface radiation is solved on a subchannel basis (Ref. 1) such that small test facilities with colder housing can be modeled more accurately. In a separate calculation, the radiation heat transfer to the droplets and vapor are calculated using the Sun et al model (Ref. 11) for the fluid radiation component.

The droplet impingement heat flux term is the same as that described earlier. However, this term is very small or negligible in the dispersed flow film boiling since the wall temperatures are much higher and the heat transfer efficiency of droplets hitting the wall is nearly zero.

Above a void fraction of 0.999, the heat transfer becomes single-phase vapor.

4.2.4.12 *Quench Front Model*

COBRA-TF uses fine variable mesh (Ref. 36) which will insert additional nodes into the heated structure if significant axial temperature gradients exist. This allows a more accurate representation of the true localized energy release from a localized portion of a heater or nuclear rod rather than the energy release from all the structures within the fluid node. Fine mesh heat transfer cells for axial and radial conduction in the structure are superimposed on the coarser hydraulic computational cells. The heat transfer package described above is applied to each of these smaller structural nodes to obtain the local heat transfer. In this fashion, the energy release at the quench front is smoother, and the effects of axial conduction in the quench front region are simulated.

4.2.4.13 *Spacer Grid Heat Transfer Models*

One of the major additions to the COBRA-TF code was the inclusion of heat transfer models for the dispersed flow film-boiling regime (void fraction greater than 0.9) which represented the experimental observations on the effects of rod bundle spacer grids. Spacer grids result in three additional heat transfer mechanisms in the rod bundle flow, namely:

- Convective heat transfer enhancement downstream of the grid,
- Rewetting of the grid structure, and
- Entrained droplet breakup caused by the grid structure.

Convective enhancement downstream of the spacer grids was observed in several single phase experiments and is due to the thinning of the thermal and velocity boundary layers on the rods as well as the additional turbulence introduced by the grid in the flow. Data from these experiments were correlated in terms of the grid blockage area in the rod bundle and an exponential multiplier, which diminishes downstream of the grid, according to Yao, Hochreiter, and Leech (Ref. 37). This correlation is used in COBRA-TF as a multiplier on the vapor convective heat transfer calculation described above for the dispersed flow heat transfer regime.

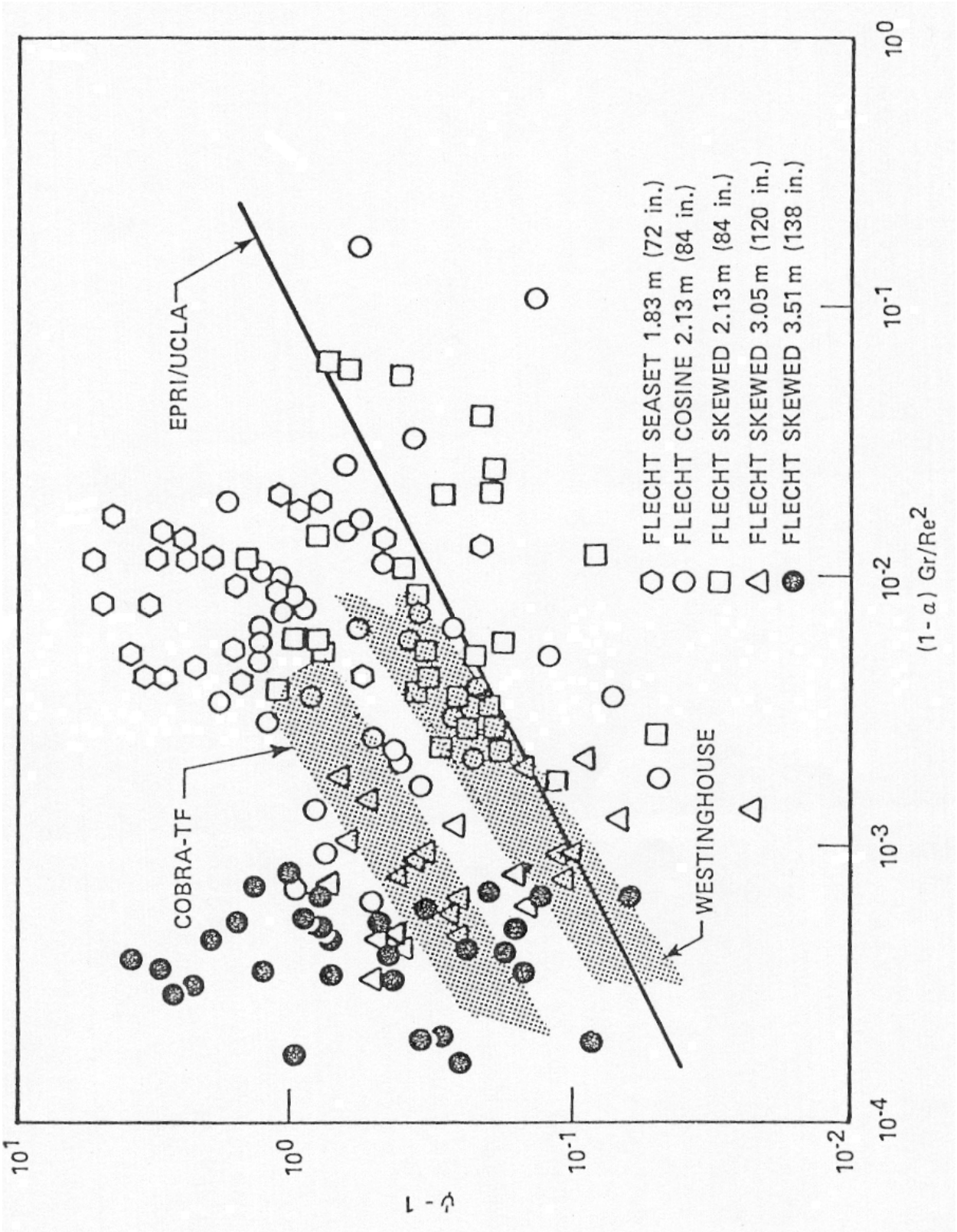

Figure 4.17 Two-Phase Enhancement: Comparison of Models and Reflood Data.

Spacer grids can be either dry, that is, with grid temperature which exceed T_{min}, or wetted with temperatures which are close to the saturation temperature. If a fraction of the grid is at the saturation temperature, it is assumed that a liquid film is present on that surface area. Since the grids are stationary, they have significant surface area; if the grid wets, a significant amount of interfacial heat transfer area is added to the interfacial area transport equation as an area source term. The result of this is more rapid de-superheating of the vapor flow in the rod bundle. As the vapor de-superheats, the driving temperature for the rod heat flux increases (T_{ROD}- T_v), and the rod wall heat flux increases and the rod cools.

There is a two zone detailed spacer grid model in COBRA-TF which calculates the location of the quench front on the grid, and the dry and wet grid temperatures considering the radiation heat transfer from the heater rods, convective heat transfer from the superheated vapor as well as the quenching of the spacer grid. The radiative heat transfer model for the spacer grid is shown in Figure 4.18. In this fashion, the fraction of the grid which is either dry or wet can be calculated as a function of the thermal-hydraulic conditions within the channel to determine the amount of grid area which should be added to the interfacial area transport equation. The additional steam generation due to the evaporation of the liquid film on the grid is also added into the hydrodynamic solution.

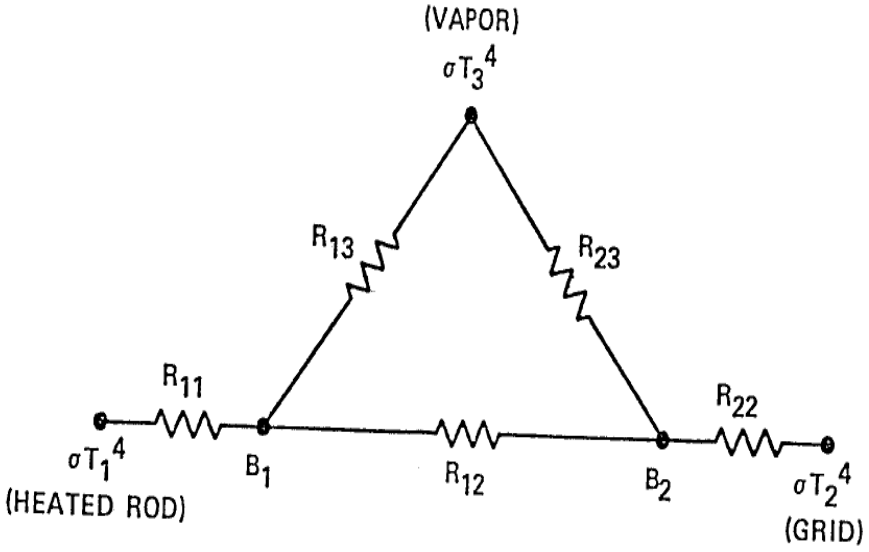

Figure 4.18 Radiation Heat Flux Network.

The third spacer grid model indicates that when high velocity entrained liquid droplets impact the grid structure, the drops can shatter producing a range of smaller "micro droplets" which are more easily evaporated. As the micro droplets are evaporated, the vapor de-superheats due to the heat taken up by evaporation as well as the addition of saturated vapor due to the droplet evaporation. Both heat transfer effects reduce the vapor temperature and result in a larger temperature difference between the vapor and the rod surface which increase the rod heat flux promoting improved cooling.

Figure 4.19 indicates the droplet breakup behavior. The parameter which was found to correlate the ratio of the shattered drop size to the initial drop size was the droplet Weber

number for flow normal to the spacer grids as seen in Figure 4.20. For low Weber numbers, the change in the drop size is not significant, at most a factor of two. For these drops, the interfacial area of the larger shattered drops was added to the interfacial area transport equation as an additional source term. For the very small drops which were generated at higher drop Weber numbers, these drops are put into the separate small-drop field described earlier. In addition, if there are small drops upstream of a spacer grid, they are also broken-up by the downstream spacer and the resulting small drop populations are then merged preserving the droplet mass, interfacial area and momentum.

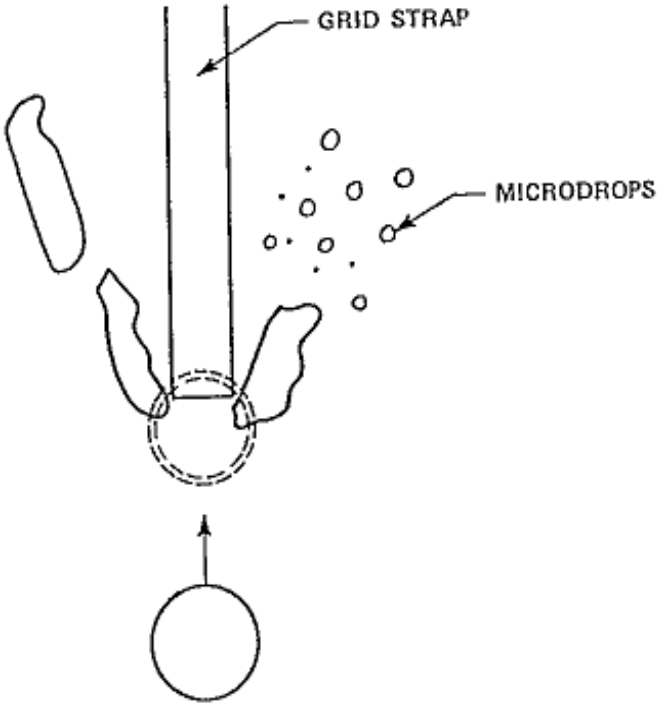

Figure 4.19 Droplet Breakup.

COBRA-TF heat transfer models, which are similar to the spacer grid models, have also been developed for flow blockage in rod bundle arrays and are described in Reference 24.

4.3 Road Map from the PIRT, to the Code Models, to the Test Instrumentation and Data Analysis

4.3.1 Single Phase Liquid Convection Below the Quench Front (Table 4.6)

The contribution of the single-phase liquid convection during a reflood transient ranks low in the PIRT. To calculate the heat transfer with the liquid single-phase (and vapor single-phase), the codes use different correlations depending on the Reynolds number. In general, the Dittus-Boelter correlation is used for turbulent flow while other correlations are used to calculate heat transfer in the laminar flow regime. These correlations are based on pipe geometry data and in general to geometries quite different than the bundle geometries. RELAP5/MOD3 uses the P/D

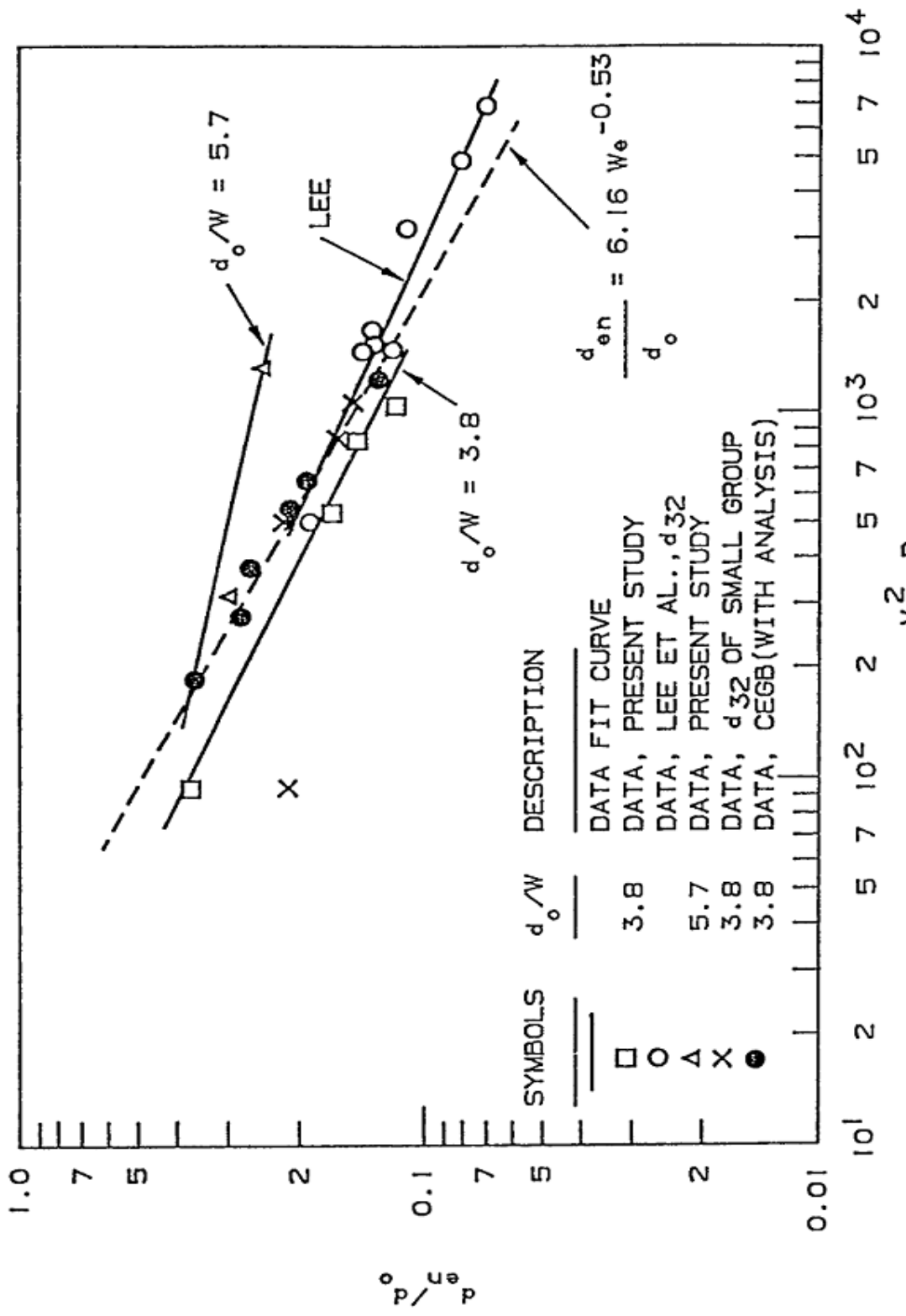

Figure 4.20 Shattered Droplet Size from Heated Grid Straps.

correction relation to account of this effect but its uncertainty is very high. The two TRAC codes do not account of this effect at all. In COBRA-TF a specific correlation was developed during FLECHT-SEASET experiments but was tuned on the 163 rod bundle geometry.
Beside the geometry effect, the flow regime during reflood is often in the transition between laminar and turbulent flow and therefore a bundle specific correlation needs to be developed to predict accurate convective heat transfer. The RBHT facility can transverse several temperature probes across the bundle at different elevations. This allows a better estimate of the bulk average temperature which is needed to assess these models.

The important phenomena were identified in the PIRT in Section 2 for the different periods or phases of the reflood transient. Examining the PIRT for single phase convective heat transfer, the items which are highly ranked are:

- The decay power which is the energy source into the fluid,
- The liquid velocity or Reynolds number,
- The liquid temperature or subcooling, and
- The convective heat transfer coefficient, which is ranked as medium.

The difference in the ranking of the liquid velocity and subcooling and the convective coefficient is that the convective fluid conditions will determine the behavior of the flow in different locations downstream, whereas the effects of uncertainty on the heat transfer coefficient for single phase heat transfer has a very small effect on the calculated peak cladding temperature.

The decay power is a test boundary condition which is controlled in the experiment and is directly measured such that this parameter is known accurately for a given test.

Although it is not given a ranking of high, convective heat transfer for the single phase convective experiments is of interest since most of the current codes use a pipe correlation as compared to a rod bundle correlation, as seen in Table 4.6. The computer codes calculate the local convective heat transfer from the local node velocity, the fluid properties, and the given hydraulic diameter of the node. The correlations for forced convection require the code to calculate a local Reynolds and Prandtl number which depends on the flow and temperature conditions within the computational node. In the RBHT experiment, the local power is calculated from the total power of the rods and the axial power distribution, such that the local value of the heat flux is known along the bundle. The heater rods are instrumented with eight thermocouples which calculate the local heater rod surface temperature from an inverse conduction calculation.

There are several subchannel fluid temperature measurements along the length of the bundle. Most of the temperature measurements have the ability to traverse across the subchannel such that the temperature distribution can be obtained within the subchannel. Therefore, the local fluid temperature or subcooling will be measured directly in the experiments. The temperature traverses will have to be velocity weighted and integrated across the subchannel area to obtain the local bulk subchannel fluid temperature.

The local subchannel flow is not directly measured in the experiment. However, the total liquid flow into the bundle is measured. The pressure drop of the bundle will already have been characterized by single phase pressure drop experiments which will confirm the losses of the spacer grids as well as the frictional loss of the total bundle. The hydraulic data can be used to

Table 4.6 Single Phase Liquid Convective Heat Transfer in the Core Component During Reflood Below the Quench Front

Process/Phenomenu	Ranking	RELAP5/MOD3.2		TRAC-B		TRAC-P		COBRA-TF	
		Does the model exist	Uncertainty	Does the model exist	Uncertainty	Does the model exist	Uncertainty	Does the model exist	Uncertainty
1ϕ Liquid Convective Heat Transfer	L								
Turbulent Forced Convection		Dittus-Boelter	30%	Dittus-Boelter	30%	Dittus-Boelter	30%	Yes, max of Dittus-Boelter or FLECHT-SEASET	15%
Laminar Forced Convection		Kays	10%	Kays	10%	Nu = 4	50%	Yes, Sparrow	50%
Effects of Geometry	L	P/D correction	H	No		No, for bundle can under predict HTC by 40%.	40%	Yes, in FLECHT-SEASET Correlation	15%
Effects of Spacers	L	Input grid loss		Input grid loss		Input grid loss		Yes, convection enhancement added, input grid loss	15%
Effects of Properties	L	Yes code calculated		Yes code calculated		Yes code calculated		Yes, code calculated	
1ϕ Liquid Natural Convection Heat Transfer	L	Churchill and Chu	L	McAdams	15%	Holman	~20%	Yes, McAddams	15%
Effects of Geometry	L	No		No		No		No	
Effects of Spacers grids	L	Input grid loss No H.T. effect	20%	Input grid loss No H.T. effect	20%	Input grid loss No H.T. effect	20%	Input grid loss No H.T. effect	20%
Effects of Properties	L	Yes code calculated		Yes code calculated		Yes code calculated		Yes, code calculates	
Decay Power	H	Input		Input		Input		Input	

benchmark a subchannel computer code such as COBRA-IV or VIPRE-II which will then be used to predict the local subchannel velocity and the subchannel Reynolds number. These code calculations can be checked, for fully developed flow, with hand calculations to confirm the flow split between types of subchannels. Given the measurements of the rod heat flux, the heater rod surface temperature, and using the fluid temperature traverses and velocities predicted by COBRA-IV, the local convective heat transfer coefficient can be calculated from the data. The COBRA-IV local subchannel velocities can also be used with the fluid properties to calculate the local fluid Reynolds and Prandtl numbers such that comparisons can be made between the correlations used in the computer codes and the RBHT data to determine if the current models are adequate. This data analysis approach has been used on the FLECHT-SEASET single phase steam tests (Ref. 26). The RBHT tests are designed to be performed over a wide range of fluid Reynolds numbers such that either a new convective correlation can be developed or an existing correlation can be confirmed.

In the case of single phase natural convection, or mixed convection, the highly ranked PIRT items include:

- Natural convection heat transfer coefficient,
- Effects of forced or free convection heat transfer,
- Liquid velocity,
- Liquid subcooling, and
- Decay power.

The local Reynolds and Grashoff numbers can also be calculated from the data using the same analysis approaches as given above to determine if forced convective heat transfer of natural circulation heat transfer exists within the subchannel. The ratio of the Grashoff to the square of the Reynolds will be calculated to determine if the flow is forced, free or mixed convection. For most reflood rates of interest, the convective heat transfer will be forced. If the heat transfer is free convection, a similar approach to that used for the forced convection heat transfer analysis can be used to determine the local heat transfer coefficient excepting that the local subchannel velocity will not be needed. If the convection is mixed, the data will be compared to conventional methods for mixed convection in which the forced and natural convection heat transfer coefficients are raised to a power (typically 3), summed (for aiding flow), and then raised to the inverse of the power (typically 1/3). The natural or mixed convective heat transfer coefficient is ranked higher as compared to the forced convection coefficient since there is very little data available for natural convection heat transfer in bundles.

4.3.2 Subcooled and Saturated Boiling Below the Quench Front (Table 4.7)

The heat transfer in this region ranks low in the PIRT but it determines the degree of subcooling at the quench front location, which in turn affects the ranking processes in that region. The Chen correlation (Ref. 4) is used in the codes to determine the heat transfer in the subcooled and saturated boiling regimes. In experiments the total heat transfer to the fluid in the two-phase region is measured while the codes need to calculate the heat transfer to each phase separately. Once the heat input in each phase is calculated the interfacial heat and mass transfer terms provide the closure to the equations. The subcooled boiling is modeled as follows:

1) convection to the liquid,

2) vapor generation at the wall,
3) vapor condensation near the wall,
4) subcooled liquid 'pumped' into the thermal boundary layer, and
5) bulk condensation (subcooled liquid core).

The fraction of vapor not condensing near the wall represents the net vapor generation term which is added explicitly into the mass-energy conservation equations. The condensation of the vapor because of the presence of vapor in the liquid core is calculated implicitly during the solution of the energy equation and it does not affect the determination of phasic heat inputs.

The convection to the liquid is calculated starting from the liquid phase Reynolds number. The code needs the local liquid bulk temperature, the local flow quality and flow velocity. The nucleate boiling component of the Chen correlation defines the amount of heat available to cause vapor generation at the wall. A fraction of this vapor condenses near the wall, whereas the rest will condense in the liquid core. The near-wall condensation is determined by the conditions (flow and thermal) of the fluid near the wall while the bulk condensation is determined by the interfacial heat transfer. Detailed void fraction measurements, void distribution, and liquid temperature during separate steady-state subcooled boiling tests should provide the information needed to assess these models.

For example, during subcooled boiling experiments, the contribution of the near wall condensation combined with the effect of subcooled liquid "pumped" into the thermal boundary layer can be calculated from an energy balance if the transverse temperature distribution of the liquid in the subchannel is measured or estimated.

Information about void fraction distribution (bubble size distribution and bubble location) are needed to estimated the interfacial heat transfer area. Measurements or estimates of bubble velocity can be used to estimate the interfacial drag. Note that the interfacial heat transfer and interfacial drag, which determines the condensation of steam in the liquid core and the slip between the two phases, rank high in the PIRT.

During saturated boiling, condensation does not take place. The code divides the total heat transfer rate in two contributions. The first is the heat removed by liquid convection, the second is the heat removed by boiling. Both components are from wall-to-liquid. Since metastable states are essentially not permitted in the code, energy absorbed by the liquid at the wall is transformed into vapor generated at the vapor-liquid interphase with an artificially large heat transfer coefficient.

This is modeled in the Chen correlation with the Reynolds number factor which is a function of the local quality. The effect of the Reynolds number is also to prevent/suppress boiling and this is accounted by the suppression factor in the nucleate boiling heat transfer component of the Chen correlation.

Similarly for the subcooled boiling regime, the code evaluates the flow rate, the quality, the temperature of the liquid and the temperature of the wall to calculate the heat transfer. The temperature of the liquid is at saturation. The interfacial heat transfer is not important in this case because the liquid superheat is prevented numerically in the code and all the energy going to the liquid is converted in vapor generation.

Table 4.7 Subcooled and Saturated Boiling in the Core Component Below the Quench Front

Process/Phenomena	Ranking	RELAP5/MOD3.2		TRAC-B		TRAC-P		COBRA-TF	
		Does the model exist	Uncertainty	Does the model exist	Uncertainty	Does the model exist	Uncertainty	Does the model exist	Uncertainty
Subcooled Boiling	L	Yes, Chen correlation	+180 -60%	Yes, Chen correlation	+180 -60%	Yes, Chen correlation	+180 -60%	Yes, Chen	+180, -60%
Effects of Geometry, P/D, De	L	Inayatov eq. (P/D)	H	No		No		No	
Effects of Spacers	L	No, H.T. effect		No, H.T. effect		No, H.T. effect		No, H.T. effect	
Effects of Properties	L	Input		Yes, code calculates		Yes, code calculates		Yes, code calculates	
Local Void Fraction (Interfacial Heat Transfer)	H	Yes code calculates interfacial area and H.T.C (see table 4.1-1)	20% for Bubbly Flow	Yes, code calculates interfacial area and HTC		Yes, code calculates interfacial area and HTC	25% for Bubbly Flow	Yes, Hancox, Rouhagi models, see Table 4- for interfacial H.T.C. and area	
Saturated Boiling	L	Chen	12%	Yes, Chen	12%	Yes, Chen	12%	Yes, Chen	12%
Effects of Geometry, P/D, De	L	Inayatov eq. (P/D)	H	No		No		No	
Effects of Spacers	L	No H.T. effects		No H.T. effects		No H.T. effects		No H.T. effects	
Effects of Properties	H	Yes, code calculates		Yes, code calculates		Yes, code calculates		Yes, code calculates	
Local Void Fraction (slip flow)	H	Yes, code calculates Slip		Yes, code calculates Slip		Yes, Code calculates slip		Yes, Code calculates slip	

Separate steady-state boiling experiments with a detailed measurement of void fraction can be used to assess the model in this region. The separate effect of the Reynolds number factor and the boiling suppression factor can be quantified in these experiments. Finally bubble velocity measurements and transverse void distribution, can be used to estimate the interfacial drag.

The PIRT table for the subcooled and saturated boiling regions are given in Table 2.2 in Section 2. The important phenomena identified in this table includes:

- Decay power,
- Local void fraction,
- Interfacial area and heat transfer, and
- Liquid subcooling.

As discussed above, decay power is a test boundary condition and is known. Local void fraction is measured using finely spaced differential pressure cells as well as using an X-ray attenuation technique. The liquid subcooling is measured using traversing temperature rakes at several different elevations in the bundle. These miniature thermocouples will traverse across the bundle between the heater rods and will measure temperature in the rod-to-rod gap, as well as at the center of the subchannel.

Several different computer code models interact to develop the local void fraction within a computational node in the case of subcooled boiling. Models for vapor generation, interfacial heat transfer such as condensation of the generated bubbles (if the liquid flow is subcooled), single phase convective heat transfer at the wall, criteria for wall voidage, bubble size at departure and interfacial drag all influence the resulting void distribution in the rod bundle for subcooled and saturated boiling below the quench front.

In the RBHT program, the total wall heat flux will be determined from the power applied in the test and the axial power shape as well as from the inverse conduction calculations using the measured heater rod temperature and the power. The local fluid temperature will be measured at many elevations using the traversing miniature thermocouples in the bundle which will indicate if the bulk liquid flow is subcooled or saturated. The axial behavior of the liquid temperature in the bundle can be measured such that the location of where the bulk flow becomes saturated can be determined.

The wall heat flux consists of two components; a direct convective component and a boiling component in similar manner as the model by Chen (Ref. 4). The axial fluid temperature distribution reflects both the wall convection heat transfer as well as the condensation of the voidage generated at the wall. If one assumes that the convective and boiling processes are separate and are additive (similar to Chen's model), the wall convective heat transfer can be estimated from the bulk flow conditions as well as the portion of the heat flux which is due to convection. Since the total wall heat flux is measured, the difference between the total and the convective heat fluxes is the boiling component. This is an estimate since the local liquid phase velocity distribution will be different at the wall because of the bubble formation.

Low void fractions, characteristic of nucleate boiling, will be very difficult to measure even with sensitive differential pressure cells. The laser illuminated digital camera system can detect the voidage but it may be difficult to quantify wall voidage since the bubbles will adhere to the heated surface. As subcooling of the bulk flow is reduced, the fraction will grow and the bubbles

will depart from the wall and will be condensed in the bulk flow. This can occur for voids of approximately 20 percent. In this situation, the finely spaced differential pressure cells data can be analyzed to obtain an average void over the cell span with more confidence. Also, the laser illuminated camera system can also be used to obtain data on the bubble diameter and velocity distributions, for low voidage flows in which there is minimum bubble interaction.

A measurement of the local void will also be obtained using an X-ray densitometer, and the finely spaced pressure drop cells, as well as visual observations. Given the void distribution, estimates of the bubble diameters and velocities, rough estimates of the product of the interfacial heat transfer and the interfacial area can be made. Therefore, the computer code models and correlations for the product of the interfacial hA_i can be compared to the rough estimates of the hA_i estimates from the data. It is expected that the uncertainties will be large. Both the axial liquid temperature gradient as well as the void fraction (which represents a net situation, that is the void generation minus the condensation) can also be used to develop and refine models for the interfacial heat transfer and area.
When the liquid reaches saturation, all the energy from the heater rods generates vapor since there is no longer any liquid subcooling. In this case saturated boiling is occurring on the heater rod surfaces and the void fraction increases. The important items from the PIRT Table 2.2 for this case are:

- Void fraction, and
- Decay power.

The void fraction in this region is ranked high since it will influence the steam velocity at the quench front and the generation of liquid entrainment. The decay power is ranked high since it represents the energy input into the fluid which will generate steam. The saturated boiling heat transfer coefficient is not ranked as a high since a large uncertainty in its value will not effect the peak cladding temperature. Note that there is an overlap between the decay power and the boiling heat transfer coefficient since all the energy generated in the rod is transferred to the fluid. If the decay power is ranked as a ”high,” in reality, the surface heat transfer coefficient is also a high.

The void distribution will be determined using the finely spaced differential pressure cells which will result in a node average void along the axial length of the bundle. In addition, an X-ray technique will be used to obtain the void distribution at specific axial locations to confirm the values obtained from the differential pressure cells.

4.3.3 Quench Front Behavior (Table 4.8)

This is the most complex region in the bundle. There are several process taking place across the quench front which rank high in the PIRT table. This is also the most difficult region to simulate with the codes because a big transition in the thermal-hydraulic conditions is experienced in a small portion of the computational domain. Moreover the hydraulic process is strongly coupled with the thermal behavior in this region. The froth region behavior significantly affects the heat transfer downstream in the film boiling region. This is where compensating errors are most likely to occur. The code has to be able to handle each separate process accurately to limit, to a minimum, extent the effect of compensating errors. Unfortunately the lack of data in this region causes the models to simulate this region poorly in most of the codes. Essentially, the codes need to calculate heat transfer from the rod to the fluid, vapor generation

and entrainment. The amount of droplets entrained in that region will determine the heat transfer downstream, in the dispersed flow region.

The codes at first calculate T_{CHF} and T_{MIN} and if the clad temperature falls between those two values then transition boiling regime is assumed. The heat transfer selection logic of COBRA-TF is shown in Figure 4.15. The present version of COBRA-TF does not have a specific transition boiling model and the heat transfer is calculated by extrapolating the dispersed flow film boiling heat transfer or the inverted annular film boiling heat transfer in that region. The models used by other codes are described in Section 4.2. A more accurate transition boiling model and a more consistent entrainment model need to be developed during the RBHT program.

Critical Heat Flux and T_{MIN} are calculated by different codes using different correlations as described in Section 4.2. In the transition boiling regime the codes calculate the total heat transfer as the sum of convective heat transfer from the wall to the vapor, radiation heat transfer to the liquid and wall-liquid direct contact heat transfer. The radiation heat transfer is a small contribution in the froth region where the wall temperature is not very high and the void fraction is low.

The code needs to predict accurately the void fraction and the slip in this region. Therefore, detailed information is needed about the void fraction distribution. An estimate of the slip is also needed and can be obtained through a mass and energy balance in the froth region when sufficient data about void fraction are available. The vapor in this region can be assumed at saturation while the liquid can be subcooled. The degree of subcooling is needed to calculate the interfacial heat transfer and net vapor generation on condensation. The void fraction distribution is also needed to calculate the radiation heat transfer component as well as to define the mechanisms of entrainment. The entrainment is a function of the vapor generation rate. Information about the size and velocity of the entrained droplets and ligaments just above the froth region are also needed to develop a mechanicistic entrainment model.

Compared to the other codes, COBRA-TF has the unique feature of a three-field approach. This is a big advantage in the froth region because continuous liquid, droplets and vapor coexist. This feature combined with proper entrainment and de-entrainment model provide a more realistic representation of the phenomena at the quench front. Data from RBHT experiments can be use to assess these separate models.

All the codes attempt to calculate the rod axial conduction at the quench front by using a fine mesh rezoning in that region. The axial conduction is a very important phenomena during reflood because it represents a flow path for the energy from the region above the quench front where the heat transfer to the liquid is low to the region below the quench front characterized by a much higher heat transfer coefficient. This component needs to be extracted during the test data analysis by solving a two-dimensional inverse conduction problem.

Other effects, such as fuel/heater rod material properties, dimensions and cladding thickness, gap heat transfer coefficient, cladding surface effects, need to be correctly simulated and measured.

Table 4.8 Quench Front Behavior in the Core Component

Process/Phenomena	Ranking	RELAP5/MOD3.2		TRAC-B		TRAC-P		COBRA-TF	
		Does the model exist	*Uncertainty*	*Does the model exist*	*Uncertainty*	*Does the model exist*	*Uncertainty*	*Does the model exist*	*Uncertainty*
Fuel /Heater Rod Quench									
Fuel/heater rod materials, ρ, C_p, k, rod diameter	H	Input		Input		Input		Input	15%
Gap heat transfer coefficient	M	FRAP-T6[1]	~100%	Yes, user specified	~100%	Yes, user specified	~±100%	For plant gap HT is adjusted to match plant calc's	~100%
Cladding materials, ρ, C_p, k	L	Input		Input		Input		Input	
Cladding surface effects	H								
• Oxides		No		No		No		Input	
• Roughness		No		No		No		No	
• Materials		Input		Input		Input		Input	
• T_{min}		Yes, code calculates		Yes, homogen. nucleation, Shumay		Yes, Nelson model		Yes, Henry Homogeneus Nucleation	
• T_{CHF}		Yes, code calculates		Yes, Baisi CHF and Chen		Yes, Biasi CHF and Chen		Yes, Zuber CHF, and Chen	

Table 4.8 Quench Front Behavior in the Core Component (Continued)

Transition Boiling Heat Transfer	H	Chen	16%	Yes, T_W-T_{Min} temperature weighting of nucleate and film boiling.		James and Bankoff: composition of nucleate and film boiling weighted with wet versus dry wall.		Yes, T_W-T_{Min} Weighting of nucleate and film boiling.	
Steam generation at quench front (interfacial H.T.)	H	Yes code calculates interfacial area and H.T.C. depending on flow regime		Yes, interfacial H.T. depend on Flow Regime		Yes, interfacial H.T. depend on Flow Regime		Yes, interfacial H.T. depends on Flow Regime Both Hot and Cold wall regime	
Decay Power	H	Input		Input		Input		Input	
Liquid entrainment at quench front which includes liquid ligaments, initial drop size, and droplet number density	H	Entrainment is calculated for the annular film flow regime)		Ishii model used for all flow regimes		Entrainment calculated for annular flow by Ishii and Mishima		Uses droplet correlation based on Flecht data and drop force balance.	
Void fraction/flow regime	H	Yes, has Flow Regime logic		Yes, has Flow Regime logic		Yes, has Flow Regime logic		Yes, has cold wall and hot wall flow regime logic	
Interfacial area	H	Yes calculated for non-equilibrium	100%	Yes, code calculates flow regime dependent	100%	Yes, code calculates flow regime dependent	100%	Yes, calculated for non-equilibrium situations. Flow Regime dependent, has hot and cold wall F.R.. Has interfacial are transport equation	50%

(1) - L.J. Sierken et al.. FRAP-T6 - A computer code for the transient analysis of oxide fule rods, EGG-CDAD-5410, April 1981.

The highly ranked items from the PIRT in Table 2.3 for the quench region are:

- Fuel/heater rod material properties, dimensions and cladding thickness,
- Gap heat transfer coefficient,
- Cladding surface effects,
- Transition boiling heat transfer(surface-liquid contact heat transfer),
- Steam generation at the quench front,
- T_{CHF} the temperature where CHF occurs (maximum limit of nucleate boiling),
- T_{MIN} the temperature at the minimum film boiling point, and
- Surface temperature.

The heater rod physical properties such as the clad conductivity, density and specific heat are known as a function of temperature from property tables. The boron nitride filler material properties such as the conductivity, specific heat and theoretical density will be determined by Purdue University Thermal Physical Property Center such that the heater rods will be well characterized. The property and geometric information is used to calculate the surface heat flux by an inverse conduction technique using an internal thermocouple. The surface temperature is also calculated using the same method. The same information is available for nuclear fuel rods such that the differences are known. The scaling analysis given in Sections 6 and 7 addresses the differences between the nuclear and the electrically heated rods.

The gap heat transfer coefficient is very high for the heater rods since they are swagged to close the gap between the boron nitride and the inside of the cladding. A typical valued of 96.875 kW/m^2-K (5000 Btu/hr-ft^2-F) is used to characterize this gap resistance. The gap heat transfer coefficient in a nuclear fuel rod is a dynamic quantity since it changes over the fuel lifetime as well as during the accident. While the fuel rod gap heat transfer coefficient has a large uncertainty, this uncertainty will not effect the total stored energy, since it will be released during quenching. However, the gap heat transfer can affect the rate at which this energy is released. Sensitivity calculations as well as nuclear rod data can be used to quantify these effects.

Cladding surface effects such as crud, oxide layers, roughness, material types, have been shown to effect the minimum film boiling temperature, T_{MIN} and the CHF temperature T_{CHF} . Both of these temperatures define the region of transition boiling.

The heater rod surface conditions will be well characterized by the Purdue University Thermal Physical Property Center as well as at Penn State. A nuclear fuel rod cladding, however, can have a range of surface conditions which affect T_{MIN} and T_{CHF}. Therefore, it has been proposed that as part of the Rod Bundle Heat Transfer Program, that a series of “bench top” experiments be performed to characterize the surface effects on both T_{MIN} and T_{CHF} using small samples of different cladding materials which have known surface conditions. The end result of this effort will be to develop specific criteria for a T_{MIN} correlation and to confirm the relationship for T_{CHF}. The literature will be reviewed and relevant data for different surfaces will be found and assessed.

Transition boiling heat transfer occurs as the fraction of the heated surface which has liquid contact increases until the entire surface is wetted and quenched. The RBHT electrical heater rods are well instrumented with internal thermocouples to measure the total wall heat flux using a radial inverse conduction calculations given the power and the internal temperature. The local

fluid thermocouples will measure the local subchannel fluid temperature which should be near or at the saturation temperature. As the rod quenches, the measured temperature can be influence by the axial conduction down the rod to the quench front since there is a very large axial temperature gradient near the quench front. Therefore, the calculation of the radial heat flux and the resulting heat transfer coefficient from the inverse conduction scheme must be corrected for the axial conduction when the quench front passes a thermocouple location.

Two-dimensional, transient calculations will be performed on the heater rods to predict the axial heat flow such that the data can take account of axial heat flux as the quench front approaches. The transition boiling heat transfer will then be calculated as the corrected heat flux divided by the difference of the heater rod surface temperature minus the local saturation temperature. The data sampling during this time period will be sufficiently rapid such that a number of data samples will be obtained as a particular location quenches. Similar calculations will be performed on the bench top experiments.

The values of T_{MIN} and T_{CHF} will be obtained directly from the data as the heater rod quenches. The local void fraction will also be available which can be used to determine if the liquid content in the flow has an effect on T_{MIN} and T_{CHF}. These values will be supplemented with similar data from the bench top experiments such that a material and surface condition specific transition boiling correlation could be developed. The RBHT heat transfer data can then be compared to different T_{MIN} and transition boiling correlations in the literature as well as those currently used in safety analysis computer codes.

Steam generation near the quench front is responsible for the downstream development of drops, liquid ligaments and or chunks which are entrained upward by the steam flow. The entrained liquid provides an additional heat sink for the heated surface since the drops evaporate in the superheated steam flow, generating additional steam at the saturation temperature, which cools the steam. The droplets are also a radiation heat sink for the heated surfaces. Local steam flows within the bundle are not measured. The exit steam and liquid flows are measured as well as the vapor temperature distribution along the bundle as well as the rod bundle total heat flux along the heater rod surfaces. The bundle heat flux represents the total energy leaving the heater rods. The rod bundle energy has several different paths, directly to the fluid by convection and radiation to steam and droplets, to the colder housing, to colder rods, and to the colder support tubes. The temperatures of all the structures in the rod bundle are measured at several elevations (heater rods, thimbles, housing, spacer grids).

The radiation network used to determine the radiation heat transfer in Sections 6 and 7 can be used to determine the expected radiation heat fluxes during a two-phase experiment. The radiation-only tests will be used to calibrate this method such that the radiation can be subtracted from the total measured heat flux to obtain the heat flow into the fluid.

Constructing a one-dimensional transient heat balance from the exit of the test section, using the measured vapor temperatures, the measured vapor flows and liquid flows, and the portion of the wall heat which is transferred to the fluid, the axial fluid quality can be calculated in the bundle above the quench front. This calculation can be carried to the top of the froth region, where the majority of the entrainment occurs.

The vapor temperature at the top of the froth region is superheated, however, it is expected that the miniature thermocouples will have wetted such that they will not yield an accurate reading of the true vapor temperature. The vapor superheat will be assumed to be the average of T_{SAT} and

the heater rod wall temperature T_{WALL}. This approach was successfully used in the analysis of the FLECHT-SEASET data. This calculations will yield the bundle average vapor and liquid flowrates at the top of the froth region. The local subchannel vapor velocities can be estimated using COBRA-IV or VIPRE-II above the froth region assuming that the droplets do not influence the vapor flow since the void fraction is very large (i.e., 0.999).

A similar transient one-dimensional energy balance calculation scheme can written from the bundle inlet to the top of the quench front. The local fluid temperatures as well as the heater rod temperatures can be used to determine if the flow is saturated or subcooled at the quench front such that the quality or subcooling can be calculated from the inlet flow conditions and the energy input into the fluid from the rod decay power, housing, and structures, as well as the heat release at the quench front. If the fluid conditions are subcooled at the quench front, the steam generation can be calculated using the difference between the energy released and the energy needed to raise the fluid temperature to the saturation temperature. This approach is reasonable for low flooding rate cases in which the flow entering the quench front is at or near saturation.

For higher flooding rate cases, additional assumptions and approximations are required since the subchannel fluid thermocouples will wet and read the saturation temperature. For high flooding rate cases (flooding rates of 6 in/s or larger), the subchannel thermocouples could read the liquid subcooling such that an estimate of the steam flow can be made. Also, for high flooding rate cases, the two-phase mixture temperature above the quench front is at or near the saturation temperature since steam superheats are small. Therefore, an equilibrium energy balance can be used to estimate the flow quality using the bundle exit flows and the rod energy which is calculated to go into the mixture. Highly ranked PIRT phenomena of steam generation at the quench front can be calculated from the data with reasonable uncertainty and compared to the computer code predictions.

Values of T_{MIN} and T_{CHF} can be obtained directly from the heater rod thermocouple data. T_{CHF} can be obtained from plots of the calculated wall heat flux against $T_{WALL} - T_{SAT}$ for the different heater rods. T_{MIN} can be obtained from the data by using a criteria that if the temperature change is greater than 27.8°C/s (50°F/s), the heater rod is wetting. The 27.8°C/s (50°F/s) is a historical value used in the FLECHT and FLECHT-SEASET programs to estimate T_{MIN}. This value will have to be verified for the RBHT facility. However, data for both T_{CHF} and T_{MIN} can be obtained to address these PIRT phenomena.

The heater rod surface temperature is also a highly ranked PIRT phenomenon as given in Table 2.3. The heater rod thermocouple directly measures temperature close to the inside cladding temperature. The outside cladding temperature is calculated from the one-dimensional inverse conduction calculation at the thermocouple location. For most of the time when the rod is in film boiling, the measured inside temperature and the calculated outside temperature are nearly identical since the heat flux is very low. Immediately near the quench front, the data have to be corrected for two-dimensional effects due to the axial conduction. In either case, the RBHT facility will provide data on the surface temperature which is a highly ranked PIRT phenomena for the quench period.

The decay power, which is ranked as high in the PIRT, will be directly simulated in the experiments over a range of powers.

Liquid entrainment at the quench front is also ranked high in the PIRT. Liquid entrainment begins at the quench front by the formation of liquid chunks, ligaments, and drops. The liquid chunks and ligaments are sheared by the high steam velocity into small particles which are then entrained as droplets at the top of the froth region. Large liquid chunks or pieces will fallback and will be sheared until they are small enough to be entrained. The bundle energy balance calculations described earlier will give the flow quality at the top of the froth region such that the bundle average liquid and vapor flowrates can be calculated from the test data. FLECHT-SEASET reflood tests indicate that the froth region thickness is approximately constant over most of the rod bundle as it refloods. Therefore, the liquid mass stored in the froth region is a constant such that the liquid flow at the top of the froth region is approximately the same as the liquid flow at the quench front. This is particularly true for lower flooding rate conditions. Using the analysis of the test data, the liquid entrainment at the quench front can be determined in the RBHT tests.

The void fraction and flow regime are also ranked high in the reflood PIRT for the quench region. The void fraction will be directly measured in the quench region using sensitive differential pressure cells with a three-inch span such that more detailed void measurements can be made as the quench front advances upward through the bundle. An X-ray attenuation technique will be used to obtain the transient chordal-average void fraction along the center plane of the bundle to obtain a time dependent void fraction. The local flow regime can also be photographed using high speed cameras or videotaped to infer the flow regime in the quench region, provided the test section windows have a minimum of wetting. Therefore, these highly ranked phenomena can be measured in the RBHT facility.

Interfacial area is also ranked high for the quench region since it effects the interfacial drag and interfacial heat transfer. There is no direct measurement of the interfacial area in the experiments. The void fraction will be measured and the liquid and vapor flowrates will be calculated from the data such that the phase velocities can be determined from the data. High speed photography can be used to infer the flow regime and hence the interfacial area. Therefore, this highly ranked PIRT phenomena can not be measured in the RBHT tests, but can be inferred from photography.

The local fluid temperature is also a highly ranked PIRT phenomenon in the quench region. The miniature fluid thermocouples which are located at different axial positions in the rod bundle will measure the liquid temperature. Liquid subcooling, if present, may be difficult to measure since most of the liquid will be at the saturation temperature for most cases. When the liquid flowrate is large combined with large liquid subcooling, the subcooled liquid temperature will be more accurately measured. Therefore, for the cases when subcooling is important, the RBHT facility can measure this highly ranked PIRT phenomenon.

4.3.4 Two-Phase Froth Region for the Core Component (Table 4.9)

The PIRT given in Table 2.4 from Section 2 indicates that several of the phenomena are highly ranked in this region. The froth region can be described as the region in which a transition is occurring between the continuous liquid or low void fraction mixture at and below the quench front; to a continuous vapor region with entrained liquid approximately one foot above the quench front. The void fraction changes very sharply from typical values of zero to 20 percent near the quench front to 0.99 or higher at the top of the froth region. The sudden change in the void fraction is the result of the large steam generation at the quench front as discussed earlier. It is this steam generation and the resulting film boiling heat transfer in the froth region which

provides the large steam velocity needed to shear and entrain the liquid upward in the rod bundle. The wall temperatures in the froth region is above the wetting temperature such that the heated surfaces are in film boiling. The film boiling heat transfer in this region has been shown to correlate well with the local void fraction. The phenomena which are highly ranked include:

- Void fraction/flow regime,
- Liquid entrainment,
- Liquid ligaments, drops sizes, number density, interfacial area,
- Film boiling heat transfer, and
- Decay power.

The components of film boiling heat trainer include the classical film boiling such as Bromley as well as drop contact heat transfer, vapor convection heat transfer as well as interfacial heat transfer and radiation heat transfer.

Void fraction and flow regime are ranked high in the PIRT for this region. Void fraction will be measured using the finely spaced differential pressure which should be accurate since the void is lower in this region. The local void can also be measured at a fixed point as the froth region passes through the location where the X-ray attentuation system is located. If there is significant vapor superheat, it maybe detected by the miniature thermocouples; however, since the void fraction is lower in the froth region as compared to the dispersed flow region, it is expected that the thermocouples will wet and will indicate the saturation temperature. The flow regime in this region is difficult to quantify; however, high speed photography can be used to indicate the features of the flow regime. Also, examples of the froth flow region exist in the FLECHT and FLECHT-SEASET high speed movies. Therefore, the RBHT program can obtain the data needed for these PIRT phenomena.

Liquid entrainment is one of the most highly ranked phenomena in the reflood PIRT since it directly determines the peak cladding temperature downstream of the froth region. The mass flowrate of the entrained liquid can be calculated, on an bundle average basis, using the energy and mass balances described earlier from the exit mass flow measurements, vapor temperatures, and the heat flux into the fluid. In the RBHT facility, additional effort has been made to design a closely coupled liquid collection tank such that the delay time from the beginning of entrainment to the detectible liquid measurement out of the bundle is minimized. Estimates of the liquid velocity can also be made using a mass and energy balance from the bundle inlet, accounting for the quench energy and the measured void fraction.

The characteristics of the entrained liquid in the froth region is also a highly ranked PIRT phenomenon. Parameters such as liquid ligaments, drop size, interfacial area, droplet number density and droplet velocities, are all highly ranked phenomena which directly effect the resulting peak clad temperature. The drops sizes and velocities will be measured by the Laser Illuminated Digital Camera System (LIDCS) near the top of the froth region. As the froth region approaches the measurement point there may be too much liquid for the laser system to properly determine the sizes and velocities. However, if there is a significant amount of liquid present, the finely spaced differential pressure cells will provide an accurate measurement of the void fraction as the froth region passes within the span of the cell. The behavior of the froth region was also measured in the FLECHT-SEASET experiments.

Table 4.9 Two-Phase Froth (Transition) Region for Core Component

Process/Phenomena	Ranking	RELAP5/MOD3.2		TRAC-B		TRAC-P		COBRA-TF	
		Does the model exist	Uncertainty	Does the model exist	Uncertainty	Does the model exist	Uncertainty	Does the model exist	Uncertainty
Void fraction/flow Regime	H	Yes, has Flow Regime logic		Yes, has Flow Regime logic		Yes, has flow regime logic		Yes, has more detailed flow regime logic	
Liquid entrainment	H	Ishii and Mishima		Ishii and Mishima		Ishii and Mishima		Force balance on drop, empirical model based on FLECHT data	
Liquid ligaments, drop sizes, interfacial area, droplet number density	H	Yes, Single liquid field, single drop size		Yes, single liquid field, drop size		Yes, single liquid field, drop size		Yes, has separate drop field, can treat two drop sizes	
Film Boiling H.T. at low void fraction classical film boiling	H	Bromley void weighted	25%	Modified Bromley, void weighted, max of pool Film Boiling and vapor convection		Modified Bromley correlation (Denham)		Bromley void weighted	25%
droplet contact heat transfer	H	No		No		No		Yes, has Ganic and Rohsenow	100%
convective vapor H.T.	M	Dittus-Boelter	30%	Dittus-Boelter	30%	Yes, max of Dougball-Rohsenow and Dittus-Boelter		Max Dittus-Boelter or FLECHT-SEASET	25%

Table 4.9 Two-Phase Froth (Transition) Region for Core Component (Continued)

interfacial H.T.	M	Yes code calculates interfacial area and H.T.C. depending on flow regime		Yes code calculates interfacial area and H.T.C. depending on flow regime		Yes code calculates interfacial area and H.T.C. depending on flow regime		Yes, code calculates interfacial area using hot wall flow regime and interfacial heat transfer	
radiation H.T. to liquid/vapor	M	Yes, with modified Bromley film boiling		Yes, with modified Bromley film boiling		Yes, with modified Bromley film boiling		Yes, with Bromley Film Boiling	
effects of spacers	M	No		No		No		Yes, if α>0.9 considers convection, rewetting droplet breakup	
Decay Power	H	Input		Input		Input		Input	

Film boiling heat transfer will be measured at many locations along the length of the electrical heater rods in the bundle. The heater rod thermocouples have been placed such that they are located at or very near the center of a differential pressure span such that the average void fraction determined from the differential pressure span can be used to correlate the resulting film boiling heat transfer. The data can be corrected for radiation heat transfer assuming that the radiation is to a liquid rich two-phase mixture within the froth region.

Radiation heat transfer can be void fraction weighted and subtracted from the total measured heater rod heat transfer. Estimates can also be made of the convective heat transfer to the vapor using the single phase heat transfer correlation which was developed earlier in the program as well as the wall and vapor temperature. Use of such a correlation assumes that the presence of the liquid has a small effect on the local velocity and temperature profiles in the steam near the wall. As the void fraction decreases, this assumption becomes invalid and the correlation will be suspect. However, for very low void fractions in the froth region, the vapor will be concentrated at the wall in a traditional inverted flow film boiling situation. The local vapor temperature measurements may also be very uncertain since the miniature thermocouples can easily wet in the froth region and will indicate only the saturation temperature, not superheat temperature such that the true vapor temperature is underestimated resulting in an over-estimate of the convective heat flux. Care will have to be used in the interpretation of these results.

Another component of the heat transfer in the froth region is direct drop-wall contact heat transfer. This individual heat transfer component is zero when the surface temperature is above the minimum film boiling temperature, T_{MIN}, and increases as the surface temperature decreases. Drop contact correlations are usually expressed as a exponential of the surface temperature which calculates a multiplier which is then applied to a nucleate boiling flux. The drop contact heat transfer cannot be measured directly in the Rod Bundle Heat Transfer facility because of the highly turbulent nature of the flow and the advancing quench front along the heater rods. The contribution of the drop contact heat transfer is accounted for in the film boiling and transition boiling heat transfer which is calculated from the measured heater rod surface temperatures and power using the inverse conduction technique, however, the precise portion of the total heat transfer attributed to drop contact cannot be separated from the total with confidence. If additional detail is needed on this phenomenon, a bench top experiment would be useful such that only the effect of the drop contact heat transfer is present. The resulting data could then be correlated into a model.

Vapor convection heat transfer is also an important PIRT phenomenon for the froth region. In this situation, the vapor is generated as a very rapidly growing film along the walls of the heater rods and then mixes with the large chunks, drops, and ligaments of liquid which are being accelerated in the froth region. The bundle average vapor flow rate can be calculated from the bundle mass and energy balance and the bundle average vapor velocity can be calculated from the measured void fraction. Measurement of the vapor superheat is uncertain.

The measurement scheme is to use miniature bare thermocouples which point into the flow. In the liquid rich froth region, there is a high probability that the thermocouples will be wetted by the liquid which is being entrained in the flow. Therefore, the miniature thermocouple probes will read the saturation or liquid temperature most of the time. For very low void fraction mixtures within the froth region, one could expect that the vapor superheat would be at or near the saturation temperature because of the large interfacial heat transfer and the lower mass flow of the vapor. As the void fraction increases within the froth region, one could expect that the

vapor temperature is between the heater rod surface temperature and the local saturation temperature such that some vapor superheat exists.

The vapor superheat data for a given test will be plotted as a function of axial position to investigate how to extrapolate the data into the froth region. This has been done in the previous FLECHT-SEASET experiments with some success. Knowing the vapor temperature, and velocity (from the energy balance and the vapor temperature), the vapor Reynolds number and a single phase convective heat flux can be calculated. Since this situation is single phase convection in a two-phase mixture, correlation is developed from droplet injection experiments. This type of a calculation will give a reasonable estimate of the portion of the total wall heat flux which is due to convection.

Heat transfer by radiation is also an important phenomenon in the froth region because of the large liquid content of the flow and the increasing heater rod surface temperatures. However, the percentage of the total heat flux due to radiation should be relatively small since the majority of the heat is transferred directly by film boiling to the low void fraction mixture. The radiation heat transfer to the liquid can be estimated for the test conditions using the void fraction and high speed movies which indicate the behavior of the liquid using the measured surface temperature and the saturation temperature. Similar calculations can be performed for radiation to the vapor using the estimated vapor temperature and the heater rod surface temperature. Again, it is expected that the total effect of radiation heat transfer is small for the froth region since the absolute value of the film boiling heat transfer is much larger in this region. The radiation modeling approach has been used in the FLECHT-SEASET program and would be modified for the RBHT facility.

As liquid is entrained and accelerated in the froth region, both interfacial shear and heat transfer occur. Models for both of these important processes are crude, at best. The interfacial area and interfacial shear are not measured directly; however, estimates of the interfacial drag (shear) times the interfacial area can be made from the data. The local quality can be calculated from a detailed mass and energy balance on the bundle, particularly in the froth region. The principal uncertainly in this calculation is the vapor temperature.
Void fraction is also measured such that the average liquid velocity in the rod bundle can be calculated. Also, by the same calculation, the average vapor velocity in the bundle can be determined at different axial locations, within and above the froth region. At this point, one would have to make assumptions which can significantly affect the calculated results. If a two-phase frictional pressure drop model is assumed, and set equal to the portion of the measured pressure drop which is believed to be caused by friction, a measure of the product of the interfacial drag and area can be calculated. Another approach is to review the high speed movies in the froth region and postulate a liquid surface area and then calculate the resulting drag.

In the case of interfacial heat transfer, the change in the local quality within the froth region will indicate the product of the interfacial heat transfer coefficient times the interfacial area. The uncertainly in this calculation is the accuracy of the measured vapor temperature. Heat transfer should be a two-step process with the wall energy being transferred to the vapor, and the resulting vapor energy causing evaporation of the entrained liquid. The axial dependence of the measured vapor temperature will have to be extrapolated into the froth region from the dispersed flow film boiling region, using the miniature thermocouples, to obtain an estimate.

To separate the heat transfer coefficient from the interfacial area, further assumptions must be made such as characterizing the liquid surface in the froth region from high speed movies, or applying an appropriate convective coefficient to the entrained liquid. Both methods are approximate and have large uncertainties but will be examined. The different models in a computer code can be compared to the data for void fraction in the froth region, and mass balance on the froth region to obtain the entrained liquid flow. The energy balance will give the bundle average liquid and vapor velocities. A computer code should match these measured and calculated quantities from the data with their particular interfacial models.

4.3.5 Dispersed Flow Film Boiling Region (Table 4.10)

In the dispersed flow film boiling region the total wall-to-fluid heat transfer is calculated by the codes as the sum of the following contributions:

1) Forced convection to the vapor,
2) Radiation heat transfer to both drops and steam, and
3) Drop direct and dry wall contact heat transfer.

The forced convection heat transfer is calculated with the Dittus-Boelter correlation by knowing the vapor Reynolds number. The vapor Reynolds number is a function of the vapor velocity, the void fraction and the vapor temperature. Some dispersed flow experiments have shown that the interfacial shear between dispersed particles and a continuous phase increases the turbulence level and enhances the convective heat transfer.

In the COBRA-TF code, this two-phase enhancement factor is approximated by an extension of the analogy between wall shear stress and heat transfer. From the momentum-heat transfer analogy, the turbulent convection heat transfer coefficient is proportional to the square root of the shear stress. The total shear stress for the two-phase is the sum of the vapor-wall shear stress and the interfacial stress due to the droplets. The ratio between the interfacial shear stress due to the droplets and the vapor-wall shear stress is a function of the vapor velocity, interfacial area the droplet velocity and the entrainment phase void fraction. These quantities can be estimated from the test data such that this effect can be quantified.

The temperature of the vapor is determined by the interfacial heat transfer and the convection from the wall. Information about the drop velocity and size distribution and the vapor temperature are also needed to estimate the interfacial heat transfer. Using steady-state droplet injection experiments, by measuring the shift in the drop size distribution as the droplets move along the channel, it may be possible to estimate the droplet evaporation rate and therefore the interfacial heat transfer.

Radiation heat transfer from wall-to-wall, wall-to-vapor, and to drops need to be analytically estimated and separated from the total heat transfer during test data analysis.

The third component is the most difficult to estimate from the test data. Fortunately this component is ranked low-medium in the PIRT. In COBRA-TF, direct wall heat transfer is a function of the deentrainment rate and the drop evaporation efficiency. The deentrainment rate is a function of the droplets concentration gradient (the concentration is zero at the wall) which is a function of the average entrainment fraction. The drop evaporation efficiency is a function of the wall superheating. The code needs information about the entrainment volume fraction, drop concentration gradient and wall temperature to estimate this component.

When the direct contact heat transfer becomes important (mostly in transition boiling), the intermittent wetting of the surface should produce localized oscillations in the temperature at the surface. These oscillations could be capture if the thermocouples response time is fast enough. The analysis of the oscillation can be an indirect way to estimate this component.

The dispersed flow film boiling region is a region of very low heat transfer located above the froth front in which the mixture consists of highly superheated steam in which small liquid droplets are entrained. The peak cladding temperature is calculated in this region and the temperature remains elevated until the froth region approaches the peak temperature axial position within the rod bundle. The important PIRT phenomena for this region are given in Table 2.5 as:

- Decay power, and
- Dispersed flow film boiling, which consists of:
  - Convective heat transfer to superheated vapor flow,
  - Dispersed phase enhancement of convective flow and heat transfer,
  - Radiation heat transfer to drops, vapor and surfaces,
  - Interfacial heat transfer between drops and superheated vapor,
  - Interfacial drag between drops and superheated vapor, and
  - Dry wall drop-contact heat transfer.

The decay power will be simulated and measured as a test condition and will be ranged over typical power values expected in a nuclear power plant.

The measurement methods used in the RBHT have been developed specifically for the dispersed flow film boiling regime since it is the most limiting region of the reflood process. The LIDCS will be used to measure the drop size and velocity at different location along the bundle. The actual flow quality will be calculated from the bundle mass and energy balance such that the bundle average flow rates for the vapor and the liquid can be obtained. Since the vapor velocity can be calculated (accounting for the vapor superheat), and the droplet velocity and quality are known, the local void fraction can be calculated. The local void fraction can also be estimated from the droplets measurements taken with the LIDCS. However, the LIDCS measurements can over-estimate the void fraction since the measurement does not record droplets which are behind the heater rods since the measuring volume is the gap between the rods.

A separate series of convective heat transfer experiments over a wide range of Reynolds numbers is planned as one of the first test series, before the actual reflood experiments. These tests will be analyzed on a subchannel basis using COBRA-IV, VIPRE-II, as well as hand calculations, to obtain the local subchannel flow for a given measured bundle inlet flowrate. The subchannel data will be correlated both on a bundle basis as well as a subchannel basis using the bundle or subchannel Reynolds number and the Nusselt number calculated from the measured wall heat flux obtained from the heater rod thermocouples. The subchannel vapor thermocouples will be used to determine the axial vapor superheat distribution. The correlation from these experiments will be compared to existing convective correlations.

Another series of separate effects experiments will examine the effects of the dispersed entrained droplets on the convective heat transfer within the rod bundle. There are different postulated phenomena which could be occurring within the dispersed flow regime. One school

Table 4.10 Dispersed Flow Region for Core Component

Process/Phenomena	Ranking	RELAP5/MOD3.2		TRAC-B		TRAC-P		COBRA-TF	
		Does the model Exist	*Uncertainty*	*Does the model exist*	*Uncertainty*	*Does the model exist*	*Uncertainty*	*Does the model exist*	*Uncertainty*
Decay Power	H	Input		Input		Input		Input	
Fuel Rod/Heater Rod properties, ρ, C_p, k	L	Input		Input		Input		Input	
Dispersed Flow Film Boiling	H	Bromley correlation for conduction across the film	18%	Modified Bromley void weighted single phase convection		Yes, modified Bromley correlation (Denham)		Yes, Sum of several individual models	
Convection to superheated vapor	H	Dittus-Boelter	30%			Yes, based on Webb-Chen correlation	Not verified for rod bundle	Yes, max of Dittus-Boelter and FLECHT-SEASET	15%
Dispersed phase enhancement of convective flow	H	No		No		Yes, somehow considered in the Webb-Chen correlation	100%	Yes, empirical correlation	>100%
Direct wall contact H.T.	L	No		No				Yes, Ganic-Rohsenow	>100%
Dry wall contact [12]	M	No		No				No	
Droplet to vapor interfacial heat transfer	H	Yes, code calculates interfacial area and H.T.C. depending on flow regime		Yes, code calculates interfacial area and H.T.C. depending on flow regime		Yes, code calculates interfacial area and H.T.C. depending on flow regime		Yes, Lee Ryley model	30%

Table 4.10 Dispersed Flow Region for Core Component (Continued)

Radiation Heat Transfer to:									
• Surfaces	M/H	No		Yes, has rod and channel radiation models		No		Yes, surface radiation model	~20%
• vapor	M/H	Yes, Sun Gonzales, Tien.	50%	Yes, Sun, Gonzales, Tien		No		Yes, Sun Gonzales, Tien	50%
• droplets	M/H	Yes, Sun Gonzales, Tien	50%	Yes, Sun, Gonzales, Tien		No		Yes, Sun Gonzales, Tien	50%
Gap heat transfer	L	FRAP-T6		Yes, code calculates		Yes, code calculates		Yes, does have dynamic gap	100%
Cladding Material	L	Input		Input		Input		Input	
Reaction Rate	M	No		Yes, Cathart, Powell		Yes, code calculates		Yes, Cathart Powell model	
Fuel Clad Swelling/Ballooning	L	No		No		No		Not in current version	

of thought is that the droplets increase the total shear which increases the turbulence level in the flow such that the single phase convective heat transfer increases. Since the Reynolds numbers are very low in superheated steam (typically 1000 to 4000), any increase in turbulence could have a significant effect.

Another thought is that the drop addition acts as a distributed heat sink within the continuous steam flow and directly affects the vapor temperature resulting in a larger temperature gradient to the wall. These and other heat transfer enhancement mechanisms will be investigated in these experiments. The local wall temperature will be measured on the heater rods to obtain the wall heat flux, the vapor temperature will be measured on a subchannel basis using the traversing miniature thermocouple probes, and the entrained droplet size, distribution, velocity and velocity distribution will be measured using the Laser Illuminated Digital Camera System. The droplet injection system will be previously characterized in a bench test, such that the initial drop size and distribution will be known. The analysis of the test data will provide a basis for the development of an improved model for these phenomena.

Separate experiments are planned to examine the surface-to-surface radiation in an evacuated bundle. The purpose to verify the data analysis program which will be used to separate the radiation heat transfer components to the surfaces, drops, and vapor, from the measured total wall heat flux such that the convective portion of the dispersed flow film boiling can be determined.

Ample heater rod, structure, grid, and housing thermocouples are placed at or very near the same elevations such that a radial temperature distribution across the bundle can be obtained. These tests will also indicate the influence of the housing and the radiation to the other surfaces within the bundle. The emissivity of the surfaces will have already been determined from previous tests to characterize the surfaces such that the surface condition uncertainty is removed from the analysis.

Radiation heat transfer components from the wall to the surfaces, drops, and vapor will be calculated from the data using the measured temperatures of the heater rods, support tubes, and housing, as well as the measured vapor temperature and the droplet temperature, which is assumed to be saturation. The uncertainty in this calculation will be reduced because the method will have been verified using radiation-only tests as well as the surface emissivity properties which were independently measured for the heater rods and surfaces. The droplet data obtained from the LIDCS will be used to determine the droplet size and area to determine the radiation from the heater rods to the drops.

Using a bundle energy balance, the local quality can be calculated along the test section. The change in the calculated quality due to the interfacial heat transfer can be obtained from the energy balance once the heat flux from the wall has been corrected for the radiation effects. The convective portion of the wall heat flux is determined from the measured value minus the radiation component. Using the energy balance data and the LIDCS data, the size and velocity of the drops are known and the number of the drops can be estimated such that the interfacial area and a droplet heat transfer coefficient can be calculated and compared to correlations used in the literature and those used in the computer codes. A similar approach can be used for the interfacial drag using the droplet information from the LIDCS and the mass and energy balance for the bundle. The above calculations from the data will be estimates since there is a droplet spectrum, not single sized droplets. The spacer grids are also postulated to shatter the entrained drops resulting in the generation of “micro” droplets which can evaporate faster.

Therefore, a Sauter mean drop size will be calculated from the distribution measure and will be used in the energy calculations. This approach has been used in the FLECHT-SEASET tests with some success, although some of the uncertainties were very large.

Dry wall contact can not be directly measured in the RBHT program as a separate heat transfer contribution to the total wall heat flux. The examination of the wall convective heat flux (once radiation effects have been subtracted from the measured total heat flux) as a function of void fraction will give some guidance on the relative importance of this component. There may be double accounting of the single phase convective enhancement of the convective flow and the dry wall contact phenomena such that they are really the same since the convective enhancement should include the effects of the dry wall phenomena.

4.3.6 Top Down Quench in Core Components (Table 4.11)

None of the phenomena identified in Table 2.6 for the top down quench were identified as a highly ranked PIRT phenomena. The most important phenomena for this period is the value of T_{MIN} which will allow the quench front to propagate down the bundle. T_{MIN} appears elsewhere as a highly ranked phenomena and is discussed there.

4.3.7 Other Effects: Spacer Grids, Housing

The spacer grids affect the total heat transfer during the reflood by:

1) enhancement of convection heat transfer to the vapor,
2) large drops are shattered by the grids, and
3) grid rewetting and deentrainment.

Specific models to account of these effects are in COBRA-TF. The information needed by the code to assess these models are:

1) temperature of the grid,
2) vapor temperature axial distribution (downstream of the grid),
3) the rod temperature axial distribution (downstream of the grid), and
4) drop velocity and size distribution.

In COBRA-TF an additional small drop field is added explicitly in the code. The model solves the small drop acceleration and interfacial heat transfer downstream the grid once the vapor flow solution is known. Information about the small drop velocity and size distribution at different position downstream the grid can be used to validate these models.

The presence of the housing which represents a distortion of the facility if compared with the real plant, must be simulated by the code. Therefore the radiation heat transfer from the rods to the housing, the heat transfer to the fluid and the quench of the housing (stored heat) need to be characterized during the experiments.

The RBHT test facility instrumentation has been designed specifically to determine the heat transfer effects of the spacer grids. The heater rod thermocouples are spaced along the rods to determine the convective enhancement of the grids, droplet breakup effects and local subchannel vapor temperature. The grids are located within the viewing regions of the windows such that the effects of the grids can be observed and measured.

Table 4.11 Top Down Quench in Core Component

Process/Phenomena	Ranking	RELAP5/MOD3.2		TRAC-B		TRAC-P		COBRA-TF	
		Does the model exist	Uncertainty	Does the model exist	Uncertainty	Does the model exist	Uncertainty	Does the model exist	Uncertainty
De entrainment of film flow	L[1]	No		No		No		Yes	
Sputtering droplet size and velocity	L	No		No		No		Yes, min size specified	100%
fuel rod/heater rod properties for stored energy ρ, C_p, k.	L[1]	Input		Input		Input		Input	
Gap heat Transfer	L[1]	FRAP-T6		Gas gap Code calculates		Yes, code calculates		Calculated by code	

Note: Some of these individual items can be ranked as high (H) within the top down quenching process; however, the entire list is ranked as low for a PWR/BWR since it occurs downstream of the PCT location.

4.4 Conclusions

The different large thermal-hydraulic computer codes have been briefly reviewed and compared against the reflood PIRT tables. While each code had the basic models for a boiling curve, and thermal and mechanical non-equilibrium, the COBRA-TF thermal-hydraulic formulation and additional detailed component models make this code an attractive choice for refined reflood development. COBRA-TF can be used on a subchannel basis to model the limiting hot fuel pin in a rod bundle. COBRA-TF is also a three-field formulation with an explicit entrained liquid field and a corresponding interfacial area transport equation which permits more accurate modeling of the entrained liquid phase, which is most important for calculating dispersed flow film boiling. Using the unique representation of the third field or entrained droplet field results in more accurate predictions of flow regimes, their transition, and the resulting heat transfer in the different regimes. There is also believed to be less chance of compensating errors, since one is not adjusting a two field model to represent the effects of three fields. Specific attention was given in COBRA-TF to the dispersed flow heat transfer model to account for the different component models which represent reflood heat transfer. Fine mesh renodalization for the heated conductors is used to better represent the quench front. Two-phase convective enhancement is accounted for in the calculations and a subchannel radiation model is used to more accurately represent radiation within a rod bundle.

COBRA-TF also models the effects of spacer grids in dispersed two-phase flow in a mechanistic manner accounting for convective effects of spacer grids, spacer grid quenching behavior and the droplet breakup caused by spacer grids. In particular, a small-droplet field has been added to COBRA-TF to model the heat transfer effects of the much smaller drops as they evaporate and provide additional cooling downstream of the grids.

As shown in the PIRT table comparisons, the formulation of the COBRA-TF code, as developed as part of the FLECHT-SEASET 163-Rod Blocked Bundle Program, has the desired basic formulation to develop the improved component models needed for dispersed flow film boiling in reflood. The Rod Bundle Heat Transfer program will utilize COBRA-TF for modeling purposes, and predictions and model validation purposes in the development of improved reflood models.

4.5 References

1. The RELAP5 Code Development Team, “RELAP5/MOD3 Code Manual Volume V: Models and Correlation”, NUREG/CR-5535, June 1995.

2. F. W. Dittus and L. M. K. Boelter, “Heat Transfer for Automobile Radiators of the Tubular Type,” University of California, Berkeley Publ. Eng, Vol. 2, No. 13, pp. 442-462, 1930.

3. S. W. Churchill and H. H. S. Chu, “Correlation Equations for Laminar and Turbulent Free Convection From a Vertical Plate,” Int. J. Heat and Mass Transfer,18, pp. 1323-1329, 1975.

4. C. Chen, “A Correlation for Boiling Heat Transfer to Saturated Fluids in Convective Flow,” Process Design and Development, 5, pp. 322-327, 1966.

5. F. D. Moles and J. R. G. Shah, “Boiling Heat Transfer to Subcooled Liquids Under Conditions of Forced Convection,” Transaction, Institution Chemical Engineers, 45, p. 39, 1949.

6. Biasi, et al., “Studies on Burnout Part 3 -- A New Correlation for Round Ducts and Uniform Heating and Its Comparison with World Data,” Energia Nucleare, 14, pp. 535-536, 1967.

7. Sjoberg and D. Caraher, “Assessment of RELAP5/MOD2 Against 25 Dryout Experiments Conducted at the Royal Institute of Technology,” NUREG/IA-0009, October 1986.

8. D. C. Groneneveld, S. C. Cheng, and T. Doan, “1986 AECL-UO Critical Heat Flux Lookup Table,” Heat Transfer Engineering, 7, 1-2, pp. 46-62, 1986.

9. C. Chen, R. K. Sundaram and F. T. Ozkaynak, “A Phenomenological Correlation for Post-CHF Heat Transfer,” NUREG-0237, June 1977.

10. Bromley, L. A., “Heat Transfer in Stable Film Boiling,” Chemical Engineering Progress, Vol. 46, No. 5, pp. 221-226, 1950.

11. H. Sun, J. M. Gonzales-Santalo and C. L. Tien, “Calculations of Combined Radiation and Convection Heat Transfer in Rod Bundles Under Emergency Cooling Conditions,” J. of Heat Transfer, pp. 414.2-420, 1976.

12. Brumfield, R. N. Houze and T. G. Theofanous, “Turbulent Mass Transfer at Free, Gas-Liquid Interphases, with Applications to Film Flows,” Int. J. of Heat and Mass Transfer, 18, pp. 1077-1081, 1975.

13. Lee and D. J. Ryley, “The Evaporation of Water Droplets in Superheated Steam,” J. of Heat Transfer, ASME, pp. 445-451, November 1968.

14. S. Plesset and S. A. Zwick, “The Growth of Vapor Bubbles in Superheated Liquids,” Journal of Applied Physics, 25, 4, pp. 493-500, 1954.

15. H. C. Unal, “Maximum Bubble Diameter, Maximum Bubble-Growth Time and Bubble Growth Rate During the Subcooled Nucleate Flow Boiling of Water up to 17.7 MN/m^2,” Int. J. Heat and Mass Transfer, 19, pp. 643-649, 1976.

16. G. Brown, “Heat Transmission of Condensation of Steam on a Spray of Water Drops,” Proceedings of the General Discussion on Heat Transfer, published by the Institution of Mechanical Engineers, pp. 49-52, September 11-13, 1951.

17. T. G. Theofanous, “Modeling of Basic Condensation Processes,” The Water Reactor Safety Research Workshop on Condensation, Silver Springs, MD, May 24-25, 1979.

18. Ishii and K. Mishima, “Correlations for Liquid Entrainment in Annular Two-Phase Flow of Low Viscous Fluid,” ANL/RAS/LWR 81-2, 1981.

19. Kataoka and M. Ishii, “Entrainment and Deposition Rates of Droplets in Annular Two-Phase Flow,” CONF-830301-11, ASME-JSME Thermal Engineering Joint Conference, Honolulu, HI, March 20, 1985.

20. Jay W. Spore, et. al., Los Alamos National Labratory. TRAC-PF1/MOD2, Vol. I, Theory Manual.

21. C. Unal, K. Tuzla, C. A. Tuzla, and J. C. Chen, “Vapor Generation Model for Dispersed Drop Flow,” in ANS Proc. 1989 National Heat Transfer Conf. (August 1989), HTC-Vol. 4, 1989.

22. Kataoka and M. Ishii, “Mechanism and Correlation of Droplet Entrainment and Deposition in Annular Two-Phase Flow,” Argonne National Laboratory Report ANL-82-44 (NUREG/CR-2885), 1982.

23. Borkowski, N. L. Wade, et.al., Idaho National Engineering Laboratory. TRAC-BF1/MOD1 Models and Correlations, July 1992.

24. C. Y. Paik, L. E. Hochreiter, J. M. Kelly, and R.J. Kohrt, “Analysis of FLECHT-SEASET163-Rod Blocked Bundle Data Using COBRA-TF,” NUREG/CR-4166, WCAP- 10375, EPRI-NP-4111, October 1985.

25. Thurgood, et al, “COBRA/TRAC: A Thermal-Hydraulic Code for Transient Analysis of Nuclear Reactor Vessels and Primary Coolant Systems,” NUREG/CR-3046, Volumes 1-5, March 1982.

26. S. Wong and L.E. Hochreiter, “Analysis of the FLECHT-SEASET Unblocked Bundle Steam Cooling and Boil-off Tests,” NRC/EPRI Westinghouse Report 8, January 1981.

27. E. M. Sparrow, et al, “Heat Transfer to Longitudinal Laminar Flow Between Cylinders,” J. Heat Transfer, Vol 83, p. 415, 1961.

28. W. T. Hancox and W. B. Nicoll, “A General Technique for the Prediction of Void Distributions in Nonsteady Two-Phased Forced Convection,” Int. J. Heat and Mass Transfer, Vol 14, 1971.

29. S. Z. Rouhani and F. Axelsson, “Calculation of Void Volume Fraction in Subcooled and Quality Boiling Regions,” Int. J. Heat and Mass Transfer, Vol. 13, 1970.

30. Zuber, et al, “The Hydrodynamic Crisis in Pool Boiling of Saturated and Subcooled Liquids,” Part II, No. 27 in International Heat Transfer Conference, Boulder, CO, 1961.

31. R. E. Henry, “A Correlation for Minimum Film Boiling Temperature,” AlChE Symposium Series 70, (138), pp. 81-90, 1974.

32. E. N. Ganic and W. M. Rohsenow, “Dispersed Flow Heat Transfer,” Int. J. Heat and Mass Transfer, Vol 20, pp. 855-866, 1977.

33. D. McCoy and T. J. Hanratty, “Rate of Deposition of Droplets in Annular Two-Phase Flow,” Int. J. Multi Phase Flow, Vol 3, pp. 319-331, 1977.

34. Drucker and V. K. Dhir, “Studies of Single and Two-Phase Heat Transfer in a Blocked Four-Rod Bundle,” EPRI-NP-3481, June 1984.

35. W. Kays, Convective Heat and Mass Transfer, McGraw-Hill, New York, 1966.

36. Kelly, “Quench Front Modeling and Reflood Heat Transfer in COBRA-TF,” Paper 79-WA/HT-63, ASME Winter Annual Meeting, New York, 1979.

37. S. C. Yao, L. E. Hochreiter, and W. Leech, “Heat-Transfer Augmentation in Rod Bundles Near Grid Spacers,” J. Heat Transfer, Vol 104, 1982.

5. ROD BUNDLE HEAT TRANSFER PROGRAM OBJECTIVES AND FACILITY MISSION

5.1 Introduction

Sections 2 and 3 identified the phenomena of interest and the existing database for reflood model development and validation over the range of conditions of interest. Section 2 also identified the individual component models and phenomena which a computer code uses to perform calculations for the complete heat transfer. Section 3 identified those existing data useful for addressing particular types of phenomena of importance to reflood heat transfer. Section 3 also provided information on the range of parameters to be selected for the various types of experiments to be performed in the RBHT program. Section 4 reviewed the different reflood heat transfer models in current computer codes and identified the current state-of-the-art needs for a best-estimate safety analysis computer code. The need for the improved analysis models becomes the objectives of the RBHT program. The needs define the specific mission of the test program as well as the analysis efforts which will compliment the experiments. The combination of specifically directed experiments and the corresponding data analysis, development of physically based heat transfer and two-phase flow models as well as implementation of these models into a best-estimate computer code will achieve the program objectives.

5.2 Rod Bundle Heat Transfer Program Objectives

The objective of the RBHT program is to provide needed, unique, separate-effects rod bundle data on specific component models which comprise the “reflood” heat transfer phenomena observed in PWR and BWR rod bundle situations for a large-break loss of coolant accident. The emphasis of the program is to provide specific experimental data and associated analysis which will enhance the understanding of the dispersed flow film boiling region which is the limiting heat transfer situation for the LOCA transient. The reflood heat transfer processes are very complex. The full range of the phenomena identified in a boiling curve occurs in the reflood heat transfer calculation as well as the multi-dimensional conduction heat transfer in the fuel rod at the quench location. The rod heat transfer is coupled to the two-phase flow behavior of the coolant such that as the stored energy from the rods is released into the fluid, the local flow regime can change and continuous liquid flow, at the quench front, can be dispersed first into slugs and ligaments then sheared into dispersed droplets. The coupling of the rod heat release drives the liquid entrainment which then provides additional cooling above the quench front.

There are several different thermal-hydraulic phenomena which interact to provide the “reflood heat transfer” which best-estimate safety analysis computer codes must predict. In the dispersed flow film boiling regime, no single phenomenon dominates. The total heat transfer is comprised of several different mechanisms as identified in Section 1 of this report. The relative importance of a particular mechanism will vary as the rod surface temperature increases or decreases, as the pressure varies, and as the flooding rate into the bundle changes. In dispersed flow film boiling, the primary heat transfer mechanism is convective heat transfer to superheated steam. It is known that the steam heat transfer coefficient can be enhanced by up to 100 percent due to the presence of entrained droplets. No suitable models currently exist for this phenomenon.

The combination of single-phase vapor heat transfer tests with the forced droplet injection tests (where drop size and flow rate are known) will result in the development of the needed model. What is needed is a series of experiments which help isolate a particular heat transfer mechanism such that its individual effects can be identified, modeled and used to predict the total heat transfer in the bundle.

Therefore, the objectives of the RBHT program are to:

1. Develop a Phenomena Identification Ranking Table (PIRT) for reflood heat transfer on a component model level and estimate the relative importance of each phenomenon for predicting reflood heat transfer,

2. Develop a test facility design which has a minimum of distortion to represent reflood heat transfer in PWR and BWR cores,

3. Assess the needs of best-estimate computer codes on their modeling approaches for reflood heat transfer and the component models used in the computer codes,

4. Perform component experiments which isolate individual phenomena which compromise reflood heat transfer,

5. Determine the effects of the fuel assembly spacer grids on the dispersed flow film boiling heat transfer downstream of the grid,

6. Develop specific component models from these experiments,

7. Add the component models into a best-estimate computer code and compare to the forced reflood heat transfer data from this series of expedients as well as other sets of reflood heat transfer data,

8. Validate the new proposed component reflood heat transfer models over their range of application, and

9. Document the results of the experiments and analysis in a form that it can be used by others.

The majority of the experiments will be separate effects tests which will isolate individual models. The separate effects tests which are proposed include:

1. Single phase flow pressure drop experiments to characterize the hydraulic behavior of the facility,

2. Heat loss experiments which characterize the heat losses to the atmosphere which are needed for modeling the facility and analyzing the test data,

3. Radiation heat transfer experiments in a evacuated bundle to assess the rod-to-surface, and rod-to rod radiation heat transfer which is needed to subtract out the radiation contribution from the total measured heat transfer,

4. Single phase steam flow convective heat transfer experiments which cover the Reynolds number range expected in a rod bundle during reflooding,

5. Single phase steam flow experiments with injected droplets over a range of conditions to simulate the dispersed two-phase flow region above the quench front,

6. Forced reflooding experiments over a wide range of conditions typical of a PWR and BWR rod bundle during reflooding,

7. Forced oscillating flow experiments which characterize the inlet flow into a reactor system during reflooding.

The proposed experiments will be performed in a building block approach such that the more complex experiments occur after the more fundamental experiments. In this fashion, additional information and desired test conditions can be modified as needed to optimize the test matrix of the forced reflooding tests which are the most difficult tests to perform. The proposed experiments will provide new unique data as well as supplement existing reflood heat transfer data but they will focus on the improvements of specific best-estimate thermal-hydraulic models rather than identifying licensing margin.

To achieve the objectives of the experiments and to capture the important thermal-hydraulic phenomena which have been identified for reflood heat transfer, several new or novel approaches are proposed for the bundle instrumentation. The characteristics of the froth region are relatively unknown. In this region, the flow changes from a liquid continuous flow to a vapor continuous flow as the rods quench and generate a significant amount of steam. The liquid flow is sheared by the steam and generates a droplet distribution which is entrained into the upper regions of the bundle where the peak cladding temperature occurs. The void fraction in the froth region varies from nearly zero to almost one in the span of approximately one-foot. There are three different measurement systems which will be used in the RBHT program:

1. A soft gamma detector with beryllium windows on the test section will measure the chordal average void fraction within the rod bundle as the dispersed flow; froth front and quench pass at selected elevations.

2. Finely spaced, very sensitive differential pressure cells will measure the local pressure along the test section and will be corrected for frictional and acceleration effects to calculate a span average void fraction. It has been demonstrated that many of the apparent functional dependencies (i.e., mass flux, subcooling, and distance from the quench front) for this heat transfer regime are primarily due to the axial profile of the void fraction in this region. Currently available data for this regime in rod bundles is insufficient for model development due to the coarse spacing (from 1 - 2 feet) used for the delta-P cells used to measure the void fraction. The RBHT program will redress this data deficiency through the use of finely spaced delta-P cells (three inch span) and by a local void fraction measurement provided by a low energy gamma-densitometer.

3. A Laser Illuminated Digital Camera System (LIDCS) will be used to measure the drop size, distribution, and velocities at the dispersed flow/froth flow boundary such that the droplet entrainment distribution can be obtained. To correctly calculate the interfacial heat transfer requires the knowledge of both the entrained droplet flow rate and droplet diameter. There is very little data of this type available for quenching rod bundles. The RBHT program will

generate the needed database through the use of advanced instrumentation, specifically through the use of the LIDCS.

At several axial locations in the rod bundle, there will also be steam probes to measure the vapor temperature in the dispersed two-phase mixture or the local fluid temperature for single-phase tests. The laser illuminated digital camera will also be used in this region to obtain the drop distribution, size, and velocity. There will also be ample heater rod temperature measurements along the bundle as well as exit and inlet flow measurements such that the bundle energy and mass balance can be performed and the total heat flux can be separated into radiation heat transfer and flow film boiling heat transfer.

Spacer grids which support the rods in the rod bundle will be instrumented as well as the rod temperatures downstream of the grids and the coolant subchannels downstream of the spacer grids. There will be laser illuminated digital camera system data taken above and below the spacer grids to observe and quantify the change in the droplet diameter and velocity distributions due to the droplet breakup caused by the spacer grids. The heater rod thermocouples and the vapor temperature measurements will also measure the local heat transfer enhancement caused by the spacer grids.

Specific bench-top experiments have been designed to aid in the instrumentation development for the RBHT program. These bench top experiments test the LIDCS for droplet measurements in an unheated 3x7 bundle and in a 3x3 heated one-third length bundle. The 3x7 experiments verify the performance of the droplet injector component which will be used in the RBHT program. These tests also confirm the ability of the laser illuminated digital camera system to measure the droplet distribution accurately. The 3x3 heated bundle experiments will specifically examine the effects of spacer grids on the entrained droplet distribution within subchannels. This heated bundle will also provide comparison data on the thermal-hydraulic effects of different spacer grid designs. The 3x3 bench test will also be used to determine the flow disturbance effects of miniature thermocouples which will be used to traverse the rod bundle. A reliable measurement of the non-equilibrium vapor temperature is desired, but since the method used is intrusive, the measurement method must be assessed to ensure that the rod bundle flow is not changed by the measurement technique.

5.3 Conclusions

The objectives of the RBHT program have been established to provide the needed data on the highly ranked PIRT phenomenon for reflood heat transfer. Experiments will be performed to isolate a specific phenomenon as best as possible so as to permit specific model development for that phenomenon. The test facility instrumentation has been designed to obtain, as best as possible, the local fluid conditions within the bundle using new and unique techniques. In this manner, the local heat transfer can be related to the local fluid conditions such that the risk of introducing compensating errors into the advanced reflood model package is minimized.

6. First Tier Scaling for the Rod Bundle Heat Transfer Test Facility

6.1 Introduction

In order to simulate actual systems (prototype), many experiments are performed at a reduced size, with different materials and different working fluids. The object of the experiment is to capture the phenomena which have been determined to be important for understanding the full size system. Scaling analyses are normally performed for the smaller size models to verify the performance of the full size system.

Scaled experiments have been used for many years in the areas of fluid mechanics for airfoil design, hydraulics for ship design as well as water tables for harbor designs and heated effluent discharges. Scaling fluids have been used in heat transfer studies to simulate high pressure fluids and other dangerous working fluids to examine critical heat flux behavior and core melt conditions. More recently, scaling has been used to simulate the thermal-hydraulic conditions expected in a nuclear reactor for postulated accident conditions. There have been several different thermal-hydraulic scaling approaches proposed by Larson (Ref. 1) and Ishii (Ref. 2) for single and two-phase systems.

A generalized scaling approach has been developed by Zuber (Ref. 3) for thermal-hydraulic systems in which a two tier scaling approach is given. An important aspect of Zuber's approach is that the scaling process can be used to help identify the most important phenomena as well as the less important phenomena such that when compromises are made, the important phenomena are correctly simulated. This approach has been refined by Wulff (Ref. 4) who recommended that the full equation be divided by a "driver term" such that the relative importance of the different terms could be assessed. Zuber (Ref. 5) also extended the methodology by using the maximum ranges to normalize variables such that correct limits would be represented. The result has been to translate the scaling analysis into a workable methodology which can be used on any general thermal-hydraulic system.

The Zuber approach was used for the scaling efforts for the Oregon State University AP-600 small break Loss of Coolant Accident (LOCA) and long term cooling experiments (Ref. 6). The combination of the Zuber and Wulff scaling methodologies were used for the other AP-600 experiments to assess possible test distortions relative to the full size reactor (Ref. 7). The combined Zuber-Wulff scaling approach is the current state-of-the-art methodology for scaling thermal-hydraulic systems.

The Zuber-Wulff scaling methodology has been used to assess the ability of the RBHT Test Facility to capture the phenomena of interest for the reflood phase of a LOCA transient such that the data can be used, with confidence, to verify and develop heat transfer and two-phase flow models for best-estimate thermal-hydraulic computer codes. In addition to verifying that the test facility can produce the desired data, the two tier scaling process also identifies possible distortions in the test facility relative to the nuclear reactor core and provides a numerical assessment of the importance of the possible distortion.

6.2 Two Tier Scaling Approach

The two tier scaling approach, as developed by Zuber, consists of "top-down" scaling approach which gives a scaling group for each transfer process as derived from the dimensionless control volume equations for the conservation of mass, momentum, and energy as written for the thermal-hydraulic system. The scaling groups which result from the normalization of the control volume equations are time ratios for the different processes which occur in the system. These groups are called "Pi" parameters. Therefore, top-down scaling or systems approach provides a method for identifying the important phenomena, derive similarity groups, weighting of the different groups to establish priorities, and providing a basis for decoupling fast and slow acting processes which have different time scales. The top-down scaling approach, which is used for both the experiment and the prototype, or full scale system, can identify the lack of similarity between the test and the prototype which indicates scaling distortions. Top-down scaling also identifies those thermal-hydraulic processes which require additional detailed analysis using a "bottom-up" scaling approach.

The bottom-up scaling approach (or process approach) addresses only those thermal-hydraulic processes which are identified as being important or can have distortions which could impact the experiment. Bottom-up scaling will focus on specific Pi terms in the system equations which govern the particular phenomena of interest. The bottom-up scaling can be used to characterize the transport terms in the control volume equations (transport of mass, momentum or energy), to establish the relationships for calculating these terms and to compare the scaled experiment to the full size prototype.

This section of the report will discuss the application of the first tier or top-down scaling for the RBHT Test Facility; the bottom-up scaling will be discussed in Section 7.

6.3 Application of the Top-down Scaling Approach

There are three equations which are examined for the RBHT Test Facility: the fluid energy equation; the solid energy (heater rod, fuel rod) equation; and, the fluid momentum equation. Each conservation equation is derived in the fashion as recommended by Zuber and Wulff. The equations are normalized and the terms are divided by the "driver term" such that the resulting Pi groups are dimensionless. This approach is applied to both the RBHT Test Facility as well as to a PWR and a BWR fuel assembly to indicate the possible non-typical effects and distortions in the test facility relative to the actual plant component.

Since the tests proposed for the RBHT Test Facility are separate effects tests, the flow at the inlet is forced, or is a prescribed boundary condition. In these situations, the fluid momentum equation has less importance as compared to the fluid energy and solid energy equations. However, since one of the primary goals of the analysis is to identify test distortions, the momentum equation will be used to examine the hydraulic behavior of the test facility relative to PWR and BWR fuel assemblies.

6.3.1 Fluid Energy Equation

A simplified fluid energy equation is written for the test bundle with the following assumptions:

- Constant forced flooding rate into the bundle,

- Zero-dimensional analysis. No radial gradients in the fluid. Single and two-phase regions are treated separately,
- No radial temperature gradient in the structures that interact with the fluid; averaged solid temperatures are used,
- The analysis represents a snapshot in time with a single phase region, a two phase region and a quench front on the rods, housing, grids, and dummy (unheated) rods,
- Once a structure is quenched, there is no longer any energy transfer to or from the fluid, flow is assumed to be single phase liquid below the quench front.

The "fluid" in the fluid energy equation is assumed to be single phase liquid below the quench front and superheated vapor in the two-phase mixture, above the quench front. The real flow above the quench front is a two-phase dispersed flow mixture. However, the vapor represents the continuous phase and is the heat sink for the heat transfer above the quench front. The interfacial heat transfer is also modeled such that the correct vapor temperature would be calculated. Modeling the superheated vapor above the quench front allows the interfacial heat transfer to be directly modeled.

The single phase liquid (below the quench front) and the superheated vapor (above the quench front) thermally connects the electrical heater rods (or fuel rods), the test section housing (no housing for a PWR, fuel can for a BWR), the spacer grids used to support the rod bundle and the dummy rods in the test bundle (control rod guide tube thimbles in a PWR and water rods in a BWR). With these assumptions, the fluid energy equation becomes:

$$\underset{(1)}{V_{1\phi}\frac{d}{dt_1}\left(\rho c_p \Delta T\right)_{1\phi}} + \underset{(2)}{V_{2\phi}\frac{d}{dt_1}\left(\rho_v e_v\right)} = \underset{(3)}{Q_{q,r}} + \underset{(4)}{Q_{q,H}} + \underset{(5)}{Q_{q,g}} + \underset{(6)}{Q_{q,DR}} + \underset{(7)}{Q_{DP}}$$

$$\underset{(8)}{-Q_{loss,H}} \underset{(9)}{-Q_{loss,g}} \underset{(10)}{-Q_{loss,DR}} \underset{(11)}{-Q_i} + \underset{(12)}{W_i h_i} \underset{(13)}{-W_o h_0} \qquad (6\text{-}1)$$

where

term 1	rate of energy change in the single phase region
term 2	rate of energy change of the vapor in the two-phase region
term 3	energy release to the fluid from the rod quenching
term 4	energy release to the fluid from the housing quenching
term 5	energy release to the fluid from the grids quenching
term 6	energy release to the fluid from the dummy rods (thimbles) quenching
term 7	energy release to the fluid from the rods above and below the quench front
term 8	energy loss to the housing
term 9	energy loss from the fluid to the spacer grids
term 10	energy loss from the fluid to the dummy rods or control rod thimbles
term 11	interfacial heat transfer between vapor and droplets
term 12	energy flow into the bundle at the inlet
term 13	energy flow out of the bundle at the exit

A listing of the nomenclature used for the equation development is given at the end of this section.

The quench front represents the dividing line between efficient cooling (nucleate boiling or forced convection) and poor cooling (film boiling, either in a froth region or dispersed flow film boiling). An alternate expression for term 6 for the energy transport into the fluid on either side of the quench front can be used. Below the quench front, the flow will be assumed to be single phase such that the energy into the fluid is equal to the decay power which is specified for the test. Above the quench front, the energy into the fluid is transported by film boiling heat transfer as well as by radiation heat transfer from the heated surfaces to the fluid. Therefore, a more general expression for the energy transfer above the quench front is given as

$$Q_{2\phi} = h_{2\phi,c} A_r \left(T_r - T_v\right) + h_{R,r/v} A_r \left(T_r - T_v\right) \tag{6-2}$$

Where $h_{2\varphi,c}$ is the convective/film boiling heat transfer coefficient, and $h_{R,r/v}$ is the radiation heat transfer coefficient from the heated rod surfaces to the fluid. The reference temperatures for both transfer processes are the rod wall temperatures (T_r) as well as the local fluid vapor (non-equilibrium) temperature (T_V). Therefore, term 7 becomes:

$$Q_{DP} = Q_{DP}\big|_{1\phi} + \left[h_{2\phi,c} A_r \left(T_r - T_v\right) + h_{R,r/v} A_r \left(T_r - T_v\right) + h_{R,r/d} A_d \left(T_r - T_{sat}\right)\right]_{2\phi} \tag{6-3}$$

The heat transfer in the two-phase region can also be written as energy flows (Btu/hr) instead of a heat transfer coefficient, area and temperature difference as

$$Q_{DP} = Q_{DP_{1\phi}} + Q_{C/FB} + Q_R \tag{6-4}$$

where $Q_{C/FB}$ represents the convective/film boiling portion of the heat transfer while Q_R represents the radiation portion of the total heat transfer from the rods to the fluid above the quench front.

The quench energy release from the heater rods (or the fuel rods), term 3 ($Q_{q,r}$), can be calculated as

$$Q_{q,r} = \rho_r c_{p,r} V_r \frac{dT_{r,q}}{dt_2} \tag{6-5}$$

where T_r is the property weighted average temperature for the heater rod (or the fuel rod) with ρ_r, $c_{p,r}$ and V_r being the rod weighted density, specific heat and volume, respectively. The temperature-time curve can be estimated from data for heater rod (Ref. 8) and/or nuclear rod quenching (Ref. 9), as well as from more accurate calculations for a heater and nuclear rods using finite difference methods. Rod quench is assumed to occur when the rod temperature reaches the minimum film boiling temperature. The effects of property differences between the electrical heater rod and the nuclear rod cladding will be considered when determining the minimum film boiling temperatures used to calculate the rod energy release for electrical heater rods and Zirconium clad fuel rods.

The test section housing heat release is given in term 4 as

$$Q_{q,H} = \rho_H c_{p,H} V_H \frac{dT_{H,q}}{dt_3} \tag{6-6}$$

and represents the heat transferred to the coolant when the housing, which is an elevated temperature, quenches. T_H represents the average housing temperature and ρ_H, $c_{p,H}$ and V_r represent the density, specific heat and volume of the housing which is quenching. The test section housing represents an atypicality or distortion of the test rod bundle relative to a PWR fuel assembly since there is no housing for the PWR assembly. However, when comparing the test facility to a BWR fuel assembly, the similarity is improved since these assemblies have a channel similar to a housing. The BWR channel is Zircaloy and not Inconel as used in the experiment; therefore, there can be differences in the minimum film boiling temperature and the resulting quench energy released to the coolant.

Term 5 represents the energy release to the coolant from the quenching of the spacer grids, which are used to position the heater rods or fuel rods, and is given as

$$Q_{q,g} = \rho_g c_{p,g} V_g \frac{dT_{g,q}}{dt_4} \tag{6-7}$$

The spacers are constructed from thin metal shim stock, typically 0.010 in thick and 1-2 in high. It is assumed that the grid will quench at once such that its entire stored energy is released to the coolant. There can be material differences between the test grids, which will be made of Inconel or stainless steel and the current generation PWR spacers which use Zircaloy. The difference in materials can lead to different minimum film boiling temperatures which in turn affect the energy release. For the experiment, the spacers, cladding surface, housing, and the dead rods are all made of Inconel, therefore, they all have the same value of T_{min}. For a PWR or BWR fuel assembly, the cladding and the spacer grids are made of Zircaloy and a T_{min} value for this material is used.

Term 6 represents the quenching of the unheated support or dummy rods in the bundle. There are four such rods used to represent the presence of guide tube thimbles in the test rod bundle and to allow bundle instrumentation to be brought out with minimum flow interference. The dummy rod quench energy is given as

$$Q_{q,DR} = \rho_{DR} c_{p,DR} V_{DR} \frac{dT_{DR,q}}{dt_5} \tag{6-8}$$

Term 7 represents the energy added to the fluid below and above the quench front, as given earlier in Equation 6-3.

Term 8 represents the heat loss from the fluid to the environment through the housing. This term will be most important above the quench front where the fluid, rod and housing temperatures are higher. The heat loss from the fluid to the housing is given as

$$Q_{loss,H} = h_{2\phi,H} A_H \left(T_v - T_H\right) + h_{R,v/H} A_H \left(T_v - T_H\right) - h_{R,H/d} A_d \left(T_H - T_{sat}\right) \tag{6-9}$$

where the first term is the convective/film boiling term, the second term represents the radiation from the superheated vapor to the housing structure, and the third term represents the radiation heat transfer from the hot housing to the entrained liquid drops. Both the convective and the radiation terms will operate on the same housing heat transfer area. The expressions for the heat transfer to the housing from the fluid can also be expressed in terms of heat flows (Btu/hr) as

$$Q_{loss,H} = Q_{2\phi,c,H} + Q_{R,H} \tag{6-10}$$

where $Q_{R,H}$ is the sum of the two radiation components.

In a similar fashion, term 9 models the fluid energy losses to the spacer grids and is given as

$$Q_{loss,g} = h_{2\phi,g} A_g \left(T_v - T_g\right) + h_{R,v/g} A_g \left(T_v - T_g\right) - h_{R,g/d} A_d \left(T_g - T_{sat}\right) \tag{6-11}$$

where the fluid will transfer heat by convection/film boiling and radiation heat transfer. This equation can also be written as heat flows as

$$Q_{loss,g} = Q_{2\phi,c,g} + Q_{R,g} \tag{6-12}$$

where $Q_{R,g}$ is the sum of the two radiation heat transfer terms.

It should be noted that Equation 6-11 is only relevant above the quench front where the vapor is significantly superheated relative to the spacer grids. The differences between the reactor and the test facility will be the geometry and materials used for the spacers. Once the spacers are quenched, there is no longer any significant heat transfer to or from the spacers and the fluid.

In a similar manner, term 10 models the fluid energy loss to the dummy rods or the control rod guide tubes for the reactor case and is given as

$$Q_{loss,DR} = h_{2\phi,DR} A_{DR} \left(T_v - T_{DR}\right) + h_{R,v/DR} A_{DR} \left(T_v - T_{DR}\right) - h_{R,v/DR} A_d \left(T_{DR} - T_{sat}\right) \tag{6-13}$$

The heat transfer from the fluid to these structures is by convection/film boiling and radiation. This only occurs above the quench front where the vapor is superheated and saturated entrained droplets exist. Once the dead rods or thimbles are quenched, there is no longer any energy transfer between these structures and the fluid.

Since the fluid energy equation is written for superheated vapor, and there are entrained droplets present, the two-phase flow above the quench front is not in thermal equilibrium. There is heat transfer between the superheated vapor and the entrained droplets, which are at the saturation temperature. The heat transfer occurs by two paths. The first is convection heat transfer in which the droplet Reynolds and Nusselt numbers depend upon the drop size and the relative velocities of the drops and vapor. The second is radiation heat transfer from vapor to droplets as they are swept along in the test section. Both terms contribute to the total interfacial heat transfer between the continuous vapor phase and the discontinuous entrained droplet

phase. The interfacial heat transfer will result in generation of additional saturated steam which mixes with the superheated steam and results in increased steam flow at a lower temperature. The droplet evaporation improves the steam as a heat sink for the heater or fuel rods.

The expression for the interfacial heat transfer becomes

$$Q_I = h_I A_d \left(T_v - T_{sat}\right) + h_{R,v/d} A_d \left(T_v - T_{sat}\right) \tag{6-14}$$

Substituting Equations 6-3 to 6-14 into Equation 6-1 gives the fluid energy equation which considers all sources of heat gain and heat loss for the fluid in the test section.

$$\begin{aligned}
Q_I &= h_I A_d \left(T_v - T_{sat}\right) + h_{R,v/d} A_d \left(T_v - T_{sat}\right) \\
&+ \rho_g c_{p,g} V_g \frac{dT_g}{dt_4} + \rho_{DR} c_{p,DR} V_{DR} \frac{dT_{DR}}{dt_5} + \\
&\left\{ Q_{DP}\big|_{1\phi} + \left[h_{2\phi,r} A_r \left(T_r - T_v\right) + h_{R,r/v} A_r \left(T_r - T_v\right) - h_{R,r/d} A_d \left(T_r - T_{sat}\right) \right] \right\} \\
&- \left[h_{2\phi,H} A_H \left(T_v - T_H\right) + h_{R,v/H} A_H \left(T_v - T_H\right) - h_{R,H/d} A_d \left(T_H - T_{sat}\right) \right] \\
&- \left[h_{2\phi,g} A_g \left(T_v - T_g\right) + h_{R,v/g} A_g \left(T_v - T_g\right) - h_{R,g/d} A_d \left(T_g - T_{sat}\right) \right] \\
&- \left[h_{2\phi,DR} A_{DR} \left(T_v - T_{DR}\right) + h_{R,v/DR} A_{DR} \left(T_v - T_{DR}\right) - h_{R,DR/d} A_d \left(T_{DR} - T_{sat}\right) \right] \\
&+ h_I A_d \left(T_v - T_{sat}\right) + h_{R,v/d} A_d \left(T_v - T_{sat}\right) + W_i h_i - W_o h_o
\end{aligned} \tag{6-15}$$

The same generalized equation can be used to represent the fluid energy in a PWR or BWR fuel assembly. The differences will be due to the geometry, materials and possible temperature limits. The boundary conditions of flow, pressure and power are the same and can be modeled in the experiments. There are also different components in the fluid energy equation as noted above. There is no housing for a PWR assembly; therefore, these terms represent a distortion of the fluid energy equation relative to a PWR assembly. There is more similarity between a BWR fuel assembly and the test facility since both have a channel surrounding the heater rods.

The next step in the Zuber-Wulff scaling process is to nondimensionalize the equation to determine the different Pi groups which represent the different transfer processes in either the test facility or in a PWR or BWR fuel assembly. A listing of the parameters used to normalize each term in Equation 6-15 is given in Table 6.1. The initial conditions and boundary conditions are used for the normalization. Ranges are selected such that they address the variability of the different parameters. The initial conditions and their definitions are given in Table 6-2.

Table 6.1 Normalizing Factors for Fluid Energy Equation

$$A_{DR}^* = \frac{A_{DR}}{A_{DR,i}}$$

$$A_g^* = \frac{A_g}{A_{g,i}}$$

$$A_H^* = \frac{A_H}{A_{H,i}}$$

$$A_r^* = \frac{A_r}{A_{r,i}}$$

$$c_p^* = \frac{c_p}{c_{p,i}}$$

$$W^* = \frac{W}{W_i}$$

$$W_o^* = \frac{W_o}{W_i}$$

$$W_i^* = \frac{W_i}{W_i}$$

$$\phi_{DP}^* = \frac{\phi_{DP}}{\phi_{DP,i}}$$

$$\rho^* = \frac{\rho}{\rho_i}$$

$$T_r^* - T_v^* = \frac{T_r - T_v}{T_{\max,r} - T_{sat}}$$

$$T_{DR,q}^* = \frac{T_{DR,q}}{T_{\min,DR} - T_{sat}}$$

$$T_{g,q}^* = \frac{T_{g,q}}{T_{\min,g} - T_{sat}}$$

$$T_{H,q}^* = \frac{T_{H,q}}{T_{\min,H} - T_{sat}}$$

$$T_{r,q}^* = \frac{T_{r,q}}{T_{\min,r} - T_{sat}}$$

$$h_I^* = \frac{h_I}{h_{I,i}}$$

$$h_{2\phi,DR}^* = \frac{h_{2\phi,DR}}{h_s}$$

$$h_{2\phi,g}^* = \frac{h_{2\phi,g}}{h_s}$$

$$h_{2\phi,H}^* = \frac{h_{2\phi,H}}{h_s}$$

$$h_{2\phi,r}^* = \frac{h_{2\phi,r}}{h_s}$$

$$h_{R,r/v}^* = \frac{h_{R,r/v}}{h_{R,r/v,i}}$$

$$h_{R,r/d}^* = \frac{h_{R,r/d}}{h_{R,r/d,i}}$$

$$h_{R,v/H}^* = \frac{h_{R,v/H}}{h_{R,v/H,i}}$$

$$h_{R,H/d}^* = \frac{h_{R,H/d}}{h_{R,H/d,i}}$$

$$h_{R,v/g}^* = \frac{h_{R,v/g}}{h_{R,v/g,i}}$$

$$h_{R,g/d}^* = \frac{h_{R,g/d}}{h_{R,g/d,i}}$$

$$h_{R,v/DR}^* = \frac{h_{R,v/DR}}{h_{R,v/DR,i}}$$

$$h_{R,DR/d}^* = \frac{h_{R,DR/d}}{h_{R,DR/d,i}}$$

$$h_{R,v/d}^* = \frac{h_{R,v/d}}{h_{R,v/d,i}}$$

Table 6.2 List of Initial Conditions and Assumptions

1. Normalization for fluid and rod properties was done on the inlet conditions for the fluid, and the initial conditions for the rod.
2. The flows were initialized on the inlet flow, W_i.
3. Time constants for structures were defined in the text of the report.
4. The temperature for a component is normalized by the expected maximum temperature variation for the component, such as

   $$T_r^* = \frac{T_r}{T_{r,CL} - T_{sat}}$$

   where $T_{r,CL}$ is the centerline temperature and T_{sat} is the saturation temperature.
5. The lengths were normalized on the full length of the bundle.
6. Pressure drop was normalized on the velocity head of the fluid.
7. The fluid momentum equation was normalized on the static head for the bundle.

The total volume is the sum of the single phase and two phase volumes. Thus,

$$V_{1\phi} + V_{2\phi} = V_T \tag{6-16}$$

The time scale for the temporal terms is assumed to be the same for single phase and two-phase flow. That is, the time constant is defined in terms of the inlet flow rate and the total fluid volume as

$$\tau_1 = \frac{\rho_i V_T}{W_i} \tag{6-17}$$

where τ_1 is used to normalize the time rate of change terms on the left hand side of Equation 6-15.

Separate time constants are used to model the quenching of the heater rods, spacer grids and the housing. During the quenching, the convection heat transfer coefficient is about 5.6782 kW/m^2-K (1000 Btu/hr-ft^2-F). The Biot number is of the order of unity for all the heat structures with the exception of the spacer grids which has a Biot number much lower than 1.0. Therefore, in general, the conductivity across the heat structures cannot be neglected. For each structure the heat removal is characterized by a time constant:

heater rods	τ_2
housing	τ_3
grids	τ_4
dummy rods	τ_5

The quench energy terms are normalized as follows:

$$Q_{q,r} = \rho_r c_{p,r} V_r \frac{dT_{r,q}}{dt_2} = \frac{\rho_{r,i} c_{p,r,i} V_{r,i} \left(T_{min,r} - T_{sat}\right)}{\tau_2} \rho_r^* c_{p,r}^* V_r^* \frac{dT_{r,q}^*}{dt_2^*} \tag{6-18}$$

$$Q_{q,H} = \rho_H c_{p,H} V_H \frac{dT_{H,q}}{dt_3} = \frac{\rho_{H,i} c_{p,H,i} V_{H,i} \left(T_{min,H} - T_{sat}\right)}{\tau_3} \rho_H^* c_{p,H}^* V_H^* \frac{dT_{H,q}^*}{dt_3^*} \tag{6-19}$$

$$Q_{q,g} = \rho_g c_{p,g} V_g \frac{dT_{g,q}}{dt_4} = \frac{\rho_{g,i} c_{p,g,i} V_{g,i} \left(T_{min,g} - T_{sat}\right)}{\tau_4} \rho_g^* c_{p,g}^* V_g^* \frac{dT_{g,q}^*}{dt_4^*} \tag{6-20}$$

$$Q_{q,DR} = \rho_{DR} c_{p,DR} V_{DR} \frac{dT_{DR,q}}{dt_5} = \frac{\rho_{DR,i} c_{p,DR,i} V_{DR,i} \left(T_{min} - T_{sat}\right)}{\tau_5} \rho_{DR}^* c_{DR}^* V_{DR}^* \frac{dT_{DR,q}^*}{dt_5^*} \tag{6-21}$$

Term 2, the temporal term representing the rate of change of energy storage within the control volume, becomes

$$V_{2\phi}\frac{d}{dt_1}(\rho_v e_v) = V_{2\phi}\frac{d}{dt_1}(\rho_v c_p \Delta T_v) \tag{6-22}$$

where

$$e_v = c_p \Delta T_v \tag{6-23}$$

and

$$\Delta T_v = T_v - T_{sat} \tag{6-24}$$

Operating on each term in Equation 6-15 using the normalizing parameters from Table 6.1 and the ranges from Table 6.2 gives

$$W_i c_{p,i}(T_f - T_i)V_{1\phi}^*\frac{d}{dt_1^*}(\rho^* c_p^* \Delta T^*)_{1\phi} + \frac{W_i \rho_{v,sat,i} c_{p,sat,i}(T_{\max,v} - T_{sat})}{\rho_i} V_2^* \frac{d}{dt_1^*}(\rho_v^* c_{p,v}^* \Delta T_v^*) =$$

$$\frac{\rho_{r,i} c_{p,r,i} V_{r,i}(T_{\min,r} - T_{sat})}{\tau_2}\rho_r^* c_{p,r}^* V_r^* \frac{dT_{r,q}^*}{dt_2^*} + \frac{\rho_{H,i} c_{p,H,i} V_{H,i}(T_{\min,H} - T_{sat})}{\tau_3}\rho_H^* c_{p,H}^* V_H^* \frac{dT_{H,q}^*}{dt_3^*}$$

$$+\frac{\rho_{g,i} c_{p,g,i} V_{g,i}(T_{\min,g} - T_{sat})}{\tau_4}\rho_g^* c_{p,g}^* V_g^* \frac{dT_{g,q}^*}{dt_4^*} +$$

$$\frac{\rho_{DR,i} c_{p,DR,i} V_{DR,i}(T_{\min} - T_{sat})}{\tau_5}\rho_{DR}^* c_{p,DR}^* V_{DR}^* \frac{dT_{DR,q}^*}{dt_5^*}$$

$$+\left\{Q_{DP,i}Q_{DP}^* + \left[h_s A_{r,i}\left(T_{\max,r} - T_{sat}\right)h_{2\phi,r}^* A_r^*\left(T_r^* - T_v^*\right) + \right.\right. \tag{6-25}$$

$$\left.\left. h_{R,r/v,i} A_{r,i}\left(T_{\max,r} - T_{sat}\right)h_{R,r/v}^* A_r^*\left(T_r^* - T_v^*\right) - h_{R,r/d,i} A_{d,i}\left(T_{\max,r} - T_{sat}\right)h_{R,r/d}^* A_d^*\left(T_r^* - T_{sat}^*\right)\right]\right\} -$$

$$\left\{\left[h_s A_{H,i}\left(T_{\max,H} - T_{sat}\right)h_{2\phi,H}^* A_H^*\left(T_v^* - T_H^*\right)\right] + \left[h_{R,v/H,i} A_{H,i}\left(T_{\max,H} - T_{sat}\right)h_{R,v/H}^* A_H^*\left(T_V^* - T_H^*\right)\right] -\right.$$

$$\left.\left[h_{R,H/d,i} A_{d,i}\left(T_{\max,H} - T_{sat,H}\right)h_{R,H/d}^* A_d^*\left(T_H^* - T_{sat}^*\right)\right]\right\} - \left\{\left[h_s A_{g,i}\left(T_{\max,g} - T_{sat}\right)h_{2\phi,g}^* A_g^*\left(T_v^* - T_g^*\right)\right]\right.$$

$$+\left[h_{R,v/g}\,A_{g,i}\left(T_{\max,g}-T_{sat}\right)h^{*}_{R,v/g}\,A^{*}_{g}\left(T^{*}_{v}-T^{*}_{g}\right)\right]-\left[h_{R,g/d,i}\,A_{d,i}\left(T_{\max,g}-T_{sat}\right)h^{*}_{R,g/d}\,A^{*}_{d}\left(T^{*}_{g}-T^{*}_{sat}\right)\right]\Bigg\}$$

$$-\Bigg\{\left[h_{s}\,A_{DR,i}\left(T_{\max,DR}-T_{sat}\right)h^{*}_{2\phi,DR}\,A^{*}_{DR}\left(T^{*}_{V}-T^{*}_{DR}\right)\right]+\left[h_{R,v/DR,i}\,A_{DR,i}\left(T_{\max,DR}-T_{sat}\right)h^{*}_{R,v/DR}\,A^{*}_{DR}\left(T^{*}_{v}-T^{*}_{DR}\right)\right]-$$

$$\left[h_{R,DR/d,i}\,A_{d,i}\left(T_{\max,DR}-T_{sat}\right)h^{*}_{R,DR/d}\,A^{*}_{d}\left(T^{*}_{DR}-T^{*}_{sat}\right)\right]\Bigg\}+\left[h_{I,i}\,A_{d,i}\left(T_{\max,v}-T_{sat}\right)h^{*}_{I}\,A^{*}_{d}\left(T^{*}_{v}-T^{*}_{sat}\right)\right]$$

$$+\left[h_{R,v/d,i}\,A_{d,i}\left(T_{\max,v}-T_{sat}\right)h^{*}_{R,v/d}\,A^{*}_{d}\left(T^{*}_{v}-T^{*}_{sat}\right)\right]+W_{i}\left(h_{f}-h_{i}\right)W^{*}_{i}\,h^{*}_{i}-W_{i}\left(h_{s}-h_{g}\right)W^{*}_{o}\,h^{*}_{o}$$

If we now divide all terms in Equation 6-25 by the "driver term" as first proposed by Wulff, one can obtain the normalized Pi time constants which represent the heat transfer processes in the rod bundle during reflood. The driver term selected is the initial decay power, Q_{DPi}, which is a test boundary condition. Therefore, each heat transfer process will be evaluated relative the initial bundle decay power. The resulting normalized Pi groups become:

$$\Pi_{1}=\frac{W_{i}c_{p,i}\left(T_{sat}-T_{i}\right)}{Q_{DP_{i}}}=\frac{1\phi\ \text{fluid sensible energy / time}}{\text{Initial decay power}} \tag{6-26}$$

$$\Pi_{2}=\frac{W_{i}\rho_{v,sat,i}c_{p,v,sat,i}\left(T_{max}-T_{sat}\right)}{\rho_{i}Q_{DP_{i}}}=\frac{\text{Vapor sensible energy / time}}{\text{Initial decay power}} \tag{6-27}$$

$$\Pi_{3}=\frac{\rho_{r,i}c_{p,r,i}V_{r,q,i}\left(T_{max,r,q}-T_{sat}\right)}{\tau_{2}\ Q_{DP_{i}}}=\frac{\text{Rod quench energy / time}}{\text{Initial decay power}} \tag{6-28}$$

$$\Pi_{4}=\frac{\rho_{H,i}c_{p,H,i}V_{H,q,i}\left(T_{min,H,q}-T_{sat}\right)}{\tau_{3}\ Q_{DP_{i}}}=\frac{\text{Housing quench energy / time}}{\text{Initial decay power}} \tag{6-29}$$

$$\Pi_{5}=\frac{\rho_{g,i}c_{p,g,i}V_{g,q,i}\left(T_{\min,g,q}-T_{sat}\right)}{\tau_{4}\ Q_{DP_{i}}}=\frac{\text{Grid quench energy / time}}{\text{Initial decay power}} \tag{6-30}$$

$$\Pi_{6}=\frac{\rho_{DR,i}c_{p,DR,i}V_{DR,q,i}\left(T_{\min,DR,q}-T_{sat}\right)}{\tau_{5}\ Q_{DP_{i}}}=\frac{\text{Dead rod quench energy / time}}{\text{Initial decay power}} \tag{6-31}$$

$$\Pi_7 = \frac{Q_{DP}\big|_{1\phi}}{Q_{DP_i}} \tag{6-32}$$

$$\Pi_8 = \frac{h_s A_{r,i}\left(T_{\max,r} - T_{sat}\right)}{Q_{DP_i}} = \frac{\text{Convective heat rate from rods to mixture vapor}}{\text{Initial decay power}} \tag{6-33}$$

$$\Pi_9 = \frac{h_{R,r/v,i} A_{r,i}\left(T_{\max,r} - T_v\right)}{Q_{DP_i}} = \frac{\text{Radiation heat rate from rods to vapor}}{\text{Initial decay power}} \tag{6-34}$$

$$\Pi_{10} = \frac{h_{R,r/d,i} A_{d,i}\left(T_{\max,r} - T_{sat}\right)}{Q_{DP_i}} = \frac{\text{Radiation heat rate from rod to drops}}{\text{Initial decay power}} \tag{6-35}$$

$$\Pi_{11} = \frac{h_s A_{H,i}\left(T_{\max,H} - T_{sat}\right)}{Q_{DP_i}} = \frac{\text{Convective heat rate from mixture to housing}}{\text{Initial decay power}} \tag{6-36}$$

$$\Pi_{12} = \frac{h_{R,v/H,i} A_{H,i}\left(T_{\max,H} - T_v\right)}{Q_{DP_i}} = \frac{\text{Radiative heat rate from vapor to housing}}{\text{Initial decay power}} \tag{6-37}$$

$$\Pi_{13} = \frac{h_{R,H/d,i} A_{d,i}\left(T_{max,H} - T_{sat}\right)}{Q_{DP_i}} = \frac{\text{Radiation heat rate from housing to drops}}{\text{Initial decay power}} \tag{6-38}$$

$$\Pi_{14} = \frac{h_s A_{g,i}\left(T_{max,g} - T_{sat}\right)}{Q_{DP_i}} = \frac{\text{Convective heat rate from vapor to grids}}{\text{Initial decay power}} \tag{6-39}$$

$$\Pi_{15} = \frac{h_{R,v/g,i} A_{g,i}\left(T_{max,g} - T_v\right)}{Q_{DP_i}} = \frac{\text{Radiation heat rate from vapor to grids}}{\text{Initial decay power}} \tag{6-40}$$

$$\Pi_{16} = \frac{h_{R,g/d,i} A_{d,i}\left(T_{max,g} - T_{sat}\right)}{Q_{DP_i}} = \frac{\text{Radiation heat rate from grids to drops}}{\text{Initial decay power}} \tag{6-41}$$

$$\Pi_{17} = \frac{h_s A_{DR,i}\left(T_{max,DR} - T_{sat}\right)}{Q_{DP_i}} = \frac{\text{Convective heat rate from vapor to dead rods}}{\text{Initial decay power}} \tag{6-42}$$

$$\Pi_{18} = \frac{h_{R,v/DR,i} A_{DR,i} \left(T_{max,DR} - T_v \right)}{Q_{DP_i}} = \frac{\text{Radiation heat rate from vapor to dead rods}}{\text{Initial decay power}} \tag{6-43}$$

$$\Pi_{19} = \frac{h_{R,DR/d,i} A_{d,i} \left(T_{max,DR} - T_{sat} \right)}{Q_{DP_i}} = \frac{\text{Radiation heat rate from dead rods to drops}}{\text{Initial decay power}} \tag{6-44}$$

$$\Pi_{20} = \frac{h_{I,i} A_d \left(T_{max,v} - T_{sat} \right)}{Q_{DP_i}} = \frac{\text{Interfacial heat transfer rate}}{\text{Initial decay power}} \tag{6-45}$$

$$\Pi_{21} = \frac{h_{R,v/d,i} A_{d,i} \left(T_{max,v} - T_{sat} \right)}{Q_{DP_i}} = \frac{\text{Radiation heat transfer from vapor to drops}}{\text{Initial decay power}} \tag{6-46}$$

$$\Pi_{22} = \frac{W_i \left(h_f - h_i \right)}{Q_{DP_i}} = \frac{W_i c_{p,i} \left(T_f - T_i \right)}{Q_{DP_i}} = \Pi_1 \tag{6-47}$$

$$\Pi_{23} = \frac{W_i \left(h_s - h_g \right)}{Q_{DP_i}} = \frac{\text{Exit mixture energy / time}}{\text{Initial decay power}} \tag{6-48}$$

Therefore, Equation 6-25 becomes

$$\begin{aligned}
&\Pi_1 V_{1\phi}^* \frac{d}{dt_1^*} \left(\rho^* c_p^* \Delta T^* \right)_{1\phi} + \Pi_2 V_{2\phi}^* \frac{d}{dt_1^*} \left(\rho_v^* c_{\rho v}^* \Delta T_v^* \right) = \Pi_3 \frac{dT_{r,q}^*}{dt_2^*} \\
&+ \Pi_4 \frac{dT_{H,q}^*}{dt_3^*} + \Pi_5 \frac{dT_{g,q}^*}{dt_4^*} + \Pi_6 \frac{dT_{DR,q}^*}{dt_5^*} + 1 + \Pi_8 h_{2\phi,r}^* A_r^* \left(T_r^* - T_v^* \right) \\
&+ \Pi_9 h_{R,r/v}^* A_r^* \left(T_r^* - T_v^* \right) - \Pi_{10} h_{R,r/d}^* A_d^* \left(T_r^* - T_{sat}^* \right) - \Pi_{11} h_{2\phi,H}^* A_H^* \left(T_v^* - T_H^* \right) \\
&- \Pi_{12} h_{R,v/H}^* A_H^* \left(T_v^* - T_H^* \right) + \Pi_{13} h_{R,H/d}^* A_d^* \left(T_H^* - T_{sat}^* \right) - \Pi_{14} h_{2\phi,g}^* A_g^* \left(T_v^* - T_g^* \right) \\
&- \Pi_{15} h_{R,v/g}^* A_g^* \left(T_v^* - T_g^* \right) + \Pi_{16} h_{R,g/d}^* A_d^* \left(T_g^* - T_{sat}^* \right) - \Pi_{17} h_{2\phi,DR}^* A_{DR}^* \left(T_v^* - T_{DR}^* \right)
\end{aligned} \tag{6-49}$$

$$-\Pi_{18} h^*_{R,v/DR} A^*_{DR}\left(T^*_v - T^*_{DR}\right) + \Pi_{19} h^*_{R,DR/d} A^*_d \left(T^*_{DR} - T^*_{sat}\right) + \Pi_{20} h^*_I A^*_d \left(T^*_v - T^*_{sat}\right)$$

$$+\Pi_{21} h^*_{R,v/d} A^*_d \left(T^*_v - T^*_{sat}\right) + \Pi_1 W^*_i h^*_i - \Pi_{23} W^*_o h^*_o$$

These Pi groups can be numerically calculated using the assumptions given in Table 6.2 for the heat transfer coefficients, heat flows and material properties. The results of the different Pi group calculations will be given in Section 6.4 of this report.

Tables 6.3 and 6.4 summarize and compare the expected values of the fluid energy equation Pi groups of the RBHT Test Facility with those of a PWR and BWR respectively. Since the rod bundle geometry models a PWR assembly, it is expected that most of the Pi groups are preserved. However, since there is no housing in a PWR assembly, to ensure similarity the Pi groups which represent the heat transfer processes associated with the housing should be small. Since the test facility has a housing similar to a BWR channel, the same Pi groups derived for the RBHT Test Facility are present for a BWR fuel assembly. Their magnitudes are expected to be slightly different because of differences in material properties.

Table 6.3 PWR Comparisons

$\Pi_{1_t} \cong \Pi_{1_{PWR}}$	Should be similar since geometry is approximately correct and flows, powers are typical.
$\Pi_{2_t} \cong \Pi_{2_{PWR}}$	Similar to Π_1 above, geometry is exact but power and flows are typical.
$\Pi_{3_t} \cong \Pi_{3_{PWR}}$	Not clear due to rod size and properties - need to check.
$\Pi_{4_t} \neq \Pi_{4_{PWR}}$	Distortion, as there is no housing in PWR.
$\Pi_{5_t} \approx \Pi_{5_{PWR}}$	Not clear how similar due to different materials and thicknesses (grids).
$\Pi_{6_t} \approx \Pi_{6_{PWR}}$	Not clear how similar due to different materials and thicknesses (dead or water rods).
$\Pi_{7_t} = \Pi_{7_{PWR}}$	Controllable boundary conditions.
$\Pi_{8_t} \overset{?}{=} \Pi_{8_{PWR}}$	Should be similar but geometry differences exist.
$\Pi_{9_t} \overset{?}{=} \Pi_{9_{PWR}}$	Should be similar but geometry differences exist.
$\Pi_{10_t} \overset{?}{=} \Pi_{10_{PWR}}$	Should be similar but geometry differences exist.
$\Pi_{11_t} \neq \Pi_{11_{PWR}}$	Distortion, as there is no housing in PWR.
$\Pi_{12_t} \neq \Pi_{12_{PWR}}$	Distortion, as there is no housing in PWR.

Table 6.3 PWR Comparisons (Continued)

$\Pi_{13_t} \neq \Pi_{13_{PWR}}$	Distortion, as there is no housing in PWR.
$\Pi_{14_t} \overset{?}{\approx} \Pi_{14_{PWR}}$	Some differences due to grid designs, materials.
$\Pi_{15_t} \overset{?}{\approx} \Pi_{15_{PWR}}$	Some differences due to grid designs, materials.
$\Pi_{16_t} \overset{?}{\approx} \Pi_{16_{PWR}}$	Some differences due to grid designs, materials.
$\Pi_{17_t} \overset{?}{\approx} \Pi_{17_{PWR}}$	Different materials, geometries, number - need to check.
$\Pi_{18_t} \overset{?}{\cong} \Pi_{18_{PWR}}$	Different materials, geometries, number - need to check.
$\Pi_{19_t} \overset{?}{\cong} \Pi_{19_{PWR}}$	Different materials, geometries, number - need to check.
$\Pi_{20_t} \approx \Pi_{20_{PWR}}$	Should be similar, as it is related to drops only and not materials, dimensions etc.
$\Pi_{21_t} \approx \Pi_{21_{PWR}}$	Should be similar, as it is related to drops only and not materials, dimensions etc.
$\Pi_{23_t} \approx \Pi_{23_{PWR}}$	Should be similar, but not exact due to geometry differences.
Note: Some of the Pi groups can be made closer by adjusting the fluid conditions. Other Pi groups reflect the materials and geometry differences between the PWR and BWR assemblies so the simulation will only be approximate.	

Table 6.4 BWR Comparisons

$\Pi_{1_t} \cong \Pi_{1_{BWR}}$	Should be similar since geometry is approximately correct (not sized for BWR) and flows, powers are typical.
$\Pi_{2_t} \cong \Pi_{2_{BWR}}$	Similar to Π_1 above, geometry is exact but power and flows are typical.
$\Pi_{3_t} \cong \Pi_{3_{BWR}}$	Not clear due to rod size and properties - need to check.
$\Pi_{4_t} \cong \Pi_{4_{BWR}}$	Not clear how similar due to different materials and thicknesses (housing).
$\Pi_{5_t} \approx \Pi_{5_{BWR}}$	Not clear how similar due to different materials and thicknesses (grids).
$\Pi_{6_t} \approx \Pi_{6_{BWR}}$	Not clear how similar due to different materials and thicknesses (dead or water rods).
$\Pi_{7_t} = \Pi_{7_{BWR}}$	Controllable boundary conditions.

Table 6.4 BWR Comparisons (Continued)

$\Pi_{8_t} \overset{?}{=} \Pi_{8_{BWR}}$	Should be similar but geometry differences exist.
$\Pi_{9_t} \overset{?}{=} \Pi_{9_{BWR}}$	Should be similar but geometry differences exist.
$\Pi_{10_t} \overset{?}{\approx} \Pi_{10_{BWR}}$	Should be similar but geometry differences exist.
$\Pi_{11_t} \overset{?}{\approx} \Pi_{11_{BWR}}$	Should be similar but housing thickness, material are different.
$\Pi_{12_t} \overset{?}{\approx} \Pi_{12_{BWR}}$	Should be similar but housing thickness, material are different.
$\Pi_{13_t} \approx \Pi_{13_{BWR}}$	Should be similar but housing thickness, material are different.
$\Pi_{14_t} \overset{?}{\approx} \Pi_{14_{BWR}}$	Some differences due to grid designs, materials.
$\Pi_{15_t} \approx \Pi_{15_{BWR}}$	Some differences due to grid designs, materials.
$\Pi_{16_t} \overset{?}{\cong} \Pi_{16_{BWR}}$	Some differences due to grid designs, materials.
$\Pi_{17_t} \overset{?}{\approx} \Pi_{17_{BWR}}$	Different materials, geometries, number - need to check.
$\Pi_{18_t} \overset{?}{\cong} \Pi_{18_{BWR}}$	Different materials, geometries, number - need to check.
$\Pi_{19_t} \overset{?}{\cong} \Pi_{19_{BWR}}$	Different materials, geometries, number - need to check.
$\Pi_{20_t} \approx \Pi_{20_{BWR}}$	Should be similar, as it is related to drops only and not materials, dimensions, etc.
$\Pi_{21_t} \approx \Pi_{21_{BWR}}$	Should be similar, as it is related to drops only and not materials, dimensions, etc.
$\Pi_{23_t} \approx \Pi_{23_{BWR}}$	Should be similar, but not exact due to geometry differences.
Note: Some of the Pi groups can be made closer by adjusting the fluid conditions. Other Pi groups reflect the materials and geometry differences between the PWR and BWR assemblies so the simulation will only be approximate.	

6.3.2 Heater Rod (Fuel Rod) Energy Equation Scaling

Equation 6-1 accounts for the energy release from the rods and other structures to the fluid and indicates some of the test distortions relative to a nuclear fuel assembly. The following analysis examines the behavior of the heater rod and a nuclear rod to determine the similarities and differences in their response to a reflood transient at or near the time that the peak cladding temperature would be calculated. In this situation, the quench front is approximately 2 or 3 ft below the peak temperature location such that there would be no axial conduction effects and one-dimensional radial heat transfer is sufficient. The analysis also considers the effects of the housing on the rod thermal response.

Two heat transfer equations are developed for the rods; an equation which describes the transient fuel, or boron nitride (BN) and heating coil power generating region; and an equation for the cladding which reflects the rod interactions with the flow field, housing and other surfaces. The assumptions for the equation development include:

- Analysis at one axial position in the bundle,
- No axial conduction, that is, far from the quench front
- Selected location on the rod is in dispersed flow film boiling, and the temperatures of the rod exceed T_{min},
- A gap heat transfer coefficient couples the fuel pellet or boron nitride and heating coil, to the cladding, and
- Heat generation is either in the fuel pellet region or in the boron nitride and heater coil region (BN).

The radial conduction equation can be written for the fuel or BN region as

$$\rho_f c_{p,f} V_f \frac{\partial T_f}{\partial t} - \frac{1}{r}\frac{\partial}{\partial r}\left(k_f r \frac{\partial T_f}{\partial r}\right) V_f = Q_f''' V_f - h_{gap} A_i (T_s - T_{ci}) \tag{6-50}$$

where Q_f''' is the volumetric heat generation for the fuel or BN region.

A similar radial conduction equation can be written for the cladding as

$$\rho_c c_{p,c} V_c \frac{\partial T_c}{\partial t} - \frac{1}{r}\frac{\partial}{\partial r}\left(k_c r \frac{\partial T_c}{\partial r}\right) V_c = h_{gap} A_i \left(T_s - T_{ci}\right) - h_c A_c \left(T_{co} - T_v\right)$$

(from pellet) (convective)

$$- h_{R,r_s} A_{R,s} \left(T_{co} - T_s\right) - h_{R,r_H} A_{R,H} \left(T_{co} - T_H\right) - h_{R,hr_{cr}} A_{R,hr_{cr}} \left(T_{co,hr} - T_{co,cr}\right) \tag{6-51}$$

(surface radiation) (housing radiation) (hot rod to cold rod radiation)

$$- h_{lw} A_{lw} \left(T_{co} - T_{sat}\right) - h_{R,r_d} A_{R,d} \left(T_{co} - T_{sat}\right) - h_{R,r_v} A_{R,v} \left(T_{co} - T_v\right)$$

(liquid contact HT) (radiation to drops) (radiation to vapor)

where the heat losses to the fluid, direct contact heat transfer, and the radiation heat transfer to the different components in the flow and bundle are indicated. This formulation allows rod-to-housing and rod to cold rod radiation heat transfer to occur. The heat transfer from the pellet or BN and heating coil to the cladding is given as

$$q = h_{gap} A_i \left(T_s - T_{ci} \right) \tag{6-52}$$

Since the region of interest for the rod is assumed to be in dispersed flow film boiling, the local void fraction is greater than 90 percent such that there is allowable radiation heat transfer between the different components in the bundle. In this situation, the region of interest is also far from the quench front.

The parameters for the normalization of Equations 6-50 and 6-51 are given in Table 6.5 and are similar to those used for the normalization of Equation 6-1. The individual temperature difference for the component temperature drop is shown in Table 6.5. In this fashion, the relative temperature differences are preserved. The time constant τ_f is the fuel pellet and or BN region time constant.

Table 6.5 Normalization Parameters for Rod Energy Equation

$$A_i^* = \frac{A_i}{A_{i,i}}, \qquad c_{p,c}^* = \frac{c_{p,c}}{c_{p,c,i}}, \qquad c_{p,f}^* = \frac{c_{p,f}}{c_{p,f,i}}$$

$$h_c^* = \frac{h_c}{h_{c,i}}, \qquad h_{gap}^* = \frac{h_{gap}}{h_{gap,i}}, \qquad h_{R,hr/cr}^* = \frac{h_{R,hr/cr}}{h_{R,hr/cr,i}}$$

$$k_f^* = \frac{k_f}{k_{f,i}}, \quad k_c^* = \frac{k_c}{k_{c,i}}, \quad Q_f^{'''*} = \frac{Q_f^{'''}}{Q_{f,i}^{'''}}, \quad r^* = \frac{r}{R_{f,i}}$$

$$t^* = \frac{t}{\tau_c}, \text{ (For clad)} \qquad t^* = \frac{t}{\tau_f} \quad \text{(For fuel)}$$

$$T_c^* = \frac{T_c}{\left(T_{ci} - T_{co} \right)}, \qquad T_f^* = \frac{T_f}{\left(T_{f,CL} - T_s \right)}$$

$$V_c^* = \frac{V_c}{V_{c,i}}, \qquad V_f^* = \frac{V_f}{V_{f,i}}$$

$$\rho_c^* = \frac{\rho_c}{\rho_{c,i}}, \qquad \rho_f^* = \frac{\rho_f}{\rho_{f,i}}$$

Using the definitions from Table 6.5 and substituting into Equation 6-50 gives

$$\frac{\rho_{f,i} c_{p,f,i} V_{f,i} \left(T_{f,CL} - T_s\right)}{\tau_f} \rho_f^* c_{p,f}^* V_f^* \frac{\partial T_f^*}{\partial t^*} - \frac{R_o k_{f,i}}{R_f^2} \frac{\left(T_{f,CL} - T_s\right)}{R_o} V_{c,i} \frac{1}{r^*} \frac{\partial}{\partial r^*} \left(k_f^* r^* \frac{\partial T_f^*}{\partial r^*} \right) V_f^* =$$

$$Q_{f,i}''' V_{f,i} Q_f'''^* V_f^* - h_{gap,i} A_{i,i} \left(T_s - T_{ci}\right) h_{gap}^* A_i^* \left(T_s - T_{ci}\right)^* \tag{6-53}$$

Equation 6-50 can be normalized by dividing each term in the equation by the "driver" term as recommended by Wulff. For this situation, the driver term is the initial power which is given as $V_{f,i} Q_{f,i}^*$. Performing the division results in the different Pi groups for the pellet or BN region of the fuel or heater rod. The Pi groups are:

$$\Pi_{24} = \frac{\rho_{f,i} c_{p,f,i} \left(T_{f,CL} - T_s\right)}{\tau_f Q_{f,i}'''} = \frac{\text{Stored energy / time}}{\text{Initial heat generation rate}} \tag{6-54}$$

$$\Pi_{25} = \frac{k_{f,i} \left(T_{f,CL} - T_s\right)}{R_{f,i}^2 Q_{f,i}'''} = \frac{\text{Clad heat conduction rate}}{\text{Initial heat generation rate}} \tag{6-55}$$

$$\Pi_{26} = \frac{V_{f,i} Q_{f,i}'''}{V_{f,i} Q_{f,i}'''} = 1 \tag{6-56}$$

Π_{26} is identically unity since this was the driver term which was used to normalize the other Pi values. The normalization of the h_{gap} term yields a Pi group which is identical to Π_{29}.

$$\Pi_{29} = \frac{h_{gap,i} A_{i,i} \left(T_s - T_{ci}\right)}{V_{f,i} Q_{f,i}'''} = \frac{\text{Heat transfer rate from pellet to clad}}{\text{Heat generation rate}} \tag{6-57}$$

The parameters used to normalize the clad conduction equation are also given in Table 6.5, where τ_c is the cladding time constant. Normalizing Equation 6-51 gives

$$\frac{\rho_{c,i} c_{p,c,i} V_{c,i} \left(T_{ci} - T_{co}\right)}{\tau_c} \rho_c^* c_{p,c}^* \frac{\partial T_c^*}{\partial t^*} -$$

$$\frac{1}{R_i^2} k_{c,i} \left(T_{ci} - T_{co}\right) V_{c,i} \frac{1}{r^*} \frac{\partial}{\partial r^*} \left(k_f^* r^* \frac{\partial T_c^*}{\partial r^*} \right) V_c^* =$$

$$h_{gap,i}A_{i,i}\left(T_s-T_{ci}\right)h^*_{gap}A^*_i\left(T_s-T_{ci}\right)^*-h_{c,i}A_{c,i}\left(T_{co}-T_{sat}\right)h^*_cA^*_c\left(T_{co}-T_v\right)^*$$

$$-h_{R,r/s,i}A_{R,s,i}\left(T_{co}-T_s\right)h^*_{R,r/s}A^*_{R,s}\left(T_{co}-T_s\right)^*-h_{R,r/H,i}A_{R,H,i}\left(T_{co}-T_H\right)h^*_{R,r/H}A^*_{R,H}\left(T_{co}-T_H\right)^*$$

$$-h_{R,hr/cr,i}A_{R,hr/cr,i}\left(T_{co,hr}-T_{co,cr}\right)h^*_{R,hr/cr}A^*_{R,hr/cr}\left(T_{co,hr}-T_{co,cr}\right)^* \tag{6-58}$$

$$-h_{\ell w,i}A_{\ell w,i}\left(T_{co}-T_{sat}\right)h^*_{\ell w}A^*_{\ell w}\left(T_{co}-T_{sat}\right)^*$$

$$-h_{R,r/d,i}A_{R,r/d,i}\left(T_{f,CL}-T_{sat}\right)h^*_{R,r/d}A^*_{R,r/d}\left(T_{co}-T_{sat}\right)^*$$

$$-h_{R,r/v,i}A_{R,r/v,i}\left(T_{f,CL}-T_{sat}\right)h^*_{R,r/v}A^*_{R,r/v}\left(T_{co}-T_v\right)^*$$

Equation 6-58 for the cladding can also be further normalized by dividing the coefficients by the driving term which is the rod initial heat generation rate. After this operation, the different Pi groups become:

$$\Pi_{27}=\frac{\rho_{c,i}c_{p,c,i}V_{c,i}\left(T_{ci}-T_{co}\right)}{\tau_cQ'''_{f,i}V_{f,i}}=\frac{\text{Clad stored energy / time}}{\text{Heat generation rate}} \tag{6-59}$$

$$\Pi_{28}=\frac{1}{R_o^2}\frac{k_{c,i}\left(T_{ci}-T_{co}\right)V_{c,i}}{Q'''_{f,i}V_{f,i}}=\frac{\text{Clad conduction heat rate}}{\text{Heat generation rate}} \tag{6-60}$$

$$\Pi_{29}=\frac{h_{gap,i}A_{i,i}\left(T_s-T_{ci}\right)}{V_{f,i}Q'''_{f,i}}=\frac{\text{Heat transfer rate from pellet to clad}}{\text{Heat generation rate}} \tag{6-61}$$

$$\Pi_{30}=\frac{h_{c,i}A_{c,i}\left(T_{co}-T_{sat}\right)}{V_{f,i}Q^*_{f,i}}=\frac{\text{Convective HT rate}}{\text{Heat generation rate}} \tag{6-62}$$

$$\Pi_{31}=\frac{h_{R,r/s,i}A_{R,r/s,i}\left(T_{co}-T_s\right)}{V_{f,i}Q'''_{f,i}}=\frac{\text{Radiation HT rate to surfaces in bundle}}{\text{Heat generation rate}} \tag{6-63}$$

$$\Pi_{32}=\frac{h_{R,r/H,i}A_{R,r/H,i}\left(T_{co}-T_H\right)}{V_{f,i}Q'''_{f,i}}=\frac{\text{Radiation HT rate to housing}}{\text{Heat generation rate}} \tag{6-64}$$

$$\Pi_{33} = \frac{h_{R,hr/cr,i}\ A_{R,hr/cr,i}(T_{co,hr} - T_{co,cr})}{V_{f,i} Q'''_{f,i}} = \frac{\text{Radiation HT rate from hot rods to cold rods}}{\text{Heat generation rate}} \quad (6\text{-}65)$$

$$\Pi_{34} = \frac{h_{\ell w,i} A_{\ell w,i} (T_{co} - T_{sat})}{V_{f,i} Q'''_{f,i}} = \frac{\text{Liquid contact HT rate}}{\text{Heat generation rate}} \quad (6\text{-}66)$$

$$\Pi_{35} = \frac{h_{R,r/d,i} A_{R,r/d,i} (T_{co} - T_{sat})}{V_{f,i} Q'''_{f,i}} = \frac{\text{Radiation HT rate to entrained drops}}{\text{Heat generation rate}} \quad (6\text{-}67)$$

$$\Pi_{36} = \frac{h_{R,r/v,i} A_{R,r/v,i} (T_{co} - T_{v})}{V_{f,i} Q'''_{f,i}} = \frac{\text{Radiation HT rate to vapor}}{\text{Heat generation rate}} \quad (6\text{-}68)$$

One can replace the radiation heat transfer representation by a more complex model which will include the material dependent emissivity. The radiation heat transfer equations can also be replaced with a calculation of the heat flow by this path within the bundle. This will be presented in Section 7.

The Pi groups presented in Equations 6-54 to 6-57 and 6-59 to 6-68 are valid for either a nuclear rod or a heater rod in a test bundle, though differences exist due to the difference in materials between the fuel rods and the electrical heater rods. Also, there is an additional term, Π_{32}, which represents the radiation from the hot rods to the test facility housing. There is no housing in a PWR fuel assembly. This is a distortion in the test facility relative to an infinitely sized PWR fuel assembly and will be addressed in Section 7 of this report. The housing effect must also be addressed in the analysis of the test data. Also, computer simulations of the test will require a structure model for the housing since the wall will communicate directly with the fluid and both directly and indirectly by radiation heat transfer with the heater rods in the interior of the bundle.

6.3.3 Momentum Equation Scaling for the RBHT Test Facility

The generalized one-dimensional integral form of the momentum equation is given by Shames (Ref. 11) and Wulff (Ref. 4) and is written for the entire test bundle as:

$$P_i - P_e = \frac{1}{g_c}\int_i^e \frac{dW}{dt}\frac{dz}{A} + \frac{1}{g_c}\left[\frac{1}{A^2}\left(\frac{W_e^2}{\rho_e} - \frac{W_i^2}{\rho_i}\right)\right] - \frac{g}{g_c}\int_i^e \rho dz \quad (6\text{-}69)$$

$$+ \frac{f}{2D_e \rho A^2 g_c}\int_i^e W|W|dz + \frac{K_T W^2}{2\rho A^2 g_c}$$

where the terms on the right hand side represent the

- inertia effects of the fluid in the volume,
- momentum flux of the fluid into and out of the volume,

- gravitational forces,
- frictional effects, and
- form losses within the volume.

The nomenclature is given at the end of this section for these equations. The momentum equation can be written for the complete bundle from the inlet to the exit. The flow in the bundle is single phase for some length and two-phase over the remaining length. The inlet is assumed to be single phase while the exit has a dispersed two-phase mixture. The saturation point is assumed to be at same location within the bundle as the quench front. Assuming that the saturation point is at the quench front is a reasonable simplification since for most reflood situations with low flooding rates (typically 0.0254 m/s, 1 in/s). The flow up to the quench front is assumed to be single phase while the flow downstream of the quench front is assumed to be in two-phase film boiling regime. Thus, the total bundle length can be split into a single phase region (from z_i to z_{sat}) and a two-phase region (from z_{sat} to z_e).

It is also assumed that the mass flow rate is only time dependent, and does not vary across the bundle cross section or along the length (this is approximately true for low flooding rate situations of interest in which the exit flows nearly equal the inlet flows). For constant low flooding rate situations, a nearly constant flow process occurs. Most of the flow which is injected into the bundle becomes entrained and flows out of the bundle as a steam/droplet mixture. Figure 6.1 shows the mass balance on FLECHT-SEASET test 31504, a 0.0254 m/s, 1 in/s, 40 psia, constant flooding rate test. Curve 1 represents the integrated injection, while curves 3 and 4 represent the integrated exit vapor and liquid flows respectively. The mass storage in the bundle is shown as curve 5 and is nearly horizontal indicating that only a portion of the injected water is stored in the bundle, while the remainder exits the bundle.

If one examines the data at the very beginning of the test; this quasi-steady situation is not true and the rate of mass accumulation nearly equals the injection rate. However, once the quench front becomes developed, as seen in Figure 6.1, the flows are quasi-steady.

Operating on the inertia term gives

$$\frac{1}{g_c}\int_i^e \frac{dW}{dt}\frac{dz}{A} = \frac{1}{g_c}\frac{dW}{dt}\frac{1}{A}\int_i^e dz = \frac{dW}{dt}\left(\frac{L_T}{A}\right)\frac{1}{g_c} \tag{6-70}$$

where L_T is the total length of the bundle.

Operating on the momentum flux term gives

$$\frac{1}{g_c}\frac{1}{A^2}\left[\left(\frac{W_e^2}{\rho_e}\right)-\left(\frac{W_i^2}{\rho_i}\right)\right] = \frac{1}{g_c}\frac{W^2}{A^2}\left[\frac{1}{\rho_m}-\frac{1}{\rho_\ell}\right] \tag{6-71}$$

where the difference in the momentum flux is due to the density difference from the bundle inlet and exit. The density at the bundle exit is a mixture density ($\rho_e = \rho_m$) that reflects the two-phase flow behavior in the bundle during reflooding. This term is also called the acceleration pressure drop in two-phase flow.

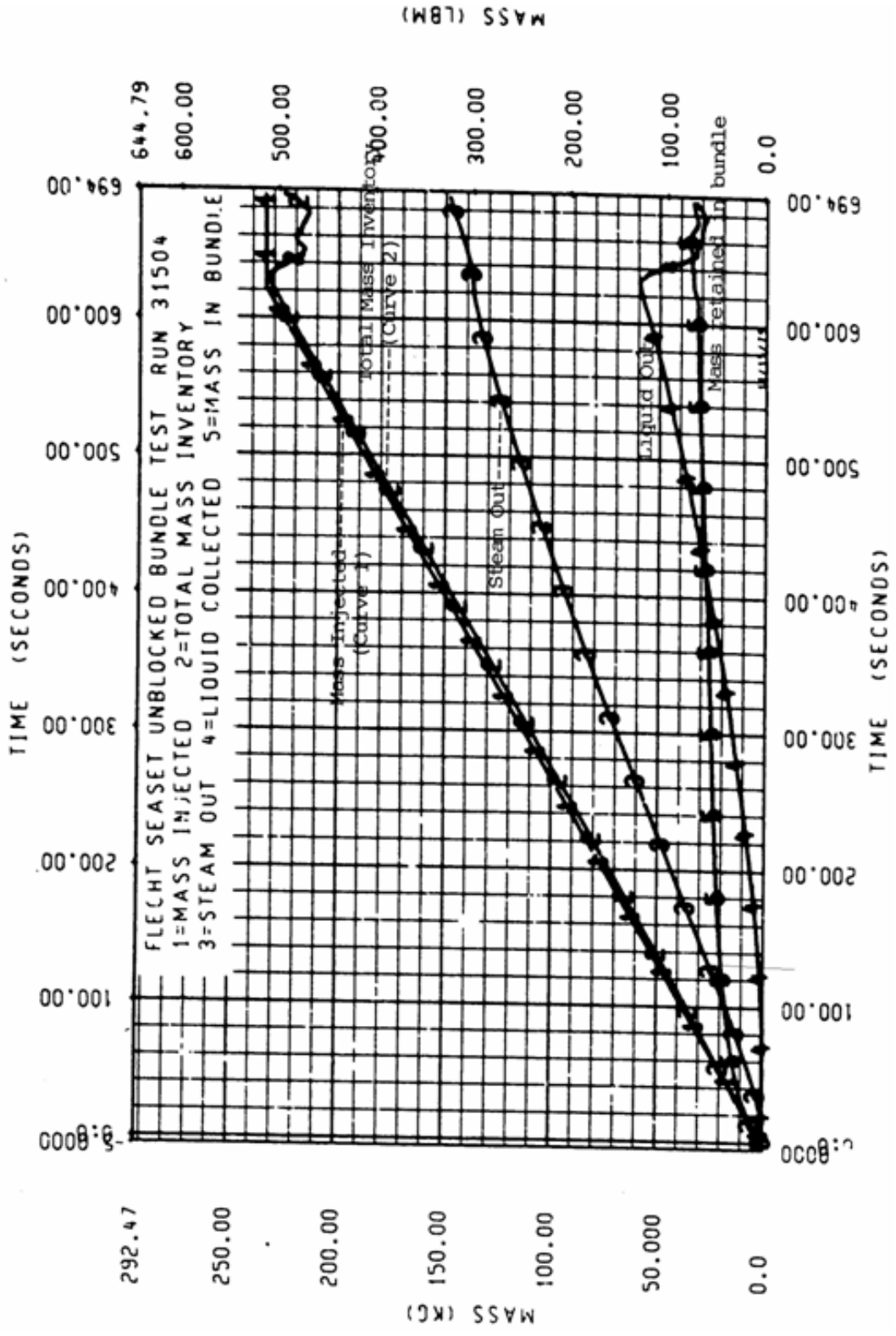

Figure 6.1 Mass Balance FLECHT–SEASET Run 31504.

The gravity term is integrated along the length of the bundle and represents the single and two-phase flow contributions to the total head in the bundle, therefore

$$\frac{g}{g_c}\int_i^e \rho dz = \frac{g}{g_c} L_{1\phi}\overline{\rho_\ell} + \frac{g}{g_c}\int_{z_{sat}}^{z_e} \rho_m dz \tag{6-72}$$

where the single phase portion of the gravitational pressure drop uses an averaged fluid density from the subcooled inlet to the saturation density for the liquid, and the two-phase region uses a mixture density.

The gravity term can be expanded in the two-phase region by representing the mixture density as

$$\rho_m = \alpha\rho_g + (1-\alpha)\rho_f \tag{6-73}$$

Inserting Equation 6-73 into Equation 6-72, and using an average void fraction in the two-phase region gives

$$\frac{g}{g_c}\int_i^e \rho dz = \frac{g}{g_c} L_{1\phi}\overline{\rho_\ell} + \frac{g}{g_c}\left[\rho_g\overline{\alpha} + \left(1-\overline{\alpha}\right)\rho_f\right]L_{2\phi} \tag{6-74}$$

The frictional terms and the form pressure loss terms can be combined for both the single phase flow region as well as the two-phase flow region assuming that the mass flow is vertically upward in the test section (the absolute sign disappears). Operating on the single phase frictional term gives

$$\frac{f}{2D_e\rho_\ell A^2 g_c} W^2 \int_{z_i}^{z_{sat}} dz = \frac{fL_{1\phi}W^2}{2D_e\rho_\ell g_c A^2} \tag{6-75}$$

and for the two-phase frictional pressure drop, one obtains

$$\frac{f}{2D_e\rho_\ell A^2 g_c}\int_{z_{sat}}^{z_e} W|W|dz = \frac{\overline{\phi_{fo}^2}\ fL_{2\phi}W^2}{2D_e\rho_f A^2 g_c} \tag{6-76}$$

where

$$\overline{\phi_{fo}^2} = \frac{\int_{z_{sat}}^{z_e}\phi_{fo}^2}{(z_e - z_{sat})} \tag{6-77}$$

is the average two-phase flow multiplier over the two-phase flow region.

A similar approach can be used for the single and two-phase form losses in the bundle. The form losses represent the spacer grids within the bundle structure. Since the quench front is

assumed to be at some intermediate position, there are a certain number of spacer grids which are in the single phase region and the remaining grids are in the two-phase region. There are typically eight grids in the rod bundle. The total form loss is given as

$$\frac{K_T W^2}{2\rho A^2 g_c} = \frac{nK_{1\phi} W^2}{2\rho_\ell A^2 g_c} + \frac{\overline{\phi_{fo}^2} \quad mK_{1\phi} W^2}{2\rho_f A^2 g_c} \tag{6-78}$$

where *n* and *m* are the number of grids in the single-phase and two-phase region respectively.

The frictional and form losses can be combined for single and two-phase flow as

$$\frac{1}{2\rho_\ell A^2 g_c}\left[\frac{fL_{1\phi}}{D_e} + nK_{1\phi}\right]W^2 + \frac{1}{2\rho_f A^2 g_c}\left[\overline{\phi_{fo}^2}\left\{\frac{fL_{2\phi}}{D_e} + mK_{1\phi}\right\}\right]W^2 \tag{6-79}$$

Substituting Equations 6-70, 6-71, 6-74 and 6-79 into Equation 6-69 gives

$$P_1 - P_2 = \frac{1}{g_c A}\frac{dW}{dt}L_T + \frac{1}{g_c}\frac{W^2}{A^2}\left(\frac{1}{\rho_m} - \frac{1}{\rho_\ell}\right) - \left[\frac{g}{g_c}L_{1\phi}\overline{\rho_\ell} + \frac{g}{g_c}\left[\rho_g\overline{\alpha} + \left(1-\overline{\alpha}\right)\rho_f\right]L_{2\phi}\right]$$

$$+ \frac{W^2}{2\rho_\ell A^2 g_c}\left[\frac{fL_{1\phi}}{D_e} + nK_{1\phi}\right] + \frac{W^2}{2\rho_f A^2 g_c}\left[\overline{\phi_{fo}^2}\left(\frac{fL_{2\phi}}{D_e} + mK_{1\phi}\right)\right] \tag{6-80}$$

We can define the total frictional and form resistance for single-phase as

$$R_{f_{1\phi}} = \frac{fL_{1\phi}}{D_e} + nK_{1\phi} \tag{6-81}$$

and for two-phase as

$$R_{f_{2\phi}} = \overline{\phi_{fo}^2}\left[\frac{fL_{2\phi}}{D_e} + mK_{1\phi}\right] \tag{6-82}$$

This equation can be normalized using the initial condition and boundary condition parameters from Table 6.2 and Table 6.6 as

$$\frac{\Delta P^* W_i^2}{2\rho_i {A_i}^2 g_c} = \left(\frac{1}{g_c}\right)\frac{W_i^2}{A_i\rho_i}\frac{L_T L^*}{V_B A^*}\cdot\frac{dW^*}{dt^*} + \frac{W_i^2}{\rho_i g_c {A_i}^2}\frac{W^{*2}}{A^{*2}}\left(\frac{1}{\rho_m^*} - \frac{1}{\rho_\ell^*}\right)$$

$$-\left[\frac{g}{g_c}L_T\rho_i L^*_{1\phi}\rho^*_\ell+\frac{g}{g_c}\alpha_e\rho_i L_T\left(\rho^*_g\alpha^*+\left(1-\alpha\right)^*\rho^*_f\right)L^*_{2\phi}\right] \tag{6-83}$$

$$+\frac{W_i^2W^{*2}}{2\rho_i A_i^2 g_c\rho^*_\ell A^{*2}}\left[R^*_{f_{1\phi}}R_{f_{1\phi_i}}\right]+\frac{W_i^2W^{*2}}{2\rho_i A_i^2 g_c\rho^*_f A^{*2}}\left[R^*_{f_{2\phi}}R_{f_{1\phi_i}}\right]$$

The bundle volume $V_B = AL_T$ can be used in equation 6-83.

Table 6.6 Normalizing Parameters for Fluid Momentum Equation

$$A^*=\frac{A}{A_i},\qquad L^*=\frac{L}{L_T},\qquad L^*_{1\phi}=\frac{L_{1\phi}}{L_T},\qquad L^*_{2\phi}=\frac{L_{2\phi}}{L_T}$$

$$\Delta P^*=\frac{\left(P_1-P_2\right)}{\left\{W_i^2\Big/\left(2g_cA_i^2\rho_i\right)\right\}},\qquad R^*_{f_{1\phi}}=\frac{R_{f_{1\phi}}}{R_{f_{1\phi,i}}},\qquad R^*_{f_{2\phi}}=\frac{R_{f_{2\phi}}}{R_{f_{1\phi,i}}}$$

where $R_{f,1\phi_i}$ refers to the total frictional and form resistance for the whole bundle in single phase flow. Thus all the (m + n) grids and the entire bundle is in single phase flow.

$$W^*=\frac{W}{W_i},\qquad \rho^*_l=\frac{\rho_l}{\rho_i},\qquad \rho^*_m=\frac{\rho_m}{\rho_i},\qquad \alpha^*=\frac{\alpha}{\alpha_e}$$

$$\left(1-\alpha\right)^*=\frac{1-\alpha}{\alpha_e}\qquad t^*=\frac{t}{\left(\rho_iV_B\Big/W_i\right)}$$

Collecting the different terms and dividing by $\frac{gL_T\rho_i}{g_c}$, the maximum gravitational driving head in the bundle as the "driving term" as recommended by Wulff gives

$$\frac{W_i^2}{2\rho_i^2A_i^2gL_T}\Delta P^*=\frac{W_i^2}{\rho_i^2A_i^2gL_T}\frac{dW^*}{dt^*}\frac{L^*}{A^{*2}}+\frac{W_i^2}{\rho_i^2A_i^2gL_T}\left(\frac{1}{\rho^*_m}-\frac{1}{\rho^*_\ell}\right)\left(\frac{W^{*2}}{A^{*2}}\right)$$

$$-\left[L^*_{1\phi}\rho^*_\ell+\alpha_e\left\{L^*_{2\phi}\left[\alpha^*\rho^*_g+\left(1-\alpha\right)^*\rho^*_f\right]\right\}\right] \tag{6-84}$$

$$+\frac{W_i^2}{2\rho_i^2A_i^2gL_T}R_{f_{1\phi_i}}\left(\frac{W^{*2}R^*_{f_{1\phi}}}{\rho^*_lA^{*2}}\right)+\frac{W_i^2}{2\rho_i^2A_i^2gL_T}R_{f_{1\phi_i}}\left(\frac{W^{*2}R^*_{f_{2\phi}}}{\rho^*_fA^{*2}}\right)$$

where the Pi groups are given as:

$$\Pi_{37} = \frac{W_i^2}{2\rho_i^2 A_i^2 g L_T} = \frac{\text{Velocity head}}{\text{Gravity head}} \tag{6-85}$$

$$\Pi_{38} = \frac{W_i^2}{A_i^2 \rho_i^2 g L_T} = \frac{\text{Velocity head}}{\text{Gravity head}} \tag{6-86}$$

$$\Pi_{39} = \frac{W_i^2}{A_i^2 \rho_i^2 g L_T} = \frac{\text{Velocity head}}{\text{Gravity head}} \tag{6-87}$$

$$\Pi_{40} = 1 \tag{6-88}$$

$$\Pi_{41} = \alpha_e = \frac{\text{Vapor head}}{\text{Total head}} \tag{6-89}$$

$$\Pi_{42} = \alpha_e = \frac{\text{Vapor head}}{\text{Total head}} \tag{6-90}$$

$$\Pi_{43} = \frac{W_i^2}{2\rho_i^2 A_i^2 g L_T} R_{f_{1\phi_i}} = \frac{\text{Single phase resistance}}{\text{Gravity head}} \tag{6-91}$$

$$\Pi_{44} = \frac{W_i^2}{2\rho_i^2 A_i^2 g L_T} R_{f_{1\phi_i}} = \frac{\text{Single phase resistance}}{\text{Gravity head}} \tag{6-92}$$

Note that Π_{37}, Π_{38}, and Π_{39} are the same or are not independent and represent the velocity head or kinetic energy of the flow relative to the maximum gravity head. Since inlet fluid conditions, geometry, and energy addition are preserved between the test and the PWR fuel assembly, the PWR plant would have the same Pi groups and these in turn will have the same numerical value. Therefore, the test facility will correctly represent the inertia effects of the fluid, the momentum flux effects and the gravitational force effects.

Π_{41} and Π_{42} represent the single-phase and two-phase gravity head terms in the momentum equation, relative to the maximum gravity head in the bundle. The two Pi groups turn out to be the same because of the normalization used.

Π_{43} represents the ratio of the single phase frictional and form pressure losses in the bundle to the maximum gravitational head in the bundle. Π_{44} represents the same ratio for the two-phase region within the bundle. Again, because of the normalization used, the two Pi groups turn out to be the same.

Comparing these terms to those for a PWR fuel assembly, differences can occur. If the spacer grids used in the test are prototypical, the form loss term will be the same for both the plant and the test. The frictional term, however, can be different since in the test there is a housing which adds additional wetted perimeter such that the hydraulic diameter is smaller for the same flow area. The smaller hydraulic diameter results in a lower Reynolds number for the same flow

Table 6.7 Pi Groups for Fluid Energy Equation

Π_i	Definition	Ratio of
Π_1	$\frac{W_i c_{p,i}(T_{sat} - T_i)}{Q_{DP_i}}$	Single phase fluid sensible energy/time Initial decay power
Π_2	$\frac{W_i \rho_{v,sat,i} c_{p,v,sat,i}(T_{max,v} - T_{sat})}{\rho_l Q_{DP_i}}$	Vapor sensible energy/time Initial decay power
Π_3	$\frac{\rho_{r,i} c_{p,r,i} V_{r,q,i}(T_{max,r,q} - T_{sat})}{\tau_2 Q_{DP_i}}$	Rod quench energy/time Initial decay power
Π_4	$\frac{\rho_{H,i} c_{p,H,i} V_{H,q,i}(T_{min,H,q} - T_{sat})}{\tau_3 Q_{DP_i}}$	Housing quench energy/time Initial decay power
Π_5	$\frac{\rho_{g,i} c_{p,g,i} V_{g,q,i}(T_{min,g,q} - T_{sat})}{\tau_4 Q_{DP_i}}$	Grid quench energy/time Initial decay power
Π_6	$\frac{\rho_{DR,i} c_{p,DR,i} V_{DR,q,i}(T_{min,DR,q} - T_{sat})}{\tau_5 Q_{DP_i}}$	Dead rod quench energy/time Initial decay power
Π_7	$\frac{Q_{DP\|_{1\phi}}}{Q_{DP_i}} = 1$	Heat generation rate Initial decay power
Π_8	$\frac{h_s A_{r,i}(T_{max,r} - T_{sat})}{Q_{DP_i}}$	Convective heat rate from rod to mixture vapor Initial decay power

Table 6.7 Pi Groups for Fluid Energy Equation (Continued)

Π_i	Definition	Ratio of
Π_9	$\frac{h_{R,r/v,i} A_{r,i} (T_{max,r} - T_v)}{Q_{DP_i}}$	Radiation heat rate from rods to vapor / Initial decay power
Π_{10}	$\frac{h_{R,r/d,i} A_{d,i} (T_{max,r} - T_{sat})}{Q_{DP_i}}$	Radiation heat rate from rod to drops / Initial decay power
Π_{11}	$\frac{h_s A_{H,i} (T_{max,H} - T_{sat})}{Q_{DP_i}}$	Convective heat rate from mixture to housing / Initial decay power
Π_{12}	$\frac{h_{R,v/H,i} A_{H,i} (T_{max,H} - T_v)}{Q_{DP_i}}$	Radiation heat rate from vapor to housing / Initial decay power
Π_{13}	$\frac{h_{R,H/d,i} A_{d,i} (T_{max,H} - T_{sat})}{Q_{DP_i}}$	Radiation heat rate from housing to drops / Initial decay power
Π_{14}	$\frac{h_s A_{g,i} (T_{max,g} - T_{sat})}{Q_{DP_i}}$	Convective heat rate from vapor to grids / Initial decay power
Π_{15}	$\frac{h_{R,v/g,i} A_{g,i} (T_{max,g} - T_v)}{Q_{DP_i}}$	Radiation heat rate from vapor to grids / Initial decay power
Π_{16}	$\frac{h_{R,g/d,i} A_{d,i} (T_{max,g} - T_{sat})}{Q_{DP_i}}$	Radiation heat rate from grids to drops / Initial decay power
Π_{17}	$\frac{h_s A_{DR,i} (T_{max,DR} - T_{sat})}{Q_{DP_i}}$	Convective heat rate from vapor to dead rods / Initial decay power

Table 6.7 Pi Groups for Fluid Energy Equation (Continued)

Π_i	Definition	Ratio of
Π_{18}	$\frac{h_{R,v/DR,i} A_{DR,i} (T_{\max,DR} - T_v)}{Q_{DP_i}}$	Radiation heat rate from vapor to dead rods / Initial decay power
Π_{19}	$\frac{h_{R,DR/d,i} A_{d,i} (T_{\max,DR} - T_{sat})}{Q_{DP_i}}$	Radiation heat rate from dead rods to drops / Initial decay power
Π_{20}	$\frac{h_{I,i} A_d (T_{\max,v} - T_{sat})}{Q_{DP_i}}$	Interfacial heat transfer rate / Initial decay power
Π_{21}	$\frac{h_{R,v/d,i} A_d (T_{\max,v} - T_{sat})}{Q_{DP_i}}$	Radiation heat rate from vapor to drops / Initial decay power
Π_{22}	$\frac{W_i c_{p,i} (T_f - T_i)}{Q_{DP_i}}$	Single phase fluid sensible energy / Initial decay power
Π_{23}	$\frac{W_i (h_s - h_g)}{Q_{DP_i}}$	Exit mixture energy/time / Initial decay power
Π_{24}	$\frac{\rho_{f,i} c_{p,f,i} \left(T_{f,CL} - T_s\right)}{\tau_f Q'''_{f,i}}$	Stored energy/time / Initial heat generation rate
Π_{25}	$\frac{k_{f,i} (T_{f,CL} - T_s)}{R_f^2 Q'''_{f,i}}$	Clad heat conduction rate / Initial heat generation rate
Π_{26}	1	Initial power / Initial heat generation rate

Table 6.7 Pi Groups for Rod Energy Equation (Continued)

Π_i	Definition	Ratio of
Π_{27}	$\frac{\rho_{c,i} V_{c,i} c_{p,c,i} (T_{ci} - T_{co})}{V_{f,i} Q'''_{f,i} \tau_c}$	Clad stored energy/time Heat generation rate
Π_{28}	$\frac{k_{c,i} V_{c,i} (T_{ci} - T_{co})}{V_{f,i} Q'''_{f,i} R_o^2}$	Clad heat conduction rate Heat generation rate
Π_{29}	$\frac{h_{gap,i} A_{i,i} (T_s - T_{ci})}{V_{f,i} Q'''_{f,i}}$	Heat transfer rate from pellet to clad Heat generation rate
Π_{30}	$\frac{h_{c,i} A_{c,i} (T_{co} - T_{sat})}{V_{f,i} Q'''_{f,i}}$	Convective HT rate Heat generation rate
Π_{31}	$\frac{h_{R,r/s,i} A_{R,r/s,i} (T_{co} - T_s)}{V_{f,i} Q'''_{f,i}}$	Radiation HT rate to surfaces in bundle Heat generation rate
Π_{32}	$\frac{h_{R,r/H,i} A_{R,r/H,i} (T_{co} - T_H)}{V_{f,i} Q'''_{f,i}}$	Radiation HT rate to housing Heat generation rate
Π_{33}	$\frac{h_{R,hr/cr,i} A_{R,hr/cr,i} (T_{co,hr} - T_{co,cr})}{V_{f,i} Q'''_{f,i}}$	Radiation HT rate from hot rods to cold rods Heat generation rate
Π_{34}	$\frac{h_{lw,i} A_{lw,i} (T_{co} - T_{sat})}{V_{f,i} Q'''_{f,i}}$	Liquid contact HT rate Heat generation rate
Π_{35}	$\frac{h_{R,r/d,i} A_{R,r/d,i} (T_{co} - T_{sat})}{V_{f,i} Q'''_{f,i}}$	Radiation HT rate to entrained drops Fuel rod heat generation rate

Table 6.7 Pi Groups for Rod Energy Equation (Continued)

Π_i	Definition	Ratio of
Π_{36}	$\frac{h_{R,r/v,i} A_{R,r/v,i} (T_{co} - T_v)}{V_{f,i} Q'''_{f,i}}$	Radiation HT rate to vapor / Fuel rod heat generation rate
$\Pi_{37} = \Pi_{38}$	$\frac{W_i^2}{2\rho_l^2 A_i^2 g L_T}$	Velocity head / Gravity head
Π_{40}	1	Maximum gravitational driving head / Total head
$\Pi_{41} = \Pi_{42}$	α_e	Vapor head / Total head
$\Pi_{43} = \Pi_{44}$	$\frac{W_i^2}{\rho_l^2 A_i^2 g L_T} R_{f_{1\phi i}}$	Single phase resistance / Gravity head

condition and hence a higher friction factor. The effects of the non-prototypical hydraulic effect of the test section housing will be calculated in Section 6.6. All the Pi groups are presented in Table 6.7.

6.4 Calculation of Pi Groups for Flow Energy Equation

6.4.1 Introduction

The fluid energy equation includes 23 Pi groups which are defined in Section 6.1. Here, the numerical values of these groups are calculated for the RBHT Test Facility, the PWR bundle and BWR bundle.

The RBHT reference conditions, given in Table 6.8 are similar to FLECHT-SEASET experiment (Run 31504) conditions. Hence, reference conditions used in the calculations are obtained from FLECHT-SEASET and then applied to the geometry and materials for each case (RBHT, PWR and BWR).

Table 6.8 RBHT Program Conditions

Flooding rate, m/s (in/s)	0.0254 (1.0)
Pressure, bar (psia)	2.67788 (40)
Inlet subcooling, degrees C (degrees F)	60 (140)
kW/m (kW/ft) at peak power location	2.3 (0.7)
Peaking factor	1.5

The fluid energy equation represents the energy balance for the fluid in the entire bundle at a given time which is selected to be the PCT time (i.e., 125 s in Run 31504). Measured values are then averaged axially to obtain the values to be used in the calculations which are shown in Table 6.9.

6.4.2 Calculation of Convective Heat Transfer Pi Groups

The Pi groups for the fluid energy equation can be categorized mainly into quench energy terms, convective heat transfer terms and radiative heat transfer terms. The present section discusses the Pi groups of the fluid energy equation.

6.4.2.1 *Methodology used for Calculations*:

The following assumptions and simplifications were used in the analysis:

1. Data from FLECHT-SEASET experiment (Run 31504) with conditions similar to the RBHT Test Facility were used; however, these values were applied to the RBHT Test Facility geometry and power shape.

Table 6.9 Reference Conditions for the Fluid Energy Equation Pi Groups

Exit Temperature, $T_{e,}$ ^{o}C (^{o}F)	260 (500)
Quench front location, m (ft)	1.2 (4.0)
Average clad temperature, $T_{c,}$ ^{o}C (^{o}F)	898.88 (1650)
Average housing temperature, $T_{H,}$ ^{o}C (^{o}F)	246.11 (475)
Average surface temperature, $T_{s,}$ ^{o}C (^{o}F)	246.11 (475)
Fluid saturation temperature, $T_{sat,}$ ^{o}C (^{o}F)	130.55 (267)
Average vapor temperature, $T_{vapor,}$ ^{o}C (^{o}F)	656.11 (1177)
Average thimble temperature, $T_{thimble,}$ ^{o}C (^{o}F)	746.66 (1376)
Average grid temperature, T_{g}, ^{o}C (^{o}F)	746.66 (1376)
Exit void fraction, α_{e}	0.999

2. The maximum temperature encountered in the run occurred at 125 s for channel 99. This was at an elevation of 1.98m (78 in). All other quantities from the FLECHT-SEASET, Run 31504 were obtained at this time (125 s).

3. The location of the quench front at 125 s was obtained from the plot of quench front location versus time in the FLECHT-SEASET report (Figure 6.6). At t = 125 s, the quench front was at the 1.2 m (4 ft) elevation. The quench front has been 'frozen' at this location for all calculations. In the calculation of the fluid energy equation Pi groups, all data used from FLECHT-SEASET report represents a snapshot in time, taken by freezing the quench front at that elevation (1.2 m [4 ft]).

4. Time averaged values over 1.2 to 3.6 m (4 to 12 ft) of the heater rod clad temperature, vapor temperature and thimble temperature were used in the calculation of the Pi groups. For the housing temperature, the maximum value of the housing temperature at that time (125 s) was used to provide a more realistic estimate of the Pi group value. This value is 410 degrees C (770 degrees F), obtained from the FLECHT SEASET report. The dummy rod temperature was taken to be the same as the maximum housing temperature. The grid temperature was set equal to the thimble temperature.

5. The heat transfer coefficient value for convection, was the time Average value obtained from data above the quench front location to the exit of the test section. This value was referenced to the fluid saturation conditions (T_{sat}).

6. The exit void fraction was assumed to be 0.999.

7. Finally, the exit temperature was obtained from the FLECHT-SEASET plot for channel 199, which gives temperature of the vapor near the exit location 3.45 m (11.5 ft). Thus T_{exit} = 260 degrees C (500 degrees F).

All values used in the calculations are summarized in Table 6.9.

6.4.2.2 *Numerical Input Quantities*:

Initial decay power:

Q_{DPi} = 2.3 kW/m (0.7 kW/ft), is the initial rod decay power (40 s into a LOCA) at the peak power location, which is equivalent to a value of 5.6 kW/rod using a peaking factor of 1.50. With 45 heated rods in the bundle, the total bundle power was 252 kW.

Inlet conditions:

Based on the information in Tables 6.8 and 6.9, the inlet properties were obtained from thermodynamic tables at a temperature of 52.77 degrees C (127 degrees F).

Areas of rods, housing, grids and dead rods above the quench front (4 ft):

a. The total rod area is calculated based on rod diameter 9.55 mm (0.374 in) and length above quench front 2.4 m (8 ft) for 45 heated rods.

b. The housing area is obtained from the product of the inner perimeter of the housing and the length of housing above the quench front.

c. The total grid area is calculated based on the product of the following:

   Area of each cell = 4 x pitch 12.6 mm (0.496 in) x height of the grid 38.1 mm (1.5 in)
   Number of cells per grid = 45
   Number of grids strops above quench front = 6

d. The total dummy rod area is based on the dummy rod diameter 9.5 mm (0.374 in) and length above quench front 2.4 m (8 ft) for four dummy rods.

6.4.2.*3 Numerical Values of the Convection Pi groups:*

The Pi groups representing the energy storage terms are

Π_1 = 0.144

Π_2 = 0.0007

For the convective energy terms for rods, housing, grids and dummy rods, a heat transfer coefficient of 56.78 W/m^2-K (10 Btu/hr-ft^2-F) was used, based on the average from the FLECHT-SEASET report (Run 31504) data. To give a more realistic value for the Pi group, Π_{11}, instead of average value of housing temperature, the maximum housing temperature of 410 degrees C (770 degrees F) at PCT time (125 s), at the 6 ft elevation was used. Also, the maximum housing temperature 410 degrees C (770 degrees F) was for the value of T_{max} of dummy rods.

Using the above information and the calculated areas, the Pi values for the various convective heat transfer terms are:

Π_8 = 0.567

Π_{11} = 0.055

Π_{14} = 0.072

Π_{17} = 0.019

The Pi group for the interfacial heat transfer is

$$\Pi_{20} = \frac{h_{I,i} A_d \left(T_{\max,v} - T_{sat}\right)}{Q_{DP_i}} = \frac{\text{Interfacial heat transfer rate}}{\text{Initial decay power}}$$

where A_d represents the interfacial area, given by the product of area of a single drop times the number of drops. The number of drops is given by

$$N_d = \frac{6\left(1-\overline{\alpha}\right)}{\pi d^3} \qquad (6\text{-}93)$$

With a mean void fraction value of 0.995, and a drop diameter of 1.016 mm (0.04 in), the number of drops is

N_d = 9.104 drops/cm^3 (149.2 drops/in^3)

The quench front is at the 4 ft elevation, hence, the number of drops in the two-phase region which extends from the location of the quench front to the bundle exit is obtained by the product of the number of drops per unit volume times the volume above the quench front.

Flow area = 45.8 cm^2 (7.0987 in^2)

Hence, the total number of drops is calculated to be 101641.

From the FLECHT-SEASET report (Page 6-26), the mean droplet velocity and mean vapor velocity are found as

$$\overline{u_d} = 6.555 \text{ m/sec } (21.5 \text{ ft/sec})$$

$$\overline{u_v} = 13.415 \text{ m/sec } (44 \text{ ft/sec})$$

The Reynolds number for drop based on the relative velocity of drops and vapor is given as:

$$\text{Re}_d = \frac{\rho_v d\left(\overline{u_v} - \overline{u_d}\right)}{\mu_v} \qquad (6\text{-}94)$$

The droplet Reynolds Number is calculated to be 803.65.

Taking a Pr_v = 1.04 from Collier and Thome (Ref. 12) and using the Lee-Ryley Correlation, the Nusselt number is

$$Nu_d = 2 + 0.74\,\mathrm{Re}_d^{0.5}\,\mathrm{Pr}^{1/3} \tag{6-95}$$

$$h_{I_{co}} = \frac{Nu_d\,k_v}{d} \tag{6-96}$$

where the thermal conductivity for vapor is obtained from Collier and Thomeas (Ref. 12) as

k_v = 0.02799027 W/m-K (0.01617 Btu/hr-ft-F)

Based on these,

$$\Pi_{20} = 0.43$$

The flow energy Pi groups for exit energy are calculated assuming the exit mass flow is equal to the inlet mass flow. Value of saturated vapor enthalpy is used from thermodynamic tables at P = 40 psia. Thus

$$\Pi_{22} = \Pi_1 = 0.144$$

$$\Pi_{23} = 0.121$$

From these, it is seen that the Pi groups representing the energy storage, the flow energy and convection from rod to vapor and the interfacial heat transfer terms are the dominant Pi groups. The other terms are very small by comparison. This clear distinction between the dominant terms and the others are in line with what is expected typically.

$$\Pi_4 = \frac{\rho_{H,i}\,c_{p,H,i}\,V_{H,q,i}\left(T_{\min,H,q} - T_{sat}\right)}{\tau_3\;Q_{DP_i}} = \frac{\text{Housing quench energy / time}}{\text{Initial decay power}}$$

$$\Pi_5 = \frac{\rho_{g,i}\,c_{p,g,i}\,V_{g,q,i}\left(T_{\min,g,q} - T_{sat}\right)}{\tau_4\;Q_{DP_i}} = \frac{\text{Grid quench energy / time}}{\text{Initial decay power}}$$

$$\Pi_6 = \frac{\rho_{DR,i}\,c_{p,DR,i}\,V_{DR,q,i}\left(T_{\min,DR,q} - T_{sat}\right)}{\tau_5\;Q_{DP_i}} = \frac{\text{Dead rod quench energy / time}}{\text{Initial decay power}}$$

6.4.3 Quench Energy groups

The Pi groups describing the heat transfer at the quench front for the rods, the housing, the grids and the surfaces (dummy rods) are the following:

The calculation is based on the input data from in Tables 6.8 and 6.9 and the methodology used in Section 6.4.2.1. In addition, the following assumptions have been made to complete the calculation:

- The same transition boiling heat transfer coefficient of $h_{q,i}$ = 5.678 kW/m^2-K (1000 Btu/hr-ft^2-F) is assumed for the structures (rods, housing, grids and surfaces);
- The same T_{min} = 550 degrees C (1022 degrees F) is assumed for all surfaces;
- The same axial quench front velocity u_q is assumed for all the structures.

where the same value of T_{min} has been used for all surfaces since the material is all Inconel. The material properties and geometry data used in the calculation are summarized in the following tables (6.10, 6.11, 6.12, 6.13):

Table 6.10 Material Properties

Material	Reference Temperature (C)	Density (kg/m^3)	Heat Capacity (J/kg-K)	Conductivity (W/m-K)
Inconel-600	1100	8254	696	24.7
Boron Nitride	1100	1910	1500	86.3
Monel K-500	1100	8470	531	34.4
Uranium Dioxide	1100	9649	326	3.9
Zircaloy-2	1100	6560	362	16.8

Table 6.11 Electrical Rod Geometry

Material	r_i (mm, in)	dr_i (mm, in)
Boron Nitride	0, 0	1.7145, 0.0675
Monel K-500	1.7145, 0.0675	1.143, 0.0450
Boron Nitride	2.8575, 0.1125	1.1811, 0.0465
Inconel-600	4.0386, 0.1590	0.7112, 0.0280
Rod surface	4.7498, 0.1870	

Table 6.12 Nuclear Rod Geometry for PWR

Material	r_i (mm, in)	dr_i (mm, in)
Uranium Dioxide	0, 0	4.18084, 0.1646
Zircaloy-2	4.18084, 0.1646	0.56896, 0.0224
Rod surface	4.7498, 0.1870	

Table 6.13 Nuclear Rod Geometry for BWR

Material	r_i (mm, in)	dr_i (mm, in)
Uranium Dioxide	0, 0	5.199, 0.2047
Zircaloy-4	5.199, 0.2047	0.810, 0.0319
Rod surface	6.0198, 0.2370	

At first we need to calculate the volume of the rod which is quenching. This is related to the assumed quench front velocity v_q and the heat structure time constant to release the stored energy:

$$V_r = A_{s,r} v_q \tau_2 \tag{6-97}$$

where $A_{s,r}$ is the cross section of one of the heater rods and is given as

$$A_{s,r} = N_r \left(\frac{\pi}{4} D_r^2 \right) \tag{6-98}$$

This expression, when substituted in the definition of Π_3 gives

$$\Pi_3 = \frac{\rho_r c_{p,r} A_{s,r} v_{q,r} \tau_2 (T_{\min,r} - T_{sat})}{Q_{DP_i} \ \tau_2} \tag{6-99}$$

Note that the time constant drops out. This is because, regardless the time constant, most of the stored energy will be released during the quenching time period. In other words, if the time constant is larger, then the energy release rate will be lower but the energy will be released by a larger volume as the quench front is advancing over the same time period. This follows from the assumption that the quench front velocity is constant.

A similar procedure is used to calculate Π_4; i.e., the energy released during quenching of the housing is

$$\Pi_4 = \frac{\rho_{H,i} c_{p,H,i} V_{H,q,i} (T_{\min,H,q} - T_{sat})}{\tau_3 Q_{DP_i}} \tag{6-100}$$

Similarly for the grid

$$\Pi_5 = \frac{\rho_{g,i} c_{p,g,i} V_{g,q,i} (T_{\min,g,q} - T_{sat})}{\tau_4 Q_{DP_i}} \tag{6-101}$$

where

$$A_{s,g} = 4\left(p \times \frac{s}{2} \right) \times 45, \tag{6-102}$$

p is the pitch, and *s* is the strop thickness.

Finally for the dummy (corner rods):

$$\Pi_6 = \frac{\rho_{DR,i} c_{p,DR,i} V_{DR,q,i} (T_{\min,DR,q} - T_{sat})}{\tau_5 Q_{DP_i}} \tag{6-103}$$

where

$$A_{s,DR} = N_{DR}\left(\frac{\pi}{4} D_{DR}^2\right) \tag{6-104}$$

and N_{DR} is the number of dead rods (in our case, 4).

Details of the calculations are reported in Appendix B.7. The values of the Pi groups are the following:

$$\Pi_3 = 0.092$$
$$\Pi_4 = 0.084$$
$$\Pi_5 = 0.022$$
$$\Pi_6 = 0.003$$

6.4.4 Thermal Radiation Heat Transfer Pi Group Calculations

The Pi groups describing the radiative heat transfer to the fluid from the structures are: Π_9 to Π_{16}. These terms require particular attention because in order to obtain these values, the solution of a radiative surface network is required. Thermal radiation heat transfer takes place between the rod surfaces, between rod and housing, between any surface to steam and droplets and between steam and droplets directly. For a given temperature field (clad, dummy rods, housing, liquid and vapor) the heat rates among the surfaces, liquid and vapor are calculated by solving a radiation network lumped model (using the RADNET Fortran computer program).

In this model, rods are lumped together and global surface view factors are calculated by combining single rod view factors obtained with the VUEFAC subroutine of the MOXY computer program (Ref. 11). Details of the view factors calculation are reported in Appendix B.1.

To account for a radial temperature distribution in the bundle, a six node radiation network has been developed, where the heater rods are divided in hot rods and cold rods (Figure 6.2). The hot rods are considered to be either the single center rod, the inner 3x3 array, or the inner 5x5 array. Sensitivity analyses (Appendix B.1) have been carried out and the inner 3x3 hot rods lumping approach was chosen to be the most appropriate.

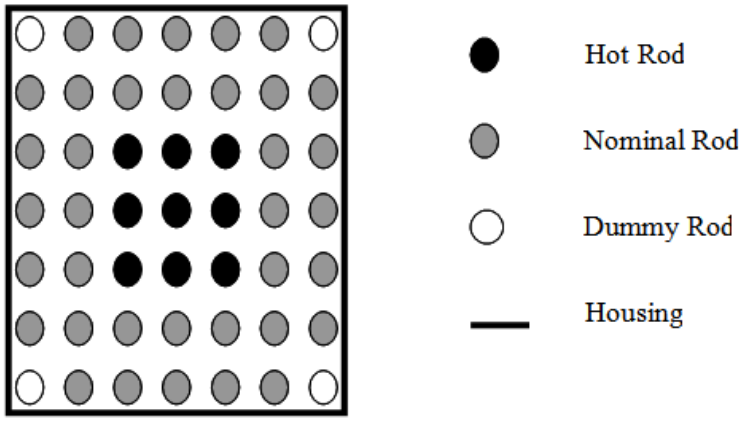

Figure 6.2 RBHT Layout.

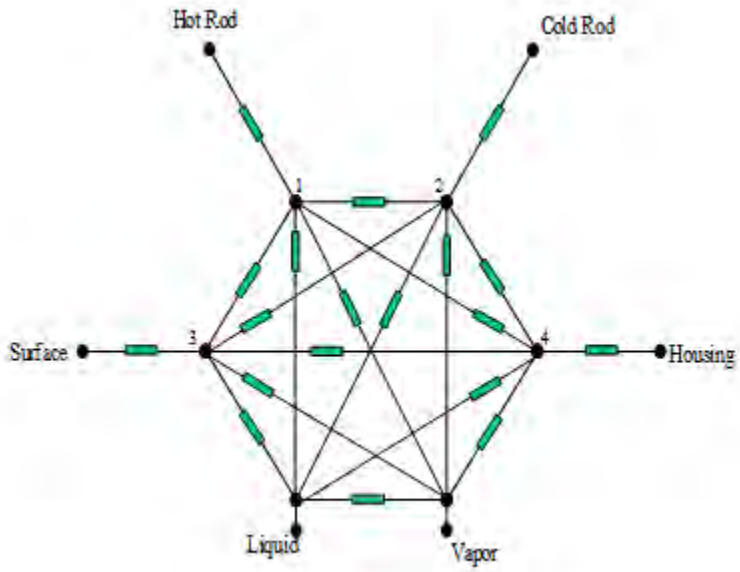

Figure 6.3 Six Node Radiation Network.

The radiation network (Figure 6.3) resistances are calculated as described in Reference 8 and Appendix B.1 while the temperature at each network node surfaces is an input for the program. The node surface temperatures are calculated by averaging measured temperature in Run 31504 of the FLECHT-SEASET experiments. These values are summarized in Table 6.9. Once the temperature is assigned to each radiative surface, the radiation network is solved for the heat rate (per unit length) between each node. In particular, the Pi groups concerned with radiation are redefined below:

$$\Pi_9 = \frac{h_{R,r/v,i} A_{r,i} \left(T_{\max,r} - T_v \right)}{Q_{DP_i}} = \frac{Q'_{r/v} \left(z_{top} - z_q \right)}{Q_{DP_i}} \qquad (6\text{-}105)$$

$$\Pi_{10} = \frac{h_{R,r/d,i} A_{d,i} \left(T_{\max,r} - T_{sat} \right)}{Q_{DP_i}} = \frac{Q'_{r/d} \left(z_{top} - z_q \right)}{Q_{DP_i}} \tag{6-106}$$

$$\Pi_{12} = \frac{h_{R,v/H,i} A_{H,i} \left(T_{\max,H} - T_v \right)}{Q_{DP_i}} = \frac{Q'_{v/H} \left(z_{top} - z_q \right)}{Q_{DP_i}} \tag{6-107}$$

$$\Pi_{13} = \frac{h_{R,H/d,i} A_{d,i} \left(T_{\max,H} - T_{sat} \right)}{Q_{DP_i}} = \frac{Q'_{H/d} \left(z_{top} - z_q \right)}{Q_{DP_i}} \tag{6-108}$$

$$\Pi_{15} = \frac{h_{R,v/g,i} A_{g,i} \left(T_{\max,g} - T_v \right)}{Q_{DP_i}} = \frac{Q'_{v/g} \Delta z_g N_g}{Q_{DP_i}} \tag{6-109}$$

$$\Pi_{16} = \frac{h_{R,g/d,i} A_{d,i} \left(T_{\max,g} - T_{sat} \right)}{Q_{DP_i}} = \frac{Q'_{g/d} \Delta z_g N_g}{Q_{DP_i}} \tag{6-110}$$

$$\Pi_{18} = \frac{h_{R,v/DR,i} A_{DR,i} \left(T_{\max,DR} - T_v \right)}{Q_{DP_i}} = \frac{Q'_{DR/v} \left(z_{top} - z_q \right)}{Q_{DP_i}} \tag{6-111}$$

$$\Pi_{19} = \frac{h_{R,DR/d,i} A_{d,i} \left(T_{\max,DR} - T_{sat} \right)}{Q_{DP_i}} = \frac{Q'_{DR/d} \left(z_{top} - z_q \right)}{Q_{DP_i}} \tag{6-112}$$

$$\Pi_{21} = \frac{h_{R,v/d,i} A_d \left(T_{\max,v} - T_{sat} \right)}{Q_{DP_i}} = \frac{Q'_{v/d} \left(z_{top} - z_q \right)}{Q_{DP_i}} \tag{6-113}$$

where

z_{top} Elevation to the top of the bundle, 3.6 m (12 ft)
z_q Elevation of the quench front, 1.2 m at 125 s (4 ft at 125 s)
Δz_g Grid axial length, 38.1 mm (1.5 in)
N_g Number of grids above quench front

The solution of the radiation network provides the radiosity or emissive power in each node, then the values in each branch can be calculated by applying the definition

$$Q_{ij} = \frac{J_i - J_j}{R_{ij}} \text{ or } Q_{ij} = \frac{J_i - E_{b,j}}{R_{ij}} \tag{6-114}$$

The six node radiation network requires two clad temperature values: the hot rod temperature and the cold rod temperature. The temperature difference between the hot rods and the cold rods is estimated from the rod-to-rod (MOXY) radiation model and is 161 degrees F when a 3x3 inner hot rods lumping approach in the bundle is assumed. Then the hot and cold rod temperature are calculated

$$\frac{9T_{hr} + 36\,T_{cr}}{45} = \overline{T} = 1650 \tag{6-115}$$

and since

$$T_{cr} = T_{hr} - \Delta T = T_{hr} - 161$$

we obtain

$$T_{hr} = 970.55^{\circ}\text{C}\ (1779\ \text{F})$$
$$T_{cr} = 880.55^{\circ}\text{C}\ (1617\ \text{F})$$

This completes the input data for the radiation network. The dimensionless group Π_9 is the radiative energy from all the rods to the vapor and is expressed as

$$\Pi_9 = \frac{Q'_{r/v}\Delta z}{Q_{DP_i}}$$

where the numerator has the units of heat rate per unit length and is the sum of two contributions: energy from hot rods to vapor and energy from nominal rods to vapor.

As already mentioned the difference Δz is the height above the quench front

$$\Delta z = z_{top} - z_q$$

and

$$Q'_{r/v} = Q'_{1v} + Q'_{2v}$$

The initial bundle decay power is

$$Q_{DP_i} = 252.0\ \text{kW}$$

As results we obtain

$$\Pi_9 = 8.55e^{-4}$$

Similarly the Pi group for the radiative energy from the rod to the liquid droplets is calculated as

$$\Pi_{10} = \frac{Q'_{r/d}\,\Delta z}{Q_{DP_i}}$$

where

$$Q'_{r/d} = Q'_{1d} + Q'_{2d}$$

and

$$\Pi_{10} = 7.06e^{-2}$$

The next two dimensionless groups represent the radiative heat transfer from the housing to the vapor and droplets, respectively

$$\Pi_{12} = \frac{Q'_{v/H}\,\Delta z}{Q_{DP_i}} \qquad \text{and} \qquad \Pi_{13} = \frac{Q'_{H/d}\,\Delta z}{Q_{DP_i}}$$

where

$$Q'_{v/H} = Q'_{4v}$$

$$Q'_{H/d} = Q'_{4d}$$

and then

$$\Pi_{12} = -8.01e^{-5}$$

$$\Pi_{13} = 2.85e^{-3}$$

The next two Pi groups for the radiative energy from the grids to the fluid are calculated by solving a separate four node radiation network (Figure 6.4). The Pi groups are defined as

$$\Pi_{15} = \frac{Q'_{v/g}\,\Delta z_g\,N_g}{Q_{DP_i}} \quad \text{and} \quad \Pi_{16} = \frac{Q'_{g/d}\,\Delta z_g\,N_g}{Q_{DP_i}}$$

where

$$Q'_{v/g} = \frac{J_2 - \sigma T_v^4}{R_{2v}}, Q'_{g/d} = \frac{J_2 - \sigma T_d^4}{R_{2d}}$$

and J_2 and R_{2v} refer to the four node radiation network. The grid vertical length and the number of grids above the quench front are

$$\Delta z_g = 1.5\text{in} \quad \text{and} \quad N_g = 6$$

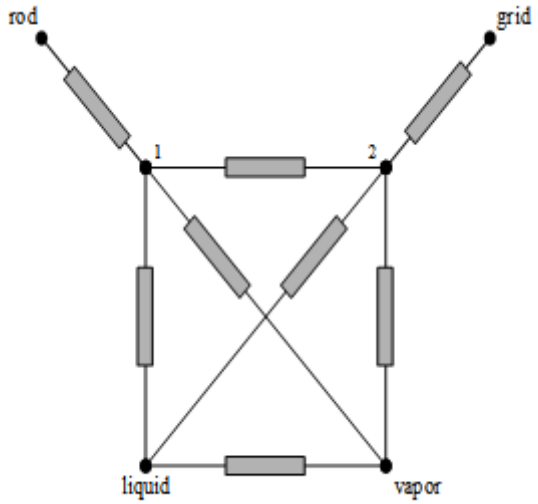

Figure 6.4 Four Node Radiation Network.

The rod-grid-liquid-vapor network resistances are calculated with the same procedure and equations described for the bundle six-node-radiation network. In this case there are only two unknowns (J_1 and J_2) which can be determined explicitly. Details of the calculation are reported in the Excel worksheet attached in Appendix B.2. The result is

$$\Pi_{15} = 6.9e^{-7}$$

$$\Pi_{16} = 0.0016$$

Finally, the radiation energy from the surfaces (unheated rods) to the fluid are represented by

$$\Pi_{18} = \frac{Q'_{v/DR}\,\Delta z}{Q_{DP_i}} \qquad \text{and} \qquad \Pi_{19} = \frac{Q'_{DR/d}\,\Delta z}{Q_{DP_i}}$$

where

$$Q'_{v/DR} = Q'_{3v} \qquad \text{and} \qquad Q'_{DR/d} = Q'_{3d}$$

as results:

$$\Pi_{18} = -3.22e^{-5} \qquad \text{and} \qquad \Pi_{19} = 6.5e^{-4}$$

The last contribution to the radiative heat transfer is expressed by the interfacial radiation heat transfer

$$\Pi_{21} = \frac{Q'_{v/d}\,\Delta z}{Q_{DP_i}}$$

which is determined directly from the network with the result that

$$\Pi_{21} = 3.9e^{-5}$$

6.4.5 Summary

Table 6.14 shows the numerical values of all the Pi groups for the fluid energy equation. As expected, stored energy, rod quench energy, convection from rod to vapor, interfacial heat transfer and flow energy terms are significant. The values of the radiation Pi groups are relatively small, thereby indicating the predominance of convection over radiation heat transfer. Though the rod quench energy term is significant, the housing, grid and the dummy rod quench energy terms are small.

6.5 Calculations of Pi groups for the Rod Energy Equation

6.5.1 Introduction

The rod energy equation includes thirteen Pi groups (from Π_{24} to Π_{36}) defined earlier. The numerical values of these groups are now calculated for the RBHT Test Facility. The reference conditions used in the calculation are obtained from the same FLECHT-SEASET experiment (Run 31504) used earlier and then applied to the geometry and materials for each case (RBHT, PWR and BWR).

The rod energy equation represents an energy balance at a given axial location within the dispersed flow film boiling region, far from the quench front at the time of the measured peak temperature. The conditions (temperature, heat transfer coefficients, etc.) are taken from FLECHT-SEASET (Run 31504) measured values at the time of PCT and at the PCT axial location. Since there are no data available for the dummy rods, their surface temperature is

Table 6.14 Numerical Values of Pi Groups - Fluid Energy Equation

Π_i	Definition	Ratio of	Value for RBHT	Value for PWR	RBHT PWR	Value for BWR	RBHT BWR
Π_1	$\frac{W_i c_{p,i}(T_{sat} - T_i)}{Q_{DP_i}}$	Single phase fluid sensible energy/time Initial decay power	0.144	0.144	1	0.144	1
Π_2	$\frac{W_i \rho_{v,sat,i} c_{p,v,sat,i}(T_{max,v} - T_{sat})}{\rho_i Q_{DP_i}}$	Vapor sensible energy/time Initial decay power	0.000	0.000	Insignificant*	0.000	Insignificant *
Π_3	$\frac{\rho_{r,i} c_{p,r,i} V_{r,q,i}(T_{max,r,q} - T_{sat})}{\tau_2 Q_{DP_i}}$	Rod quench energy/time Initial decay power	0.092	0.066	1.394	0.105	0.876
Π_4	$\frac{\rho_{H,i} c_{p,H,i} V_{H,q,i}(T_{min,H,q} - T_{sat})}{\tau_3 Q_{DP_i}}$	Housing quench energy/time Initial decay power	0.084	0	Does not exist as Π term for PWR is zero	0.009	Insignificant *
Π_5	$\frac{\rho_{g,i} c_{p,g,i} V_{g,q,i}(T_{min,g,q} - T_{sat})}{\tau_4 Q_{DP_i}}$	Grid quench energy/time Initial decay power	0.022	0.009	Insignificant*	0.012	Insignificant *
Π_6	$\frac{\rho_{DR,i} c_{p,DR,i} V_{DR,q,i}(T_{min,DR,q} - T_{sat})}{\tau_5 Q_{DP_i}}$	Dead rod quench energy/time Initial decay power	0.003	0.001	Insignificant*	0.000	Insignificant *
Π_7	$\frac{Q_{DP\|_{1\phi}}}{Q_{DP_i}}$	Heat generation rate Initial decay power	1	1	1	1	1
Π_8	$\frac{h_s A_{r,i}(T_{max,r} - T_{sat})}{Q_{DP_i}}$	Convective heat rate from rod to mixture vapor Initial decay power	0.567	0.567	1	0.719	1.268

Table 6.14 Numerical Values of Pi Groups - Fluid Energy Equation (Continued)

Π_9	$\frac{h_{R,r/v,i} A_{r,i} (T_{max,r} - T_v)}{Q_{DP_i}}$	Radiation heat rate from rods to vapor / Initial decay power	0.000	0.000	Insignificant*	0.000	Insignificant *
Π_{10}	$\frac{h_{R,r/d,i} A_{d,i} (T_{max,r} - T_{sat})}{Q_{DP_i}}$	Radiation heat rate from rod to drops / Initial decay power	0.071	0.074	0.959	0.116	0.612
Π_{11}	$\frac{h_s A_{H,i} (T_{max,H} - T_{sat})}{Q_{DP_i}}$	Convective heat rate from mixture to housing / Initial decay power	0.055	0	Does not exist as Π term for PWR is zero	0.07	0.786
Π_{12}	$\frac{h_{R,v/H,i} A_{H,i} (T_{max,H} - T_v)}{Q_{DP_i}}$	Radiation heat rate from vapor to housing / Initial decay power	0.000	0	Does not exist as Π term for PWR is zero	0.000	Insignificant *
Π_{13}	$\frac{h_{R,H/d,i} A_{d,i} (T_{max,H} - T_{sat})}{Q_{DP_i}}$	Radiation heat rate from housing to drops / Initial decay power	0.000	0	Does not exist as Π term for PWR is zero	0.000	Insignificant *
Π_{14}	$\frac{h_s A_{g,i} (T_{max,g} - T_{sat})}{Q_{DP_i}}$	Convective heat rate from vapor to grids / Initial decay power	0.072	0.072	1	0.093	0.774
Π_{15}	$\frac{h_{R,v/g,i} A_{g,i} (T_{max,g} - T_v)}{Q_{DP_i}}$	Radiation heat rate from vapor to grids / Initial decay power	0.000	0.000	Insignificant*	0.000	Insignificant *
Π_{16}	$\frac{h_{R,g/d,i} A_{d,i} (T_{max,g} - T_{sat})}{Q_{DP_i}}$	Radiation heat rate from grids to drops / Initial decay power	0.002	0.002	1	0.002	1
Π_{17}	$\frac{h_s A_{DR,i} (T_{max,DR} - T_{sat})}{Q_{DP_i}}$	Convective heat rate from vapor to dead rods / Initial decay power	0.019	0.019	1	0.023	0.826

Table 6.14 Numerical Values of Pi Groups - Fluid Energy Equation (Continued)

Π_{18}	$\frac{h_{R,v/DR,i} A_{DR,i} (T_{max,DR} - T_v)}{Q_{DP_i}}$	Radiation heat rate from vapor to dead rods Initial decay power	0.000	0.000	Insignificant*	0.000	Insignificant *
Π_{19}	$\frac{h_{R,DR/d,i} A_{d,i} (T_{max,DR} - T_{sat})}{Q_{DP_i}}$	Radiation heat rate from dead rods to drops Initial decay power	0.000	0.000	Insignificant*	0.000	Insignificant *
Π_{20}	$\frac{h_{I,i} A_d (T_{max,v} - T_{sat})}{Q_{DP_i}}$	Interfacial heat transfer rate Initial decay power	0.43	0.43	1	0.43	1
Π_{21}	$\frac{h_{R,v/d,i} A_d (T_{max,v} - T_{sat})}{Q_{DP_i}}$	Radiation heat rate from vapor to drops Initial decay power	0.000	0.000	Insignificant*	0.000	Insignificant *
Π_{22}	$\frac{W_i c_{p,i} (T_f - T_i)}{Q_{DP_i}}$	Single phase fluid sensible energy Initial decay power	0.144	0.144	1	0.144	1
Π_{23}	$\frac{W_o (h_s - h_g)}{Q_{DP_i}}$	Exit mixture energy/time Initial decay power	0.121	0.121	1	0.121	1

* - Both numbers are very small, so the ratio is insignificant

assumed equal to the housing temperature. The complete list of data and assumptions is given in Table 6.15.

6.5.2 Convection and Stored Energy Pi Groups

The convection and stored energy Pi groups are Π_{24}, Π_{25}, Π_{26}, Π_{27}, Π_{28}, Π_{29}, Π_{30}, and Π_{34}. The values of the Pi groups are calculated for both the electric rod and the nuclear rod. The reference conditions and the input that is used in the calculation are tabulated in Table 6.15. Both types of rods are modeled as infinite cylinders. The temperature at the various locations such as centerline, surface, clad inside and clad outside surface are calculated simply by applying the concepts of conduction resistance for cylindrical geometries.

Table 6.15 Reference Conditions for Rod Energy Equation Pi Groups

Rod peak power, kW/m (kW/ft)	2.3 (0.7)
PCT time (sec)	125
PCT axial location, m (ft)	1.95 (6.5)
Clad temperature (PCT), T_{ci}, ^oC (F)	1148.88 (2100)
Housing temperature, T_H, ^oC (F)	426.66 (800)
Surface temperature, T_s, ^oC (F)	426.66 (800)
Saturation temperature, T_{sat}, ^oC (F)	130.55 (267)
Vapor temperature, T_v, ^oC (F)	898.88 (1650)
Gap heat transfer coefficient, kW/m^{2}K (Btu/hr-ft^2-F) h_{gap} (Nuclear Rod) h_{gap} (Electrical Rod)	 5.678 (1000) 28.39 (5000)

To account for the correct heat transfer, based on the maximum temperature difference (T_{CL} - T_{sat}), the value of the heat transfer coefficient is taken to be h = 56.78 W/m^2-K (10 Btu/hr-ft^2-F). This is again based on the same FLECHT-SEASET (Run 31504) data.

Also, to simulate the gap that exists between the inside of the clad and the fuel pellet or the boron nitride insulator, a gap heat transfer coefficient is used:

h_{gap} = 28.39 kW/m^{2}K (5000 Btu/hr-ft^2-F), for electrical rods
h_{gap} = 5.678 kW/m^{2}K (1000 Btu/hr-ft^2-F), for nuclear rods

which are representative values for these rods.

The heat generation rate per unit volume, Q_i''', is calculated from the kW/ft rating at peak location 2.3 kW/m (0.7 kW/ft) and the diameter of the fuel element, D_f = 9.5 mm (0.374 in). We get Q_i''' = 1.469 x 10^8 W/m^3 (4329012.6 Btu/hr-ft^3).

Material properties tabulated in Table 6.10 and the dimensions of the electrical rod from Table 6.11 are used for the calculation of the Pi terms.

The fuel time constant τ_f and clad time constant τ_c are obtained by solving a double-lumped model for the rod. Three time constants are calculated from these models that represent respectively the fuel resistance (UO_2 or BN and Monel), the clad resistance and the film resistance. Results are reported in the following Table 6.16:

Table 6.16 Comparison of Calculated Time Constants

Time constant (sec)	RBHT	PWR	BWR
Fuel, τ_f	0.55	3.99	5.98
Clad, τ_c	0.36	0.68	1.15
Film, τ_{film}	0.74	0.24	0.36

The fuel time constant τ_f and clad time constant τ_c are used in groups Π_{24} and Π_{27}, respectively. The calculation of the P_{34} group defining direct contact heat transfer requires some explanation,

$$\Pi_{34} = \frac{h_{lw,i} A_{lw,i} \left(T_{co} - T_{sat}\right)}{Q'''_{f,i} V_{f,i}} = \frac{\text{Liquid contact HT rate}}{\text{Heat generation rate}}$$

To calculate the direct contact heat transfer for the dispersed droplet field, the Forsland Rohsenow correlation is used as follows

$$q''_{dcht} = (0.2)(1.276)(1-\alpha_v)^{2/3}\left[\frac{g\rho_f \rho_g H^*_{fg} k^3}{(T_w - T_{sat})\mu_g D_d}\right]^{1/4}(T_w - T_{sat}) \qquad (6\text{-}116)$$

In the calculations, it is assumed that the liquid is saturated such that $H^*_{fg} = h_{fg}$.

The properties are evaluated at 60 psia and the calculations are performed for different void fractions and wall superheats. The droplet area is calculated assuming a uniform distribution of drops. Only drops within a diameter of the rod can interact. The number of drops is given by

$$N_d = \frac{6\left(1-\overline{\alpha}\right)}{\pi d^3} \qquad (6\text{-}117)$$

With a mean void fraction value of 0.995, and a drop diameter of 0.04 in, the number of drops is calculated as

N_d = 9.104 drops/cm^3 (149.2 drops/in^3)

The drops (max) that can interact with the rod are those which are within one drop diameter of the rod surface.

Rod diameter = 9.5 mm (0.374 in)
Rod diameter + diameter of two drops = 0.374 in + 2·(0.04 in) = 11.53 mm (0.454 in)
Area of the region occupied by two drops = $(22/7)\cdot(0.454^2 - 0.374^2) = 33.55\ \text{mm}^2$ $(0.052\ \text{in}^2)$
Subchannel area = $(\text{pitch})^2$ - area of rod = $88.135\ \text{mm}^2$ $(0.13661\ \text{in}^2)$

The area fraction of the drops that can hit the rod is the ratio of the area occupied by two drops to the subchannel area.

Area fraction = 0.052/0.13661 = 0.395

From the information of the area fraction and the number of drops per cubic inch, the resultant number of drops that can contact the wall is calculated as

(0.395)·(149.2) = 59 drops.

Since only one side of a drop contacts the rod, the total contact area is given as:

Total contact area = 0.5 (spherical area per drop)·(Resultant number of drops) = 95.66 mm^2 $(0.14828\ \text{in}^2)$

Knowing all the values for the variables in equation 6-116, the heat flux is calculated for various values of $(T_w - T_{sat})$. From this, the heat transfer coefficient can also be calculated. For the Pi group calculation, the values of heat transfer coefficient, the contact area and the heat generation rate are known. The numerical value of the Pi group can be evaluated for various values of $(T_{co} - T_{sat})$, each time using the appropriate value of h. The value of Π_{34} tabulated in the result is for a temperature difference of 537.77 degrees C (1000 degrees F). The calculated Pi values are given in Table 6.17.

Table 6.17 Convection and Stored Energy Pi Groups for Electrical/Nuclear Rod

π group	Electrical Rod	Nuclear Rod PWR
π_{24}	0.965	1.180
π_{25}	0.182	0.182
π_{26}	1	1
π_{27}	0.110	0.04
π_{28}	0.016	0.016
π_{29}	0.73	0.73
π_{30}	0.73	0.73
π_{34}	0.005	0.005

6.5.3 Thermal Radiation Heat Transfer Pi Groups

The radiative heat transfer from the rod is expressed by the terms Π_{31}, Π_{32}, Π_{33}, Π_{35}, and Π_{36}. The reference rod, for which the energy balance is described, is assumed to be a rod in the central region of the bundle, specifically in the inner 3x3 sub-array. These Pi groups describe the radiative heat transfer from the hot rod to dummy rods, to housing, to liquid droplets, to vapor and to the nominal rods in the outer region of the bundle. Due to the housing, the outer region of the bundle will be at a lower temperature compared to the inner region. This will cause a radial temperature distribution across the bundle which will drive rod-to-rod radiative heat transfer from the center region. A detailed model to address this phenomenon has been developed and is described in Section 7.

The same phenomenon exists for the Pi groups for the rod equation, as

$$\Pi_{31} = \frac{h_{R,r/s,i} A_{R,r/s,i} \left(T_{co} - T_s\right)}{Q'''_{f,i} V_{f,i}} = \frac{Q_{r/s}}{Q'''_{f,i} V_{f,i}} \tag{6-118}$$

$$\Pi_{32} = \frac{h_{R,r/H,i} A_{R,r/H,i} \left(T_{co} - T_H\right)}{Q'''_{f,i} V_{f,i}} = \frac{Q_{r/H}}{Q'''_{f,i} V_{f,i}} \tag{6-119}$$

$$\Pi_{33} = \frac{h_{R,hr/cr,i} A_{R,hr/cr,i} \left(T_{co,hr} - T_{co,cr}\right)}{Q'''_{f,i} V_{f,i}} = \frac{Q_{hr/cr}}{Q'''_{f,i} V_{f,i}} \tag{6-120}$$

$$\Pi_{35} = \frac{h_{R,r/d,i} A_{R,r/d,i} \left(T_{co} - T_{sat}\right)}{Q'''_{f,i} V_{f,i}} = \frac{Q_{r/d}}{Q'''_{f,i} V_{f,i}} \tag{6-121}$$

$$\Pi_{36} = \frac{h_{R,r/v,i} A_{R,r/v,i} \left(T_{co} - T_v\right)}{Q'''_{f,i} V_{f,i}} = \frac{Q_{r/v}}{Q'''_{f,i} V_{f,i}} \tag{6-122}$$

These dimensionless groups are calculated by solving the six node radiative network already discussed in the previous section. In this case, a different set of boundary conditions is used from previously discussed (Table 6.2).

The radiative heat transfer from the rod to the surfaces (unheated rods) is described by

$$\Pi_{31} = \frac{Q_{r/s}}{Q'''_{f,i} V_{f,i}}$$

where $Q_{r/s}$ and $Q'''_{f,i}V_{f,i}$ have both dimensions of heat rate per unit length. The heat rate $Q_{r/s}$ is the energy flowing from one of the hot rods (inner 3x3 sub-array) to the dummy rods and the normalization factor $Q'''_{f,i}V_{f,i}$ is based to the peak power location:

$$Q'''_{f,i}V_{f,i} = 0.7 \text{ kW/ft} = 2296 \text{ W/m} \tag{6-123}$$

From the network solution

$$Q_{r/s} = Q_{13}$$

The heat rate is identically zero since the view factor from the inner 3x3 rods to the unheated rods at the corners is identically zero. As a consequence, the resistance R_{12} becomes infinite and

$$\Pi_{31} = 0.0$$

The same procedure is applied for the calculation of the next Pi group representing the direct radiative heat transfer from the rod to the housing

$$\Pi_{32} = \frac{Q_{r/H}}{Q'''_{f,i}V_{f,i}}$$

where

$$Q_{r/H} = Q_{14}$$

which gives

$$\Pi_{32} = 0.0272$$

The radiative heat transfer from the hot rod to the cold rods (rod-to-rod) radiation is expressed by

$$\Pi_{33} = \frac{Q_{hr/cr}}{Q'''_{f,i}V_{f,i}}$$

where

$$Q_{hr/cr} = Q_{12}$$

which gives

$$\Pi_{33} = 0.388$$

The heat rate from the hot rod to the droplet and the vapor, respectively, is described by

$$\Pi_{35} = \frac{Q_{r/d}}{Q'''_{f,i} V_{f,i}}$$

$$\Pi_{36} = \frac{Q_{r/v}}{Q'''_{f,i} V_{f,i}}$$

From the network, Qr/d and Qr/v are

$$Q_{r/d} = Q_{1l}$$

$$Q_{r/v} = Q_{1v}$$

The calculated result becomes

$$\Pi_{35} = 0.154$$

$$\Pi_{36} = 7.88e^{-4}$$

The results of the calculations are summarized in Table 6.18. As seen in the table, the rod-to-rod radiative heat transfer (hot rod to cold rod) is the largest contribution. This term can also be seen as an indirect path for radiative heat transfer from the inner rods to the housing. In fact the housing reduces the temperature of the external rods because of radiation heat transfer. This generates a radial temperature gradient among the rods which drives energy from the inner region to the outer region of the bundle. This effect is more prototypical for a BWR than a PWR fuel assembly due to the fuel channel used for BWRs, and will be discussed further.

This analysis overestimates the effect of the housing because the housing thermal resistance in the azimuthal direction is not considered since only one node is used to simulate the housing.

To model this effect, the housing must be split in many separate surfaces with each surface thermally connected by azimuthal conductivity. This has been done in the more detailed COBRA-TF subchannel model described in Section 9. The COBRA-TF results indicate that the corners of the housing are at a lower temperature than the rest of the housing temperature predicted by the BUNDLE simple conduction model. In other words, for the same heat stored in the housing the more exposed portion of the housing surface will be at a higher temperature than predicted by a single surface model. This will reduce the heat removed by radiation from the heater rods.

Table 6.18 Numerical Values of Pi Groups - Rod Energy Equation

Π_i	Definition	Ratio of	Value for RBHT	Value for PWR	RBHT PWR	Value for BWR	RBHT BWR
Π_{24}	$\frac{\rho_{f,j} c_{p,f,j} (T_{f,CL} - T_z)}{\tau_f Q'''_{f,j}}$	Stored energy/time / Initial heat generation rate	0.965	1.180	0.818	1.160	0.832
Π_{25}	$\frac{k_{f,j} (T_{f,CL} - T_z)}{R_f^2 Q'''_{f,j}}$	Clad heat Conduction rate / Initial heat generation rate	0.182	0.182	1.0	0.11	1.655
Π_{26}	1	Initial power / Initial heat generation rate	1	1	1	1	1
Π_{27}	$\frac{\rho_{c,j} V_{c,j} c_{p,c,j} (T_{ci} - T_{co})}{V_{f,j} Q'''_{f,j} \tau_c}$	Clad stored energy/time / Heat generation rate	0.110	0.040	2.75	0.051	2.157
Π_{28}	$\frac{k_{c,j} V_{c,j} (T_{ci} - T_{co})}{V_{f,j} Q'''_{f,j} R_o^2}$	Clad conduction heat rate / Heat generation rate	0.016	0.016	1	0.009	1.778
Π_{29}	$\frac{h_{gap,j} A_{i,j} (T_z - T_{ci})}{V_{f,j} Q'''_{f,j}}$	Heat transfer rate from pellet to clad / Heat generation rate	0.73	0.73	1	0.565	1.292
Π_{30}	$\frac{h_{c,j} A_{c,j} (T_{co} - T_{sat})}{V_{f,j} Q'''_{f,j}}$	Convective HT rate / Heat generation rate	0.73	0.73	1	0.556	1.313
Π_{31}	$\frac{h_{R,\%,j} A_{R,\%,j} (T_{co} - T_z)}{V_{f,j} Q'''_{f,j}}$	Radiation HT rate to surfaces in bundle / Heat generation rate	0.00	0.235	0	0.336	0

Table 6.18 Numerical Values of Pi Groups - Rod Energy Equation (Continued)

Π_{32}	$\frac{h_{R,r/H,i} A_{R,r/H,i} (T_{co} - T_H)}{V_{f,i} Q'''_{f,i}}$	Radiation HT rate to housing Heat generation rate	0.027	0	Does not exist as Π term for PWR is zero	0.030	0.9
Π_{33}	$\frac{h_{R,hr/cr,i} A_{R,hr/cr,i} (T_{co,hr} - T_{co,cr})}{V_{f,i} Q'''_{f,i}}$	Radiation HT rate from hot rods to cold rods Heat generation rate	0.388	0.064	6.063	0.324	1.197
Π_{34}	$\frac{h_{W,i} A_{W,i} (T_{CO} - T_{sat})}{V_{f,i} Q'''_{f,i}}$	Liquid contact HT rate Heat generation rate	0.005	0.005	1	0.005	1
Π_{35}	$\frac{h_{R,r/d,i} A_{R,r/d,i} (T_{co} - T_{sat})}{V_{f,i} Q'''_{f,i}}$	Radiation HT rate to entrained drops Fuel rod heat generation rate	0.154	0.159	0.969	0.259	0.595
Π_{36}	$\frac{h_{R,r/v,i} A_{R,r/v,i} (T_{co} - T_v)}{V_{f,i} Q'''_{f,i}}$	Radiation HT rate to vapor Fuel rod heat generation rate	0.000	0.001	Insignificant *	0.00	Insignificant *

* - Both numbers are very small, so the ratio is insignificant.

6.5.4 Summary

The Pi groups obtained for the rod energy equation indicate that the significant terms are the convective heat transfer to the surrounding fluid, the radiation from hot rod to cold rod and radiation to entrained drops. Property differences between the electrical rod and the nuclear rod exist and hence the Pi groups involving the properties of the rods are different. One particular Pi group, Π_{24}, is about 20 percent higher for the nuclear rod. This is because of the low thermal conductivity of UO_2 and also due to the fact that at start up, a nuclear rod has very high amount of stored energy. The effect of this difference will be discussed in Section 7.

6.6 Calculation of Pi Groups for Flow Momentum Equation

The flow momentum equation Pi groups are calculated using the given inlet conditions of 40 psia, 140 degrees F subcooling, and flooding rate 25.4 mm/s (1 in/s) and flow area. The inlet is assumed to be single phase and the exit is dispersed two-phase mixture. The quench front is assumed to be at the 1.2 m (4 ft) elevation and two grids are underwater; therefore, there are six grids in the two phase region. Hydraulic diameter is calculated based on the wetted perimeter and flow area. Based on this hydraulic diameter, the Reynolds number and the single phase friction factor (f = 64/Re) are calculated.

For two phase frictional pressure drop, all the two phase mixture is assumed to be liquid, so that a two-phase multiplier can be used. The exit void fraction is taken to be 0.999. For an average quality of 50 percent and low pressure conditions, it is appropriate to assume an average two-phase flow multiplier, $\overline{\phi_{fo}^2}$, to be 100.

Table 6.19 shows numerical values for all the Pi groups for the fluid momentum equation.

Table 6.19 Fluid Momentum Pi Groups

π Group	Value
$\pi_{37} = \pi_{38} = \pi_{39}$	$8.9e^{-6}$
π_{40}	1
$\pi_{41} = \pi_{42}$	0.999
$\pi_{43} = \pi_{44}$	$7.0e^{-4}$

The only Pi group of significance is $\Pi_{40,}$ which represents the liquid gravity head pressure drop. All other non dimensional groups are insignificant by comparison. This was expected since the differential pressure cells have been used to infer average void fraction in previous FLECHT and FLECHT-SEASET experiments because the frictional and acceleration effects are small.

The calculated Pi groups, along with their definitions, are reported in Table 6.20.

Table 6.20 Numerical Values of Pi Groups - Fluid Momentum Equation

Π_i	Definition	Ratio of	Value for RBHT	Value for PWR	RBHT PWR	Value for BWR	RBHT BWR
$\Pi_{37} = \Pi_{38} = \Pi_{39}$	$\frac{W_i^2}{2\rho_i g A^2 L_T}$	Velocity head / Gravity head	0.000	0.000	1 (Identical numbers, very close to zero)	0.000	1 (Identical numbers, very close to zero)
Π_{40}	1	Maximum gravitational driving head / Gravity head	1	1	1	1	1
$\Pi_{41} = \Pi_{42}$	α_g	Vapor head / Gravity head	0.999	0.999	1	0.999	1
$\Pi_{43} = \Pi_{44}$	$\frac{W_i^2}{2\rho_i^2 g A^2 L_T} R_{f_{tp}}$	Total single phase frictional resistance / Gravity head	0.000	0.000	1 (Identical numbers, very close to zero)	0.000	1 (Identical numbers, very close to zero)

6.7 Calculation of PWR and BWR Pi Groups

6.7.1 Introduction

Pi groups calculated for the RBHT Test Facility, a PWR and BWR assembly is given in Tables 6.14, 6.18 and 6.20. The values obtained were compared, and distortions due to scaling identified. Using this approach, it can be seen whether or not the RBHT Test Facility replicated prototypic behavior. The closer the values of the Pi group are for the test facility and the PWR or the BWR, the more similar is the behavior. The Pi groups which are not dependent on the material properties but only on the fluid conditions should be similar. Those Pi groups which are a function of the material properties will be different for the test facility and the PWR or the BWR, since the material properties are different.

Table 6.3 compares the different Pi groups for the test facility and a PWR fuel assembly and indicates possible test distortions relative to the fuel assembly being modeled. These comparisons indicate that many of the Pi terms are preserved since the rod bundle geometry models that of a PWR fuel assembly and the initial conditions are preserved in the tests relative to the reactor. However, there is no housing in the PWR fuel assembly. So to ensure similarity, the Pi groups which represent the heat transfer processes associated with the housing must be small relative to the other transport terms in Equation 6-26.

Similarly, Table 6.4 compares the Pi groups for the test facility to the Pi groups for the BWR fuel assembly. Since the BWR assembly has a channel surrounding the fuel rods, the same terms and Pi groups derived for the RBHT Test Facility are also present for the BWR fuel assembly. The terms can have different magnitudes since the materials are different between the test and the BWR fuel assembly.

6.7.2 Calculation of Pi Groups for PWR

The Pi groups for the fluid energy, which represent the flow energy, energy storage, convection to rods, housing, grids and dummy rods were evaluated for a PWR. Firstly, there is no housing for a PWR, hence the convection heat transfer from the vapor to the housing is zero. Those Pi groups which are dependent only on the flow conditions and independent of the material properties, will be the same for the test facility and the PWR, since the geometry, including the dimensions of rods, grids, etc. for the test facility and the PWR are the same.

Therefore, the fluid energy storage, flow energy, and convection Pi groups are all identical for the PWR. Thus, the only Pi groups that will be different are the quench terms and those involving radiation heat transfer.

The PWR quench energy groups Π_3, Π_4, Π_5 and Π_6 are calculated using the same method as for the RBHT Test Facility, however, the PWR core material properties and geometry are used (Zircaloy, UO_2, etc.). Note that in this case the housing is not present and the scaling group describing the quench of the housing is zero by definition. The calculated values are reported in Table 6.14.

The thermal radiation Pi groups for the PWR are calculated with a modified version of the RADNET computer program to account for the typical Westinghouse 17x17 rod bundle geometry. In a PWR, the housing is not present and only portion of the core section is considered. The situation assumed in the calculation is that of a hot assembly surrounded by eight colder assemblies as depicted in Figure 6.5. To reduce the size of the problem, this core portion (nine assemblies) is assumed to be 90 degrees symmetric. Moreover, because of the geometry, radiation from the hot assembly cannot penetrate beyond seven rows into the cold rods. This reduces the problem to a 15x15 array. Thimble locations are described in the same Figure 6.5. At this point, the VUEFAC subroutine of the MOXY code is used to calculate the single rod-to-rod view factors matrix and these values are combined to produce the global view factors. The node surface areas are calculated in the computer program RADNET, as described in Appendix B.1.

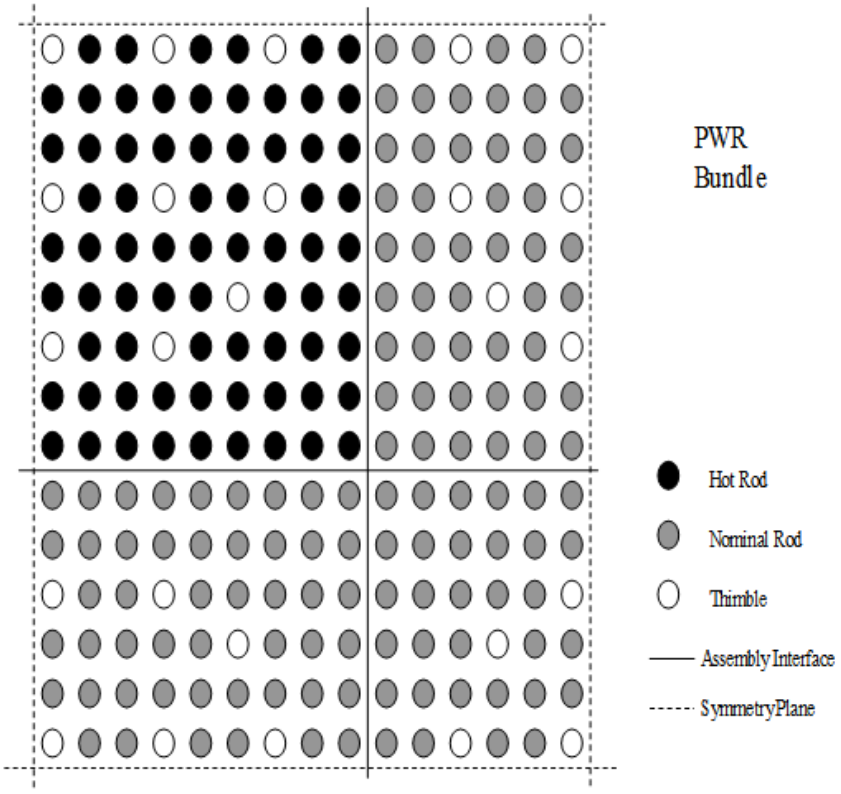

Figure 6.5 PWR Bundle Lumping Approach.

To simulate the absence of the housing in a PWR core, the resistances from each node to node 4 in the network are set to a very large number (practically infinite). Then the same node temperatures for the RBHT Test Facility are applied at the network external nodes and the program is solved for the radiosity in the other nodes. Finally, following the same procedure utilized for the RBHT case, the PWR fluid energy equation Pi groups for radiation heat transfer are calculated.

The numerical values for PWR Pi groups for the radiation terms for the fluid energy and rod energy equations are shown in Tables 6.14 and 6.18.

Similar to the RBHT, the fluid momentum Pi groups are calculated for the PWR and results are reported in Table 6.20.

The Pi group for the interfacial heat transfer will be the same for the test facility, PWR and BWR.

Comparing these terms to that for the test facility, minor differences can be seen. The spacer grids used in the test are prototypical, so the form loss term will be the same for both the plant and the test. The frictional term, however, can be different since in the test there is a housing which adds additional wetted perimeter such that the hydraulic diameter is smaller for the same flow area. The smaller hydraulic diameter results in a lower Reynolds number for the same flow condition and hence a higher friction factor, but the differences in the values are quite small. The emissivity of Inconel 600 is slightly lower than Zircaloy and this causes some differences in radiation terms.

6.7.3 Calculation of Pi Groups for BWR

The Pi groups for the fluid energy, which represent the flow energy, energy storage, convection to rods, housing, grids and dead rods have been evaluated for a BWR. Since the BWR fuel assembly is surrounded by a channel, which acts as a housing, the Pi groups related to the housing are not zero as in a PWR. It should be noted that the Pi groups which are dependent only on the flow conditions and independent of the material properties and geometry are the same for the RBHT Test Facility and the BWR fuel assembly.

In the fluid energy equation, based on the above, it is evident that the Pi groups representing the fluid energy storage terms and, the flow energy terms, Π_1, Π_2, Π_7, Π_{22} and Π_{23}, will be the same as that of the test facility, as they depend only on the flow conditions. The interfacial heat transfer term, (Π_{20}) will also be the same as it depends only on the fluid condition and the number of drops. The Pi groups for the convection to rod, housing, grid and dead rod will be different because of a different rod diameter for a BWR fuel rod.

The stored energy and convection terms for the rod energy equation Pi groups for BWR are somewhat different because the dimensions of the rod is different for a BWR compared to a PWR. Also the time constants for the cladding and the fuel are higher for a BWR. These Pi groups are presented in Tables 6.14 and 6.18.

The BWR quench energy groups are calculated by the same method used for the RBHT Test Facility, using BWR core material properties and geometry (Zircaloy, UO_2, etc.). For simplicity, the same T_{min} is assumed in the calculation for both Zircaloy and Inconel. Note that in this case the housing is represented by the channel walls. The quench energy Pi groups for the BWR are shown in Table 6.14.

To calculate the thermal radiation Pi groups for the BWR, the RADNET computer program was modified to account for the different bundle geometry typical of a typical GE 8x8 rod bundle. In this case the housing is represented by the channel walls. The situation assumed in the calculation is a 4x4 hot assembly surrounded by two rows of colder assembly as depicted in Figure 6.6. The cold surfaces are the two water rod in

the center of the channel. The VUEFAC subroutine of the MOXY code is used to calculate the single rod-to-rod view factors matrix and then by combining properly these values, the global view factors and node surface area are calculated in the RADNET computer program, as described in Appendix B.1 for the RBHT Test Facility.

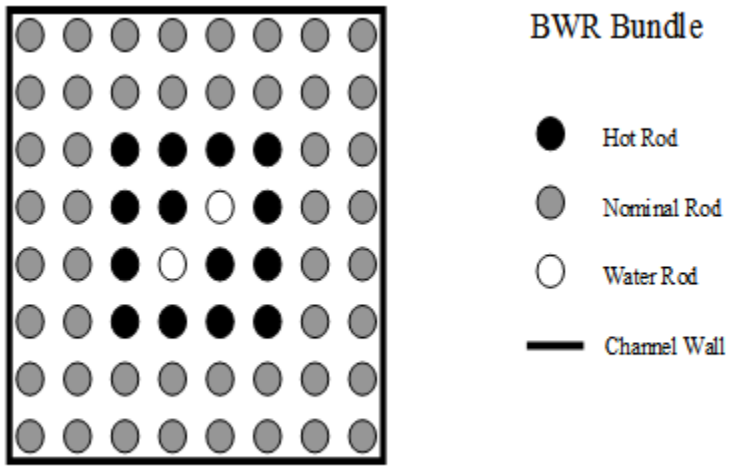

Figure 6.6 BWR Bundle Lumping Approach.

The same node temperatures used for the RBHT Test Facility are applied at the network external nodes and the program solves for the radiosity in the other nodes. Finally, following the
same procedure utilized for the RBHT case, we calculate the BWR fluid energy equation Pi groups for the radiation heat transfer. The numerical values are reported in Tables 6.14 and 6.18.

The Pi groups for the fluid momentum equation for the BWR will be the same as that of a PWR, based on the conditions of flooding rate of 1 in/s.

6.8 Conclusions

The fluid energy equation, the rod energy equation and the bundle fluid momentum equations have been developed for the RBHT Test Facility. These equations were made dimensionless using the initial and boundary conditions such that dimensionless Pi groups were developed to examine similitude between the RBHT Test Facility and a PWR and a BWR fuel assembly. From the scaling analysis, it is found that the presence of a test housing leads to extra Pi groups for this structure relative to a PWR fuel assembly, thereby indicating that distortion in the test is possible.

The test facility is actually a closer representation to a BWR fuel assembly which also has a Zircaloy channel or shroud surrounding the fuel rods. Therefore, for code modeling and validation purposes, the effect of the test housing must be modeled including the rod-to-rod and rod-to- housing radiation heat transfer. The housing effects must also be considered in the analysis of the test data to determine effect of radiation.

The housing had a less important effect on the fluid momentum equation since it only affected the hydraulic diameter and resulting fluid Reynolds number and friction factor such that the frictional component of the fluid pressure drop would be somewhat larger than a PWR fuel assembly. Since the majority of the pressure drop in the bundle is due to the spacer grid form losses and the elevation head and since the prototypical grids are used in the test bundle, the hydraulic distortion is negligible.

There also can be some difference in the PWR/BWR Pi groups relative to the test due to the material differences as seen in Tables 6.14, 6.18 and 6.20. These effects are relatively small and can be accounted for in the analysis of the data.

Comparisons of the derived Pi groups for the test and a PWR and a BWR fuel assembly indicate that if prototypical fluid conditions are used in the tests, and the bundle geometry is retained, there is a very strong similarity between the bundle and the PWR and BWR fuel assemblies and the data should be applicable to either reactor fuel assembly type.

6.9 References

1. Larson, T. K., et al, "Scaling Criteria and Assessment of Semi-scale Mod-3 Scaling for Small-Break Loss of Coolant Transients," EGG-SEMI-5121, 1980.

2. Ishii, M. and I. Kataoka, "Scaling Criteria for LWRs under Single-Phase and Two-Phase Natural Circulation," Proc. Joint ANS/NRC Meeting on Basic Thermal-Hydraulic Mechanisms in LWR Analysis, NUREG/CP-0043, Bethesda, MD, 1982.

3. Zuber, N., "An Integrated Structure and Scaling Methodology for Severe Accident Analysis, Appendix D, A Hierarchical Two-Tiered Scaling Analysis", NUREG/CR-5809, 1991.

4. Wulff, W., "Scaling of Thermal Hydraulic Systems," Nuclear Engr. and Design, Vol 163, pg. 359-395, 1996.

5. Zuber, N., "Presentation at March 28, 1997 ACRS Thermal Hydraulic Phenomena Subcommittee Meeting," Rockville, MD.

6. Reyes, J. R., Hochreiter, L. E. and L. Lau, "AP600 Low Pressure Integral systems Test at Oregon State University, Facility Scaling Report," WCAP-14270, 1995.

7. Brown, W. L., Hochreiter, L. E. and M. J. Loftus, "AP600 Scaling and PIRT Closure Report", WCAP-14727, 1997.

8. Lee, N., Wong, S., Yeh, H.C. and L. E. Hochreiter, "PWR FLECHT-SEASET Unblocked Bundle Forced and Gravity Reflood Task Data Evaluation and Analysis Report," NUREG/CR-2256, 1981.

9. Mohr, C. L. et al., "Prototypic Thermal-Hydraulic Experiment in NRU to simulate Loss-of-Coolant Accidents," NUREG/CR-1882, 1981.

10. Kreith, F. and M. S. Bohn, “Principles of Heat Transfer,” Fourth Edition, Harper and Row Publishers, New York, 1986.

11. Evans, D.R., “The MOXY Core Heat Transfer Program: View Factor Model Improvements,” RE-E-77-114, 1977.

12. Collier, J. G. and J. R. Thome, “Convective Boiling and Condensation,” Oxford Science Publications, Oxford, 1994.

13. “An Integrated Structure and Scaling Methodology for Severe Accident Technical Issue Resolution,” NRC Research, NUREG/CR - 5809, Nov 1991.

14. Lewis, E. E., “Nuclear Power Reactor Safety,” John Wiley & Sons, New York, 1977.

7. SECOND TIER SCALING FOR THE ROD BUNDLE HEAT TRANSFER TEST FACILITY

7.1 Introduction

Following the two-tier scaling methodology approach, Section 6 examined the "Top Down" scaling of the RBHT Test Facility relative to a PWR fuel assembly as well as a BWR fuel assembly. The individual Pi groups were calculated from the normalized conservation equations for the test facility, a PWR fuel assembly and a BWR fuel assembly. The calculations indicated which terms in the conservation equations were dominant for each configuration. The ratio of the Pi group calculations for the test and either the PWR or BWR fuel assembly indicated where the test facility had possible scaling distortions. The distortions were larger for the representation of the PWR fuel assembly by the RBHT test facility as compared to a BWR fuel assembly since there is no fuel assembly channel in the PWR fuel assembly, as compared to the test facility, while the BWR fuel assembly contains a fuel channel.

The top-down scaling analysis indicated three areas where scaling distortion could exist in the RBHT test facility relative to a PWR or BWR fuel assembly. They are:

1. The presence of the housing which can act as a radiation and convection heat sink for the fluid and heater rods, as well as a heat source to the fluid as the housing quenches. The housing also changes the hydraulic diameter of the outer subchannels slightly such that there is lower flow in the outer subchannels, and correspondingly higher flow in the center of the bundle. However, this effect is small.

2. The material differences between the electrical heater rods and the nuclear rods which include a gap between the fuel pellet and the cladding

3. The material differences in the cladding which can affect the T_{min} value and hence the quenching rate of the heater rods verses nuclear rods. Also included in this difference are the local effects of the surface, including roughness and oxide layer.

The bottom-up scaling effort has been performed specifically to examine these differences so that identified distortions can be assessed and methods found to account for or minimize their effects in the testing, data reduction, and data analysis. In the bottom-up scaling approach, analysis was performed to determine the radiation heat transfer effects of the test section housing relative to an infinite size rod bundle. These calculations would tend to over-emphasize the distortion of the test relative to a PWR fuel assembly. The BWR fuel assembly channel is similar to that of the RBHT facility so the distortion is less.

Calculations were also performed modeling a fuel rod, with its properties and the fuel- pellet gap as well as the electrical heater rod, to determine the heat released at quench as well as the stored energy effects and maximum temperatures and radial temperature distributions.

The differences in cladding material on the value of T_{min} were assessed by comparing Inconel and Zircaloy cladding quench data from different tests. These comparisons indicated that Zircaloy quenches at a higher temperature relative to stainless steel or Inconel cladding.

The analysis and data comparisons for each of the identified areas of distortion are given in the remainder of this Section.

7.2 Housing Effects and Studies

7.2.1 Introduction

One of the main distortions of the RBHT facility compared to a PWR fuel assembly is the presence of the housing, which represents a heat sink for radiative heat transfer from the rods. The housing can also be a heat source for the fluid later into the transient because of the release of its stored energy during the quench time period.

To address housing effects in more detail, a single rod-to-rod, rod-to-housing model based on the MOXY computer program (Ref. 1) was developed. MOXY was used to calculate the view factors matrix while a new program was written, called BUNDLE, to calculate the combined conduction-convection-radiation heat transfer in a cross section of the rod bundle. The BUNDLE program considers a cross section with each rod simulated individually, as well as the housing.

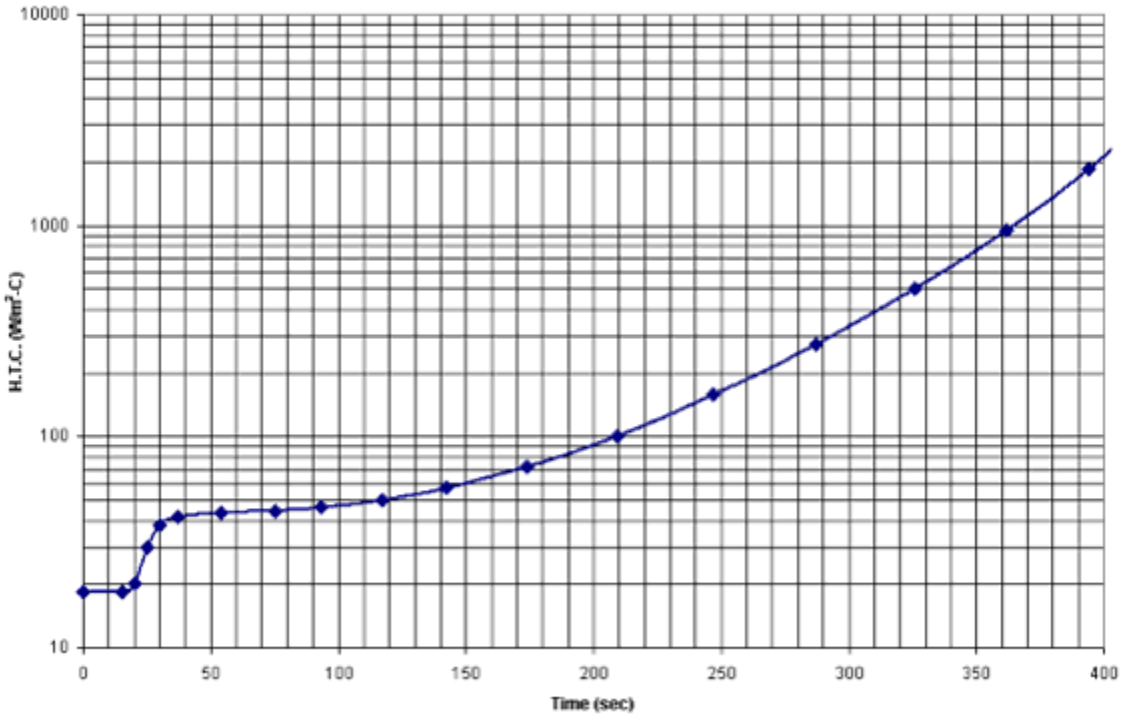

Figure 7.1 Convective Heat Transfer Coefficient (FLECHT-SEASET Run 31504).

The VUEFAC subroutine was extracted from the MOXY computer program and included in BUNDLE to calculate the view factors matrix. The program calculates the temperature field in the bundle cross section during the reflood transient. The model solves thermal conduction in the rods and the housing, convection heat transfer to the fluid and radiative heat transfer among

the rods and the housing surfaces. Convection to the fluid is simulated by assigning the time history of the heat transfer coefficient estimated from the FLECHT-SEASET Run 31504 test data (Ref. 2), as shown in Figure 7.1. In addition, when the temperature in the hottest rod falls below T_{min}, the heat transfer coefficient is set to a very large value 5678 W/m^2-K (1000 Btu/hr-ft^2-F) to force all the structures to quench at that time.

The radiative heat transfer to the droplets and to the vapor is neglected in the BUNDLE program while fluid is assumed transparent to the radiation. The thermal radiation heat transfer between the surfaces and the fluid (steam and droplets) is considered in the simplified lumped parameter approach using the RADNET computer program described in Section 6.4.4. More details of the model as well as the computer program list can be found in Appendices C.1 and C.2. The base case was a 7x7 bundle with four zero power (dummy) rods in the corner of the array. The other parameters are given in Table 7.1.

Table 7.1 Input Data

Rod Power (kW/rod)	5.0 kW/ft.
Power radial distribution	Uniform
Wall surface emissivity	0.80
Bundle heat loss (h_{out}), W/m^2-K (Btu/hr-ft^2 -F)	0
Fluid convective heat transfer coefficient (h_{in})	See Figure 7.1
Initial temperature dummy rods, ^{o}C (^{o}F)	232.22 (450)
Initial temperature power rods, ^{o}C (^{o}F)	871.11 (1600)
Initial (pre-heating) temperature, ^{o}C (^{o}F)	232.22 (450)
Fluid temperature, ^{o}C (^{o}F)	147.5 (268) (T_{sat})

The heat transfer coefficient at the inside surface of the housing is assumed equal to the convective heat transfer coefficient used for the heater rods and is based on FLECHT-SEASET Test data.

7.2.2 Results

Figure 7.2 shows the clad temperature of the center rod, the inner 3x3 and 5x5 array averages, the housing and cold (dummy) rods surface temperature. The PCT temperature is reached at about 50 s while the maximum housing temperature is reached later at about 200 s. At about 250 s the clad temperature at the hottest rod falls below T_{min} and all structures are quenched. Note that the quenching time of the housing is larger than that for the other structures. Figure 7.3 shows the heat rate (W/m) release from the rods to the housing and the heat released from the housing to the fluid. The heat transfer rate is very high when the housing quenches. Figure 7.4 shows the same results with an expanded y-axis. The maximum heat transfer rate from the rods to the housing is about 25 percent of the heat generated in the bundle. The housing

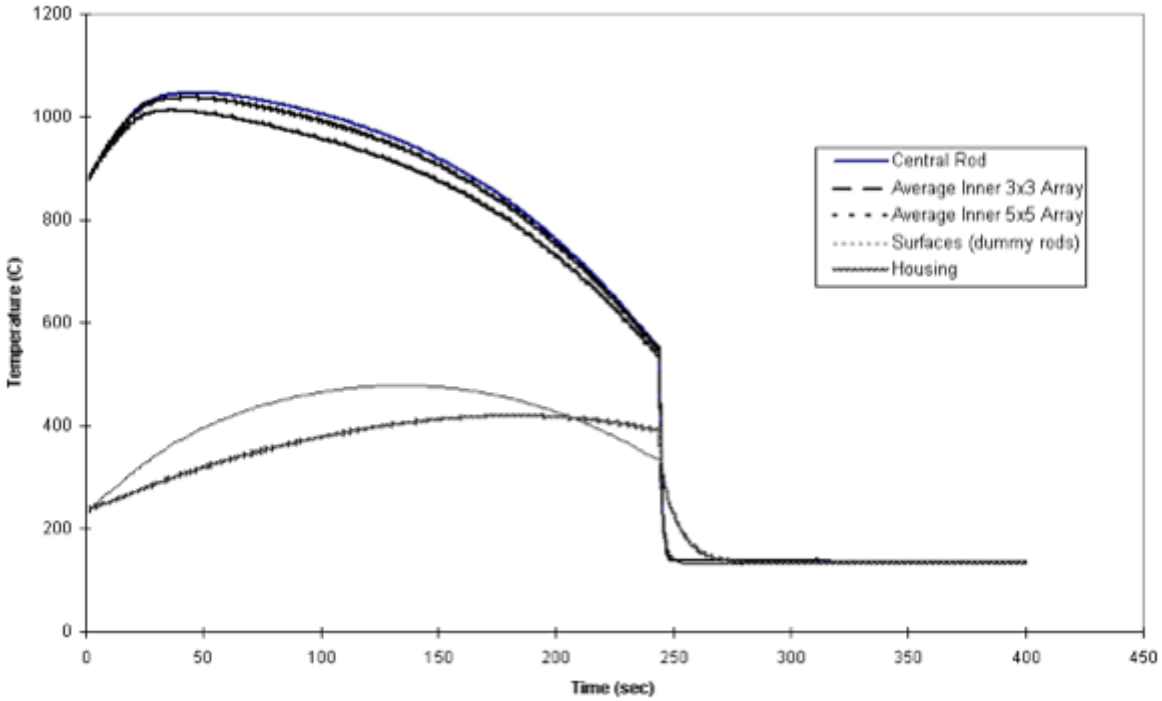

Figure 7.2 Wall Surface Temperature in the 7x7 Bundle (Base Case).

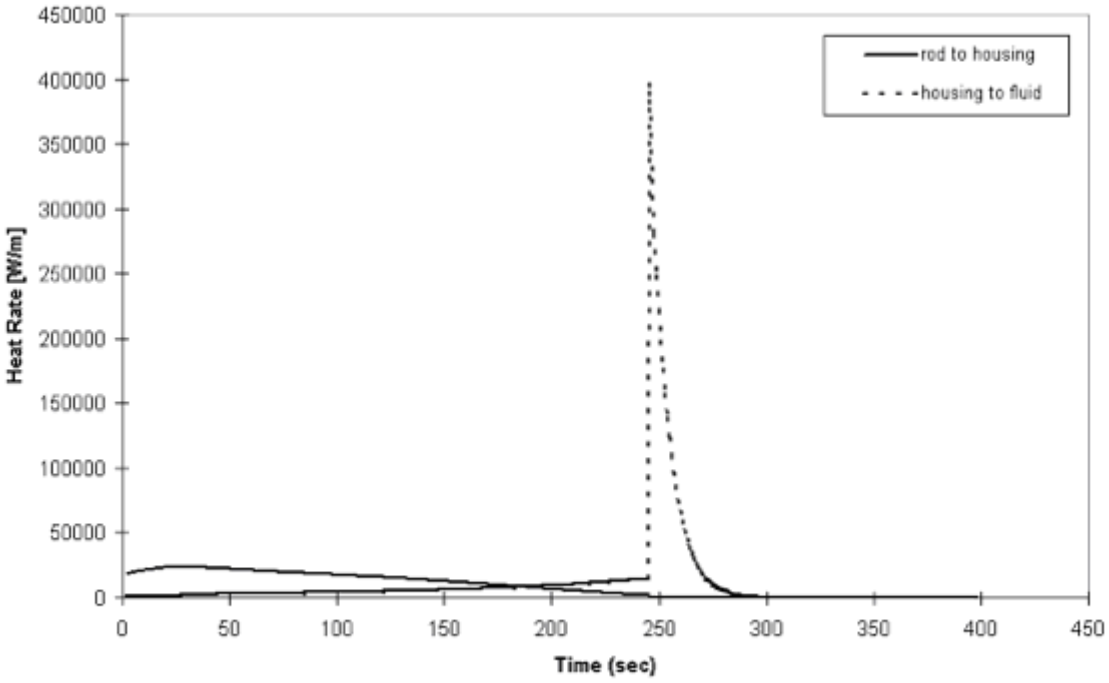

Figure 7.3 Heat Rate To and From the Housing in the 7x7 Bundle (Base Case) (Bundle Linear Power = 103000 W/m).

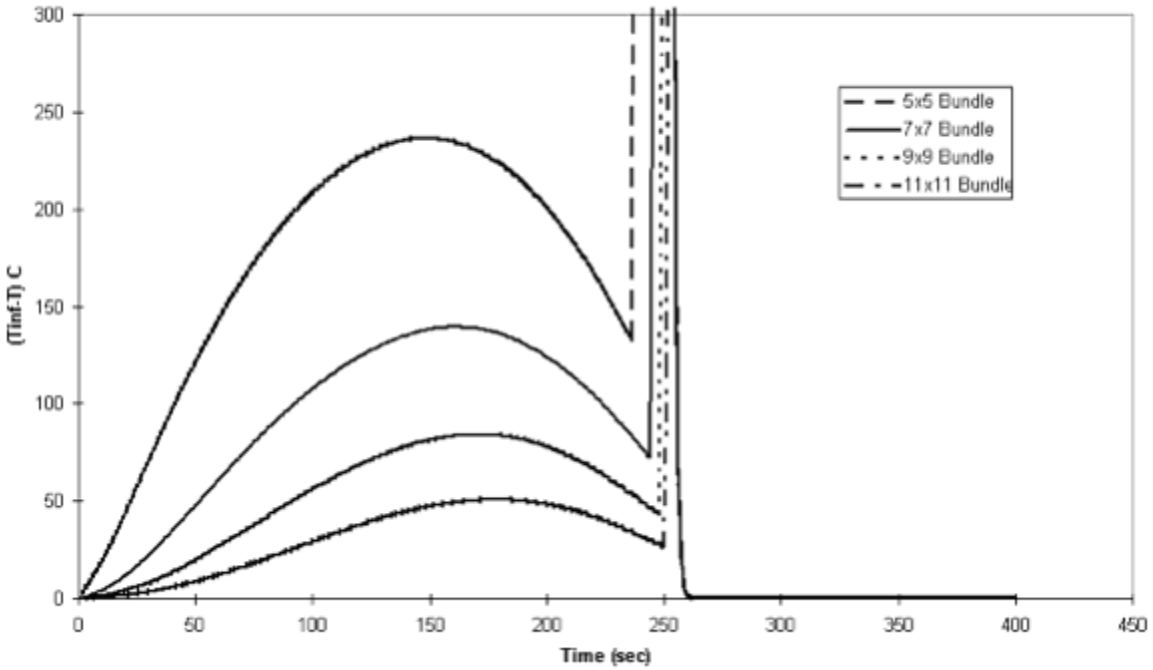

Figure 7.4 Clad Temperature Drop in the Inner 3x3 Array Because of Radiative Heat Transfer in a Finite Size Bundle Array.

releases energy to the fluid early in transient by convection to the steam and later to the mixture during the quench time.

The heat transfer from the rods to the fluid, particularly from the outer rods, can be a two-step process in which the energy first passes to the housing via radiation and then to the fluid by convection. This is described by Figure 7.4 which shows that the radiative heat rate from the rods to the housing reaches its maximum value of 24 kW/m at about 35 s, then decreasesalmost linearly to 2 kW/m at about 245 s, when quench occurs. In the same time period, the convective heat rate from the housing to the fluid rise from nearly 0 to about 15 kW/m. Then the remaining energy stored in the housing is released during the quench period which last about 20-30 s. During quenching, the convective heat rate from the housing to the fluid increases to 400 kW/m.

Note that the temperature gradient which develops radially across the bundle as a consequence of the presence of the housing is overestimated by these calculations because of the assumptions used. In reality, thermal radiation from the rods to the fluid (droplets and vapor) will tend to reduce the temperature of the inner rods, therefore, the heat transfer to the external rods and the housing will be lower than the calculated value. Another effect is the convective heat transfer coefficient, which is assumed uniform in the calculation. In reality, the convective heat transfer coefficient will be higher in the center region of the bundle. Again, this effect will reduce the temperature gradient across the bundle.

Quasi steady-state calculations were carried out for the FLECHT 15x15 bundle using a radiative network approach (Ref. 3) similar to the one described in Section 6. In this case the radiative heat transfer from the inner rods to the housing was estimated to be 10 to 20 percent of the convective heat transfer depending on the flow conditions. Note that the FLECHT bundle was larger than the 7x7 RBHT bundle.

Sensitivity studies were performed to the base case (Table 7.1) to optimize the facility designing by reducing the scaling bias where possible, as follows:

1. bundle size (3x3, 5x5, 7x7,…,17x17,infinite)
2. housing thickness
3. housing pre-heating
4. surfaces emissivity
5. radial power distribution
6. dummy rods (cold-surfaces) contribution

Results are summarized in the following and presented in Figures 7.5 through 7.10.

7.2.2.1 *Bundle Size*

The calculation of the clad temperature for an infinite array with a constant radial power distribution results in a rod-to-rod temperature gradient which is zero since radiative heat transfer does not take place and the clad temperature is determined only by the fluid convection. An indication of the radiative heat transfer contribution for a finite array is the difference between the average clad temperature in the central rods sub-array as calculated for a finite size bundle and the same value calculated for an infinite size bundle. The selected sub-array is the inner 3x3 rods and the temperature drop defined is $\Delta T_{\infty} = \Delta T_{\infty} - T_{3x3}$. This temperature difference represents the facility distortion when compared to the temperature expected when the same boundary condition are applied in a real PWR core which is essentially an infinite array.

Figure 7.4 shows the value of ΔT_{∞} for different bundle sizes (5x5, 7x7, 9x9 and 11x11). The time at which the quench is occurring is earlier in the finite bundle respect to the infinite bundle case. As a consequence, the significant clad temperature drop which is experience during the quench is earlier than in the small bundle size. This effect is indicated in Figure 7.5, which shows the difference between the clad temperature in the hypothetical infinite bundle and the clad temperature in the finite size bundle. Figure 7.4 shows that the quench time is anticipated by about 17 s in 5x5 bundle, by about 7-8 s in the 7x7 bundle and a smaller value for larger bundle sizes.

Before the quenching, the maximum temperature distortion is reached between 150 and 200 s into the transient, depending on the bundle size. For the 7x7 bundle, a maximum value of 138 degrees C (250 degrees F) is predicted, the maximum distortion decreases to 83 degrees C (150 degrees F) for a 9x9 bundle and to 55.6 degrees C (100 degrees F) for an 11x11 bundle. For the 5x5 bundle size the maximum temperature distortion is up to 222.4 degrees C (400 degrees F) which is much larger than the 138 degrees C (250 degrees F) maximum temperature distortion experienced in a 7x7 bundle. In conclusion, when compared to the infinite bundle array, the 7x7 bundle is good compromise when low costs and scaling biases are

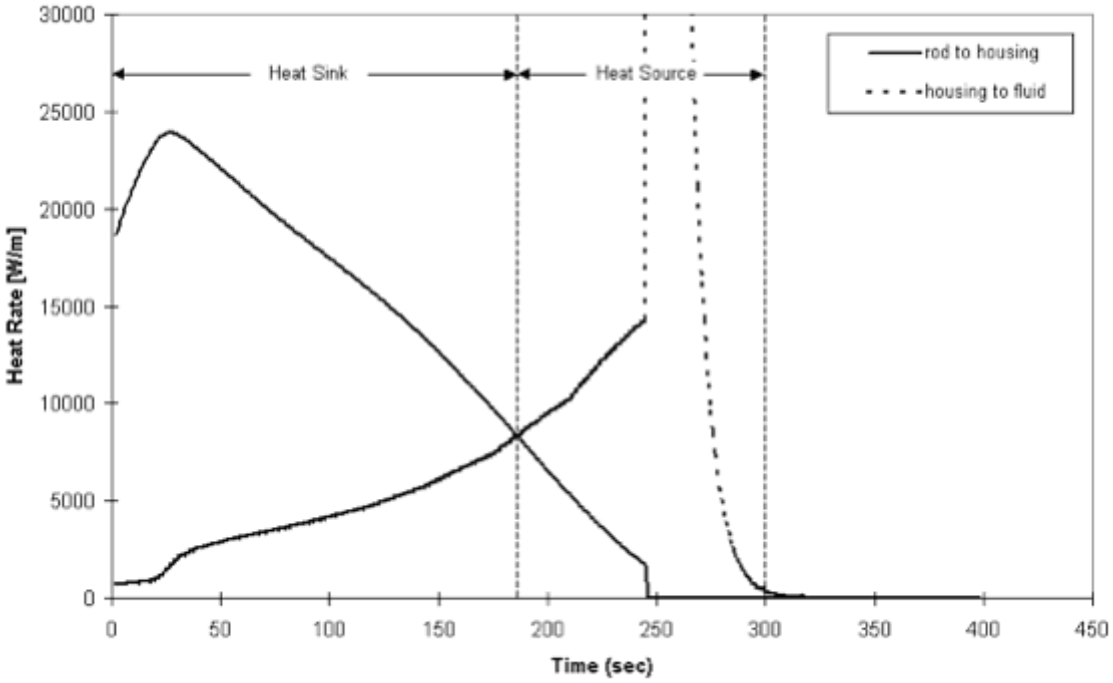

Figure 7.5 Heat Rate To and From the Housing in the 7x7 Bundle (Base Case) (Bundle Linear Power = 103000 W/m).

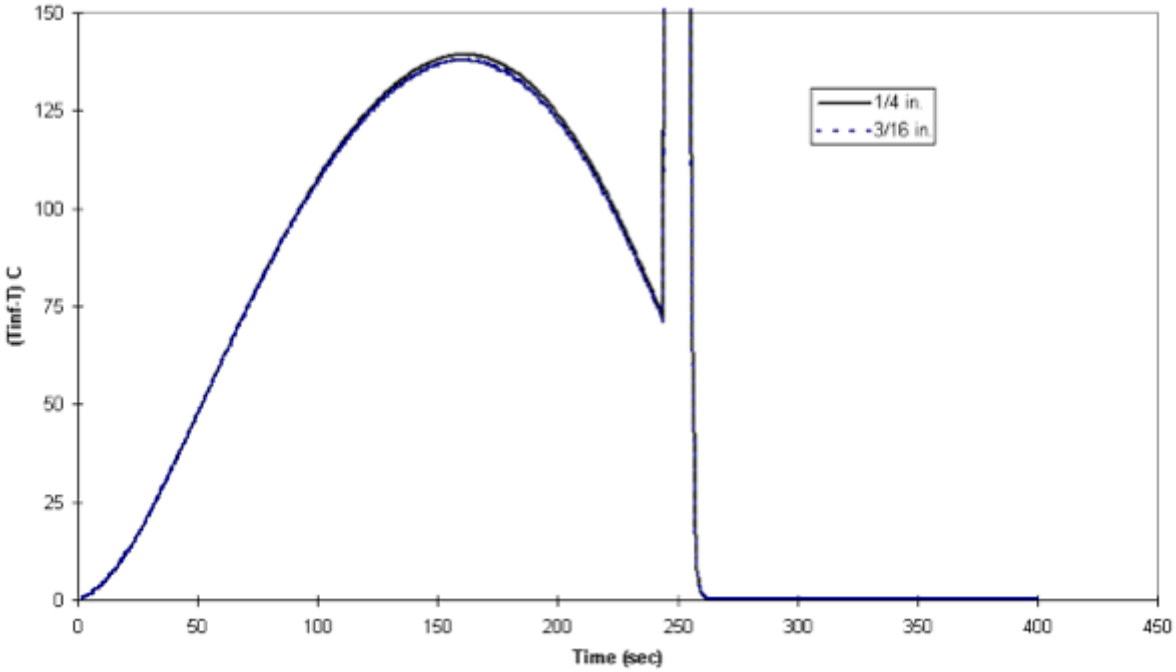

Figure 7.6 Inner 3x3 Rod Array Clad Temperature Bias in RBHT Bundle Housing Thickness Sensitivity.

both a concern in the facility design. A larger bundle will provide a more prototypic behavior with a reduced temperature bias but the costs due to the additional rods increases dramatically.

7.2.2.2 *Housing Thickness*

The housing is both a heat sink and a heat source during the reflood transient, and represents a bias which should be minimized by reducing its thickness to a minimum. The housing is a heat sink for the thermal radiation from the external rods and is a heat source to the fluid as the quench front approaches, as seen in Figure 7.5. The housing heat release is very large during quenching. A 6.35 mm (¼ in) thick housing was chosen to provide enough strength for the facility operation. To quantify the effect of the housing thermal inertia, two sensitivity cases were run with 6.35 and 4.76 mm ($^3/_{16}$ and ¼ in) thick housing. Results shown in Figure 7.6 indicate that in this range the solution is insensitive to the housing thickness. In conclusion the variation of the housing thermal inertia is negligible in the thickness range of interest.

7.2.2.3 *Housing Preheating*

To reduce the rod temperature drop introduced by the presence of the housing, the housing could be pre-heated before the reflood begins to reduce the radiative heat transfer between the rods and the housing during the early part of the reflood. An optimum preheating temperature value will exist. A high temperature reduces the radiative transfer between rods and housing; however, it increases the metal heat release to the fluid during quenching. The base case considered an initial housing temperature of 250 degrees C (450 degrees F) while the sensitivity case assumed an initial housing temperature of 556 degrees C (1000 degrees F). Results are shown in Figure 7.7. The temperature drop ΔT_{∞} for the center 3x3 array is lower for higher pre-heating temperature, 556 degrees C (1000 degrees F), but the difference between the two cases is less than 40 degrees F, indicating that initial heating has a weak effect.

7.2.2.4 *Surface Emissivity*

Some uncertainty exists in surface emissivity, which is a function of surface conditions (roughness, oxidation, etc.). Emissivity, in turn, affects radiative heat transfer. For oxidized Inconel-600, the literature provides emissivity values ranging from 0.7 and 0.9. A sensitivity analysis was performed to address this effect. Figure 7.8 shows that the temperature uncertainty introduced by the emissivity uncertainty is less than 11 degrees C (20 degrees F).

7.2.2.5 *Axial Power Distribution*

The base case considers a uniform radial profile with zero power in the four corner rods. The possibility of increasing the peripheral rods to provide a “shield” to rod-to-housing heat transfer was investigated. A 20 percent increase in power was applied to the external rods while keeping the same (5.0 kW/rod) power in the interior rods (i.e., the total power in the bundle increases by about 9 percent). Figure 7.9 shows that the maximum value of ΔT_{∞} decreases of about 20 degrees F.

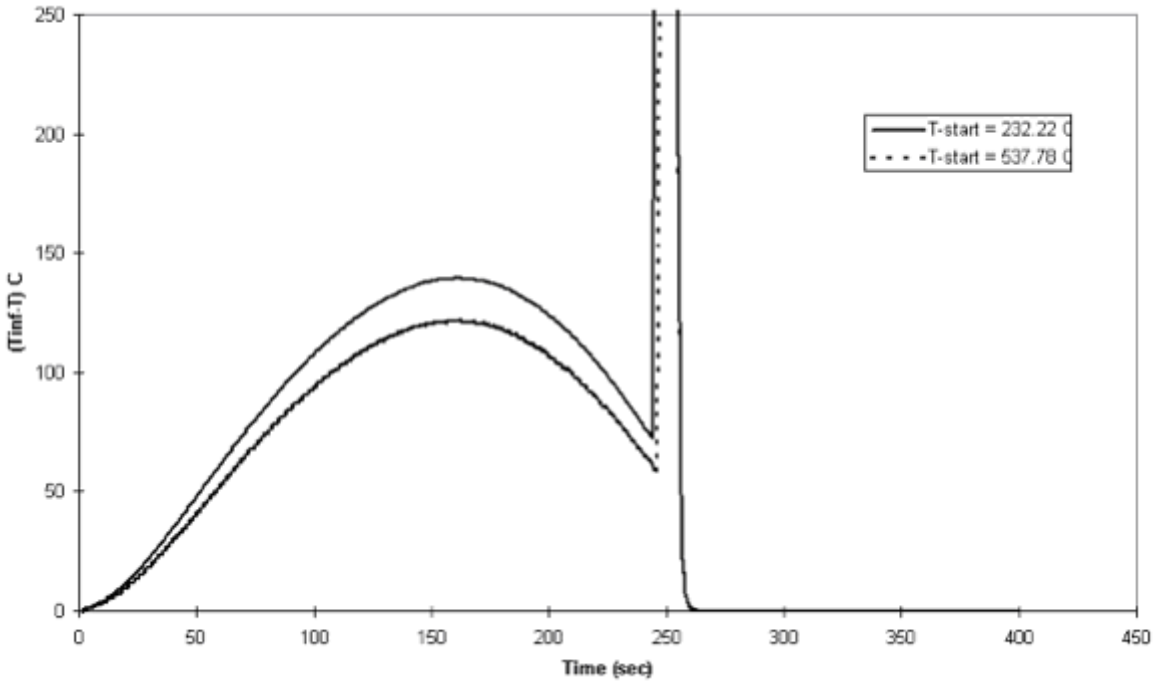

Figure 7.7 Inner 3x3 Rod Array Clad Temperature Bias in RBHT Bundle Housing Initial (Pre-Heating) Temperature Sensitivity.

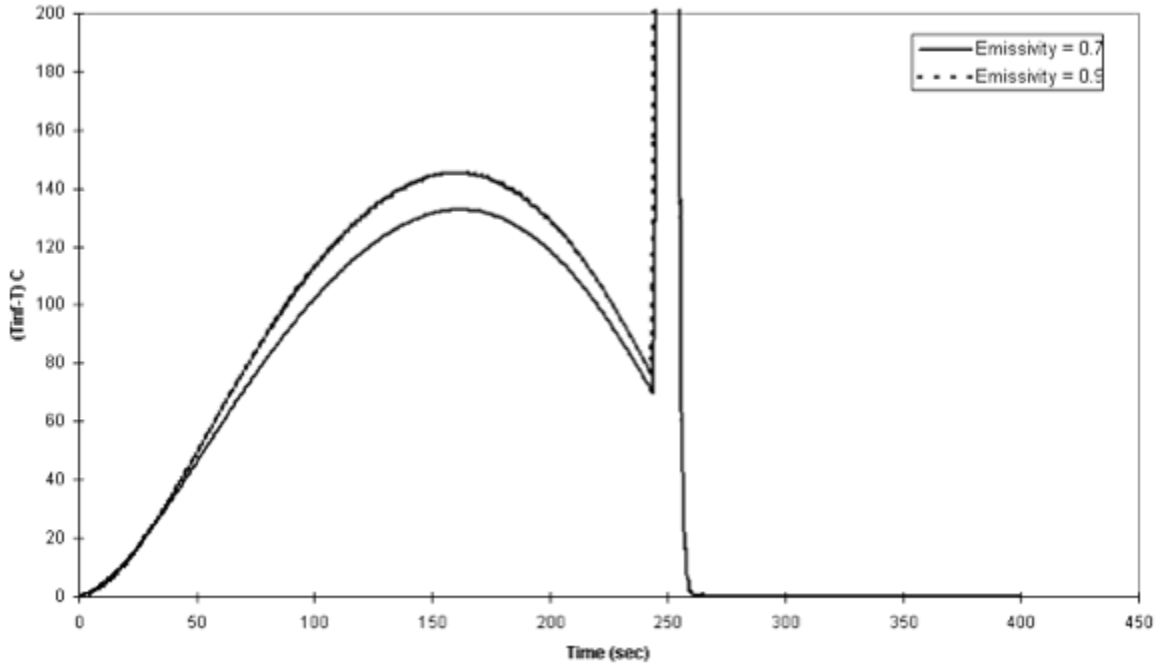

Figure 7.8 Inner 3x3 Rod Array Clad Temperature Bias in RBHT Bundle Wall Emmissivity Sensitivity.

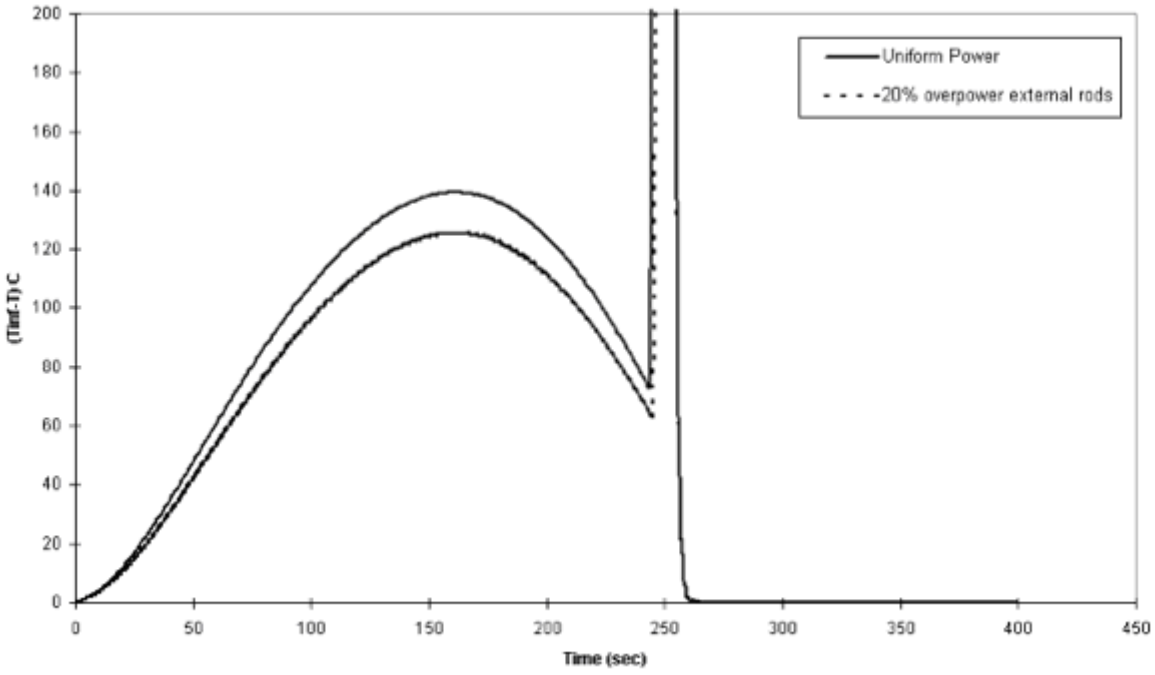

Figure 7.9 Inner 3x3 Rod Array Clad Temperature Bias in RBHT Bundle Radial Power Distribution Sensitivity.

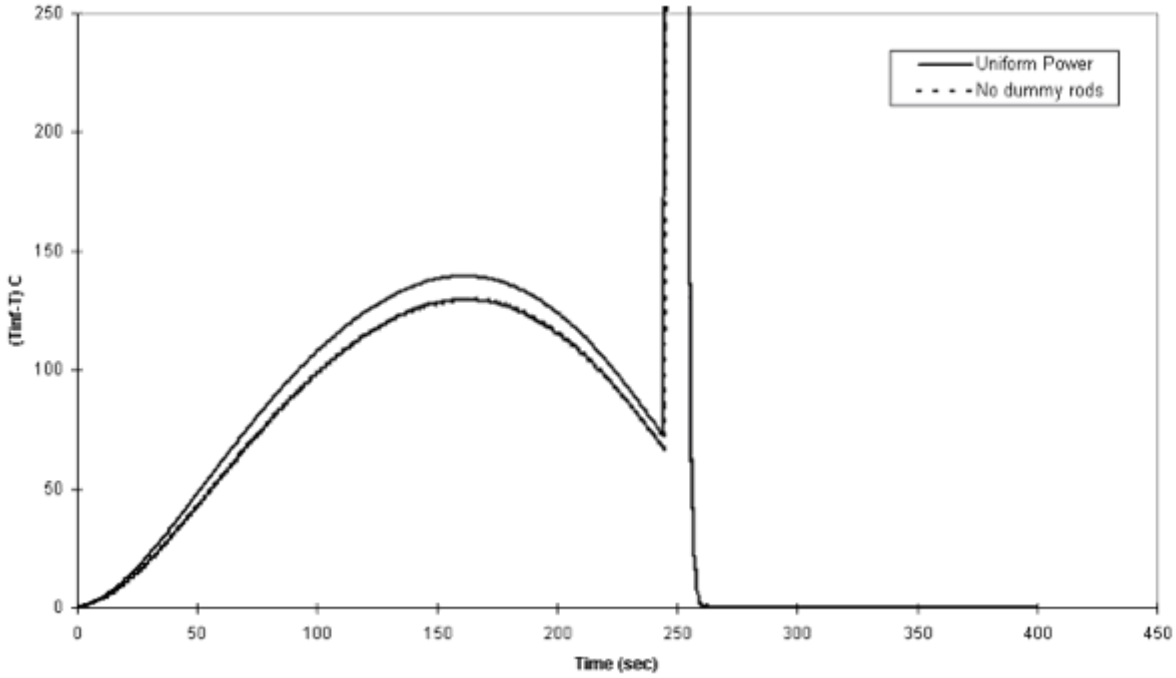

Figure 7.10 Inner 3x3 Rod Array Clad Temperature Bias in RBHT Bundle Dummy Rods Effect.

7.2.2.6 *Effect of the Corner Dummy Rods*

The effect of the dummy rods in the four corners of the bundle is shown in Figure 7.10. The calculation is based on the same rod power (5.0 kW/rod) and the total power of the bundle is the same of the previous sensitivity case (9 percent greater than the base case). The effect of the dummy rods is to decrease ΔT_{∞} by about 10 degrees F. This is a secondary effect to the radiative heat transfer from the inner rods in the bundle. The conclusion from the six sensitivity studies is that the parameter of most importance is bundle size. A large gain (~50 percent) occurs in increasing the bundle size from 5x5 to 7x7. Further gains are made by increasing the bundle size to 11x11, however, the facility cost would increase accordingly by approximately a factor of four. The other parametric variations are small by comparison.

7.3 Material Differences

7.3.1 Introduction

Another issue which arose from the scaling analysis is the rod material differences. The electrical heater rods use Inconel-600 instead of Zircaloy for the clad and Boron Nitride instead of Uranium Dioxide. The electric power is generated only in an annulus area inside the rod where the heating element, Monel K-500, is located. Another difference is the gap conductance which is assumed to be 5679 W/m^2-K (1000 Btu/hr-ft^2-F) for a nuclear rod and 28385 W/m^2-K (5000 Btu/hr-ft^2-F) for the electrical rod. A detailed analysis was performed to quantify the transient temperature response distortion of an electrical rod when compared with a nuclear rod.

The BUNDLE computer program was used to simulate a transient conduction problem for a single rod. The radiation heat transfer is turned off for this case. The transient was basically a step change in the convection heat transfer coefficient while keeping constant rod power and fluid temperature. The step change was applied after a steady-state was reached where the surface temperature is assumed to be at T_{min}. This transient can be a simplified view of the quench process. Consistent with Section 6, T_{min} was set to 550 degrees C (1022 degrees F). The initial convective heat transfer coefficient is calculated assuming a steady state condition where the rod surface temperature is exactly at T_{min}. The conditions of the transient are given in Table 7.2.

7.3.2 Rod Comparison

Figure 7.11 shows the temperature profile at the initial steady state for both the heater rod and the nuclear rod with a clad surface temperature of 550 degrees C (1022 degrees F). The difference in the profiles is because of conductivity: UO_2 is about a factor 20 lower than the BN/Monel conductivity; therefore, the nuclear rod has a higher centerline temperature than the electric rod for the same clad surface temperature.

An additional contribution to the above difference is the gap conductance which larger for the heater rod by approximately a factor of five. This effect is shown in Figure 7.12.

Table 7.2 Input Data

Rod Power (kW/rod)	0.7 kW/ft.
Fluid temperature, ^{o}C (^{o}F)	131 (267)
Initial heat transfer coefficient, W/m^2-K (Btu/hr-ft^2 -F)	183.4 (32.3)
Final heat transfer coefficient, W/m^2-K (Btu/hr-ft^2 -F)	5679 (1000)
Initial $T_{clad} = T_{min}$	550 (1022)
Conductivity of UO_2, W/m-K (Btu/hr-ft-F)	2.4 (1.4)
Conductivity of BN, W/m-K (Btu/hr-ft-F)	85.9 (49.6)
Gap Conductance (nuclear rod), W/m^2-K (Btu/hr-ft^2 -F)	5679 (1000)
Gap Conductance (electrical rod), W/m^2-K (Btu/hr-ft^2 -F)	28385 (5000)

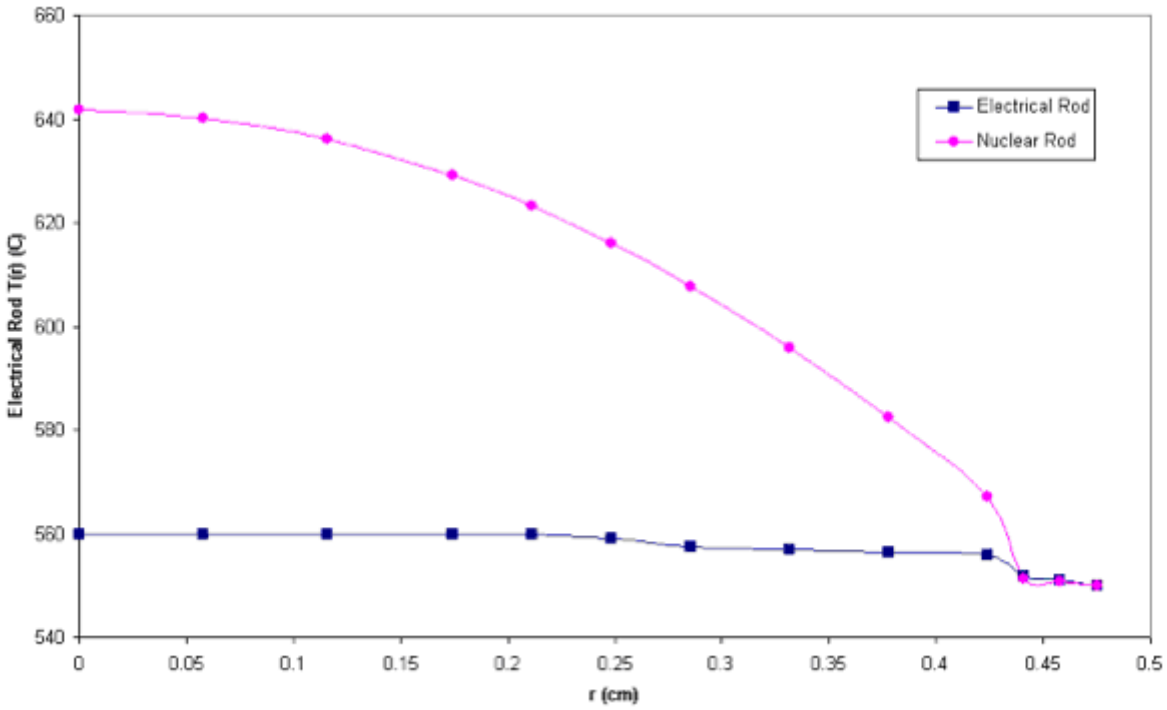

Figure 7.11 Steady-State Temperature Profile.

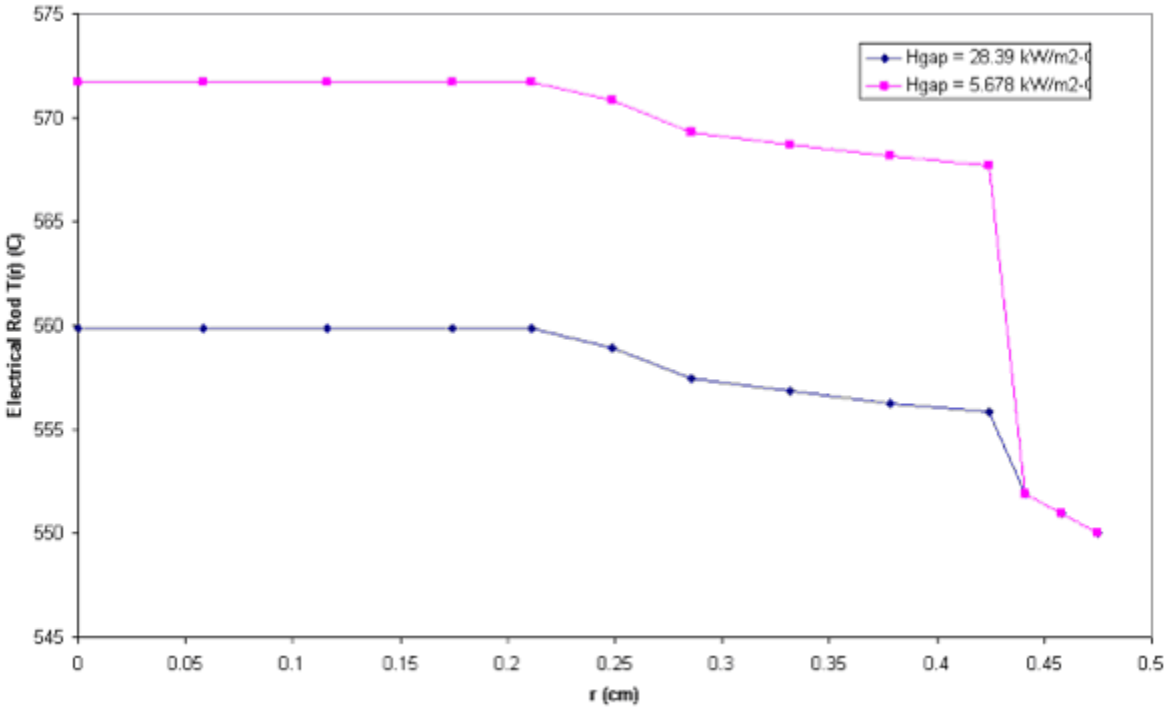

Figure 7.12 Electrical Rod Steady-State Temperature Profile Gap Resistance Sensitivity.

The top-down analysis indicated that the stored energy in the fuel region is comparable between the nuclear rod and heater rod. On the other hand, more energy is stored in the Inconel cladding than Zircaloy cladding so that the total amount of stored energy is somewhat larger for the heater rod. The larger amount of energy which resides in the cladding of the heater rod is released quickly during quenching, as shown in Figure 7.13. Figure 7.14 shows the amount of stored energy released during the transient. This value was calculated by integrating over time the power released minus the power generated as:

$$E_{quench} = \int_o^t (q(t) - q_o)dt$$

where

$q(t)$ = Power released to the fluid

q_o = Rod Power (0.7kW/ft)

t_o = Initiation of quench

Figure 7.14 shows that the electrical rod releases a larger amount of energy more quickly. The time constant for the energy release is consistent with that calculated with a simple double-lumped approach, described in Section 6.

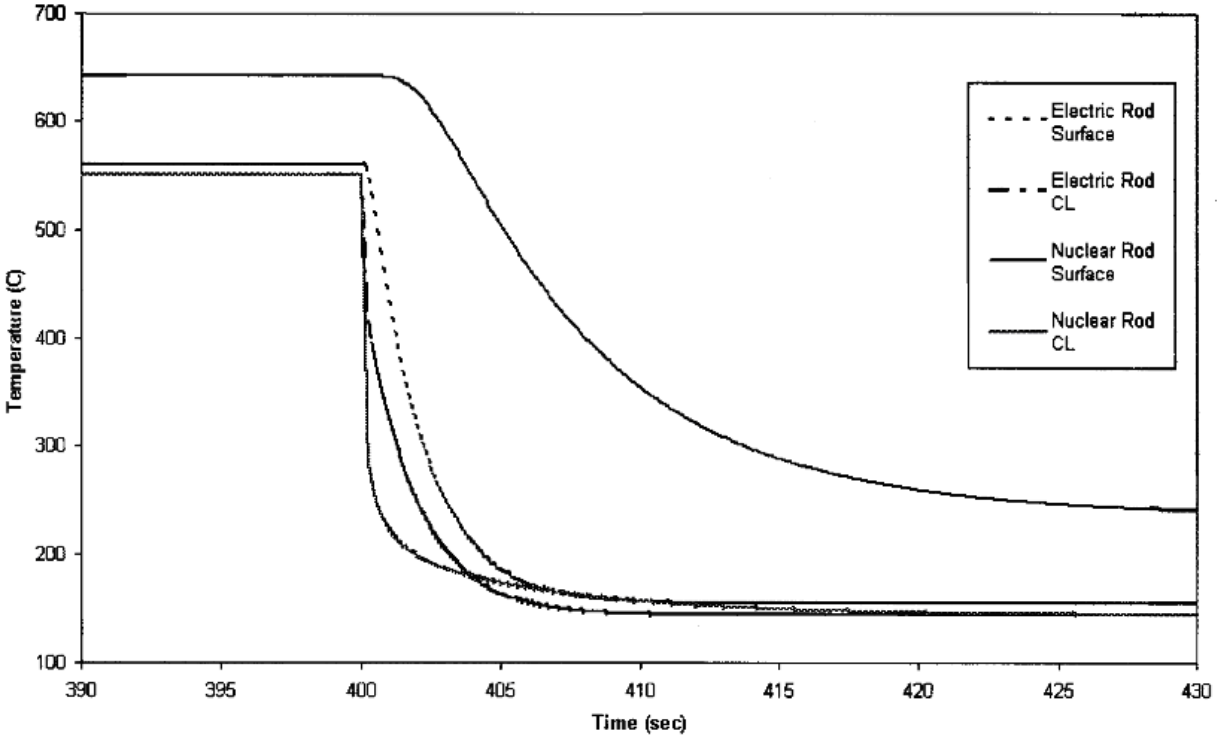

Figure 7.13 Rod Quenching.

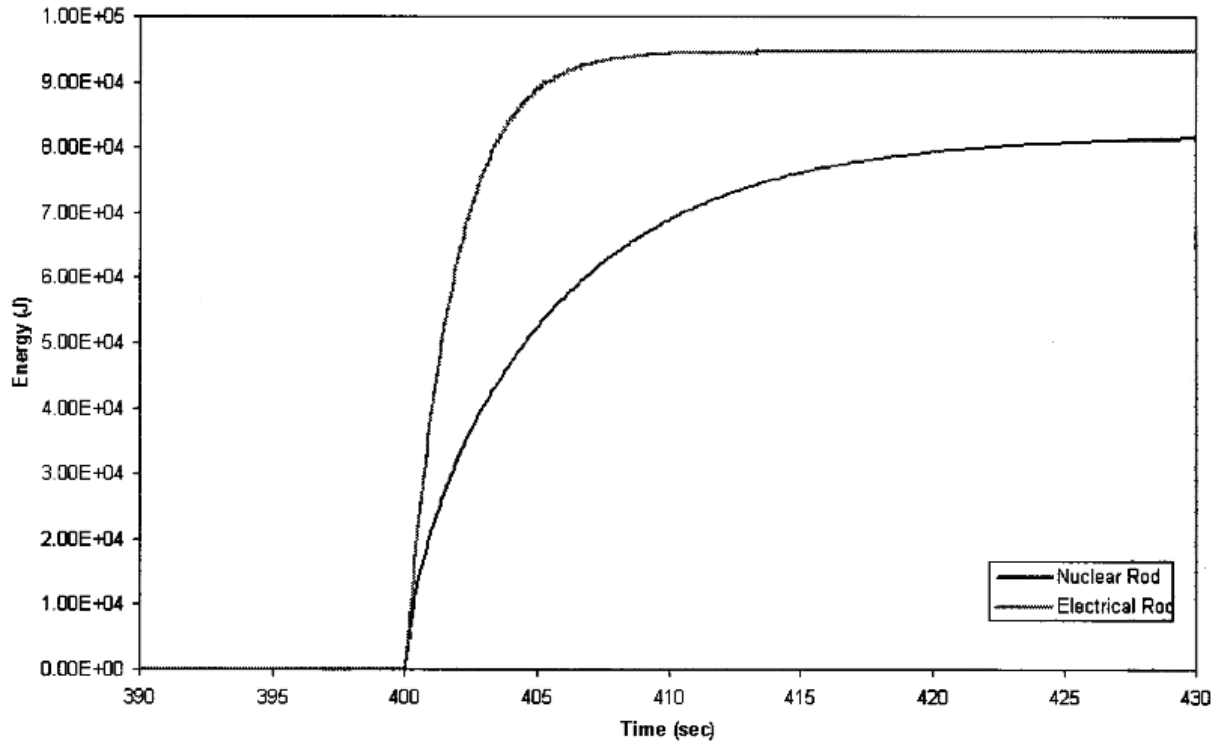

Figure 7.14 Rod Quench Energy Release.

7.4 Surface Properties Differences

The surface properties which can affect the reflood behavior are the wall surface emissivity and the factors that determine minimum film boiling temperature $T_{min.}$

The Zircaloy surface emissivity can be slightly higher than the Inconel-600 even though the uncertainty in its real value is sometimes larger than the difference between the two materials. The wall emissivity depends on many factors such as temperature and oxidation of the surface. The effect of the wall emissivity on the rod-to-rod and rod-to-housing radiative heat transfer was addressed by the sensitivity analysis presented in Section 7.2.

Figure 7.15 shows the distribution (Ref. 6) of experimental rewet temperatures based on Westinghouse G-1 and G-2 blowdown experiments (Refs. 7 and 8). A mean value of 536 degrees C (998 degrees F) was found. Prototypic thermal hydraulic experiments (Ref. 9) for Zircaloy cladding indicate an average value of 575 degrees C (1068 degrees F). Zircaloy will quench at higher temperature than stainless steel or Inconel.

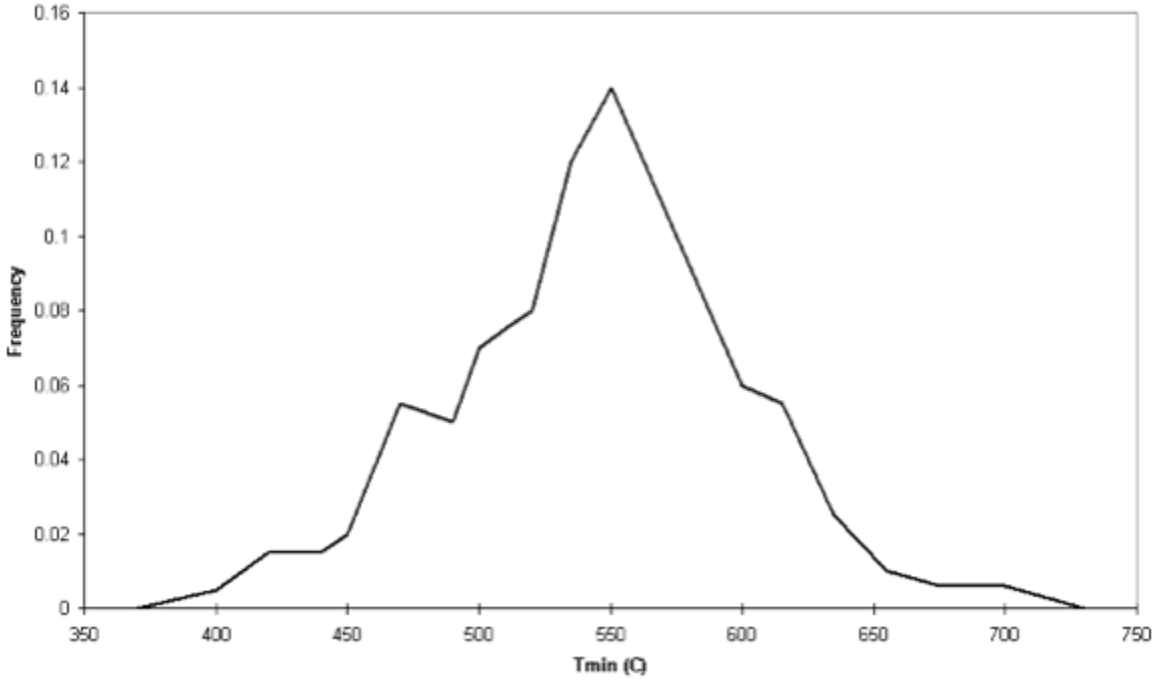

Figure 7.15 Distribution of Measured Rewet Temperatures During Westinghouse G-1 and G-2 Blowdown Rod Bundle Experiments.

7.5 Scaling Conclusions

The three areas where scaling distortion could exist between the RBHT Test Facility and a PWR or BWR fuel assembly were indicated during the first tier scaling analysis described in Section 6. Section 7 presented the bottoms-up scaling analysis and addressed these distortions in more detail.

During the early part of reflood, the housing acts as both a radiation and convection heat sink for the fluid and heater rods, whereas with the approach of the quench front it acts as a heat source. The presence of the housing causes a radial temperature distribution across the bundle which in turn drives energy from the inner portion of the bundle to the housing. As a result, during the transient, the temperature in the inner region of the RBHT bundle is lower than the temperature in an ideal case.

The effect of the housing is less important for a large bundle since the inner region is shielded by the outer region of the bundle. Sensitivity analyses were performed to quantify the housing distortion for different bundle sizes, from 5x5 to 11x11 arrays. The distortion decreases significantly when the bundle size is increased from 5x5 to 7x7, while for further increases the distortion reduction is progressively less and less significant. A 7x7 bundle size is a reasonable compromise between cost and scaling distortion. For a 7x7 array, the maximum temperature distortion to the inner 3x3 rod array with respect to an infinite (no-housing) bundle is about 121 degrees C (250 degrees F).

Sensitivity studies were performed to evaluate the effects of the housing thickness, housing initial temperature, emissivity, radial power distribution and dummy rods contribution. These were found to be of second order importance. Their effect on the temperature in the center region is about 28 degrees C (50 degrees F) at most.

The material differences between the electrical heater rods and the nuclear rod, which also includes a gap between the fuel pellet and the cladding, is the second major facility distortion. The analysis shows that the quench time can be affected by material properties. The stored energy is 15 percent larger in the heater rod compared with the nuclear rod. The amount of energy in the fuel region is similar. The difference resides in the Inconel cladding of the heater rod. The conductivity of the “fuel” region of the electrical rod is 20 times higher than the nuclear rod. Therefore, if we assume the same heat transfer coefficient at the quench front, the stored energy is released more rapidly in the heater rod versus the nuclear rod. This introduces a bias in the experiments which must be determined. This bias will be lower than predicted by this simplified analysis. In fact, if more energy is released to a given volume of liquid, the heat transfer coefficient will decrease and this will in turn reduce the heat release rate in the electric rod.

In addition, differences of the cladding material on the value of T_{min} were assessed by comparing Inconel and Zircaloy cladding quench data from different tests. These comparisons indicated that there is a difference. The Zircaloy cladding will quench at a higher temperature relative to stainless steel or Inconel cladding.

7.6 References

1. Evans, D. R., “The MOXY Core Heat Transfer Program: View Factor Model Improvements”, RE-E-77-114, February 1977.

2. Lee, N., Wong, S., Yeh, H.C. and Hochreiter., L.E. - “PWR FLECHT-SEASET Unblocked Bundle, forced and gravity reflood task. Data evaluation and analysis report”. - WCAP-9891, November 1981.

3. Yao, S.C., Dodge, C. and Hochreiter, L.E., “A simple Method for Calculating Radiative Heat Transfer in Rod Bundles With Droplets and vapors as Absorbing Media” - (Technical Note), J. Heat Transfer 101, ASME, 736, 1979.

4. Sun, K.H., et al., “Calculation of combined radiation and convection heat transfer in rod bundles under emergency cooling conditions”, - J. Heat Transfer 98, ASME, 4141-420, 1976.

5. Kreith, F. and Bohn, M.S. - “Principles of Heat Transfer (Fourth Edition)” - Harper & Row, Publishers Inc., New York, 1986.

6. Zhang J., Bajorek S. M., Kemper R M., Hochreiter L. E., “WCOBRA-TRAC Analysis of ORNL High Flow Rod Bundle Film Boiling Tests”, National Heat Transfer Conference, ANS-HTC- Vol. 10, Baltimore, MD, 1997.

7. Cunningham, J. P., et al., “ECCS Heat Transfer Experiments with Upper Head Injection,” WCAP-8100, Vols 1 & 2, October 1974 and January 1975.

8. Andreycheck, T. S., et al., “Blowdown Experiments with Upper Head Injection in G-2 17x17 Rod Array Facility,” WCAP-8582, Vols 1 & 2, Jan. 1976 and Aug. 1976.

9. Mohr, C. L., at al., “Prototypic Thermal Hydraulic Experiments in NRU to simulate LOCA”, NUREG-CR-1882.

8. Instrumentation Requirements for the Rod Bundle Heat Transfer Test Facility

8.1 Introduction

The objective of the RBHT Program is to provide data on the key thermal-hydraulic phenomena of interest for dispersed flow film boiling and reflood heat transfer. Instrumentation requirements were developed to provide the needed data. The required information was identified in the PIRT given in Section 2. As the PIRT indicates, information is needed to develop and/or validate specific heat transfer and two-phase flow models. Since the objective is to develop the component models which comprise "reflood heat transfer," data will be obtained to view the component models as identified in the PIRT.

One of the more important objectives of the RBHT Program is to obtain new information on the mechanism of liquid entrainment at the quench front. This requires detailed measurements of the void fraction, droplet size, droplet velocity, and local heat transfer from the heater rods. The liquid entrainment at the quench front and the resulting droplet field downstream is responsible for the improved cooling at the upper elevations in the rod bundle where the peak cladding temperature occurs. Codes currently have difficulty predicting the correct amount of liquid entrainment as well as the timing of the entrainment. The instrumentation used in the RBHT Program will help resolve this modeling issue.

The instrumentation plan and layout will follow the lessons learned from the FLECHT (Ref. 1) and FLECHT-SEASET (Ref. 2) reflood heat transfer programs as well as the ACHILLES (Ref. 3) experimental program. Both sets of FLECHT experiments and the Rod Bundle Heat Transfer experiments are separate effects tests with prescribed boundary and initial conditions. While there are needs for very specific data, which is difficult to measure, proven instrumentation will be used with redundant measurement techniques where possible and developmental instrumentation will be verified using bench-top experiments before installing in the test bundle. In addition, bundle mass and energy balances will be used to calculate parameters of interest from the data.

8.2 Instrumentation Requirements

Perhaps the most basic requirement is to perform transient mass and energy balances on the test facility. Inlet flow, pressure, coolant temperature, outlet vapor flow, pressure, and liquid flow will be measured. Since the reflood tests are transients, there will be mass accumulation within the bundle. The mass accumulation will be measured using sensitive differential pressure (DP) cells with fine axial spacing. This approach was used successfully in the FLECHT and FLECHT-SEASET programs and mass balances were typically within five percent. The DP resolution in the current facility is finer than FLECHT.

To obtain an axial void fraction distribution requires the use of several different measurements. These include inlet and exit measurements of each phase and axial heat flux into the coolant. The axial quality distribution above the quench front and the amount of evaporation can be calculated from the data. Similarly, the void distribution along the heated bundle can also be determined to indicate the flow and heat transfer regimes and the information can be used to correlate the measured heat transfer data.

The differential pressure drop measurements must be corrected for frictional pressure drop, as well as any acceleration pressure drop, to infer local void fraction.

Since the quality is non-equilibrium, measurements of the true vapor temperature are needed as well as the wall heat flux into the fluid. Different techniques have been tried to measure the vapor temperature in a dispersed non-equilibrium two-phase flow as part of the FLECHT-SEASET program (Ref. 2), as well as elsewhere (Refs. 4, 5, 6 and 7). The technique that appears to be best is the use of miniature thermocouples which are placed normal to the flow and which point into the flow. As the froth region approaches, the thermocouples will wet since the droplet number density increases as the void fraction decreases. Very small thermocouples have a fast response time to allow the thermocouple to recover rapidly from being wetted by entrained droplets. In this fashion, a reasonable measure of the non-equilibrium vapor temperature can be achieved. Therefore, ample miniature thermocouples will be placed into the different subchannels along the axial length of the bundle. In addition, since the spacer grids can promote improved cooling downstream of the spacer, fluid thermocouples will be placed at these locations. The local quality can be calculated wherever a local vapor temperature exists in the bundle.

The experimental program will be structured to help separate the thermal-hydraulic phenomena which are observed during “reflood heat transfer. The test facility will be characterized hydraulically by measuring the rod bundle frictional losses. The spacer grid form losses will also be measured. Therefore, the two-phase differential pressure measurements can be corrected for frictional losses and form losses using single-phase data and an appropriate two-phase multiplier. Sufficient, sensitive, differential pressure cells will be arranged along the bundle to measure the rod bundle frictional losses and the grid losses over a range of Reynolds numbers.

Radiation-only experiments will determine, in-situ, the fraction of radiation heat flux which is transmitted from the inner rods to the housing, unheated dummy rods, and the outer peripheral row of rods. Values of the heater rod emissivity will be obtained from independent measurements using the pre-production heater rods which were tested at similar conditions. This data will help validate a multi-node model radiation network which can then be used to calculate the portion of the total heat transfer due to radiation in the bundle during reflood. The convective or dispersed flow film boiling portion of the total measured heat transfer can then be calculated from the total measured heat transfer by subtracting out the radiation portion. The data will also be used to validate the detailed COBRA-TF subchannel radiation heat transfer model for the test facility. Therefore, there is a requirement for sufficient thermocouple instrumentation on the heater rods, housing, and the dead or support rods at different planes within the bundle.

Electric heater rods will simulate fuel rods and will have the capability to simulate decay power at 40 seconds following reactor scram. These rods will have an internal heating coil with a prescribed axial power shape. Thermocouples will be placed along the rods to cover the complete axial length of the bundle. There will be thermocouples at specific elevations to obtain the radial temperature distribution dependence in the bundle. Heat flux will be determined from an inverse conduction calculation using the thermocouple data. In addition, the experiments are designed for computer code validation purposes; therefore, the thermocouples and the differential pressure cells will be arranged within the bundle with the following considerations:

- The overall bundle energy distribution will be determined during the transient;

- Thermocouples will be placed upstream and downstream of spacers to see their effects;

- Thermocouples will be placed on the spacer grids to determine their temperature and quench time;

- Thermocouples will be placed on the housing and dummy rods for rod-to-dummy rod, and rod-to-housing radiation heat transfer calculations; and

- Thermocouples will be placed at the center of the differential pressure cell spans such that one can then more easily relate the measured heat transfer to the local void fraction.

The experiments and instrumentation plan has been designed to allow a transient mass and energy balance to be performed.

In addition to heat transfer and the vapor and structure temperatures, data are needed on the flow behavior in the test bundle. In the froth region, data are needed on local void fraction distribution, interfacial area, and droplet/liquid ligament size. Also in the dispersed flow regime, data are needed on the droplet size, velocity, and number density for wall-to-drop radiation heat transfer, and the vapor-to-drop radiation and convective heat transfer. There is also evidence that entrained droplets enhance the convective heat transfer (Refs. 1 and 2) either by increasing turbulence, adding a distributed heat sink, or both. There is a requirement, therefore, that data be obtained on drop sizes, velocities, and number densities, to characterize the droplet mechanics of the dispersed two-phase region so interfacial area and droplet Weber numbers can be calculated from the test data. If the vapor flow rates and temperatures are known from other measurements, slip or relative droplet velocity can be calculated from the drop velocity measurements.

The flow regime must be characterized in the froth region where the liquid changes from continuous liquid dispersed droplet flow (continuous vapor). Therefore, the test section will require windows which will permit viewing and photographing the transient flow at important time periods in the transient.

8.3 Proposed New Instrumentation

While the RBHT Program is not intended to be an instrumentation development program, several new techniques will be used to obtain the data needed as identified by the PIRT. A soft-gamma ray measuring devise or X-ray system will be used at selected fixed elevations along the lower portion of the bundle. The gamma densitometer will give chordal average densities of the two-phase flow mixture as the flow regime changes from a dispersed droplet flow to the froth region and finally to solid water. This technique has been used in the past for void fraction measurements in rod bundles as indicated in Reference 8. To minimize attenuation of the soft gamma ray, beryllium inserts will be used in the test housing instead of quartz. The transient gamma ray measurements will provide an independent validation of the void fraction obtained from the finely spaced differential pressure measurements.

Droplet information has been traditionally obtained using high speed photography and laborious methods to obtain drop sizes and velocities, by examining droplet behavior frame-by-frame from the high speed film. Newer techniques will be used in the RBHT Program utilizing a pulsed

laser technique in conjunction with a fine grid digital camera. This system is called a Laser Illuminated Digital Camera System (LIDCS). The pulsed laser provides backlighting as well as the focus volume for pictures in the center subchannels of the rod bundle. This measurement technique employs software to determine the droplet size spectrum, Sauter mean drop size, droplet velocities, drop velocity distribution and an estimate of the droplet number density. These data can be used to estimate the interfacial area of the entrained droplet phase. The pulsed laser and digital camera technique has not been applied to rod bundle heat transfer before; therefore, to verify the performance of the system and confirm the accuracy of the measurements, a series of "bench-top" experiments are being performed to develop the data reduction and analysis methods to analyze the droplet data.

There will also be new techniques used for more traditional measurements in the rod bundle. There will be very finely instrumented regions of differential pressure cells with three-inch spans along the bundle to calculate a more localized void fraction from the data in the froth region and dispersed regions. Note, however, that the dispersed region void fraction could be within the uncertainty of the pressure cell after corrections. These data will be used to help correlate the measured heat transfer with the local void fraction. There will also be miniature fluid thermocouples which will act as steam probes to measure the local vapor temperature. In addition there will also be traversing vapor measurements within the bundle at selected locations to give the subchannel local temperature. This technique will be verified in a small heated bench experiment.

These techniques and measuring systems will provide new, more accurate, more reliable data for computer code model development and validation.

8.4 Instrumentation Plan Comparison to the PIRT

The PIRT tables in Section 2 listed the key thermal-hydraulic models and or parameters which are needed for developing and validating component models which comprise reflood heat transfer. Most of the items identified in the PIRT tables can be measured directly. Some can be determined from analysis of the test data, and some can be determined from the literature, while others will not be fully separable from the measurements made. Tables 8.1 to 8.8 reproduce the PIRT tables from Section 2 and indicate how the specific phenomena will be measured. All PIRT items are given in these tables regardless of ranking; however, instrumentation and use of new measuring techniques have been oriented specifically to obtaining data for the highly ranked PIRT phenomena.

As the tables indicate, nearly all the highly ranked phenomena will be measured directly or calculated from the experimental data. When a parameter is directly calculated from the experimental data, the calculation uses the transient mass and energy balance on the test section to calculate the radially averaged fluid properties. A code is not used at this stage of the analysis so the data analysis is independent of the code to be validated by the experiments.

There will be some difficulties in measuring the effects of the different cladding used in the rod bundle experiments as compared to the Zircaloy cladding used in the fuel rods. This difference was discussed in the scaling analysis in Sections 6 and 7. The effects of the difference in the materials are small except for the minimum film boiling temperature. For this parameter, data from the literature, FLECHT tests with Zircaloy cladding (Ref. 9) and NRU experiments (Ref. 10) can provide guidance on the most appropriate value to be used. A similar situation exists for the differences in the heater rod surface emissivity and the emissivity for Zircaloy rods. Here,

Table 8.1 Single Phase Liquid Convective Heat Transfer in the Core Component During Reflood Below the Quench Front

Process/Phenomena	Ranking	Basis	RBHT Program
Convective Heat Transfer	M	1φ Convective H.T. data has been correlated for rod bundles, uncertainty will not affect PCT, can effect point of boiling.	Will measure T_s, T_f and power below quench front so forced convective H.T. or natural convection H.T. can be calculated.
Geometry	L	Hydraulic diameter has been shown to be acceptable for pitch-to-diameter ratio of 1.3.	
Spacer Grids	L	Effects of spacers in 1φ convective H.T. are known effects known for natural convection. No impact on PCT uncertainty.	Models exist for spacer H.T. multiplier. The effects of spacers will be measured with detailed axial T/C placement.
Material Properties	L	Property effects are accounted for in analysis for 1φ H.T. Little uncertainty.	Property effects can be calculated from T_s and T_b.
Liquid Velocity (Reynolds Number)	M	Determine convective heat transfer.	Will measure total flow, T_w, T_f. Can calculate heat transfer from data and correlate. Local flow can be calculated from subchannel code (COBRA, VIPRE) or by hand calculation.
Liquid Subcooling	M	Liquid is heat sink.	Fluid temperatures will be measured with miniature steam probes; selected T/C's can traverse.
Decay Power	H	Source of energy for rods, boundary condition for test.	Will be simulated.

Table 8.2 Subcooled and Saturated Boiling – Core Component Below the Quench Front

Process/Phenomena	*Ranking*	*Basis*	RBHT Instrumentation and Measurements
Subcooled Boiling Heat Transfer and Heat Flux, Split of Energy Between Liquid and Vapor Production	M	A significant variation in the subcooled boiling heat transfer coefficient will not affect the PCT uncertainty since rod is quenched.	Will measure rod temperature (surface), local fluid temperatures (selectively) and power such that total wall heat flux can be calculated. Bundle average quality can be calculated from an energy balance. Codes use the Chen Model which has a superposition of convection and boiling. The RBHT can be used to test this type of correlation since both T_s and q^2 are measured. However, it will be difficult to determine directly the heat flux split between convection and boiling without using the correlation.
Geometry, P/D, De	L	Boiling effects in rod bundles have been correlated for our P/d, De range with acceptable uncertainty.	The void fraction will be measured along the test section using ΔP cells, and at fixed locations with a soft gamma ray detector.
Spacers	L	Locally enhances heat transfer; Correlations/ Models are available, acceptable uncertainty.	Effects of spacer grids can be measured with the detailed axial T/C placement on the heater rods.
Material Properties	L	Data exists for the range of conditions, little uncertainty.	
Local Void Fraction	M	Data exists for tubes and rod bundles.	The void fraction will be measured along the test section using ΔP cells, and at fixed locations with a low energy gamma ray detector. This is a difficult measurement since the void is very low and attached to the heater rods.
Liquid Subcooling	M	Determines the condensation of vapor, energy split.	Subcooling will be measured with miniature T/C's, and traversing T/C's.
Interfacial Heat Transfer Area	M	Determines net vapor generation.	Movies can be taken at different positions but very difficult to obtain interfacial area.
Decay Power	H	Energy source for heat transfer.	Will be simulated over a range of conditions.
Saturated Boiling Heat Transfer and Heat Flux	M	Similar to subcooled boiling, data is available for our P/D, De range. The uncertainty of Saturated Boiling H.T. coefficient will not significantly impact the PCT since rod is quenched.	Rod wall temperature and heat flux will be measured as well as the fluid temperature (saturation).
Geometry, P/D, De	L	Data exists in the range of P/D, De with acceptable uncertainties.	

Table 8.2 Subcooled and Saturated Boiling – Core Component Below the Quench Front (Continued)

Process/Phenomena	*Ranking*	*Basis*	RBHT Instrumentation and Measurements
Spacer Grids	L	Locally enhances heat transfer, Correlations/ Models are available, with acceptable uncertainty.	The effect of the spacer grids can be detected from axial heater rod thermocouples.
Material Properties	L	Data exists for our range of conditions, little uncertainty.	
Local Void Fraction	H	Provides the fluid conditions as the flow enters the quench front region and total steam flow which effects the liquid entrainment.	The void fraction will be measured along the test section using ΔP cells, and at fixed locations with a low energy gamma ray detector.
Decay Power	H	Source of energy for rods, boundary condition for the test.	Will be simulated.

Table 8.3 Quench Front Behavior in the Core Component

Process/Phenomena	*Ranking*	*Basis*	RBHT Instrumentation and Measurements
Fuel/Heater Rod Materials, and Thickness. ρ, C_p, k, Rod Diameter	H	These properties effect the stored energy in the fuel/heater rod and its quench rate, uncertainty directly impacts PCT.	Inconel Heater Rods will be used. Heater rod properties will be known from direct measurements.
Gap Heat Transfer Coefficient	M	Second largest resistance in fuel rod. Affects heat release rate from fuel pellet. Gap heat transfer coefficient has large uncertainty, but its impact on PCT is smaller since all stored energy is redistributed much earlier than reflood, timing may change however.	Heater rods do have a gap like fuel rods since they are swagged. High gap conductivity is used for heater rods (5000 Btu/Hr -ft^2 -F since rods are swagged. Gap effects cannot be directly simulated with conventional heaters.
Cladding Surface Effects • Oxides • Roughness • Materials • T_{min} • T_{CHF}	H	Since Zircaloy oxidizes, the oxide layer will quench sooner due to its low conductivity, compared to Inconel. Also roughness of oxide layer promotes quenching. The surface condition effects T_{min} which is the point where quenching is initiated. Quenching is a quasi-steady two-dimensional process. Values of T_{min} and T_{CHF} can be estimated. Large uncertainty but relatively less impact on PCT.	Inconel will be used for the cladding since repeated tests will be performed. Other data on Zircaloy quench will be sought and compared to Inconel and specific T_{min} models, such that a simple model can treat both materials. Separate bench tests will be performed to characterize T_{min} for different surfaces and materials.
Transition Boiling Heat Transfer (surface - liquid contact heat transfer)	H	Determines the rate of heat release at Quench Front directly impacts PCT, large uncertainty.	Depends on wall super heat. Low super heats, give high values, high super heats give low values. Quasi-steady, two-dimensional process. Estimates can be made using the closely spaced heater rod T/C's to obtain the axial conduction effects as well as a two-dimensional model of the heat rod. Calculate heat flux by inverse conduction methods.
Steam Generation at Quench Front	H	It is the rapid amount of steam generation which creates the liquid entrainment, large uncertainty and impact on PCT.	This is a quasi-steady two-dimensional process. Steam generation rate can be calculated from the heater rod T/C's, total energy and the bundle mass and energy balance.

Table 8.3 Quench Front Behavior in the Core Component (Continued)

Process/Phenomena	*Ranking*	*Basis*	RBHT Instrumentation and Measurements
T_{CHF}	H	Clad temperature when the critical heat flux is obtained, Used to develop the boiling curve and transition boiling.	Measured by heater rod T/C's some 2-dimensional correction may be needed.
T_{min}	H	Clad temperature at minimum film boiling point, Demarcation between good and poor cooling is needed to develop boiling curve.	Measured by heater rod T/C's. Some 2-dimensional correction effects may be needed. Separate bench tests will also be performed to measure T_{min} and T_{CHF} for different surfaces.
Surface Temperature	H	Cladding temperature indicates which heat transfer regime the surface is experiencing.	Measured by heater rod T/C's, may need some 2-dimensional correction effects.
Spacer Grid	M	Steam generation at the quench front is the dominant effect and the resulting heat transfer is very large, location could impact entrainment due to wetting of the grid and vapor acceleration through the grid.	Axial placement of heater rod T/C's will show grid affects if any.
Radiation Effects, Wall to Liquid, Vapor	L	The convective effects of the vapor generation dominates, wall temperatures are low.	Can calculate from the data via energy balance to obtain estimate.
Decay Power	M	Stored energy is the primary source of energy for rods.	Will be simulated in tests.
Void Fraction/Flow Regime	H	Determines the wall heat transfer since large α results in dispersed flow, low α in film boiling. Directly impacts PCT.	Void fraction will be measured (estimated) using ΔP cells **,** and gamma densitometers, and high-speed movies.
Interfacial Area	H	Determines the initial configuration of the liquid as it enters the froth region directly impacts liquid/vapor heat transfer and resulting PCT downstream.	Interfacial area can be estimated from high-speed photography if windows remain dry. Void fraction will also be measured with DP cells and gamma densitometer.
Fluid Temperature	H	Influences the quench rate and net vapor generation. Important for high flooding rates, with high subcooling.	Local miniature fluid temperatures will measure fluid temperature at many axial positions.

Table 8.4 Two-Phase Froth (Transition) Region for Core Component

Process/Phenomena	*Ranking*	*Basis*	RBHT Instrumentation and Measurements
Void Fraction/Flow Regime	H	Void fraction/flow regime helps determine the amount of vapor-liquid heat transfer, which affects the downstream vapor temperature at PCT, large uncertainty.	Average void fraction will be measured with DP cells. Vapor superheat will be estimated from miniature fluid T/C's.
Liquid Entrainment	H	Significant generation of steam in the froth and quench regions helps create liquid entrainment.	Can be calculated from the rod bundle energy balance, however, assumption must be made on vapor temperature. Mass stored in froth region is measured by cells, and gamma measurements.
Liquid Ligaments, Drop Sizes, Interfacial Area, Droplet Number Density	H	Liquid flow characteristics determine the interfacial heat transfer in the transition region as well as the dispersed flow region, large uncertainty.	The flow regime, interfacial area, droplet size, and droplet velocities will be estimated by high-speed photography, and laser measurements.
Film Boiling Heat Transfer at Low Void Fraction Classical Film Boiling (Bromley)	H	Film boiling heat transfer is the sum of the effects listed below in the adjacent column. Each effect is calculated separately and is added together in a code calculation, large uncertainty.	Will measure the total heat transfer. Vapor heat transfer will be estimated from the bundle energy balance. The difference is the film boiling and direct contact heat transfer.
Droplet Contact Heat Transfer	H	Wall temperature is low enough that some direct wall-to-liquid heat transfer is possible, with high heat transfer rates, large uncertainty.	Some data exists on wall surface. Difficult to separate this component from total heat flux.
Convective Vapor Heat Transfer	M	Vapor convective heat transfer relatively less important since the liquid content in the flow is large and the vapor velocities are low, but large uncertainty.	Calculate from bundle energy balance using measured vapor temperatures**,** bundle exit liquid and vapor flows, total heat flux (corrected for radiation).
Interfacial Heat Transfer	M	Interfacial heat transfer effects are relatively small since the steam superheat is low, large uncertainty exists.	Interfacial heat transfer will be inferred from the vapor temperature measurements and flow as calculated from bundle energy balance.

Table 8.4 Two-Phase Froth (Transition) Region for Core Component (Continued)

Process/Phenomena	*Ranking*	*Basis*	RBHT Instrumentation and Measurements
Radiation Heat Transfer to Liquid/Vapor	M	The radiation heat transfer effects are also small since the rod temperatures are low.	Radiation tests will help isolate the different components. Increased radiation will exit in the tests due to the two phase mixture since there will be wall-to-mixture radiation in addition to surface-to-surface radiation.
Spacer Grids	M	The velocities and Reynolds numbers are low in this region such that droplet breakup and mixing are not as important. Drop deposition could occur.	Axial placement of heater rod T/C's will measure the effects of spacers.
Decay Power	H	Source of power for rods.	Will be simulated.

Table 8.5 Dispersed Flow Region for Core Component

Process/Phenomena	*Ranking*	*Basis*	RBHT Instrumentation and Measurements
Decay Power	H	Energy source which determines the temperature of the heater rods, and energy to be removed by the coolant.	Power is a controllable parameter in the experiment
Fuel Rod/Heater Rod properties, ρ, C_p, k	L	Properties can be modeled. Stored energy release is not important at this time.	Data on heater rod properties will be independently measured.
Dispersed Flow Film Boiling (Components given below)	H	Dispersed flow film boiling modeling has a high uncertainty which directly effects the PCT.	Current plan for tests is to perform a bundle energy balance to obtain local quality. The convective heat transfer will be calculated using steam-only tests such that a 1φ convective correlation for RBHT facility will be available. Specific tests will also be run to determine the effects of convective enhancement and radiation heat transfer such that the different heat transfer effects should be separable from the total heat transfer measured in a reflood test.
Convection to Superheated Vapor	H	Principal mode of heat transfer as indicated in FLECHT-SEASET experiments.	Similar convective behavior is expected in the RBHT tests, as in the FLECHT-SEASET tests, except that the spacer grids may have a larger effect because of mixing vane design.
Dispersed Phase Enhancement of Convective Flow	H	Preliminary models indicate that the enhancement can be over 50% in some cases.	A series of separate tests will be performed to examine this heat transfer effect which will be compared to the single-phase convection tests.
Gap Heat Transfer	L	Controlling thermal resistance is dispersed flow film boiling heat transfer resistance. Large gap heat transfer uncertainties are not important, but fuel centerline temperature is affected.	Heater rods will not simulate the gap heat transfer, but not needed for this regime.
Cladding Material	L	Cladding material in the tests is Inconel which has the same conductivity as Zircaloy. Nearly the same temperature drop will occur.	Test will use Inconel.
Oxidation Rate	M	Inconel will not oxidize while Zircaloy will, and create a secondary heat source at very high PCTs, Zircaloy reaction can be significant at high temperature.	Oxidation not simulated in tests since cladding is Inconel.

Table 8.5 Dispersed Flow Region for Core Component (Continued)

Process/Phenomena	*Ranking*	*Basis*	RBHT Instrumentation and Measurements
Fuel Clad Swelling/Ballooning	L	Ballooning can divert flow from the PCT location above the ballooning region. The ballooned cladding usually is not the PCT location. Large uncertainty.	Flow blockage is not simulated but was modeled in FLECHT-SEASET. Heat transfer was improved.
Direct Wall Contact Heat Transfer	L	Wall temperatures are significantly above T_{min} such that no contact is expected.	Will verify no contact from the literature. This component cannot be directly measured in the RBHT tests but we can estimate its effects. Separate small-scale tests are needed.
Droplet Dry Wall Contact	M	Iloeje indicates this heat transfer mechanism is less important than vapor convection.	This component cannot be separated out of the total heat flux data in the RBHT tests. Separate smaller scale tests are needed. This effect will be captured in the measured total heat flux.
Droplet-to-Vapor Interfacial Heat Transfer	H	Interfacial heat transfer reduces the vapor temperature, which is the heat sink for the wall.	The axial vapor temperature distribution will be measured, and the bundle average quality will be calculated to obtain the evaporation. Also, drop sizes and velocities will be measured.
Radiation Heat Transfer • Surfaces • Vapor • Droplets	 H/M H/M H/M	Important at higher bundle elevations (H) where convective heat transfer is small since the vapor is highly superheated. Very important for BWR reflood with sprays and colder surrounding channel. Large uncertainty.	Separate tests will be used to characterize the radiation behavior of the RBHT test facility with no convection. The surface emissivity will be independently measured. Radiation Heat Transfer will be calculated for the forced flooding tests.

Table 8.6 Top Down Quench in Core Components

Process/Phenomena	*Ranking*	*Basis*	RBHT Instrumentation and Measurements
Deentrainment of Film Flow	L[1]	Film flow quenches the heater rod. High uncertainty.	The top-down quench front will be measured but deentrainment of drops onto the liquid film will not be measured.
Sputtering Droplet Size and Velocity	L	Droplets are sputtered off at the quench front and reentrained upward. Since the sputtering front is above PCT location, no direct impact. Entrained, sputtered drops affect total liquid entrainment, as well as the steam production in the steam generators.	If the top quench front progresses downward such that it is within a viewing location then droplet size and velocity can be estimated from high-speed movies and laser measurements. Quench locations will be determined from heater rods T/C's and housing T/C's.
Fuel Rod/Heater Rod Properties for Stored Energy ρ, C_p, k.	L[1]	These properties are important since they determine the heat release into the coolant. However, since this occurs above PCT level, no impact.	Heater rod stored energy is approximately the same as the fuel rod. The conductivity of the heater rod is larger than the fuel rod so heat is released quicker.
Gap Heat Transfer	L[1]	Affects the rate of energy release from fuel/heater rod.	No gap heat transfer simulated.

(1) Some of these individual items can be ranked as high (H) within the top down quenching process; however, the entire list is ranked as low for a PWR/BWR since it occurs downstream of the PCT location.

Table 8.7 Preliminary PIRT for Variable Reflood Systems Effects Tests

Process/Phenomena	*Ranking*	*Basis*	RBHT Instrumentation and Measurements
Upper Plenum - Entrainment/Deentrainment	M	Upper plenum will fill to a given mixture level after which the remaining flow will be entrained into the hot leg, large uncertainty.	A non-scaled upper plenum will be simulated in the tests; it should be easier liquid to entrain relative to a plant. Differential pressure cells will indicate mass storage.
Hot Leg - Entrainment, Deentrainment	L	Hot legs have a relatively small volume and liquid entering the hot leg will be entrained into the steam generator plena, medium uncertainty.	Hot leg entrainment can be simulated up to the separator which will separate the liquid flow.
Pressurizer	L	Pressurizer is filled with steam and is not an active component-small uncertainty.	Pressurizer will not be simulated.
Steam Generators	H	The generators evaporate entrained droplets and superheat the steam such that the volumetric vapor flow increases (particularly at low pressure). The result is higher steam flow downstream of the generators, high uncertainty since a good model is needed. FLECHT-SEASET data exist.	The steam generators will not be simulated, but the aspects of the higher steam flow will be accounted for when specifying the inlet flooding rates. Flow pressure drop across simulated resistance will be measured.
Reactor Coolant Pumps	H	Largest resistance in the reactor coolant system, directly affects the core-flooding rate, low uncertainty.	The resistance will be represented in the test to give approximate inlet flooding rate response observed in the system calculations.
Cold Leg Accumulator Injection	H	Initial ECC flow into the bundle.	Accumulator flow rates will be scaled, simulated, and measured.
Cold Leg Pumped Injection	H	Pumped injection is the liquid source for majority of the reflood transient.	Pumped injection will be simulated and measured.
Pressure	H	Low pressure (~35 psia) significantly affects vapor volumetric flow steam binding decreases the bundle flooding rate.	Pressure range will be simulated and measured.
Injection Subcooling	M/H	Lower subcooling will result in more boiling below the quench front, additional vapor to vent.	Subcooling range will be simulated.
Downcomer wall heat transfer	H	The heat transfer from the downcomer walls raises the ECC fluid temperature as it enters the core, resulting in more steam generation.	Simulate affect by varying the inlet temperature.

Table 8.7 Preliminary PIRT for Variable Reflood Systems Effects Tests (Continued)

Process/Phenomena	*Ranking*	*Basis*	RBHT Instrumentation and Measurements
Lower Plenum Wall Heat Transfer	M	Same effect as downcomer.	Simulate the metal heat effect by varying the inlet temperature. A non-scaled upper plenum will be simulated in the tests; it should be easier liquid to entrain relative to a plant. Differential pressure cells will indicate mass storage.
Break	L	Excess ECC injection spills out of vessel, break ΔP helps pressurize reactor system.	Break not simulated.

Table 8.8 High Ranked BWR Core Phenomena

Process/Phenomena	Basis	RBHT Instrumentation and Measurements
Core Film Boiling	PCT occurs in film boiling.	Film boiling components will be measured by heater rod T/C's, data will be corrected for radiation.
Upper Tie Plate CCFL	Hot assembly is in cocurrent up-flow above CCFL limit.	Similar behavior as PWR reflooding.
Channel-bypass Leakage	Flow bypass will help quench the BWR fuel channel.	The housing in the RBHT test will approximate a BWR channel, no leakage flow simulated; housing T/C's will indicate quench location.
Steam Cooling	A portion of the dispersed flow film boiling heat transfer.	Simulated in RBHT tests.
Dryout	Transition from nucleate boiling and film boiling.	Not simulated in RBHT tests.
Natural Circulation Flow	Flow into the core and system pressure drops.	Flow range can be simulated in RBHT, using pumped flow.
Flow Regime	Determines the nature and details of the heat transfer in the core.	Since pressures, heat flux, temperature, and flows can be simulated, flow regimes will be representative, measurements of void fraction by cells, gamma densitometer, high speed photography.
Fluid Mixing	Determines the liquid temperature in the upper plenum for CCFL break down.	Not simulated in RBHT, but hot assembly is calculated to be in upflow.
Fuel Rod Quench Front	Heat release from the quench front will determine entrainment to the upper region of the bundle.	Heater rod T/C's will indicate the quench front behavior.
Decay Heat	Energy source for heat transfer.	Will simulate in RBHT as a boundary condition.
Interfacial Shear	Affects the void fraction and resulting droplet and liquid velocity in the entrained flow.	Is not directly measured, can estimate for different flow regimes from data.
Rewet: Bottom Reflood	BWR hot assembly refloods like PWR.	Simulated in RBHT.
Rewet Temperature	Determines quench front location.	RBHT will use different materials than fuel rod; bench tests will be used to support the RBHT data.
Top Down Rewet	Top of the hot assembly will rewet in a similar manner as PWR.	Will be simulated in RBHT.

Table 8.8 High Ranked BWR Core Phenomena (Continued)

Process/Phenomena	Basis	RBHT Instrumentation and Measurements
Void Distribution	Gives the liquid distribution in the bundle.	Will be measured with differential pressure cells, gamma densitometer, and/or x-ray techniques.
Two-Phase Level	Similar to quench front location, indicates location of nucleate and film boiling.	Will be measured with heater rod T/C's and differential pressure cells to obtain axial void distribution.

however, the differences become smaller once the heater rod surface is oxidized. The emissivity of the oxidized surface approaches 0.9 for either metal. The determination of T_{min} for different surface conditions and material types is a candidate for a bench-type test and analysis.

In the dispersed flow film boiling region, the portion of the wall heat flux due to radiation heat transfer (to vapor, surfaces, housing, and droplets) can be separated from the measured total wall heat flux obtained from the inverse conduction calculation using the heater rod thermocouples. What cannot be easily separated from the remaining portion of the wall heat flux, in the froth flow regime, is the direct contact heat transfer. This mode of heat transfer occurs just above the quench front where the wall is near the minimum film boiling temperature. There have been models developed for this phenomenon by Forslund and Rohsenow (Ref. 11), Iloeji (Ref. 12) and Pederson (Ref. 13) and others (see Section 2) which can be used to separate this specific component from the remaining film boiling and convective heat transfer term. Different options and models will be used to assess the magnitude of this heat transfer component. For forced flooding experiments, instrumentation will be required to measure the variable flow into and out of the bundle. Previous experiments have concentrated on only the positive oscillatory flow (Ref. 14) such that there is no reverse flow out of the bundle. ERSEC (Ref. 14) are the closest tests which simulate positive and negative flows. The FLECHT-SEASET tests simulated stepped flows which reflected the effects of the steam binding in PWRs. An injection scheme and measurement plan will be developed to measure the instantaneous flow into the bundle.

8.5 Conclusions

The instrumentation requirements were developed using the PIRT tables as a guide for the important phenomena for the different test types, which the experiments must capture for code development and verification. The Rod Bundle Heat Transfer Test Facility will employ ample instrumentation proven to perform in previous rod bundle experiments. There will also be state-of-the-art instrumentation to measure details of the two-phase flow field in a non-intrusive manner. The combination of the different techniques provides a robust instrumentation plan for the Rod Bundle Heat Transfer program so the most important phenomena identified in the PIRT can be measured or calculated from the data.

8.6 References

1. Lilly, G.P., Yeh, H.C., Hochreiter, L.E., and Yamaguchi, N., “PWR FLECHT Skewed Profile Low Flooding Rate Test Series Evaluation Report,” WCAP-9183.

2. Lee, N., Wong, s., Yeh, H.C., and Hochreiter, L.E., “PWR FLECHT-SEASET Unblocked Bundle, Forced and Gravity Reflood Task Data Evaluation and Analysis Report,” NRC/EPRI/Westinghouse Report No. 10, WCAP-9891, NUREG/CR-2256, RPRI NP-2013, November 1981.

3. Denham, M.K., Sowitt, D. and K.G. Pearson, “ACHILLES Unballooned Cluster Experiments, Part I, Description of ACHILLES Rig Test Section and Experimental Procedures,” AEEW-R2336, November 1989.

4. Loftus, M.J., Hochreiter, L.E., Conway, C.E., Rosal, E.R., and Wenzel, A.H., “Non-Equilibrium Vapor Temperature Measurements in Rod Bundle and Steam Generator Two-

Phase Flows," Proceedings of the Third CSNI Specialist Meeting on Transient Two-Phase Flow, March 1981.

5. Ihle, P., and Rust, K., "Influence of Spacers on the Heat Transfer During the Reflood Phase of a Pressured Water Reactor Loss of Coolant Accident," Nuclear Research Center, Karlsruhe, KFK Report 3178. September 1982.

6. Lilly, G.P., Yeh, H.C., Hochreiter, L.E., and Yamaguchi, N., "PWR FLECHT Cosine Low Flooding Rate Test Series Evaluation Report," WCAP-8838, 1977.

7. Unal, C., "An Experimental Study of Thermal Nonequilibrium Convective Boiling in Post-Critical-Heat-Flux Region in Rod Bundles," Ph.D. Dissertation, Lehigh University, 1985.

8. Jiang, Y and Rezkallah, K. S., "An Experimental Study of the suitability of Using a Gamma Densitometer for Void Fraction Measurement in Gas-Liquid Flow in a Small Diameter Tube," Measurement Science and Technology, Vol. 4, pp. 496-505, 1993.

9. Cadek, F.F., Dominicis, D.P., and R.H. Leyse, "FLECHT Final Report," WCAP-7665, April 1971.

10. Mohr, C.L., et.al., "Data Report for Thermal-Hydraulic Experiment 2 (TH-2), NUREG/CR-2526, PNL-4164, November 1982.

11. Forslund, R.P., and Rohsenow, W.M., "Dispersed Flow Film Boiling," J.Heat Trans. 90 (6), 399-407, 1968.

12. Iloeje, O.C., Plummer, D.N., Griffith, P., and Rohsenow, W.M., "An Investigation of the Collapse and Surface Rewet in Film Boiling in Vertical Flow," J. Heat Trans. ,Vol. 97, pp. 166-172, 1975.

13. Pedersen, C.O., "The Dynamics and Heat Transfer Characteristics of Water Droplets Impinging on a Heated Surface," Ph.D. Thesis, Carnegie Institute of Technology, 1967

14. Clement, P., Deruaz, R., and Veteau, J.M., "Reflooding of a PWR Bundle Effect of Inlet Flow Rate Oscillations and Spacer Grids," European Two-Phase Flow Group Meeting, Paris, June 1982.

9. DEVELOPING A FACILITY INPUT MODEL

9.1 Introduction

The COBRA-TF computer code (Refs. 1, 2 and 3) was used to model the RBHT Test Facility. The objective was to perform pre-test calculations to obtain information about the range of the parameters to expect during reflood transient. This analysis also provided a basis to develop the test matrix and indicate the maximum temperature conditions reached in the bundle for a given set of conditions.

The COBRA-TF code was developed at the Pacific Northwest Laboratory under the sponsorship of the NRC to provide best-estimate thermal-hydraulic analyses of a LWR vessel during LOCAs. The two-phase flow is described with a two-fluid, three-field model. Thermal radiation and grid spacer effects are also included in the code, as well as a more detailed dispersed flow film boiling model as described in Section 4. The code was developed for use with either rectangular Cartesian or subchannel coordinates.

Two COBRA-TF models of the RBHT Test Facility were developed: a two-channel model and a more detailed individual subchannel model. The two-channel model was used to examine the local fluid conditions within the test facility for comparison with a plant. This model does not account for rod-to-rod or rod-to-housing radiation heat transfer from the inner channel which exists in the test bundle. The model does account for the test section housing and calculates the convection heat transfer to the housing as well as the energy released from the housing as it quenches.

A more detailed 1/8th sector of the test facility was modeled on a subchannel basis with each subchannel, individual heater rod surface, and the gap between rods uniquely modeled. The subchannel capability of COBRA-TF allows more accurate representation of small rod bundle arrays since each individual rod can be modeled with different surfaces for radiation heat transfer, so rod-to-rod and rod-to-housing radiation heat transfer can be modeled more accurately. In this fashion, the radial temperature gradient which develops due to the radiation heat losses to the test section housing can be simulated. There are specific experiments planned in the RBHT program to examine radiation-only heat transfer within the rod bundle and to the test section housing. The emissivities of the rods and housing will be measured.

Both the two-channel and the subchannel model were used for pre-test analysis. Since the two-channel calculations run much quicker and are easier to analyze, the majority of the pre-test calculations used this model. The more detailed model was used selectively for specified tests to examine the detail of the flow structure within the rod bundle.

9.2 Two-Channel Model

9.2.1 Input Deck Description

The analysis considered a 7x7 rod array comprised of forty-five heater rods, four unheated rods, and the surrounding housing. The facility modeling approach was to divide the test facility into four sections and five fluid channels. As shown in Figure 9.1, channels one and five represent the lower and upper plenums, respectively. Channel two models the low end fitting of the rod bundle. The third element is the actual heated length of the rod bundle and contains two fluid

channels. Channel three is the inner channel and encompasses a total of sixteen 'hot' rods; this includes the nine center rods and summation of the fractional parts of the rods that lie on the channel's boundary as shown in Figure 9.2. The second core channel, channel four, is comprised of the remaining twenty-nine heater rods, the four unheated rods, and the housing.

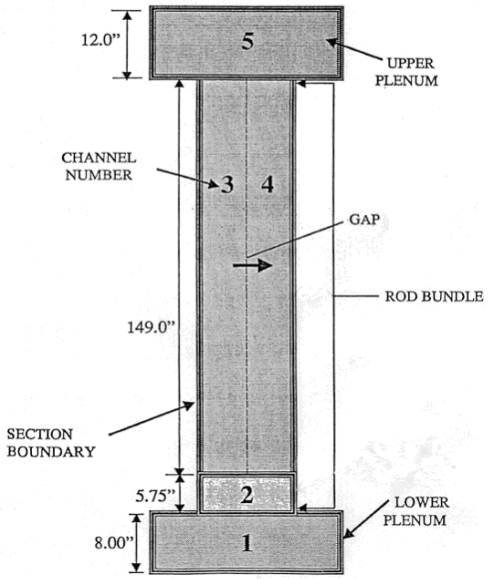

Figure 9.1 RBHT - Partitioning of Sections, Channels and Gaps.

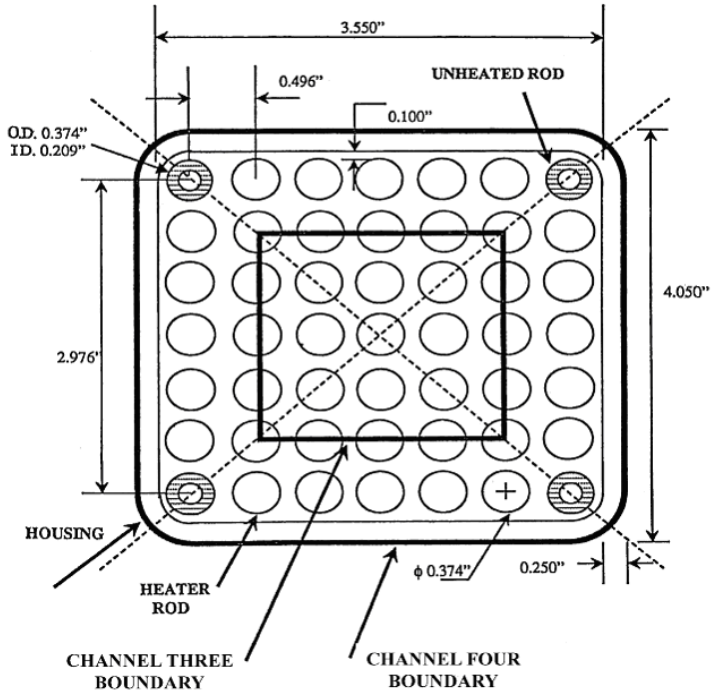

Figure 9.2 RBHT - Test Section 7x7 Rod Bundle Array Cross Section.

Three geometry types, *hrod*, *tube* and *wall*, were employed to represent the components of the test section. The *hrod* type signifies a solid cylinder and, thus, was employed to model the heater rods. As shown in Figure 9.3, successive layers of Boron Nitride, Monel K-500, Boron Nitride and Inconel 600 constitute the material composition of each rod. The unheated rods, of *tube* geometry, consist solely of Inconel 600.

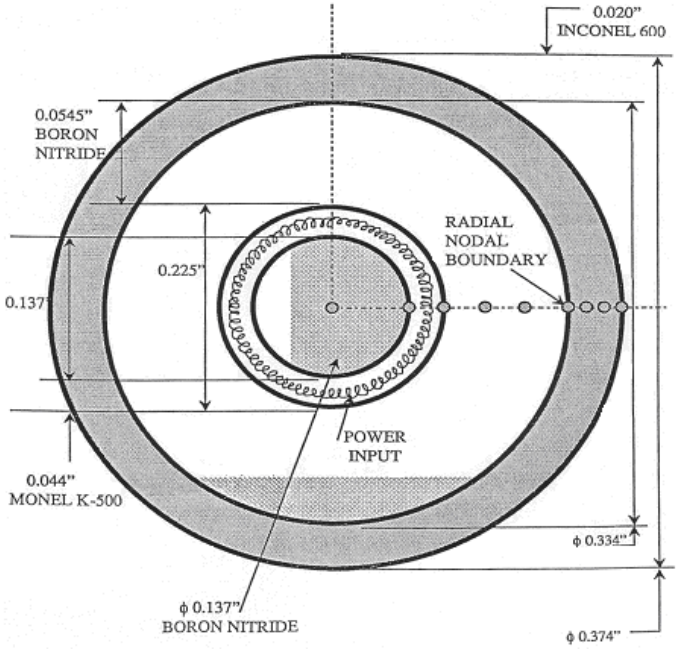

Figure 9.3 RBHT Heater Rod - Radial Dimensions, Materials and Noding Scheme.

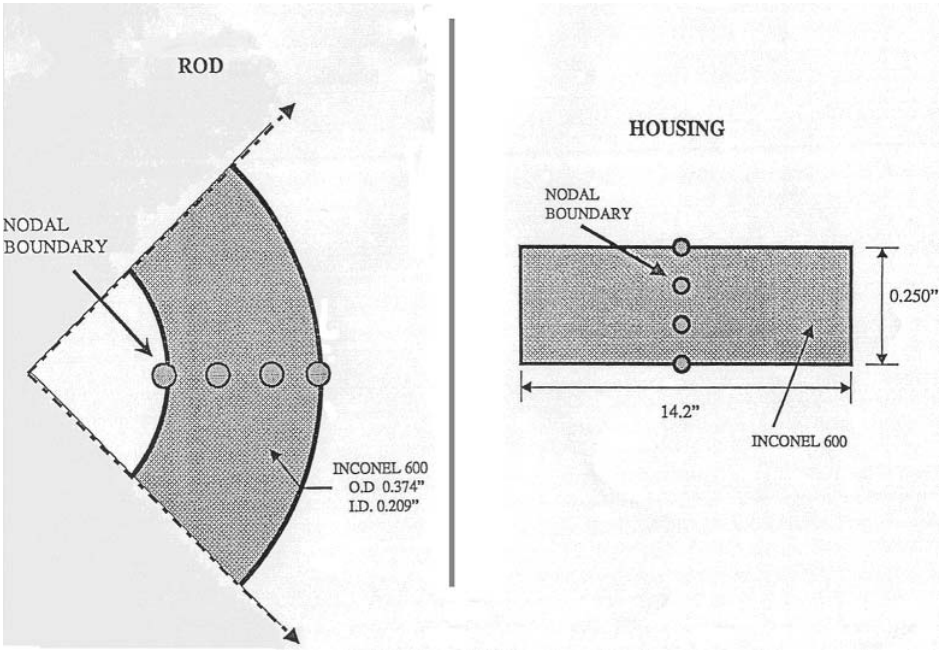

Figure 9.4 RBHT - Radial Dimensions, Materials and Noding Scheme.

The housing was modeled as a single wall with a cross-sectional area and wetted perimeter equal to the sum of the four individual sides. Both radial and axial noding were specified in the input model. As seen in Figure 9.4, there are three radial nodes for the Inconel 600 unheated rods and housing.

Radial noding in the heater rods is shown in Figure 9.3. The first two material segments of the rods (Boron Nitride and Monel K-500) both feature only one node, while three nodes each were allocated to the latter two segments. Axially, a total of twenty-eight nodes were specified, distributed as follows: two in the lower plenum, one in the lower end fitting, twenty-two in the heated length, and three in the upper plenum. Nodal boundaries in the heated length as shown in Figure 9.5 align with the grid locations, an ideal situation from a computational standpoint. Consequently, since the first grid is located 63.754 mm (2.51 in) from the bottom of the rod bundle, the first axial node in the heated length is 63.754 mm (2.51 in) from the bottom of the core.

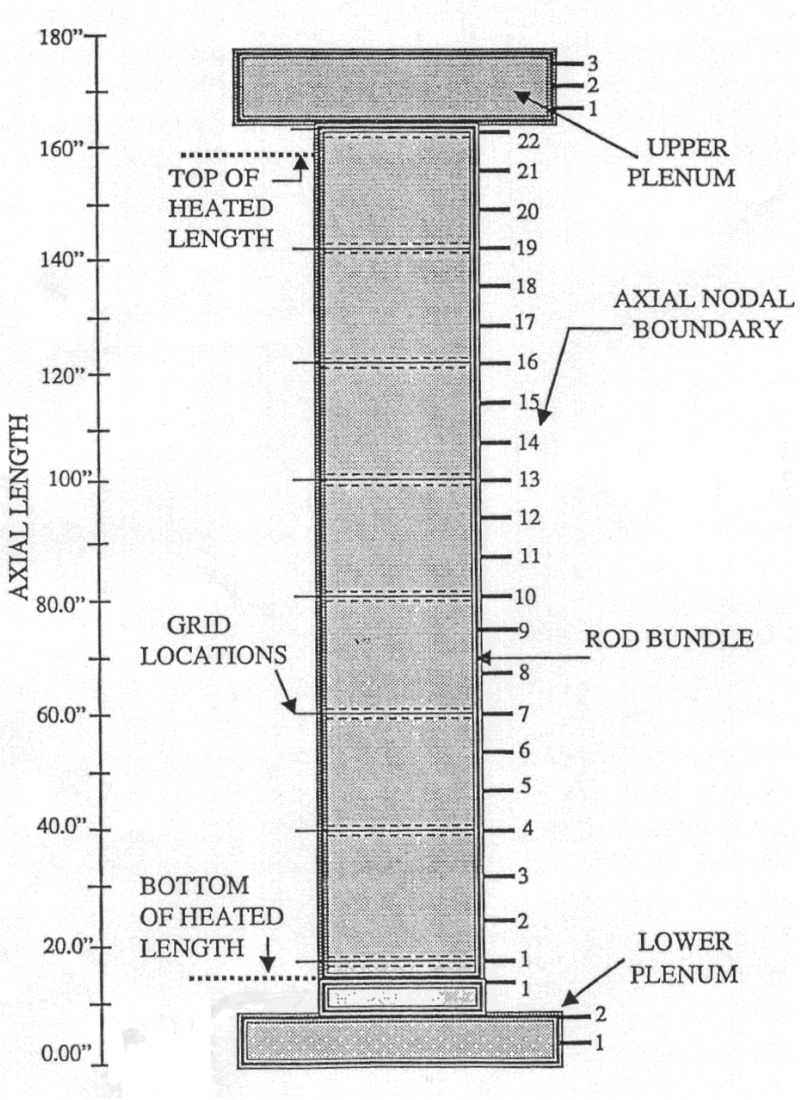

Figure 9.5 RBHT - Axial Dimensions and Nodal Scheme.

The major approximation made by this input model was to neglect radiation heat transfer. COBRA-TF does not have the capability to calculate radiation effects across channel boundaries unless the individual subchannels are modeled. Rather, it can only calculate radiation within each channel in which the rods are lumped. Each rod within a channel is considered to be at the same temperature; therefore, wall-to-wall radiation effects within the channel boundaries are neglected.

9.2.2 Results of Two-Channel Model

At the time this report was written, work was still continuing, so the results presented in this section are preliminary.

The analysis considered three flooding transients with different flooding rates: 20.32, 25.4 and 38.1 mm/s (0.8, 1.0 and 1.5 in/s). A constant pressure (40 psia) was set in the upper plenum. The water inlet subcooling was 48.89 degrees C (120 degrees F). The axial power shape is shown in Figure 9.6 which is the axial shape to be used in the RBHT tests. The initial power was chosen to be 0.7 kW/ft at the peak power location of 2.7432 m (108 in) from the bottom of the heated length. The decay power factor is the ANS-1971 +20 percent and is shown in Figure 9.7. This parameter will be ranged to cover the ANS-1979 decay heat standard as well as to provide overlap with existing data. In the actual experiments, the initial rod temperature will be determined by an adiabatic heat-up, not simulated in this analysis. The initial peak temperature was assumed to be 815 degrees C (1500 degrees F), and the local rod initial temperature was calculated based on the local power factor. The initial housing temperature was assumed to be a uniform value of 260 degrees C (500 degrees F). The simulation was carried out for 500 s.

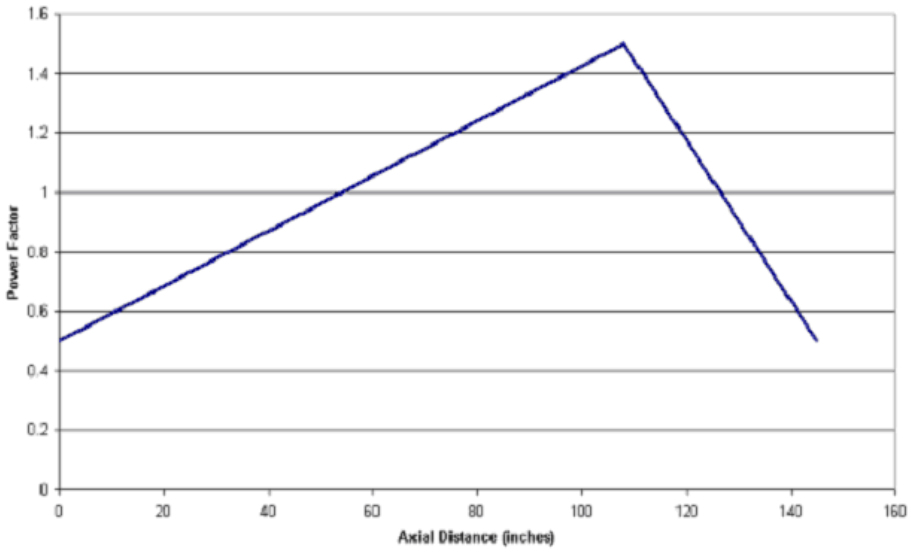

Figure 9.6 Axial Power Shape.

The 25.4mm/s (1.0 in/s) flooding rate results are shown in Figures 9.8 through 9.15. Figure 9.8 shows the quench front location versus time. The quench front rises relatively rapidly during the first 180 s**,** then it slows down. The average quench front velocity between 200 and 500 s is 2.438 mm/s (0.096 in/s). Figure 9.9 shows the hot rod clad temperature at different elevations. The peak clad temperature (PCT) 1354 degrees C (2470 degrees F) is reached at about 170 s at the peak power location.

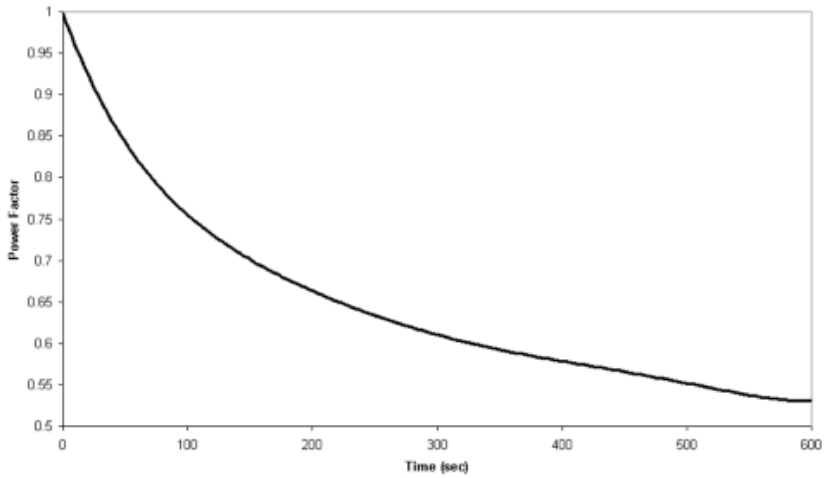

Figure 9.7 Power Decay.

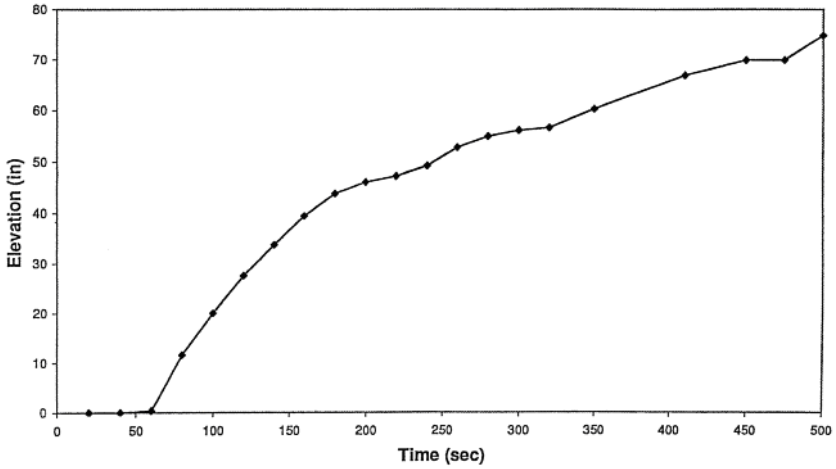

Figure 9.8 Quench Front - 1.0 in/s Reflooding Rate.

The housing temperature at different elevations is given in Figure 9.10**,** showing that the maximum temperature is reached at the same heater rod peak locations. The axial distribution of hot rod temperature is shown in Figure 9.11. Figure 9.12 shows the vapor temperature at different locations above the quench front. The effect of the grids is to reduce the vapor temperature downstream of the grids and, as a consequence, this reduces the clad temperature at the same locations. This effect is visible in Figures 9.11 and 9.12.

Figures 9.13 and 9.14 show respectively the vapor flow rate and the entrained liquid flow rate at the outlet of the bundle. An almost quasi-steady-state is reached at the end of the transient where the total of vapor, continuous liquid, and droplets flow rates almost matches the inlet subcooled liquid flow rate.

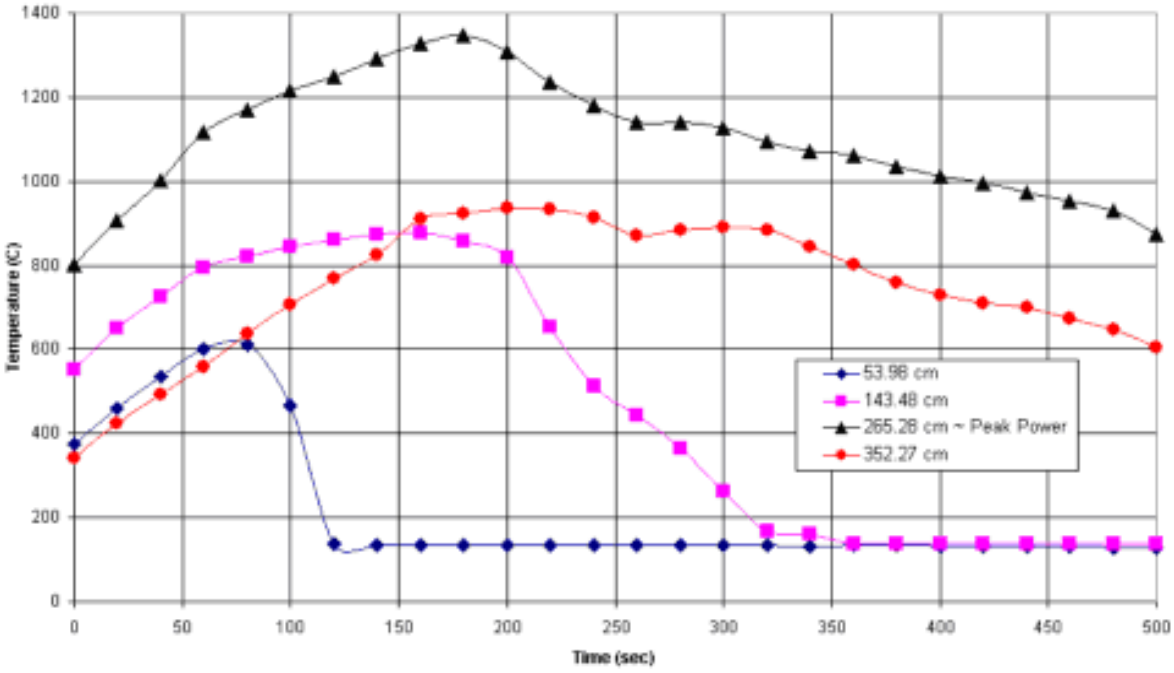

Figure 9.9 Hot Rod Clad Temperature - 2.54 cm/s (1.0 in/s) Reflooding Rate.

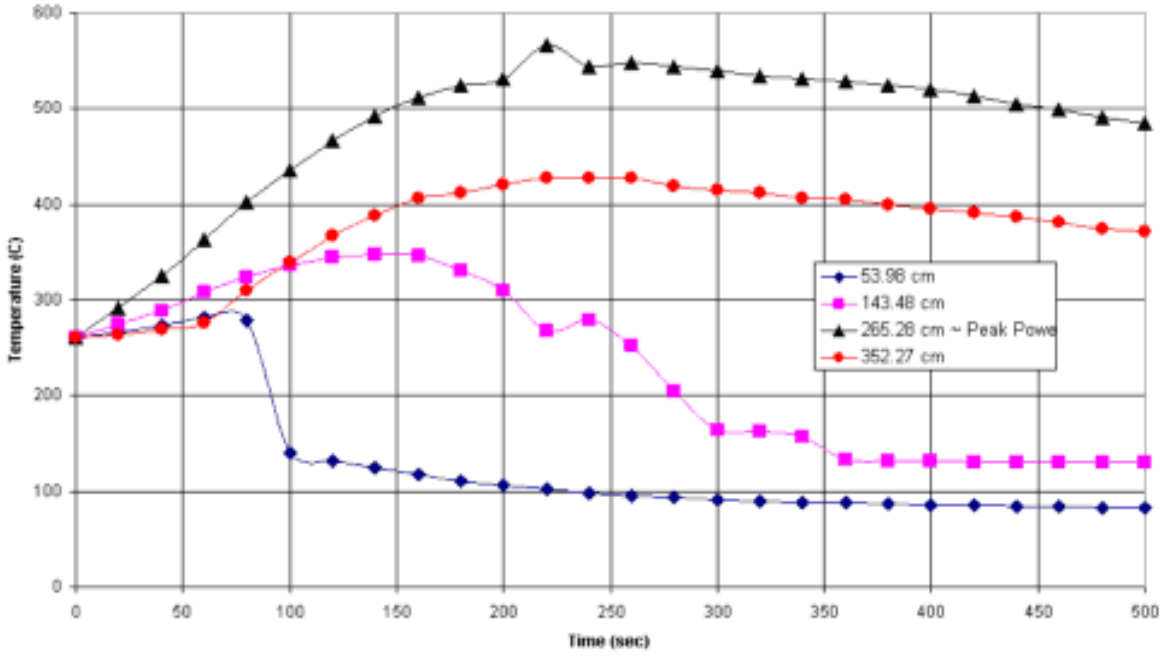

Figure 9.10 Housing Temperature - 2.54 cm/s (1.0 in/s) Reflooding Rate.

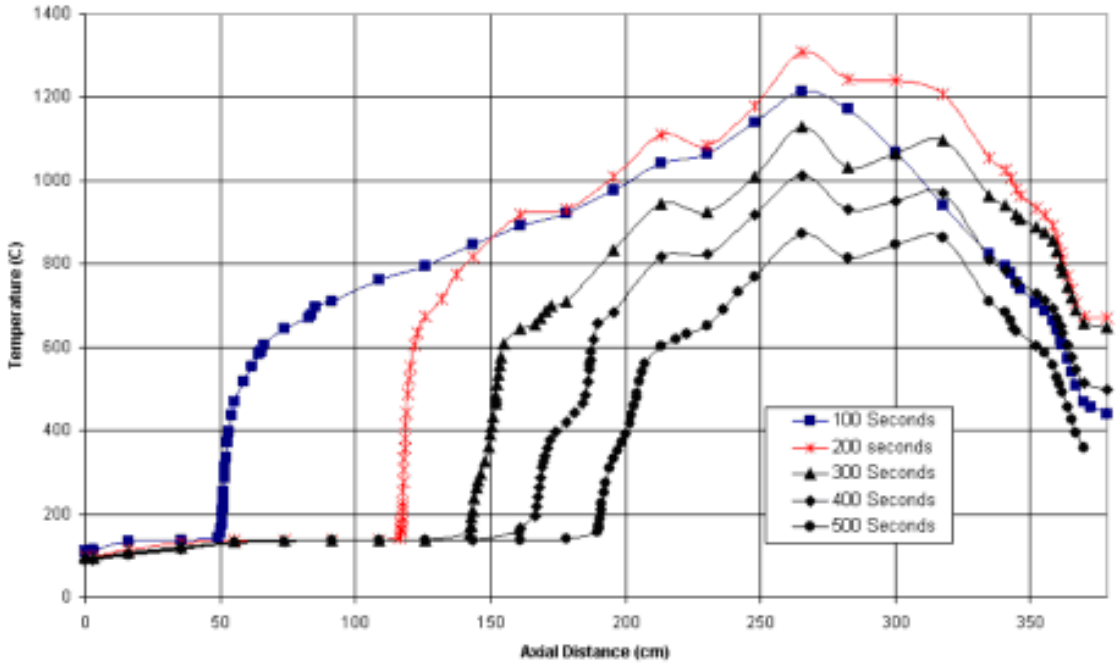

Figure 9.11 Hot Rod Clad Temperature - 2.54 cm/s (1.0 in/s) Reflooding Rate.

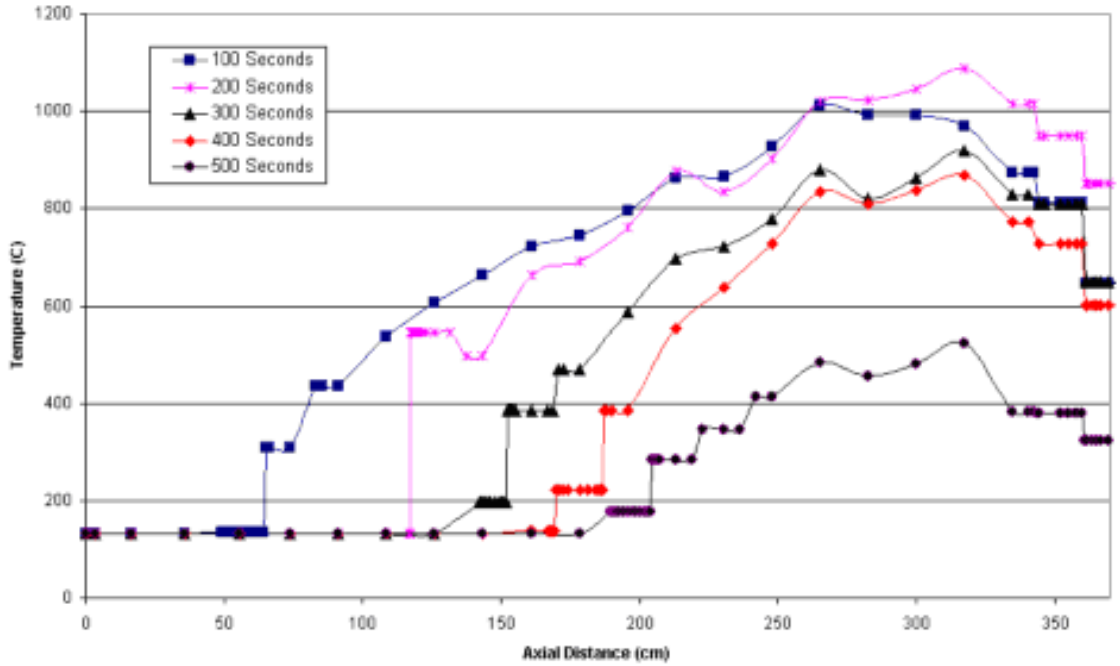

Figure 9.12 Vapor Temperature - 2.54 cm/s (1.0 in/s) Reflooding Rate.

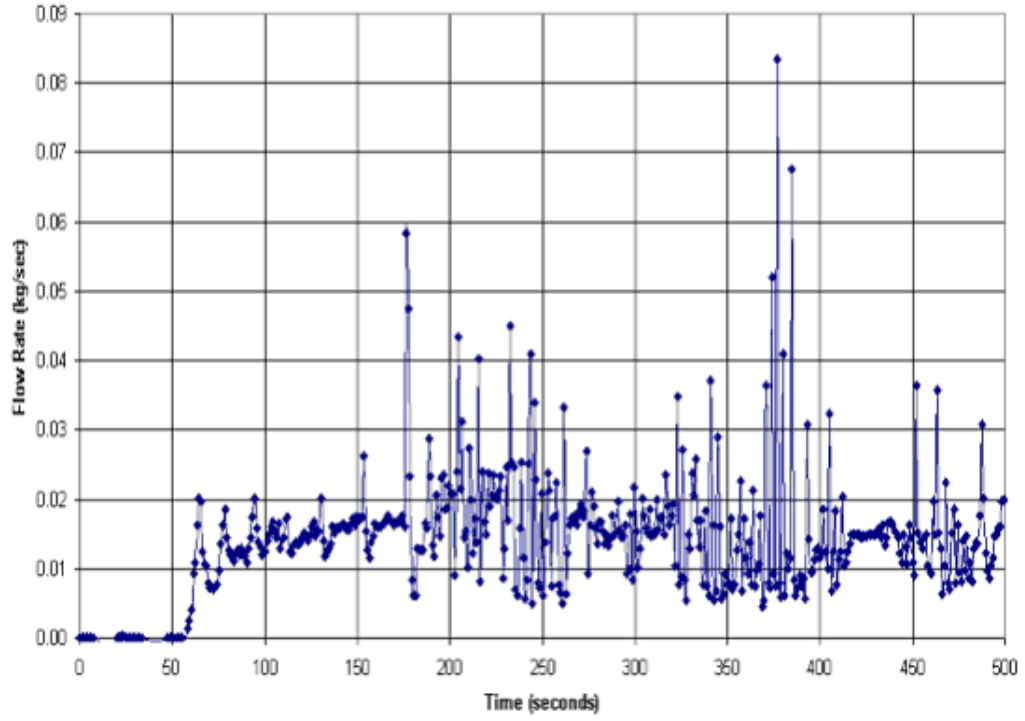

Figure 9.13 Vapor Flow Rate at Outlet of Rod Bundle - 2.54 cm/s (1.0 in/s) Reflooding Rate.

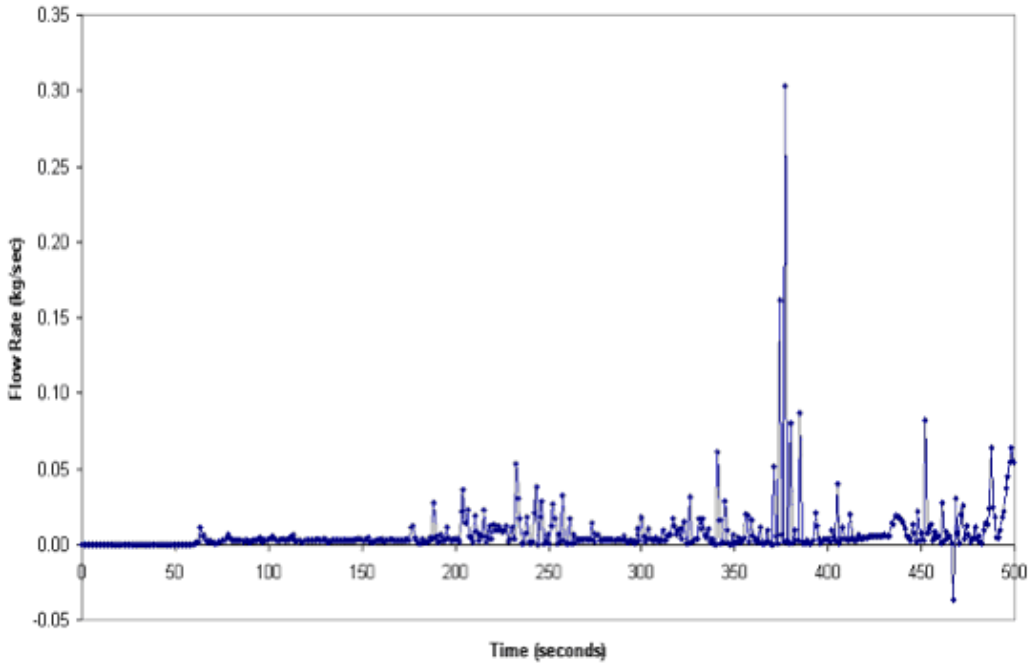

Figure 9.14 Entrainment Flow Rate at Outlet of Rod Bundle - 2.54 cm/s (1.0 in/s) Reflooding Rate.

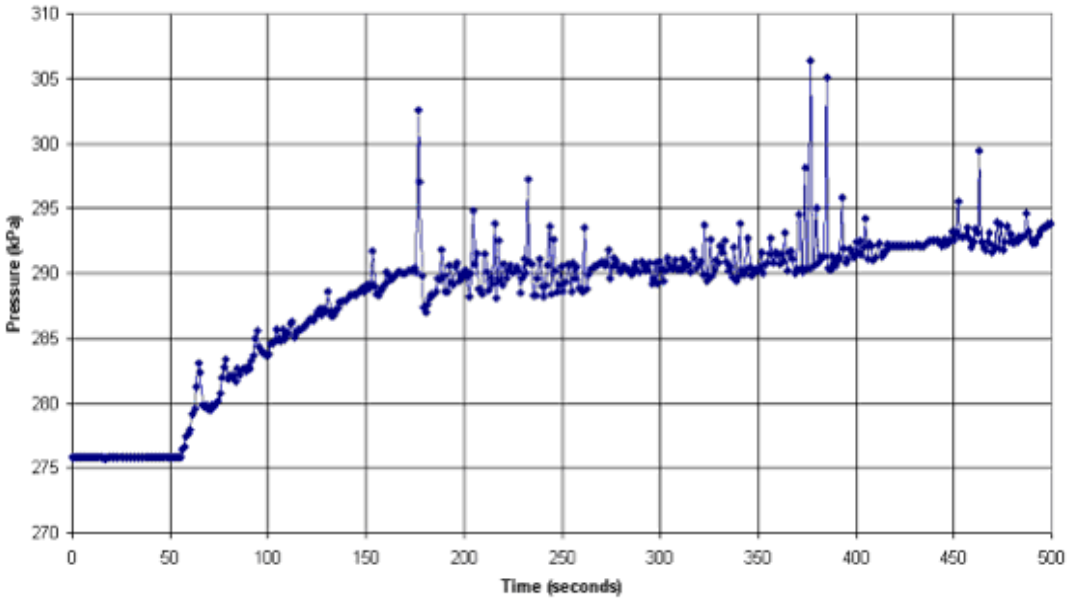

Figure 9.15 Pressure at Inlet of Rod Bundle - 2.54 cm/s (1.0 in/s) Reflooding Rate.

Finally, Figure 9.15 shows the pressure at the inlet of the bundle. Since pressure is fixed at 40 psia at the outlet of the bundle**,** the inlet pressure is the result of the gravity head and pressure drop across the bundle.

Similar results were obtained with the inlet flow rates of 20.3 mm/s (0.8 in/s) and 38.1 mm/s (1.5 in/s). Results are not shown in detail for these two cases, but it is interesting to calculate the range of vapor Reynolds numbers in this range of flooding rate. Figures 9.16, 9.17 and 9.18 show the vapor Reynolds number for respectively 20.3, 25.4 and 38.1 mm/s (0.8, 1.0 and 1.5 in/s) cases. These figures indicate that the vapor Reynolds number can be within the laminar and transition regimes, as well as turbulent flow.

The droplet Weber number was calculated for the 25.4 mm/s (1.0 in/s) flooding rate at 425 s into the transient when the flow conditions present a smooth, quasi-steady state behavior. The droplet Weber number is based on

$$We = \frac{\rho_v \left(u_v - u_e\right)^2 d_d}{\sigma} \tag{9-1}$$

where the droplet diameter is calculated from the equation

$$d_d = \frac{6\alpha_e}{A_i} \tag{9-2}$$

The droplet Weber number is calculated just above the quench front and at the bundle outlet using the variable values obtained from the code output shown in Table 9.1:

Table 9.1 Weber Number Parameters at 425 s

Symbol	Description	Value just above the quench front	Value at the top of the bundle
α	Entrainment phase void fraction	0.0029	0.0003
ρ_v	Vapor density, kg/m^3 (lbm/ft^3)	0.9772 (0.061)	0.636 (0.0397)
σ	Surface tension, N/m (lbf/ft)	0.0535 (0.00366)	0.0535 (0.00366)
u_v	Vapor velocity, m/s (ft/s)	5.94 (19.49)	16.67 (54.69)
u_e	Entrainment phase (droplet) velocity, m/s (ft/s)	1.109 (3.64)	11.433 (37.51)
A_i	Interface Area (ft^2/ft^3)	9.79	1.48

The calculated value of the Weber number ranges from 7.4 just above the quench front to 3.9 at the top of the bundle.

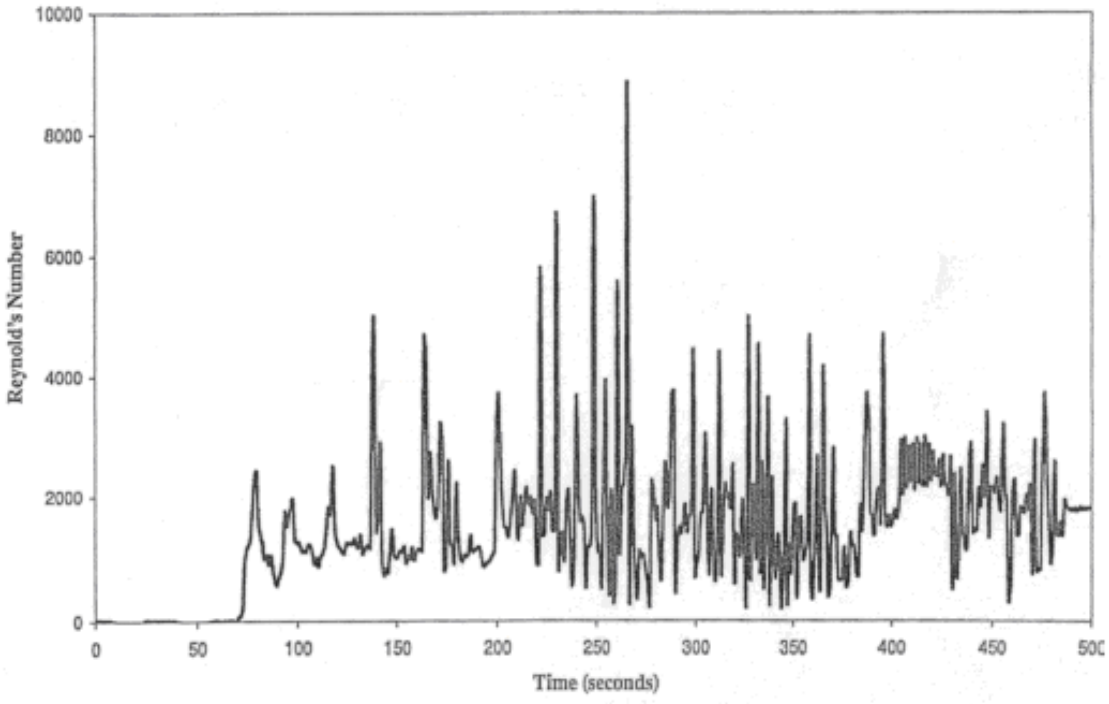

Figure 9.16 Vapor Reynolds Number - 2.032 cm/s (0.8 in/s) Reflooding Rate.

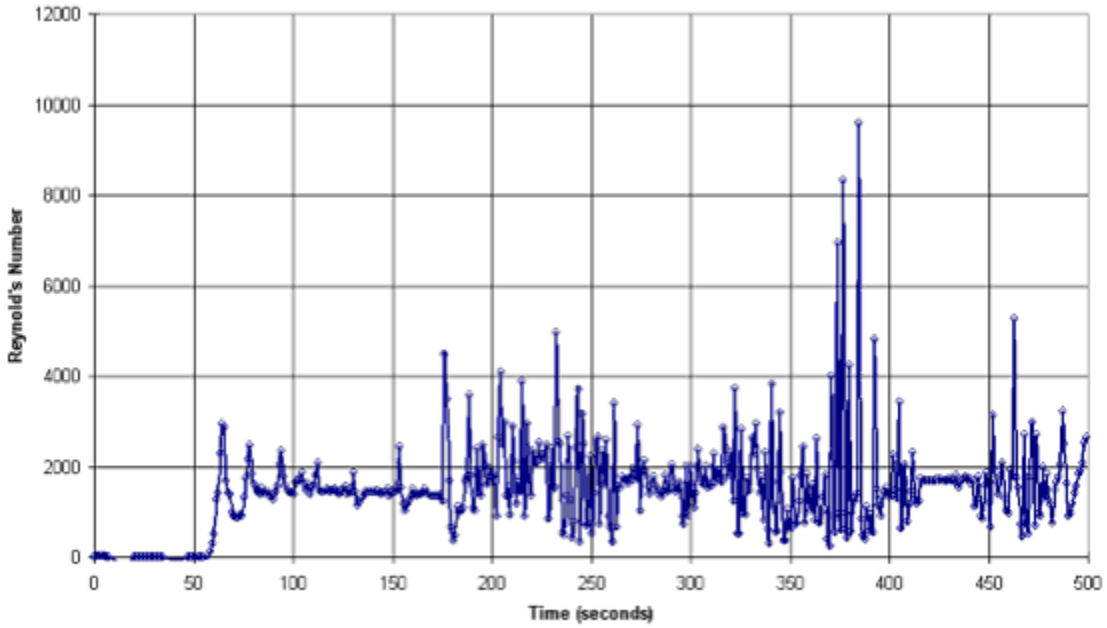

Figure 9.17 Vapor Reynolds Number - 2.54 cm/s (1.0 in/s) Reflooding Rate.

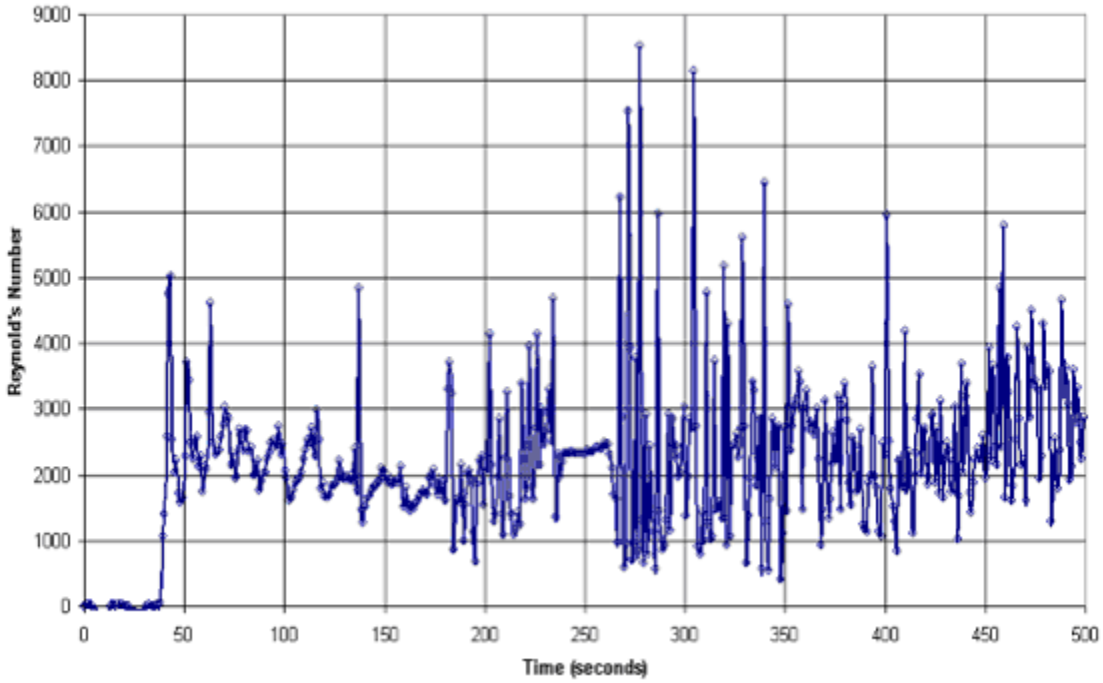

Figure 9.18 Vapor Reynolds Number - 3.81 cm/s (1.5 in/s) Reflooding Rate.

9.3 Individual Subchannel Model

9.3.1 Input Deck Description

A detailed COBRA-TF subchannel model of the RBHT test section was developed to examine the effects of rod-to-rod and rod-to-housing radiation as well as the subchannel flow behavior during refloods. The RBHT test section is assumed to have 1/8 symmetry which enables COBRA-TF to model the bundle with ten rods, ten channels, 12 gaps, and four wall sections, as seen in Figure 9.19. Each rod is divided into four surfaces with each surface oriented towards a channel. The heater rod surfaces are connected thermally by azimuthal conduction heat flow paths. Partial rods have less then four surfaces**,** with the number dependent upon rod orientation. The composition and noding of the rods and housing are identical to the description of the two-channel model in Section 9.2.

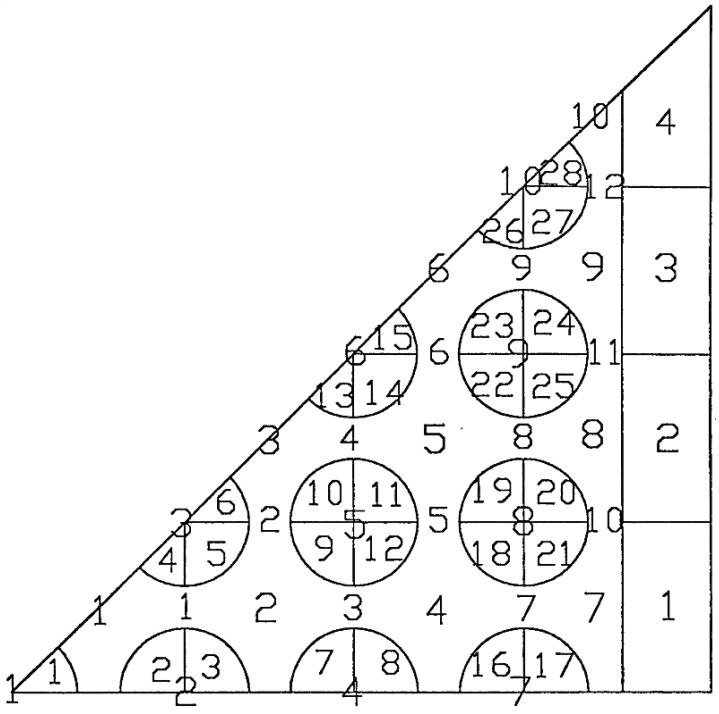

Figure 9.19 Nodal Diagram for Subchannel Model.

The subchannel model uses the same power profile and linear power densities as the two-channel model, the peak linear power being at 2.7432 m (108 in) and 2,297 W/m (0.7 kW/ft). The axial noding of the test section is identical to the two-channel model described in Section 9.2 with 22 nodes and eight spacer grids except the test section contains ten, not two channels. The plenum is modeled at the top and bottom of the test section to provide inlet and exit boundary conditions. An intermediate section with three channels is used to link the test section to the plenums; COBRA-TF does not allow more than six channels to be directly linked to one channel. Figure 9.20 shows the axial nodal diagram for the subchannel model.

Each rod is modeled with four separate surfaces. The COBRA-TF radiation model exchanges radiation between surfaces of the rods and surfaces in the four adjoining channels**,** and the

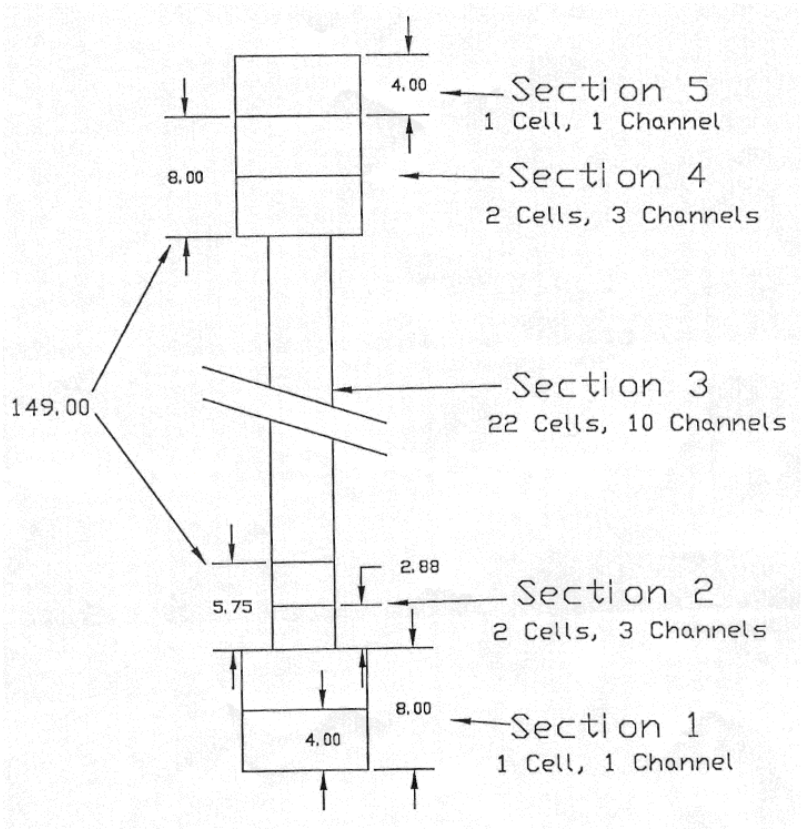

Figure 9.20 Axial Nodal Diagram for Subchannel Model.

channel walls through the rod gaps. Because of the symmetry planes (1/8 symmetry) the net radiation across a line of symmetry is zero. The azimuthal conduction model allows heat to be conducted around the rods from hot surfaces oriented toward the center of the bundle to the cold surfaces nearer the bundle housing.

Initial temperature distributions in the test section are taken from a COBRA run from which the bundle is initially at saturation, 130 degrees C (267 degrees F), and heated about 110 s until the peak rod temperature is 870 degrees C (1600 degrees F). This procedure is the prescribed pre-test heatup phase.

9.3.2 Results of Subchannel Model

To determine the effect of the housing on the bundle temperature distribution, the subchannel model was run with and without the ten radiation channels. The inlet conditions were set to zero such that the bundle was heated in an adiabatic manner in a stagnant steam environment. However, as the bundle was heated, steam convective currents developed and steam was released from the top pressure boundary to maintain the system pressure at 40 psia. Also, the bundle underwent convective heat transfer from the hot rods to the unheated surfaces because natural circulation paths were set in motion between grid spans.

The bundle was heated for 50 s to obtain the peak rod temperature at 870 degrees C (1600 degrees F). The results presented in Figure 9.21 are taken at the peak power location at the end of the 50 s heat-up. All temperature information on Figure 9.21 is in Celsius.

Initial temperatures at the peak location were:

Heated Rods: 870 degrees C (1600 degrees F)
Corner Rod: 340 degrees C (645 degrees F)
Housing: 250 degrees C (482 degrees F)

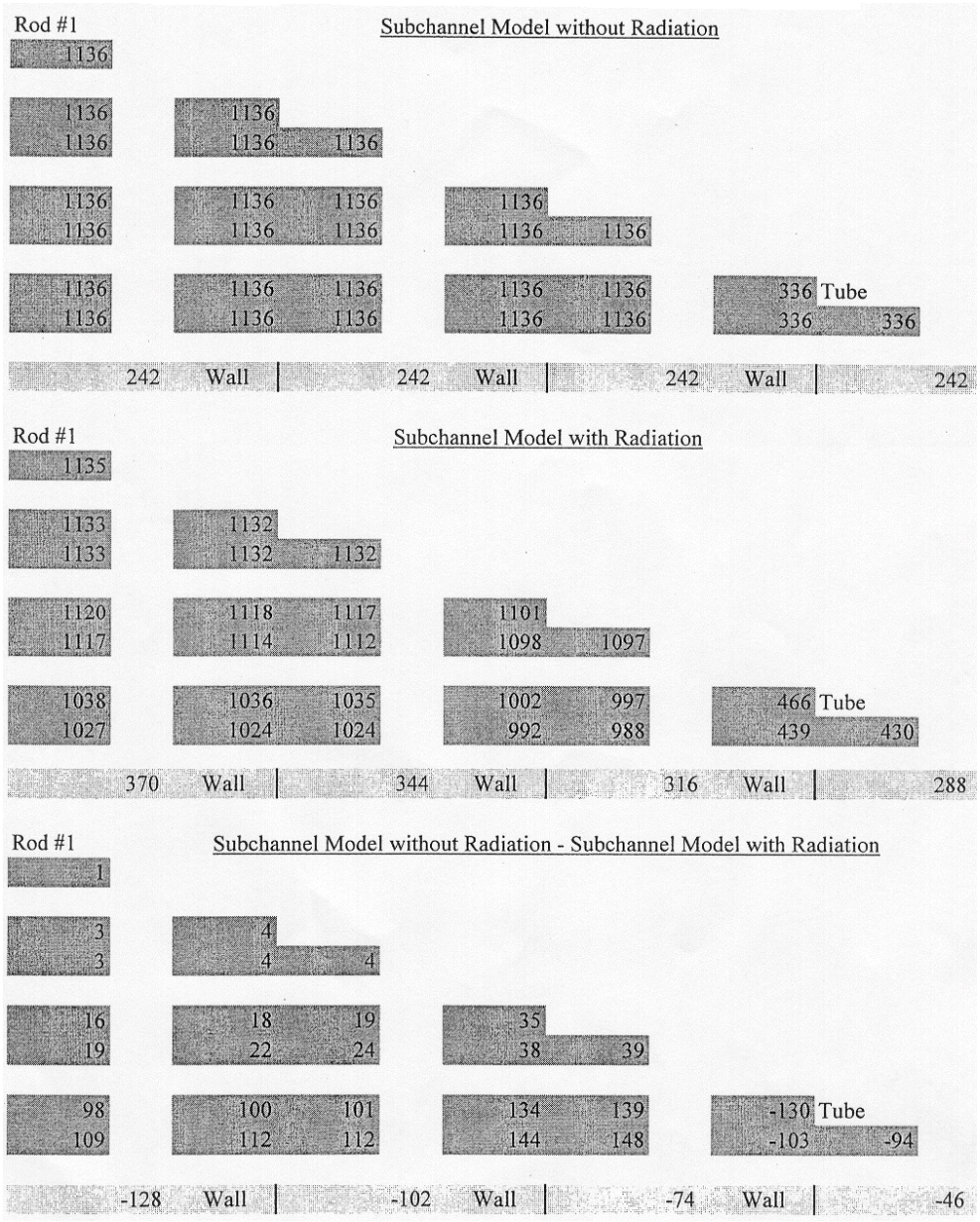

Figure 9.21 Temperature Distributions after 50 s Heatup (in degrees C).

These results confirm the assumption that the central 5x5 array of rods can be assumed to be at the same temperature. For the central rods the maximum temperature difference is 39 degrees

C (70 degrees F). The outermost row of rods is quite effective in shielding the remainder of the rods.

The detailed subchannel model will be used to selectively analyze the test facility to establish the exact test facility test conditions.

9.4 Conclusions

Two COBRA-TF models were developed for the RBHT Test Facility. A two-channel model represents the 7x7 rod bundle by splitting the bundle into two channels. One channel describes the inner, hotter rods and another describes the peripheral rods. The peripheral rods (in this case) are colder due to the presence of the housing, which provides a heat sink because of convective heat transfer. The two-channel model does not include radiation heat transfer. This was modeled with a more detailed subchannel model.

The detailed subchannel model was developed. The adiabatic heat-up phase for the RBHT Test Facility was simulated. Results show that radiation heat transfer is especially important for the rods facing the housing. The central 5x5 array of rods have practically uniform temperature with a maximum temperature difference of 39 degrees C (70 degrees F). The outer most row of rods is quite effective in shielding the remainder of the rods.

These preliminary results show the values of parameters to be expected during reflood of the RBHT bundle and provide the range of fluid vapor Reynolds and droplet Weber numbers for those conditions which should be compared with expected conditions in PWR and/or BWR reflood.

9.5 References

1. C. Y. Paik et al., “Analysis of FLECHT SEASET 163-Rod Blocked Bundle Data Using COBRA-TF,” NUREG/CR-4166, 1975.

2. Thurgood, M. J., et al., “COBRA-TRAC: A Thermal-Hydraulic Code for Transient Analysis of Nuclear Reactor Vessels and Primary Coolant Systems,” NUREG/CR-3046 (PNL 4385), Volumes 1-5, 1982.

3. Wheeler, C. L., et al., “COBRA-IV-I: An Interim Version of COBRA for Thermal Hydraulic Analysis of Rod Bundle Nuclear Fuel Elements and Cores,” BNWL- 1962, 1973.

10. ROD BUNDLE HEAT TRANSFER TEST MATRIX

10.1 Introduction

A test matrix for the RBHT tests was developed. The range of conditions is given and the objectives for the proposed tests are described. Some of the proposed tests were compared to the conditions and types of tests described in Section 3 to show how the proposed tests overlap and complement the existing database. The strategy in developing the test matrix was to use a "building block" approach in which simpler experiments are performed first to quantify a particular heat transfer mechanism. Additional complications of two-phase flow film boiling behavior are added in later experiments. The proposed test conditions bracket those expected in postulated LOCA.

10.2 Types of Tests Which are Proposed

The types of tests proposed include:

1. Steady-state liquid flow characterization tests to determine the rod bundle frictional pressure drop and the spacer grid loss coefficients. These tests will provide the bundle-specific hydraulic information to be used in the TRAC and COBRA-TF models.

2. Heat loss experiments to characterize the facility heat loss to the environment. These tests will provide the heat loss boundary information to be modeled in the COBRA-TF model, and to verify the scaling calculations for heat losses.

3. Radiation-only tests with an evacuated rod bundle. These tests will be performed over a range of rod bundle powers to achieve a wide range of heater rod surface temperatures, characteristic of those expected for dispersed flow film boiling. The bundle will be evacuated such that heat transfer will be by radiation only with no convective currents within the bundle. These tests will characterize the rod-to-rod and rod-to-housing radiation heat transfer. The objective will use the measured emissivities to characterize the rod bundle and housing surfaces such that the radiation heat transfer component can be subtracted from the total dispersed flow film boiling transfer as well as to verify that the outer row of heater rods effectively shields the inner 5x5 rows of rods. These tests will provide the data for the rod-to-rod and rod-to-surface radiation heat transfer models in TRAC and COBRA-TF. Modeling of this type of tests has been successfully performed using COBRA-TF in the past (Refs. 1 and 2).

4. Subcooled and saturated boiling experiments at low flows and low pressure. The objectives will be to provide data which can be utilized to validate the boiling models and correlations currently used. The experiments will be conducted in a steady-state manner and the heat transfer and void distributions will be measured along the rod bundle.

5. Convective steam cooling tests over a wide range of Reynolds numbers to determine the single-phase convective heat transfer in superheated steam. The analysis of the FLECHT-SEASET 161 rod bundle data (Ref. 3) indicates that for low flooding rates where the vapor becomes highly superheated, the vapor Reynolds numbers can decrease sufficiently to the laminar flow or transition flow regime. Therefore, these tests will characterize single-phase convective heat transfer cooling without the complications of a dispersed droplet field. Data

from these tests will be compared to rod bundle steam cooling data from the ORNL tests (Ref. 4) and the FLECHT-SEASET tests (Ref. 5), and other data sets for consistency.

6. Steam cooling tests with injected droplets at the entrance of the test bundle. A droplet injection system will be designed to inject drops of a known initial size and velocity into the heated rod bundle subchannels over a range of liquid flows such that quasi-steady state dispersed flow film boiling experiments can be conducted. An estimate of the droplet flow can be made from the FLECHT-SEASET 161 rod bundle tests as well as calculations from COBRA-TF. The objective of these experiments will be to examine the effects of a highly dispersed phase of entrained liquid droplets on convective heat transfer within the rod bundle.

   These tests will be simpler to analyze since the additional effects of the rod quench front movement, quench heat release and generation of the entrainment will be minimized. Since these tests will be quasi-steady, the Laser-Illuminated Digital Camera Systems (LIDCS) can be used at selected elevations to track the droplets and measure their size and velocity distributions, such that the change of the droplet interfacial area can be measured and compared to predictions.

   The LIDCS can be positioned upstream and downstream of spacer grids to determine the grid effects on the drop field. Also, local vapor temperature will be measured from steam probes, as well as the exit liquid and vapor temperature flow. From this, a mass and energy balance can be written for the bundle to calculate the quality change along the bundle, and therefore the axial steam flow. Radiation heat transfer can be calculated using the measured rod and surface temperatures, and this value can be subtracted from the measured total heater rod wall heat flux, resulting in the dispersed flow film boiling contribution to the total wall heat flux. The convective heat flux can then be compared to the single-phase convective heat flux based on the steam cooling tests to determine under what conditions convective heat transfer enhancement is enhanced by the evaporating droplets in the flow. A similar approach was used in the analysis of the FLECHT-SEASET 161 rod bundle experiments, but the lack of separate radiation only tests and good single-phase steam cooling tests resulted in significant data scatter. The inclusion of the radiation only and the steam cooling tests will reduce the uncertainties in the data analysis as well as the modeling uncertainties to avoid compensating errors as much as possible. These tests represent a unique contribution to the rod bundle dispersed flow film boiling literature.

7. Forced reflooding experiments will be performed to compliment the existing data, as determined from Task 2. The forced reflooding tests will also overlap the steam cooling and the droplet injection two-phase experiments. The forced reflooding experiments will contain all the elements of the experiments performed earlier with the additional complications of the heater rod quench front movement, quench heat release, and entrainment expected for reactor conditions, for a prescribed set of initial and boundary conditions.

   The focus of these experiments is to examine entrainment at the quench front within the froth region. The LIDCS and gamma densitometers will be used to determine the flow regime and the behavior of the entrained phase over a range of pressure, inlet flow, inlet subcooling, heater rod power, and heater rod initial temperatures. In addition, the data above the quench front can be analyzed in the same fashion as the FLECHT-SEASET 161 rod bundle data and the steam cooling tests with droplet injection to determine the wall heat flux components due to radiation heat transfer and film boiling.

These tests will serve as validation experiments for the models to be developed from the simpler component tests described above. Some of the data for selected tests can be designed as "blind" test data to be released to only the NRC for blind test predictions for the merged TRAC computer code. The COBRA-TF model developed in Task 8 will be used for pre-test calculations to determine the test matrix conditions for these experiments.

8. Gravity reflood experiments or variable inlet injection experiments will also be performed. These experiments will examine the system response on the inlet-flooding rate into the test bundle and the resulting heat transfer within the bundle. In the experiments described above, inlet flow conditions are prescribed boundary conditions. Actual inlet flow in a reactor system is a dependent parameter which depends upon the steam generation rate within the core, driving head in the downcomer, and pressure losses in the reactor piping, steam generators and pumps. The resistances for the generator, pump, and associated piping will be simulated using an orifice at the test section outlet. The parameters of interest are the orifice resistance, injection flow rate into the downcomer, initial rod bundle temperature, inlet subcooling, and rod bundle power levels. There will be a Laser-Illuminated Digital Camera System and gamma densitometer data to examine the gravity flow behavior within the bundle, effects of the spacer grids, and resulting entrainment. The tests will be modeled using COBRA-TF, which will have been improved as part of the program effort.

10.3 Range of Conditions Considered for the Experiments

The range of conditions used to establish the test matrix covers the postulated calculated reflood transit. Typical calculated reflood conditions were obtained from Westinghouse (Ref. 5), Framatome (Ref. 6), and Siemens (Ref. 7). Westinghouse compared the ranges of existing data to their model to show that it had been tested over the range of model application.

The composite table of all the predicted conditions from the reactor vendor calculations is given in Table 10.1. The table is subdivided into each of the different heat transfer regimes and the range of the calculated plant conditions is given for each. As can be seen, there is a large variation in parameters such as liquid and vapor Reynolds number, liquid subcooling and vapor superheat. The range of pressures is small since all plants reflood at low pressures. The Westinghouse plant parameters were extracted from best-estimate WCOBRA/TRAC calculations, while the plant parameters from Framatome and Siemens were taken from their Appendix K evaluation model calculations.

The liquid Reynolds number was based on the inlet flow and the bottom cell in the bundle which was single phase liquid. The vapor Reynolds number was based on the local vapor superheat, and the calculated vapor flow rate in the dispersed flow film-boiling region of the bundle. The wall superheat is from the calculated peak cladding temperature for the calculation. The liquid subcooling and the vapor superheat are also given.

Using Table 10.1 as a guide, a test matrix was developed to capture most of the range of conditions which the vendor and NRC safety analysis computer codes are required to calculate. Not all the heater rod temperature conditions will be directly simulated in the RBHT test program since many of the test conditions are at very high heater rod temperatures (>1093 degrees C, >2000 degrees F) which can limit the lifetime of the heater rods. Since the RBHT test program strategy is to reuse the expensive heater rods in two bundles builds, the very high temperature tests will be conducted in the second bundle build. Also, data are available from the FLECHT-

SEASET program in which several tests were run at very high temperatures, near or at the licensing limit, which can be used with the RBHT data to cover the full range of calculated conditions for reflood heat transfer model development.

Table 10.1 Range of PWR Reflood Conditions

Heat Transfer Regime	PWR Range of Conditions
Single Phase Liquid	
Re_l	5500 - 25000
P (bar) [psia]	1.38 - 3.10 [20 - 45]
$T_{sub} = T_{sat} - T_l$ (^oC) [^oF]	< 44 [< 80]
Single Phase Vapor	
Re_v	2500 - 9500
P (bar) [psia]	1.38 - 3.10 [20 - 45]
$T_{sat} = T_v - T_{sat}$ (^oC) [^oF]	333 - 778 [600 - 1400]
Subcooled Boiling	
Re_l	5500 - 25000
P (bar) [psia]	1.38 - 3.10 [20 - 45]
$T_{sub} = T_{sat} - T_l$ (^oC) [^oF]	< 44 [<80]
Saturated Nucleate Boiling	
Re_l	5500 - 25000
P (bar) [psia]	1.38 - 3.10 [20 - 45]
$T_{sat} = T_w - T_{sat}$ (^oC) [^oF]	2.78 - 16.7 [5 - 30]
Transition Boiling	
Re_l	5500 - 25000
Re_v	2500 - 9500
P (bar) [psia]	1.38 - 3.10 [20 - 45]
$T_{sub} = T_{sat} - T_l$ (^oC) [^oF]	0 - 44 [0 - 80]
Inverted Annular Film Boiling	
P (bar) [psia]	1.38 - 3.10 [20 - 45]
$T_{sat} = T_v - T_{sat}$ (^oC) [^oF]	222 - 333 [400 - 600]
$T_{sub} = T_{sat} - T_l$ (^oC) [^oF]	0 - 11.1 [0 - 20]
Dispersed Flow Film Boiling	
Re_v	2500 - 9500
P (bar) [psia]	1.38 - 3.10 [20 - 45]
$T = T_w - T_{sat}$ (^oC) [^oF]	222 - 1056 [400 - 1900]
$T_{sub} = T_{sat} - T_l$ (^oC) [^oF]	0 [0]
$T_v = T_w - T_v$ (^oC) [^oF]	< 1000 [<1800]

The other source for the test conditions are those conditions obtained from the analysis of the FLECHT-SEASET test data and the earlier FLECHT Cosine (Ref. 8) and the FLECHT Skewed (Ref. 9) reports. In these tests, a mass and energy balance was used to calculate the axial quality behavior along the test bundle at different times using the non-equilibrium steam vapor temperature measurements. The vapor Reynolds number, void fraction, calculated quality, and rod temperatures are shown in Figures 10.1 to 10.3 for FLECHT-SEASET test 31504, which is a 25.4 mm/s (1 in/s) flooding rate test at 2.76 bars (40 psia), 66.7 degrees C (120 degrees F) inlet subcooling, peak power of 2.3 kW/m (0.7 kW/ft) and an initial cladding temperature of 871 degrees C (1600 degrees F). As the figures indicate, the high vapor temperatures result in very low vapor Reynolds numbers, well within the laminar region. The vapor Reynolds number is approximately proportional to $1/T_v^2$ such that as the vapor superheats, the Reynolds number decreases, even for relatively high vapor velocities (Ref. 3).

10.4 Proposed Preliminary Test Matrix

A preliminary test matrix for the RBHT Test Facility is given in this section. A sufficient number of COBRA-TF calculations have been performed to specify the range of conditions for the tests as an envelope for the test facility design. Therefore, parameters such at flows, temperature limits, pressures, and powers have been broadly specified for the facility design to specify thermal-hydraulic conditions which provide data.

The Tests are divided into the same classifications as given in Section 10.2 and reflect the building-block approach for characterizing the test facility as well as minimizing the duty on the heater rods.

1. Steady-state flow characterization of the test facility, designed to provide the detailed pressure drop and loss coefficient information of the test facility so the facility can be modeled accurately. The Reynolds number range of interest covers laminar, transition, and fully turbulent ranges; therefore, the grid loss coefficients will be a strong function of the Reynolds number. The tests will be performed with the rod bundle unpowered, at approximately 2.68 bars (40 psia), and using subcooled water. The Reynolds number range that will be investigated is 1500 - 25000. Several tests and repeat tests, approximately 25 valid tests total, will be performed to characterize the grid loss coefficients, rod bundle frictional losses and the total bundle pressure loss.

2. Heat loss experiments to determine the heat loss characteristics of the facility. These tests will be performed in two steps. The first series of tests will be with the rod bundle unpowered using the hot water from the accumulator tank at 1.34 bars (T_{sat} = 108.9 degrees C) [20 psia (T_{sat} = 228 degrees F)], and 4.02 bars (T_{sat} = 145 degrees C) [60 psia (T_{sat} = 293 degrees F)]. The bundle will be filled with hot water and the temperature distribution, as a function of time will be measured. The heat losses will be calculated from the data. Approximately three valid tests will be performed with an additional repeat test. The higher temperature heat loss data will be obtained as part of the radiation only and steam cooling tests. It should be noted that all heated tests will have sufficient instrumentation to characterize the heat losses.

3. Radiation only tests with the facility evacuated to minimize free convection currents within the rod bundle. These tests will be used to characterize the rod-to-rod and rod-to-housing heat transfer within the bundle, and to verify the radiation heat losses given in Sections 6 and 7. These tests will be performed using a constant power calculated to give maximum temperatures of 260, 538, and 816 degrees C at 2.76 bars (500, 1000, and 1500 degrees F at 40 psia) in a quasi-steady fashion. The tests will provide data for heat loss calculations. Heat loss should equal the bundle power if the temperature is constant. Pre-test calculations using both MOXY and COBRA-TF will be performed to estimate the target power level for the given peak temperature. Approximately six tests with repeat tests will be performed.

4. Subcooled and saturated steady-state boiling experiments will be performed over a range of inlet subcooling, from approximately -17-27 degrees C (1 - 80 degrees F), with a pressure range of 1.34 to 4.02 bars (20 to 60 psia). The liquid flow rate and temperature will be varied to cover the liquid Reynolds range from approximately 4000 to 30000. The heater rods will be powered and the test section total power needed to develop boiling will be calculated using COBRA-IV or VIPRE-II subchannel codes. Simpler calculations will also be

performed as a check. The heater rods should not exceed critical heat flux since the objective is to investigate stable nucleate and saturated boiling. Approximately 30 tests will be performed including repeat tests. The specific test matrix will be completed after the pre-test calculations have been performed for the range of conditions.

5. Convective steam cooling steady-state tests over a wide range of vapor Reynolds numbers from 1500 to 30000 with pressure variations from 1.34 to 4.02 bars (20 to 60 psia). As with the boiling tests in Part 4 above, pre-test predictions of the steam cooling tests will be made using COBRA-IV and/or VIPRE-II subchannel codes to help determine the test power. Simpler calculations will also be performed as a check. The bundle will be heated to a maximum temperature of 538 degrees C (1000 degrees F) to determine the consequence of temperature on the steam physical properties; i.e., the local Reynolds number. The tests will also be analyzed using the subchannel vapor temperature measurements with COBRA-IV and/or VIPRE-II. The data will be reduced to obtain local heat transfer and Reynolds numbers. Approximately 30 tests will be performed after the pre-test predictions have been performed.

6. Steady-state dispersed flow film boiling tests in which droplets, of known size and velocity, are injected into the steam flow for the same conditions as the steam only convective cooling tests. The test conditions will be preserved between these two different experiments to determine the effects of the droplets on the flow and resulting heat transfer behavior. The amount of the liquid flow will be estimated from the FLECHT-SEASET data and scaled appropriately for the RBHT Test Facility. The same scaling logic will have already been used for the 3x3 heated bench test. The heated bench test will have already been performed to qualify the LIDCS, which will measure the drop size and velocity. The range of vapor Reynolds numbers is the same as the steam cooling tests, from 1500 - 30000. The pressure will be varied from 1.34 to 4.02 bars (20 to 60 psia), and the initial drop size will be varied from approximately 0.5 to 1.52 mm (0.02 to 0.06 in). The initial drop velocity will be estimated from COBRA-TF pre-test calculations and from FLECHT-SEASET data. The initial drop velocity is a function of the inlet quality to be simulated. The rod bundle will be heated and the maximum temperature will be kept below 816 degrees C (1500 degrees F), with most tests temperatures peaking at 538 degrees C (1000 degrees F) to prolong the bundle life.

7. Forced reflood experiments over a range of inlet flooding rates, which will correspond to liquid Reynolds of approximately 4000 to 25000 and vapor Reynolds numbers from 1500 to 30000. The tests will be performed over the pressure range of 1.34 to 4.02 bars (20 to 60 psia) with inlet subcoolings of approximately 2.78 to 66.7 degrees C (5 to 120 degrees F), and peak rod powers chosen not to exceed 1000 degrees C (1800 degrees F). The initial temperatures and powers will be determined by pre-test predictions using COBRA-TF. The code calculations will also be used to verify the range of Reynolds numbers within the bundle. There will be approximately 20 forced reflood tests.

8. Gravity reflood and or variable reflood tests. The purpose is to examine the effect of variable inlet flow on entrained liquid which is carried to upper regions of the bundle. In a PWR, the inlet flow initially surges into the core as the downcomer fills and its head increases. The two-phase froth front and liquid continuous flow regime can penetrate further into the bundle than the quench front to produce inverted annular film boiling. However, the head in the core region quickly comes in equilibrium with the downcomer head and the flow into the bundle decreases. The water in the bundle quickly heats and boils and

entrainment from the bundle increases. Water above the quench front tends to be entrained and carried through the bundle, providing improved cooling at the upper elevations.

These tests will use a stepped variable inlet flooding rate and will vary the flooding rate time history, inlet subcooling and the system pressure. The variable flooding rate tests will be integrated into the forced flooding experiments so that the final low flooding rate period will overlap with the forced flooding rate tests. Approximately five tests are planned.

10.5 Conclusions

Eight different types of experiments have been planned for the RBHT Test Facility to characterize the facility as well as to obtain data on dispersed flow film boiling. The experiments cover the ranges of conditions which best estimate and Appendix K reflood models are required to calculate. Hydraulic heat loss characterization experiments will be conducted. Single phase liquid boiling experiments, radiation only experiments, and single phase steam convection heat transfer experiments will also be performed to characterize the facility. In this fashion, the modeling uncertainties of the test facility are reduced.

The tests are structured in a building block approach to separate and understand the components of dispersed flow film boiling, so there is less of a chance of compensating error being applied in a specific heat transfer mode.

The precise test conditions will be developed. There is a need to perform further pre-test predictions to select the range of rod powers and initial temperatures to provide the data needed while at the same time, to minimize the duty on the heater rods. The facility design envelope is sufficiently broad to be able to perform tests over a wide range of initial and boundary conditions.

10.6 References

1. Chiou, J. S. and L. E. Hochreiter, “Combined Radiation and Dispersed Flow Film Boiling in a BWR Rod Bundle with Top Spray,” Proceedings of 26th National Heat Transfer Conference, Philadelphia, PA, 1989.

2. Hochreiter, L.E. and J. S. Chiou, “COBRA-TF Analysis of SVEA Spray Cooling Experiments,” Proceedings of 26th National Heat Transfer Conference, Philadelphia, PA, 1989.

3. Lee, N., S. Wong, H. C. Yeh, and L. E. Hochreiter, “PWR FLECHT-SEASET Unblocked Bundle, Forced and Gravity Reflood Test Data Evaluation and Analysis Report,” NUREG/CR-2256, 1981.

4. Yoder, G., et al, “Dispersed Flow Film Boiling in Rod Bundle Geometry, Steady-State Heat Transfer Data and Correlation Comparisons,” NUREG/CR-2435, 1982.

5. Bajorek, S. M., Letter to L.E. Hochreiter on “Calculated Range of Conditions for PWR Reflood Transients,” June 1998.

6. Nithianandan, C.K., Framatome Technologies, Letter to L.E. Hochreiter on “Calculated Range of Conditions for PWR Reflood Transients,” September 1998.

7. O’Dell, L., Siemens, Letter to L.E. Hochreiter on “Calculated Range of Conditions for PWR Reflood Transients,” September 1998.

8. Lilly, G.P., H. C. Yen, L. E. Hochreiter, and N. Yamaguchi, “PWR FLECHT Cosine Low Flooding Rate Test Series Evaluation Report”, WCAP-8838, 1977.

9. Lilly, G.P., H. C. Yeh, L. E. Hochreiter, and N. Yamaguchi, “PWR FLECHT Skewed Profile Low Flooding Rate Test Series Evaluation Report,” WCAP-9183, 1977.

11. Test Facility Design

11.1 Introduction

The RBHT Test Facility is designed to conduct systematic separate-effects tests under well-controlled conditions in order to generate fundamental rod bundle heat transfer data including single phase steam cooling tests, low flow boiling tests, steam flow tests with injected droplets and inverted annular film boiling and dispersed flow film boiling heat transfer. The facility is capable of operating in both forced and variable flow reflood modes covering wide ranges of flow and heat transfer conditions at pressures from 1.34 to 4.02 bars (20 psia to 60 psia).

11.2 General Design Description

The RBHT Test Facility consists of the following major components, shown schematically in Figure 11.1:

- A test section consisting of a lower plenum, a low-mass housing containing the heater rod bundle, and an upper plenum
- Coolant injection and steam injection systems
- Closely coupled phase separation and liquid collection systems
- An injection system
- A pressure fluctuation damping tank and steam exhaust piping

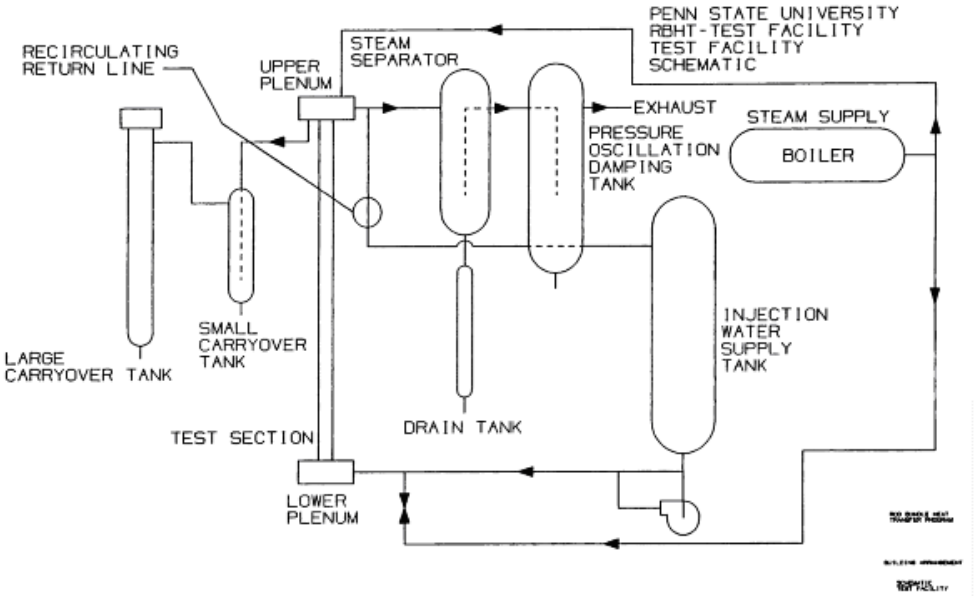

Figure 11.1 RBHT Test Facility Schematic.

11.3 Detailed Component Design Description

The various components of the RBHT Test Facility are described in the following paragraphs. All components are well insulated to minimize heat losses to the environment.

11.3.1 Test Section

The test section consists of the heater rod bundle, the flow housing, and the lower and upper plenums, as shown in Figure 11.2.

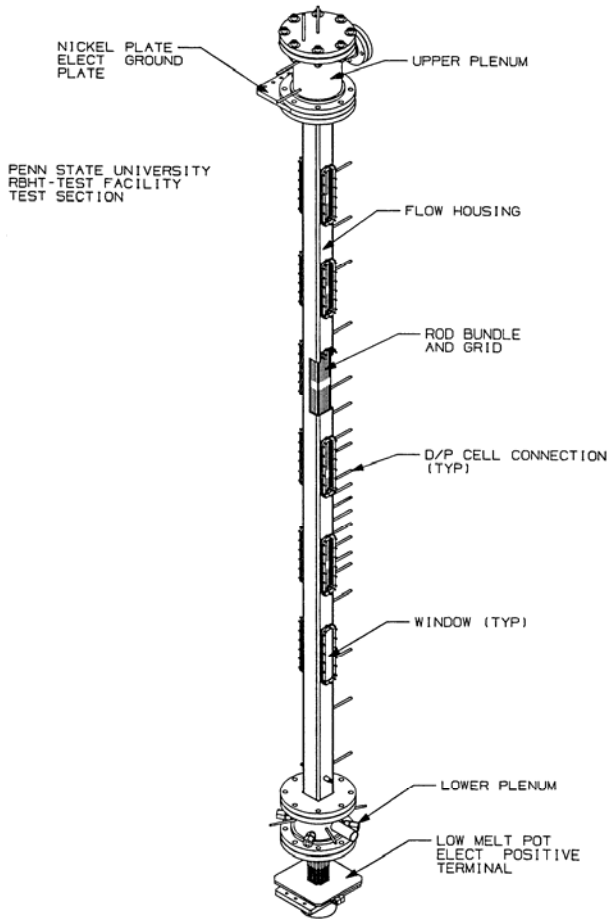

Figure 11.2 Test Section Isometric View.

The heater rod bundle simulates a small portion of a 17x17 reactor fuel assembly. The electrically powered heater rods have a diameter of 9.5 mm (0.374 inches) arranged in a 7x7 array with a 12.598 mm (0.496 in) pitch, as shown in Figure 11.3. The heater rod specifications are listed in Table 11.1. The bundle has 45 heater rods and four unheated corner rods. The corner rods are used to support the bundle grids and the grid and fluid thermocouple leads. The support rods are made from Inconel 600 tubing having a diameter of 9.525 mm (0.375 in), a wall thickness of 2.108 mm (0.083 in), and have a length of 3.96 m (156 in). The heater rods are

Table 11.1 General Specifications

Operating Pressure	200 psi
Maximum Sheath Temperature	220 degrees F
Heater Rod (Schematic Drawing)	
Design Power	10.0 kW
Design Voltage	57V
Design Current	175.4A
Design Resistance (@ 1000 degrees F)	0.325 Ω
Electrical Resistance (@ 70 degress F)	0.306 Ω ± 5 percent
Axial Power Profile	Linear 0.5/1.5/0.5 (See Figure 11.5)
Heated Length	144 in
Average Linear Power	0.83 kW/ft
Peak Linear Power	1.25kW/ft
Outside Diameter	0.374 ± 0.002 in
Overall Sheath Length	172 in
Electrode Length	8 in
Electrode Diameter	0.230 ± 0.002 in
Extension Length - Top	8 ± 0.25 in
Sheath Surface Finish	As Swaged (63 μin or better)

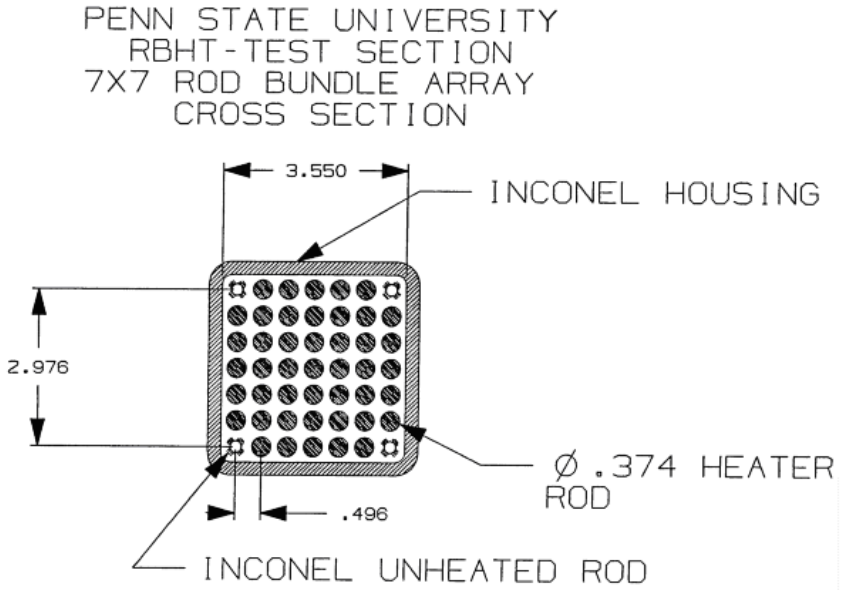

Figure 11.3 Rod Bundle Cross Sectional View.

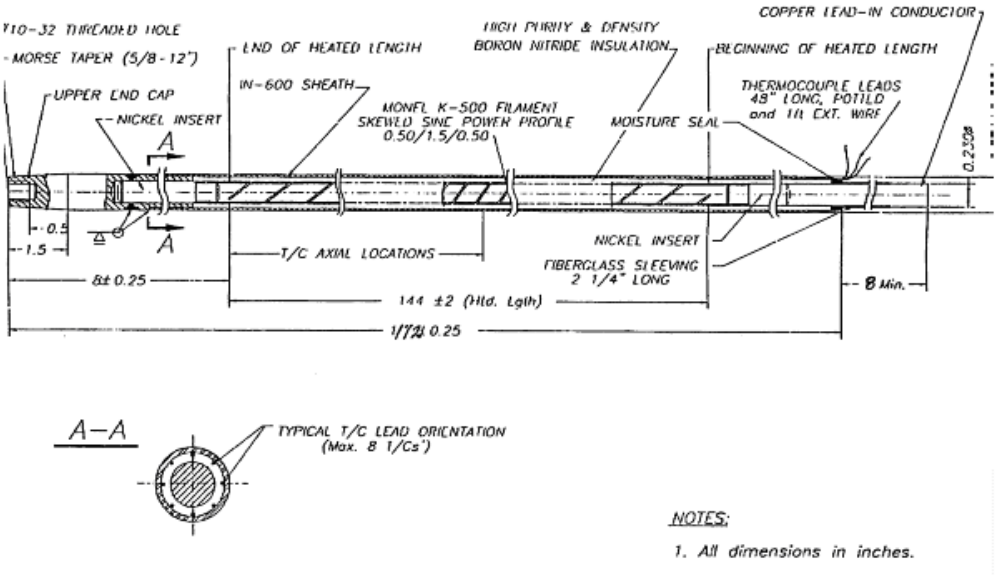

Figure 11.4 Heater Rod.

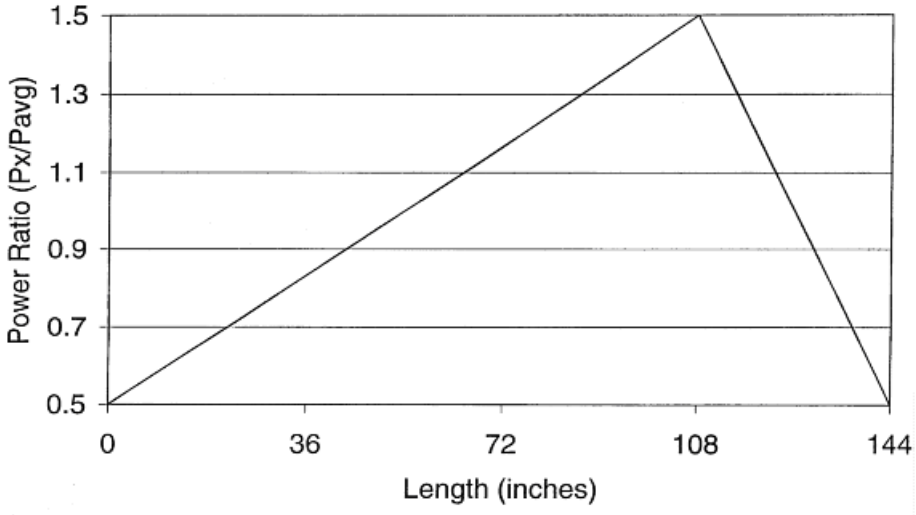

Figure 11.5 Heater Rod Axial Power Profile.

single ended and consist of a Monel 500 electrical resistance element filled and surrounded by hot pressed boron nitride (BN) insulation, and enclosed in an Inconel 600 cladding, as shown in Figure 11.4. This material was chosen for its high strength and low thermal expansion coefficient at high temperatures, which minimizes rod bowing and failure at high temperature operating conditions since it was desired to reuse the heater rods for a second bundle build. The heater rods have a 3.657 m (12 ft) heated length with a skewed axial power profile, as shown in Figure 11.5, with the peak power located at the 2.74 m (9 ft) elevation. The maximum-to-average power ratio (P_{min}/P_{avg}) is 1.5 and the minimum-to-average power ratio (P_{min}/P_{avg}) is 0.5 at both ends of the heated length. The bundle has a uniform radial power distribution.

Power to each rod is provided by a 60 volt, 12,600 amp, 750 kW DC power supply. Each rod is rated for 10 kW, and designed to operate at 13.8 bars (200 psig) at a maximum temperature of 1204 degrees C (2200 degrees F), but because of its solid construction can be operated at up to 103.4 bars (1500 psig). Each rod is instrumented with eight 0.508 mm (20 mil) diameter ungrounded thermocouples attached to the inside surface of the Inconel sheath at various locations. All of the thermocouple leads exit at the heater rod bottom end. Thermocouple specifications are shown in Table 11.2. The Inconel 600 thermocouple sheath is compatible with the heater rod cladding and housing material to reduce thermal expansion and minimize the possibility of thermocouple failure during the thermocycling operations.

Table 11.2 Thermocouple Specifications

Type	Premium grade ANSI Type K
Diameter	0.02 in
Sheath	Inconel 600
Insulation	MgO
Junction	Ungrounded, BN backfilled
Length	Up to 18 ft
Resistance, Lead to Sheath	$1x10^{11}$ Ω at 50 V
Length beyond Heater Sheath	48 in

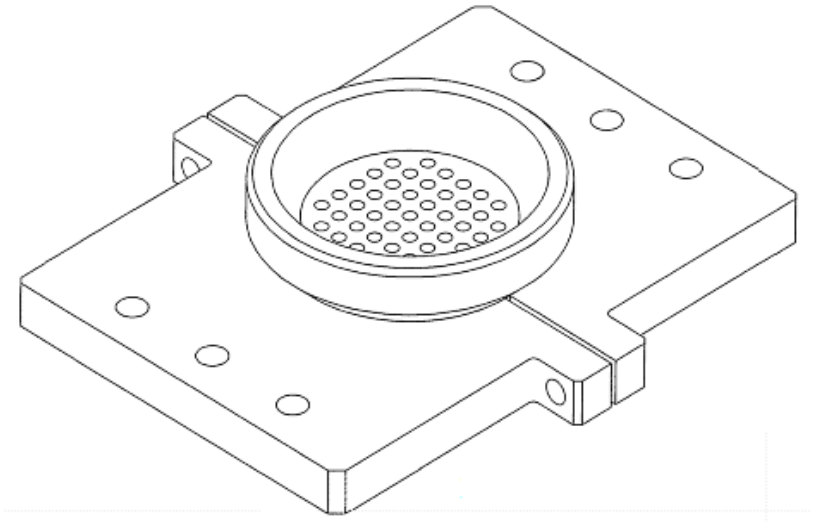

Figure 11.6 Low-Melt Reservoir.

The rod bundle has eight grids located 0.522 m (20.55 in) apart except for the spacing between the first and second grids, which are 588.26 mm (23.16 in) apart. The first grid is located 101.854 mm (4.01 in) above the bottom of the heated length. The grid elevations are similar to the ones found in a 17x17 fuel assembly. The grids, in conjunction with the corner support rods, form the heater rod bundle support structure. The heater rod top extensions are attached to the 2.4 cm (1 in) thick nickel ground plate by means of a Morse taper that provides a good electrical contact. The heater rod bottom extension and copper electrode extend through the lower plenum-O ring pressure seal plate. The copper electrodes, which are 5.842 mm (0.230 in) in diameter and 203 mm (8 in) long, extend through holes drilled in the low-melt reservoir shown in Figure 11.6. This reservoir serves as the electrical power supply positive side connection. It contains a low temperature melting alloy that melts at about 71.11 degrees C (160 degrees F) which is an excellent conductor, thus providing a good electrical contact to each heater rod.

The flow housing provides the pressure and flow boundary for the heater rod bundle. It has a square geometry. Its nominal inside dimensions are 90.17 mm^2 (3.55 in^2), and wall thickness 6.35 mm (0.25 in), as shown in Figure 11.7. The housing is made out of Inconel 600, the same material used for the heater rod cladding and thermocouple sheaths. As pointed out previously, the high strength of Inconel 600 at elevated temperatures will minimize housing distortion during testing. The 6.35 mm (0.25 in) wall thickness is the minimum allowable for operating at 4.0 bars (60 psia) and 537.77 degrees C (1000 degrees F), taking into consideration the cutouts to accommodate the large windows and the numerous pressure and temperature penetrations through the walls. The empty housing has a flow area of 81.29 cm^2 (12.60 in^2). With the rod bundle in place the flow area is 45.80 cm^2 (7.1 in^2). This area is 8.2 percent larger than the ideal flow area of a 7x7 rod bundle configuration. The excess flow area is due to the flow housing inside dimensional tolerance and the space needed to insert the rod bundle in the housing. The gap between the outer rods and the flow housing inner wall is 2.54 mm (0.1 in) wide.

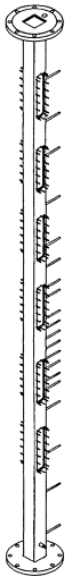

Figure 11.7 Low Mass Flow Housing Assembly.

The flow housing has six pairs of windows. Each window provides a 50.8x292.1 mm (2x11.5 in) viewing area. Each pair of windows is placed 180 degrees apart and located axially at elevations overlapping rod bundle spacer grids, thus providing a viewing area about 88.9 mm (3.5 in) below and 152.4 mm (6 in) above the corresponding spacer grids. The windows will facilitate the measurement of droplet size and velocity using a Laser Illuminated Digital Camera System (LIDCS). The two-phase void fraction will be measured using a X-ray densitometer, as well as sensitive differential pressure (DP) cells. In addition, high speed movies using diffused back lighting can be taken during the experiments, if desired, for visualization and flow regime information. The windows are made out of optical grade fused quartz and are mounted on the housing by means of a bolted flange and Thermiculite high temperature gasketing material, as shown in Figure 11.8.

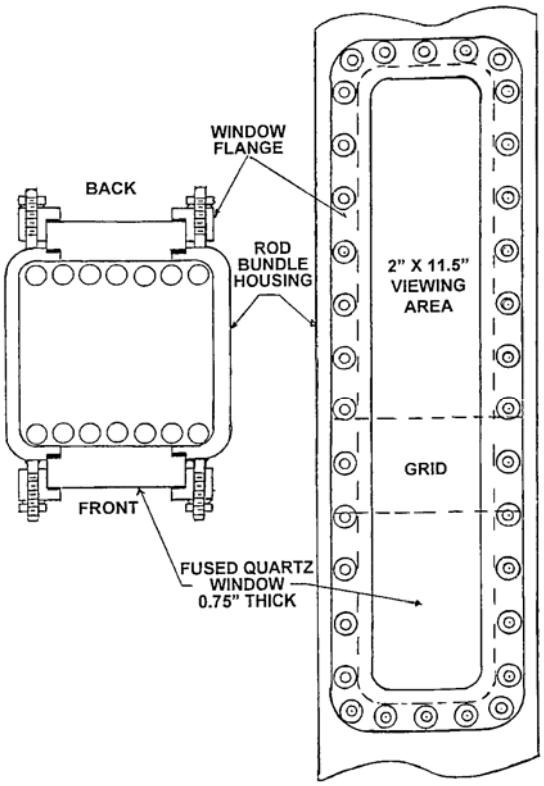

Figure 11.8 Housing Window.

The flow housing has 22 pressure taps located at various elevations, as shown in Figure 11.7. The pressure taps are connected to sensitive DP cells, providing measurements to calculate single-phase friction losses for determining bare rod bundle and grid loss coefficients. Nine of these pressure taps are located about 76.2 mm (3 in) apart to provide detailed void fraction measurements in the froth region above the quench front. The flow housing is supported from the nickel plate and upper plenum, allowing it to freely expand downward, thus minimizing thermal buckling and distortion.

11.3.2 Lower Plenum

The lower plenum is attached to the bottom of the flow housing. The lower plenum is made out of nominal 203.2 mm (8 in) schedule 40, 304 stainless steel pipe with an inside diameter of 201.6 mm (7.937 in), a height of 203.2 mm (8 in), and a volume of 6569.5 cm^3 (0.232 ft^3), as shown in Figure 11.9. The lower plenum is used as a reservoir for the coolant prior to injection into the rod bundle during reflood. It connects to the injection water line and steam cooling line. It has two penetrations for thermocouples monitoring the coolant temperature prior and during reflood, and a pressure tap for static and differential pressure measurements.

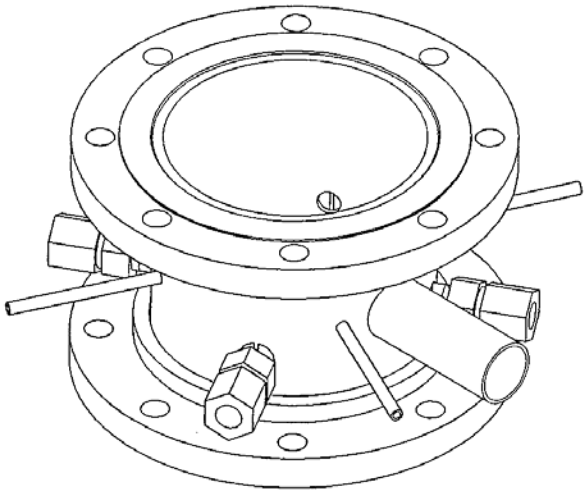

Figure 11.9 Lower Plenum.

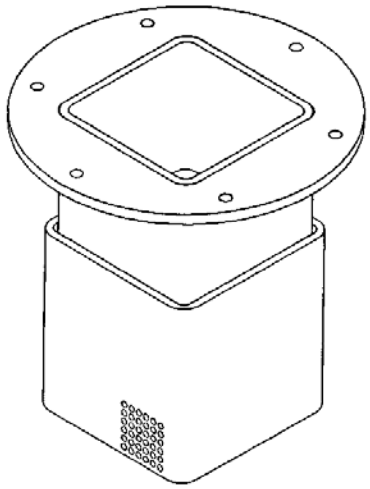

Figure 11.10 Lower Plenum Flow Baffle.

The lower plenum also has four Conax fittings with multiple probes sealing glands for the bundle grid, steam probes, and support rod wall thermocouple extensions that are routed through the bottom of the rod bundle. It contains a flow baffle, which is attached to the flow housing bottom flange. The flow baffle has a square geometry, similar to the flow housing, as shown in Figure 11.10. The flow baffle wall has numerous small diameter holes that act as a flow distributor and flow straightener to provide an even flow distribution into the rod bundle.

11.3.3 Upper Plenum

The upper plenum serves as the first stage for phase separation and liquid collection of the two-phase effluent exiting the rod bundle. The liquid phase separates due to the sudden expansion from the bundle to the larger plenum flow area. The de-entrained liquid is collected around the flow housing extension in the upper plenum. The extension acts as a weir preventing the separated liquid from falling back into the heater rod bundle. The upper plenum vessel configuration is shown in Figure 11.11. The vessel is made from a 203.2 mm (8 in) 304 stainless steel pipe with an inside diameter of 201.6 mm (7.937 in) and a height of 304.8 mm (12 in). It has a volume of 9825.95 cm^3 (0.347 ft^3). The plenum has a 76.2 mm (3 in) pipe flanged connection to the steam separator and two penetrations for fluid thermocouples. It is covered with a 203.2 mm (8 in) 304 stainless steel blind flange. This flange has a 25.4 mm

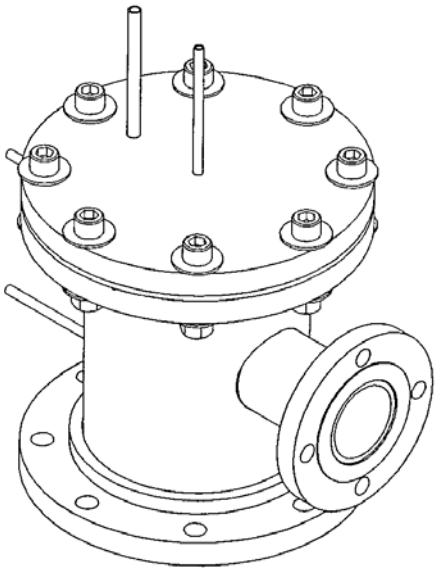

Figure 11.11 Upper Plenum.

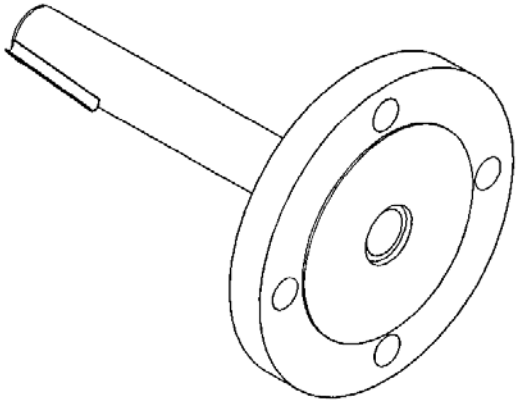

Figure 11.12 Exhaust Line Baffle.

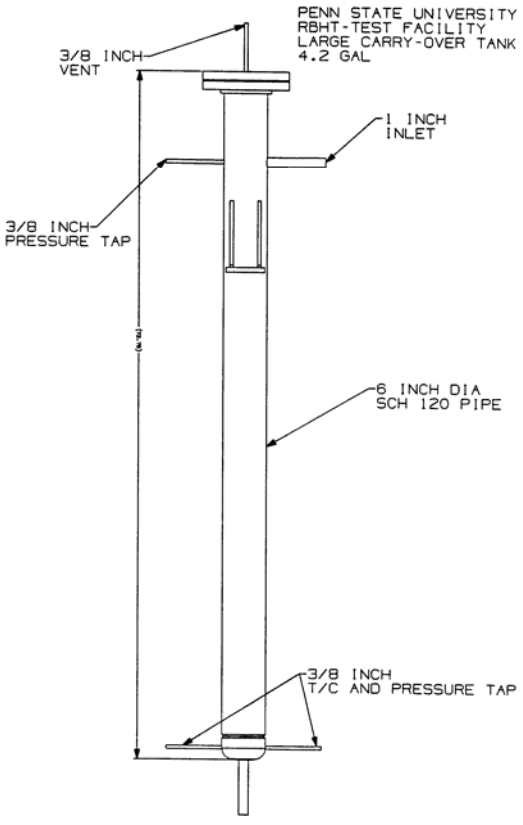

Figure 11.13 Large Carryover Tank.

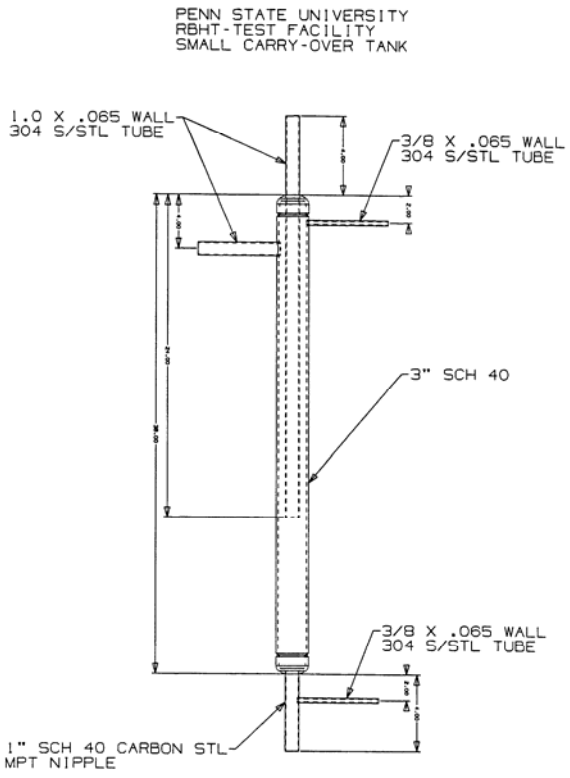

Figure 11.14 Small Carryover Tank.

(1 in) penetration for steam injection, venting, and connecting the safety relief valve and rupture disc assembly. It also has a pressure tap penetration for static and differential pressure measurements. In addition, the upper plenum contains an exhaust line baffle, shown in Figure 11.12. The baffle is used to further de-entrain water from the steam, and prevents water dripping from the upper plenum cover flange to be carried out by the exhaust steam. The baffle has a 76.2 mm (3 in) flange connection at one end. It is inserted through the upper plenum exit nozzle, and it is bolted between the nozzle flange and the flange of the pipe going to the steam separator.

11.3.4 Carryover Tanks

The de-entrained liquid from the upper plenum drains into the top of a 25.6 mm (1 in) tube which extends inside a small carryover tank to detect and measure the carryover liquid as soon as possible. This tank, shown in Figure 11.14, is connected close coupled in series with a larger carryover tank, shown in Figure 11.13, which collects and measures the amount of liquid overflow from the smaller carryover tank. The small carryover tank has a volume of about 4247.53 mm^3 (0.15 ft^3) to more accurately measure the water being collected as a function of time. This tank is made from a 76.2 mm (3 in) schedule 40 pipe having an overall length of 0.9144 m (36 in) including the end caps. The large carryover tank is made from a 101.6 mm (4 in) schedule 40 pipe with a bottom end cap and top flanges having an overall length of 152.4 mm (6 ft) and a capacity of 15007.9 mm^3 (0.53 $feet^3$). Each tank is connected with 25.4 mm (1 in) flexible hose, and has a 1 in drain tube, and 9.525 mm (3/8 in) tubes with wall penetrations for installing fluid and level meters.

11.3.5 Steam Separator and Collection Tanks

The wet steam exhausted from the upper plenum flows through a steam separator (or dryer), shown in Figure 11.15, where carryover liquid droplets are further separated from the steam. The droplets are collected in a small collection tank, shown in Figure 11.16, attached to the bottom of the steam separator. The steam separator relies on centrifugal force action to provide 99 percent dry steam. The separated liquid is drained into a collection tank where a DP cell is used as a level meter to measure the liquid accumulation. The steam separator is fabricated from a 355.6 mm (14 in) diameter 316 stainless steel pipes and is 914.4 mm (36 in) long. It has 50.8 mm (2 in) connecting nozzles, a 25.4 mm (1 in) drain, and a 12.7 mm (0.5 in) top vent. It also has two pressure taps for liquid level measurements and two 38.1 mm (1.5 in) side nozzle connections. The drain tank is a small vessel with a capacity of 0.0113 m^3 (0.4 ft^3). It is made from a 101.6 mm (4 in) schedule 10, 304 stainless steel pipe with an overall length of 121.9 mm (48 in), including both end caps. It has a 25.4 mm (1 in) drain nozzle, a 25.4 mm (1 in) pipe top connection to the steam separator, pressure taps and fluid thermocouple connections.

11.3.6 Pressure Oscillation Damping Tank

The dry steam from the steam separator flows into a pressure oscillation-damping tank. As its name implies, it is used to dampen pressure oscillations in the upper plenum caused by rapidly oscillating steam generation rates in the heater rod bundle during reflood. This effect is coupled to the characteristics of the pressure control valve, which is located downstream in the steam exhaust line. It is desirable to have a smooth pressure control in order to minimize uncertainties when calculating mass balances, steam generation rates, and heat transfer coefficients in the heater rod bundle, and avoid the pressure control valve causing oscillations in the bundle as it cycles. The tank has a volume of 0.227 m^3 (8 ft^3), which is approximately equal to the total

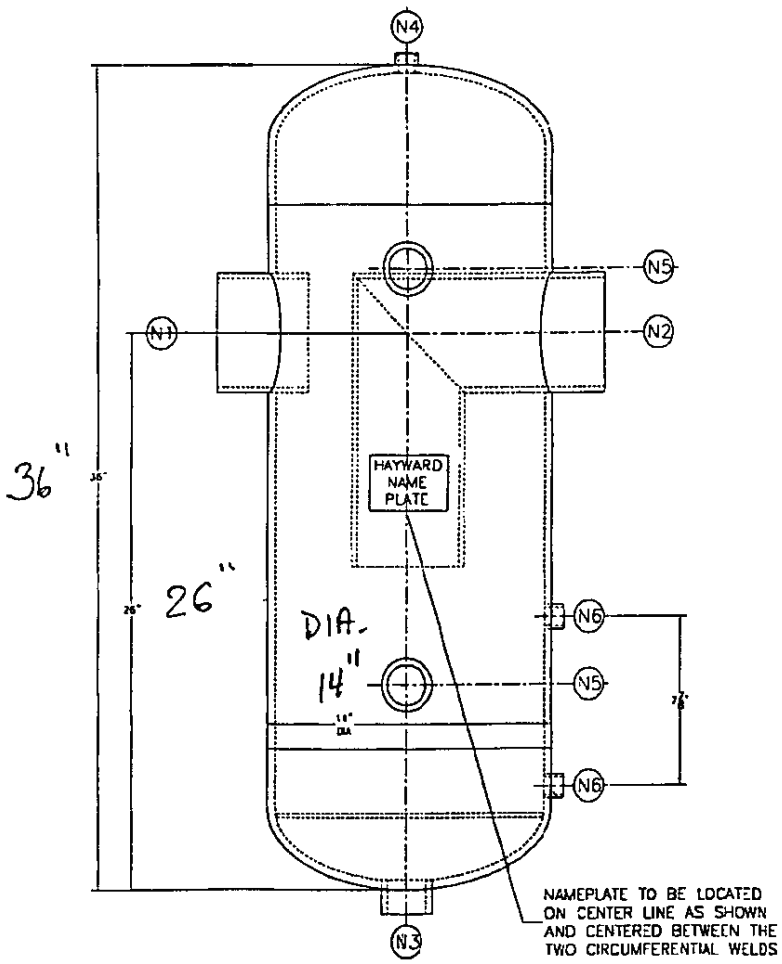

Figure 11.15 Steam Separator.

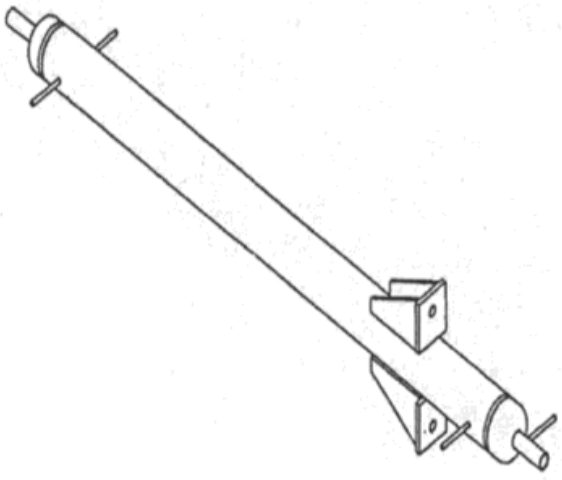

Figure 11.16 Steam Separator Collection Tank.

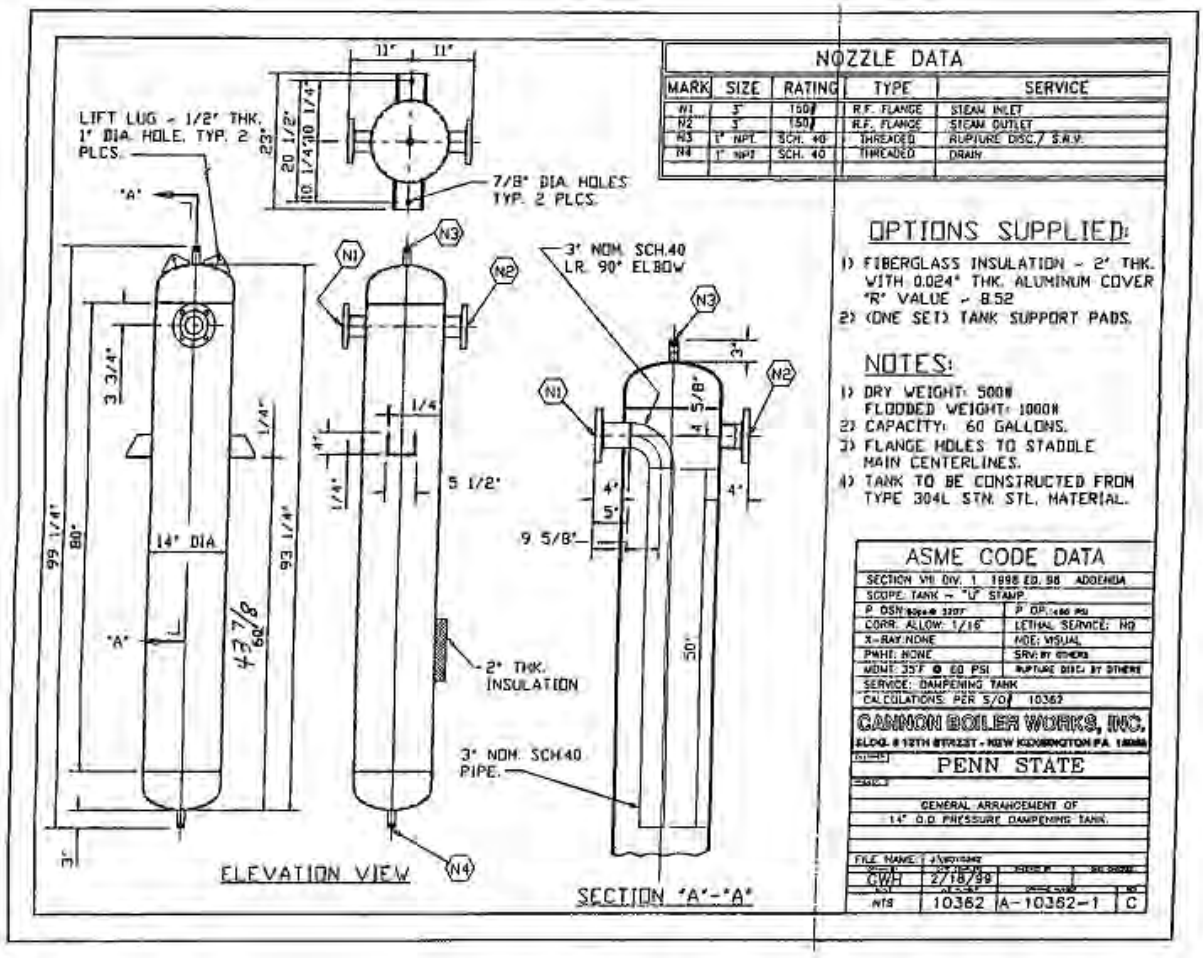

Figure 11.17 Pressure Oscillation Damping Tank.

volume of the rest of the test facility. This design criterion was used successfully in the ACHILLES reflood test facility (Refs. 1, 2, 3, 4, 5 and 6). The pressure tank is fabricated from a 355.6 mm (14 in), 304 stainless steel standard schedule pipe by 2.59 m (102 in) long, as shown in Figure 11.17. Inside the tank is a 76.2 mm (3 in), schedule 40, 304 stainless steel pipe that provides a tortuous path for the steam flow to expand into a large volume, thus damping pressure oscillations. The inlet and outlet nozzles are 76.2 mm (3 in) in diameter with flanges. The vent and drain lines are made of 25.4 mm (1 in) pipe. There are 9.53 mm (3/8 in) tube penetrations for a fluid thermocouple and two static pressure taps. The tank walls are heated with clamp-on strip heaters up to about 10 degrees above saturation temperatures to prevent steam condensation.

11.3.7 Exhaust Piping

The steam flowing out of the pressure oscillation-damping tank is exhausted through a 76.2 mm (3 in) schedule 40, 304 stainless steel pipes, shown schematically in Figure 11.20. The exhaust line has a Vortex flowmeter, a 76.2 mm (3 in) V-Ball pressure control valve, and a muffler at the exit to minimize the noise caused by steam blowing into the atmosphere. The pressure control valve is activated by a signal from a static pressure transmitter located on the upper plenum.

The line is also instrumented with a static pressure transmitter, fluid thermocouples, and outer wall thermocouples. The 76.2 mm (3 in) line has flow-straightening vanes which reduce the pipe length requirements upstream of the Vortex meter in order to obtain accurate flow measurements. This line has strapped-on electrical heaters to keep the wall temperature about 11.11 degrees C (20 degrees F) above saturation to insure that single-phase steam flow measurements are made by the Vortex flowmeter.

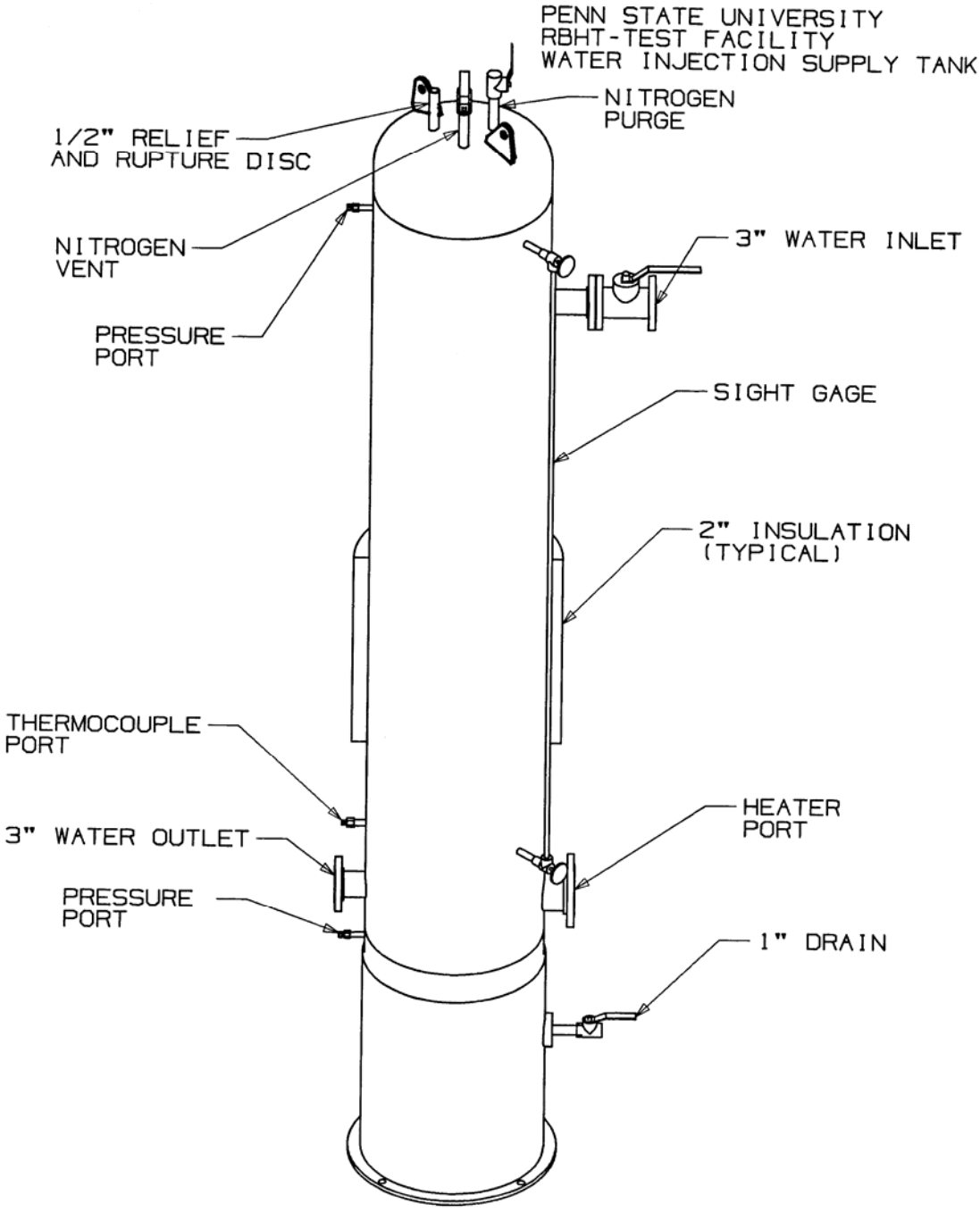

Figure 11.18 Injection Water Supply Tank.

11.3.8 Injection Water Supply Tank

The injection water system consists of a water supply tank, a circulating pump, and interconnecting lines to the test section lower plenum. The water supply tank, shown in Figure 1118, has a capacity of 200 gal. It is designed for 4.0 bar (60 psia) and 154.44 degrees C (310 degrees F). The tank is equipped with a submersible electrical heater to heat the injection water to specified test temperatures. The tank is pressurized by a nitrogen supply system, which regulates the over-pressure needed for the forced flooding injection tests. The tank has inlet and outlet nozzles, pressure taps for level measurements, fluid and wall thermocouples. Water from the tank can be circulated through the test section by a centrifugal pump with a capacity up to 250 gpm which is needed to perform liquid single-phase flow tests.

11.3.9 Water Injection Line

The water injection line, shown schematically on Figure 11.20, consists of a 50.8 mm (2 in) diameter 304 stainless steel tubing with a 2.7686 mm (0.109 in) wall. It is rated for 60 psia (4.0 bar) and 154.44 degrees C (310 degrees F) service. This line has a Coriolis Effect type flowmeter, a V-ball control valve, a quick opening solenoid valve, and appropriate shut-off and drain valves. It also has penetrations for static pressure and fluid thermocouples, and outside wall thermocouples. The line has tracer electrical cable type heater to maintain the water being injected at the proper test inlet temperatures. The water injection line can also be extended to the downcomer during gravity reflood tests.

11.3.10 Steam Supply

A boiler with a capacity of 2613 kg (5760 lbs) per hour at 10 bar (150 psia) provides steam for the single phase steam cooling , pressure drop and water droplet injection tests. It also provides steam for preheating the test components prior to testing. The boiler is connected to the lower plenum by means of a 50.8 mm (2 in), 304 stainless steel tube. It is equipped with a Vortex flowmeter to measure steam flows, fluid and wall thermocouples, a V-ball control valve, and a quick acting solenoid valve. The boiler is also connected to the upper plenum to provide steam for preheating the test components prior to testing.

11.3.11 Droplet Injection System

A system to inject water droplets into the test section has been included in the RBHT design. The droplet injection system consists of six 2.38 mm (3/32 in) O.D. stainless steel tubes entering through the test section at the 1.295 m (51 in) elevation. The tubes run perpendicular to the heater rods and penetrate through both sides of the housing as seen in Figure 11.19. The tubes can be easily removed when not needed so they do not interfere with other types of tests. Water is supplied to the injector tubes from the injection water supply tank as described in Section 11.3.8 and a series of small holes are drilled in the tubes to inject water directly into each of the 36 subchannels.

11.4 Test Facility Instrumentation

The test facility instrumentation is designed to measure temperatures, power, flows, liquid levels, pressures, void fractions, and droplet sizes, distribution, and drop velocities. The vapor velocity cannot be directly measured in a two-phase dispersed flow, but it can be calculated at

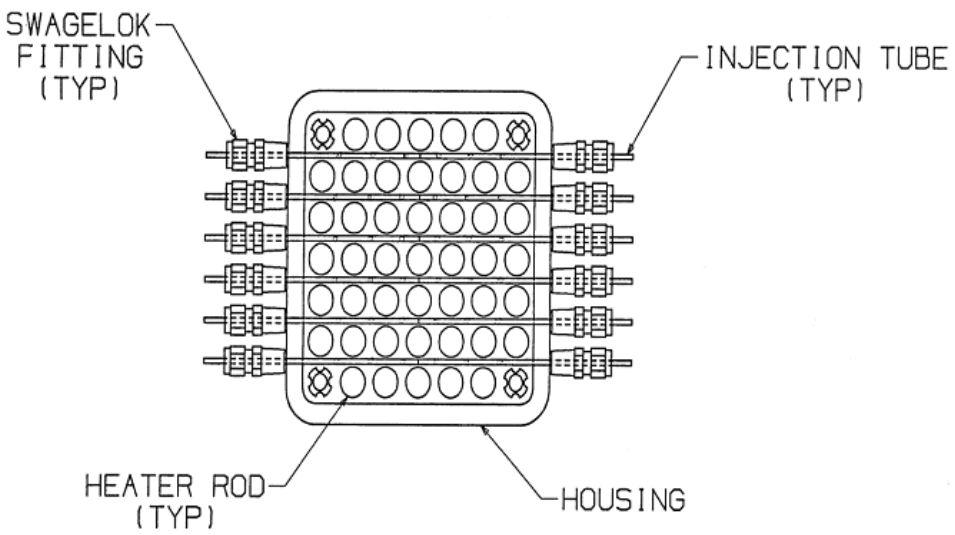

Figure 11.19 Droplet Injection Schematic.

different axial positions from the data. Overall and transient mass and energy balances, mass inventories, carryover liquid and steam flows as a function of time can be calculated. Heater rod power, temperature, and fluid temperature are used to calculate heat fluxes and heat transfer coefficients, quench times, rod bundle energy losses, convective and radiation heat transfer to steam, droplets, grids, support rods, and housing. Effects of grids, support rods and housing behavior during reflood can be determined. Void fraction can be determined from the pressure drop measurements below the quench front and in the froth level above the quench front. The laser illuminated digital camera measurements are used to determine droplet entrainment behavior and droplet effects on heat transfer, and steam desuperheating above the quench front.

11.4.1 Loop Instrumentation and Controls

Loop instrumentation is shown schematically in Figure 11.20, and the instrumentation and data acquisition channels are listed in Table 11.3. There are 61 instrumentation channels assigned to the collection of electrical power, fluid and wall temperatures, levels, flows, differential pressures, and static pressure measurements. The injection water supply tank has three fluid and three wall thermocouples to monitor water and wall temperatures during heat-up prior to testing. A DP transmitter used as a level meter to determine water mass in the tank and mass depletion during reflood testing. A static pressure transmitter which monitors the nitrogen overpressure and controls the nitrogen flow needed to maintain a constant pressure during forced injection reflood tests.

The water injection line is equipped with a Coriolis Effect Micromotion flowmeter that directly measures mass flows up to 454 kg/min (1000 lbs/min) with an accuracy of plus or minus eleven hundredths of a percent (±0.11 percent) of the flow rate. The steam line has a Rosemount Vortex shedding flowmeter to measure flow up to 7.08 m^3/min (250 ft^3/min) with an accuracy of plus or minus 65 hundredths of a percent (±0.65 percent) of the flow rate. Each flowmeter is connected through a pneumatic controller to a V-ball flow control valve. Each line has a fluid thermocouple to measure water or steam temperature during heat-up and forced injection

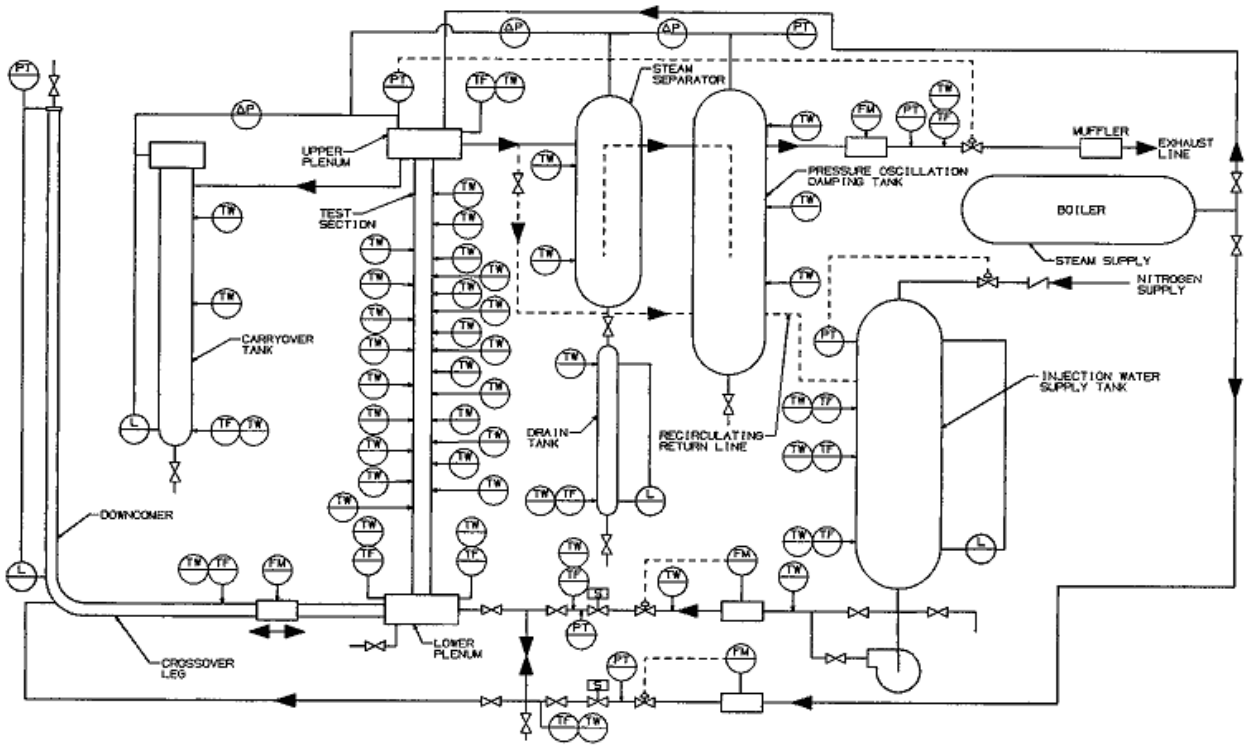

Figure 11.20 Loop Instrumentation Schematic.

testing. The injection line has three wall thermocouples to monitor wall temperatures during heat-up and during testing. One of these thermocouples in conjunction with a temperature controller regulates the power to an electrical heating cable wrapped around the injection line. The heating cable is used to heat-up the injection line wall and to maintain the injection water at the required injection temperature.

The carryover tank instrumentation consists of one fluid thermocouple, three wall thermocouples, and a liquid level meter which measures the amount of carryover liquid being collected during testing. In addition, a DP transmitter is connected from the top of the carryover tank to the upper plenum to determine the static pressure in the carryover tank.

The steam separator and drain tank are instrumented with two wall thermocouples to monitor wall temperatures during heat-up. The drain tank has a fluid thermocouple to measure temperatures of de-entrained liquid being collected during testing. The volume of de-entrained water is measured with a level meter connected across the drain tank. A DP transmitter is connected between the steam separator and upper plenum.

The pressure oscillation damping tank has three wall thermocouples which are used to monitor vessel walls during heat-up, and to insure that the vessel wall is at a temperature above saturation to prevent condensation. One wall thermocouple in conjunction with a temperature controller monitors the power applied to clamp-on heaters that heat up the tank to the desired wall temperature.

The exhaust line is equipped with a Rosemount Vortex shedding flowmeter which, in conjunction with a static pressure transmitter and fluid thermocouple measurements, is used to calculate steam volumetric flows up to 7.08 m^3/min (250 ft^3/min). The flowmeter has an accuracy of plus or minus 65 hundredths of a percent (±0.65 percent) of the flow rate. The exhaust line also has wall thermocouples to measure pipe wall temperatures. One wall thermocouple in conjunction with a temperature control regulates the power going to clamp-on heaters which are used for heating the pipe walls up to a temperature above saturation of about 11 degrees C (~20 degrees F) to prevent steam condensation and to insure accurate single phase steam flow measurements. The exhaust line has a V-ball pressure control valve this valve is controlled by a static pressure transmitter through a pneumatic controller connected to the top of the upper plenum in order to maintain constant test section pressure during testing.

11.4.2 Test Section Instrumentation

The test section is heavily instrumented to obtain the data described at the beginning of Section 11.4.

The test section instrumentation consists of the heater rod bundle and flow housing, the lower plenum, and the upper plenum groups. The heater rod bundle and flow housing instrumentation is shown schematically in Figure 11.21 and listed in Table 11.3. Figure 11.21 shows the instrumentation axial locations in relation to heater rod heated length, heater axial power profile, grids, housing pressure taps, and windows.

Five grids have thermocouples attached to their surfaces in order to determine quenching behavior during reflood. Eight groups of heater rods have thermocouples at different elevations to cover, as much as possible, the entire rod bundle heated length. The radial location of each heater rod group is shown in Figure 11.22. The radial locations of instrumentation rods were chosen in order to be able to characterize heat transfer of hot rods simulated by the center rods, rod-to-rod and rod-to-housing radiation heat transfer. For this purpose, heater rod thermocouples, steam probes, and housing wall thermocouples are located at the same elevations. In addition, symmetrical location of the same group of instrumented heater rods will help in the data analysis and will determine any anomalies in the radial flow distribution through the rod bundle. Rod thermocouples are also placed at varying distances downstream from a grid to determine the decreasing heat transfer gradient between grid spans. The steam probe or fluid thermocouples are located at short distances upstream and downstream of a grid to determine the effect of water droplets being shattered by the grids on droplet size and distribution, and the de-superheating effect on steam temperatures in the disperse flow regime.

The vapor or steam temperature will be measured using miniature thermocouples which are attached to the spacer grids or are used for traversing. These are very small bare thermocouples that have a fast response time such that they can follow the vapor temperature accurately in a dispersed, non-equilibrium, two-phase flow. As the froth front approaches, the number and sizes of the droplets increase which can lead to wetting of these thermocouples. Experiments performed as part of the FLECHT-SEASET program indicated that very small bare thermocouples would provide reliable vapor superheat ready for the longest time period until they quench as the froth region approached. While the Lehigh vapor probe was considered, it is too large and causes a flow distribution effect which is not typical of the bundle. The Lehigh probe would block 68 percent of the gap between adjacent heat rods. The effect of the probe would be to distort the data downstream of the sensing location. Such flow distribution

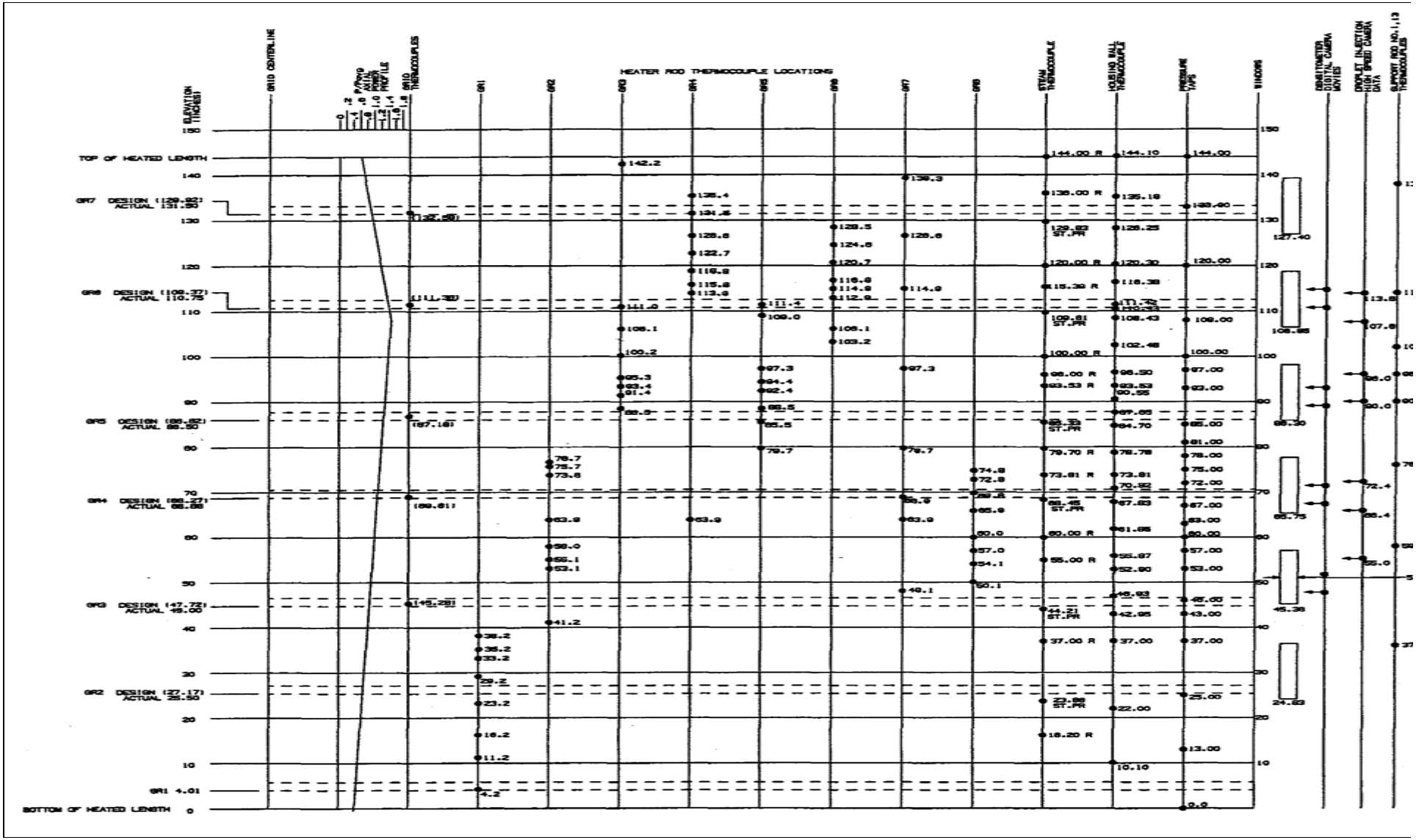

Figure 11.21 Rod Bundle and Housing Instrumentation Axial Locations.

Table 11.3 Instrumentation and Data Acquisition Channel List

SLOT 1			
CHAN	NAME	PANEL/ INPUT #	Slot, SCP & SCP #
497	**Pnl1-Therm2S**	**1-0**	**1-E1508A-0**
418	Lg CT fl	1-1	1-E1508A-0
419	Lg CT wall-t	1-2	1-E1508A-0
420	Lg CT wall-m	1-3	1-E1508A-0
421	Lg CT wall-b	1-4	1-E1508A-0
422	Sm CT fl	1-5	1-E1508A-0
423	Sm CT wall-t	1-6	1-E1508A-0
424	Sm CT wall-b	1-7	1-E1508A-0
1	HR_B1-48.1	1-8	1-E1508A-1
2	HR_B1-63.9	1-9	1-E1508A-1
3	HR_B1-68.9	1-10	1-E1508A-1
4	HR_B1-79.7	1-11	1-E1508A-1
5	HR_B1-97.3	1-12	1-E1508A-1
6	HR_B1-114.9	1-13	1-E1508A-1
7	HR_B1-126.6	1-14	1-E1508A-1
8	HR_B1-139.3	1-15	1-E1508A-1
9	HR_D1-48.1	1-16	1-E1508A-2
10	HR_D1-63.9	1-17	1-E1508A-2
11	HR_D1-68.9	1-18	1-E1508A-2
12	HR_D1-79.7	1-19	1-E1508A-2
13	HR_D1-97.3	1-20	1-E1508A-2
14	HR_D1-114.9	1-21	1-E1508A-2
15	HR_D1-126.6	1-22	1-E1508A-2
16	HR_D1-139.3	1-23	1-E1508A-2
17	HR_F7-48.1	1-24	1-E1508A-3
18	HR_F7-63.9	1-25	1-E1508A-3
19	HR_F7-68.9	1-26	1-E1508A-3
20	HR_F7-79.7	1-27	1-E1508A-3
21	HR_F7-97.3	1-28	1-E1508A-3
22	HR_F7-114.9	1-29	1-E1508A-3
23	HR_F7-126.6	1-30	1-E1508A-3
24	HR_F7-139.3	1-31	1-E1508A-3

SLOT 2			
CHAN	NAME	PANEL/ INPUT #	Slot, SCP & SCP #
499	**Pnl3-Therm2S**	**3-0**	**2-E1508A-0**
392	U Plen wall-b	3-1	2-E1508A-0
399	Sup Tnk fl-t	3-2	2-E1508A-0
400	Sup Tnk fl-m	3-3	2-E1508A-0
401	Sup Tnk fl-b	3-4	2-E1508A-0
402	Sup Tnk wall-t	3-5	2-E1508A-0
403	Sup Tnk wall-m	3-6	2-E1508A-0
404	Sup Tnk wall-b	3-7	2-E1508A-0
49	HR_B2-4.2	3-8	2-E1508A-1
50	HR_B2-11.2	3-9	2-E1508A-1
51	HR_B2-16.2	3-10	2-E1508A-1
52	HR_B2-23.2	3-11	2-E1508A-1
53	HR_B2-29.2	3-12	2-E1508A-1
54	HR_B2-33.2	3-13	2-E1508A-1
55	HR_B2-35.2	3-14	2-E1508A-1
56	HR_B2-38.2	3-15	2-E1508A-1
57	HR_C2-41.2	3-16	2-E1508A-2
58	HR_C2-53.1	3-17	2-E1508A-2
59	HR_C2-55.1	3-18	2-E1508A-2
60	HR_C2-58	3-19	2-E1508A-2
61	HR_C2-63.9	3-20	2-E1508A-2
62	HR_C2-73.8	3-21	2-E1508A-2
63	HR_C2-75.7	3-22	2-E1508A-2
64	HR_C2-76.7	3-23	2-E1508A-2
65	HR_D2-103.2	3-24	2-E1508A-3
66	HR_D2-106.1	3-25	2-E1508A-3
67	HR_D2-112.9	3-26	2-E1508A-3
68	HR_D2-114.9	3-27	2-E1508A-3
69	HR_D2-116.8	3-28	2-E1508A-3
70	HR_D2-120.7	3-29	2-E1508A-3
71	HR_D2-124.6	3-30	2-E1508A-3
72	HR_D2-128.5	3-31	2-E1508A-3

Table 11.3 Instrumentation and Data Acquisition Channel List (Continued)

SLOT 1			
CHAN	NAME	PANEL/ INPUT #	Slot, SCP & SCP #
498	**Pnl2-Therm2S**	**2-32**	**1-E1508A-4**
385	L Plen fl-t	2-33	1-E1508A-4
386	L Plen fl-b	2-34	1-E1508A-4
387	L Plen wall-t	2-35	1-E1508A-4
388	L Plen wall-b	2-36	1-E1508A-4
389	U Plen fl-t	2-37	1-E1508A-4
390	U Plen fl-b	2-38	1-E1508A-4
391	U Plen wall-t	2-39	1-E1508A-4
25	HR_D7-48.1	2-40	1-E1508A-5
26	HR_D7-63.9	2-41	1-E1508A-5
27	HR_D7-68.9	2-42	1-E1508A-5
28	HR_D7-79.7	2-43	1-E1508A-5
29	HR_D7-97.3	2-44	1-E1508A-5
30	HR_D7-114.9	2-45	1-E1508A-5
31	HR_D7-126.6	2-46	1-E1508A-5
32	HR_D7-139.3	2-47	1-E1508A-5
33	HR_A6-48.1	2-48	1-E1508A-6
34	HR_A6-63.9	2-49	1-E1508A-6
35	HR_A6-68.9	2-50	1-E1508A-6
36	HR_A6-79.7	2-51	1-E1508A-6
37	HR_A6-97.3	2-52	1-E1508A-6
38	HR_A6-114.9	2-53	1-E1508A-6
39	HR_A6-126.6	2-54	1-E1508A-6
40	HR_A6-139.3	2-55	1-E1508A-6
41	HR_A4-48.1	2-56	1-E1508A-7
42	HR_A4-63.9	2-57	1-E1508A-7
43	HR_A4-68.9	2-58	1-E1508A-7
44	HR_A4-79.7	2-59	1-E1508A-7
45	HR_A4-97.3	2-60	1-E1508A-7
46	HR_A4-114.9	2-61	1-E1508A-7
47	HR_A4-126.6	2-62	1-E1508A-7
48	HR_A4-139.3	2-63	1-E1508A-7

SLOT 2			
CHAN	NAME	PANEL/ INPUT #	Slot, SCP & SCP #
500	**Pnl4-Therm2S**	**4-32**	**2-E1508A-4**
407	Sup Ln fl	4-33	2-E1508A-4
408	Sup Ln wall	4-34	2-E1508A-4
409	Sup Ln wall	4-35	2-E1508A-4
410	Sup Ln wall	4-36	2-E1508A-4
414	St Sup fl	4-37	2-E1508A-4
415	St Sup wall	4-38	2-E1508A-4
428	St Sep fl	4-39	2-E1508A-4
73	HR_E2-50.1	4-40	2-E1508A-5
74	HR_E2-54.1	4-41	2-E1508A-5
75	HR_E2-57	4-42	2-E1508A-5
76	HR_E2-60	4-43	2-E1508A-5
77	HR_E2-65.9	4-44	2-E1508A-5
78	HR_E2-69.8	4-45	2-E1508A-5
79	HR_E2-72.8	4-46	2-E1508A-5
80	HR_E2-74.8	4-47	2-E1508A-5
81	HR_F2-4.2	4-48	2-E1508A-6
82	HR_F2-11.2	4-49	2-E1508A-6
83	HR_F2-16.2	4-50	2-E1508A-6
84	HR_F2-23.2	4-51	2-E1508A-6
85	HR_F2-29.2	4-52	2-E1508A-6
86	HR_F2-33.2	4-53	2-E1508A-6
87	HR_F2-35.2	4-54	2-E1508A-6
88	HR_F2-38.2	4-55	2-E1508A-6
89	HR_F3-50.1	4-56	2-E1508A-7
90	HR_F3-54.1	4-57	2-E1508A-7
91	HR_F3-57	4-58	2-E1508A-7
92	HR_F3-60	4-59	2-E1508A-7
93	HR_F3-65.9	4-60	2-E1508A-7
94	HR_F3-69.8	4-61	2-E1508A-7
95	HR_F3-72.8	4-62	2-E1508A-7
96	HR_F3-74.8	4-63	2-E1508A-7

Table 11.3 Instrumentation and Data Acquisition Channel List (Continued)

SLOT 3			
CHAN	NAME	PANEL/ INPUT #	Slot, SCP & SCP #
501	**Pnl5-Therm2S**	**5-0**	**3-E1508A-0**
429	St Sep wall-t	5-1	3-E1508A-0
430	St Sep wall-b	5-2	3-E1508A-0
431	St Sep Dr wall-t	5-3	3-E1508A-0
432	St Sep Dr wall-b	5-4	3-E1508A-0
435	Acc wall-t	5-5	3-E1508A-0
436	Acc wall-m	5-6	3-E1508A-0
437	Acc wall-b	5-7	3-E1508A-0
97	HR_F4-79.7	5-8	3-E1508A-1
98	HR_F4-85.5	5-9	3-E1508A-1
99	HR_F4-88.5	5-10	3-E1508A-1
100	HR_F4-92.4	5-11	3-E1508A-1
101	HR_F4-94.4	5-12	3-E1508A-1
102	HR_F4-97.3	5-13	3-E1508A-1
103	HR_F4-109	5-14	3-E1508A-1
104	HR_F4-111.4	5-15	3-E1508A-1
105	HR_F5-41.2	5-16	3-E1508A-2
106	HR_F5-53.1	5-17	3-E1508A-2
107	HR_F5-55.1	5-18	3-E1508A-2
108	HR_F5-58	5-19	3-E1508A-2
109	HR_F5-63.9	5-20	3-E1508A-2
110	HR_F5-73.8	5-21	3-E1508A-2
111	HR_F5-75.7	5-22	3-E1508A-2
112	HR_F5-76.7	5-23	3-E1508A-2
113	HR_F6-4.2	5-24	3-E1508A-3
114	HR_F6-11.2	5-25	3-E1508A-3
115	HR_F6-16.2	5-26	3-E1508A-3
116	HR_F6-23.2	5-27	3-E1508A-3
117	HR_F6-29.2	5-28	3-E1508A-3
118	HR_F6-33.2	5-29	3-E1508A-3
119	HR_F6-35.2	5-30	3-E1508A-3
120	HR_F6-38.2	5-31	3-E1508A-3

SLOT 4			
CHAN	NAME	PANEL/ INPUT #	Slot, SCP & SCP #
503	**Pnl7-Therm2S**	**7-0**	**4-E1508A-0**
453	Qtz Win4-B	7-1	4-E1508A-0
454	Qtz Win5-A	7-2	4-E1508A-0
455	Qtz Win5-B	7-3	4-E1508A-0
456	Qtz Win6-A	7-4	4-E1508A-0
457	Qtz Win6-B	7-5	4-E1508A-0
440	Ex Pipe fl	7-6	4-E1508A-0
441	Ex Pipe wall	7-7	4-E1508A-0
145	HR_B6-4.2	7-8	4-E1508A-1
146	HR_B6-11.2	7-9	4-E1508A-1
147	HR_B6-16.2	7-10	4-E1508A-1
148	HR_B6-23.2	7-11	4-E1508A-1
149	HR_B6-29.2	7-12	4-E1508A-1
150	HR_B6-33.2	7-13	4-E1508A-1
151	HR_B6-35.2	7-14	4-E1508A-1
152	HR_B6-38.2	7-15	4-E1508A-1
153	HR_B5-41.2	7-16	4-E1508A-2
154	HR_B5-53.1	7-17	4-E1508A-2
155	HR_B5-55.1	7-18	4-E1508A-2
156	HR_B5-58	7-19	4-E1508A-2
157	HR_B5-63.9	7-20	4-E1508A-2
158	HR_B5-73.8	7-21	4-E1508A-2
159	HR_B5-75.7	7-22	4-E1508A-2
160	HR_B5-76.7	7-23	4-E1508A-2
161	HR_B4-88.5	7-24	4-E1508A-3
162	HR_B4-91.4	7-25	4-E1508A-3
163	HR_B4-93.4	7-26	4-E1508A-3
164	HR_B4-95.3	7-27	4-E1508A-3
165	HR_B4-100.2	7-28	4-E1508A-3
166	HR_B4-106.1	7-29	4-E1508A-3
167	HR_B4-111	7-30	4-E1508A-3
168	HR_B4-142.2	7-31	4-E1508A-3

Table 11.3 Instrumentation and Data Acquisition Channel List (Continued)

SLOT 3			
CHAN	NAME	PANEL/ INPUT #	Slot, SCP & SCP #
502	**Pnl6-Therm2S**	**6-32**	**3-E1508A-4**
446	Qtz Win1-A	6-33	3-E1508A-4
447	Qtz Win1-B	6-34	3-E1508A-4
448	Qtz Win2-A	6-35	3-E1508A-4
449	Qtz Win2-B	6-36	3-E1508A-4
450	Qtz Win3-A	6-37	3-E1508A-4
451	Qtz Win3-B	6-38	3-E1508A-4
452	Qtz Win4-A	6-39	3-E1508A-4
121	HR_E6-50.1	6-40	3-E1508A-5
122	HR_E6-54.1	6-41	3-E1508A-5
123	HR_E6-57	6-42	3-E1508A-5
124	HR_E6-60	6-43	3-E1508A-5
125	HR_E6-65.9	6-44	3-E1508A-5
126	HR_E6-69.8	6-45	3-E1508A-5
127	HR_E6-72.8	6-46	3-E1508A-5
128	HR_E6-74.8	6-47	3-E1508A-5
129	HR_D6-103.2	6-48	3-E1508A-6
130	HR_D6-106.1	6-49	3-E1508A-6
131	HR_D6-112.9	6-50	3-E1508A-6
132	HR_D6-114.9	6-51	3-E1508A-6
133	HR_D6-116.8	6-52	3-E1508A-6
134	HR_D6-120.7	6-53	3-E1508A-6
135	HR_D6-124.6	6-54	3-E1508A-6
136	HR_D6-128.5	6-55	3-E1508A-6
137	HR_C6-41.2	6-56	3-E1508A-7
138	HR_C6-53.1	6-57	3-E1508A-7
139	HR_C6-55.1	6-58	3-E1508A-7
140	HR_C6-58	6-59	3-E1508A-7
141	HR_C6-63.9	6-60	3-E1508A-7
142	HR_C6-73.8	6-61	3-E1508A-7
143	HR_C6-75.7	6-62	3-E1508A-7
144	HR_C6-76.7	6-63	3-E1508A-7

SLOT 4			
CHAN	NAME	PANEL/ INPUT #	Slot, SCP & SCP #
504	**Pnl8-Therm2S**	**8-32**	**4-E1508A-4**
442	Ex Pipe wall	8-33	4-E1508A-4
443	Ex Pipe wall	8-34	4-E1508A-4
394	Pwr Sup W	8-35	4-E1508A-4
395	Pwr Sup V	8-36	4-E1508A-4
396	Pwr Sup Cur	8-37	4-E1508A-4
397	Test Sect V	8-38	4-E1508A-4
398	Test Sect Cur	8-39	4-E1508A-4
169	HR_B3-50.1	8-40	4-E1508A-5
170	HR_B3-54.1	8-41	4-E1508A-5
171	HR_B3-57	8-42	4-E1508A-5
172	HR_B3-60	8-43	4-E1508A-5
173	HR_B3-65.9	8-44	4-E1508A-5
174	HR_B3-69.8	8-45	4-E1508A-5
175	HR_B3-72.8	8-46	4-E1508A-5
176	HR_B3-74.8	8-47	4-E1508A-5
177	HR_C3-79.7	8-48	4-E1508A-6
178	HR_C3-85.5	8-49	4-E1508A-6
179	HR_C3-88.5	8-50	4-E1508A-6
180	HR_C3-92.4	8-51	4-E1508A-6
181	HR_C3-94.4	8-52	4-E1508A-6
182	HR_C3-97.3	8-53	4-E1508A-6
183	HR_C3-109	8-54	4-E1508A-6
184	HR_C3-111.4	8-55	4-E1508A-6
185	HR_D3-88.5	8-56	4-E1508A-7
186	HR_D3-91.4	8-57	4-E1508A-7
187	HR_D3-93.4	8-58	4-E1508A-7
188	HR_D3-95.3	8-59	4-E1508A-7
189	HR_D3-100.2	8-60	4-E1508A-7
190	HR_D3-106.1	8-61	4-E1508A-7
191	HR_D3-111	8-62	4-E1508A-7
192	HR_D3-142.2	8-63	4-E1508A-7

Table 11.3 Instrumentation and Data Acquisition Channel List (Continued)

SLOT 5			
CHAN	NAME	PANEL/ INPUT #	Slot, SCP & SCP #
505	**Pnl9-Therm2S**	**9-0**	**5-E1508A-0**
393	UP Exit P	9-1	5-E1508A-0
406	Sup Tnk Pr	9-2	5-E1508A-0
411	Sup Ln Pr	9-3	5-E1508A-0
416	St Sup Pr	9-4	5-E1508A-0
439	Acc Pr	9-5	5-E1508A-0
444	Ex Pipe Pr	9-6	5-E1508A-0
412	Sup Ln FM	9-7	5-E1508A-0
193	HR_E3-63.9	9-8	5-E1508A-1
194	HR_E3-113.9	9-9	5-E1508A-1
195	HR_E3-115.8	9-10	5-E1508A-1
196	HR_E3-118.8	9-11	5-E1508A-1
197	HR_E3-122.7	9-12	5-E1508A-1
198	HR_E3-126.6	9-13	5-E1508A-1
199	HR_E3-131.5	9-14	5-E1508A-1
200	HR_E3-135.4	9-15	5-E1508A-1
201	HR_E4-88.5	9-16	5-E1508A-2
202	HR_E4-91.4	9-17	5-E1508A-2
203	HR_E4-93.4	9-18	5-E1508A-2
204	HR_E4-95.3	9-19	5-E1508A-2
205	HR_E4-100.2	9-20	5-E1508A-2
206	HR_E4-106.1	9-21	5-E1508A-2
207	HR_E4-111	9-22	5-E1508A-2
208	HR_E4-142.2	9-23	5-E1508A-2
209	HR_E5-63.9	9-24	5-E1508A-3
210	HR_E5-113.9	9-25	5-E1508A-3
211	HR_E5-115.8	9-26	5-E1508A-3
212	HR_E5-118.8	9-27	5-E1508A-3
213	HR_E5-122.7	9-28	5-E1508A-3
214	HR_E5-126.6	9-29	5-E1508A-3
215	HR_E5-131.5	9-30	5-E1508A-3
216	HR_E5-135.4	9-31	5-E1508A-3

SLOT 6			
CHAN	NAME	PANEL/ INPUT #	Slot, SCP & SCP #
507	**Pnl11-Therm2S**	**11-0**	**6-E1508A-0**
425	CT-UP DP	11-1	6-E1508A-0
433	St Sep-UP DP	11-2	6-E1508A-0
438	St Sup-Acc DP	11-3	6-E1508A-0
362	FH DP-(0-144)	11-4	6-E1508A-0
363	FH DP-(0-12)	11-5	6-E1508A-0
364	FH DP-(12-25)	11-6	6-E1508A-0
365	FH DP-(25-37)	11-7	6-E1508A-0
241	HR_D4-50.1	11-8	6-E1508A-1
242	HR_D4-54.1	11-9	6-E1508A-1
243	HR_D4-57	11-10	6-E1508A-1
244	HR_D4-60	11-11	6-E1508A-1
245	HR_D4-65.9	11-12	6-E1508A-1
246	HR_D4-69.8	11-13	6-E1508A-1
247	HR_D4-72.8	11-14	6-E1508A-1
248	HR_D4-74.8	11-15	6-E1508A-1
249	GRD2-fl-D-4/d2-b2	11-16	6-E1508A-2
250	GRD2-wall-D-4/a-2	11-17	6-E1508A-2
251	GRD3-fl-D-4/d2-b2	11-18	6-E1508A-2
252	GRD3-fl-D-2/d1-b2	11-19	6-E1508A-2
253	GRD3-fl-D-6/c3-b2	11-20	6-E1508A-2
254	GRD3-wall-E-3/c-1	11-21	6-E1508A-2
255	GRD3-wall-D-4/a-2	11-22	6-E1508A-2
256	GRD3-wall-C-5/d-3	11-23	6-E1508A-2
257	GRD4-fl-D-4/d2-b2	11-24	6-E1508A-3
258	GRD4-fl-D-2/d1-b2	11-25	6-E1508A-3
259	GRD4-fl-D-6/c3-b2	11-26	6-E1508A-3
260	GRD4-wall-E-3/c-1	11-27	6-E1508A-3
261	GRD4-wall-D-4/a-2	11-28	6-E1508A-3
262	GRD4-wall-C-5/d-3	11-29	6-E1508A-3
263	GRD5-fl-D-4/d2-b2	11-30	6-E1508A-3
264	GRD5-fl-D-2/d1-b2	11-31	6-E1508A-3

Table 11.3 Instrumentation and Data Acquisition Channel List (Continued)

SLOT 5			
CHAN	NAME	PANEL/ INPUT #	Slot, SCP & SCP #
506	Pnl10-Therm2S	10-32	5-E1508A-4
413	Drop Inj FM	10-33	5-E1508A-4
417	St Sup FM	10-34	5-E1508A-4
445	Ex Pipe FM	10-35	5-E1508A-4
405	Sup Tnk Lvl	10-36	5-E1508A-4
426	Lg CT Lvl	10-37	5-E1508A-4
427	Sm CT Lvl	10-38	5-E1508A-4
434	St Sep Lvl	10-39	5-E1508A-4
217	HR_D5-88.5	10-40	5-E1508A-5
218	HR_D5-91.4	10-41	5-E1508A-5
219	HR_D5-93.4	10-42	5-E1508A-5
220	HR_D5-95.3	10-43	5-E1508A-5
221	HR_D5-100.2	10-44	5-E1508A-5
222	HR_D5-106.1	10-45	5-E1508A-5
223	HR_D5-111	10-46	5-E1508A-5
224	HR_D5-142.2	10-47	5-E1508A-5
225	HR_C5-63.9	10-48	5-E1508A-6
226	HR_C5-113.9	10-49	5-E1508A-6
227	HR_C5-115.8	10-50	5-E1508A-6
228	HR_C5-118.8	10-51	5-E1508A-6
229	HR_C5-122.7	10-52	5-E1508A-6
230	HR_C5-126.6	10-53	5-E1508A-6
231	HR_C5-131.5	10-54	5-E1508A-6
232	HR_C5-135.4	10-55	5-E1508A-6
233	HR_C4-88.5	10-56	5-E1508A-7
234	HR_C4-91.4	10-57	5-E1508A-7
235	HR_C4-93.4	10-58	5-E1508A-7
236	HR_C4-95.3	10-59	5-E1508A-7
237	HR_C4-100.2	10-60	5-E1508A-7
238	HR_C4-106.1	10-61	5-E1508A-7
239	HR_C4-111	10-62	5-E1508A-7
240	HR_C4-142.2	10-63	5-E1508A-7

SLOT 6			
CHAN	NAME	PANEL/ INPUT #	Slot, SCP & SCP #
508	Pnl12-Therm2S	12-32	6-E1508A-4
265	GRD5-fl-D-6/c3-b2	12-33	6-E1508A-4
266	GRD5-wall-E-3/c-1	12-34	6-E1508A-4
267	GRD5-wall-D-4/a-2	12-35	6-E1508A-4
268	GRD5-wall-C-5/d-3	12-36	6-E1508A-4
269	GRD6-fl-D-4/d2-b2	12-37	6-E1508A-4
270	GRD6-fl-B-4/c2-a1	12-38	6-E1508A-4
271	GRD6-fl-F-4/c2-b3	12-39	6-E1508A-4
272	GRD6-wall-E-3/c-1	12-40	6-E1508A-5
273	GRD6-wall-D-4/a-2	12-41	6-E1508A-5
274	GRD6-wall-G-4/b-3	12-42	6-E1508A-5
275	GRD6-wall-C-5/d-3	12-43	6-E1508A-5
276	GRD7-fl-D-4/d2-b2	12-44	6-E1508A-5
277	GRD7-fl-D-2/d1-b2	12-45	6-E1508A-5
278	GRD7-fl-D-6/c3-b2	12-46	6-E1508A-5
279	GRD7-wall-D-4/a-2	12-47	6-E1508A-5
280	SPR1-37.2	12-48	6-E1508A-6
281	SPR1-59.1	12-49	6-E1508A-6
282	SPR1-76.8	12-50	6-E1508A-6
283	SPR1-90.7	12-51	6-E1508A-6
284	SPR1-96.6	12-52	6-E1508A-6
285	SPR1-102.5	12-53	6-E1508A-6
286	SPR1-114.4	12-54	6-E1508A-6
287	SPR1-138.2	12-55	6-E1508A-6
288	SPR13-37.2	12-56	6-E1508A-7
289	SPR13-59.1	12-57	6-E1508A-7
290	SPR13-76.8	12-58	6-E1508A-7
291	SPR13-90.7	12-59	6-E1508A-7
292	SPR13-96.6	12-60	6-E1508A-7
293	SPR13-102.5	12-61	6-E1508A-7
294	SPR13-114.4	12-62	6-E1508A-7
295	SPR13-138.2	12-63	6-E1508A-7

Table 11.3 Instrumentation and Data Acquisition Channel List (Continued)

SLOT 7			
CHAN	NAME	PANEL/ INPUT #	Slot, SCP & SCP #
509	**Pnl13-Therm2S**	**13-0**	**7-E1508A-0**
296	ST. PR-R1-16.2-A	13-1	7-E1508A-0
297	ST. PR-R1-16.2-B	13-2	7-E1508A-0
298	ST. PR-R1-16.2-C	13-3	7-E1508A-0
299	ST. PR-R2-37-A	13-4	7-E1508A-0
300	ST. PR-R2-37-B	13-5	7-E1508A-0
301	ST. PR-R2-37-C	13-6	7-E1508A-0
302	ST. PR-R3-55-A	13-7	7-E1508A-0
303	ST. PR-R3-55-B	13-8	7-E1508A-1
304	ST. PR-R3-55-C	13-9	7-E1508A-1
305	ST. PR-R4-60-A	13-10	7-E1508A-1
306	ST. PR-R4-60-B	13-11	7-E1508A-1
307	ST. PR-R4-60-C	13-12	7-E1508A-1
308	ST. PR-R5-73.81-A	13-13	7-E1508A-1
309	ST. PR-R5-73.81-B	13-14	7-E1508A-1
310	ST. PR-R5-73.81-C	13-15	7-E1508A-1
311	ST. PR-R6-76-A	13-16	7-E1508A-2
312	ST. PR-R6-76-B	13-17	7-E1508A-2
313	ST. PR-R6-76-C	13-18	7-E1508A-2
314	ST. PR-R7-79.7-A	13-19	7-E1508A-2
315	ST. PR-R7-79.7-B	13-20	7-E1508A-2
316	ST. PR-R7-79.7-C	13-21	7-E1508A-2
317	ST. PR-R8-93.53-A	13-22	7-E1508A-2
318	ST. PR-R8-93.53-B	13-23	7-E1508A-2
319	ST. PR-R8-93.53-C	13-24	7-E1508A-3
320	ST. PR-R9-96-A	13-25	7-E1508A-3
321	ST. PR-R9-96-B	13-26	7-E1508A-3
322	ST. PR-R9-96-C	13-27	7-E1508A-3
323	ST. PR-R10-100-A	13-28	7-E1508A-3
324	ST. PR-R10-100-B	13-29	7-E1508A-3
325	ST. PR-R10-100-C	13-30	7-E1508A-3
326	ST. PR-R11-115.39-A	13-31	7-E1508A-3

SLOT 8			
CHAN	NAME	PANEL/ INPUT #	Slot, SCP & SCP #
511	**Pnl15-Therm2S**	**15-0**	**8-E1508A-0**
358	FH24-wall-129.25	15-1	8-E1508A-0
359	FH25-wall-135.18	15-2	8-E1508A-0
360	RB-IF1-fl-(-1)-A	15-3	8-E1508A-0
361	RB-IF2-fl-(-1)-B	15-4	8-E1508A-0
366	FH DP-(37-43)	15-5	8-E1508A-0
367	FH DP-(43-46)	15-6	8-E1508A-0
368	FH DP-(46-53)	15-7	8-E1508A-0
369	FH DP-(53-57)	15-8	8-E1508A-1
370	FH DP-(57-60)	15-9	8-E1508A-1
371	FH DP-(60-63)	15-10	8-E1508A-1
372	FH DP-(63-67)	15-11	8-E1508A-1
373	FH DP-(67-72)	15-12	8-E1508A-1
374	FH DP-(72-75)	15-13	8-E1508A-1
375	FH DP-(75-78)	15-14	8-E1508A-1
376	FH DP-(78-81)	15-15	8-E1508A-1
377	FH DP-(81-85)	15-16	8-E1508A-2
378	FH DP-(85-93)	15-17	8-E1508A-2
379	FH DP-(93-97)	15-18	8-E1508A-2
380	FH DP-(97-100)	15-19	8-E1508A-2
381	FH DP-(100-108)	15-20	8-E1508A-2
382	FH DP-(108-120)	15-21	8-E1508A-2
383	FH DP-(120-133)	15-22	8-E1508A-2
384	FH DP-(133-144)	15-23	8-E1508A-2
458	Rem Close	15-24	8-E1535A-3
459	Rem Start/Stop	15-25	8-E1535A-3
460	Rem Reset	15-26	8-E1535A-3
461	RELAY 3 - NO	15-27	8-E1535A-3
462	I/O Disc	15-28	8-E1535A-3
463	Pull-Up+/I/O Disc-	15-29	8-E1535A-3
464	*Not Available*	*15-30*	*8-E1535A-3*
465	*Not Available*	*15-31*	*8-E1535A-3*

Table 11.3 Instrumentation and Data Acquisition Channel List (Continued)

SLOT 7			
CHAN	NAME	PANEL/ INPUT #	Slot, SCP & SCP #
510	**Pnl14-Therm2S**	**14-32**	**7-E1508A-4**
327	ST. PR-R11-115.39-B	14-33	7-E1508A-4
328	ST. PR-R11-115.39-C	14-34	7-E1508A-4
329	ST. PR-R12-120-A	14-35	7-E1508A-4
330	ST. PR-R12-120-B	14-36	7-E1508A-4
331	ST. PR-R12-120-C	14-37	7-E1508A-4
332	ST. PR-R13-136-A	14-38	7-E1508A-4
333	ST. PR-R13-136-B	14-39	7-E1508A-4
334	ST. PR-R13-136-C	14-40	7-E1508A-5
335	FH1-wall-10.1	14-41	7-E1508A-5
336	FH2-wall-22	14-42	7-E1508A-5
337	FH3-wall-37	14-43	7-E1508A-5
338	FH4-wall-42.95	14-44	7-E1508A-5
339	FH5-wall-46.93	14-45	7-E1508A-5
340	FH6-wall-52.9	14-46	7-E1508A-5
341	FH7-wall-55.87	14-47	7-E1508A-5
342	FH8-wall-61.85	14-48	7-E1508A-6
343	FH9-wall-67.83	14-49	7-E1508A-6
344	FH10-wall-70.82	14-50	7-E1508A-6
345	FH11-wall-73.81	14-51	7-E1508A-6
346	FH12-wall-78.78	14-52	7-E1508A-6
347	FH13-wall-84.7	14-53	7-E1508A-6
348	FH14-wall-87.65	14-54	7-E1508A-6
349	FH15-wall-90.55	14-55	7-E1508A-6
350	FH16-wall-93.53	14-56	7-E1508A-7
351	FH17-wall-96.5	14-57	7-E1508A-7
352	FH18-wall-102.48	14-58	7-E1508A-7
353	FH19-wall-108.43	14-59	7-E1508A-7
354	FH20-wall-110.43	14-60	7-E1508A-7
355	FH21-wall-111.42	14-61	7-E1508A-7
356	FH22-wall-116.38	14-62	7-E1508A-7
357	FH23-wall-120.3	14-63	7-E1508A-7

SLOT 8			
CHAN	NAME	PANEL/ INPUT #	Slot, SCP & SCP #
512	**Pnl16-Therm2S**	**16-32**	**8-E1508A-4**
482	Spare1	16-33	8-E1508A-4
483	Spare2	16-34	8-E1508A-4
484	Spare3	16-35	8-E1508A-4
485	Spare4	16-36	8-E1508A-4
486	Spare5	16-37	8-E1508A-4
487	Spare6	16-38	8-E1508A-4
488	Spare7	16-39	8-E1508A-4
489	Spare8	16-40	8-E1508A-5
490	Spare9	16-41	8-E1508A-5
491	Spare10	16-42	8-E1508A-5
492	Spare11	16-43	8-E1508A-5
493	Spare12	16-44	8-E1508A-5
494	Spare13	16-45	8-E1508A-5
495	Spare14	16-46	8-E1508A-5
496	Spare15	16-47	8-E1508A-5
466	PS-PWR OUTA	16-48	8-E1532A-6
467	PS-PWR OUTB	16-49	8-E1532A-6
468	IF RATEA	16-50	8-E1532A-6
469	IF RATEB	16-51	8-E1532A-6
470	CNTL3A	16-52	8-E1532A-6
471	CNTL3B	16-53	8-E1532A-6
472	CNTL4A	16-54	8-E1532A-6
473	CNTL4B	16-55	8-E1532A-6
474	CNTL5A	16-56	8-E1532A-7
475	CNTL5B	16-57	8-E1532A-7
476	CNTL6A	16-58	8-E1532A-7
477	CNTL6B	16-59	8-E1532A-7
478	CNTL7A	16-60	8-E1532A-7
479	CNTL7B	16-61	8-E1532A-7
480	CNTL8A	16-62	8-E1532A-7
481	CNTL8B	16-63	8-E1532A-7

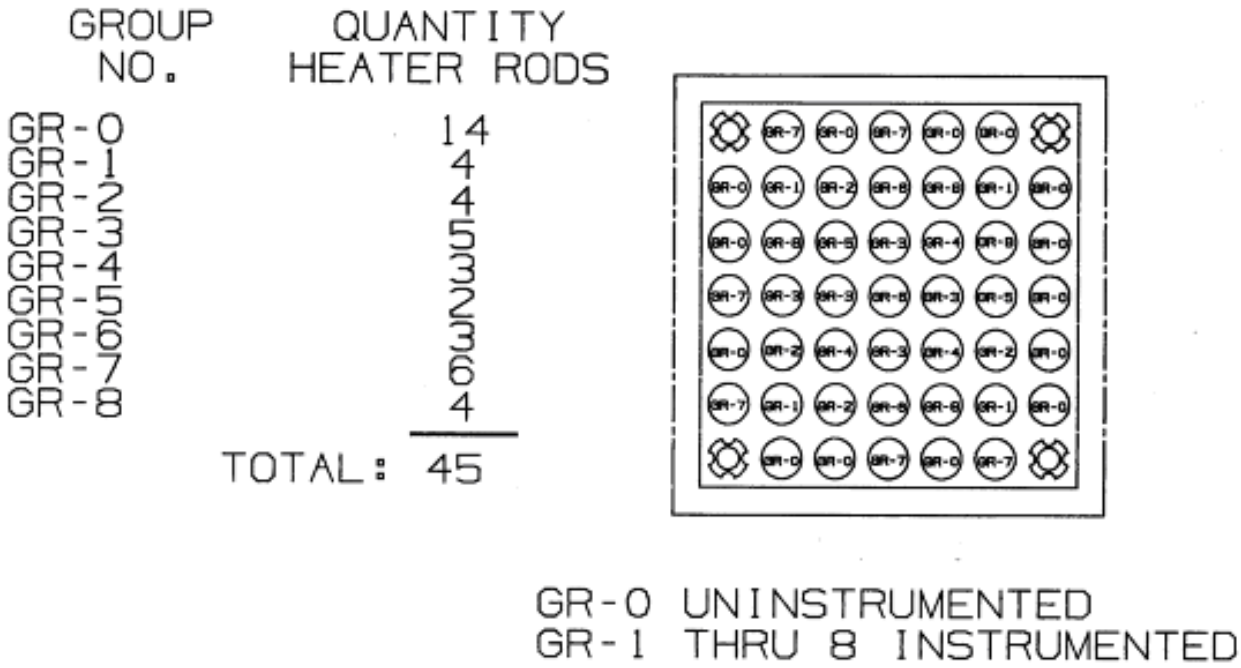

Figure 11.22 Instrumented Heater Rod Radial Locations.

effects were observed in the Lehigh data as well as the INEL single tube data which used these probes.

In addition, there will be traversing vapor temperature measurement probes mounted on rakes with multiple thermocouples. The traversing steam probe rakes will be installed at the mid span between grids at the upper rod bundle elevations. The steam probes will measure steam temperatures in the rod bundle flow subchannels and the gap between the heater rods during the dispersed flow regime. The conceptual design of a tranversing steam probe rake is shown in Figure 11.23. Each rake consists of three 0.381 mm (15 mil) diameter ungrounded thermocouples mounted on a 0.356 mm (14 mil) thick by 6.35 mm (¼ in) wide inconel strip. The thermocouples are spaced 12.6 mm (0.496 inch) apart which correspond to the heater rod spacing in the bundle. The thermocouple tips are located facing the steam flow. A 2.39 mm (94 mil) diameter tube attached to the strip is used to traverse the steam probe rake across the rod bundle. This tube also carries the thermocouples leads outside the flow housing through a extension tube and a pressure seal arrangement. This instrument is now in the development phase and will be tested in the nine rod bundle bench test prior to installing it on the large rod bundle.

Two fluid thermocouples are placed 24.5 mm (1 in) below the bottom of the bundle heated length such that injection water temperatures are monitored prior and when reflood is started. There are 22 DP transmitters are connected to the housing wall pressure taps providing measurements to calculate single phase bare bundle and grid friction losses, bundle mass inventory and void fraction during reflood. Nine DP cells are connected to pressure taps located 76.2 mm (3 in) apart to provide detail mass inventory, and void fraction data in the froth region above the quench front. In addition, heater rod and housing wall thermocouples are placed at the pressure tap mid spans locations to determine convective and radiant heat

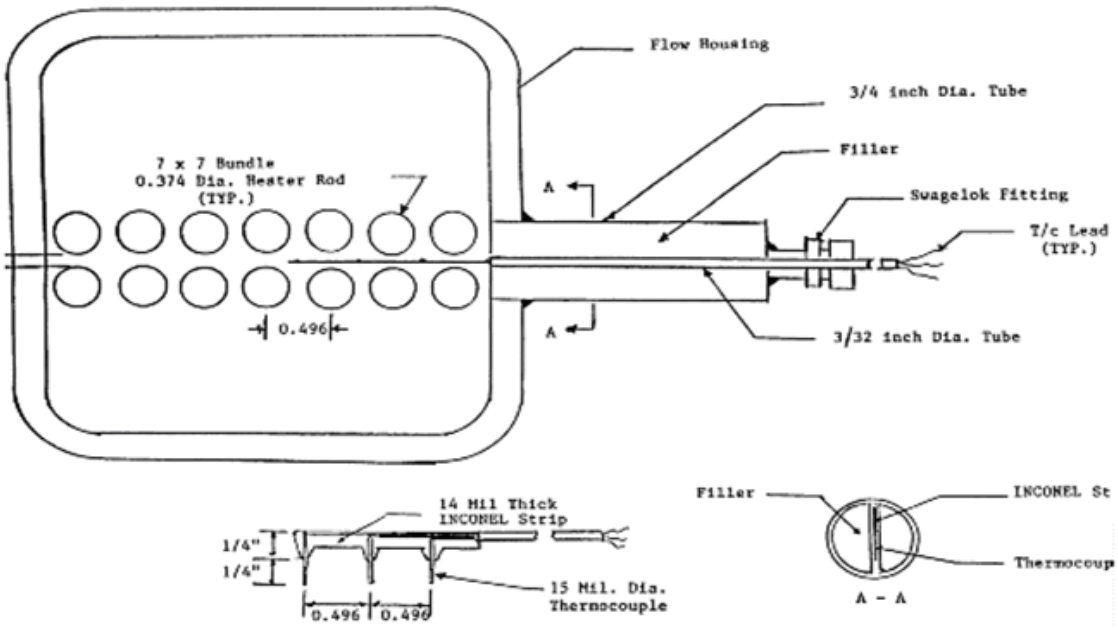

Figure 11.23 Traversing Steam Probe Rake.

transfer coefficients in the froth region where the differential pressure cells will give the average void fraction.

As described in Section 11.3.1, the flow housing has six pairs of windows at the following elevations: 685.8, 1193.8, 1752.6, 2260.6, 2768.6, 3302.0 and 3962.4 mm (27, 47, 69, 89, 109, 130 and 156 in). Each pair of windows are 180 degrees apart. The window lenses are made from optical grade fused quartz and provide a 50.8x292.1 mm (2x11.5 in) viewing area. The windows are positioned about 88.9 mm (3.5 in) below and 152.4 mm (6 in) above grid numbers 2, 3, 4, 5, 6 and 7. The windows will be preheated to prevent wetting during the time when dispersed flow is occurring and LCDS measurements are being made. The windows will be heated using infrared heaters on each window and by pulsing the rod bundle for preheating the flow housing walls. The infrared heaters will be removed just before a test is started. Two significant measurements above and below the grid can be made through the windows: void fraction measurements with a Gamma Densitometer, and entrained water droplet size, velocity, and distribution with the LIDCS. High speed movies can also be shot through this window to observe the different two-phase flow regimes during testing.

There can be up to three densitometers or an x-ray detector located at different elevations during testing. The bottom densitometer will measure void fractions as the quench front approaches this location, while the other densitometers will measure void fraction in the dispersed flow regimes.

The Gamma Densitometer system which could be used is shown schematically in Figure 11.24. There are three systems each at different elevations consisting of an AM 241, 120 mCi, 59.5 KeV gamma ray source, a Reuter-Stokes gas proportional counter, a preamplifier and an amplifier, high voltage power supply, a single channel analyzer, and a rate meter. The radiation beam intensity is measured across the center gap among the bundle heater rods. The beam is

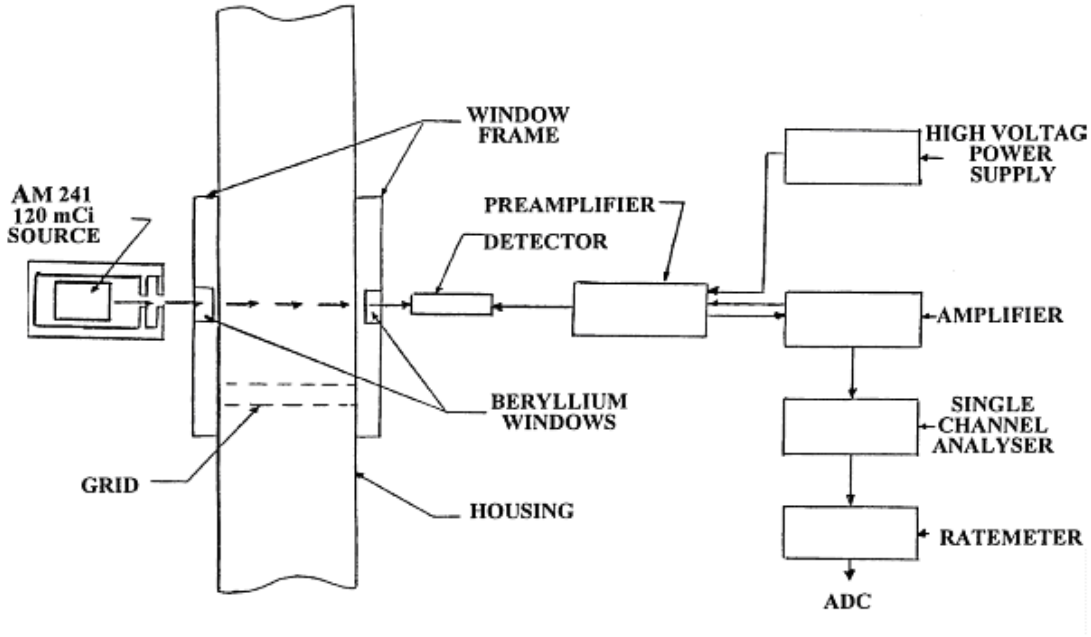

Figure 11.24 Densitometer Schematic.

passed through a small beryllium window fabricated from an S 200F alloy sheet. These windows are mounted on a metal plate that replaces the glass window lenses. The densitometer provides a cordial average void fraction across the bundle. The three densitometers are located at various elevations during a test.

A droplet imaging system known as VisiSizer has been developed in conjunction with Oxford Lasers of Acton, MA, to measure the size and velocity of water droplets entrained in the steam flow of the RBHT test section. VisiSizer uses a pulsed infrared laser to image water droplets on a 1000x1000 pixel high-resolution black and white digital camera through a set of windows in the bundle housing. The LIDCS setup used for VisiSizer is shown schematically in Figure 11.25.

A digital system such as VisiSizer was chosen over conventional high-speed cameras because of issues with reliability and speed of data acquisition. A high-speed camera is capable of only a few seconds of imaging and is a tedious process that does not give instantaneous results. Each frame of a standard imaging technique would need to be analyzed by hand. The VisiSizer system is capable of analyzing 12 to 13 frames per second for an indefinite period of time. Film from the FLECHT-SEASET tests show much less image quality than images taken with VisiSizer in the experiments performed so far. However, VisiSizer is incapable of measuring anything other than complete droplets. This makes it an inadequate tool for gathering information about the entrainment front where there are ligaments and other unusual water behavior. Therefore, it is still a possibility that a high-speed camera will be used in tandem with VisiSizer for preliminary RBHT tests.

An infrared laser is used with the system because it is capable of passing through the quartz viewing windows and being absorbed by the water droplets entrained in the steam flow.

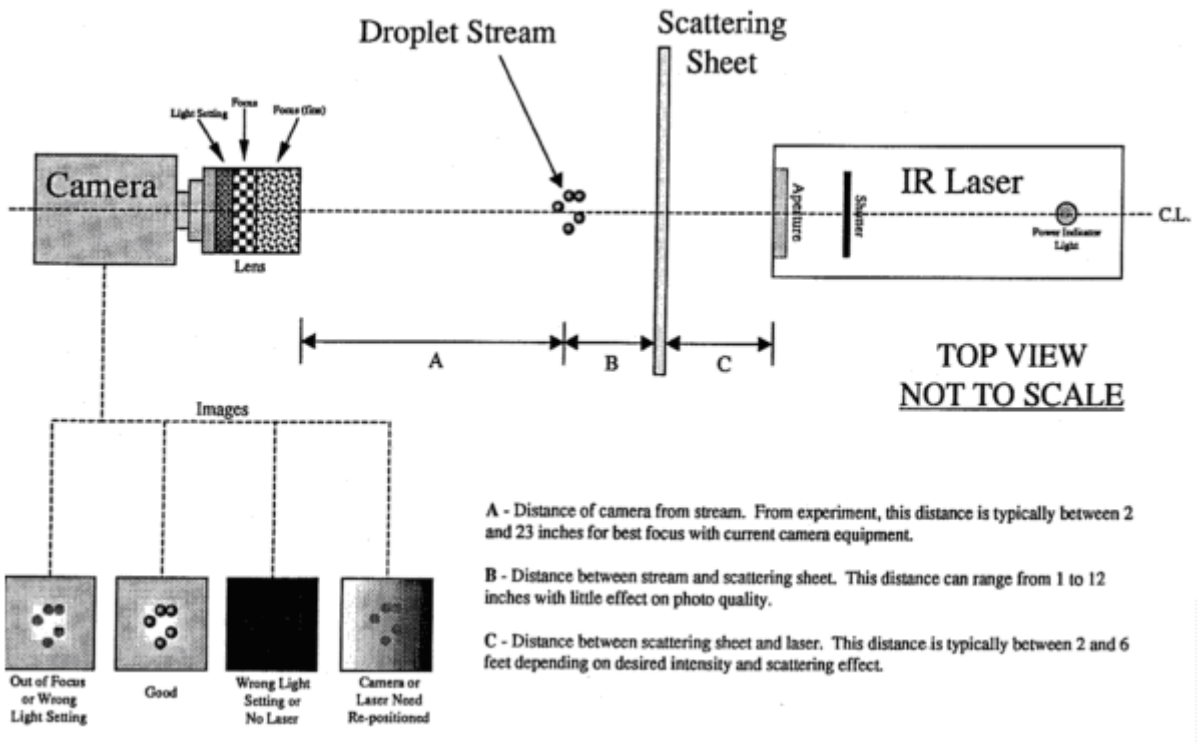

Figure 11.25 Laser Illuminated Digital Camera System Setup

Because the infrared rays are absorbed by the water droplets, the resulting droplet shadows can be recorded by the digital camera. So far, there has been no effect of laser light scattering from rods to droplets. Pictures taken in and out of the rod bundle have the same imaging characteristics, droplet analyzing capability, and clarity. A band pass laser light filter is placed in front of the digital camera to eliminate non-infrared light from other sources and an anti-glare attachment is used to eliminate any illumination interference from outside the viewing area. In addition, rod bundle geometry has little effect in the measurement of droplet distributions and velocities.

The frames captured by the camera are fed back to a computer at approximately 12 to 13 frames per second. The software can analyze each frame for droplet size and velocity and write the recorded data to a size and velocity data array. The software program determines droplet sizes by determining the area of black versus white pixels in each droplet image. Once the droplet area is determined, the program calculates the perimeter of the droplet image to determine the sphereosity of the droplet. The VisiSizer system is capable of determining the surface area based on diameter of any and all droplets. At any droplet concentration that is measurable with the system, an accurate measure of the total droplet surface area can be obtained. So far, number fluxes of up to six droplets per frame in velocity mode (12 droplet images) have been analyzed successfully with the droplets in a very narrow viewing area. There is the capability to increase this droplet number flux by several times using larger and multiple viewing areas.

Operating the laser in a double pulse mode enables the VisiSizer system to measure both droplet diameter and velocity for a particular probe volume. The laser pulses twice with a

known pulse delay (on the order of 1 ms) while the camera shutter remains open, creating two images in the same frame of each droplet. The distance between images is then determined and the velocity calculated. These velocity characteristics are enough to characterize the behavior of the flow despite the fact that the droplets are only captured in a single frame.

The local distribution of droplets will be determined for a known probe volume governed by the software settings. Droplets that lie out of this probe volume on either side of the line of sight will be rejected based on focus. The opposite sides of the probe volume will be set by the spacing of the rods in the bundle. Each droplet is recorded in a two-dimensional array according to size and velocity. The droplet sizes are recorded in lognormal bins while the velocity bin size is user defined. Data for the transient reflood experiments is recorded in user defined quasi-steady state time periods. At the end of each time period the data is saved and a new array is opened. Arrays characterized by similar droplets populations can then be combined for better statistical results.

The VisiSizer will enable the experimenters to collect a vast amount of information about the droplet flow in the test section. The information will be collected in an easy to handle data array and all information will be written to a CD-ROM to ensure the information will be available for later use.

The droplet injection system described in Section 11.3.12 has been constructed so that RBHT can collect steady state information on droplet behavior. The injection system creates droplets of a known size and flow rate in the test section. The injection tubes are easily removed and replaced. This enables multiple injection sizes to be used as needed. The flow rate of the injection is controlled through a series of valves and flow meters. These factors should allow for the production of various droplet sizes. VisiSizer can study the droplet flow and distribution before a grid and then the system can be moved to image droplets immediately after the grid with the same conditions. In this way the effects of a spacer grid on the droplet diameter distribution can be determined.

The four corner support rods are unheated, they are used to support the bundle grids and to support grid and steam probes thermocouple leads going out of the bundle. These rods are instrumented with eight thermocouples attached at various elevations corresponding to heater rods and housing wall thermocouples. The purpose of this arrangement is to quantify radiation heat transfer losses to unheated surfaces and determine their behavior during reflood.

The DC power supply can be controlled by regulating the voltage, current, or total power output. The voltage drop across the heater rod bundle is measured by a voltmeter connected to voltage taps at the Low-Melt pot and the Nickel Ground Plate. The electrical current is measured by a copper shunt calibrated for 15,000 amps proportional to an output signal of 0-50 mV.

The Lower Plenum is instrumented with two fluid and two wall thermocouples. The fluid thermocouples monitor the injection water temperature prior and during testing. The wall thermocouples measure the vessel wall during heat-up and testing. One of the wall thermocouples in conjunction with a temperature controller regulates electrical power to clamp-on heater rods to maintain the vessel wall at inlet temperatures.

The Upper Plenum is also instrumented with two fluid thermocouples and two wall thermocouples. The fluid thermocouples measure steam and carryover liquid during testing. The wall thermocouples monitor vessel wall temperatures during heat-up and testing. The

Upper Plenum is also instrumented with a static pressure transmitter which measures and controls the test section pressure during testing.

11.4.3 Data Acquisition System

The control and data acquisition system provides control functions and data collection functions for the RBHT Test Facility. This system consists of two parts, the computer and display terminals residing in the control room, and the VXI mainframe and terminal panels residing in the test facility. The two parts are connected via an industry standard IEEE 1394 (Firewire) serial control and data interface.

The computer provides the display, control, and data storage functions. It has the capability of displaying control function setpoints and process variables, and critical operating parameters during tests, along with selected variables such as various rod temperatures displayed in real-time during the experiment. This system will provide dial, meter, and strip-chart functions as required. The computer collects and saves data from the various instruments, such as voltage, current, pressure, level, flow, and temperature; and provides control functions such as heater rod power, injection water pressure, upper and lower plenum temperature, etc.

The instrumentation part of this system, residing in the test facility, consists of an industry standard VXI mainframe (Vme bus with extensions for Instrumentation) from Hewlett-Packard (HP E8401A), and a set of terminal panels (HP E1586A). The VXI mainframe contains a Firewire controller card (HP E8491A) and several (currently seven) state-of-the-art data acquisition and control cards (HP E1419A). The terminal panels provide the isothermal reference junctions needed for the thermocouples, as well as the voltage and current-loop input/output (i/o) interface to the RBHT Test Facility. These terminal panels are connected to the HP E1419A cards with SCSI cables. Seven cards yield a capability of 448 i/o. The VXI mainframe can hold up to 12 cards, and the Firewire interface can support up to 16 mainframes.

Each E1419A card can support up to eight signal conditioning plug-ons (scp's), conditioning eight channels each. Each E1509A scp contains low-pass antialiasing filters, fixed at 7 Hz. Because of this, the scan rate for each channel must be greater than or equal to the Nyquist rate of 14 Hz. The maximum a/d conversion rate on each HP E1419A card is nominally 100 kHz, but is controlled to the rate the user requires. The seven cards can be synchronized to perform the scans simultaneously. The theoretical maximum scan rate for each channel (on any individual card) is 100,000/64 = 1,562.5 Hz, if all 64 channels are scanned. (Note that the actual scan rate would be less because of multiplexer switching, amplifier settling times due to gain changes, etc. There are different scp's available from HP providing different filter values to scan at these rates.) The normal data-scanning rate will be 2 Hz during the majority of the tests, but this rate can be increased to 10 Hz for specific times during testing.

11.5 RBHT Test Facility Improvement

Significant improvements related to other rod bundle testing programs, listed in Section 3.0 Literature Review have been incorporated in the RBHT Test Facility. These improvements are:

- A low mass square flow housing design which better fits a square rod bundle array and minimizes the housing mass and the excess rod bundle flow area.

- The six pairs of windows which provide large viewing areas below and above grid locations, making it possible to observe and make void fraction and droplet measurements during reflood testing.

- The possible use of Densitometers or X-ray detectors to obtain void fraction measurements in the subcooled, quench, and froth level regions.

- The use of a Laser Illuminated Digital Camera System to measure entrained water droplets sizes, distribution, and velocities in the dispersed flow regions.

- The use of a traversing steam probe rake to measure simultaneously steam temperatures in the flow subchannel and in the rod-to-rod gap.

- DP transmitter axially located 3 in apart in conjunction with heater rod and flow housing wall thermocouples to obtain detailed void fraction and heat transfer information.

- Water droplets injection system in conjunction steam injection to study the droplet-steam cooling effects on heat transfer and grids.

- Addition of a large pressure oscillation-damping tank to minimize test section oscillations observed in the FLECHT and FLECHT-SEASET tests.

- The incorporation of closely coupled liquid collection tanks and piping to reduce delay times for liquid collection.

11.6 Conclusions

The RBHT Test Facility has been designed as a flexible rod bundle separate-effects test facility which can be used to perform single-phase and two-phase experiments under well-controlled laboratory conditions to generate fundamental reflood heat transfer data. The facility is capable of operating in both forced and variable reflood modes covering wide ranges of flow and heat transfer conditions at pressures up to 4.02 bars (60 psia). It is heavily instrumented to meet all the instrumentation requirements developed under Task 7. It can be used to conduct all types of the planned experiments according to the test matrix developed under Task 9. It is considered that the RBHT Test Facility with its robust instrumentation represents a unique NRC facility for the in-depth studies of the highly ranked reflood phenomena identified in the PIRT table developed under Task 1**,** and will produce the data and analysis needed to refine reflood heat transfer models in the current safety analysis computer codes.

11.7 References

1. Denham, M.K., D. Jowitt, and K.G. Pearson, “ACHILLES Unballooned Cluster Experiments, Part 1: Description of the ACHILLES Rig, Test Section, and Experimental Procedures,” AEEW-R2336, Winfrith Technology Centre (Commercial in Confidence), Nov. 1989.

2. Denham, M.K. and K.G. Pearson, “ACHILLES Unballooned Cluster Experiments, Part 2: Single Phase Flow Experiments,” AEEW-R2337, Winfrith Technology Centre (Commercial in Confidence), May 1989.

3. Pearson, K.G. and M.K. Denham, “ACHILLES Unballooned Cluster Experiments, Part 3: Low Flooding Rate Reflood Experiments,” AEEW-R2339, Winfrith Technology Centre (Commercial in Confidence), June 1989.

4. Pearson, K.G. and M.K. Denham, “ACHILLES Unballooned Cluster Experiments, Part 4: Low Pressure Level Swell Experiments,” AEEW-R2339, Winfrith Technology Centre (Commercial in Confidence), July 1989.

5. Dore, P. and M.K. Denham, “ACHILLES Unballooned Cluster Experiments, Part 5: Best Estimate Experiments,” AEEW-R2412, Winfrith Technology Centre (Commercial in Confidence), July 1990.

6. Dore, P. and D.S. Dhuga, “ACHILLES Unballooned Cluster Experiments, Part 6: Flow Distribution Experiments,” AEA-RS-1064, Winfrith Technology Centre (Commercial in Confidence), December 1991.

12. CONCLUSIONS

The initial phase of the RBHT Program, which aims at designing a flexible, well-instrumented rod bundle test facility for conducting reflood experiments to aid in the development of dispersed flow film boiling models for the NRC's thermal-hydraulics code, was completed and documented in this report. Based upon the results obtained in the initial phase, i.e., Tasks 1 through 10, the following are concluded:

1. The thermal-hydraulics heat transfer phenomena that dominates the reflood transient is dispersed flow film boiling, which is the limiting (lowest heat transfer from fuel to fluid) heat transfer situation for the LOCA transient. The RBHT Program will emphasize this phase in providing specific experimental data and associated analysis to improve the understanding of the dispersed flow film boiling region.

2. The heat transfer rates in the dispersed flow film-boiling region are very low, and several competing mechanisms are responsible for the total wall heat flux. No single mechanism dominates the heat transfer process such that all the competing mechanisms must be modeled with roughly equal precision. Separate-effect data at the subcomponent levels isolating the particular contribution of each competing mechanism to the total wall heat flux will be simulated in the RBHT Test Facility.

3. The single largest uncertainty in predicting the dispersed film boiling heat transfer is the liquid entrainment from the froth region just above the quench front. In this region, the steam generation from the rod quenching results in very large vapor velocities which entrain and shear liquid ligaments into droplets. The entrained droplets provide cooling by several different mechanisms in the upper elevations of the rod bundle where the resulting peak clad temperatures occur. To address the liquid entrainment and resulting droplet flow, specific tests are planned which will isolate the droplet behavior. Also, state-of-the-art instrumentation will be used to obtain drop size and velocities as well as the local void fraction.

4. The RBHT Test Facility is designed to permit separate-effect component experiments isolating each highly ranked reflood phenomenon as best as possible so as to permit model development for particular phenomenon and to minimize the risk of introducing compensating error in the advanced reflood model package.

5. The proposed experiments to be performed in the RBHT Test Facility will provide new data on reflood heat transfer as well as supplementing existing data for model development and code validation. They will also focus on the improvements of specific best-estimate thermal-hydraulics models of importance to the highly ranked phenomena rather than identifying licensing margin.

6. Results of the two-tier scaling analysis indicate that if prototypical fluid conditions are used in the tests and the bundle geometry is retained by using the prototypical spacer grids, there is very strong similarity between the RBHT test bundle and the PWR and BWR fuel assemblies. The data to be obtained in the RBHT Test Facility should be applicable to either reactor fuel assembly type.

7. The effects of the gap conductance and the rod materials differences between electrical

and nuclear fuel rods are small with the possible exception of the minimum film boiling temperature. Other literature or bench type tests can determine the appropriate value for fuel rod cladding. The presence of a test housing in the proposed RBHT facility can lead to some distortion in the tests and it should be accounted for in the test analyses.

8. One important objective of the program is to obtain new information on the mechanism of liquid entrainment at the quench front as the resulting droplet field downstream is responsible for the improved cooling at the upper elevations in the rod bundle where the clad temperature peaks. The instrumentation requirements will include detailed measurements of the local void fraction, droplet size, droplet velocity, and droplet number density in the droplet field.

9. To determine the local heat transfer, a reliable measurement of the non-equilibrium vapor temperature is needed. This has been included in the instrumentation requirements. Instrumentation will also be placed upstream and downstream of the spacer grids to see their effects. Additional instrumentation requirements have been identified using the PIRTs as a guide for the important phenomena for the different test types which the experiments must capture for the code development and validation.

10. The instrumentation plan developed in the RBHT Program, which involves the use of ample instrumentation proven to perform in previous rod bundle experiments as well as state-of-the-art instrumentation specifically developed for dispersed two-phase flow measurements, represents a robust diagnostic plan that allows all the highly ranked phenomena to be either directly measured or calculated directly from the experimental data.

11. The RBHT Test Facility meets all the instrumentation requirements developed in Task 7 and can be used to conduct all of the planned experiments according to the test matrix developed in Task 9. It presents a unique NRC facility that can be used to provide new data at the subcomponent levels for the fundamental assessment of the physical behavior upon which the code constitutive heat transfer and flow models are based.

12. In addition to obtaining separate-effect reflood data, the RBHT Test Facility is designed to perform mechanistic studies of the highly ranked phenomena to develop new or improved models for implementation in the NRC merged code. Thus, it will aid in the refinement of the NRC's thermal-hydraulics code and will help maintain the NRC's leadership in the reactor thermal-hydraulics safety analysis area.

APPENDIX A1. LITERATURE REVIEW

Appendix A1: FLECHT Low Flooding Rate Cosine Test Series

Dates When Tests Were Performed: 1974 - 1975

References:

R1 Rosal, E. R. et al, "FLECHT Low Flooding Rate Cosine Test Series Data Report," WCAP-8651, Dec 1975.

R2 Lilly, G.P.,Yeh, H. C.,Hochreiter, L. E., and N. Yamaguchi, "PWR FLECHT Cosine Low Flooding rate Test Series Evaluation Report," WCAP-8838, March 1977.

Availability of Data:

Plots of selected data exist in the data report in R1. The raw data and reduced and analyzed data exists at Westinghouse on CDC 6600 and 7600 Magnetic tapes. This data has been in storage at the Westinghouse facilities. Microfiche of the raw data and analyzed data exist at the Westinghouse Engineering offices in Monroeville, PA. It is not clear if any of this data was put on the INEL data bank.

Test Facility Description, Types of Tests

The FLECHT Low Flooding Rate Cosine Test Series was a continuation of the FLECHT reflood heat transfer program started in the late 1960's and focused on low forced flooding rates tests at low pressures to provide a broader data range for the Appendix K licensing basis during the reflood period. The overall objective of the test program was to obtain data that would be useful for calculating the reflood behavior of PWRs following a postulated Loss Of Coolant Accident.

The tests were performed using a 10x10 rod bundle with 91 active electrical heater rods and nine guide tube thimbles in which instrumentation was placed. The rod bundle was placed inside a thick walled 19.05 mm (0.75 in square housing which was heated externally for the tests. There was excess flow area around the bundle such that the housing had to be heated to preserve the correct power-to-flow area of a PWR fuel assembly. The heater rods were 10.72 mm (0.422 in) in diameter and were arranged on a square pitch of 14.3 mm (0.563 in) and had a heated length of 3.66 m (12 ft). The electrical heater rods used a 1.66 cosine power distribution which was approximated by different pitch heating coils. The facility layout is shown in Figure A1.1 and the bundle geometry is given in Figure A1.2 from R2. A radial power distribution was used in these experiments to simulate or bound the rod-to-rod power distribution in a PWR fuel assembly. One feature which was unique in this test series is that there were a large number of variable inlet flooding rates tests performed to better simulate the gravity reflood behavior of the PWR. There were also low initial clad temperature test performed to simulate lower power regions in the core that could have quenched during blowdown or during Upper Head Injection which was a newer high-pressure accumulator installed on PWRs which had Ice Condenser Containment.

The ranges of conditions include:

Constant Flooding Rates	10.16 - 38.1 mm/s (0.4 - 1.5 in/s)
Upper Plenum Pressure	172.37 - 413.685 kPa (25 - 60 psia)
Initial Clad Temperature (At Peak Location)	148.88 - 871.11 degrees C (300 - 1600 degrees F)
Initial Peak Power (At Peak Location)	1.673 - 3.1167 kW/m (0.51 - 0.95 kW/ft)
Inlet Subcooling	11.11 - 100 degrees C (20 180 degrees F)
Variable Inlet Flooding Rate	Ranged from 0.3048 m/s (12 in/s) for 5 s and 20.32 mm/s (0.8 in/s) onward, to 50.8 mm/s (2 in/s) for 20 s and 25.4 mm/s (1 in/s) onward
Continuously Variable Flooding	There were two tests which simulated the average variable flooding rate from the FLECHT-SEASET Phase B systems tests.
Housing Temperature Tests	Housing initial temperature varied from 140 - 371.11 degrees C (284 - 700 degrees F)
FLECHT Repeat Tests	There were six repeat tests of previously performed FLECHT reflood tests.
Bundle and Housing Stored Energy Tests	Three different housing temperatures were used
Supplemental Entrainment	These were entrainment tests with several disconnected heater rods and failed rods over a range of flooding rates and pressures to provide additional data.

Instrumentation and Data From Tests

The heater rods were instrumented with several thermocouples to measure the inside cladding surface temperature. The heat flux from the cladding surface was calculated form the thermocouple response using an inverse conduction computer program called DATAR. This program should still exist at Westinghouse and has been replaced by an improved version called DATARH. The thimbles shown in Figure A2.2 were unheated tubes which receive radiant heat from the heater rods. The temperatures of the thimbles were measured using thermocouples welded to the inside of the tubes. Housing temperatures were measured along the length of the housing to characterize its heat release as the bundle quenched. The inlet flow and water temperature were measured as well as the pressure in the exit or upper plenum. There were separators and collection tanks at the exit of the test section such that the existing steam and water flows could be separated and individually measured. There were also sensitive differential pressure cells every two feet along the housing to measure the bundle

mass storage. The spacing is too sparse to obtain an accurate indication of local void fraction, however, the cells will indicate the mass stored in the bundle.

One of the more important pieces of data is the steam probe measurements at the 2.1366, 3.048 and 3.81 m (7, 10 and 12.5 ft) elevations. These were shielded aspirating thermocouples which could measure the vapor superheat until the quench front would approach and fill the probe with water. The steam probes indicated the high degree of superheat in the dispersed two-phase flow above the quench front.

This FLECHT Test Series was the first to perform a mass and energy balance down the test section to determine the local quality conditions and the split of the heat transfer between radiation to drops, vapor and housing, and steam convection with entrained droplets. There are calculated values of the real quality for seven tests which span the matrix at different times in the transient. The analysis indicated, for the first time, that the convection is enhanced when droplets are entrained. The analysis also indicated the importance of the radiation heat transfer. The Appendix A in Reference 1 gives the details of the calculational method.

Conclusions

The FLECHT Low Flooding Rate Cosine tests do have some data which would be of interest for improved reflood modeling. In addition to the heater rod temperatures, the measurement of the vapor temperature at the 2.1366, 3.048 and 3.81 m (7, 10 and 12.5 ft) elevations are of value since these data indicate the degree of non-equilibrium within the flow. The pressure drop measurements are too coarse to be used as an indicator of the void fraction within the bundle. However, these measurements can be used to indicate the mass rate of accumulation within the bundle such that a complete mass balance can be calculated from the data for the tests.

The conditions which were simulated are also useful from a code analysis and validation effort since a large range of conditions were simulated, in particular a variable inlet flooding rate and a continuously variable inlet flooding rate which simulates gravity reflooding. These experiments would be useful to assess the code performance.

This is not sufficient data to make code model changes without the potential for compensating error. More detailed data is needed which identify code calculated parameters such as vapor superheat, convective enhancement, radiation to drops, rods, vapor and housing, droplet sizes and velocities along the bundle, and the void distribution in the froth region. These types of measurements are missing such that the code can only be compared to the cladding temperatures, quench front, and the overall mass balance.

Therefore while these tests are useful in determining the overall reflood heat transfer, they provide very limited data which can be used to assess the reflood phenomena which was identified in the PIRT. Therefore, limited effort should be spent modeling these tests.

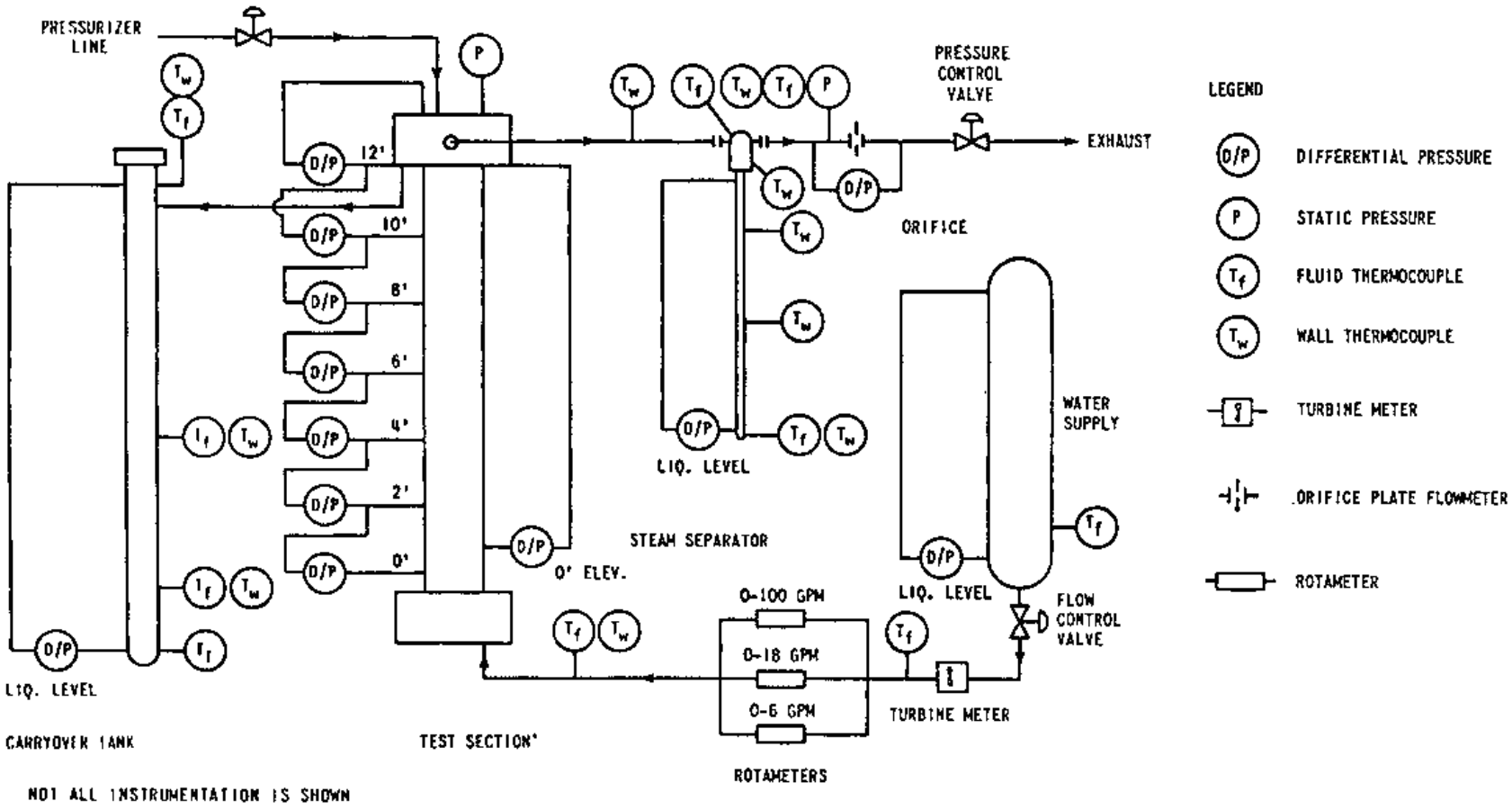

Figure A1.1 FLECHT Low Flooding Rate Test Configuration.

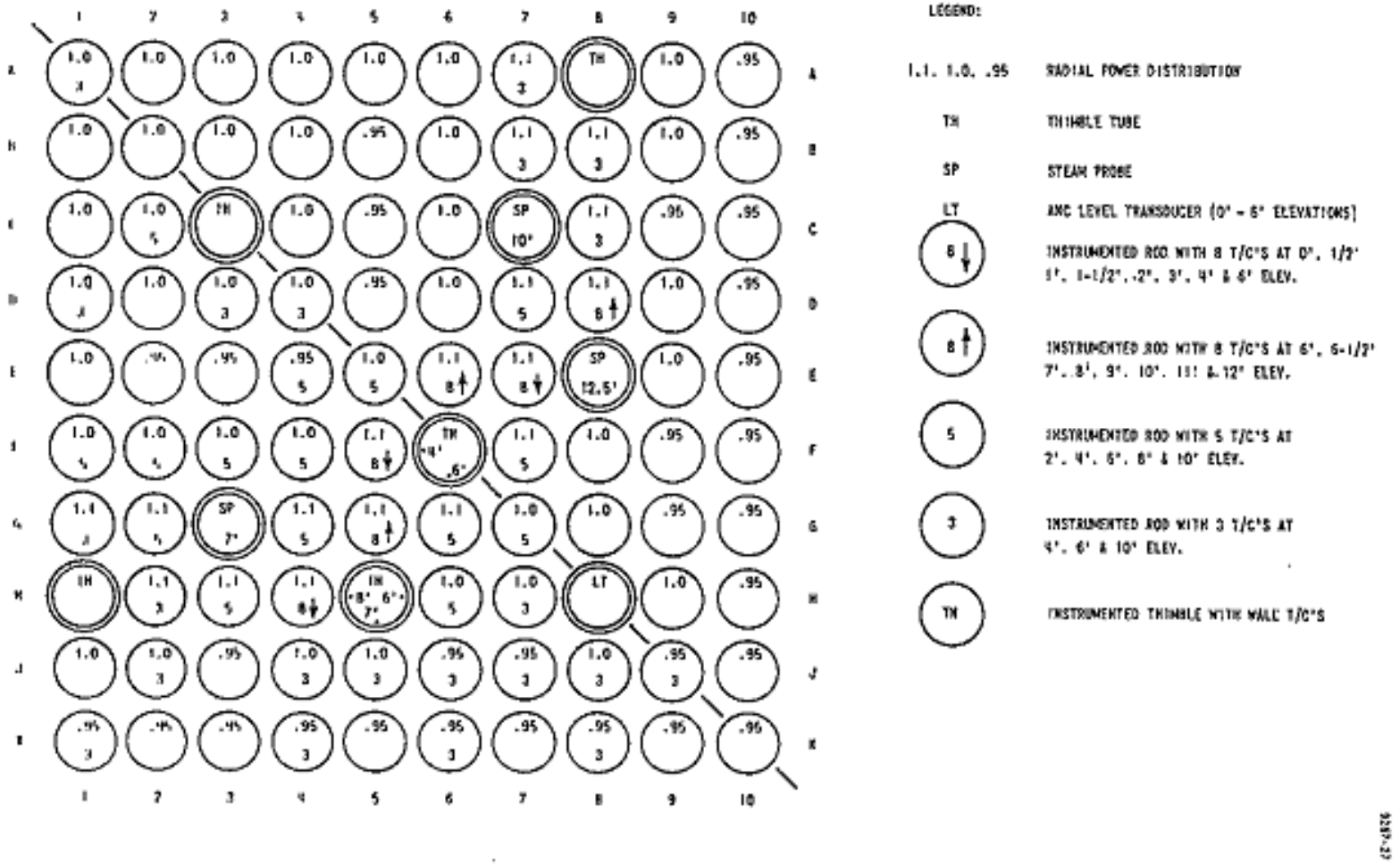

Figure A1.2 Rod Bundle Instrumentation for FLECHT Low Flooding Rate Tests.

APPENDIX A2. LITERATURE REVIEW

Appendix A2: FLECHT Low Flooding Rate Skewed Test Series

Dates When Tests Were Performed: 1976-1977

References:

R3 Rosal, E. R. et al, "FLECHT Low Flooding Rate Skewed Test Series Data Report," WCAP-9108, May 1977.

R4 Lilly, G. P., Yeh, H. C., Dodge, C. E., and S. Wong, "PWR FLECHT Skewed Profile Low Flooding Rate Test Series Evaluation Report," WCAP-9183, Nov. 1997.

Availability of Data:

Plots and tables of selected data are given in R3 for the different tests. Some of the basic quantities which were measured and calculated from the bundle mass and energy balance (given in R4) such as the local non-equilibrium quality, portion of the rod energy which is due to radiation and convective film boiling, and energy absorbed by the drops above the quench front. Two skewed power tests and one low flooding rate cosine test were analyzed in detail, which can be used for computer code comparison purposes. A heat transfer correlation was also developed which was a function of the distance above the quench front and is given in Reference R4. The skewed profile data was also compared to the cosine power shape data for the same test conditions.

The raw test data and the analyzed test data are available at Westinghouse on CDC 7600 magnetic tapes. Some selected tests have been brought forward to the new UNIX system at Westinghouse. Microfiche exist for the measured data as well as the analyzed test data at Westinghouse Engineering Offices in Monroeville, PA. It is believed that some of the transient temperature data were placed in the NRC data bank at INEL.

Test Facility Description, Types of Tests

The FLECHT Low Flooding Rate Skewed Tests were a continuation of the FLECHT Low Flooding Rate Cosine Tests which were performed in the 1975 time frame. The rod diameter used was 10.719 mm (0.422 in) on a square pitch of 14.33 mm (0.563 in). These tests were intended to provide data for supporting the Appendix K reflood heat transfer models for different possible axial power shapes for analysis of the Loss Of Coolant Accident.

There were two unique differences in the skewed tests as compared to the earlier cosine tests. The axial power shape was skewed to the top of the bundle with a peak of 1.35 at 3.048 m (10 ft), and a low mass circular housing was used for the first time in the FLECHT program.

The test facility is shown in Figure A2.1 and is similar to that for the low flooding rate cosine tests. The power shape is shown in Figure A2.2 and the bundle cross section is given in Figure A2.3. The bundle contained 105 electrical heater rods, six guide tube thimbles, eight metal filler rods and the ANC liquid level probe. The use of the filler rods permitted the square pitch rod array to fit into the circular housing with a minimum of excess flow area. There was additional

instrumentation added to the skewed test facility as compared to the low flooding rate cosine tests. There was more extensive thermocouple instrumentation within the bundle, there were differential pressure cells every foot instead of every two feet, close coupled tanks were attached to the upper plenum to collect and separate the liquid entrainment, and a more reliable exit flow measurement was used to measure the exiting steam flow from the bundle.

There was a radial power profile which was similar to the low flooding rate cosine bundle as seen in Figure A2.3. There were instrumented control rod guide tubes and aspirating steam probes in the rod bundle. The steam probes were at 2.1336, 3.048 and 3.3528 m (7, 10 and 11 ft). Selected guide tube thimbles were also instrumented with wall thermocouples.

The range of conditions which were investigated were similar to the low flooding rate cosine tests and included:

Constant Flooding Rate	17.78 - 152.4 mm/s (0.7 - 6.0 in/s)
Upper Plenum Pressure	137.896 - 413.685 kPa (20 - 60 psia)
Initial Clad Temperature (At Peak Location)	263.89 - 871.11 degrees C (507 - 1600 degrees F)
Initial Peak Power (At Peak Location)	1.4764 - 3.3808 kW/m (0.45 - 1.0 kW/ft)
Inlet Subcooling	4.44 - 55.55 degrees C (8 - 100 degrees F)
Variable Inlet Flooding Rate	Ranged from 152.4 mm/s (6 in/s) for 5 seconds to 20.32 mm/s (0.8 in/s), to 38.1 mm/s (1.5 in/s) for 100 s to 12.7 mm/s (0.5 in/s) onward
Cosine Overlap Tests	Tests were performed to overlap Cosine and Skewed test conditions
Hot and Cold Channel Tests	Tests were performed with portions of the bundle hot and the remainder cold
Transient Pressure and Subcooling Tests	Tests were performed in which the inlet flow, system pressure, and the inlet subcooling varied with time

There were also repeat tests which were performed to insure that the bundle geometry was not distorted. There were a total of 75 powered experiments. Very early on in the program, two heater rods failed at the beginning of testing. As the number of thermal cycles increased in the test bundle, additional heater rods failed later.

Instrumentation and Data From Tests

The electrical heater rods were instrumented with several thermocouples at the different elevation which gave good coverage for the length of the bundle. However, there were no thermocouples placed around the spacer grids which would indicate a spacer grid effect on the two-phase flow. The liquid carried out of the test section was measured as well as the exiting

steam vapor. The mass storage within the test section was also measured using delta P cells at one-foot intervals along the length of the housing. From these measurements, a transient mass balance could be performed on the test to help validate the data. Typically the mass balances were within five percent.

There were three aspirating steam probes at the 2.1336, 3.048 and 3.3528 m (7, 10 and 11 ft) elevations, as well as the exit pipe of the test section, to verify that the steam flow measurement was single phase. Using the flow measurements at the bundle exit, the actual steam non-equilibrium temperature, and the integrated wall heat flux between the steam probe locations; an energy balance can be performed to obtain the local quality and therefore the local steam and liquid flow. The change in the calculated quality indicates how much of the rod bundle surface heat flux goes into evaporating the entrained liquid droplets. The calculation was carried to the quench front where the vapor temperature was assumed to be the average of the rod temperature and the saturation temperature.

A simple radiation network was developed to separate the radiation heat transfer component from the total measured wall heat flux on the heater rods. Knowing the total wall heat flux, and subtracting the radiation heat flux, the convective wall heat flux can be determined. In the dispersed flow film boiling, this is the heat flux to the superheated vapor which contains entrained liquid droplets. The Nusselt number for the convective flux was calculated and compared to the Nusselt number that typical single-phase correlations would predict. It was observed that the convective Nusselt number calculated from the test data lied significantly above the limits calculated with conventional single phase convective correlations. Also, since the flow was superheated steam at low pressure, the calculated vapor Reynolds number was quite small, from 1500 to 10,000. These data and that of the low flooding rate cosine tests indicated that the presence of entrained liquid droplets could enhance the convective nature of the single phase vapor significantly at low vapor Reynolds numbers.

Conclusions

The FLECHT Low Flooding Rate Skewed Power Tests do have data which would be of interest for improved computer code modeling for the reflood heat transfer process. In particular, the different axial power shape used in these tests is very useful for assessing computer codes which may have been “tuned” to a cosine power shape. The pressure drop measurements are improved in the skewed bundle tests such that a more local void fraction (one-foot increments), can be determined and used to assess the local heat transfer. The void fractions and overall pressure drop are also used in the test bundle mass balances along with the inlet flows and exit flows. Typically the mass balances were within five percent.

There were a large number of experiments which were performed over a wide range of conditions, some of which specifically over-lapped with the low flooding rate cosine tests. These overlap experiments are particularly useful for code validation purposes, since the accuracy of the computer code predictions for different axial power shapes can be assessed. A Best-Estimate computer code must be able to calculate a range of different axial power shapes to determine the most limiting shape.

While the data from the skewed series of experiments as well as the data analysis of these tests was improved over the low flooding rate cosine tests; there was still the lack of sufficient vapor temperature distribution and information in the test bundle such that the axial distribution of the local qualities could be more accurately determined. The data was analyzed to determine the

heat flux split between radiation heat transfer and convective-dispersed flow film boiling heat transfer using a simplified radiation network approach. When the resulting convective-film boiling heat transfer (from the data) was compared to calculated single phase heat transfer correlation at the same vapor Reynolds number, the calculated data convective-film boiling transfer was significantly higher. Since the single phase correlation used the measured vapor temperature and the calculated vapor flow rate from the quality and energy balance, it is believed that the improved heat transfer is due to the presence of the entrained droplets which can add to the turbulence level in the flow at the low vapor Reynolds numbers. This phenomenon of enhanced convective-dispersed flow film boiling was identified in this report as well as in the low flooding rate report.

Therefore, the Low Flooding Rate Skewed Power reflood tests are useful in determining the overall heat transfer processes and some of individual models and phenomena which compromise the reflood heat transfer process.

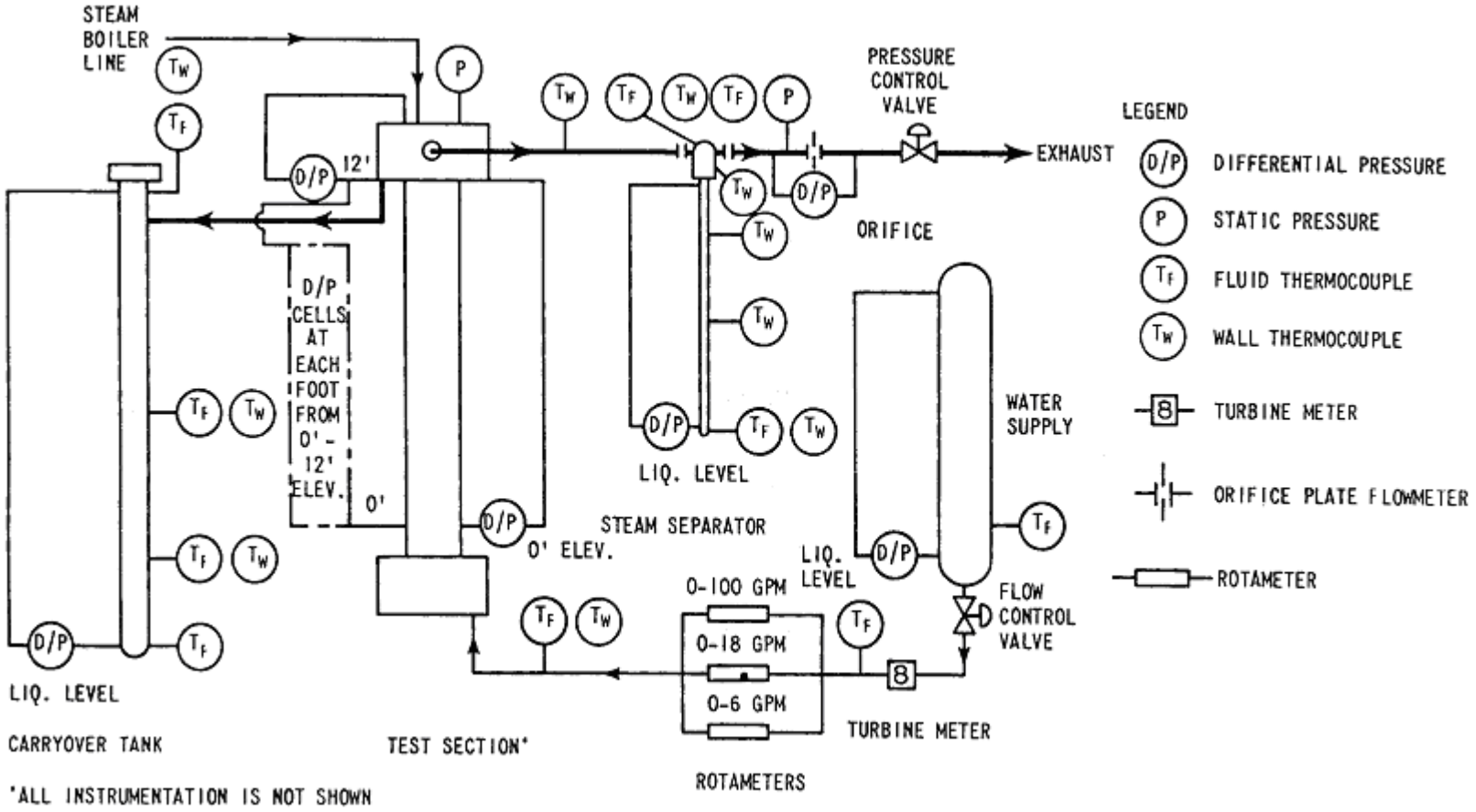

Figure A2.1 FLECHT Low Flooding Rate Test Facility Schematic.

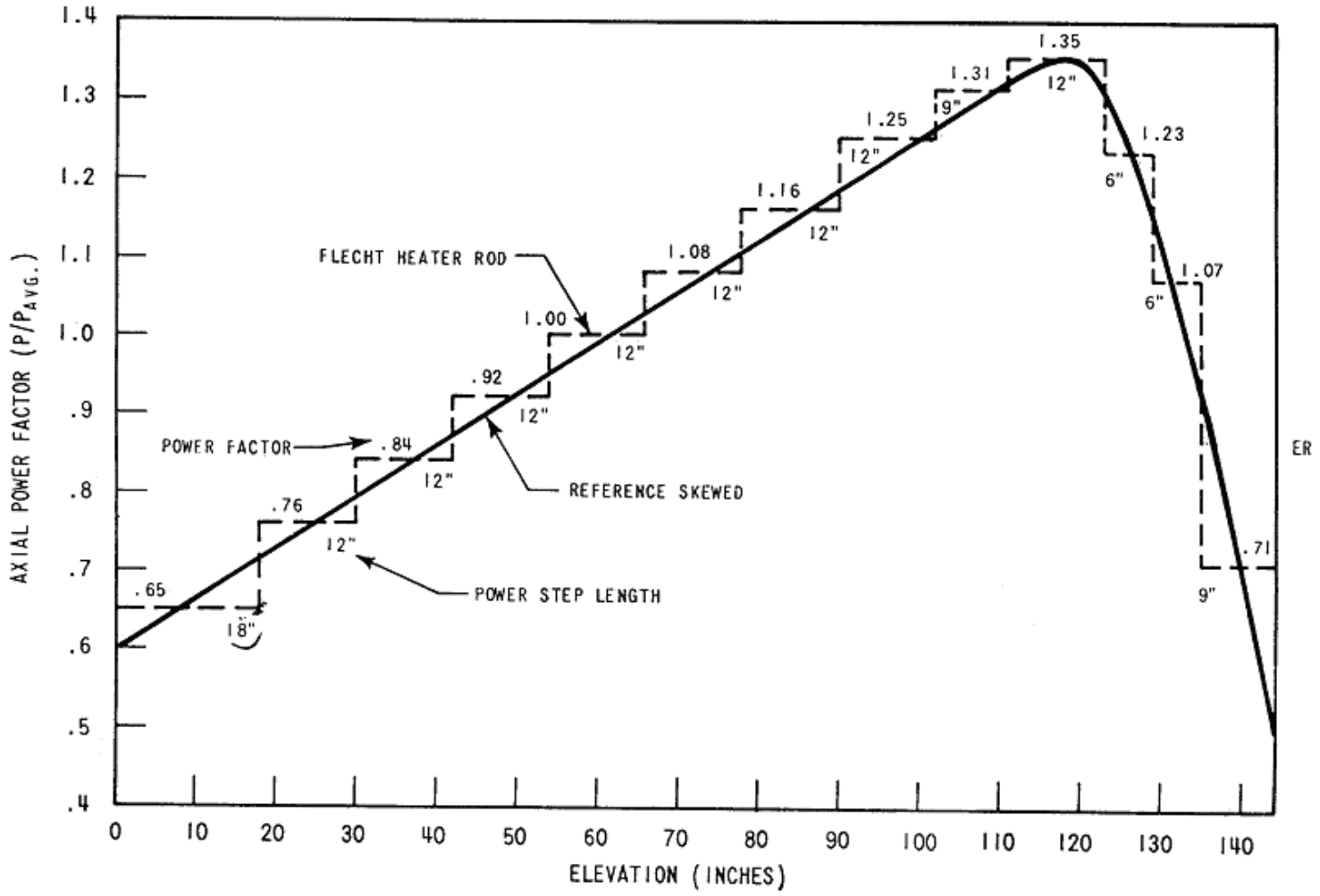

Figure A2.2 FLECHT Low Flooding Rate Test Power Shape.

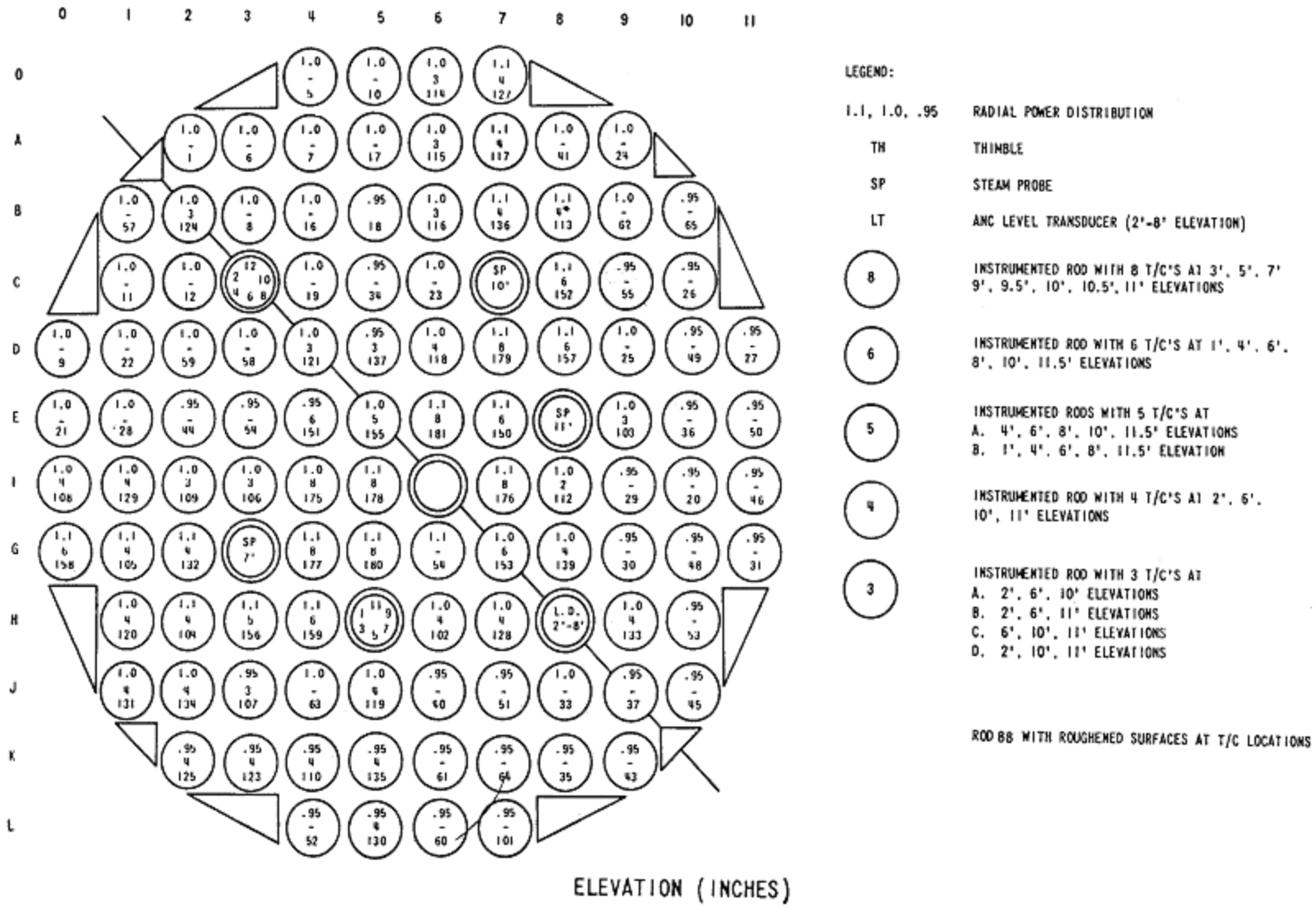

Figure A2.3 FLECHT Low Flooding Rate Test Rod Bundle Cross Section.

APPENDIX A3. LITERATURE REVIEW

Test Facility Name: Westinghouse FLECHT-SEASET 21-Rod Bundle Test Facility.

Dates When Tests Were Performed: 1977-1982

References:

R5 M. J. Loftus, et. al., "PWR FLECHT SEASET 21-Rod Bundle Flow Blockage Task Data and Analysis Report," NUREG/CR-2444, EPRI NP-2014, ECAP-992, Vol. 1 and Vol. 2, September 1982.

Availability of Data:

Volume 1 contains data and limited analysis from the 21-Rod Bundle FLECHT-SEASET Program. Volume 2 contains sampling of data tables and plots collected for the unblocked bundle (Configuration A) and five blocked bundle configurations, (B, C, D, E and F). All the valid measured data are available in the NRC data bank.

Test Facility Description, Types of Tests

Low forced flooding rate, gravity reflood, and single phase flow tests were performed in the 21-Rod bundle FLECHT-SEASET Test Facility. The overall objectives of these tests were to determine effects of various flow blockages of reflooding behavior and to aid in development/assessment of computational models in predicting reflooding behavior of flow blockage configurations for the 163-Rod flow blockage bundle test.

The tests were performed using a 5x5 rod bundle array typical of a 17x17 power fuel assembly. The bundle contained 21 active electrical heater rods and four triangular shaped filler strips placed at the corners in order to minimize excess flow areas due to the circular low mass flow housing as shown in Figure A3.1. The heater rods were 0.0095 m (0.374 in) in diameter and 3.24 m in length. The electrical heater rods used a 1.66 peak to average axial power distribution with a chopped cosine shape, which was approximately simulated by different pitch coils in the electrical heating element. The heater rod bundle had a uniform radial power profile. Spacer grids were of a simple egg-crate style installed 0.533 m (21 in) apart. The tests were conducted in a heavily instrumented facility as indicated in the reference Reports.

Four types of tests were conducted: hydraulic characteristics tests, steam cooling tests, forced reflood tests, and gravity reflood tests. The hydraulic characteristics tests were performed to determine the pressure losses associated with rod friction, grids, and blockage sleeves. The steam cooling tests were performed to measure single-phase heat transfer effects of unblocked and blocked configurations. Forced reflood tests were performed to measure the two-phase flow heat transfer effects of unblocked configurations. The gravity reflood tests were performed to measure heat transfer effects during the PWR-simulated gravity reflood injection for unblocked and blocked configurations.

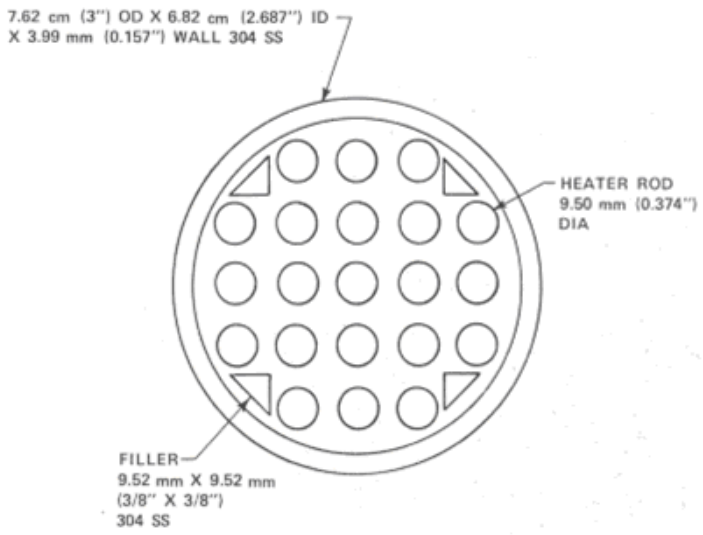

Figure A3.1 Schematic of the Test Bundle.

The range of conditions included:

Constant Flooding Rates:	10.2 - 152 mm/s (0.4 - 6.0 in/s)
Upper Plenum Pressure:	0.14 - 0.28 MPa (20 - 40 psia)
Initial Clad Temperature: (At Peak Location)	260 - 871 degrees C (500 - 1600 degrees F)
Inlet Subcooling:	3 - 78 degrees C (5 - 140 degrees F)
Variable Steps in Flooding Rates:	20 - 152 mm/s (0.8 - 6.8 in/s)
Injection Gravity Reflood: (Variable Steps)	0.09 - 0.82 kg/s (0.2 - 1.8 lb/s)
Housing Temperature Tests: (At Peak Location)	222 - 546 degrees C (431 - 1015 degrees F
Repeat Tests:	There were 2 repeat tests of the Unblocked Configuration (A)

Conclusions

Comparisons of calculated and measured temperatures generally showed good agreement. Nusselt numbers calculated from the steam cooling data were compared with the Dittus-Boelter heat transfer correlation as a function of Reynolds number. The results showed that, in general, the Dittus-Boelter correlation under predicts the heat transfer coefficient for Reynolds numbers less than 2500 and is in agreement for values about Reynolds numbers greater than 10,000. Comparisons of the FLECHT-SEASET 21-Rod Bundle tests with the Rod Bundle PIRT are given in Tables A3.1 to A3.4.

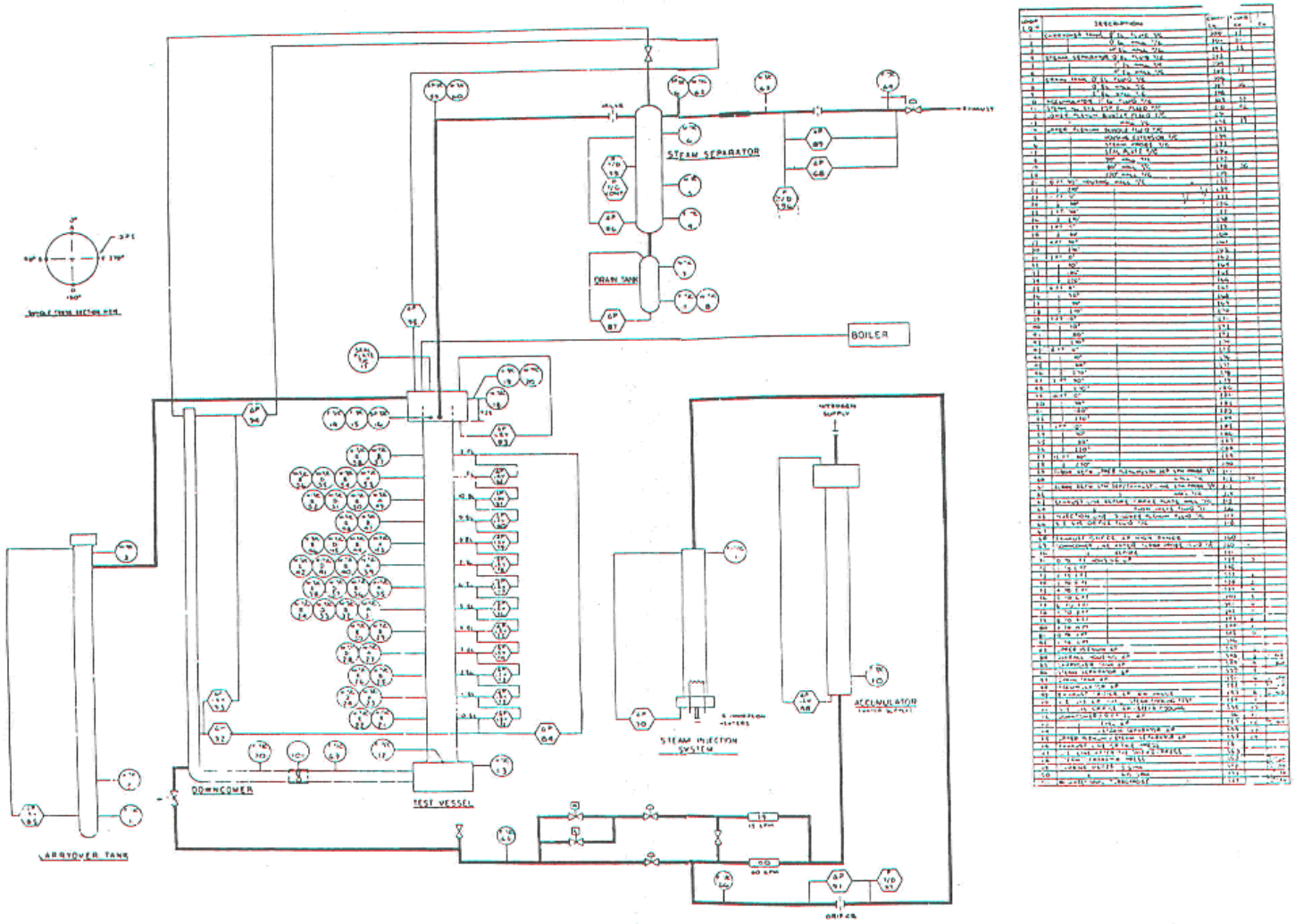

Figure A3.2 21-Rod Bundle Flow Blockage Task Instrumentation Schematic Diagram.

Table A3.1 Assessment of FLECHT-SEASET Unblocked 21-Rod Bundle Test to RBHT PIRT: Dispersed Flow Region for Core Component

Process/Phenomena	Ranking	Basis	FLECHT-SEASET 21-Rod Bundle
Decay Power	H	Energy source which determines the temperature of the heater rods, and energy to be removed by the coolant.	Known, measured initial condition.
Fuel Rod/Heater Rod properties, ρ, C_p, k	L	The exact properties can be modeled and stored energy release is not important at this time.	Heater rod properties are known and approximate those of nuclear rod.
Dispersed Flow Film Boiling	H	Dispersed flow film boiling modeling has a high uncertainty which directly effects the PCT.	Only 2 T_v measurements, and no valid α measurements were made.
• Convection to superheated vapor	H	Principle mode of heat transfer as indicated in FLECHT-SEASET experiments[4].	Total heat transfer was measured, convective H.T. was estimated from data.
• Dispersed phase enhancement of convective flow	H	Preliminary models indicate that the enhancement can be over 50% in source cases[2].	Comparisons of estimate convective H.T. to conventional correlation showed 2ϕ enhancement. No model for this.
• Direct wall contact H.T.	L	Wall temperatures are significantly above T_{min} such that no contact is expected.	Only total heat transfer was measured, this component was not isolated.
• Dry wall contact[12]	M	Iloeje[12] indicates this H.T. Mechanism is less important than vapor convection.	Only total wall heat transfer was measured, this component was not isolated.
• Droplet to vapor interfacial heat transfer	H	The interfacial heat transfer reduces the vapor temperature which is the heat sink for the wall heat flux.	No measurements
• Radiation Heat transfer to: • Surfaces • Vapor • Droplets	 M/H M/H M/H	This is important at higher bundle elevations (H) where the convective heat transfer is small since the vapor is so highly superheated. Very important for BWR reflood with sprays, and colder surrounding can. Large uncertainty.	Radiation to vapor was estimated.
Gap heat transfer	L	Controlling thermal resistance is the dispersed flow film boiling heat transfer resistance. The large gap heat transfer uncertainties can be accepted, but fuel center line temperature will be impacted.	Not present. Heater rods have no gap.
Cladding Material	L	Cladding material in the tests is Inconel which has the same conductivity as zircalloy nearly the same temperature drop will occur.	Used stainless steel clad.
Reaction Rate	M	Inconel will not react while Zircalloy will react and create a secondary heat source at a very high PCTs, Zirc reaction can be significant	Not present
Fuel clad swelling/ballooning	L	Ballooning can divert flow from the PCT location above the ballooning region. The ballooned cladding usually is not the PCT location. Large uncertainty.	Ballooning was simulated with sleeves attached to heater rods in bundle configurations B, C, D, E and F. Enhance factors on H.T. were calculated

Table A3.2 Assessment of FLECHT-SEASET Unblocked 21-Rod Bundle Test to RBHT PIRT: Top Down Quench in Core Components

Process/Phenomena	Ranking	Basis	FLECHT-SEASET 21-Rod Bundle
De-entrainment of film flow	L[1]	The film flow is the heat sink needed to quench the heater rod. This has high uncertainty.	Top down quenching was observed in some tests.
Sputtering droplet size and velocity	L	The droplets are sputtered off at the quench front and are then re-entrained upward. Since the sputtering front is above the PCT location, no impact. The entrained sputtered drops do not affect the total liquid entrainment into the reactor system, as well as the steam production, in the steam generators.	Details at top quench front were not measured. Only the total heat transfer was measured.
Fuel rod/heater rod properties for stored energy: ρ, c_p and k.	L[1]	These properties are important since they determine the heat release into the coolant. However, since this occurs above the PCT level, no impact.	Heater rod properties are known.
Gap heat transfer	L[1]	Affects the rate of energy release from the fuel/heater rod.	No gap in heater rods.

Note: Some of these individual items can be ranked as High (H) within the top down quenching process; however, the entire list is ranked as low (L) for a PWR/BWR since it occurs downstream of the PCT location.

Table A3.3 Assessment of FLECHT-SEASET Unblocked 21-Rod Bundle Test to RBHT PIRT: Preliminary PIRT for Gravity Reflood Systems Effects Tests

Process/Phenomena	Ranking	Basis	FLECHT-SEASET 21-Rod Bundle
Upper Plenum-Entrainment/De-entrainment	M	The plenum will fill to a given void fraction after which the remaining flow will be entrained into the hot leg, large uncertainty.	Not measured.
Hot leg - Entrainment, de-entrainment.	L	The hot legs have a small volume and any liquid swept with the hot leg will be entrained into the steam generator plenums, medium uncertainty.	Not measured.
Pressurizer	L	Pressurizer is filled with steam and is not an active component, small uncertainty.	Not measured.
Steam Generators	H	The generators evaporate entrained droplets and superheat the steam releases (particularly at low pressures). The result is a higher steam flow downstream of the generators. High uncertainty since a good model is needed. FLECHT-SEASET data exists for reflood.	Not measured. Not measured.
Reactor Coolant Pumps	H	This is the largest resistance in the reactor coolant system which directly affects the core flooding rate-low uncertainty.	Not measured. Variable flows were simulated to model accumulator and pumped injections, also continuous by variable flooding rate tests were performed.
Cold leg accumulator injection	H	Initial ECC flow into the bundle.	Not measured, variable flows are simulated to model accumulator and pumped injection , also continuous by variable flooding rate tests were performed.
Cold leg pumped injection	H	Pumped injection maintains the core cooling for the majority of the reflood transient.	Low pressure (20 psia) simulated.

Table A3.3 Assessment of FLECHT-SEASET Unblocked 21-Rod Bundle Test to RBHT PIRT: Preliminary PIRT for Gravity Reflood Systems Effects Tests (Continued)

Process/Phenomena	Ranking	Basis	FLECHT-SEASET 21-Rod Bundle
Pressure	H	Low pressure (20 psia) significantly impacts the increased vapor volume flow rate, which decreases the bundle flooding rate.	Low pressure (20 psia) simulated.
Injection Subcooling	M/H	Lower subcooling will result in boiling below quench front such that there is additional vapor to vent.	Low subcooling simulated.
Downcomer Wall Heat Transfer	H	The heat transfer from the downcomer walls can raise the ECC fluid temprature as it enters the core, resulting in more steam generation.	Not measured.
Lower Plenum Wall Heat Transfer	M	Source effect as downcomer but less severe.	Not measured.
Break	L	Excess ECC injection spills, but break ΔP helps pressurize reactor system.	Not measured.

Table A3.4 Assessment of FLECHT- SEASET Unblocked 21-Rod Bundle Test to RBHT PIRT: High Ranked BWR Core Phenomena

Process/Phenomena	Basis	FLECHT-SEASET 21-Rod Bundle
Core Film Boiling	PCT is determined in film boiling period.	Total heat transfer is measured.
Upper Tie Plate CCFL	Hot assembly is in co-current flow above CCFL limit.	Not applicable.
Channel-Bypass Leakage	Flow bypass will help quench the BWR fuel assembly core.	Not applicable.
Steam Cooling	A portion of the dispersed flow film boiling heat transfer.	Steam cooling heat transfer is estimated from data.
Dryout	Transition from nucleate boiling and film boiling.	Quench front is measured.
Natural Circulation Flow	Flow into the core and system pressure drops.	Not measured.
Flow Regime	Determines the nature and details of the heat transfer in the core.	Not measured.
Fluid Mixing	Determines the liquid temperature in the upper plenum for CCFL break down.	Not measured.
Fuel Rod Quench Front	Heat release from the quench front will determine entrainment to the upper region of the bundle.	Quench front data exists.
Decay Heat	Energy source for heat transfer.	Measured as initial/boundary conditions.
Interfacial Shear	Affects the void fraction and the resulting droplet and liquid velocity in the entrained flow.	Not measured.
Rewet: Bottom Reflood	BWR hot assembly refloods like PWR.	Total reflood heat transfer measured.

Table A3.4 Assessment of FLECHT- SEASET Unblocked 21-Rod Bundle Test to RBHT PIRT: High Ranked BWR Core Phenomena (Continued)

Process/Phenomena	Basis	FLECHT-SEASET 21-Rod Bundle
Rewet Temperature	Determines the quench front point on the fuel rod.	Quench temperature measured.
Top Down Rewet	Top of the hot assembly fuel will rewet in a similar manner as PWR.	Top down rewet quench front measured.
Void Distribution	Gives the liquid distribution in the bundle.	Not measured.
Two-Phase Level	Similar to quench front location, indicates the location of nucleate and film boiling.	Measured by rod TC's. Collapsed level measured, two phase level measured by DP cells.

APPENDIX A4. LITERATURE REVIEW

Appendix A4: FLECHT-SEASET 161-Rod Unblocked Bundle Tests

Dates When Tests Were Performed: 1981-1982

References:

R6 Loftus, M. J., et al," PWR FLECHT-SEASET Unblocked Bundle Forced and Gravity Reflood Task Data Report," NUREG/CR-1532, September 1981.

R7 Lee, N. ,Wong, S., Yeh, H.C., and Hochreiter, L.E., "PWR FLECHT-SEASET Unblocked Bundle Forced and Gravity Task, Data Evaluation and Analysis Report," NUREG/CR-2256, February 1982.

R8 Wong, S. and Hochreiter, L.E., "PWR FLECHT-SEASET Analysis of Unblocked Bundle Steam-Cooling and Boil-off Tests," NUREG/CR-1533, May 1981.

Availability of Data:

Plots and tables of selected data are given in R6 for each of the tests. These tests are similar to the Low Flooding Rate Cosine Tests excepting that the rod array used in the FLECHT-SEASET tests used the newer 17x17 array while the Low Flooding Rate Cosine and Skewed Power Tests used the older 15x15 rod array. There are selected tests which were analyzed in detail in Reference 2, particularly Test 31504 which is a 40 psia, 1 in/s constant reflood test. There was additional instrumentation on the test bundle which permitted more accurate mass and energy balances for the two-phase dispersed flow region of the bundle. There were also several high-speed movies of the different tests taken at the three, six and nine-foot windows. The drop diameter and droplet velocities were obtained and are given in R7. A heat transfer correlation was developed as a function of the distance from the quench front for both the 15x15 and 17x17 rod bundle geometry.

The raw data in engineering units is available from the NRC Data Bank for selected tests. All the data exists at Westinghouse on Microfiche, including the analyzed data. The analyzed data and the row data in engineering units also exists at Westinghouse in storage on older computer tapes. It is not clear at this time if the data can be assessed.

Test Facility Description, Types of Tests

The FLECHT-SEASET Unblocked Bundle tests were the first publicly available reflood experiments on the newer 17x17 fuel array which was adopted by the utilities in the 1980's. This fuel array used fuel rod of approximately 9.5 mm (0.374 in) on a square pitch of 12.60 mm (0.496 in).

The experiments used a 1.66 chopped cosine power shape which was the same as the FLECHT Low Flooding Rate Cosine Tests. The tests were used to help confirm the conservatism in the Appendix K rule as well as to be used for reflood safety analysis computer code assessment. Two of the experiments were also used as US Standard Problem 9 in which

different parties predicted two FLECHT-SEASET unblocked bundle reflood transients. The unblocked bundle tests were also used as a basis for determining the effects of flow blockage within the rod bundle which simulated the ballooning and bursting of the Zircaloy cladding.

The majority of the tests were separate effects constant and or variable reflood tests. There were also limited gravity reflood scoping experiments as well. In addition, there were boil-off and steam cooling tests performed as well as given in R8.

The 161-rod bundle unblocked bundle did have problems with the electrical heater rod. The new smaller diameter rods, with smaller inside wall thermocouples, proved to be less reliable then the previous larger 10.719 mm (0.422 in) diameter rods. Several of the heater rod thermocouples failed in the initial transient tests such that the bundle instrumentation became degraded. Consequently, the 161-rod bundle was rebuilt by replacing heater rods approximately one-half way into the testing program. Those individuals using the test data must verify the proper channel and rod location since new rods were used in several different locations. The full channel list for all tests is given in R6.

The 161-rod bundle also used the thin wall circular housing so as to minimize the housing radiation heat sink effects as well as the housing heat release effects. Figure A4.1 shows the cross-section of the rod bundle and Figure A4.2 shows the facility flow diagram. The majority of these tests were conducted with a uniform radial power profile for ease of analysis, as well as obtaining a statistical distribution for the hot spot temperatures and heat transfer coefficient.

The 161-rod bundle was much more heavily instrumented as compared to the previous FLECHT test bundles. Most of the heater rods were instrumented and would have eight thermocouples per rod. Rods were located in symmetric positions such that complete coverage over the bundle length was achieved. The differential pressure cells were located one foot apart as in the skewed bundle tests and the data was used to determine the mass balance as well as for the average void fraction over the given cell span. There was no specific thermocouple placement relative to the grids, and the spacer grids were not instrumented; however, the axial placement was sufficiently fine that the data does indicate the heat transfer improvements caused by the spacer grids. The FLECHT egg-crate spacer grids were used and are the same as those used in previous FLECHT tests. One of the objectives of the 161 rod bundle tests was to provide improved data for the development and validation of safety analysis computer codes. To this end, there were additional aspirating steam probes added to the guide tube thimbles. Some of the steam probes aspirated the flow out the bottom of the bundle while other probes aspirated out the top of the bundle. It was discovered that the bottom probes would not indicate the true steam temperature since they were more easily wetted during the transient. The probes which are regarded as unreliable are given in R6.

The range of conditions which were examined was similar to the Low Flooding Rate FLECHT tests and included:

Constant Flooding Rates	11.43 - 154.94 mm/s (0.45 - 6.1 in/s)
Upper Plenum Pressure	137.895 - 413.685 kPa (20 - 60 psia)
Initial Clad Temperature (At Peak Location)	256.66 - 1118.33 degrees C (494 - 2045 degrees F)

Initial Peak Power (At Peak Location)	1.312 - 3.2808 kW/m (0.40 - 1.0 kW/ft)
Radial Power Distribution Similar to FLECHT Tests	Uniform - FLECHT
Inlet Liquid Temperature	51.11 - 125 degrees C (124 - 257 degrees F)
Variable Flooding Rate Tests	161.544 mm/s (6.36 in/s) for 5 s; 20.828 mm/s (0.82 in/s) onward; 165.862 mm/s (6.53 in/s) for 5 s; 24.892 mm/s (0.98 in/s) for 25 s; 15.748 mm/s (6.36 in/s) onward
Gravity Injection Tests	147.32 mm/s (5.8 in/s) for 15 s; 19.94 mm/s (0.785 in/s) onward

There were other tests performed such as hot and cold channel tests to examine the effects of liquid entrainment, repeat tests to verify that the bundle was performing in a repeatable manner overlap tests with the previously performed 15x15 cosine experiments and steam cooling tests. The steam cooling tests are given in Reference 3 and investigated the steam cooling in the bundle over a Reynolds number range of approximately 1500 to 25000. The test matrix for this test series is given as Table A4.1, along with the measured peak cladding temperatures.

There was a significant number of power cycles performed on the test bundle which led to heater rod distortion at the end of the test program. An analysis was performed to determine when the effects of distortion became evident in the data. This analysis is given in Reference 1 and should be consulted when modeling the tests from this program such that only valid data is used.

High-speed movies were taken for a number of tests at the three, six, and nine-foot windows with camera speeds up to 2000 frames/sec. The movie data was reduced and analyzed to obtain droplet size and velocity data which was then compared to values from the literature as well as calculations. It was found that a log-normal distribution fit the droplet diameter data reasonably well while there was no real correlation of the droplet velocity with the droplet diameter or any other parameter.

An empirical reflood heat transfer correlation was developed from the 161-rod bundle experiments. The heat transfer correlation was a function of the distance above the quench front as well as the bundle initial conditions of power, pressure, flooding rate, inlet subcooling, and initial power. This correlation was used to predict the heat transfer above the quench. In addition, a quench front correlation was also developed such that given a set of system conditions; the dispersed flow film boiling heat transfer above the quench front in the PCT region could be predicted. The correlation was also used the older 15x15 FLECHT Low Flooding Rate Cosine and Skewed Power test data for developing the correlation.

The unique area that the 161-rod bundle tests addressed was the analysis of the test data above the quench front in the film boiling region. The analysis methods which were first developed as part of the FLECHT Low Flooding Rate Test Series were expanded upon in the

FLECHT-SEASET program. There was increased instrumentation for axial vapor temperature measurements along the test bundle which could then be used with the exit flow measurements to calculate the local actual quality in the test bundle, from an energy balance, such that the local liquid and vapor velocities could be determined. From the calculations of the vapor flows, velocities, and temperatures, the local vapor Reynolds number could be calculated such that a convective heat transfer could be predicted from different single-phase correlations. The effects of the vapor superheat on the calculated Reynolds number were significant since superheated steam flows at 15.24 m/s (50 ft/s) could result in a Reynolds number in the laminar regime. The results from the energy balance were also used with the high-speed movie from the analysis of the droplet data to calculate the void fraction in the flow. The measured void fraction from the differential pressure cells is not as accurate in the highly dispersed flow regime when the flow has very little liquid content.

The wall heat flux was also decomposed using a six node radiation heat transfer network such that the radiation heat transfer from the inner hot rods, outer cold rods, guide tube thimbles, housing, droplets, and vapor could be calculated. Once the radiation component of the hot rods was calculated, the convective-dispersed flow film boiling portion of the rod heat transfer could be determined by subtracting the calculated radiation heat transfer from the measured total heat transfer which was calculated from an inverse conduction calculation using the heater rod thermocouple and local power. The convective-dispersed flow film boiling heat transfer was also compared to the single phase heat transfer one would predict using the same vapor Reynolds number, wall temperature and vapor temperature conditions. As with the FLECHT tests, the convective dispersed flow heat transfer data gave much higher values of the Nusselt number when compared to the Nusselt number calculated form the same conditions for a single-phase vapor. The interpretation of this difference is that the droplets are acting to enhance the heat transfer in the flow by acting as additional turbulence promoters, as well as temperature sinks which change the local bulk temperature profile. The comparisons indicate that the droplet effects are the greatest at the lowest vapor Reynolds numbers where the natural turbulence in the flow is the smallest. Therefore, the drops could be promoting increased turbulence in the flow which provides for increased heat transfer. It was also observed that as the liquid content of the flow increased, the difference between the convective dispersed flow film boiling heat transfer and the predicted single phase heat transfer also increased.

The 161-rod bundle tests also clearly showed that two different two-phase regions exist above the quench front. A lower void fraction, liquid rich froth or transition region, exists at and just above the quench front for the forced flooding tests. The length of this region depends on the flooding rate value relative to the quench velocity. The larger the flooding rates relative to the quench velocity (which is conduction controlled), the longer the froth region. The froth region was observed and appears as liquid ligaments which are sheared into increasingly smaller droplets from the steam flow generated at the quench front and the higher wall temperature in the quench front region. The vapor shearing effects generate the entrained droplets which then provide cooling at the upper elevations of the test bundle in the non-equilibrium dispersed flow film-boiling regime.

Conclusions

The FLECHT-SEASET 161-rod unblocked bundle experiments represent the best reflood experiments which were performed. It was recognized in the test planning that data was

needed for advanced reflood computer code development such that an effort was made to obtain additional local heat transfer and fluid flow data in addition to the total heater rod heat transfer data for an empirical correlation. The mass balances on the tests were generally very good such that the data can be used with confidence, however, one must be careful of the vapor measurements as indicated earlier since some of the steam probes did not function as desired. Also because of heater rod problems, the bundle was rebuilt so that channel designation relative to specific heater rods may have changed. These changes are documented in the reports such that the user can correctly obtain the data for a given test.

The analysis for the test data is the most complete of all the FLECHT test series. Test 31504 was analyzed in detail with several plots given in the reports which can be used for computer code validation. There is also an amount of very good droplet size and velocity information which can also be used for computer code validation. If all the data is used for the validation, not just the heater rod temperatures, one can more realistically assess a computer code reflood heat transfer model since the test measurements include the rod surface temperature, vapor temperature, drop size, drop velocity as well as the local quality, void fraction, and heat flux split between radiation heat transfer and convective dispersed flow film boiling heat transfer.

Two of the FLECHT-SEASET tests were used as US Standard Problem 9 for the purposes of code validation. It is strongly recommended that these data be used for validating the NRC merged code.

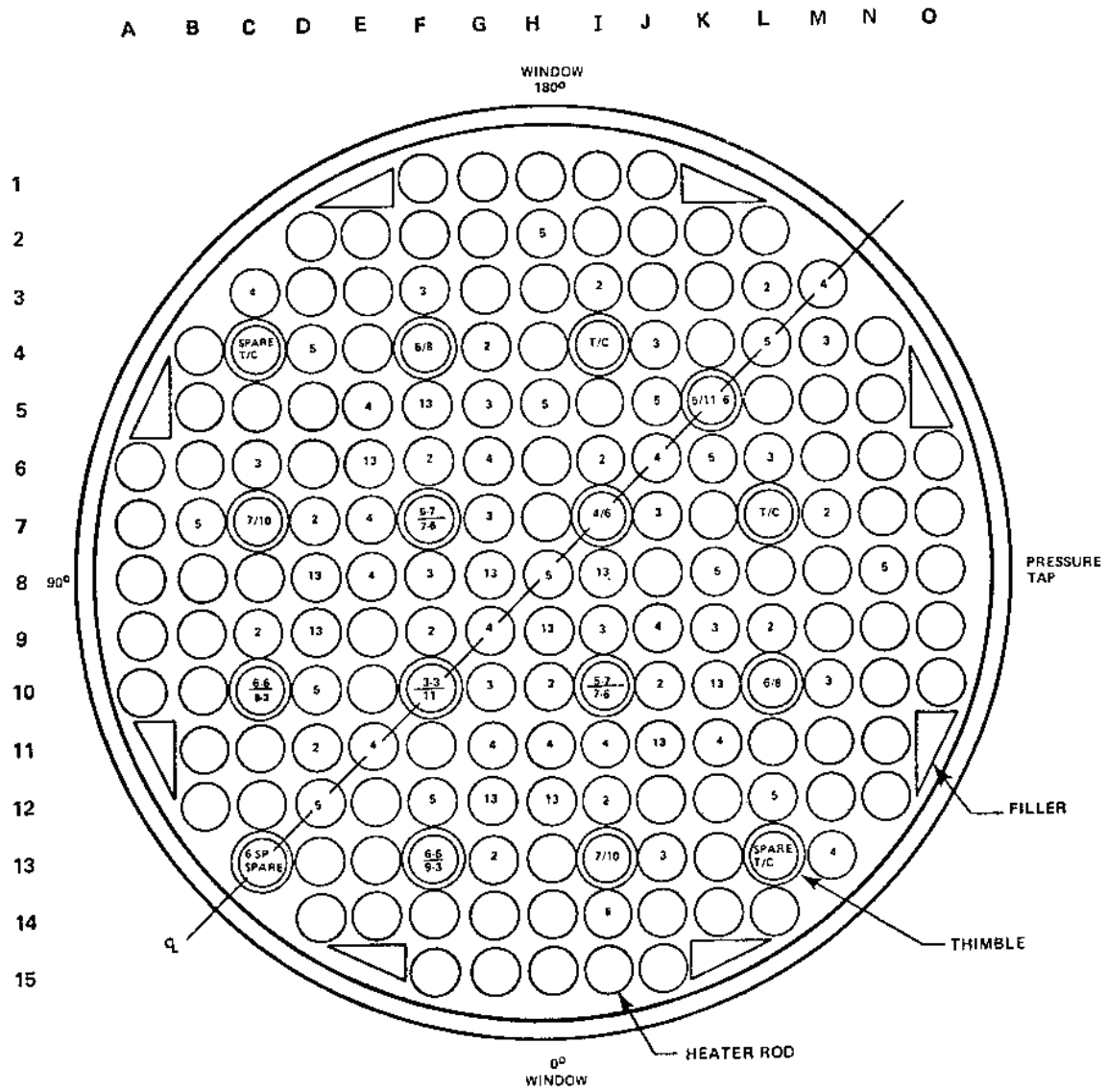

BUNDLE STATISTICS

HOUSING INSIDE DIAMETER	194.0 mm (7.625 in.)
HOUSING WALL THICKNESS	5.08 mm (0.200 in.)
ROD DIAMETER	9.50 mm (0.374 in.)
THIMBLE DIAMETER	12.0 mm (0.474 in.)
ROD PITCH	12.6 mm (0.496 in.)
CROSS-SECTIONAL FLOW AREA	15571 mm^2 (24.136 $in.^2$)
FILLER DIMENSIONS	18.8 x 8.43 mm (0.741 x 0.332 in.)
161 HEATER RODS	— —
16 THIMBLES	— —
8 FILLERS	— —

Figure A4.1 FLECHT-SEASET Rod Bundle Cross Section.

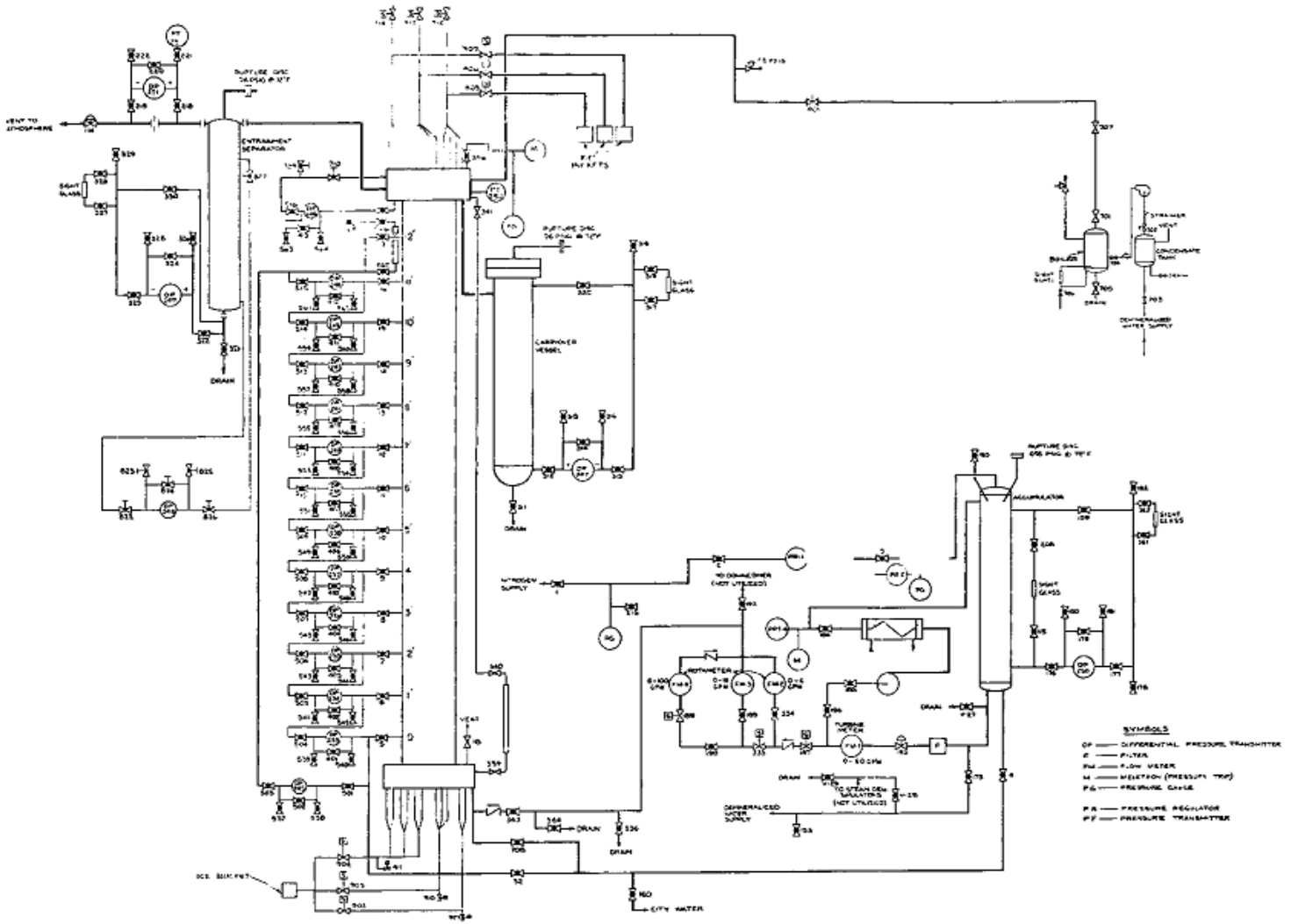

Figure A4.2 FLECHT-SEASET Facility Flow Diagram.

Table A4.1 FLECHT-SEASET Unblocked Bundle Reflood Test Data Summary

Test No.	Run No.	Actual Test Conditions: Upper Plenum Pressure [MPa (psia)]	Rod Initial T_{clad} at 1.83m (72 in.) [°C(°F)]	Rod Peak Power [kw/m (kw/ft)]	Flooding Rate [mm/sec (in./sec)]	Coolant Temperature [°C(°F)]	Radial Power Distribution	Results: Hottest Rod T/C and Elevation [m(in.)]	Initial Temperature [°C(°F)]	Maximum Temperature [°C(°F)]	Temperature Rise [°C(°F)]	Turn-around Time (sec)	Quench Time (sec)	Bundle Quench Time (sec)	Disconnected Rod Location
CONSTANT FLOODING RATE															
1	31701	0.28 (40)	872 (1601)	2.3 (0.70)	155 (6.1)	53 (127)	Uniform	9I-1.78(70)	893 (1640)	923 (1694)	30 (54)	5	55	114	4G, 5G
2	31302	0.28 (40)	869 (1597)	2.3 (0.69)	76.5 (3.01)	52 (126)	Uniform	8E-1.70(67)	889 (1631)	932 (1710)	43 (79)	8	124	262	4G, 5G, 6J, 11G
3	31203	0.28 (40)	872 (1601)	2.3 (0.70)	38.4 (1.51)	52 (126)	Uniform	9L-1.93(76)	870 (1597)	1037 (1898)	167 (301)	63	246	435	4G, 5G
	33903	0.28 (40)	881 (1619)	2.3 (0.70)	40.1 (1.58)	52 (125)	Uniform	7K-1.98(78)	868 (1594)	1048 (1919)	180 (325)	68	220	335	4G, 5G, 11I, 11J, 11K, 12IJK, 13JK
	34103	0.28 (40)	885 (1626)	2.4 (0.74)	38.1 (1.50)	51 (123)	Uniform	7K-1.98(78)	872 (1601)	1089 (1992)	217 (391)	71	241	381	4G, 5G, 11IJK, 12IJK, 13JK
4	31504	0.28 (40)	863 (1585)	2.3 (0.70)	24 (0.97)	51 (123)	Uniform	8K-1.98(78)	820 (1507)	1150 (2101)	330 (593)	130	325	594	4G, 5G
	35304[a]	0.28 (40)	915 (1679)	2.4 (0.74)	25.9 (1.02)	51 (124)	Uniform	9F-1.93(76)	797 (1467)	1230 (2246)	433 (779)	125	249	499	4G, 5G, 11IJK, 12IJK, 13JK,
5	31805	0.28 (40)	871 (1600)	2.3 (0.70)	21 (0.81)	51 (124)	Uniform	11K-1.98(78)	851 (1563)	1232 (2250)	381 (687)	134	419	691	4G, 5G
6	34006	0.27 (39)	882 (1620)	1.3 (0.40)	15 (0.59)	51 (124)	Uniform	7K-1.98(78)	864 (1587)	1163 (2126)	299 (539)	175	327	566	4G, 5G, 11IJK, 12IJK, 13JK
7	34907[a,b]	0.28 (40)	897 (1648)	1.4 (0.42)	11 (0.45) 76 (3.0)	51 (123)	Uniform	9F-1.98(78)	836 (1538)	1230 (2246)	394 (708)	203	326	385	4G, 5G, 11IJK, 12IJK, 13JK
	35807[a]	0.28 (40)	886 (1628)	0.89(0.27)	10 (0.41)	50 (121)	Uniform	9F-1.88(74)	849 (1560)	1182 (2160)	333 (600)	217	368	734	4G, 5G, 11IJK, 12IJK, 13JK
PRESSURE AT CONSTANT FLOODING RATE															
8	31108	0.13 (19)	871 (1600)	2.3 (0.70)	79.0 (3.11)	33 (91)	Uniform	9I-1.78(70)	884 (1624)	938 (1720)	54 (96)	10	156	364	4G, 5G
9	34209	0.14 (20)	889 (1636)	2.4 (0.72)	27.2 (1.07)	32 (90)	Uniform	7K-1.98(78)	854 (1570)	1161 (2121)	307 (551)	127	427	701	4G, 5G, 11IJK, 12IJK, 13JK

a. Significant rod bundle distortion occurred between 1.52 and 2.27 m (60 and 90 in.)

b. Scrammed at 279 seconds because of high rod temperature

Table A4.1 FLECHT-SEASET Unblocked Bundle Reflood Test Data Summary (Continued)

		As-Run Test Conditions						Results							
Test No.	Run No.	Upper Plenum Pressure [MPa (psia)]	Rod Initial T_{clad} at 1.83m (72 in.) [°C(°F)]	Rod Peak Power [kw/m (kw/ft)]	Flooding Rate [mm/sec (in./sec)]	Coolant Temperature [°C(°F)]	Radial Power Distribution	Hottest Rod T/C and Elevation [m(in.)]	Initial Temperature [°C(°F)]	Maximum Temperature [°C(°F)]	Temperature Rise [°C(°F)]	Turn-around Time (sec)	Quench Time (sec)	Bundle Quench Time (sec)	Disconnected Rod Location
10	34610	0.14 (20)	892 (1637)	1.4 (0.42)	21 (0.82)	32 (90)	Uniform	6D-1.88 (74)	845 (1554)	1052 (1926)	207 (372)	137	310	507	4G, 5G, 11J, 12J, 13J
11	3471[a]	0.13 (19)	888 (1630)	1.4 (0.42)	17 (0.67)	33 (91)	Uniform	9E-1.93 (76)	855 (1571)	1119 (2045)	264 (474)	135	361	600	4G, 5G, 11J, 12J, 13J
12	35212[a,c]	0.14 (20)	879 (1613)	1.4 (0.42)	11 (0.43) 178 sec 79 (3.1)	32 (89)	Uniform	9E-1.83 (72)	830 (1526)	1231 (2247)	401 (721)	173	236	294	4G, 5G, 11J, 12J, 13J
	35912[a]	0.14 (20)	889 (1632)	0.89 (0.27)	11 (0.42)	34 (93)	Uniform	9G-2.29 (90)	802 (1476)	1128 (2062)	326 (586)	289	558	789	4G, 5G, 11J, 12J, 13J
13	32013	0.41 (60)	887 (1629)	2.3 (0.70)	26.4 (1.04)	66 (150)	Uniform	6L-1.93 (76)	846 (1555)	1171 (2139)	325 (584)	115	269	461	4G, 5G
SUBCOOLING															
14	32114	0.28 (40)	893 (1639)	2.3 (0.70)	25-51 (1.0-1.22)	125 (257)	Uniform	6L-1.88 (74)	840 (1544)	1189 (2172)	349 (628)	114	405	633	4G, 5G
	35114	0.28 (40)	892 (1638)	2.4 (0.74)	25 (0.98)	123 (253)	Uniform	9D-1.83 (72)	886 (1628)	1192 (2178)	306 (550)	123	394	651	4G, 5G, 11J, 12J, 13J
15	31615	0.14 (20)	876 (1609)	2.3 (0.70)	0 (0)		Uniform	11H-1.70 (67)	881 (1617)	1220 (2228)	339 (611)	57			4G, 5G
	34815[a]	0.14 (20)	895 (1643)	2.4 (0.74)	25 (0.98)	94 (221)	Uniform	7J-1.83 (72)	870 (1597)	1178 (2152)	308 (555)	132	562	919	4G, 5G, 11J, 12J, 13J
16	34316	0.28 (40)	889 (1631)	2.4 (0.74)	25 (0.97)	51-119 (124-246)	Uniform	6D-1.88 (74)	849 (1560)	1207 (2206)	358 (646)	107	349	592	4G, 5G, 11J, 12J, 13J
INITIAL CLAD TEMPERATURE															
17	30817	0.27 (39)	531 (987)	2.3 (0.70)	38.6 (1.52)	53 (128)	Uniform	10J-1.98 (78)	519 (965)	832 (1530)	313 (565)	84	219	395	4G, 5G
18	30518	0.28 (40)	256 (494)	2.3 (0.70)	38.9 (1.53)	52 (126)	Uniform	8H-1.98 (78)	246 (475)	653 (1208)	407 (732)	96	187	344	4G, 5G
19	30619	0.136 (19.5)	256 (494)	2.3 (0.70)	38.9 (1.53)	36 (96)	Uniform	2H-1.98 (78)	243 (469)	727 (1340)	484 (871)	142	292	572	4G, 5G

c. Scrammed at 178 seconds because of high rod temperature

Table A4.1 FLECHT-SEASET Unblocked Bundle Reflood Test Data Summary (Continued)

Test No.	Run No.	As-Run Test Conditions						Results							
		Upper Plenum Pressure [MPa (psia)]	Rod Initial T_{clad} at 1.83m (72 in.) [°C(°F)]	Rod Peak Power [kw/m (kw/ft)]	Flooding Rate [mm/sec (in./sec)]	Coolant Temperature [°C(°F)]	Radial Power Distribution	Hottest Rod T/C and Elevation [m(in.)]	Initial Temperature [°C(°F)]	Maximum Temperature [°C(°F)]	Temperature Rise [°C(°F)]	Turn-around Time (sec)	Quench Time (sec)	Bundle Quench Time (sec)	Disconnected Rod Location
20	34420	0.27 (39)	1119 (2045)	2.4 (0.74)	38.9 (1.53)	51 (124)	Uniform	7J-1.83 (72)	1102 (2016)	1207 (2205)	105 (189)	34	222	376	4G, 5G, 11J3K, 12J3K, 13J3K
ROD PEAK POWER															
21	30921[d]	0.27 (39)	879 (1614)	1.3 (0.40)	38.9 (1.53)	52 (126)	Uniform	9F-1.78 (70)	882 (1629)	949 (1740)	62 (111)	17	152	158	4G, 5G
	31021	0.28 (40)	880 (1615)	1.3 (0.40)	38.6 (1.52)	52 (126)	Uniform	9F-1.78 (70)	891 (1635)	941 (1726)	50 (91)	14	158	271	4G, 5G
22	31922	0.14 (20)	883 (1621)	1.3 (0.40)	27.2 (1.07)	35 (95)	Uniform	6F-1.83 (72)	883 (1621)	975 (1787)	92 (166)	70	229	435	4G, 5G
23	30223	0.27 (39)	258 (497)	1.3 (0.40)	37.8 (1.49)	54 (129)	Uniform	6F-1.93 (76)	261 (501)	455 (852)	194 (351)	44	113	181	None
	30323	0.27 (39)	259 (499)	1.3 (0.40)	38.6 (1.52)	52 (126)	Uniform	6F-1.98 (78)	256 (494)	459 (859)	203 (365)	57	115	171	None
24	34524	0.28 (40)	878 (1612)	3.0 (1.0)	39.9 (1.57)	52 (125)	Uniform	7J-1.83 (72)	873 (1604)	1204 (2199)	331 (595)	89	266	520	4G, 5G, 11J3K, 12J3K, 13J3K
RADIAL POWER DISTRIBUTION															
25	Not run														
26	35426[a]	0.28 (40)	886 (1627)	2.54 (0.773) 2.42 (0.737) 2.08 (0.633)	25.7 (1.01)	52 (126)	FLECHT	9F-1.93 (76)	814 (1497)	1229 (2243)	415 (746)	113	240	485	4G, 5G, 11J3K, 12J3K, 13J3K
	36026[a]	0.28 (40)	900 (1651)	2.42 (0.737) 2.31 (0.703) 2.19 (0.667)	25 (1.0)	51 (124)	FLECHT	11F-1.88 (74)	862 (1583)	1174 (2145)	312 (562)	113	286	475	4G, 5G, 11J3K, 12J3K, 13J3K
27	Not run														
28	Not run														
REPEAT TESTS															
29	35304														

d. Scrammed because of high-temperature thermocouple failure at 125 seconds

Table A4.1 FLECHT-SEASET Unblocked Bundle Reflood Test Data Summary (Continued)

As-Run Test Conditions						Results							
Upper Plenum Pressure [MPa (psia)]	Rod Initial T_{clad} at 1.83m (72 in.) [°C(°F)]	Rod Peak Power [kw/m (kw/ft)]	Flooding Rate [mm/sec (in./sec)]	Coolant Temperature [°C(°F)]	Radial Power Distribution	Hottest Rod T/C and Elevation [m(in.)]	Initial Temperature [°C(°F)]	Maximum Temperature [°C(°F)]	Temperature Rise [°C(°F)]	Turn-around Time (sec)	Quench Time (sec)	Bundle Quench Time (sec)	Disconnected Rod Location
NG RATE													
0.28 (40)	889 (1631)	2.3 (0.70)	162 (6.36) 5 sec 21 (0.82) onward	52 (125)	Uniform	6L-1.93 (76)	843 (1550)	1148 (2099)	305 (549)	131	337	639	4G, 5G
0.14 (20)	888 (1630)	2.3 (0.70)	166 (6.53) 5 sec 25 (0.98) 200 sec 16 (0.62) onward Injection Rate kg/sec (lbm/sec)	31 (88)	Uniform	6K-1.98 (78)	823 (1514)	1146 (2096)	323 (582)	142	546	964	4G, 5G
0.27 (39)	878 (1611)	2.3 (0.70)	5.80 (12.8) 15 sec 0.785 (1.73) onward	52 (125)	Uniform	10H-1.78 (70)	891 (1636)	910 (1670)	19 (34)	4	121	174	4G, 5G
0.28 (40)	871 (1600)(e) 591 (1096)(f)	2.3 (0.70)(e) 1.3 (0.40(f)	5.9 (13) 15 sec 0.807 (1.78) onward	52 (125)	Hot/ cold channels	10H-1.78 (70)	906 (1664)	925 (1697)	19 (33)	6	76	181	4G, 5G

Table A4.1 FLECHT-SEASET Unblocked Bundle Reflood Test Data Summary (Continued)

		As-Run Test Conditions						Results							
Test No.	Run No.	Upper Plenum Pressure [MPa (psia)]	Rod Initial T_{clad} at 1.83m (72 in.) [°C(°F)]	Rod Peak Power [kw/m (kw/ft)]	Injection Rate [kg/sec (lbm/sec)]	Coolant Temperature [°C(°F)]	Radial Power Distribution	Hottest Rod T/C and Elevation [m(in.)]	Initial Temperature [°C(°F)]	Maximum Temperature [°C(°F)]	Temperature Rise [°C(°F)]	Turn-around Time (sec)	Quench Time (sec)	Bundle Quench Time (sec)	Disconnected Rod Location
39	Not run														
HOT AND COLD CHANNELS															
40	Not run														
41	Not run														
42	Not run														
43	Not run														
AXIAL TEMPERATURE DISTRIBUTION															
44	33544	0.27 (39)	196 (385)(g) (0 to 3) 874 (1605)	2.3 (0.69)	5.85 (12.9) 15 sec 0.780 (1.72) onward	52 (125)	Uniform	11K-1.93 (76)	877 (1610)	908 (1668)	31 (58)	8	121	213	4G, 5G
	33644	0.27 (39)	182 (359)(g) (0 to 3) 877 (1610)	2.3 (0.70)	5.81 (12.8) 15 sec 0.789 (1.76) onward	52 (125)	Uniform	7D-1.93 (76)	884 (1623)	930 (1705)	46 (82)	9	104	250	4G, 5G
STEAM COOLING															
45 46	32652 through 33056 36160 through 37170														
OVERLAP COSINE TESTS															
47	Not run														
48	Not run														

g. Axial temperature distribution - simulated gravity reflood

Table A4.1 FLECHT-SEASET Unblocked Bundle Reflood Test Data Summary (Continued)

Test No.	Run No.	As-Run Test Conditions						Results							
		Upper Plenum Pressure [MPa (psia)]	Rod Initial T_{clad} at 1.83m (72 in.) [°C(°F)]	Rod Peak Power [kw/m (kw/ft)]	Flooding Rate [mm/sec (in./sec)]	Coolant Temperature [°C(°F)]	Radial Power Distribution	Hottest Rod T/C and Elevation [m(in.)]	Initial Temperature [°C(°F)]	Maximum Temperature [°C(°F)]	Temperature Rise [°C(°F)]	Turn-around Time (sec)	Quench Time (sec)	Bundle Quench Time (sec)	Disconnected Rod Location
COMPARISON WITH WESTINGHOUSE PROPRIETARY REFLOOD DATA															
49	33749 33849[h]	0.27 (39) 0.28 (40)	745 (1374) 745 (1374)	1.9 (0.57) 1.9 (0.57)	26.9 (1.06) 25.9 (1.02)	61 (142) 58 (138)	Uniform Uniform	11K-1.88 (74) 8K-1.98 (78)	730 (1346) 705 (1302)	1017 (1861) 1025 (1878)	287 (515) 320 (576)	103 105	250 254	430 437	4G, 5G 4G, 5G
50	35050[a]	0.14 (20)	758 (1397)	1.6 (0.48)	25.9 (1.02)	43 (109)	Uniform	9D-1.83 (72)	758 (1397)	958 (1758)	200 (361)	98	243	433	4G, 5G, 11JK 12JK, 13JK
POWER DECAY															
51	Not run														

APPENDIX A5. LITERATURE REVIEW

Test Facility Name: FEBA - Flooding Experiments with Blocked Arrays.

Dates When Tests Were Performed: 1977

References:

R9 P. Ihle, K. Rust, "FEBA - Flooding Experiments with Blocked Arrays Evaluation Report," KfK 3657, March 1984.

R10 P. Ihle, K. Rust, "FEBA - Flooding Experiments with Blocked Arrays Data Report 1, Test Series I through IV," KfK 3658, March 1984.

R11 P. Ihle, K. Rust, "FEBA - Flooding Experiments with Blocked Arrays Data Report 2, Test Series V through VIII," KfK 3659, March 1984.

Availability of Data:

Reduced instrument responses are presented in References R9 to R11 in a variable versus time plot format. Tables and figures describing instrument locations are provided. Results are presented in 'almost SI' units. A listing of computer channel numbers and of data identification are available on tapes or in the USNRC/RSR Data Bank.

Test Facility Description, Types of Tests

The test facility is designed for a separate effect test program involving a constant flooding rate and a constant back pressure to allow investigation of the influence of coolant channel blockages independently of system effect.

Figure A5.1 shows a scheme of the test facility. The coolant water is stored in tank and during operation the flow is forced into the bundle with a back pressure control system. A 1x5 as well as 5x5 rod array are placed in a full length stainless steel housing which have a wall thickness of 1/4 in. The heater rods were 10.75 mm (0.423 in) in diameter and were arranged on a square pitch of 14.3 mm (0.563 in) and had a heated length of 3.90 m (12.8 ft) for the 5x5 rod bundle tests and 2.9 m (9.5 ft) for the 1x5 rod bundle tests. The axial power profile is shown in Figure A5.2. Top-down quenching was prevented in the experiments by using a particular upper plenum design (Figure A5.3).

The ranges of conditions include:

Constant Mass Flow Rate	2.0 - 9.5 cm/s (0.8 - 3.7 in/s)
Pressure	2.0 - 6.2 bar (29.4 - 91.1 psia)
Initial Clad Temperature	368 - 794 degrees C (694 - 1461 degrees F)
Power Axial Peak Factor	1.19

Initial Average Power	120 percent ANS: 40s after Reactor Trip
Inlet Temperature	40 - 125 degrees C (104 - 257 degrees F)
Initial Housing Temperature	275 - 760 degrees C (527 - 1400 degrees F)
Flow Blockage Ratio	0, 62, 90 and 90+62 percent
Flow Blockage Geometry	Various

The FEBA 5x5 rod bundle program consisted of eight test series with different grid spacer and sleeve blockage arrays within the bundle (Figure A5.4). Series I tests are baseline tests with undisturbed bundle geometry. Series II tests investigate the grid spacer effect on the axial temperature profile at bundle mid-plane. Series III and IV tests consider 90 and 62 percent blockage at bundle midplane respectively. Series V tests consider both the blockage and the grid spacer effects while Series VI tests have double blockage and investigate on the possibility of a hot region between the two blockages. Finally Series VII and VIII tests investigate on cooling enhancement downstream the blockages.

Instrumentation and Data From Tests

Thermocouples (Chromel-Alumel) are imbedded in each of the rods as shown in Figure A5.5 and A5.6. They are used to measure cladding, sleeve, grid spacers and housing temperatures at different locations (Figure A5.7). Fluid temperatures were measured with three different thermocouples (Figure A5.8) and probes in order to provide information about two separate phases. The signals of all three fluid thermocouples indicated roughly same temperature during most part of reflood. Radiation effect for the unshielded thermocouple was not detected however shielding let to earlier quenching of the shielded thermocouples. Pressure and pressure differences were measured with pressure transducers. In addition to inlet and outlet pressure, the pressure differences along the midplane as well as along both the lower and upper portion of the bundle were measured. The flooding rate was measured with a turbine flow meter. The amount of water carry over was measured continuously by a pressure transducer on the water collecting tank. All data were digitally recorded with a scan frequency of 10 Hz.

The water level rising in the lower plenum at the onset of reflood was detected by thermocouples. In some tests high-frequency probes were used to detect the presence of water in the flow channel.

Conclusions

The FEBA experiments provide very good information concerning the separate effect of grids and blocked bundle regions on the heat transfer during reflood. Separate tests were run with the same boundary conditions with and without grids, with and without blockage to address this effect. On the other hand, very little effort has been dedicated to investigating the single thermal-hydraulic process involved in the heat transfer during reflood (droplets behavior, entrainment, etc.). This does not provide sufficient data to develop and validate mechanistic models to be used in best-estimate code.

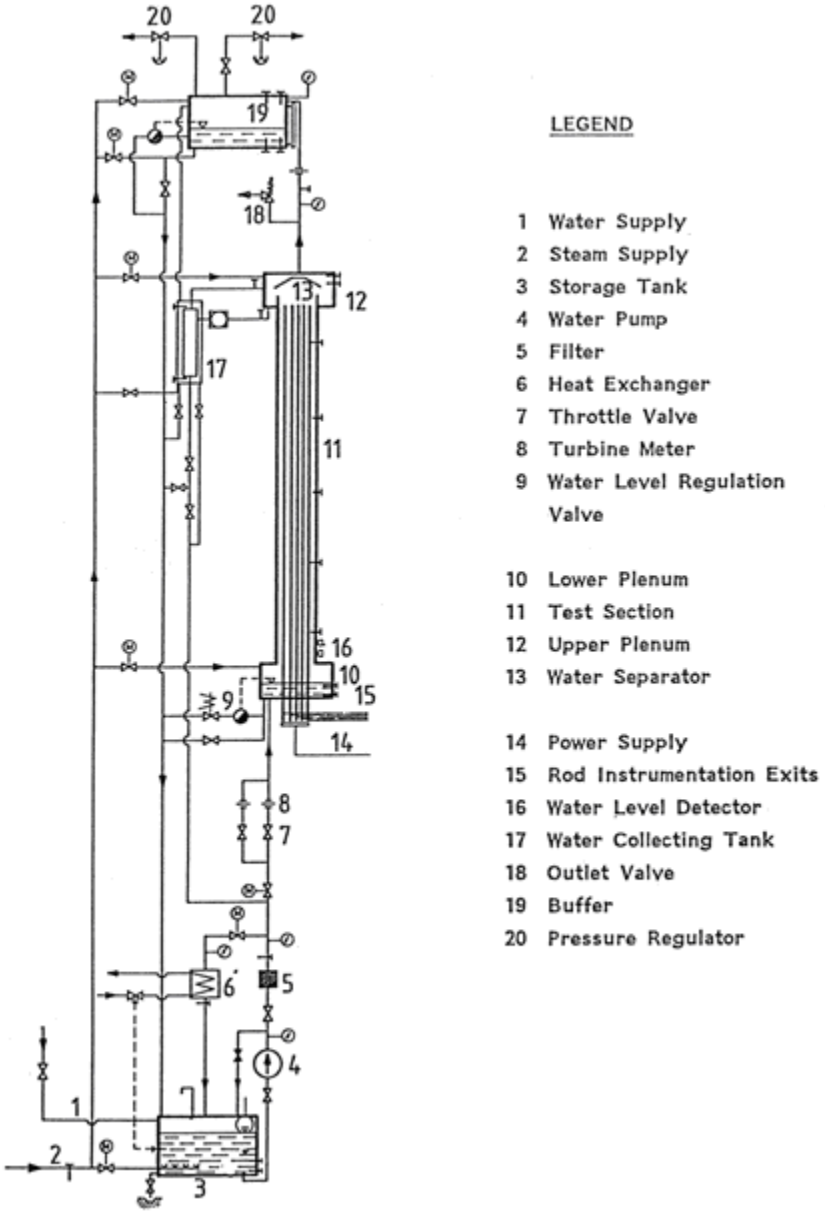

Figure A5.1 FEBA Test Facility.

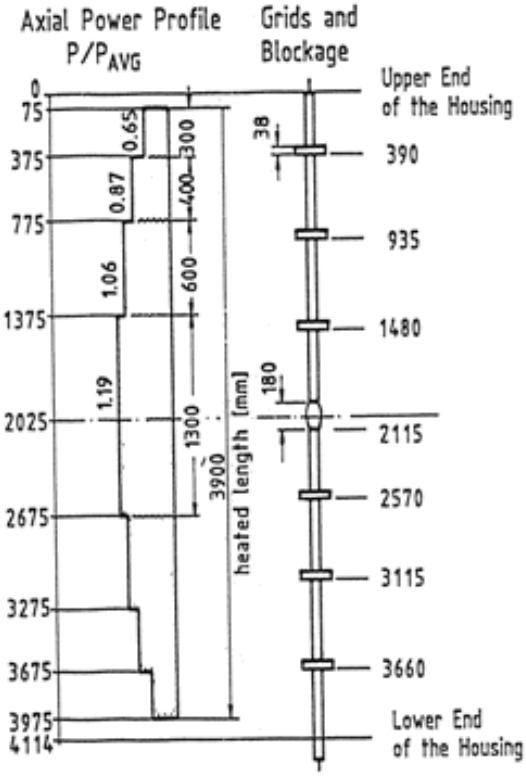

Figure A5.2 Axial Power Profile.

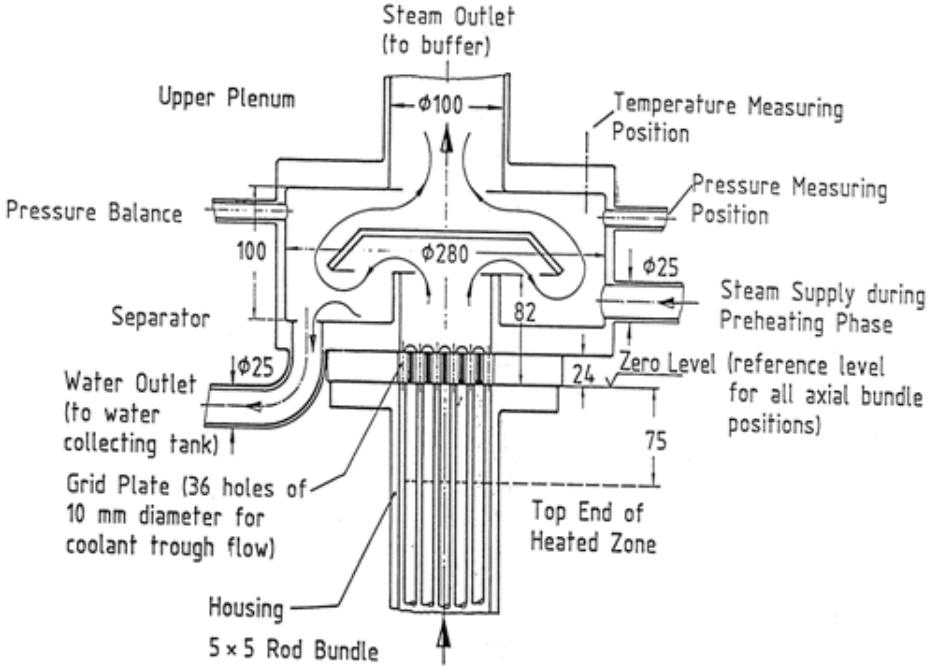

Figure A5.3 Upper Bundle End and Upper Plenum.

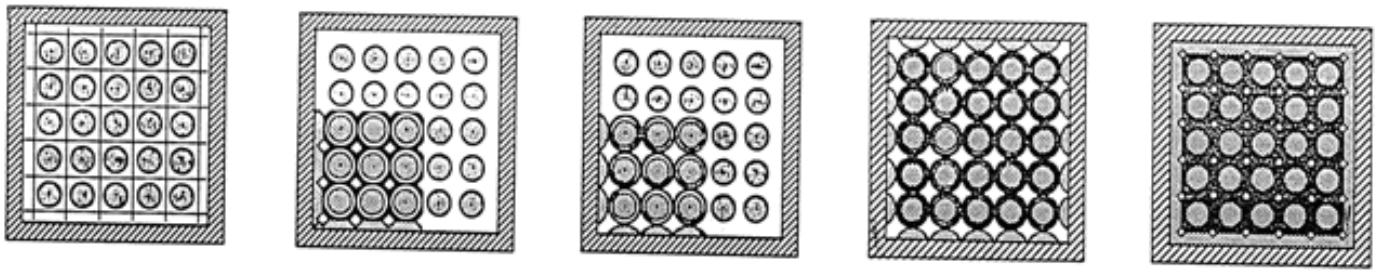

Test Series I
Test Series II

Test Series III
Test Series V
Test Series VI
90% Blockage

Test Series IV
Test Series VI
62% Blockage

Test Series VII
62% Blockage

Test Series VIII
90% Blockage

FLOODING PARAMETERS

Test Series		I	II	III	IV	V	VI	VII	VIII
Flooding Velocity (cold bundle) Constant During Each Test	cm/s	3.8, 5.8	3.8, 5.8	3.8, 5.8	3.8, 5.8 (2.2, 10.)	2.2, 3.8 5.8	2.2, 3.8 5.8	3.8, 5.8 (2.2)	3.8, 5.8 (2.2)
System Pressure Constant During Each Test	bar	2, 4, 6	2, 4, 6	2, 4, 6	2, 4, 6 (4)	4	4	2, 4, 6 (4)	2, 4, 6 (2, 4)
Feedwater Temperature Constant During Each Test	°C	40 °C, some few tests with 80 °C							
Max. Cladding Temperature (at start of reflooding)	°C	between 700 and 800 °C, some few tests between 600 and 700°C							
Max. Housing Temperature (at start of reflooding)	°C	between 600 and 700 °C, some few tests between 500 and 600°C							
Bundle Power	kW	at start of reflooding 200 kW, 120% ANS decay heat transient 40 s after shutdown, some few tests with constant bundle power							

Steam Cooling Tests: Test series VII and VIII include steady state and transient tests for which low bundle power and system pressures of 2, 4 and 6 bar were selected.

Figure A5.4 5x5 Rod Bundle, Test Matrix for Series I Through VIII.

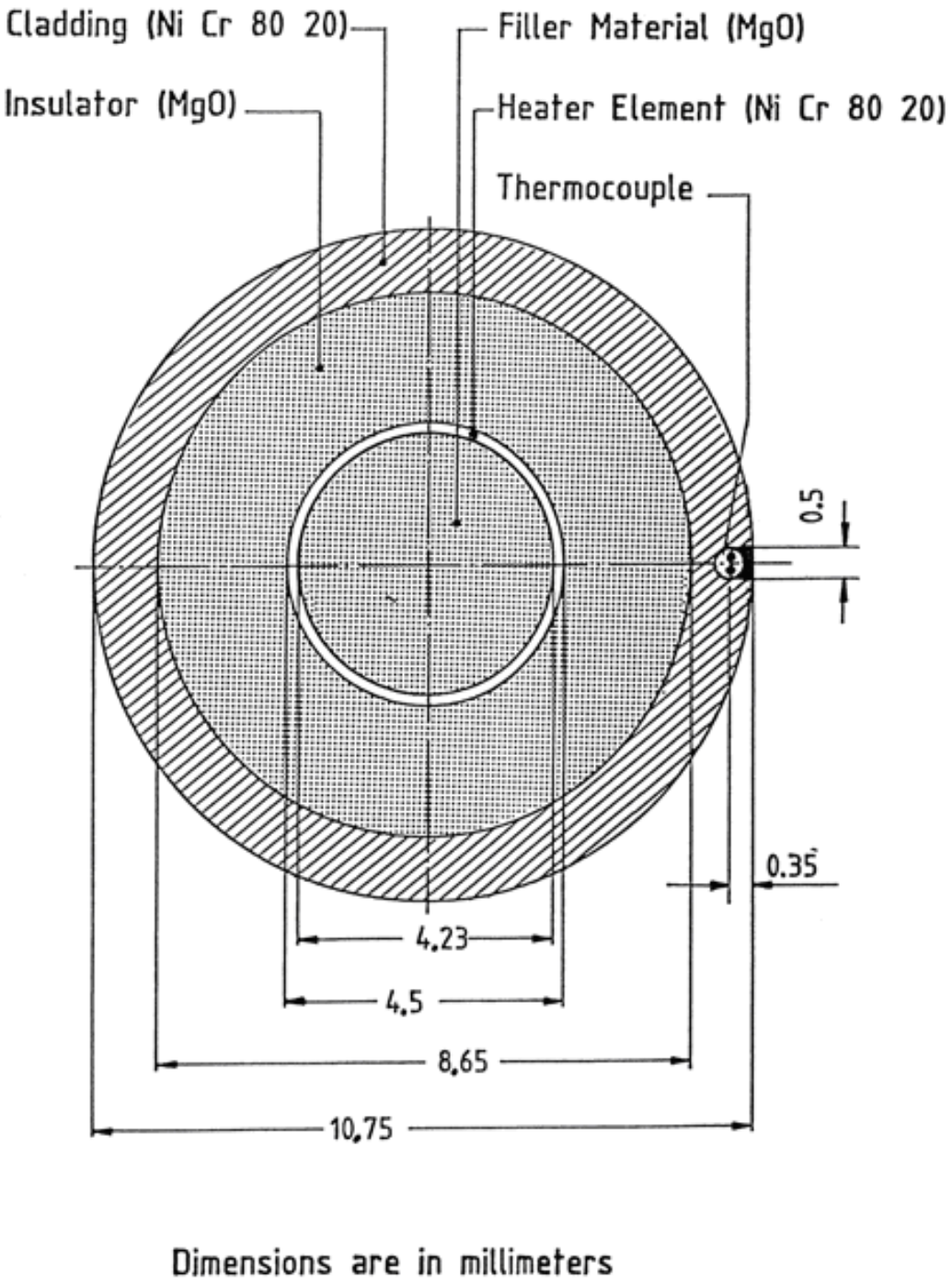

Figure A5.5 Rod Geometry and Location of Thermocouple.

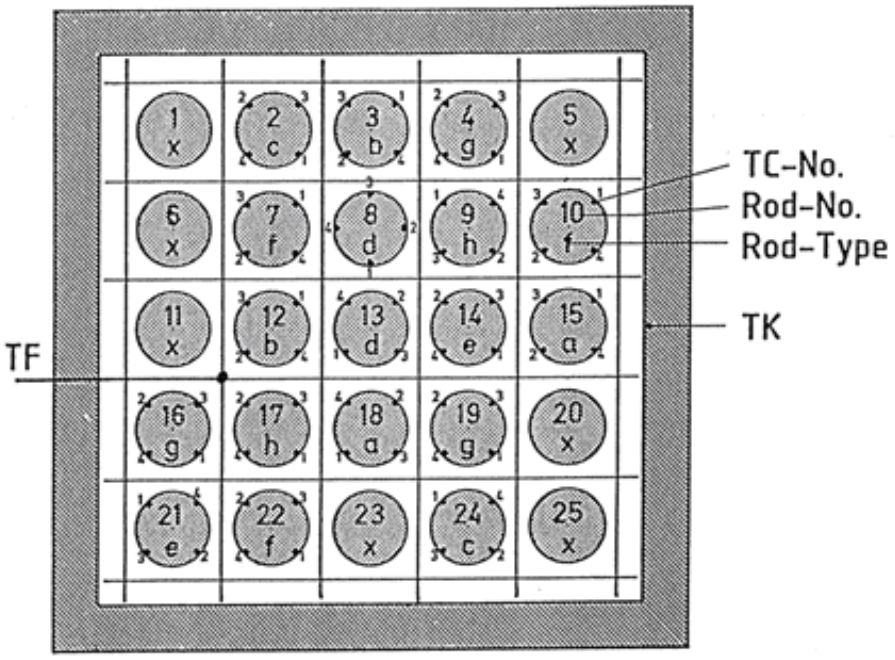

Rod Type	TC No.	Axial Level mm
a	1	2225
	2	2770
	3	3315
	4	3860
b	1	45
	2	590
	3	1135
	4	1680
c	1	3725
	2	3825
	3	3925
	4	4025
d	1	2025
	2	2025
	3	2025
	4	2025

Rod Type	TC No.	Axial Level mm
e	1	2075
	2	2125
	3	2175
	4	2225
f	1	2125
	2	2225
	3	2325
	4	2425
g	1	1625
	2	1725
	3	1825
	4	1925
h	1	1925
	2	2025
	3	2125
	4	2225

Rod Type	TC No.	Axial Level mm
x	without TC's	

Figure A5.6 Radial and Axial Location of Cladding, Fluid and Housing T/C's for Test Series I.

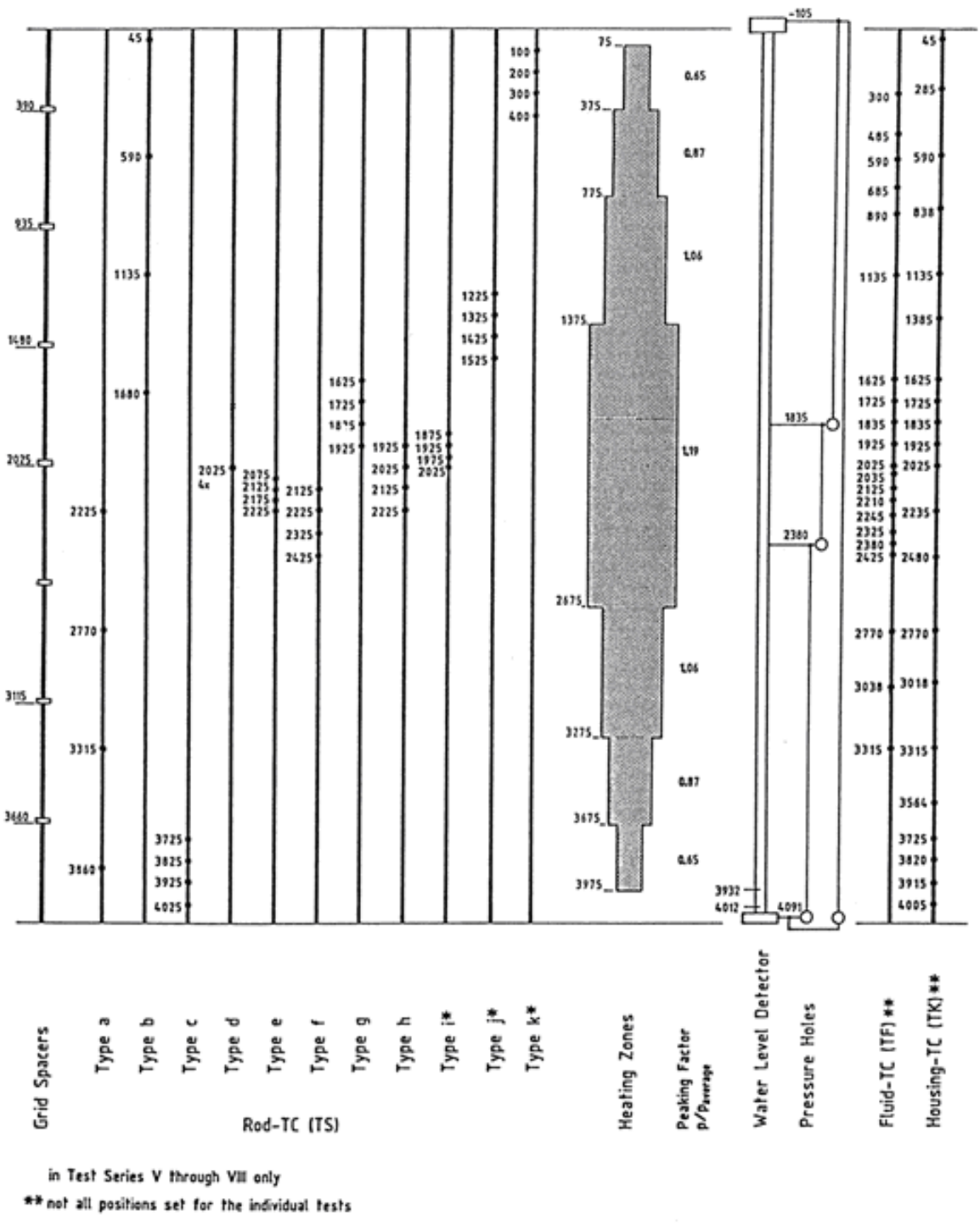

Figure A5.7 Axial Locations of Various Thermocouples in 5x5 Rod Bundle.

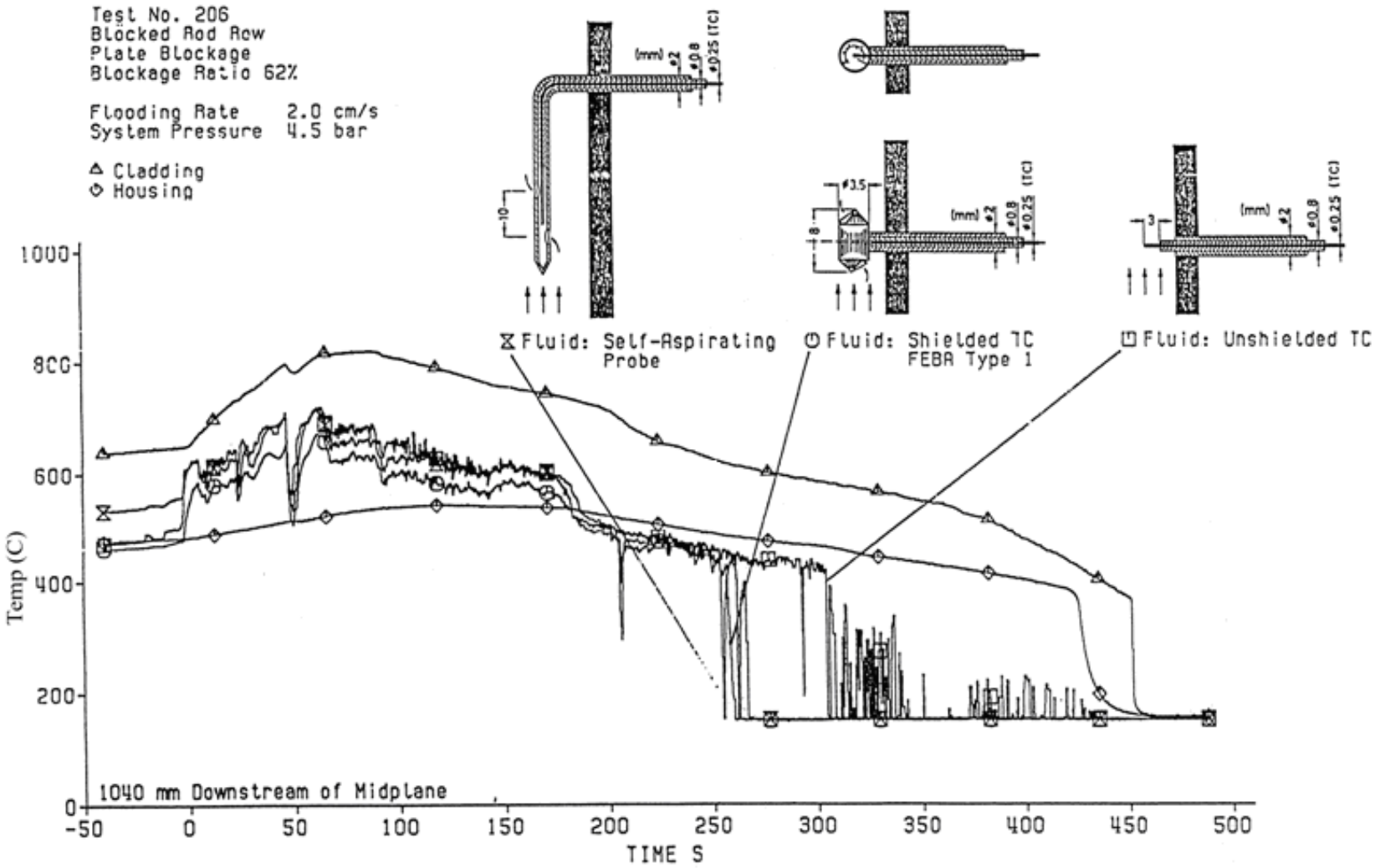

Figure A5.8 5-Rod Row: Comparison of Different Fluid Temperature Measuring Devices.

Table A5.1 Assessment of FEBA Test to RBHT PIRT: Single Phase Liquid Convective Heat Transfer in the Core Component During Reflood Below the Quench Front

Process/Phenomena	Ranking	Basis	FEBA
Subcooled Boiling	L	A significant variation in the subcooled boiling H.T. coefficient will not effect the PCT uncertainty since rod is quenched.	Temperature measurements (fluid and clad) are available but void fraction data are insufficient.
-Effects of Geometry, P/D, De	L	Boiling effects in rod bundles have been correlated for our P/d, De range with acceptable uncertainty[8].	P/D = 1.33 for tests.
-Effects of Spacers	L	Locally enhances H.T.; Correlations/ Models are available,acceptable uncertainty.	Separate tests with and without grid spacer have been run to address the effect.
-Effects of Properties	L	Data exists for our Range of Conditions, little uncertainty.	Insufficientα data.
Saturated Boiling	L	Similar to subcooled boiling, data is available for our P/D, De range. The uncertainty of Saturated Boiling H.T. coefficient will not significantly impact the PCT since rod is quenched.	Heater rod and fluid temperatures are available, but void fraction data are insufficient.
-Effects of Geometry, P/D, De	L	Data exists in the range of P/D, De with acceptable uncertainties[8].	P/D = 1.33
-Effects of Spacers	L	Locally enhances H.T., Correlations/ Models are available[8], with acceptable uncertainty.	Separate tests with and without grid spacer have been run to address the effect.
-Effects of Properties	L	Data exists for our range of conditions, little uncertainty.	Insufficient void fraction data.
Decay Power	H	Source of energy for rods, boundary condition for the test.	Measured.

Table A5.2 Assessment of FEBA Test to RBHT PIRT: Subcooled and Saturated Boiling in the Core Component Below the Quench Front

Process/Phenomena	Ranking	Basis	FEBA
Subcooled Boiling	L	A significant variation in the subcooled boiling H.T. coefficient will not effect the PCT uncertainty since rod is quenched.	Temperature measurements (fluid and clad) are available but void fraction data are insufficient.
-Effects of Geometry, P/D, De	L	Boiling effects in rod bundles have been correlated for our P/d, De range with acceptable uncertainty[8].	P/D = 1.33 for tests.
-Effects of Spacers	L	Locally enhances H.T.; Correlations/ Models are available,acceptable uncertainty.	Separate tests with and without grid spacer have been run to address the effect.
-Effects of Properties	L	Data exists for our Range of Conditions, little uncertainty.	Insufficient data.
Saturated Boiling	L	Similar to subcooled boiling, data is available for our P/D, De range. The uncertainty of Saturated Boiling H.T. coefficient will not significantly impact the PCT since rod is quenched.	Heater rod and fluid temperatures are available, but void fraction data are insufficient.
-Effects of Geometry, P/D, De	L	Data exists in the range of P/D, De with acceptable uncertainties[8].	P/D = 1.33
-Effects of Spacers	L	Locally enhances H.T., Correlations/ Models are available[9], with acceptable uncertainty.	Separate tests with and without grid spacer have been run to address the effect.
-Effects of Properties	L	Data exists for our range of conditions, little uncertainty.	Insufficient void fraction data.
Decay Power	H	Source of energy for rods, boundary condition for the test.	Measured.

Table A5.3 Assessment of FEBA Tests to RBHT PIRT: Quench Front Behavior in the Core Component

Process/Phenomena	Ranking	Basis	FEBA
Fuel /Heater Rod Quench			
Fuel/heater rod materials, ρ, C_p, k, rod diameter	H	These properties effect the stored energy in the fuel/heater rod and its quench rate, uncertainty directly impacts PCT.	Rod properties are known, as are dimensions, stored energy can be calculated.
Gap heat transfer coefficient	M	Second largest resistance in fuel rod. Can limit heat release rate from fuel pellet. Gap heat transfer coefficient has large uncertainty, but its impact on PCT is smaller since all stored energy will be released, timing may change however.	0.5mm gap is present between rod and sleeve in blocked bundle experiments. Rod and sleeve temperatures are measured.
Cladding materials ρ, C_p, k	L	Both Inconel and Zirc have approximately same conductivity most existing data is on stainless steel. Small uncertainty.	Cladding material properties are known Ni-Cr 80-20 cladding was used.
Cladding surface effects • Oxides • Roughness • Materials • T_{min} • T_{CHF}	H	Since zirc can oxidize, the oxide layer will quench sooner due to its low conductivity, verses Inconel or Zirc. Also roughness from oxide promotes easier quenching. The surface condition effects T_{min} which is the point where quenching is initiated[9], [10]. Quenching is a quasi-steady two-dimensional process, values of T_{min} and T_{CHF} can be estimated. Large uncertainty and impact on PCT.	Surface properties effects were not addressed in the analysis and insufficient information are available.
Transition Boiling Heat Transfer	H	Determines the rate of heat release at Quench Front directly impacts PCT, large uncertainty.	Insufficient data.
Steam generation at quench front	H	It is the rapid amount of steam generation which creates the liquid entrainment, large uncertainty and impact on PCT.	Not given in the data analysis.

Table A5.3 Assessment of FEBA Tests to RBHT PIRT: Quench Front Behavior in the Core Component (Continued)

Decay Power	H	Source of Energy for Rods, boundary condition for the test.	Measured.
Liquid entrainment at quench front which includes liquid ligaments, initial drop size, and droplet number density	H	Liquid entrainment cools the PCT location downstream, directly impacts PCT, high uncertainty.	Total water carryover is measured but no information is available on droplets size, density, velocity etc.
Void fraction/flow regime	H	Determines the wall heat transfer since large α results in dispersed flow, low α is film boiling. Directly impacts PCT.	Only coarse (ΔP) measurements are available. Insufficient data.
Interfacial area	H	Determines the initial configuration of the liquid as it enters the transition region directly impacts liquid/vapor heat transfer and resulting PCT downstream.	Insufficient instrumentation.

Table A5.4 Assessment of FEBA Tests to RBHT PIRT: Froth Region for the Core Component

Process/Phenomena	Ranking	Basis	FEBA
Void fraction/flow Regime	H	Void fraction/flow Regime helps determine the amount of vapor-liquid heat transfer which effects the downstream vapor temperature at PCT, large uncertainty.	DP measurements are too coarse to calculate the void fraction.
Liquid ligaments, drop sizes, interfacial area, droplet number density	H	Liquid surface characteristics determine the interfacial heat transfer in the transition region as well as the dispersed flow region, large uncertainty.	Insufficient instrumentation.
Film Boiling H.T. at low void fraction classical film boiling (Bromley)	H	The film boiling heat transfer is the sum of the effects listed below in the adjacent column. Each effect is calculated separately and is added together in a code calculation, large uncertainty.	Only rod heat transfer can be calculated from data.
- droplet contact heat transfer	H	Wall temperature is low enough that some direct wall-to-liquid heat transfer is possible with a high heat transfer rate, large uncertainty.	No data or analysis is available.
- convective vapor H.T.	M	Vapor convective heat transfer is not quite as important since the liquid content in the flow is large and the vapor velocities are low, but large uncertainty.	Estimated using Dittus-Boelter correlation.
interfacial H.T.	M	Interfacial heat transfer effects are also smaller since the steam temperature is low, but large uncertainty.	No data available.
radiation H.T. to liquid/vapor	M	The radiation heat transfer effects are also small since the rod temperatures are low.	No data available.
effects of spacers	M	The velocities and Reynolds numbers are low in this region such that droplet breakup and mixing are not as important. Drop deposition could occur.	Measured. Separate tests with and without grid spacer were run to investigate the effect.
Decay Power	H	Source of power for rods.	Measured.

Table A5.5 Assessment of FEBA Tests to RBHT PIRT: Dispersed Flow Region for the Core Component

Process/Phenomena	Ranking	Basis	FEBA
Radiation Heat Transfer to: - Surfaces - Vapor - Droplets	 M/H M/H M/H	This is important at higher bundle elevations (H) where the convective heat transfer is small since the vapor is highly superheated. Very important for BWR reflood with spays and colder surrounding can. Large uncertainty.	Radiation heat transfer was not considered in data analysis.
Gap Heat Transfer	L	Controlling thermal resistance is the dispersed flow film boiling heat transfer resistance. The large gap heat transfer uncertainties can be accepted, but fuel centerline temperature will be impacted.	A 0.5 mm gap is present between rod and sleeve in the blocked bundle experiments. Rod and sleeve temperature were measured in this case.
Cladding Material	L	Cladding material use din the tests is Inconel which has the same thermal conductivity as zircaloy. Nearly the same temperature drop will occur.	Used Ni-Cr 80-20 clad.
Reaction Rate	M	Inconel will not react while zircaloy will react and create a secondary heat source at very high PCTs. Zirc reaction can be significant.	Not present.
Fuel Clad Swelling/Ballooning	L	Ballooning can divert flow from the PCT location above the ballooning region. The ballooned cladding usually is not the PCT location. Large uncertainty.	The effect of clad ballooning was extensively investigated since it was the main issue of FEBA experiment campaign. Large amount of data is available.

Table A5.6 Assessment of FEBA Tests to RBHT PIRT: Top Down Quench in Core Components

Process/Phenomena	Ranking	Basis	FEBA
De-Entrainment of Film Flow	L[1]	The film flow is the heat sink needed to quench the heater rod. This has high uncertainty.	Top down quenching was prevented in these tests by design.
Sputtering Droplet Size and Velocity	L	The droplets are sputtered off at the quench front and are then re-entrained upward. Since the sputtering front is above the PCT location, no impact. The entrained sputtered drops do affect the total liquid entrainment into the reactor system, as well as the steam production in the steam generators.	Not applicable since top-down quenching was prevented.
Fuel Rod/Heater Rod Properties for Stored Energy: r, c_p, k.	L[1]	These properties are important since they determine the heat release into the coolant. However, since this occurs above PCT level, no impact.	Not applicable since top-down quenching was prevented.
Gap Heat Transfer	L[1]	Affects the rate of energy releases from the fuel/heater rod.	Not applicable since top-down quenching was prevented.

Note: Some of these individual items can be ranked as high (H) within the top down quenching process; however, the entire list is ranked as low for a PWR/BWR since it occurs downstream of the PCT location.

Table A5.7 Assessment of FEBA Tests to RBHT Preliminary PIRT for Gravity Reflood Systems Effects Tests

Process/Phenomena	Ranking	Basis	FEBA
Upper Plenum-Entrainment/De-Entrainment	M	The plenum will fill to a given void fraction after which the remaining flow will be entrained into the hot leg, large uncertainty.	Not applicable.
Hot Leg - Entrainment, De-Entrainment.	L	The hot legs have a small volume and any liquid swept with the hot leg will be entrained into the steam generator plenums, medium uncertainty.	Not applicable.
Pressurizer	L	Pressurizer is filled with steam and is not an active component, small uncertainty.	Not applicable.
Steam Generators	H	The generators evaporate entrained droplets and superheat the steam releases (particularly at low pressures). The result is a higher steam flow downstream of the generators. High uncertainty since a good model is needed. FLECHT-SEASET data exists for reflood.	Not applicable.
Reactor Coolant Pumps	H	This is the largest resistance in the reactor coolant system which directly affects the core flooding rate- low uncertainty.	Not applicable.
Cold Leg Accumulator Injection	H	Initial ECC flow into the bundle.	Not applicable.
Cold Leg Pumped Injection	H	Pumped injection maintains the core cooling for the majority of the reflood transient.	Not applicable.
Pressure	H	Low pressure (20 psia) significantly impacts the increased vapor volume flow rate, which decreases the bundle flooding rate.	Low pressure (30 psia) simulated.
Injection Subcooling	M/H	Lower subcooling will result in boiling below quench front such that there is additional vapor to vent.	Low subcooling simulated.
Downcomer Wall Heat Transfer	H	The heat transfer from the downcomer walls can raise the ECC fluid temprature as it enters the core, resulting in more steam generation.	Not applicable.
Lower Plenum Wall Heat Transfer	M	Source effect as downcomer but less severe.	Not applicable.
Break	L	Excess ECC injection spills, but break ΔP helps pressurize reactor system.	Not applicable.

Table A5.8 Assessment of FEBA Tests to RBHT PIRT for High Ranked BWR Core Phenomena

Process/Phenomena	Basis	FEBA
Core Film Boiling	PCT is determined in film boiling period.	Total heat transfer is measured.
Upper Tie Plate CCFL	Hot assembly is in co-current flow above CCFL limit.	Not applicable.
Channel-Bypass Leakage	Flow bypass will help quench the BWR fuel assembly core.	Not applicable.
Steam Cooling	A portion of the dispersed flow film boiling heat transfer.	Steam cooling heat transfer is estimated from data.
Dryout	Transition from nucleate boiling and film boiling.	Quench front is measured.
Natural Circulation Flow	Flow into the core and system pressure drops.	Not applicable.
Flow Regime	Determines the nature and details of the heat transfer in the core.	Movies exist to determine flow regime.
Fluid Mixing	Determines the liquid temperature in the upper plenum for CCFL break down.	Not applicable.
Fuel Rod Quench Front	Heat release from the quench front will determine entrainment to the upper region of the bundle.	Quench front data exists.
Decay Heat	Energy source for heat transfer.	Measured as initial/boundary conditions.
Interfacial Shear	Effects the void fraction and the resulting droplet and liquid velocity in the entrained flow.	Not measured.
Rewet: Bottom Reflood	BWR hot assembly refloods like PWR.	Total reflood heat transfer measured.
Rewet Temperature	Determines the quench front point on the fuel rod.	Quench temperature measured.
Top Down Rewet	Top of the hot assembly fuel will rewet in a similar manner as PWR.	Top down rewet quench front measured.

Table A5.8 Assessment of FEBA Tests to RBHT PIRT for High Ranked BWR Core Phenomena (Continued)

Process/Phenomena	Basis	FEBA
Void Distribution	Gives the liquid distribution in the bundle.	Not measured.
Two-Phase Level	Similar to quench front location, indicates the location of nucleate and film boiling.	Measured by rod TC's. Collapsed level measured, two-phase level measured by DP cells.

APPENDIX A6. LITERATURE REVIEW

Test Facility Name: Oak Ridge National Laboratory Thermal-Hydraulic Test Facility (THTF).

Dates when tests were performed: 1980 - 1982.

References:

R12 Mullins, C. B., et al., "ORNL Rod Bundle Heat Transfer Test Data," NUREG/CR - 2525, Vol. 1 to Vol. 5, 1982.

R13 Yoder, G. L., et al., "Dispersed Flow Film Boiling in Rod Bundle Geometry - Steady State Heat Transfer Data and Correlations Comparisons," NUREG/CR - 24351, 1982.

Availability of Data:

Reduced instrument responses are presented in Reference R12 for transient film boiling in upflow. Microfiche of the reduced data in graphical form exist along with three types of tables to assist the reader in using the data. The first table lists instrumentation in terms of instrument function, type and location. The second table lists instruments in the order they appear graphically in the microfiche. The third table lists instruments alphabetically in terms of the instrument application number (IAN). In addition to the transient data, steady state data exist in Reference R13 for dispersed flow film boiling. The data are presented in two separate sets of tables, one in SI units and the other in English units, listing fluid conditions, surface conditions and correlation - predicted versus experimentally determined heat transfer coefficients.

Test Facility Description, Types of Tests

Both the transient and steady state experiments were performed in the Thermal-Hydraulic Test Facility (THTF), as shown in Figure A6.1. The THTF was a heavily instrumented non-nuclear pressurized water loop containing 64 full-length rods arranged in an 8x8 bundle; 60 of the rods were electrically heated (see Figure A6.2). The rod diameter was 0.0095 m (0.374 in) and the rod pitch was 0.0127 m (0.501 in) on a square lattice, typical of PWRs with 17xl7 fuel rod assemblies. Figure A6.3 shows a simplified cross section of a typical fuel rod simulator. The axial and radial power profile was flat. The heated length of the bundle was 3.66 m (12 ft) and there were eight spacer grids in the heated length, as shown in Figure A6.4. The spacer grids were of the egg crate type installed 0.61 m (2 ft) apart.

Two types of tests were performed, one transient and the other steady state. The transient tests were initiated by breaking the outlet rupture disk assembly. Although the THTF had a rupture disk assembly at the inlet, it was not employed to assure a unidirectional flow up through the test section. At the same time the outlet rupture disk was broken, the pump was tripped and

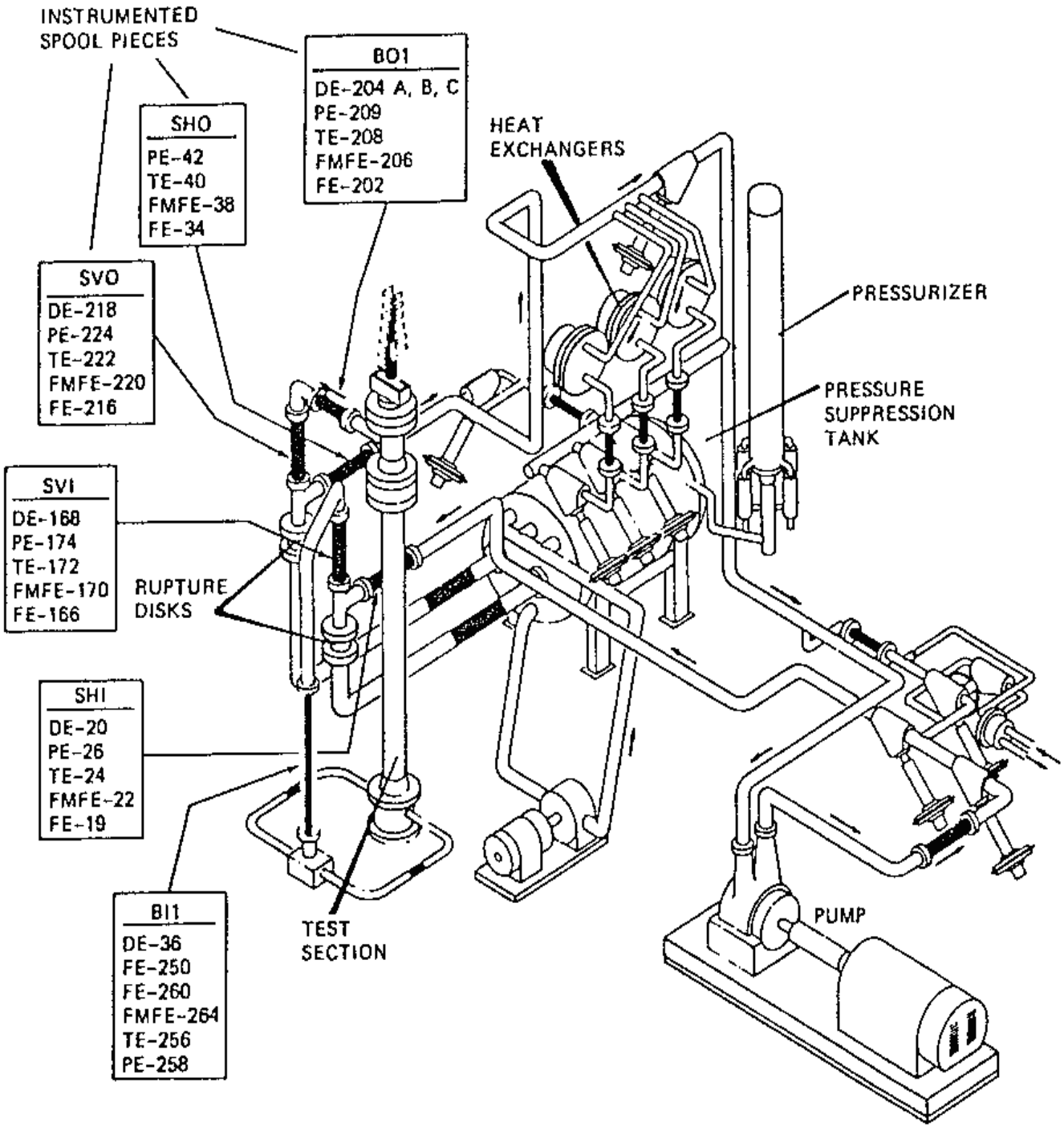

Figure A6.1. THTF System with Instrumented Spool Pieces Labeled.

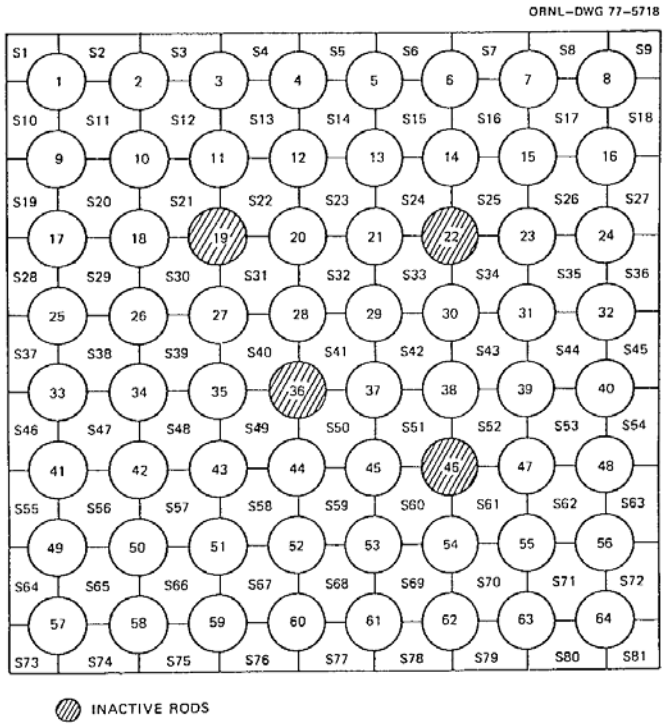

Figure A6.2. Identification of THTF Heater Rods, Subchannel Location, and Inactive Rods in THTF Heater Bundle.

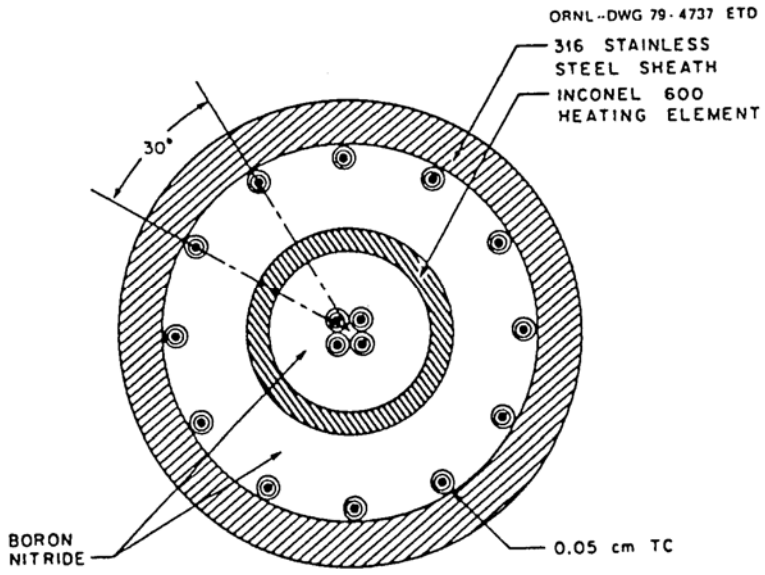

Figure A6.3. Cross-Section of a Typical Fuel Rod Simulator.

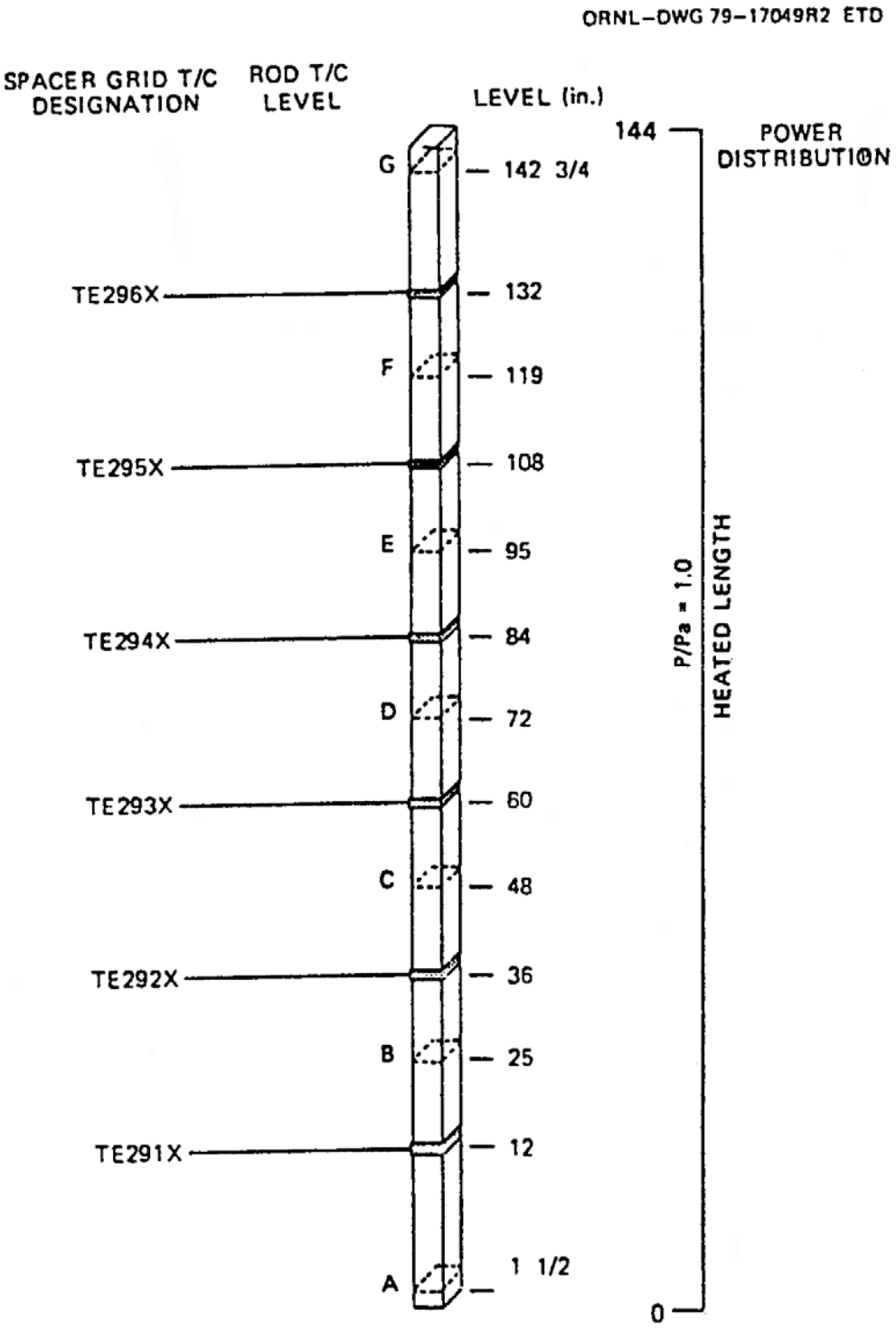

Figure A6.4. Axial Locations of Spacer Grid and Thermocouples.

bundle power was ramped up to about 6-8 MW. After the initial power ramped up, the bundle power remained at this high level until most of the sheath temperatures at level G in the bundle reached 811 degrees K (1000 degrees F). The bundle power was then ramped down to maintain high rod sheath temperatures in the upper bundle without reaching the safety limit of 1116 degrees K (1550 degrees F). All test series including test 3.03.6AR, test 3.06.6B and test 3.08.6C were conducted under reactor accident-type conditions to obtain transient film boiling data. The ranges of conditions are given are given below:

Test 3.03.6AR

Mass Velocity	136 – 502 kg/m^{2}s ($1x10^5$ to $3.7x10^5$ lbm/hr - ft^2)
Quality	23 – 100 percent
Pressure	5 – 10 MPa (700 – 1500 psi)
Heat Flux	158 – 1000 kW/m^2 ($5x10^4$ to $3.2x10^5$ Btu/hr - ft^2)

Test 3.06.6B

Mass Velocity	136 – 610 kg/m^{2}s ($1x10^5$ to $4.5x10^5$ lbm/hr - ft^2)
Quality	5 – 100 percent
Pressure	6 – 13 MPa (875 – 1900 psi)
Heat Flux	158 – 630 kW/m^2 ($5x10^4$ to $2x10^5$ Btu/hr - ft^2)

Test 3.08.6C

Mass Velocity	330 – 1090 kg/m^{2}s ($2.4x10^5$ to $8x10^5$ lbm/hr - ft^2)
Quality	35 – 100 percent
Pressure	6.6 – 11.7 MPa (950 – 1700 psi)
Heat Flux	160 – 1100 kW/m^2 ($5x10^4$ to $3.5x10^5$ Btu/hr-ft^2)

In the steady state tests, the working fluid flowed from the pump through two control values, past the inlet rupture disk assembly and through a vertical spool piece before it entered the external downcomer. The working fluid then flowed through two spool pieced in the downcomer and entered the test section. The fluid was heated as it flowed along the rods within the test section. It then left the test section from the upper plenum, past through the three outlet spool pieces and the heat exchangers, and returned to the pump. During the run, the loop was adjusted to provide the desired inlet fluid temperature and inlet pressure. The bundle power was then increased until the dryout point was at the desired position in the bundle. The steady state operating conditions were assumed to have been reached when the operating pressure and rod surface temperatures stabilized. A total of 22 steady-state tests were performed. The ranges of conditions were:

Mass Velocity	226 – 806 kg/m^{2}s ($1.66x10^5$ to $5.94x10^5$ lbm/hr - ft^2)
Quality	0 – 100 percent
Pressure	4.4 – 13.4 MPa (635 – 1938 psi)
Heat Flux	320 – 940 kW/m^2 ($1x10^5$ to $3x10^5$ Btu/hr - ft^2)

Instrumentation and Data from Tests

The bundle was fully instrumented with thermocouples at various axial locations (i.e., at A, B, C, D, E, F and G levels) to measure the rod temperatures and in-bundle fluid temperatures. At each axial location where a rod had thermocouples, there were three individual thermocouples spaced azimuthally around the rod. In-bundle fluid temperatures were measured using thermocouples extending a short distance from the rod surface into the fluid as well as thermocouples mounted on the spacer grids. Rods 36 and 46 also contained gamma densitometer instrumentation for measuring in-bundle fluid density. Two flow measurement sites were positioned at each end of the test section containing the rod bundle. Differential pressure and pressure instrumentation was made at various locations along the heated bundle. In addition, there was instrumentation located in the entire piping system including the outlet nozzle, vertical outlet and external downcomer spool pieces.

In the transient tests, local bundle fluid conditions were calculated with the homogeneous two-phase flow and thermodynamic equilibrium thermal-hydraulics code RLPSFLUX. The transient data were compared to six existing film boiling correlations. Results of the comparisons were presented in Reference R12. In the steady state tests, mass and energy conservation relationship were used to calculate equilibrium fluid conditions within the rod bundle. These fluid conditions, along with calculated rod surface temperatures, were used to evaluate the six film boiling correlations as well as single-phase vapor correlation. Results of the comparisons were presented in Reference R13. In addition to the dispersed flow film boiling data, results were also obtained for the spacer grid effects, which had beneficial influence on the heat transfer due to a boundary layer breakup-rebuild process at the grids.

Conclusions

The ONRL/THTF tests provide both transient and steady state film boiling heat transfer data in rod bundle geometry. In general, the steady state results support the conclusions reached in the analysis of the transient results. The experimentally determined heat transfer coefficients may be useful as they have been compared to various existing heat transfer correlations. It is found that the Dougall-Rohsenow correlation often overpredicts the heat transfer coefficient whereas the Groeneveld-Delorme correlation tends to underpredict the heat fluxes near dryout but improves as distance from dryout increases. On the other hand, the Groeneveld 5.7, Groeneveld 5.9 and Condie-Bengston IV correlations give better agreement with the experimental data.

It should be noted that although the steady state and the transient data appear to be consistent with each other, the bundle fluid conditions in both cases are determined from mass and energy conservation consideration based on the assumption of thermodynamic equilibrium. However, non-equilibrium conditions probably exist within the bundle. Thus, a more sophisticated calculational method accounting for the effect of non-equilibrium is needed to determine the actual bundle fluid conditions. Non-equilibrium also implies that liquid droplets can be present in the flow when equilibrium qualities are calculated to be larger than unity.

The ORNL/THTF tests have been focused on the case of dispersed flow film boiling in upflow under high-pressure high-temperature conditions. The data may provide some relevant information in the dispersed flow region for core component in the RBHT PIRT Table 5. However, the results are not applicable to single phase liquid corrective heat transfer in the core component during reflood below the quench front (RBHT PIRT Table 1), subcooled and saturated boiling in the core component below the quench front (RBHT PIRT Table 2), quench front behavior in the core component (RBHT PIRT Table 3), froth region for the core component (RBHT PIRT Table 4), top down quench in core component (RBHT PIRT Table 6), and gravity reflood system effects (RBHT PIRT Table 7).

Even in the dispersed flow region, the ORNL/THFT data must be used with caution. This is because the pressure range of 4.4 - 13.4 MPa (635 - 1938 psi) explored in the THTF tests is very high, more characteristic of a PWR or BWR blowdown situation. Thus the results may not be directly applicable to transient stage of reflood heat transfer in rod bundles.

Table A6.1 Assessment of ORNL/THTF Data to RBHT PIRT: Dispersed Flow Region for Core Component

Process/Phenomena	Ranking	Basis	ORNL/THTF Data
Decay power	H	Energy source which determines the temperature of the heater rods, and energy to be removed by the coolant.	Known, measured as initial/boundary conditions.
Fuel Rod/Heater Rod properties, ρ, c_p, k	L	The exact properties can be modeled and stored energy release is not important at this time, environmentally.	Heater rod properties are known and approximate those of nuclear rod.
Dispersed Flow Film Boiling	H	Dispersed flow film boiling modeling has a high uncertainty which directly effects the PCT.	Total head transfer coefficients for DFFB have been obtained from the transient and steady state data covering a wide range of mass velocities, qualities and pressures. The coefficients have been compared to existing correlations.
Convection to superheated vapor	H	Principle mode of heat transfer as indicated in FLECHT-SEASET experiments[4].	Total convection heat transfer has been determined.
Dispersed phase enhancement of convective flow	H	Preliminary models indicted that the enhancement can be over 50% in source cases[13].	This component was not isolated.
Direct wall contact H. T.	L	Wall temperatures are significantly above Tmin such that no contact is expected.	This component was not isolated.
Dry wall contact[12]	M	Iloeje[12] indicates this H. T. Mechanism is less important than vapor convection.	This component was not determined.
Droplet to vapor interfacial heat transfer	H	The interfacial heat transfer reduces the vapor temperature which is the heat sink for the wall heat flux.	The quality is known but the interfacial surface area is not.
Radiation Heat Transfer to: • surfaces • vapor • droplets	 M/H M/H M/H	This is important at higher bundle elevations (H) where the convective heat transfer is small since the vapor is so highly superheated. Very important for BWR reflood with sprays, and colder surrounding can. Large uncertainty.	Can be estimated from the data on surface temperatures and fluid conditions.

Table A6.1 Assessment of ORNL/THTF Data to RBHT PIRT: Dispersed Flow Region for Core Component (Continued)

Gap heat transfer	L	Controlling thermal resistance is the dispersed flow film boiling heat transfer resistance. The large gap heat transfer uncertainties can be accepted, but fuel center line temperature will be impacted.	Not present. Heater rods have no gap.
Cladding Material	L	Cladding material in the tests is Inconel which has the same conductivity as zircalloy nearly the same temperature drop will occur.	Used stainless steel clad.
Reaction Rate	M	Inconel will not react while Zircalloy will react and create a secondary heat source at very high PCTs, Zirc reaction can be significant.	Not present.
Fuel Clad Swelling/Ballooning	L	Ballooning can divert flow from the PCT location above the ballooning region. The ballooned cladding usually is not the PCT location. Large uncertainty.	Not present.

APPENDIX A7. LITERATURE REVIEW

Test Facility Name: FRIGG-2 36-Rod Loop (Sweden)

Dates When Tests Were Performed: 1965-1968

References:

R14 Becker, K. M., Flinta, J., and Nylund, O., "Dynamic and Static Burnout Studies for the Full Scale 36-Rod Marviken Fuel Element in the 8 MW Loop FRIGG," Paper presented at the Symposium on Two-Phase Flow Dynamics, Eindhoven, September 1967.

R15 Nylund, O., et al., "Measurements of Hydrodynamic Characteristics, Instability Thresholds, and Burnout Limits for 6-Rod Clusters in Natural and Forced Circulation," ASEA and AB Atomenergi Report FRIGG-1, 1967.

R16 Nylund, O., Becker, K. M., Eklund, R., Gelius, O., Haga, I., Herngorg, G., Rouhani, Z., and Akerhielm, F., "Hydrodynamic and Heat Transfer Measurements on a Full Scale Simulated 36-Rod Marviken Fuel Element with Uniform Heat Flux Distribution," ASEA and AB Atomenergi Report FRIGG-2, 1968.

Availability of Data:

The experimental investigation simulates the fuel element of a Swedish heavy water cooled Marviken BVRR with 35 uniformly heated heater rods and a unheated (but larger in diameter) center rod simulating the control rod. Experimental data available from the FRIGG-2 tests, all under pressures up to 50 bar (711 psi), are single- and two-phase pressure drops; burnout (or critical heat flux) in natural and forced circulation; natural circulation mass velocity as a function of total power and inlet subcooling; the stability limit; as well as the details about the system during transient conditions. Additionally, a unique output of the FRIGG-2 tests is the axial and radial void distributions measured by the Cobalt-60 gamma-ray densitometer system. The results have been compared to data obtained from in the previous six-rod tests (R15, FRIGG- 1) and to predictions with existing correlations and models. All pressure drop data are consistently agreeable between FRIGG-2, FRIGG-1, and actual Marviken conditions. The natural circulation burnout value is very close to that of forced circulation, but both are about 20 percent low compared to predictions by the Becker correlation. This is believed to be due to the unfavorable conditions in the inner subchannels of the uniformly heated bundle. The results of natural circulation mass velocity, stability limit, and transient behavior at different power levels agree well with the calculation. Calculations indicate that the conditions in a real Marviken boiling channel are somewhat more favorable than in the FRIGG-2 experiment. This suggests that sufficient margins against burnout and hydrodynamic instability are present in the Marviken reactor.

Test Facility Description, Types of Tests

The primary purpose of FRIGG-2 tests was to obtain the burnout values of the 36-rod bundle at different mass fluxes and inlet subcoolings to simulate the core conditions of a Marviken BWR. The geometric features of the test section are:

Number of heated rods:	35	Rod diameter:	13.8 mm (0.5433 in)
Number of unheated rods:	1	Unheated rod dia.:	20 mm (0.7874 in)
Circular housing diameter:	160 mm (6.30 in)	Number of spacers:	8
Average hydraulic dia.:	26.9 mm (1.06 in)	Heated hydraulic dia.:	36.6 mm (1.44 in)
Heated length (uniform):	4375 mm (172 in)	No. of burnout T/C's:	4

Tests were run with 35 rods electrically heated and one center rod unheated. Both the axial and radial power profiles are uniform. A cross-sectional view of the test section is shown in Figure A7.1, indicating the placement pattern of the unheated center rod and 35 heated rods in three orbital rows. The flow diagram of the FRIGG-2 loop is shown in Figure A7.2. For burnout tests FRIGG-2 requires a significant DC electrical power: 80 MW, 80 kA, and DC voltage regulation from 0 to 200 V. The heater rods were of a type with coaxial feeder rod eliminating the electromagnetic forces between the rods. Most of the heat is produced in the 0.8 mm stainless steel canning of the rod, which is isolated from the center copper conductor. This means that the reactor fuel time constant (or heat capacity) is <u>not</u> correctly simulated. There are four electrically isolated burnout detectors (or thermocouples) measuring temperatures at different elevations and there wires running axially along the inside surface of the stainless steel canning. If a burnout event is detected by any of the burnout detectors in the bundle, the DC power applied to the bundled would be immediately reduced by 20 percent within 0.1 s and the histories of all important fluid and thermal parameters are recorded. These burnout conditions are the primary objective of the FRIGG-2 tests.

A secondary but important test of FRIGG-2 is the void fraction measurement in both the axial and radial directions of the bundle. The measurement system comprises one gamma source, Co-60, and four scintillation detectors with adjustable collimators. The pulses from the detectors are amplified, analyzed and counted in separate scalars built into the data collection system. The penetration paths of the four gamma beams can be changed between three prefixed radial positions within the bundle. The void at a certain level is thus evaluated from the twelve measurements covering different parts of the bundle. This gives a rather good cross sectional mean value of the void and also information about the radial void distribution. The void measurement system is moved up and down the test section by means of an electric elevator that allows for axial void distribution measurement.

Other instrumentation includes: Chromel-alumel thermocouples for fluid temperature distribution measurement; fast response differential pressure (DP) cells with venturi units and turbine flow meters for mass velocity measurement; and impedance void gauge to measure the outlet quality. Standard single and two-phase pressure drops at all test conditions are also measured using differential and absolute pressure sensors.

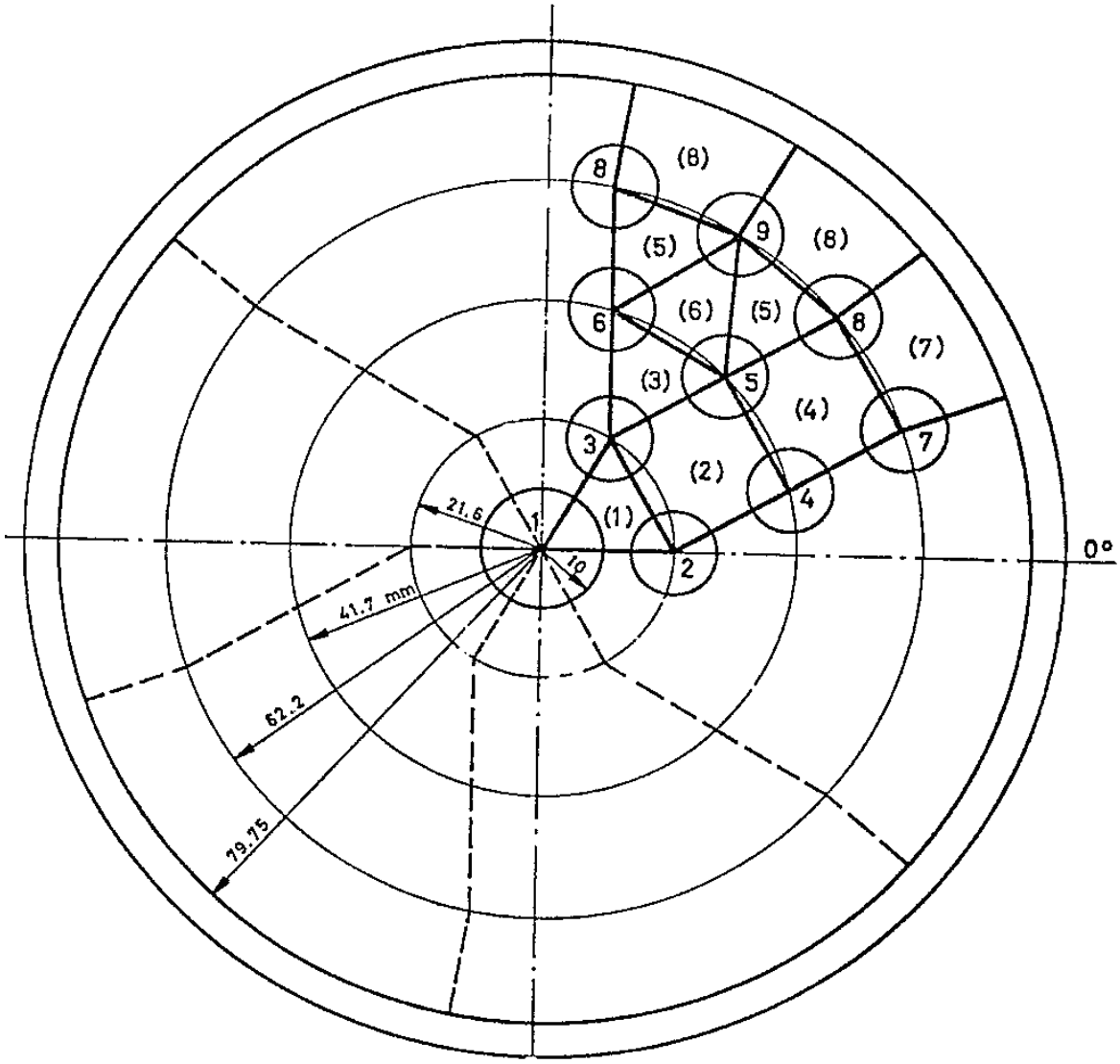

Figure A7.1. 36-Rod Bundle of the FRIGG-2.

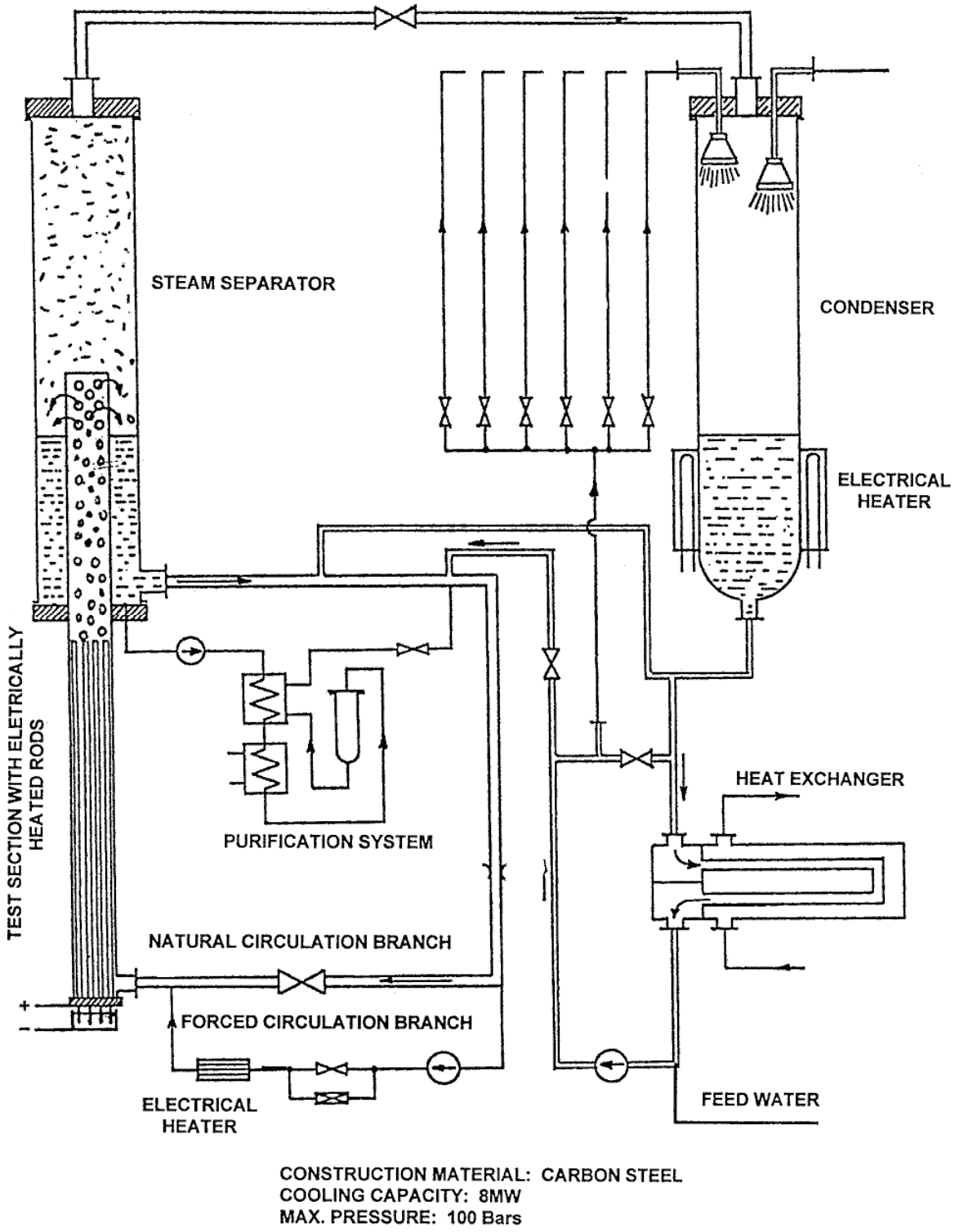

Figure A7.2. Flow Diagram of the FRIGG-2 Loop.

The ranges of test conditions include:

Single-Phase (Cold) Mass Flux	840 - 3195 kg/m^2-s (0.618 – 2.35x10^6 lbm/ft^2-hr)
Two-Phase Mass Flux	366 - 1492 kg/m^2-s (0.269 – 1.098x10^6 lbm/ft^2-hr)
Pressure	50 bar (711 psi)
Rod Temperature	measured with thermocouples serving as burnout detectors
Average Heat Flux	8.1 - 103 W/cm^2 (0.0257 – 0.326x10^6 Btu/ft^2-hr)
Exit Quality	2.2 - 51.5 percent
ΔT_{sub}	2.4 - 29.4 degrees C
Flow Regimes	Liquid 1-ϕ, bubbly, transition, annular (typical of BWR).
Void Fraction	0 - 100 percent

Instrumentation and Data from Tests

Each of the heater rods was instrumented with four thermocouples. These thermocouples are primarily for burnout detectors and thus calibration is not necessary. Neither was any visualization view port provided, such that the identification of flow regimes was based on empirical correlations from the state of local quality. Heat transfer information were mainly derived from the voltage and current parameters of the DC power system, thus only global heat flux (rather than local heat flux) were obtained. Although the heater rods were pushed to the burnout limits in order to obtain the critical heat flux (CHF), the normal BWR operating mass flux range was maintained. Therefore the post-LOCA reflood (or blowdown) scenarios were not addressed, neither were the radiation heat transfer and dispersed flow film boiling phenomena as normally encountered in a uncovered core during reflood. However, the FRIGG-2 gamma-ray densitometer experiments provided valuable information on the axial and radial distribution of void faction. It could facilitate the physical correlation between void fraction, local quality, and interfacial slip.

Extensive single and two-phase flow pressure drop data were obtained in the FRIGG-2 tests. These pressure drop data are specific to the Marviken reactor core condition, but have compared favorably with the Martinelli-Nelson and Becker correlations.

The only complete natural circulation curve was also obtained at conditions close to the Marviken reactor's. However, by far, the most important data obtained from the FRIGG-2 tests are the CHF data for the particular fuel type and grid spacer pattern, as well as the void fraction distribution of the 36-rod bundle.

Conclusions

For the burnout experiments in FRIGG-2, all independent parameters (mass flux, inlet subcooling, pressure, and power to the bundle) have been carefully and independently controlled. Due to the uniform axial and radial power profiles of FRIGG-2, which resulted in a less favorable heat transfer condition in FRIGG-2 as compared to the actual Marviken core, the

measured burnout data were approximately 20 percent lower than those predicted. This points out the major deficiency of the uniform power profiles of FRIGG-2. Follow-up tests using the actual Marviken reactor's power profiles have been suggested and recognized.

The natural circulation mass flow rate in Marviken is 10-15 percent above the experimental values of FRIGG-2 in the power range of interest, while there is a close agreement between the calculated and measured FRIGG-2 flows. The differences are attributed to the Marviken's coolant (heavy water); larger radial heat loss of Marviken channel; and distributed power profiles of Marviken fuel assembly.

Although the FRIGG-2 facility has improved our understanding of the burnout limits and natural circulation flows of a simulated Marviken core, it did not address the heat transfer phenomena associated with post-LOCA reflood conditions, in which the quench front progression, froth region propagation, and dispersed flow film boiling are of major interest. However, the relevant heat transfer information of FRIGG-2 is assessed against the RBHT PIRT in the following Tables A7.1 through A7.3:

Table A7.1 Assessment of FRIGG-2 36-Rod Bundle Test to RBHT PIRT: Single Phase Liquid Convective Heat Transfer in the Core Component During Reflood Below the Quench Front

Process/Phenomena	Ranking	Basis	FRIGG-2 36-Rod Bundle Test
1ϕLiquid Convective Heat Transfer	L	1ϕConvective H.T. data ha been correlated for rod bundles, uncertainty will not effect PCT.	Flows are substantially higher than proposed RBHT reflood flows.
• Effects of Geometry	L	De varies radially	P/D varies radially
• Effects of Spacers	L	Effects of spacers in 1ϕ convective H.T. is known. No impact on PCT uncertainty.	Rod T/C's are used for burnout detectors only.
• Effects of Properties	L	Property effects are accounted for in analysis for 1ϕH.T. little uncertainty.	Insufficient instrumentation for T_b.
1ϕLiquid Natural Convection H.T.	M	Must test Gr/Re^2 to determine regime.	Natural circulation flow measured, but at powers substantially higher than the decay power.
• Effects of Geometry	L	Limited data exists which can be used as a guide, should have little uncertainty on PCT.	Insufficient instrumentation for T_b.
• Effects of Spacers	L	Effect unknown for natual convection, but enhances H.T. No impact on PCT uncertainty.	Insufficient rod T/C instrumentation.
• Effects of Properties	L	Accounted for in dimensionless parameters, little uncertainty.	Insufficient instrumentation for T_b.
Decay Power	H	Source of energy for rods, boundary convection for test.	Decay power not simulated

Table A7.2 Assessment of FRIGG-2 36-Rod Bundle Test to RBHT PIRT: Subcooled and Saturated Boiling in the Core Component During Reflood Below the Quench Front

Process/Phenomena	Ranking	Basis	FRIGG-2 36-Rod Bundle Tests
Subcooled Boiling	L	A significant variation in the subcooled boiling H. T. coefficient will not effect the PCT uncertainty since rod is quenched.	Heater rod temperatures are measured, but only used as burnout detectors.
• Effects of Geometry, P/D, De	L	Boiling effects in rod bundles have been correlated for our P/d, De range with acceptable uncertainty.	P/D varies radially
• Effects of Spacers	L	Locally enhanced H. T.	Not quantified by the experiments
• Effects of Properties	L	Data exists for our Range of Conditions, little uncertainty.	Heater rods do not simulate nuclear rods
Saturated Boiling	L	Similar to subcooled boiling, data is available for our P/D, De range. The uncertainty of Saturated Boiling H. T. coefficient will not significantly impact the PCT since rod is quenched.	Heater rod temperatures are available, but only used as burnout detectors.
• Effects of Geometry, P/D, De	L	Data exists in the range of P/D, De with acceptable uncertainties.	P/D varies radially
• Effects of Spacers	L	Locally enhanced H. T., Correlations/ Models are available, with acceptable uncertainty.	Not quantified by the experiments.
• Effects of Properties	L	Data exists for our range of conditions, little uncertainty.	Heater rods do not simulate nuclear rods
Decay Power	H	Source of energy for rods, boundary condition for the test.	Tests were conducted at Marviken operating power, not at decay power.

Table A7.3 Assessment of FRIGG-2 36-Rod Bundle Test to RBHT PIRT for High Ranked BWR Core Phenomena

	Process/Phenomena	Basis	FRIGG-2 36-Rod Bundle Tests
Core			
•	Film Boiling	PCT is at the end of the heated length, but not measured.	Only occurs in dryout DNB tests
•	Upper Tie Plate CCFL	Hot Assembly is in co-current up flow above CCFL limit.	Not applicable
•	Channel-bypass Leakage	Flow bypass will help quench the BWR fuel assembly core.	Not applicable
•	Steam Cooling	A portion of the Dispersed Flow Film Boiling Heat Transfer.	Pot-dryout condition, not enough H.T. measurement
•	Dryout	Transition from nucleate boiling and film boiling.	Indicated from the burnout detectors
•	Natural Circulation Flow	Flow into the core and system pressure drops.	At Marviken's normal power
•	Flow Regime	Determines the nature and details of the heat transfer in the core.	Bubbly, transitional, and annular flows identified from flow-regime map, typical of BWR.
•	Fluid Mixing	Determines the liquid temperature in the upper plenum for CCFL break down.	Not applicable
•	Fuel Rod Quench Front	Heat release from the quench front will determine entrainment to the upper region of the bundle.	Not applicable
•	Decay Heat	Energy source for heat transfer	Not applicable
•	Interfacial Shear	Effects the void fraction and resulting droplet and liquid velocity in the entrained flow.	Insufficient measurement
•	Rewet: Bottom Reflood	BWR hot assembly refloods like PWR.	Not applicable
•	Rewet Temepratures	Determines the quench front point on the fuel rod.	Not applicable
•	Top Down Rewet	Top of the hot assembly fuel will rewet in a similar manner as PWR.	Not applicable
•	Void Distribution	Gives the liquid distribution in the bundle.	Measured by the gamma-ray densitometer
•	Two-Phase Level	Similar to quench front locations, indicates location of nucleate and film boiling.	Not applicable

APPENDIX A8. LITERATURE REVIEW

Test Facility Name: General Electric 9-Rod Bundle Facility

Dates When Tests Were Performed: 1968-1970

References:

R17 Lahey, R. T., and Schraub, F. A., "Mixing, Flow Regimes, and Void Fraction for Two-Phase Flow in Rod Bundles," *Two-Phase Flow and Heat Transfer in Rod Bundles*, ASME, Nov. 1969.

R18 Lahey, R. T., Shiralkar, B. S., and Radcliff, D. W., "Two-Phase Flow and Heat Transfer in Multirod Geometries: Subchannel and Pressure Drop Measurements in a Nine-rod Bundle for Diabatic and Adiabatic Conditions," GEAP-13049, AEC, 1968.

Availability of Data:

In the 3x3 9-rod bundle configuration for typical BWR operating conditions, there are three types of geometrical subchannels: comer, side, and center subchannels. Subchannels are also classified into hot (locally heated), cold (unheated), and uniform (uniformly heated) subchannels. Data for all test points are available in tabulated form for all types of subchannel. Bundle average mass flux, bundle average exit quality, measured subchannel mass flux, and subchannel quality are tabulated against the test points in Refereces R17 and R18. Substantial differential pressure drop data for both single- and two-phase flows are available in the same references. Other reduced or analyzed data are also available in graphic format that include: subchannel quality-vs-average quality; subchannel energy flux-vs-subchannel mass flux; subchannel quality-vs-subchannel type; subchannel mass flux-vs-subchannel type; etc. Single-phase friction factors are graphed against the Reynolds number, while two-phase friction multipliers are graphed against flow quality and favorably compared with the Martinelli-Nelson correlation.

Test Facility Description, Types of Tests

The primary purpose of this investigation was to obtain the mass flux and enthalpy distribution in a simulated rod bundle for a BWR. The geometric features of the test section are:

Number of rods	9	Rod diameter	14.48 mm (0.570 in)
Radius of channel corner	10.16 mm (0.400 in)	Rod-rod clearance	4.287 mm (0.168 in)
Rod-wall clearance	3.429 mm (0.135 in)	Hydraulic diameter	12.04 mm (0.474 in)
Heated length	1.83 m (72 in)		

Tests were run with all nine rods electrically heated. The radial local peaking was either uniform or a peaking pattern typical of BWR conditions. A cross-sectional view of the test section is shown in Figure A8.1, indicating the corner, side, and center subchannels. One of the unique features of the facility is that provisions are made for bringing static and differential pressure lines at the same axial location but for different subchannels. To measure the flow in any given subchannel, that subchannel is isolated at some point from the rest of the channel. The subchannel flow, also referred as sample flow as shown in Figure A8.2, can then be taken through special ducting to another point outside the test section, where both the flow rate and enthalpy can be measured. Flow splinters made of thin metal sheets are used to separate and isolate flow of a subchannel at the end of the heated length. Such an isolated flow is guided through a tube before passing out the test section flange and entering a heat exchanger (calorimeter) as shown in Figure A8.2. The condensed flow is monitored by a turbine flow meter for subchannel flow measurement.

The sample enthalpy was determined by a heat balance on the calorimeter. For this purpose, the cooling water flow and temperature rise are carefully measured to provide as accurate energy information as possible. The outlet thermocouples are inserted beyond a right- angle bend in the piping to ensure good mixing in the water. Pressure drop measurements were also made during both single- and two-phase tests. All pressure drop measurements were corrected-for the hydrostatic head in the pressure tap lines based on the average density of water between the relevant pressure taps.

The ranges of test conditions include:

Single-Phase (Cold) Mass Flux	422.67 - 3089.21 kg/m^2-sec (0.311 - 2.273x10^6 lbm/ft^2-hr)
Two-Phase Mass Flux	505.58 - 1603.72 kg/m^2-sec (0.372 - 1.180x10^6 lbm/ft^2-hr)
Pressure	75.84 - 82.74 bar (1100 - 1200 psi)
Rod Temperature	not measured
Average Heat Flux	690.63 - 2513.4 kW/m^2-K (0.219 - 0.797x10^6 Btu/ft^2-hr)
Exit Quality	3.1 - 44.4 percent
Δh_{sub}	674.54 - 1239.76 kJ/kg (290 - 533 Btu/lbm)
Flow Regimes	Liquid 1-ϕ, bubbly, transition, annular

Instrumentation and Data from Tests

The heater rods were not instrumented with thermocouples. Thus, little local heat transfer information could be obtained. Neither was any visualization view port provided, such that the identification of flow regimes was based on empirical correlations from the state of local quality. Since the heater rods were sufficiently cooled under the normal BWR operating conditions and the issues of DNB and LOCA/reflood were not addressed, radiation heat transfer was not a important factor. However, flow and enthalpy distributions among the subchannels that are unique to BWR conditions were carefully measured and addressed. The tests were able to measure flow, enthalpy, and derive local quality in each individual subchannel. Thus the facility can yield some significant information on the heterogeneous flow core, of which the cross flow phenomenon is of importance.

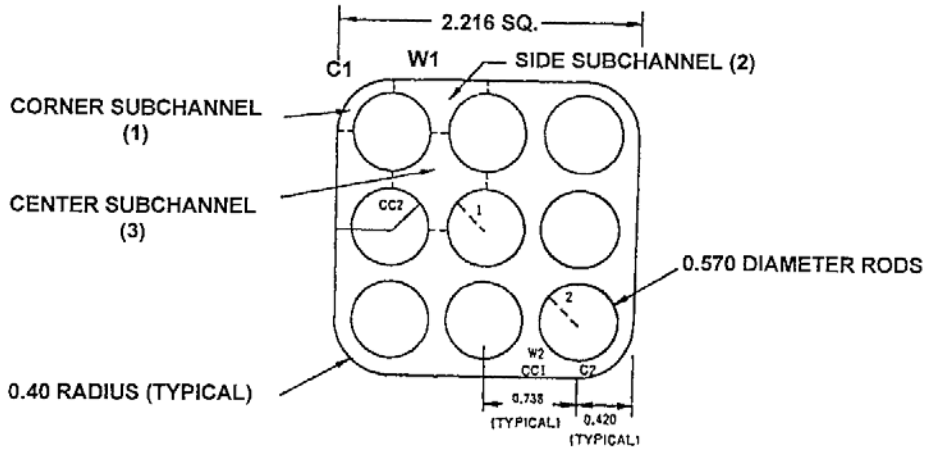

SECTION "A-A
(NOTE SPLITTER POSITIONS FOR THE VARIOUS SUBCHANNELS)

Figure A8.1 Positions of Pressure Taps for Setting Isokinetic Conditions.

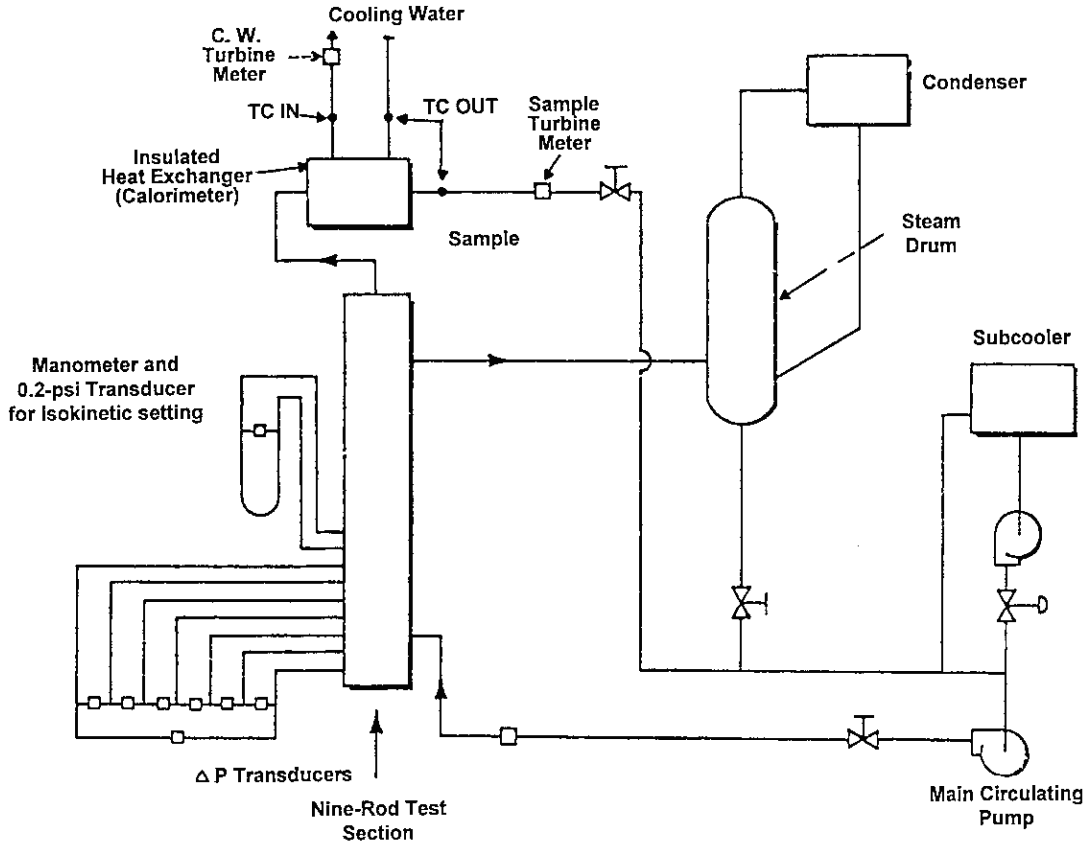

Figure A8.2 Schematic of Loop Showing Sampling Circuit.

While the heater rods were uniformly heated in the axial direction, the radial power distribution was controlled by peaking the individual transformers. Thus the flow, enthalpy, and quality distributions across the subchannels due to radial power peaking were also unique output of the facility.

Pressure drop data for single (cold) and two-phase flow tests were obtained for frictional loss correlation. At the same axial locations, cross-flow phenomenon (between subchannels) was interpreted from the pressure differential between subchannels (non-isokinetic cases).

Conclusions

Subchannel test data were taken for a 9-rod bundle in typical BWR operating conditions. In general the following observations are made:

1. The corner subchannel runs a mass flux and quality below the bundle average values.
2. The side subchannel has mass flux and quality approximately equal to or slightly less than the bundle average.
3. The center subchannel has both mass flux and quality above the bundle average values.
4. There is an observable, though somewhat inconsistent, tendency for the subchannels to approach bundle average condition in the regions of slug-annular flow-regime transition.
5. The effect of heat flux on subchannel enthalpy distribution was small for low flows, but showed a strong effect at the high flows.
6. The effect of the bundle average mass flux on subchannel mass flux distribution was to increase the mass flux in the comer and center subchannels, and decrease the mass flux in the side subchannels, as the bundle average mass flux was increased.
7. The effect of heat flux on subchannel mass flux distribution was to decrease the mass flux in the comer subchannel but leave the mass flux in other subchannels relatively unchanged.
8. The adiabatic single-phase friction factor for the clean 9-rod bundle under consideration was slightly higher than the smooth-tube friction factor, for all Reynolds numbers.
9. The two-phase friction drop multiplier showed only a very minor flow effect, and the data was well correlated by the classical Martinelli-Nelson curve.

Although this facility and work improved our understanding of subchannel flow and energy diversions in typical BWR conditions, it did not address the heat transfer phenomena associated with post-LOCA reflood conditions, in which the quench front progression, froth region propagation, and dispersed flow film boiling are of major interest. However, the relevant heat transfer information is assessed against the RBHT PIRT in the following Tables A8.1 and A8.2:

Table A8.1 Assessment of General Electric 9-Rod Bundle Tests to RBHT PIRT: Subcooled and Saturated Boiling in the Core Component Below the Quench Front

Process/Phenomena	Ranking	Basis	GE 9-Rod Bundle Tests
Subcooled Boiling	L	A significant variation in the subcooled boiling H. T. coefficient will not effect the PCT uncertainty since rod is quenched.	Heater rod temperatures are not measured, but subchannel flow, temperature, quality are measured.
• Effects of Geometry, P/D, De	L	Boiling effects in rod bundles have been correlated for our P/d, De range with acceptable uncertainty.	P/D = 1.295 for tests.
• Effects of Spacers	L	Locally enhanced H. T.; Correlations/Models are available, acceptable uncertainty.	Subchannel flow and enthalpy should be redistributed by the spacers, but was not investigated.
• Effects of Properties	L	Data exists for our Range of Conditions, little uncertainty.	No heater rod temperature measurement
Saturated Boiling	L	Similar to subcooled boiling, data is available for our P/D, De range. The uncertainty of Saturated Boiling H. T. coefficient will not significantly impact the PCT since rod is quenched.	Heater rod temperatures are not available, but subchannel flow, temperature, and quality are measured.
• Effects of Geometry, P/D, De	L	Data exists in the range of P/D, De with acceptable uncertainties.	P/D = 1.295.
• Effects of Spacers	L	Locally enhanced H. T., Correlations/ Models are available, with acceptable uncertainty.	Subchannel flow and enthalpy should be redistributed by the spacers, but was not investigated.
• Effects of Properties	L	Data exists for our range of conditions, little uncertainty.	No heater rod temperature measurement.
Decay Power	H	Source of energy for rods, boundary condition for the test.	Test were conducted at BWR operating power, not at decay power.

Table A8.2 Assessment of General Electric 9-Rod Bundle Tests to RBHT PIRT for High Ranked BWR Core Phenomena

	Process/Phenomena	Basis	General Electric 9-Rod Bundle Tests
Core			
•	Film Boiling	PCT is at the end of the heated length, but not measured.	Not applicable
•	Upper Tie Plate CCFL	Hot Assembly is in co-current up flow above CCFL limit.	Not applicable
•	Channel-bypass Leakage	Flow bypass will help quench the BWR fuel assembly core.	Subchannel cross flow observed
•	Steam Cooling	A portion of the Dispersed Flow Film Boiling Heat Transfer.	Not applicable
•	Dryout	Transition from nucleate boiling and film boiling.	Not applicable
•	Natural Circulation Flow	Flow into the core and system pressure drops.	Not applicable
•	Flow Regime	Determines the nature and details of the heat transfer in the core.	Bubbly, transitional, and annular flows identified from flow-regime map.
•	Fluid Mixing	Determines the liquid temperature in the upper plenum for CCFL break down.	Not applicable
•	Fuel Rod Quench Front	Heat release from the quench front will determine entrainment to the upper region of the bundle.	Not applicable
•	Decay Heat	Energy source for heat transfer	Not applicable
•	Interfacial Shear	Effects the void fraction and resulting droplet and liquid velocity in the entrained flow.	Not applicable
•	Rewet: Bottom Reflood	BWR hot assembly refloods like PWR.	Not applicable
•	Rewet Temepratures	Determines the quench front point on the fuel rod.	Not applicable
•	Top Down Rewet	Top of the hot assembly fuel will rewet in a similar manner as PWR.	Not applicable
•	Void Distribution	Gives the liquid distribution in the bundle.	Not directly measured, however, the enthalpy distribution of the 9-rod bundle was measured.
•	Two-Phase Level	Similar to quench front locations, indicates location of nucleate and film boiling.	Identified from the flow-regime map.

APPENDIX A9. LITERATURE REVIEW

Test Facility Name: PNL LOCA Simulation Program at NRU Reactor, Chalk River, Canada

Dates When Tests Were Performed: October 1980 - November 1981

References:

R19 C. L. Mohr, et. al., "Data Report for Thermal-Hydraulic Experiment 2 (TH-2)", NUREC/CR-2526, PNL-4164, November 1982.

R20 C. L. Mohr, et. al., "Data Report for Thermal-Hydraulic Experiment 3 (TH-3)", NUREC/CR-2527, PNL-4165, March 1983.

Availability of Data:

Graphical data demonstrating fuel cladding temperature control using the preset reflood flow and temperature feedback. Photographs of guard and test fuel used are shown. Data in graphical form on the test assembly temperatures, cooling flow and the neutronic environment are also presented. Data is available in both SI and British units. Microfiche of the entire report is available with NTIS.

Test Facility Description, Types of Tests

The TH-2 included 14 tests. A schematic of the test train used is depicted in Figure A9.1. The fuel assembly consists of a 6x6 segment of a 17x17 PWR fuel assembly with four corner rods removed, providing a basic fuel array of 32 rods. The 20 guard rods in the outer row reduced the heat net heat transfer from the inner test rods during the test. All the inner 12 test fuel rods were arranged in cruciform pattern. All the 32 unpressurized fuel rods were filled with helium. The core configuration is shown in Figure A9.2.

The following table gives the test fuel rod design variables:

Cladding Material	Zircaloy-4
Cladding Outside Diameter (OD)	0.963 cm (0.379 in)
Cladding Inside Diameter (ID)	0.841 cm (0.331 in)
Pitch (Rod to Rod)	1.275 cm (0.502 in)
Fuel Pellet OD	0.826 cm (0.325 in)
Fuel Pellet Length	0.953 cm (0.375 in)
Active Fuel Length	3.66 m (12 ft)

The TH-2 experiment included a preconditioning phase and 14 successive tests, each having a pre-transient and transient phase. The average test assembly fuel rod power during preconditioning was ~18.7 kW/m (5.7 kW/ft) with the U-2 loop providing water cooling; this was also used for the TH-3 experiment. System loop pressure was held at 8.63 MPa (1250 psia). The pre-transient stage for the TH-3 tests was conducted with the steam cooling provided by the U-1 loop at a mass flow rate of ~0.379 kg/s (~3000 lbm/hr) and a reactor power of ~7.4 MW.

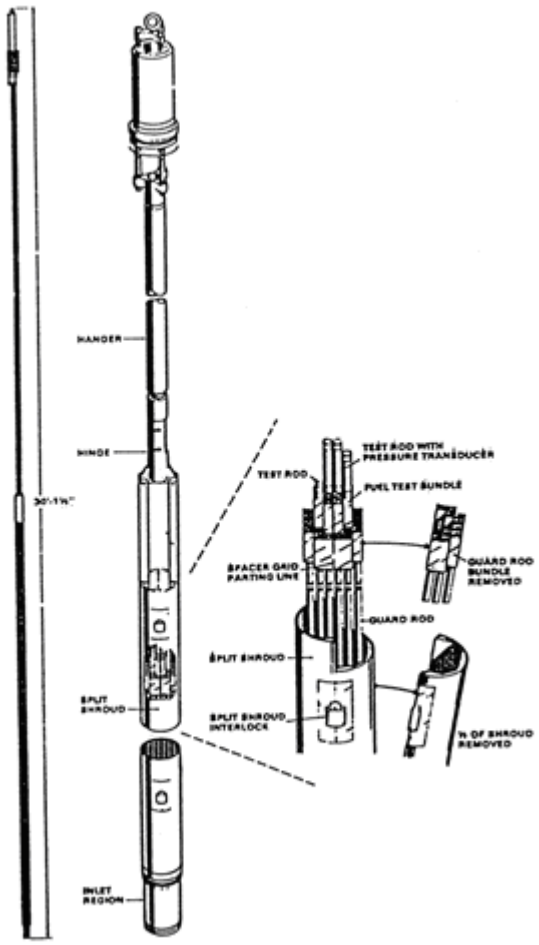

Figure A9.1 Schematic of NRU Loss-of-Coolant Accident Test Train.

This enabled the total assembly power to remain constant, even though the peak cladding temperature varied from test to test. The transient phase of TH-3 commenced when the steam coolant flow was reduced from ~3000 lbm/hr to 0, with the reactor power being maintained at about 7.4 MW. No preconditioning operation was conducted for the TH-3 experiment.

The test conditions measured during the TH-2 and TH-3 experiments are described in Tables A9.1 and A9.2, respectively.

Instrumentation and Data from Tests

The instrumentation for the TH-2 experiment included: 24 self-powered neutron detectors (SPNDs), 115 fuel rod thermocouples, 18 steam probe thermocouples and four closure head thermocouples. The instrumentation was located at 21 elevations along the test train assembly. These are shown in Figure A9.3.

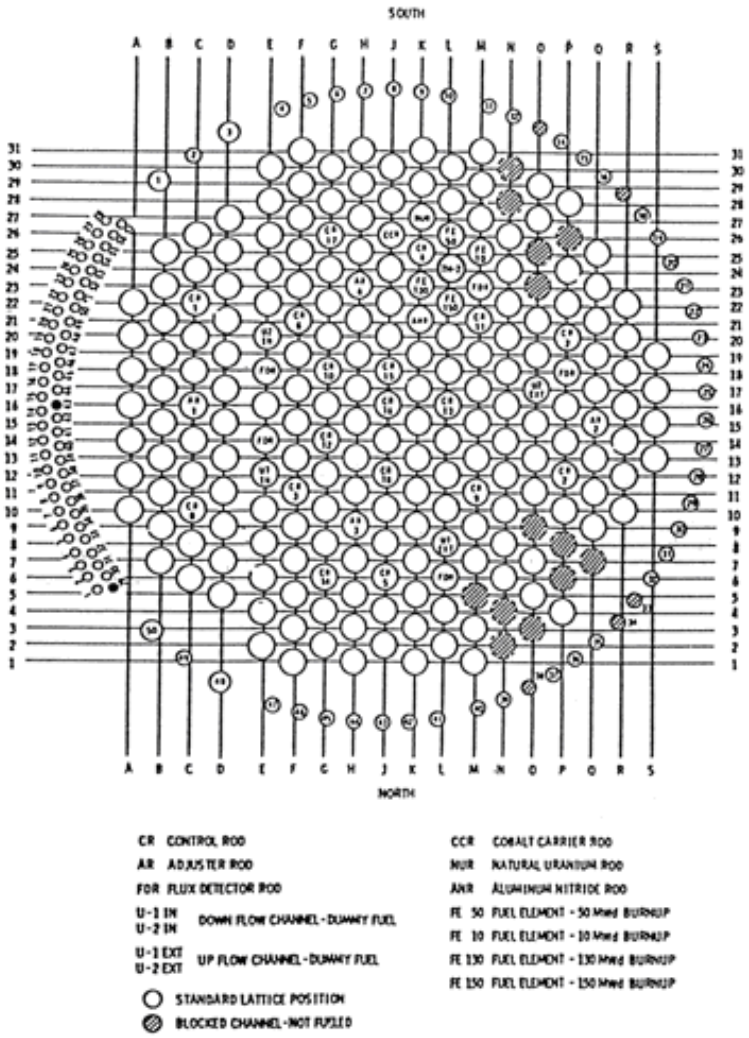

Figure A9.2 NRU Reactor Core Configuration.

The instrumentation for the TH-3 experiment included: 24 SPNDs, 69 fuel rods thermocouples, four hanger thermocouples and four closure head thermocouples. The instrumentation was located at 22 elevations along the test train assembly. These are shown in the Figure A9.4.

Thermal-hydraulic data was obtained by turbine flowmeters and thermocouples. Local coolant temperatures were measured with steam probe thermocouples that protruded into the coolant channel and with thermocouples attached to the shroud. Azimuthal temperature variations were measured by thermocouples located at the fuel centerline and attached to the inside of the cladding surface. The cladding temperature was monitored by cladding thermocouples that were spot welded to the interior cladding surface.

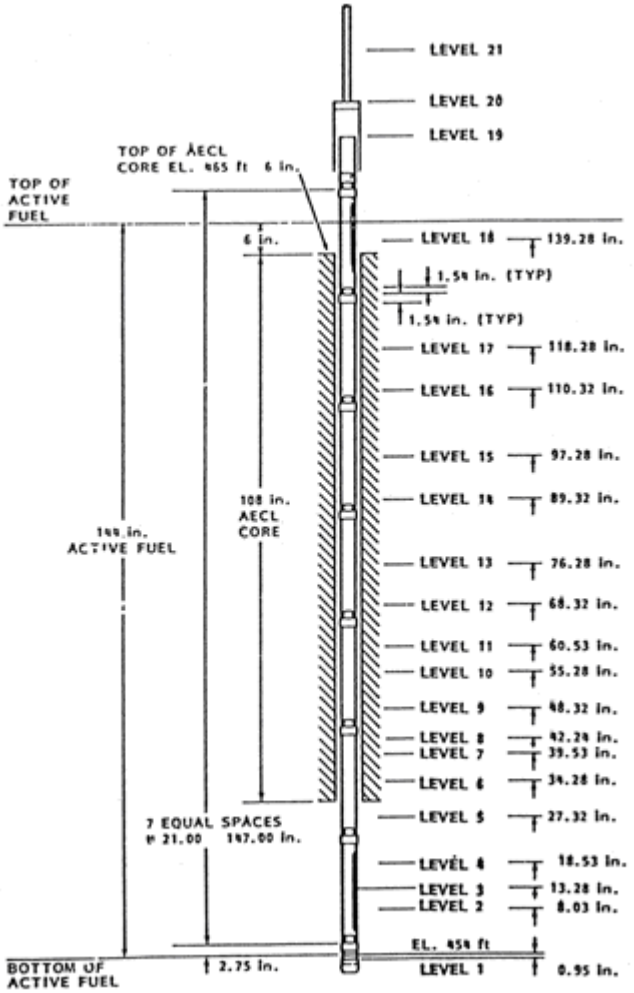

Figure A9.3 Instrumentation Levels in the TH-2 Test Assembly.

The SPNDs provided neutron flux measurements within the fuel bundle. These measurements were made at opposite corners of the stainless steel shroud at several elevations, ranging from 13.3 - 139.3 in above the bottom of the fuel column. The SPNDs provide a measure of the radial neutron flux gradient and neutron flux distribution over the vertical axis of the test assembly. These could also detect the coolant density variations (through flux changes) associated with the quench front that passed each SPND during the reflood phase of the transient. The instrument signals were monitored on a real-time basis with the DACS (Data Acquisition and Control System). The recorded data characterized the coolant flow rates, temperature neutron flux and operating history.

The reflood flow measurement system included a Fisher-Porter turbine flowmeter in the high flow rate and a series connected Barton and Fisher-Porter turbine flowmeters in the parallel low flow rate line. Steam probe temperature history provided independent measurements of the reflood coolant level in the test assembly.

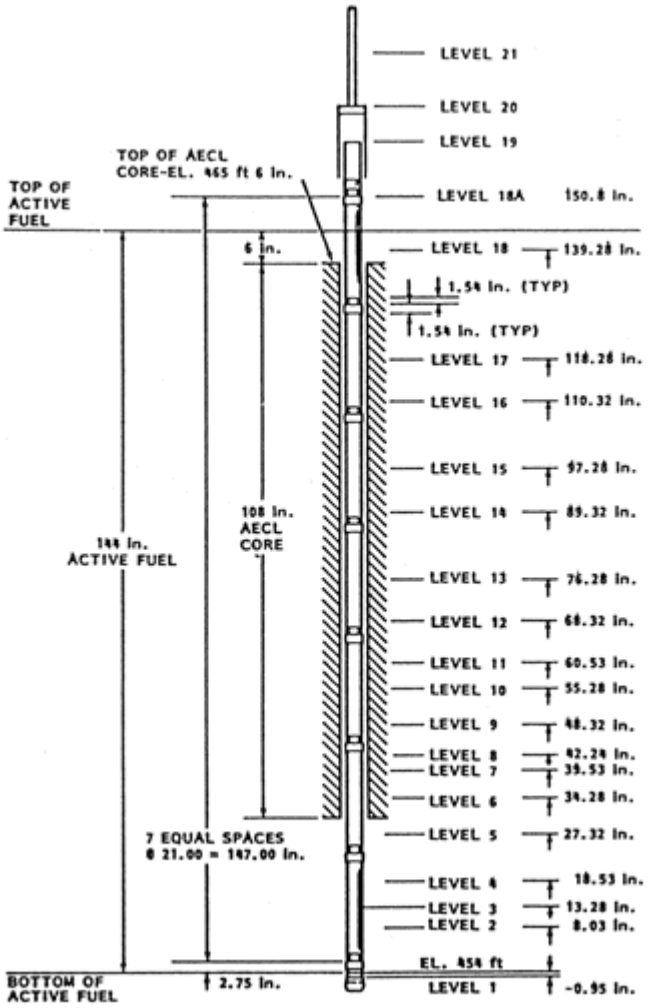

Figure A9.4 Instrumentation Levels in the TH-3 Test Assembly.

Conclusions

These tests give the average fuel rod cladding temperatures during pre-conditioning, pre-transient and transient phases. Also available are the test coolant and shroud temperatures. However, these tests do not have enough data to make code model changes without the potential for compensating errors. Many of the heat transfer phenomena such as droplet to vapor interfacial heat transfer, dry wall contact are not simulated, though overall wall heat transfer is measured. Therefore, while these tests are useful in simulating the overall reflood heat transfer, they provide limited data which can be used to assess the reflood phenomena which was identified in the PIRT table for the RBHT Program.

Table A9.1 Measured Conditions for the TH-2 Experiment[1]

Parameter	Preconditioning	Reflood Calibration	Transient TH-2.01	Transient TH-2.02	Transient TH-2.03	Transient TH-2.04	Transient TH-2.05	Transient TH-2.06
Reactor power, MW	127	0	-7.4	-7.4	-7.4	-7.4	-7.4	-7.4
Test assembly power, kW		0						
Coolant	U-2 water	U-1 steam/ reflooding	U-1 steam/re-flooding	U-1 steam/re-flooding	U-1 steam/re-flooding	U-1 steam/re-flooding	U-1 steam/re-flooding	U-1 steam/re-flooding
Coolant flow, kg/s (lbm/h)	0 to 16.30 (0 to 129,400)	0.378 (3000)	0.380 (3010)	0.383 (3040)	0.382 (3030)	0.382 (3030)	0.382 (3030)	0.381 (3020)
Reflood delay, s	NA	0	NA					
Reflood rates, m/s (in/s)	NA	0.0508 (2.0), 0.0254 (1.0), 0.0508 (2.0)						
Pretransient cladding temperatures, K (° F)	NA	NA	707 (813)					
Peak cladding temperature (PCT), K(° F)	700 (800)	433 (320)	1005 (1350)					
Reactor conditional trip criteria (PCT), K(° F)	NA	NA	978 (1300)	1103 (1525)	1103 (1525)	1144 (1600)	1144 (1600)	1144 (1600)
Bundle quench time, [a] s								
Type of test	NA	Reflood	Adiabatic	Transient	Transient	Transient	Transient	Transient
Type of reflood control			NA	LCS [b]	DACS[c] after 85 s	DACS after 85 s	DACS after 85 s	DACS after 85 s

Table A9.1 Measured Conditions for the TH-2 Experiment (Continued)

Parameter	Transient TH-2.07	Transient TH-2.08	Transient TH-2.09	Transient TH-2.10	Transient TH-2.11	Transient TH-2.12	Transient TH-2.13	Transient TH-2.14
Reactor power, MW	-7.4	-7.4	-7.4	-7.4	-7.4	-7.4	-7.4	-7.4
Test assembly power, kW						138.7	143.8	142.8
Coolant	U-1 steam/ reflooding	U-1 steam/ reflooding	U-1 steam/ reflooding	U-1 steam/ reflooding	U-1 steam/ reflooding	U-1 steam/ reflooding	U-1 steam/ reflooding	U-1 steam/ reflooding
Coolant flow, kg/s (lbm/h)	0.383 (3040)	0.378 (3000)	0.379 (3010)	0.378 (3000)	0.378 (3000)	0.378 (3000)	0.378 (3000)	0.378 (3000)
Reflood delay, s							NA	
Reflood rates, m/s (in/s)						unable to read from paper	0	unable to read from paper
Pretransient cladding temperatures, K (F)						743 (877)	783 (869)	737 (867)
Peak cladding temperature (PCT), K(F)						1174 (1653)	1013 (1364)	1274 (1834)
Reactor condi tional trip crite ria (PCT), K(F)	1144 (1600)	1144 (1600)	1144 (1600)	1144 (1600)	1144 (1600)	1144 (1600)	1144 (1600)	1144 (1600)
PCT turnaround time, [a] s						273	33	244
Bundle quench time, [a] s						306	NA	338
Type of test	Transient	Transient	Transient	Transient	Transient	Transient	Adiabatic	Transient
Type of reflood control	DACS after 95 s	DACS after 95 s	DACS after 95 s	DACS after 95 s	DACS after 95 s	DACS after 95 s	NA	DACS after 95 s

(1) TH-2.12 and TH-2.14 were the principal

(a) Time after initiation of transient,

(b) LCS-Loop Control System,

(c) DACS - Data Acquisition and Control System

Table A9.2 Measured Conditions for the TH-3 Experiment

Parameter	Preconditioning	Reflood Calibration	Test TH-3.01	Test TH-3.02	Test TH-3.03
Reactor power, MW	127	0	7.4	7.4	7.4
Test assembly power, kW		0	141.5	134.6	133.5
Coolant	U-2 water	U-1 steam/ reflooding	U-1 steam/ reflooding	U-1 steam/ reflooding	
Coolant flow, kg/s (lbm/h)	0 to 16.30 (0 to 129,400)	0.0254, 0.508 (1.0, 2.0)	0.379 (3010)	0.379 (3004)	0.379 (3009)
Reflood delay, s	NA	NA	NA	9	3
Reflood rates, m/s (in/s)	NA	NA	NA	0.0823(3.24) for 8 s 0.0549(2.16) for 40 s 0.0366(1.44) for 16 s 0.0244(0.96) for 28 s 0.127 (0.5) for 162 s	0.0828(3.26) for 8 s 0.0574(2.26) for 40 s 0.0371(1.46) for 16 s 0.0224(0.88) for 28 s 0.0124(0.49) for 18 s 0.0191(0.75) for 40 s 0.0097(0.38) for 96 s 0.0147(0.58) for 28 s 0.0102(0.4) for 130s
Pretransient cladding temperatures, K (° F)	NA	NA	723 (842)	723 (842)	717 (830)
Peak cladding temperature (PCT), K(° F)	700 (800)		1008 (1354.4)	1318 (1912)	1283 (1850)
Reactor conditional trip criteria (PCT), K(° F)	NA	NA	978 (1300)	1172 (1650)	1200 (1700)
PCT turnaround time, [a] s	NA	NA	35	193	257
Bundle quench time, [a] s	NA	NA	NA	277	407
Type of test	NA	Reflood	Adiabatic	Transient	Transient
Type of reflood control	NA	LCS [b]	NA	DACS [d] after 90 s	DACS after 90 s

(a) Time after initiation of transient,

(b) LCS-Loop Control System,

(c) DACS - Data Acquisition and Control System

Table A9.3 Assessment of NRU Inpile Reflood Data to RBHT PIRT: Dispersed Flow Region for Core Component

Process/Phenomena	Ranking	Basis	NRU Inpile Reflood Data
Decay Power	H	Energy source which determines the temperature of the heater rods, and the energy removed by the coolant.	Known
Fuel Rod/Heater Rod properties, ρ, C_p, k	L	The exact properties can be modeled and stored energy release is not important at this time, environmentally.	Known properties and dimensions.
Dispersed Flow Film Boiling	H	Dispersed flow film boiling modeling has a high uncertainty which directly effects the PCT.	PCTs known for the tests.
Convection to superheated vapor	H	Principal mode of heat transfer as indicated in FLECHT-SEASET experiments[4]	Not determined
Dispersed phase enhancement of convective flow	H	Preliminary models indicated that the enhancement can be over 50% in source cases[13].	Not determined
Direct wall contact H.T.	L	Wall temperatures are significantly above T_{min} such that no contact is expected.	Not determined
Dry wall contact[12]	M	Iloje indicates that H.T. Mechanism is less important than vapor convection.	Not determined
Droplet to vapor interfacial heat transfer.	H	The interfacial heat transfer reduces the vapor temperature which is the heat sink for the wall heat flux.	Not determined
Radiation Heat Transfer to: • Surfaces • Vapor • Droplets	 M/H M/H M/H	This is important at higher bundle elevations (H) where the convective heat transfer is small since the vapor is so highly superheated. Very important for BWR reflood with sprays, and colder surrounding can. Large uncertainty.	May be estimated from the values of test rod temperatures and the flow conditions

Table A9.3 Assessment of NRU Inpile Reflood Data to RBHT PIRT: Dispersed Flow Region for Core Component (Continued)

Process/Phenomena	Ranking	Basis	NRU Inpile Reflood Data
Gap heat transfer	L	Controlling thermal resistance is the dispersed flow film boiling heat transfer resistance. The large gap heat transfer uncertainties can be accepted, but the fuel center line temperature will be impacted.	Gap existed and gap conductance can be estimated.
Cladding Material	L	Cladding material in the tests is Inconel which has the same conductivity as Zircaloy, nearly same temperature drop will occur.	Used Zircaloy-4.
Reaction Rate	M	Inconel will not react while Zircaloy will react and create a secondary heat source at very high PCTs, zirc reaction can be significant.	Should exist because zircaloy is used.
Fuel Clad Swelling/Ballooning	L	Ballooning can divert flow from the PCT location above the ballooning region. The ballooned cladding usually is not the PCT location. Large uncertainty.	This effect was modeled in the tests.

Table A9.4 Assessment of NRU Inpile Reflood Data to RBHT PIRT: High Ranked BWR Core Phenomena

Process/Phenomena	Basis	NRU Inpile Reflood Data
Core Film Boiling	PCT is determined in film boiling period.	PCT is determined in the tests.
Upper Tie Plate CCFL	Hot assembly is in co-current flow above CCFL limit.	Not simulated.
Channel-Bypass Leakage	Flow bypass will help quench the BWR fuel assembly core.	Not simulated.
Steam Cooling	A portion of the dispersed flow film boiling heat transfer.	Simulated but overall heat transfer was measured.
Dryout	Transition from nucleate boiling and film boiling.	Quench front location is not known.
Natural Circulation Flow	Flow into the core and system pressure drops.	Not applicable.
Flow Regime	Determines the nature and details of the heat transfer in the core.	Dispersed flow film boiling.
Fluid Mixing	Determines the liquid temperature in the upper plenum for CCFL break down.	Not applicable.
Fuel Rod Quench Front	Heat release from the quench front will determine entrainment to the upper region of the bundle.	Simulated with nuclear rods.
Decay Heat	Energy source for heat transfer.	Simulated.
Interfacial Shear	Affects the void fraction and the resulting droplet and liquid velocity in the entrained flow.	Not measured.
Rewet: Bottom Reflood	BWR hot assembly refloods like PWR.	Measured.
Rewet Temperature	Determines the quench front point on the fuel rod.	Measured.

Table A9.4 Assessment of NRU Inpile Reflood Data to RBHT PIRT: High Ranked BWR Core Phenomena (Continued)

Process/Phenomena	Basis	NRU Inpile Reflood Data
Top Down Rewet	Top of the hot assembly fuel will rewet in a similar manner as PWR.	Not measured.
Void Distribution	Gives the liquid distribution in the bundle.	Not measured.
Two-Phase Level	Similar to quench front location, indicates the location of nucleate and film boiling.	Measured.

APPENDIX A10. LITERATURE REVIEW

Appendix A10: ACHILLES Reflood Heat Transfer Tests

Dates when Tests Were Performed: 1989 - 1991

References:

R21 Denham, M. K., Jowitt, D., and K. G. Pearson, "ACHILLES Unballooned Cluster Experiments, Part 1: Description of the ACHILLES Rig, Test Section, and Experimental Procedures," AEEW-R2336, Winfrith Technology Centre (Commercial in Confidence), November 1989.

R22 Denham, M. K., and K. G. Pearson, "ACHILLES Unballooned Cluster Experiments, Part 2: Single Phase Flow Experiments," AEEW-R2337, Winfrith Technology Centre (Commercial in Confidence), May 1989.

R23 K.G. Pearson and M. K. Denham, " ACHILLES Unballooned Cluster Experiments, Part 3: Low Flooding Rate Reflood Experiments," AEEW-R2338, Winfrith Technology Centre (Commercial in Confidence), June 1989.

R24 K.G. Pearson and M.K. Denham, "ACHILLES Unballooned Cluster Experiments, Part 4: Low Pressure Level Swell Experiments," AEEW-R2339, Winfrith Technology Centre (Commercial in Confidence), July 1989.

R25 Dore, P and M.K. Denham, "ACHILLES Unballooned Cluster Experiments, Part 5: Best Estimate Experiments," AEEW-R2412, Winfrith Technology Centre, (Commercial in confidence), July 1990.

R26 Dore, P. and D.S. Dhuga, "ACHILLES Unballooned Cluster Experiments, Part 6: Flow Distribution Experiments," AEA-RS-1064, Winfrith Technology Centre (Commercial in Confidence), December 1991.

Availability of Data:

The ACHILLES experiments were performed as part of the safety case for PWRs in the United Kingdom. The ACHILLES tests were funded by the Central Electricity Generating Board (CEGB) and were performed by the United Kingdom Atomic Energy Authority (UKAEA) at the Winfrith Laboratories. The data does have some release restrictions and is not unlimitedly available to the general public. However, more recently, data has been released to interested parties and governments as part of cooperative data exchange. Some of the data was used for an International Standard Problem. Westinghouse has been able to obtain some of the data directly from the CEGB provided that reference was given to the CEGB in the reports prepared by Westinghouse. Therefore, the data should be available to the Nuclear Regulatory Commission.

Test Facility Description, Types of Tests

The ACHILLES tests were specifically conducted to support the PWR (Sizewell) safety case in the United Kingdom in the late 1980's and early 1990's. Since these tests were performed after the FLECHT-SEASET tests, the authors had made some improvements which are of value for the current Rod Bundle Heat Transfer Program. The testing consisted of specific test series which were used to examine specific safety issues and safety analysis issues. Specifically, experiments were performed to examine:

- Low reflooding rate behavior similar to FLECHT-SEASET and FLECHT,
- Best-Estimate Reflood tests were performed to assess a realistic LOCA transient,
- Single-phase flow distribution tests were performed to examine the flow uniformity and single-phase heat transfer within the rod bundle, and
- Low-pressure level swell experiments were also performed to validate drift flux/void fraction relationships.

There were also gravity feed reflood tests with loop resistance simulated, and variable injection reflood tests which simulated evaluation model type system response. There were also oscillating inlet flow injection tests.

One of the purposes of the ACHILLES test program was to examine the heat transfer performance of a fuel assembly with high blockages caused by the swelling of the zirc cladding (sausage ballooning problem). This issue had been resolved in the U.S. but it still remained as an open item in the United Kingdom safety case for the PWR. The reports given in the review only discuss the unblocked or unballooned configuration of the test program. There is a continuation of the ACHILLES test program which specifically examines flow blockages of up to 80 percent to address the clad swelling issues during a LOCA. These tests will not be discussed here.

The ACHILLES bundle is shown in Figure A10.1 and contains a total of 69 heater rods of 9.5 mm (0.374 in) in diameter on a square pitch of 12.6 mm (0.496 in) and have 3.66 m (12 ft) of heated length. ACHILLES used production Inconel mixing vane grids supplied by Westinghouse. All rods were heated in ACHILLES such that there was no simulation of the guide tube thimbles in the bundle such as in the FLECHT-SEASET experiments. However, experiments were performed in ACHILLES to examine the effects of increased surface-to-surface radiation heat transfer by performing tests with selective unpowered heater rods. Figure A10.2 indicates the flow loop schematic for the ACHILLES facility. There was ample flexibility built into the test facility such that both single phase, two-phase, forced reflood injections could be performed, as well as oscillatory injection and gravity injection tests with little facility modifications. The test bundle was contained within a circular shroud of wall thickness of 6.5 mm (0.26 in) and a pressure capability of 6 bars (approximately 90 psia). There were no filler rods in the test bundle design which resulted in excess flow area for the square array of rods within the circular housing. To compensate for the excess flow area and to better simulate an infinite array of fuel rods, the ACHILLES housing was heated with zonal heaters which had a

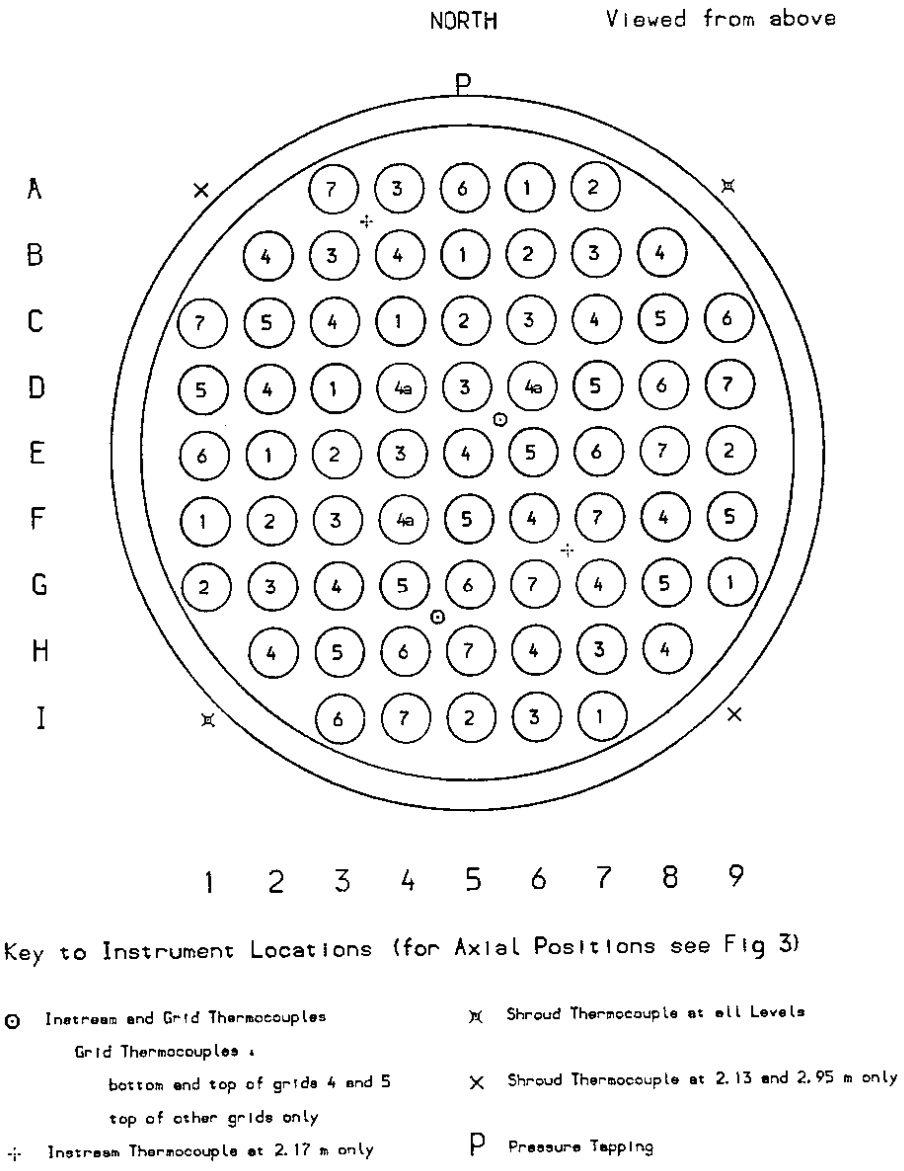

Figure A10.1 Cross Section of ACHILLES 69-Rod Bundle.

total power of 46 kW. These heaters provided a similar axial temperature distribution as the heater rods.

The heater rods were manufactured by RAMA corporation, the same company that made the FLECHT-SEASET heater rods. A chopped cosine power shape with a peak-to-average of 1.4 was used. These rods used Inconel cladding, and could have up to six thermocouples per rod installed. The axial distribution of the heater rod thermocouples and the other instrumentation is shown in Figure A10.3. One unique feature of the ACHILLES bundle is that the instrumentation plan was developed with the idea of examining the heat transfer effects of the spacer grids both upstream and downstream of the grids.

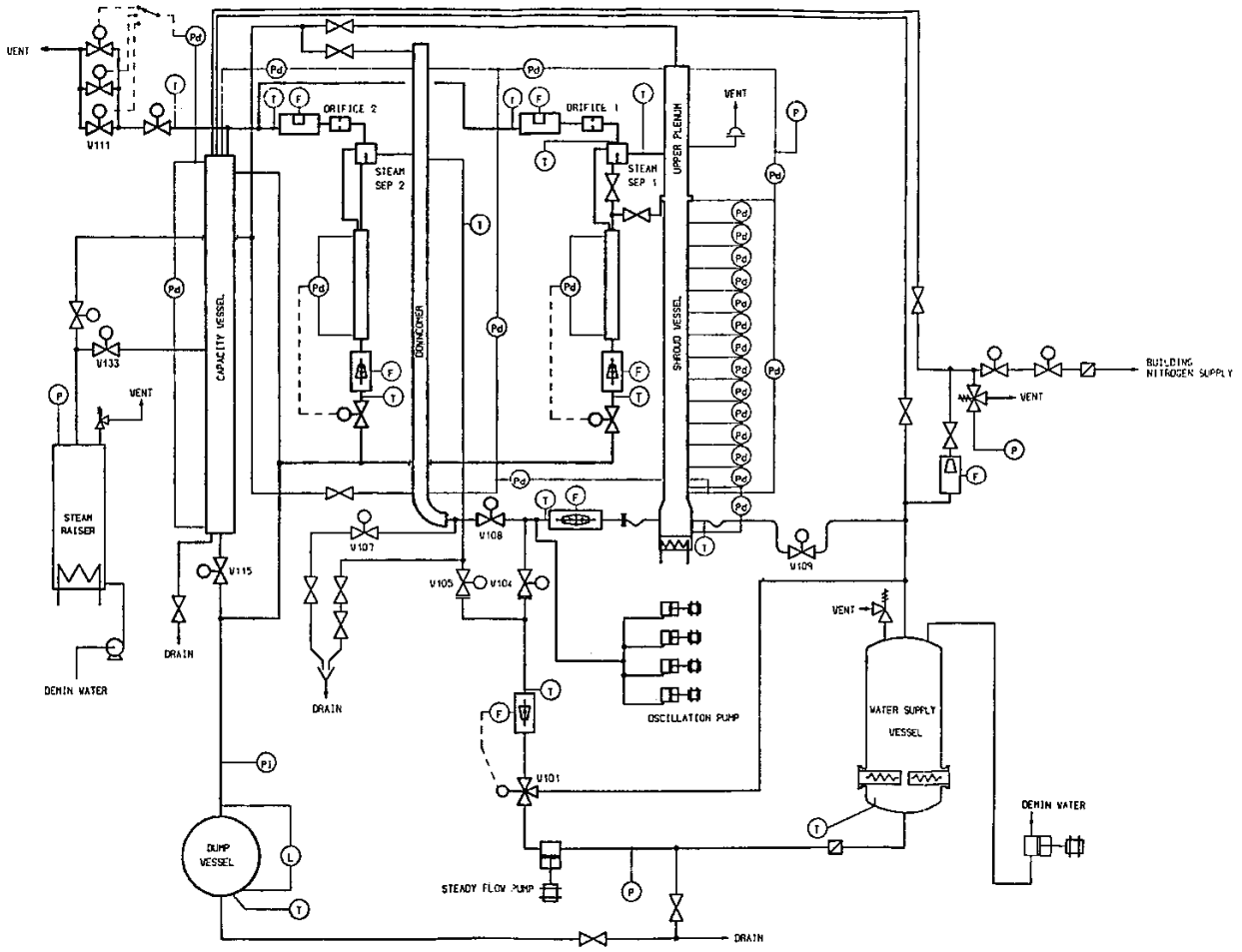

Figure A10.2 Schematic of ACHILLES Flow Loop.

The grids used were Inconel production 17x17 spacer grids with mixing vanes. These grids were instrumented with 0.5 mm (0.20 in) thermocouples which were attached to the grids using Inconel shim stock which was spot-welded to the spacer. The attachment method was designed to minimize the flow disturbance and the effects of the thermocouple lead leading to early grid rewet. Each grid had two thermocouples attached to the spacer at the top and lower edges at different radial positions. The data indicates that this installation method worked well and only one-grid thermocouples failed.

The vapor temperature was measured in the rod bundle at different axial location, up steam and down stream of spacer grids using 1 mm (0.040 in) thermocouples which were swagged to a tip size of 0.5 mm (0.020 in). There is an uncertainly analysis given in the report which indicates that f or the conditions used in the ACHILLES tests, the vapor temperature uncertainty is only 13 degrees C (23.4 degrees F) which is consistent with the uncertainty which was derived in the FLECHT-SEASET program. It is mentioned in Reference R22 that the vapor temperature measurements did have an effect on the entrained droplets with the probe causing additional

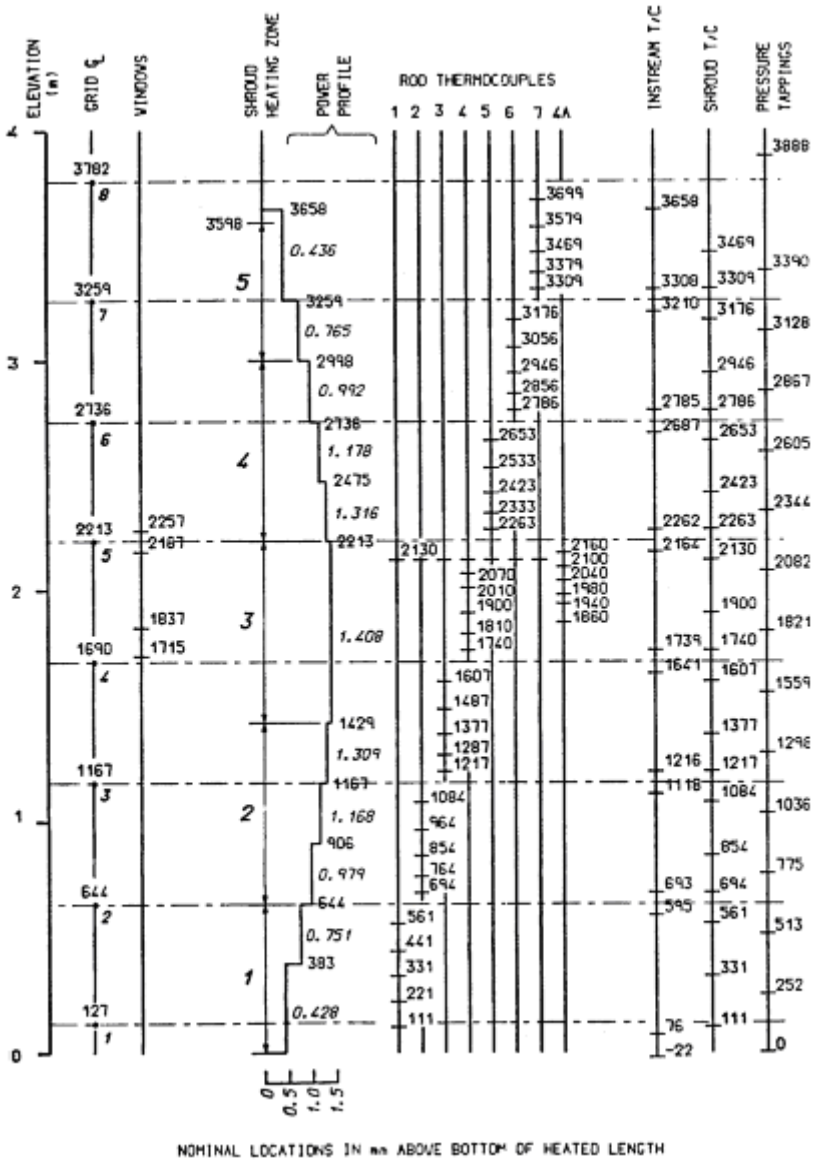

Figure A10.3 Axial Locations in Test Section.

droplet breakup and slowing down of larger droplets. There is insufficient data presented to draw an independent conclusion of these effects.

There were additional pressure taps placed along the shroud such that the pressure drops across the spacer grids were obtained as well as the frictional pressure drop in the rod bundle section. The pressure drop information was used to infer void fraction; however, there was no frictional or acceleration pressure drop corrections to the data such that the void fractions given for ACHILLES are lower then those expected.

The shroud had windows at the mid-plane for photographic purposes with the view being through specific rows of heater rods. The windows were very small such that they could be heated by the rods during heat-up before each test. The windows were set back from the inside edge to avoid direct droplet impact which would have caused the window to wet. From the report, it appears that the windows would stay dry until the quench front was within the grid span where the windows were located. One could interpret this as having the top of the froth front approaching the window before the window wetted.

Tests were performed using a four-cylinder piston pump which superimposed an oscillating flow on the forced flooding rate. The period and magnitude of the flow and oscillation frequency could be adjusted for different sensitivity tests. The bi-directional flow probe showed reverse flow, but is not clear if “real” reverse flow occurred. One significant observation is that with oscillatory flow, the grids quickly rewet as compared to constant forced injection flow. The same situation occurred for initially high injection flows.

An improved photographic droplet diameter and velocity measuring technique was developed as part of the ACHILLES program in which a pulse of green light was shined into the open camera shutter, followed by a pulse of red light. The duration of each pulse was short and there was a fixed time between the two pulses. This approach produced two images of a droplet which were of different color such that the drop size and velocity could be inferred from the prints. The filming rate was 100 frames/s; clips of shots were taken during a given test. Two cameras were also able to focus on different subchannels such that a reasonable droplet distribution across the bundle could be determined. It was observed that the droplet flow was not uniform with more liquid in the outermost channel near the wall. The outermost channel has the larger hydraulic diameter and hence the greater steam flows as compared to the inner regions of the bundle which could explain the observed trend. The report included droplet distribution plots for selected tests.

The test matrix for the low flooding rate tests is given in Table A10.1. One parameter to note is that they purposely controlled the power such that very high heater rod temperatures never occurred and the maximum temperatures were very similar. Details of the reference test and the effects for the different sensitivity tests are given in Reference R23. The temperature rise values were different. Table A10.2 gives the test numbers for the droplet distribution experiments. Table A10.3 gives the conditions for the single-phase air flow distribution experiments and for the voidage distribution experiments. Each series of tests is discussed in Reference R22. The test matrix for the best-estimate or realistic Reflood tests is given in Table A10.4 from Reference R25.

The authors did perform a similar analysis as in the FLECHT and FLECHT-SEASET tests in which the actual quality was calculated at the bundle cross sections where vapor measurements existed. The same or similar exit flow measurements were made in the ACHILLES tests as in the FLECHT and FLECHT-SEASET tests such that a bundle heat and mass balance could be determined. However, the authors did not attempt to separate the radiation component from the total measured heat transfer such that their estimates of the convective dispersed flow film boiling heat transfer results in higher heat transfer coefficients then would be the case in the FLECHT and FLECHT-SEASET experiments. However, very similar trends were observed, with very low vapor Reynolds number flows and enhancement of the dispersed flow film boiling heat transfer above the single phase convection heat transfer limit for the same fluid conditions.

The effects of the spacer grids were analyzed and a correlation was suggested for the convective enhancement of the local heat transfer downstream of the grid. There were also some very informative plots of the vapor temperatures and the spacer grid temperatures which showed that when the grid quenches, the vapor temperature downstream of the grid decreases.

The axial distribution of the heater rod thermocouples gave an excellent indication of the quench front along the bundle. These authors did display their data more as axial plots for different time periods such that additional information good be obtained with fewer figures. Variable reflood rates, oscillatory flooding rates, and stepped flooding rates would easily quench the spacer grids and they remained wetted throughout the transient. The very high flooding rates also quenched the miniature thermocouples used to measure the vapor temperature. Some of these thermocouples could dry out later in the tests and would indicate the presence of superheated vapor.

The best-estimate tests had more favorable test initial conditions such that the heat transfer was higher and the bundle would quench more easily. The same or similar phenomenon was observed in these tests excepting that the transients were shorter and the temperatures were lower.

Single-phase heat transfer and flow tests were also conducted using air as the fluid. A specially constructed hot film probe was used for the air velocity distribution which confirmed that a bypass effect was occurring in the ACHILLES bundle due to the large excess flow area located on the outside edge of the bundle between the heater rods and the shroud. Single-phase effects of the spacer grids were also determined and compared to a previous correlation. We need to verify the axial distribution of the thermocouples in the RBHT test to make sure that we can detect the decaying heat transfer trend downstream of the spacer grids.

One of the more unique data obtained in the ACHILLES program is the droplet or liquid distribution across the bundle using the photographic technique. Again, this distribution is distorted and shows more liquid at the edge of the bundle where the steam mass flow is higher due to the increased bypass flow at this location. The opposite would be expected in an infinite bundle since the center rods would be hotter creating a thermal syphon which should result in increased entrainment.

Conclusions

The ACHILLES Reflood experiments potentially represent some of the best reflood data available for computer code validation. However, a two-channel model which includes crossflow should be used to represent the inner region of the bundle which has the correct flow are per rod, while an outer channel would represent the outer region of the bundle where there is excess flow area. Also, the computer code would have to model the housing or shroud which also supplies energy to the fluid. Computer codes such as the TRAC- P series, and COBRA-TF and COBRA-TRAC have the ability to model these effects. However, the flow diversion, excess flow area, and housing heat release effects must be assessed as test distortions. Also, if they are first order effects, it will be difficult to determine what models in the candidate code need improving since the test distortions could mask the model requirements resulting in compensating error being introduced into the code.

There is some unique data from the ACHILLES tests which are not available from other tests such as the subchannel droplet distribution data, spacer grid loss coefficient data, instrumentated spacer grid and local fluid temperature data, along with very finely spaced heater rod thermocouple data which shows the heat transfer effects of the spacer grids and quench front. The differential pressure data was taken using small spans both between grids and across spacer grids. This data needs to be corrected for frictional pressure drop and acceleration pressure drop in order to be used for inferring the local void fraction. Once this is performed, the local heat transfer can then be correlated with the void fraction.

The tests cover a wide range of conditions which are equally applicable to evaluation of model calculations as well as best-estimate reflood conditions such that an ample set of data is available. Also the tests include oscillating inlet flow, stepped forced flooding rate tests, and gravity reflood tests.

It is strongly recommended that these data be screened and selected ACHILLES tests be obtained from CEGB and added to the NRC data bank and analyzed with the TRAC-M code and COBRA-TF. These tests can also be used for comparison purposes with the Rod Bundle Heat Transfer Tests.

Table A10.1 Summary of Low Flooding Rate Reflood Experiments

Run Number	Description	Pressure bar	Steady Reflood Rate cm/s	Inlet Subcooling °C	Initial Rod Power KW	Initial Temp °C	Results at 2.13 m		Grid Centre Rewet Time		
							Max Temp (°C)	Rewet Time (s)	Grid 4 (s)	Grid 5 (s)	Grid 6 (s)
Forced Reflood											
A1R027	Medium Constant Power	2.4	2.0	28	2.0	662	879	418	120	189	207
A1R028	High Constant Power	2.1	2.0	22	2.5	654	964	606	121	283	452
A1R029	90% ANS + 2σ	2.1	2.0	24	3.9	651	1082	678	141	382	532
A1R030	Base Case (70% ANS + 2σ)	2.1	2.0	24	3.0	651	971	515	120	263	323
A1R032	50% ANS + 2σ	2.1	2.0	24	2.3	653	879	416	120	206	199
A1R033	Low Flow, Constant Power	2.1	1.0	22	1.5	654	960	589	206	416	608
A1R035	Maximum Flow	2.2	10.0	25	3.0	652	666	210	27	22	23
A1R036	Maximum Flow and Subcooling	2.1	10.0	55	3.0	649	682	154	32	24	24
A1R037	Low Flow, Decreasing Power	2.1	1.0	23	1.8	652	960	533	130	264	344
A1R040	Varying Flow	2.1	Fig 56	23	3.0	648	889	571	9	3	3
A1R042	Base Case Repeat 1	2.1	2.0	23	3.0	653	974	525	125	240	304
A1R044	Low Pressure	1.4	2.0	24	3.0	652	987	687	136	312	450
A1R045	High Pressure	4.1	2.0	23	3.0	650	947	340	106	150	198
A1R046	Low Initial Temperature	2.1	2.0	23	3.0	505	878	453	90	143	91
A1R047	High Inlet Subcooling	2.1	2.0	53	3.0	653	984	460	113	183	288
A1R048	High Flow	2.1	4.0	24	3.0	654	801	355	32	31	18
A1R053	Base Case Repeat 2	2.1	2.0	24	3.0	653	974	522	96	160	272
A1R055	80% ANS + 2σ	2.1	2.0	24	3.4	655	1014	582	96	214	346
A1R056	60% ANS + 2σ	2.1	2.0	24	2.6	652	923	453	96	149	200
A1R059	4 Unpowered Rods	2.1	2.0	24	3.0	654	947	482	97	155	231
A1R061	4 Unpowered Rods, Low Shroud Temp	2.1	2.0	25	3.0	653	919	452	81	117	166
A1R063	1 Unpowered Rod	2.1	2.0	25	3.0	656	963	520	77	144	240
A1R072	High Shroud Power	2.1	2.0	24	3.0	657	963	588	90	161	287
A1R073	Low Shroud Temperature	2.1	2.0	24	3.0	667	958	475	82	73	177
A1R074	Base Case Repeat 3	2.1	2.0	25	3.0	654	969	518	102	104	226
A1R114	Combination of 40 and 61	2.1	Fig 59	16	3.0	657	828	512	2	2	2
A1R117	Very Low Shroud Temperature	2.1	2.0	24	3.0	675	909	345	68	115	227
Flow Oscillations											
A1R050	Maximum Amplitude	2.1	2.0	17	3.0	652	966	690	10	10	10
Gravity Reflood											
A1G041	Gravity Base Case	2.3	2.0	27	3.0	656	897	463	20	6	5
A1G051	High Pressure	4.2	2.0	26	3.0	651	850	313	2	2	2
A1G052	High Inlet Subcooling	2.2	2.0	53	3.0	652	907	405	2	4	3

Table A10.2 Droplet Distribution Experiments

Run No	Description	Sub-Chan	Window	Inlet Sub Cool (C)	Init Temp at 2.13 m Rod E5 (C)	Init Temp at 2.13 m Shroud (C)	Results at 2.13 m Max Temp (C)	Results at 2.13 m Rewet Time (s)
Hot Shroud Experiments								
A3R014		D0	3	23	647	599	960	540
A3R025		D0	3	24	645	598	947	521
A3R021		D1	3	23	644	599	947	523
A3R019		D2	3	19	647	599	953	552
A3R020		D3	3	24	648	598	952	528
A3R018		D4	3	18	645	597	940	553
A3R001	Base Case	D5	3,4	23	646	600	958	526
A3R002		D5	1,2	23	645	597	961	524
A3R006		D5	3,4	23	649	595	950	527
A3R013		D6	3	23	648	600	950	519
A3R003		D7	3,4	21	645	598	960	540
A3R012		D8	3	25	646	597	950	510
A3R005		D9	3,4	23	646	600	960	535
Cool Shroud Experiments								
A3R017		D0	3	21	657	399	940	498
A3R022		D1	3	23	656	399	946	500
A3R023		D2	3	22	656	399	947	510
A3R024		D3	3	21	656	400	941	498
A3R009	Base Case	D5	3,4	23	652	399	945	493
A3R008		D7	3,4	23	650	399	950	492
A3R011		D8	3	24	652	398	940	491
A3R010		D9	3	23	653	398	940	473

Table A10.3 Airflow and Voidage Distribution Experiments

Air Flow Distribution Experiments

Run No	Description	Inlet Re No	Cluster Power (kW)	Cluster Temp (°C)	Scan Period (s)	Log Time (s)
Repeat Heat Transfer Experiments						
A3A015	Examined	5000	15	350	2	2000
A3A016	temperature	5000	15	350	2	2000
A3A026	asymmetry	5000	15	350	2	2000
A3A027		5000	15	350	2	2000
A3A036		1000	3	350	8	8000
A3A035		1750	5.5	350	5	5000
A3A034		3000	10	350	3	3000
A3A033		9000	25	350	1	1000
Isothermal Flow Distribution Experiments						
A3A029	Measured	3000	0	23	2	2000
A3A030	radial	3000	0	21	2	2000
A3A031	Velocity	3000	0	22	2	2000
A3A028		5000	0	23	2	2000
A3A032		5000	0	23	2	2000

Voidage Distribution Experiments

Run No	Description	Press (bar)	Flow Rate (dm^3/s)	Sub-Cool (°C)	Cluster Power (kW)
Air/Water					
A3L037	Commission	1.0	3.0	-	0
Boil-down					
A3L038		1.2	d/c	-	20
A3L039		1.0	d/c	-	20
Steady-boiling					
A3L040		1.2	d/c	4	20
A3L041		1.2	0.08	4	20
A3L042		1.2	0.08	4	40
A3L043		1.2	0.08	4	60
A3L044		1.2	0.08	4	80
A3L045	Base Case	1.2	0.08	50	40
A3L046	Power	1.2	0.08	50	60
A3L047	Flow	1.2	0.11	50	40
A3L048	Pressure	2.0	0.08	50	40
A3L049	A3R condition	2.0	0.15	86	105

d/c - downcomer connected to shroud vessel

Table 10A.4 Summary of Best Estimate Reflood Experiments

FORCED REFLOOD

Run Number	Description	Rig Pressure (bar)	Initial Flow (cm/s)	Surge Volume (dm³)	Subcooling (K)	Initial Temperature (°C)	Quench front Elevation after Initial Surge (m)	Results at 2.13 m Max Temp (°C)	Results at 2.13 m Rewet Time (s)
A1B088[1]	High Initial Temp	3	30	19.2	10	650	0.19	720	266
A1B091	High Initial Temp	3	30	20.0	10	650	0.34	716	254
A1B092	Low Initial Temp	3	30	20.1	10	500	0.56	624	172
A1B094	Base Case Repeat	3	30	20.5	10	550	0.53	658	184
A1B095	High Inlet Subcooling	3	30	20.9	50	550	0.66	621	183
A1B096	Low Initial Temp	3	30	20.8	10	400	0.70	536	115
A1B097	Low Pressure	2	30	21.4	10	550	0.42	696	333
A1B098[2]	Low Downcomer Level	3	30	10.8	10	550	0.32	683	194
A1B099	EM Comparison	3	30	20.6	20	650	0.44	737	319
A1B100	High Surge Rate	3	60	18.0	10	550	0.52	666	233
A1B101	High Surge Rate	3	100	21.4	10	550	0.53	665	223
A1B112	Base Case	3	30	21.2	10	550	0.43	666	240

Notes
All Condition as Base Case unless stated.
[1] Initial Temperature high at bottom of test-section only
[2] Initial Downcomer Level 50%.

NATURAL REFLOOD

Run Number	Description	Rig Pressure (bar)	Surge Volume (dm³)	Subcooling (K)	Initial Temperature (°C)	OR1/OR2[1]	Quench front Elevation after Initial Surge (m)	Results at 2.13 m Max Temp (°C)	Results at 2.13 m Rewet Time (s)
A1B087	Flow Resistance	3	9.3	10	650	0/0	0.33	734	265
A1B089	Flow Resistance	3	25.9	10	650	0/300	0.42	798	308
A1B102	Flow Resistance	3	21.7	10	650	25/300	0.33	812	300
A1B103	Flow Resistance	3	18.9	10	650	35/200	0.33	796	278
A1B104	Flow Resistance	3	22.9	10	550	35/200	0.68	755	268
A1B105	High Initial Temp	3	17.1	10	650	35/100	0.33	784	275
A1B106	Base Case	3	19.0	10	550	35/100	0.38	738	248
A1B107	Low Initial Temp	3	20.6	10	400	35/100	0.74	613	169
A1B108	High Inlet Cooling	3	24.3	50	550	35/100	0.7	740	214
A1B109	Low Pressure	2	24.0	10	550	35/100	0.57	777	341
A1B110[2]	Odd Initial Temp	3	23.7	10	550	35/100	0.96	709	225
A1B111	Flow Resistance	3	10.0	10	550	35/0	0.16	711	254
A1B123	Base Case Repeat	3	18.1	10	550	35/100	0.33	732	254

Notes
All Condition as Base Case unless stated.
[1] OR1 & OR2 k values based on Area = 3578 mm².
[2] Initially, Bottom 1.0 m of Cluster at Saturation Temperature.

APPENDIX A11. LITERATURE REVIEW

Appendix A11: Lehigh 9-Rod Bundle Tests

Dates When Tests Were Performed: 1982 - 1986

References:

R27 Tuzla, K., Unal, C., Badr, O., Neti, S., Chen, J.C., "Thermodynamic Nonequilibrium in Post-Critical-Heat-Flux Boiling in a Rod Bundle," NUREG-CR 5095, Vol. 1-4, June 1998.

R28 Unal C., Tuzla, K., Badr, O., Neti, S., Chen, J.C., "Convective Boiling in a Rod Bundle: Traverse Variation of Vapor Superheat Temperature Under Stabilized post-CHF Conditions," Int. J. Heat and Mass Transfer, Vol. 34, No. 7, pp. 1695-1706, 1991.

Availability of Data:

The data for these experiments is contained in Volumes 2 - 4 of Reference R27. Raw data are not available from the original source.

Test Facility Description, Types of Tests

The rods were 9.5 mm (0.374 in) in diameter and were arranged in a square pitch of 12.6 mm (0.496 in) as shown in Figure A11.1. The actual test section of the facility was 1.22 m (4 ft) long with one spacer grid located at 0.762 m (30 in) from the bottom as shown in Figure A11.2. The rods had a linear power profile to provide a constant heat flux over the length of the test section. Each subchannel had the same wetted perimeter and this resulted in about 39 percent of excess flow area in the bundle. The excess flow area was to account for the housing effect.

Coolant Mass Flow Rate	6.6×10^{-4} - 0.1694 kg/s (3×10^{-4} - 0.077 lbm/s)
Inlet Subcooling	40 - 0.55 degrees C (72 - 1 degrees F)
Pressure	102.042 - 119.97 kPa (14.8 - 17.4 psi)
Initial Shroud Temperature	301.67 - 398.89 degrees C (575 - 750 degrees F)
Initial Rod Temperature	593.33 degrees C (1100 degrees F)
Heat Flux	5 - 4312 kW/m^2
Linear Heat Generation (Constant Over the Length)	1.3123 to 11.483 kW/m (0.4 to 3.5 kW/ft)
Constant Flooding Rates	1.016 to 4.064 mm/s (0.04 to 0.16 in/s)

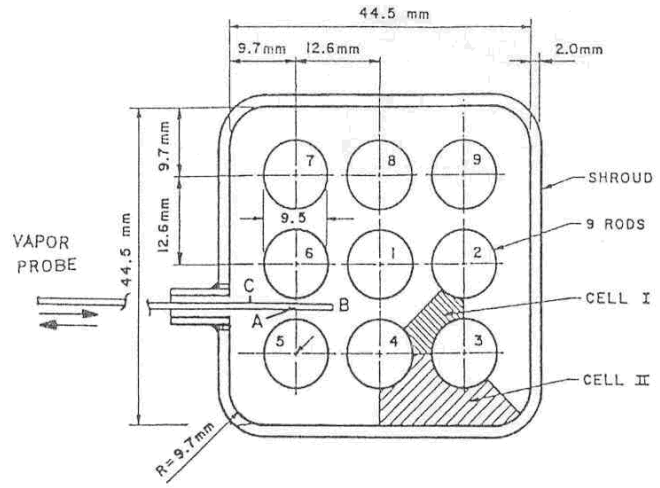

Figure A11.1 Cross-Sectional View of Test Bundle.

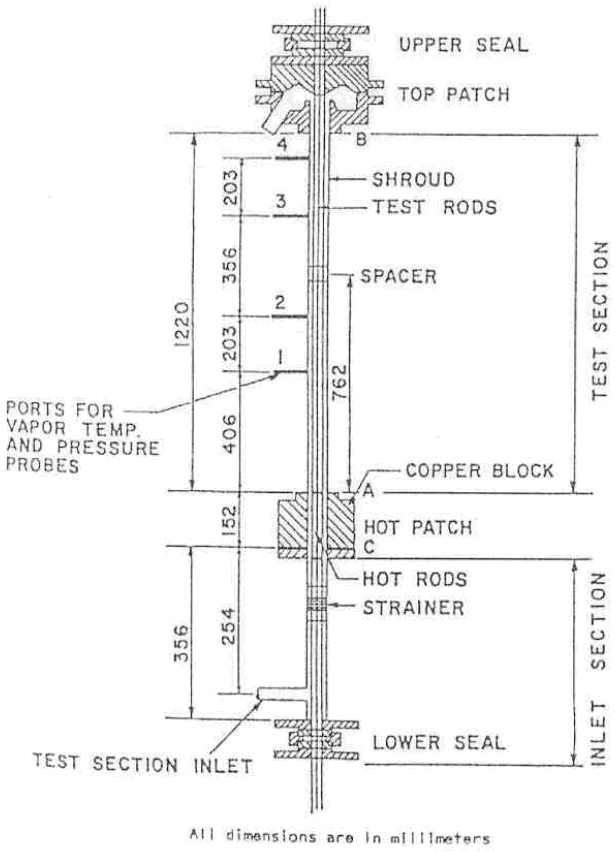

Figure A11.2 Schematic of Test Section Support System.

Instrumentation and Data From Tests

There were eight thermocouples imbedded in each of the nine heater rods at 152.4 mm (6 in) intervals. Due to limitations of the data collection system, only 80 channels could be monitored for any given test. The arrangement of thermocouple elevations has one disturbing shortcoming. There are no thermocouples located at identical elevations and angles to allow for checking of the symmetry of the test section. The pressure cells were spaced too far apart to be able to make a calculation of the void fraction. Two aspirating steam probes were located at 609.6 mm (24 in) and 965.2 mm (38 in), respectively. These probes were traversed through the bundle in several experiments to measure the traverse variation of vapor superheat. The vapor temperature difference was reduced from 120 to 40 degrees C superheat when the inlet quality was increased from 0.04 to 0.40. Effects of dispersed droplet cooling were evident after the grid as well.

The data presented in Figures A11.3 to A11.7 and Tables A11.1 to A11.4 shows a pronounced effect caused by the spacer grid located at the 762 mm (30 in) elevation. This information might be used in evaluating the effects of spacer grids in two-phase-dispersed droplet flow. The data also showed a small error caused by the steam probes.

Conclusions

This series of tests is of limited use to the RBHT Program. The information gathered using a traversing steam probe is the most significant contribution.

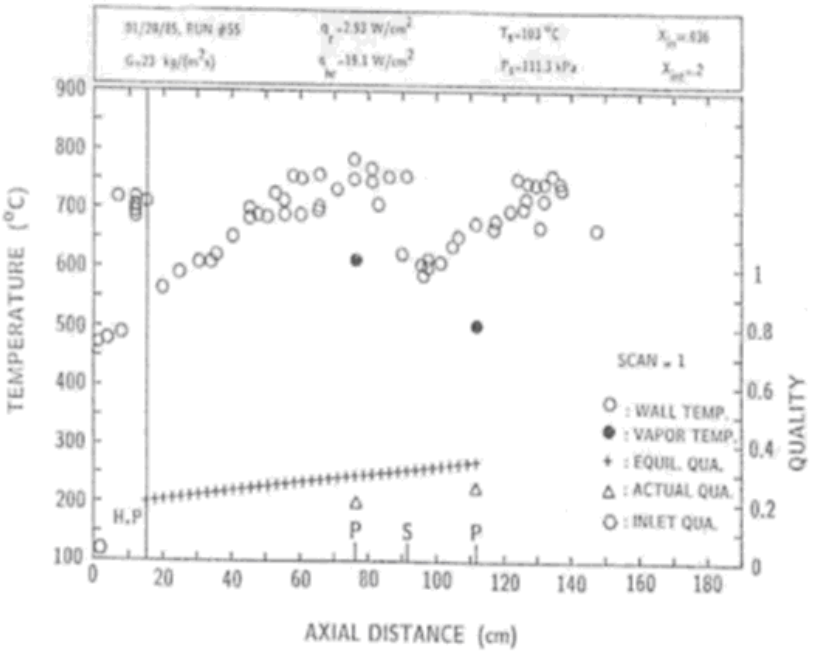

Figure A11.3 Sample Plot of Temperature and Steam Quality Data for the Stabilized Quench Front Experiments.

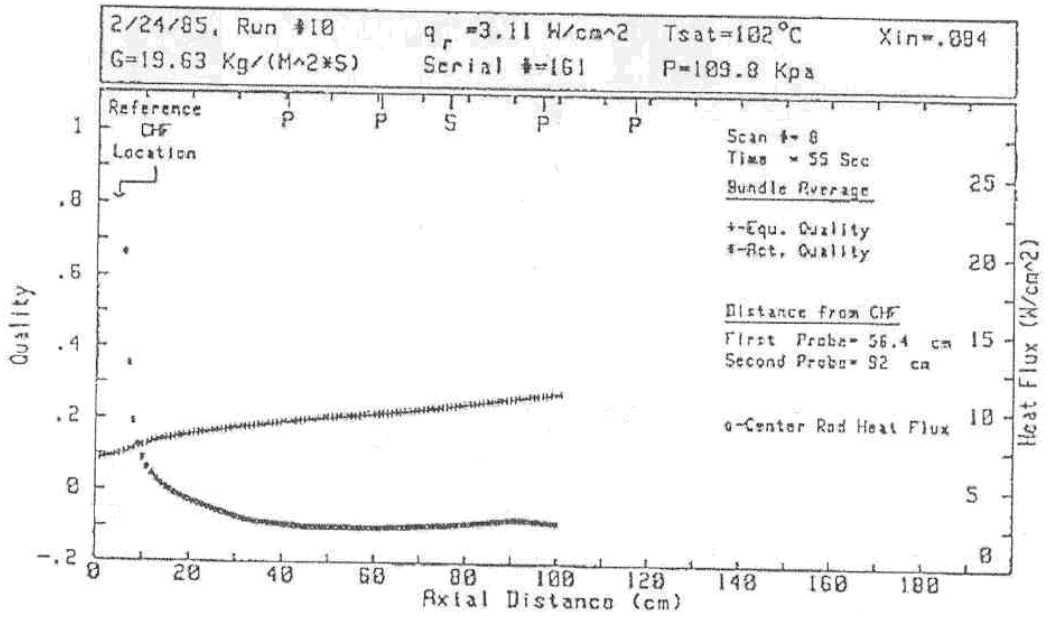

Figure A11.4 Sample Plot of Heat Flux and Steam Quality Data for the Advancing Quench Front Experiments.

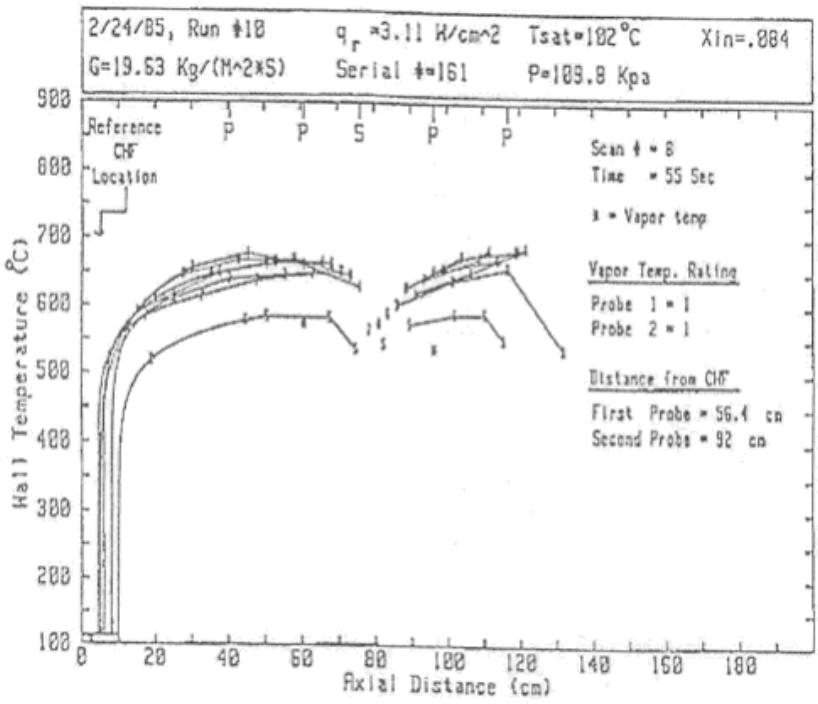

Figure A11.5 Sample Plot of Rod and Steam Temperature Data for the Advancing Quench Front Experiments.

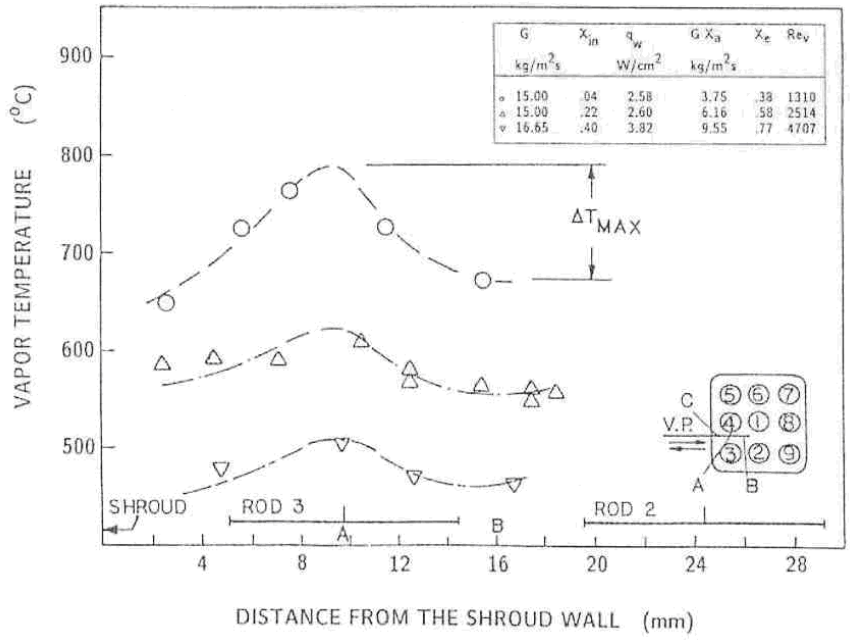

Figure A11.6 Typical Transverse Vapor Temperature Profiles for Various Vapor Qualities.

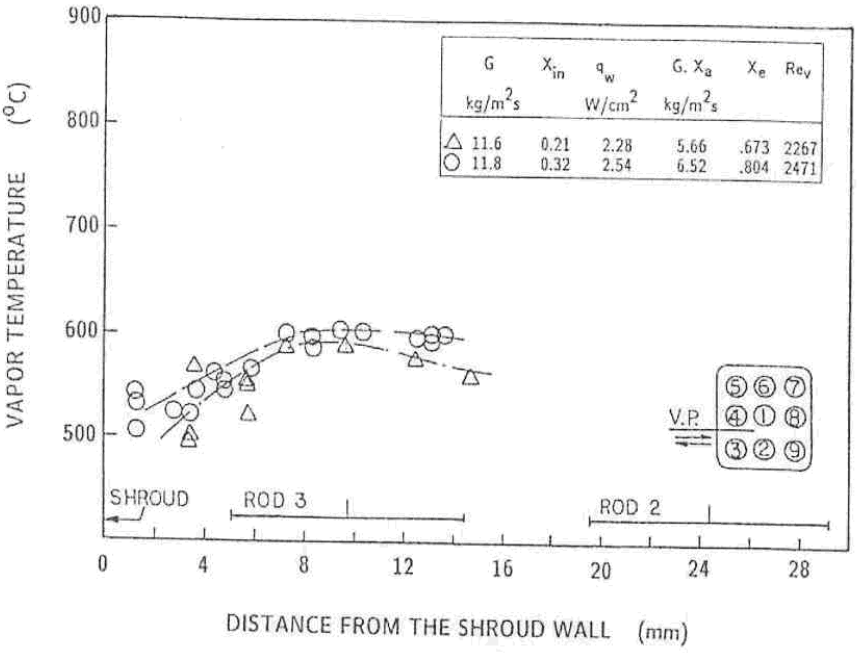

Figure A11.7 Typical Transverse Vapor Temperature Profiles Downstream of the Grid Spacer.

Table A11.1 Sample Tabulation of a Stabilized Quench Front Data Point (See Table A11.2 for Nomenclature)

INLET QUALITY	= .219	
INLET MASS FLUX	= 15.00	Kg/M^2s
TEST-ROD HEAT FLUX	= 2.60	W/cm^2
HOT-ROD HEAT FLUX	= 16.89	W/cm^2
HOT-PATCH HEAT FLUX	= 12.82	W/cm^2
INLET PRESSURE	= 110.0	Kpa
SAT. TEMPERATURE	= 102.3	C

VAPOR SUPERHEAT TEMPERATURE

AT Z=76.2 CM TV1 = 561.0 C	AT Z=111.8 CM TV2 = 366.0 C
RATING OF TV1 = 1	RATING OF TV2 = 4
XA1 = .408	XA2 = .527
XE1 = .579	XE2 = .651

SHROUD				TEST RODS							
ZS (CM)	QRS (W/CM2)	ZS (CM)	TS (C)	ZT (CM)	XE	TR1 (C)	TR3 (C)	TR4 (C)			
18.7	.93	1.3	501.	15.2	.45	701					
25.9	1.24	5.5	495.	20.3	.46			558			
33.2	1.26	9.7	475.	25.4	.48		584				
40.4	1.21			30.5	.49	596					
47.5	1.04	34.3	582.	35.6	.50			610			
54.7	.81	60.2	669.	40.6	.51		643				
61.9	.57	66.1	689.	45.7	.52	674			TR9	687	
69.0	.50	83.1	686.	48.3	.52				TR7	696	
76.2	.50	90.2	611.	50.8	.53			672			
83.4	.43	97.8	619.	53.5	.53				TR6	729	
90.5	1.38	104.9	643.	55.9	.54		709		TR5	683	
97.7	1.25	117.4	679.	58.4	.54				TR8	746	
104.9	.98	125.7	695.	61.0	.55	738					
112.1	.82	130.8	676.	66.0	.56			746			
119.2	.43			71.1	.57		734				
126.4	.20			76.2	.58	772		750			
133.6	1.06			81.3	.59			747	TR2	756	
				86.4	.60		758				
				91.4	.61	757					
				96.5	.62			617	TR2	609	
				101.6	.63		638				
				106.7	.64	687					
				111.8	.65			712			
				116.8			694				
				121.9		728					
				124.5					TR7	770	
				127.0				770	TR2	739	
				129.4					TR6	774	
				132.1			743		TR5	768	
				134.6					TR8	772	
				137.1		768			TR9	746	
				147.3			700				

Table A11.2 Definition of Parameters Used in Table A11.1

QRS	= shroud heat flux (local)
TR 1	= surface temperature of test rod number 1
TR 3	= surface temperature of test rod number 3
TR 4	= surface temperature of test rod number 4
TR 5	= surface temperature of test rod number 5
TR 6	= surface temperature of test rod number 6
TR 7	= surface temperature of test rod number 7
TR 8	= surface temperature of test rod number 8
TR 9	= surface temperature of test rod number 9
TS	= shroud surface temperature
TV 1	= vapor temperature obtained from first probe
TV 2	= vapor temperature obtained from second probe
XA 1	= actual quality at the first vapor probe location
XA 2	= actual quality at the second vapor probe location
XE	= equilibrium quality
XE 1	= equilibrium quality at the first vapor probe location
XE 2	= equilibrium quality at the second vapor probe location
ZS	= shroud axial location (reference to hot-patch inlet)
ZT	= Test section axial location (reference to hot-patch inlet)

Table A11.3 Sample Tabulation of an Advancing Quench Front Data Point (See Table A11.4 for Nomenclature)

SERIAL NO: 161

INLET QUALITY	= .084		
INLET MASSFLUX	= 19.63 Kg/M^2s	TEST-ROD ELEC FLUX	= 3.11 W/cm^2
INLET PRESSURE	= 109.0 KPa	SCAN NUMBER	= 8
SAT. TEMPERATURE	= 102.3 C	TIME OF SCAN	= 55 SEC

DF CONDITIONS, RATING=2

DEV.	DIS. CM	VEL. CM/S	QUAL.
R1	4.5	.16	.093
R4	5.1	.13	.095
R3	8.1	.00	.111
R6	6.0	.15	.100
R7	4.5	.13	.093
R8	7.9	.12	.110
SH	9.9	.11	.120

VAPOR TEMPERATURE

AT Z= 61.0 CM	TV1 = 575 C		
RATING OF	TV1 = 1		
	XA1 = .149		
	XE1 = .213		
DIST. FROM CHF	= 56.4 CM		
AT Z= 94.5 CM	TV2 = 534 C		
RATING OF	TV2 = 1		
	XA2 = .191		
	XE2 = .266		
DIST. FROM CHF	= 92.0 CM		

SHROUD

ZS CM	QRS W/CM^2	ZS CM	TS C
3.6	1.4	17.2	517
10.8	1.8	45.3	577
17.9	1.2	51.0	583
25.1	1.2	69.0	602
32.3	1.1	75.3	633
39.4	1.0	82.8	543
46.6	.9	89.8	572
53.8	.8	102.0	588
60.9	.8	110.0	509
68.1	.9	115.0	550
75.3	1.2		
82.5	1.2		
89.6	.9		
96.8	.8		
104.0	.7		
111.1	.6		
118.3	.5		

TEST RODS

ZT CM	XE	TR1 C	TR4 C	TR3 C	TR6 C	TR7 C	TR8 C
0.0	.084	106	—	—	—	—	—
2.5	.089	—	—	—	—	100	—
5.1	.095	—	122	—	—	—	—
7.6	.109	—	—	—	519	—	—
10.2	.121	—	—	521	—	—	—
12.7	.133	—	—	—	—	—	545
15.2	.141	590	—	—	—	—	—
17.8	.147	—	—	—	—	503	—
20.3	.153	—	609	—	—	—	—
22.9	.159	—	—	—	609	—	—
25.4	.163	—	—	610	—	—	—
27.9	.168	—	—	—	—	—	644
30.5	.172	655	—	—	—	—	—
33.0	.176	—	—	—	—	613	—
35.6	.180	—	645	—	—	—	—
38.1	.184	—	—	—	648	—	—
40.6	.188	—	—	658	—	—	—
43.2	.192	—	—	—	—	—	666
45.7	.195	676	—	—	—	—	—
48.3	.198	—	—	—	—	637	—
50.8	.202	—	661	—	—	—	—
53.3	.205	—	—	—	663	—	—
55.9	.207	—	—	645	—	—	—
58.4	.210	—	—	—	—	—	660
61.0	.213	659	—	—	—	—	—
63.5	.216	—	—	—	—	647	—
66.0	.219	—	663	—	—	—	—
68.6	.222	—	—	—	660	—	—
71.1	.226	—	—	650	—	—	—
73.7	.230	—	—	—	—	—	643
76.2	.234	626	—	—	—	—	—
78.7	.238	—	—	—	—	563	—
81.3	.242	—	572	—	—	—	—
83.8	.247	—	—	—	587	—	—
86.4	.251	—	—	601	—	—	—
88.9	.255	—	—	—	—	—	626
91.4	.259	619	—	—	—	—	—
94.0	.263	—	—	—	—	639	—
96.5	.267	—	651	—	—	—	—
99.1	.270	—	—	—	654	—	—
101.6		—	—	637	—	—	—
104.1		—	—	—	—	—	673
106.7		651	—	—	—	—	—
109.2		—	—	—	—	672	—
111.8		—	682	—	—	—	—
114.3		—	—	—	670	—	—
116.8		—	—	657	—	—	—
119.4		—	—	—	—	—	682
121.9		686	—	—	—	—	—

Table A11.4 Definition of Parameters Used in Table A11.3

DEV	= device
DIS	= distance
QRS	= shroud's heat flux (local value)
QUAL	= equilibrium quality
R1	= test rod #1
R3	= test rod #3
R4	= test rod #4
R6	= test rod #6
R7	= test rod #7
R8	= test rod #8
SH	= shroud
TR 1	= surface temperature of test rod number #1
TR 3	= surface temperature of test rod number #3
TR 4	= surface temperature of test rod number #4
TR 6	= surface temperature of test rod number #6
TR 7	= surface temperature of test rod number #7
TR 8	= surface temperature of test rod number #8
TS	= surface temperature of the shroud
TV1	= vapor temperature of first vapor probe elevation
TV2	= vapor temperature of second vapor probe elevation
XA 1	= actual quality at the first vapor probe location
XA 2	= actual quality at the second vapor probe location
XE	= equilibrium quality
XE 1	= equilibrium quality at the first vapor probe location
XE 2	= equilibrium quality at the second vapor probe location
ZS	= shroud axial location (reference to hot-patch outlet)
ZT	= test section axial location (reference to hot-patch outlet)

APPENDIX B1. RADIATION HEAT TRANSFER NETWORK AND CALCULATION OF PI GROUPS

Description of the Radiation Network

In order to calculate the radiative heat transfer from the rods to the surfaces and the housing, a six node radiation network (Figure 6.3) has been developed which includes radiation heat transfer to droplets and vapor. The network resistances discussed in Section 7 (Refs. 7-2, 7-3 and 7-4) are defined as follows:

$$\frac{1}{R_{ii}} = \frac{\varepsilon_w}{1-\varepsilon_w} A_i$$

$$\frac{1}{R_{ij}} = (1-\varepsilon_l)(1-\varepsilon_v) A_i F_{ij}$$

$$\frac{1}{R_{il}} = \varepsilon_l (1-\varepsilon_v) A_i$$

$$\frac{1}{R_{iv}} = \varepsilon_v (1-\varepsilon_l) A_i$$

$$\frac{1}{R_{lv}} = \varepsilon_l \varepsilon_v \sum_{i=1}^{4} A_i$$

where

A_i radiating area per unit length for the i-th radiating wall surface
F_{ij} view factor from node 'i' to node 'j'
ε_w wall emissivity
ε_l, ε_v drop and vapor emissivity

The view factors are calculated by summing up single rod-to-rod, rod-to-housing and rod-to-surfaces view factors which are calculated with the VIEWFAC subroutine of MOXY computer program (Ref. 7-1):

$$F_{12} = \sum_{j} \frac{\sum_{i=1}^{49} A_i F_{ij}}{\sum_{i=1}^{49} A_i}, \quad \text{where } j = j_{CR} \text{ and } i \neq j_{CR} \quad (j_{CR} \text{ are the cold rods indices})$$

$$F_{13} = \sum_j \frac{\sum_{i=1}^{49} A_i F_{ij}}{\sum_{i=1}^{49} A_i}, \quad \text{where} \quad j = j_S \quad \text{and} \quad i \neq j_S, j_{CR} \quad (j_S \text{ are surfaces indices: 1,7,43,49})$$

$$F_{14} = \frac{\sum_{i=1}^{49} A_i F_{iN}}{\sum_{i=1}^{49} A_i}, \quad \text{where} \quad i \neq j_S, j_{CR}$$

$$F_{23} = \sum_j \frac{\sum_{i=1}^{49} A_i F_{ij}}{\sum_{i=1}^{49} A_i}, \quad \text{where} \quad j = j_S \quad \text{and} \quad i = j_{CR}$$

$$F_{24} = \frac{\sum_{i=1}^{49} A_i F_{iN}}{\sum_{i=1}^{49} A_i}, \quad \text{where} \quad i = j_{CR}$$

$$F_{34} = \frac{A_1 F_{1N} + A_7 F_{7N} + A_{43} F_{43N} + A_{49} F_{49N}}{A_1 + A_7 + A_{43} + A_{49}}$$

Assuming that the droplet and vapor media are optically thin, the drop and vapor emissivities ε_l and ε_v are calculated with the following formula:

$$\varepsilon_l = 1 - e^{-a_l L_m}$$

$$\varepsilon_v = 1 - e^{-a_v L_m}$$

where the beam length L_m is defined as follows for rod bundle geometry:

$$L_m = 0.85 D_h$$

Assuming the droplets in the geometric scattering regime, the liquid absorption coefficient is calculated by the following formula which is based on Reference 7-4 with the additional assumption of considering a single drop size group (Sauter mean diameter):

$$a_l = 0185 \pi . d^2 n_d$$

where d is the drop Sauter mean drop diameter (m) while the number of droplet per unit volume n_d is calculated from the void fraction:

$$n_d = \frac{6(1-\alpha)}{\pi.d^3}$$

where the Sauter mean diameter and the void fractions are inputs in the program. The vapor absorption coefficient a_v is calculated with the following formula:

$$a_v = 9.84 \cdot 10^{-5} P \left[18.66 \left(\frac{555}{T_w} \right)^2 - \left(\frac{555}{T_w} \right)^4 \right]$$

where P is the pressure (kPa) and T_w is the wall temperature (K).

Solution of the Radiation Network

Kirchhoff Law is applied to nodes 1, 2, 3 and 4:

$$\frac{J_1 - \sigma.T_{hr}^4}{R_{11}} + \frac{J_1 - J_2}{R_{12}} + \frac{J_1 - J_3}{R_{13}} + \frac{J_1 - J_4}{R_{13}} + \frac{J_1 - \sigma.T_l^4}{R_{1l}} + \frac{J_1 - \sigma.T_v^4}{R_{1v}} = 0.0$$

$$\frac{J_2 - \sigma.T_{cr}^4}{R_{22}} + \frac{J_2 - J_1}{R_{12}} + \frac{J_2 - J_3}{R_{23}} + \frac{J_2 - J_4}{R_{24}} + \frac{J_2 - \sigma.T_l^4}{R_{2l}} + \frac{J_2 - \sigma.T_v^4}{R_{2v}} = 0.0$$

$$\frac{J_3 - \sigma.T_s^4}{R_{33}} + \frac{J_3 - J_1}{R_{13}} + \frac{J_3 - J_2}{R_{23}} + \frac{J_3 - J_4}{R_{34}} + \frac{J_3 - \sigma.T_l^4}{R_{3l}} + \frac{J_3 - \sigma.T_v^4}{R_{3v}} = 0.0$$

$$\frac{J_4 - \sigma.T_h^4}{R_{44}} + \frac{J_4 - J_1}{R_{14}} + \frac{J_4 - J_2}{R_{24}} + \frac{J_4 - J_3}{R_{34}} + \frac{J_4 - \sigma.T_l^4}{R_{4l}} + \frac{J_4 - \sigma.T_v^4}{R_{4v}} = 0.0$$

where J_i are the radiosities in the network nodes.

For a given temperature field (T_{hr}, T_{cr}, T_s, T_h, T_l and T_v), the equations are solved for the unknowns (J_1, J_2, J_3 and J_4). Then the heat rate across each resistance in the network can be calculated as:

$$Q_{ij} = \frac{J_j - J_i}{R_{ij}}$$

The previous procedure has been implemented in the Fortran program called RADNET attached in Appendix B5.

Another input to the RADNET computer program is how hot versus cold rods are lumped together in the bundle. It can be recognized that for given boundary conditions, the result is dependent on how hot and cold rods are lumped together in the model. Sensitivity studies have carried out where the hot rods sub-array has been assumed to be the central rod, the inner 3x3 array or the inner 5x5 array. For example, the Pi group π_{30} (see later) calculated with the three different lumping approaches is:

$$\pi_{30,cr} = 0.567$$

$$\pi_{30,3x3} = 0.388$$

$$\pi_{30,5x5} = 0.345$$

It is important to note that this is the group affected most while the effect of different lumping approach on the other groups is less important. Results from the detailed rod-to-rod model calculations discussed in Section 7 show that the temperature is practically uniform in the inner 3x3 array while the temperature drops in the periphery due to the effect of the housing. Thus, the inner 3x3 hot rods lumping approach is the most appropriate and was chosen in the dimensionless groups calculation.

APPENDIX B2. ROD GRID RADIATION NETWORK FOR RBHT

Inputs

H grid	1.5	in	0.0381	m
N grids	6			
rod diameter	0.374	in	0.0094996	m
rods pitch	0.496062992	in	0.0126	m
rod power	5.6	kW		
pressure	40	psia	272.1088435	kPa
liquid temperature	267	F	403.6955556	K
vapor temperature	1177	F	909.2511111	K
rod temperature	1650	F	1172.028889	K
grid temperature	1376	F	1019.806667	K
void fraction	0.995			
droplets Sauter mean diameter			0.001	m
wall emissivity			0.8	

Calculation

bundle hydraulic diameter			0.011789932	m
droplet density			9554140.127	Ndrp/m^3
liquid absorption coefficient			5.55	m^{-1}
beam length			0.010021442	m
liquid emissivity			0.054100549	
vapor absorption coefficient			0.182435145	m^{-1}
vapor emissivity			0.000542019	
rod area (based on Hgrid) Ar	1.76154	in^2	0.001136475	m^2
grid area (per rod) Ag	2.976	in^2	0.001919996	m^2
1/R11			0.004545901	
1/R22			0.007679985	
1/R12			0.001074409	
1/R1L			6.14506E-05	
1/R1V			5.82665E-07	
1/R2L			0.000103817	
1/R2V			9.84373E-07	
1/RLV			8.96264E-08	
A11			0.005682342	
A22			0.008859194	
A12=A21			-8.96264E-08	
C1			486.4733384	
C2			471.1878606	

APPENDIX B3. ROD GRID RADIATION NETWORK FOR PWR

Inputs

H grid	1.5	in	0.0381	m
N grids	6			
rod diameter	0.374	in	0.0094996	m
rods pitch	0.496063	in	0.0126	m
rod power	5.6	kW		
pressure	40	psia	272.10884	kPa
liquid temperature	267	F	403.69556	K
vapor temperature	1177	F	909.25111	K
rod temperature	1650	F	1172.0289	K
grid temperature	1376	F	1019.8067	K
void fraction	0.995			
droplets Sauter mean diameter			0.001	m
wall emissivity			0.9	

Calculation

bundle hydraulic diameter			0.0117899	m
droplet density			9554140.1	$Ndrp/m^3$
liquid absorption coefficient			5.55	m^{-1}
beam length			0.0100214	m
liquid emissivity			0.0541005	
vapor absorption coefficient			0.1824351	m^{-1}
vapor emissivity			0.000542	
rod area (based on Hgrid) Ar	1.76154	in^2	0.0011365	m^2
grid area (per rod) Ag	2.976	in^2	0.00192	m^2
1/R11			0.0102283	
1/R22			0.01728	
1/R12			0.0010744	
1/R1L			6.145E-05	
1/R1V			5.827E-07	
1/R2L			0.0001038	
1/R2V			9.844E-07	
1/RLV			8.963E-08	
A11			0.0113647	
A22			0.0184592	
A12=A21			-8.963E-08	
C1			1094.4211	
C2			1059.9296	

APPENDIX B4. ROD GRID RADIATION NETWORK FOR BWR

Inputs

H grid	1.5	in	0.0381	m
N grids	6			
rod diameter	0.4830709	in	0.01227	m
rods pitch	0.6377953	in	0.0162	m
rod power	5.6	kW		
pressure	40	psia	272.10884	kPa
liquid temperature	267	F	403.69556	K
vapor temperature	1177	F	909.25111	K
rod temperature	1650	F	1172.0289	K
grid temperature	1376	F	1019.8067	K
void fraction	0.995			
droplets Sauter mean diameter			0.001	m
wall emissivity			0.9	

Calculation

bundle hydraulic diameter			0.0149768	m
droplet density			9554140.1	Ndrp/m^3
liquid absorption coefficient			5.55	m^{-1}
beam length			0.0127303	m
liquid emissivity			0.068215	
vapor absorption coefficient			0.1824351	m^{-1}
vapor emissivity			0.000868	
rod area (based on Hgrid) Ar	2.2752638	in^2	0.0014679	m^2
grid area (per rod) Ag	2.976	in^2	0.00192	m^2
1/R11			0.0132112	
1/R22			0.01728	
1/R12			0.0013666	
1/R1L			0.0001	
1/R1V			1.187E-06	
1/R2L			0.0001309	
1/R2V			1.553E-06	
1/RLV			2.006E-07	
A11			0.014679	
A22			0.018779	
A12=A21			-2.006E-07	
C1			1413.6388	
C2			1059.9923	

APPENDIX B5. FORTRAN PROGRAM RADNET

```
program radnet
c
      dimension f(50,50),area(50)
            dimension pir(50)
      dimension ir(50)
c
      common/cgauss/ a(10,10),b(10),c(10),na
      common/temp/t(10),eb(10),tl,tv,ebl,ebv,q(10)
      common/resist/ r(10,10)
c
      data sig/5.67E-08/
      data pi/3.141592654/
c
c.....input values
      nhot=9
      trmed=1650.0
            thr=2100.0
            ts=800.0
            th=800.0
            tl=267.0
            tv=1650.0
            hqch=4.0
            qrod=2296.6
c
      hcore=12.0
            qtot=qrod*45.0
            qhr=qrod*float(nhot)
      nsurf=4
      nrod=49
      ncold=nrod-nhot-nsurf
      n=nrod+1
      drod=0.0095
      dh=0.01178
            dtemp=155.0
            if (nhot.eq.9) dtemp=161.0
            if (nhot.eq.25) dtemp=170.0
            if (thr.eq.0.0) thr=trmed+ncold*dtemp/float(ncold+nhot)
            tcr=thr-dtemp
            write(6,*) thr,tcr
c
c.....pressure in psia
      press=40.0
      alp=0.995
      dd=0.001
      ew=0.8
      timax=500.0
c
c.....end of inputs
c
      do 301 i=1,49
      ir(i)=2
  301  continue
```

```
      if (nhot.eq.1) then
      ir(25)=1
      endif
      if (nhot.eq.9) then
      ir(17)=1
      ir(18)=1
      ir(19)=1
      ir(24)=1
      ir(26)=1
      ir(31)=1
      ir(32)=1
      ir(33)=1
      endif
      if (nhot.eq.25) then
      ir(9)=1
      ir(10)=1
      ir(11)=1
      ir(12)=1
      ir(13)=1
      ir(16)=1
      ir(20)=1
      ir(23)=1
      ir(27)=1
      ir(27)=1
      ir(30)=1
      ir(34)=1
      ir(37)=1
      ir(38)=1
      ir(39)=1
      ir(40)=1
      ir(41)=1
      endif
c
      ir(1)=3
      ir(7)=3
      ir(43)=3
      ir(49)=3
c
      shrod=float(nhot)*pi*drod
      scrod=float(ncold)*pi*drod
      ssrf=float(nsurf)*pi*drod
      shou=0.3607
      nd=6.0*(1.0-alp)/(pi*dd**3.0)
      al=0.185*nd*pi*dd**2.0
      press=press*100.0/14.7
c
c.....calculate global view factors with inner hot rods array considered
c
      do 11 i=1,n
      do 12 j=1,n
      read(9,*) ni,nj,f(i,j)
   12  continue
      read(9,*) area(i)
   11  continue
c
```

```
      fhrcr=0.0
      do 101 j=1,nrod
      fsum=0.0
      asum=0.0
      if (ir(j).ne.2) goto 101
      do 102 i=1,nrod
      if (ir(i).ne.1) goto 102
      fsum=fsum+area(i)*f(i,j)
      asum=asum+area(i)
  102 continue
      fhrcr=fhrcr+fsum/asum
  101 continue
c
      fsum=0.0
      asum=0.0
      fhrh=0.0
      do 202 i=1,nrod
      if (ir(i).ne.1) goto 202
      fsum=fsum+area(i)*f(i,n)
      asum=asum+area(i)
  202 continue
      fhrh=fsum/asum
c
      fsum=0.0
      asum=0.0
      fcrh=0.0
      do 302 i=1,nrod
      if (ir(i).ne.2) goto 302
      fsum=fsum+area(i)*f(i,n)
      asum=asum+area(i)
  302 continue
      fcrh=fsum/asum
c
      fhrs=0.0
      do 401 j=1,nrod
      fsum=0.0
      asum=0.0
      if (ir(j).ne.3) goto 401
      do 402 i=1,nrod
      if (ir(i).ne.1) goto 402
      fsum=fsum+area(i)*f(i,j)
      asum=asum+area(i)
  402 continue
      fhrs=fhrs+fsum/asum
  401 continue
c
      fcrs=0.0
      do 501 j=1,nrod
      fsum=0.0
      asum=0.0
      if (ir(j).ne.3) goto 501
      do 502 i=1,nrod
      if (ir(i).ne.2) goto 502
      fsum=fsum+area(i)*f(i,j)
      asum=asum+area(i)
```

```
  502  continue
       fcrs=fcrs+fsum/asum
  501  continue
c
       asum=area(1)+area(7)+area(43)+area(49)
       fs1=area(1)*f(1,n)
       fs2=area(7)*f(7,n)
       fs3=area(43)*f(43,n)
       fs4=area(49)*f(49,n)
       fsh=(fs1+fs2+fs3+fs4)/asum
c
c......calculate network resistances
c
       ebl=sig*tl**4.0
       ebv=sig*tv**4.0
       av=9.84e-5*press*(18.66*(555.0/tv)**2.0 - (555.0/tv)**4.0)
       xlm=0.85*dh
       el=1.0-exp(-al*xlm)
       ev=1.0-exp(-av*xlm)
       r(1,1)=(1.0-ew)/(ew*shrod)
       r(1,2)=1.0/((1.0-el)*(1.0-ev)*shrod*fhrcr)
       r(1,3)=1.0/((1.0-el)*(1.0-ev)*shrod*fhrs)
       r(1,4)=1.0/((1.0-el)*(1.0-ev)*shrod*fhrh)
       r(1,5)=1.0/(el*(1.0-ev)*shrod)
       r(1,6)=1.0/(ev*(1.0-el)*shrod)
c
       r(2,1)=r(1,2)
       r(2,2)=(1.0-ew)/(ew*scrod)
       r(2,3)=1.0/((1.0-el)*(1.0-ev)*scrod*fcrs)
       r(2,4)=1.0/((1.0-el)*(1.0-ev)*scrod*fcrh)
       r(2,5)=1.0/(el*(1.0-ev)*scrod)
       r(2,6)=1.0/(ev*(1.0-el)*scrod)
c
       r(3,1)=r(1,3)
       r(3,2)=r(2,3)
       r(3,3)=(1.0-ew)/(ew*ssrf)
       r(3,4)=1.0/((1.0-el)*(1.0-ev)*ssrf*fsh)
       r(3,5)=1.0/(el*(1.0-ev)*ssrf)
       r(3,6)=1.0/(ev*(1.0-el)*ssrf)
c
       r(4,1)=r(1,4)
       r(4,2)=r(2,4)
       r(4,3)=r(3,4)
       r(4,4)=(1.0-ew)/(ew*shou)
       r(4,5)=1.0/(el*(1.0-ev)*shou)
       r(4,6)=1.0/(ev*(1.0-el)*shou)
c
       r(5,1)=r(1,5)
       r(5,2)=r(2,5)
       r(5,3)=r(3,5)
       r(5,4)=r(4,5)
       r(5,5)=0.0
       r(5,6)=1.0/(ev*el*(shrod+scrod+ssrf+shou))
c
       r(6,1)=r(1,6)
```

```
      r(6,2)=r(2,6)
      r(6,3)=r(3,6)
      r(6,4)=r(4,6)
      r(6,5)=r(5,6)
      r(6,6)=0.0
c
      na=4
c
      t(1)=273.14+(thr-32.0)/1.8
      t(2)=273.14+(tcr-32.0)/1.8
      t(3)=273.14+(ts-32.0)/1.8
      t(4)=273.14+(th-32.0)/1.8
            t(5)=273.14+(tl-32.0)/1.8
            t(6)=273.14+(tv-32.0)/1.8
      do 10 i=1,6
      eb(i)=sig*t(i)**4.0
 10   continue
c
      call matrix
      call gauss
c
      do 351 i=1,na
      q(i)=(c(i)-eb(i))/r(i,i)
351   continue
      q(5)=0.0
      q(6)=0.0
      do 352 i=1,na
      q(5)=q(5)+(c(i)-eb(5))/r(i,5)
      q(6)=q(6)+(c(i)-eb(6))/r(i,6)
352   continue
      qvl=(eb(6)-eb(5))/r(5,6)
      q(5)=q(5)+qvl
            q(6)=q(6)-qvl
c
            q12=(c(1)-c(2))/r(1,2)
            q13=(c(1)-c(3))/r(1,3)
            q23=(c(2)-c(3))/r(2,3)
            q14=(c(1)-c(4))/r(1,4)
      q24=(c(2)-c(4))/r(2,4)
            q1l=(c(1)-eb(5))/r(1,5)
            q1v=(c(1)-eb(6))/r(1,6)
      q2l=(c(2)-eb(5))/r(2,5)
            q2v=(c(2)-eb(6))/r(2,6)
            q3l=(c(3)-eb(5))/r(3,5)
            q3v=(c(3)-eb(6))/r(3,6)
            q4l=(c(4)-eb(5))/r(4,5)
            q4v=(c(4)-eb(6))/r(4,6)
c
c.....pi groups in the flow energy equation
            pir(1)=(q1v+q2v)/qtot
            pir(2)=(q1l+q2l)/qtot
            pir(3)=q4v/qtot
            pir(4)=q4l/qtot
            pir(5)=q3v/qtot
            pir(6)=q3l/qtot
```

```
            pir(7)=qvl/qtot
c
c......pi groups in the rod energy equation
            pir(8)=q13/qhr
            pir(9)=q14/qhr
            pir(10)=q12/qhr
            pir(11)=q1l/qhr
            pir(12)=q1v/qhr
c
c......correction to account for the above quench length
      corf=(hcore-hqch)/hcore
            do 701 i=1,7
            pir(i)=pir(i)*corf
 701   continue
c
      write(6,*) 'RV = ', pir(1)
            write(6,*) 'RL = ', pir(2)
            write(6,*) 'HV = ', pir(3)
            write(6,*) 'HL = ', pir(4)
            write(6,*) 'SV = ', pir(5)
            write(6,*) 'SL = ', pir(6)
            write(6,*) 'VL = ', pir(7)
            write(6,*)
      write(6,*) 'RS = ', pir(8)
            write(6,*) 'RH = ', pir(9)
            write(6,*) 'RR = ', pir(10)
            write(6,*) 'RL = ', pir(11)
            write(6,*) 'RV = ', pir(12)
c
      stop
      end
c
c
      subroutine matrix
c
      common/cgauss/ a(10,10),b(10),c(10),na
      common/temp/t(10),eb(10),tl,tv,ebl,ebv,q(10)
      common/resist/ r(10,10)
c
      do 10 i=1,na
      b(i)=0.0
      do 10 j=1,na
      a(i,j)=0.0
   10  continue
c
      do 101 i=1,na
      b(i)=eb(i)/r(i,i)+ebl/r(i,5)+ebv/r(i,6)
      do 102 j=1,na
      if (i.ne.j) then
      a(i,j)=-1.0/r(i,j)
      else
      do 103 k=1,6
      a(i,i)=a(i,i)+1.0/r(i,k)
  103  continue
      endif
```

```
  102  continue
  101  continue
c
      return
      end
c
c
      subroutine gauss
c
      common/cgauss/ a(10,10),b(10),c(10),na
c
      k=1
   20  temp = 1.0/a(k,k)
      j=k
   30  a(k,j) = a(k,j)*temp
      if (j.eq.na) goto 40
      j=j+1
      goto 30
   40  b(k) = b(k)*temp
      j=k+1
   50  temp = a(j,k)
      l=k
   60  a(j,l) = a(j,l)-a(k,l)*temp
      if (l.eq.na) goto 70
      l=l+1
      goto 60
   70  b(j) = b(j)-b(k)*temp
      if (j.eq.na) goto 80
      j=j+1
      goto 50
   80  if (k.eq.na-1) goto 90
      k=k+1
      goto 20
   90  continue
      c(na) = b(na)/a(na,na)
      i=1
  120  sum = 0.0
      j=na-i+1
  100  sum = sum+a(na-i,j)*c(j)
      if (j.eq.na) goto 110
      j=j+1
      goto 100
  110  c(na-i) = b(na-i)-sum
      if (i.eq.na-1) goto 130
      i=i+1
      goto 120
  130  continue
c
      return
      end
c
```

APPENDIX C1. BUNDLE MODEL DESCRIPTION

A full model of a square lattice rod bundle was developed to calculate the cross section temperature distribution during the reflood transient. The model includes the rod-to-rod and rod-to-housing thermal radiation heat transfer as well as the radial heat conduction in the rods and the housing. The convection heat transfer between rods and fluid as well as housing and fluid is simulated by inputting a convective heat transfer coefficient time history. The fluid temperature is another input value and it is kept constant during the transient.

The view factor matrix is calculated with the VUEFAC subroutine of MOXY computer program (Ref. 7-1). The conduction heat transfer is computed in each of the fuel rods, subject to the transient heat flux boundary condition of combined convection and radiation heat transfer. The radiative heat transfer computations are based on assumptions of gray and diffuse surfaces. The model neglects absorption, emission, or scattering of radiation by steam and droplets contained between surfaces. The radiation heat transfer between the surfaces and vapor was taken into account in the lumped model described in Section 6 (RADNET computer program).

Conductive Heat Transfer

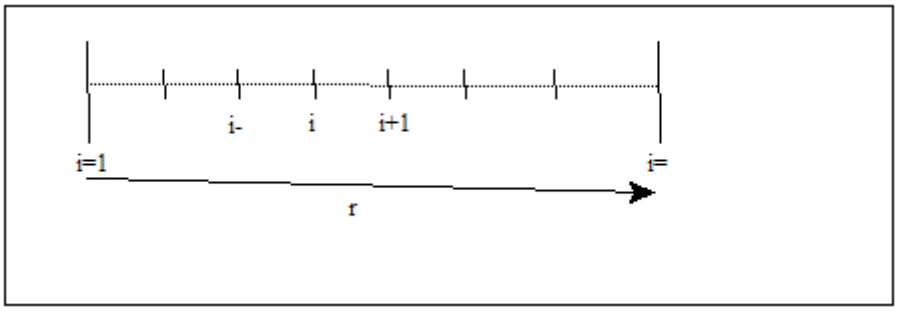

The heat conduction in fuel rods, solid inactive rods and housing is computed by numerical integration of the one-dimensional Fourier heat conduction equation:

$$\frac{1}{r}\frac{\partial}{\partial r}\left(kr\frac{\partial T}{\partial r}\right)+q'''=\rho c_p\frac{\partial T}{\partial t}$$

where q''' is zero for the inactive rods. The equation is discretized as follows:

$$\frac{\rho c_{p,1}V_1}{\Delta t}\left(T_1^{n+1}-T_1^n\right)=Q_1+2\pi\left[k_1\frac{T_2^n-T_1^n}{2}\right]$$

$$\frac{\rho c_{p,i}V_i}{\Delta t}\left(T_i^{n+1}-T_i^n\right)=Q_i+2\pi\left[k_i\left(r_i+\frac{dr_i}{2}\right)\left(\frac{T_{i+1}^n-T_i^n}{dr_i}\right)-k_{i-1}\left(r_i-\frac{dr_{i-1}}{2}\right)\left(\frac{T_i^n-T_{i-1}^n}{dr_{i-1}}\right)\right]$$

$$\frac{\rho c_{p,N} V_N}{\Delta t}\left(T_N^{n+1} - T_N^n\right) = Q_N - 2\pi\left[k_{N-1}\left(r_N - \frac{dr_{N-1}}{2}\right)\left(\frac{T_N^n - T_{N-1}^n}{dr_{N-1}}\right)\right] - 2\pi r_N\left[q_{rod}^n + h\left(T_N^n - T_f\right)\right]$$

where

$$V_i = \pi\left[r_i\left(dr_{i-1} + dr_i\right) + \frac{dr_i^2 - dr_{i-1}^2}{4}\right]$$

The equation for the heat conduction in the housing is:

$$\frac{\partial}{\partial x}\left(k\frac{\partial T}{\partial x}\right) + q''' = \rho c_p \frac{\partial T}{\partial t}$$

Again, this is solved numerically with the following equations:

$$\frac{\rho c_{p,1} dx}{\Delta t}\left(T_1^{n+1} - T_1^n\right) = k_1\left(\frac{T_2^n - T_1^n}{dx}\right) - h_{loss}\left(T_1^n - T_{out}\right)$$

$$\frac{\rho c_{p,i} dx}{\Delta t}\left(T_i^{n+1} - T_i^n\right) = k_i\left(\frac{T_{i+1}^n - T_i^n}{dx}\right) - k_{i-1}\left(\frac{T_i^n - T_{i-1}^n}{dx}\right)$$

$$\frac{\rho c_{p,N} dx}{\Delta t}\left(T_N^{n+1} - T_N^n\right) = -k_{N-1}\left(\frac{T_N^n - T_{N-1}^n}{dx}\right) - h\left(T_N^n - T_f\right) - q_{rad}^n$$

Once the radiative heat rate q_{rad}^n is calculated from the radiation transport equations, the previous equations are solved for the temperature field at time t_{n+1}.

Radiative Heat Transfer

The equations governing the radiative heat transfer are the following:

$$J_1 - \left(1 - \varepsilon_i\right)\sum_{j=1}^{N} F_{ij} J_j = \varepsilon_i E_{b,i} \qquad \text{(i = 1, 2, ... N)}$$

where

J_i radiosity of the i[th] surface
$E_{b,i}$ blackbody emissive power of the i[th] surface
F_{ij} view factor matrix
E_i emissivity of the i[th] surface

Once the temperature field is known by solving the conduction equation at time t_n the emissive power $E_{b,i}$ can be calculated. Then the previous system is solved for the radiosities J_i and the radiative heat fluxes at time t_n are calculated from the following equation:

$$q^{n}_{rad,1} = \frac{\varepsilon_i}{1-\varepsilon_i}(E_{b,i} - J_i)$$

The radiative heat fluxes are applied as the wall boundary condition for the conduction equation which is used to evaluate the temperature field at time t_{n+1}.

The program herein presented can operate also in a steady state mode. In this case the conduction equation is not solved while the temperature field is calculated iteratively. The source list of the Fortran program called BUNDLE is attached in Appendix C2.

APPENDIX C2. FORTRAN PROGRAM BUNDLE

```
program bundle
c
      implicit double precision (a-h,o-z)
      dimension d(1000),pwf(1000)
      dimension a(1001,1001),b(1001)
c
      common /vf/ f(1001,1001),area(1001)
      common/heat/q(1001),qrad(1001),qconv(1001),temp(1001),
     +  emiss(1001),bs(1001),qold(1001)
      common/heat1/tfad,tenvad,h,hout,hmin,qct,qrt,qt
      common/geoint/nrod,n,nl
            common/geo/vrod(1000)
      common/temp/told(1001)
      common/converg/alfa
      common/printc/tpcv,nprt1,nprt2,imod
c
      common/trans1/regsze(4),ql(1000),qr(1000),tr(1000,100),th(100)
      common/trans2/ndreg,ndx,ndr,npc,np1,ntab,ntab2,ifrad,inuc
      common/trans3/dt,tmax,time,tft,s,tenv,hloss,qavg,htrs,trst,
     +              tdst,thst,tmin,fdcy,hgap
      common/trans4/tme(100),hft(100),tmep(100),pdcy(100),tmix(100)
c
      data pi/3.141592654/
      data sig/5.67D-08/
c
      open(unit=8,file='bd.inp')
      open(unit=11,file='bd.out')
      open(unit=12,file='bd.dmp')
      open(unit=13,file='bd.flx')
c
      write(11,800)
      write(12,600)
      write(13,700)
      read(8,*) nl
      write(11,812) nl,nl
            read(8,*) inuc
      read(8,*) dd,p,drh
      write(11,801) dd
      write(11,802) p
      write(11,803) drh
      read(8,*) pwavg
      write(11,804) pwavg
      read(8,*) emirod,emihs
      write(11,805) emirod
      write(11,806) emihs
      read(8,*) hf,tf,tmin
      write(11,807) hf
      write(11,808) tf
      hf=hf*5.679
      tf=(tf-32.0)*5.0/9.0 + 273.14
```

```
          tmin=(tmin-32.0)*5.0/9.0 + 273.14

read(8,*) hloss,tenv
     write(11,809) hloss
     write(11,810) tenv
     hloss=hloss*5.679
     tenv=(tenv-32.0)*5.0/9.0 + 273.14
     read(8,*) s
     write(11,813) s
     s=s*0.0254
c
     hmin=0.2
c
     write(11,811)
     nrod=nl*nl
     n=nrod+1
     k1=1
     k2=k1+nl-1
     do 500 i=1,nl
     read(8,*) (pwf(k),k=k1,k2)
     write(11,903) (pwf(k),k=k1,k2)
     k1=k1+nl
     k2=k2+nl
 500  continue
c
     read(8,*) err
     read(8,*) imod,ifrad
c
     if (imod.eq.0) goto 510
c
c.....read transient data
     read(8,*) dt,tmax,nprt1,nprt2
     read(8,*) (regsze(i),i=1,4)
     do 505 i=1,4
     regsze(i)=regsze(i)*0.0254
          rsum=rsum+regsze(i)
          vrod(i)=(rsum**2.0-(rsum-regsze(i))**2.0)*pi
 505  continue
     read(8,*) hgap
          hgap=hgap*5.679
     read(8,*) ndreg,ndx
c      read(8,*) tft
c      tft=(tft-32.0)*5.0/9.0 + 273.14
     read(8,*) ntab
     do 507 i=1,ntab
     read(8,*) tme(i),hft(i),tmix(i)
     hft(i)=hft(i)*5.679
          tmix(i)=(tmix(i)-32.0)*5.0/9.0 + 273.14
 507  continue
     read(8,*) ntab2
     do 508 i=1,ntab2
     read(8,*) tmep(i),pdcy(i)
 508  continue
     read(8,*) trst,tdst,thst
     trst=(trst-32.0)*5.0/9.0 + 273.14
```

```
            tdst=(tdst-32.0)*5.0/9.0 + 273.14
            thst=(thst-32.0)*5.0/9.0 + 273.14

c
c
c....'pwavg' is the radial average power in kW/ft
c
 510  feet=0.3048
      pwl=pwavg*1000./feet
      tpcv=tf+pwl/(hf*pi*dd*0.0254)
c
      call vufac(nl,dd,p,drh)
c
      do 301 i=1,n
      do 302 j=1,n
 302  continue
      area(i)=area(i)*0.0254
 301  continue
c
      do 401 i=1,nrod
      d(i)=dd*0.0254
      ql(i)=pwf(i)*pwl
      emiss(i)=emirod
 401  continue
      emiss(n)=emihs
      qavg=pwl/(pi*d(1))
c
      if (imod.eq.1) goto 2000
c
c.....Set dimensionless variables
c
      tfad=(sig*tf**4.0d0/qavg)**0.25d0
      tenvad=(sig*tenv**4.0d0/qavg)**0.25d0
      tguess=tfad
      h=hf/(qavg**0.75d0 * sig**0.25d0)
      hout=hloss/(qavg**0.75d0 * sig**0.25d0)
      do 501 i=1,nrod
      q(i)=pwf(i)
 501  continue
      q(n)=0.0
c
c.....Start Iteration loop
c
      if (h.lt.hmin) then
      alfa=1.0
      nitmax=1000
      goto 150
      endif
c
      write(6,*) 'ALFA = ?'
      read (6,*) alfa
      write(6,*) 'NITER = ?'
      read (6,*) nitmax
c
 150  niter=0
```

```
c
c.....Initial guess for temperature
c

      do 201 i=1,n
      temp(i)=tfad
 201  continue
c
1001  niter=niter+1
c
      call rads
      call conv
c
c.....check for convergence
      eps=0.0
      elast=0.0
      do 240 i=1,n
      tnew=temp(i)
      eps=abs(tnew-told(i))
      eps=max(elast,eps)
      elast=eps
      told(i)=tnew
 240  continue
      write(6,*) niter,eps
      if (niter.gt.nitmax) goto 1002
      if (eps.gt.err) goto 1001
1002  continue
      goto 2100
c
c.....transient calculation
c
2000  call trans
      goto 9001
c
c.....print results steady state
c
2100  call print
c
c
 600  format(5x,'TIME',4x,'TCR-1',4x,'TCR-N',4x,'TWR-N',4x,'T0R-N',
     +       4x,'THO-1',4x,'THO-N',4x,'TN3x3',4x,'TN5x5',4x,'TN7x7',/)
 700  format(5x,'TIME',3x,'Q-RtoH',3x,'Q-RtoF',3x,'Q-HtoF',3x,
     +       'Q-LOSS',3x,'T-RODS',3x,'T-SURF',3x,'T-HOUS',//)
 800  format(/,40x,'CALCULATION RBHT',
     +      //,3x,'INPUT DATA')
 801  format(3x,'Rod Diameter              (in)          = ',F8.3)
 802  format(3x,'Rods Array Pitch          (in)          = ',F8.3)
 803  format(3x,'Distance Rods-to-Housing  (in)          = ',F8.3)
 804  format(3x,'Rod Average Power         (kW)          = ',F8.3)
 805  format(3x,'Rod Surface Emissivity    (-)           = ',F8.3)
 806  format(3x,'Housing Surface Emissivity (-)          = ',F8.3)
 807  format(3x,'Bundle Covection H.T.C.  (Btu/hr-F-ft2)= ',F8.3)
 808  format(3x,'Fluid Temperature         (F)           = ',F8.3)
```

```
809  format(3x,'Housing Heat Losses H.T.C. (Btu/hr-F-ft2)= ',F8.3)
 810  format(3x,'Enviroment Temperature     (F)          = ',F8.3)
 811  format(//,3x,'RODS POWER FACTOR',///)
 812  format(//,3x,'Bundle Array Size          (-)          = ',3x,
    +       I2,'x',I2)
 813  format(3x,'Housing Thickness          (in)         = ',F8.3)
 903  format(20(1x,F7.2))
c
9001  stop
      end
c
c*********************************************************************
c
      subroutine trans
c
      implicit double precision (a-h,o-z)
c
      common/trans1/regsze(4),ql(1000),qr(1000),tr(1000,100),th(100)
      common/trans2/ndreg,ndx,ndr,npc,np1,ntab,ntab2,ifrad,inuc
      common/trans3/dt,tmax,time,tft,s,tenv,hloss,qavg,htrs,trst,
     +              tdst,thst,tmin,fdcy,hgap
      common/trans4/tme(100),hft(100),tmep(100),pdcy(100),tmix(100)
      common/heat/q(1001),qrad(1001),qconv(1001),temp(1001),
     +  emiss(1001),bs(1001),qold(1001)
      common/geoint/nrod,n,nl
      common /vf/ f(1001,1001),area(1001)
      common/printc/tpcv,nprt1,nprt2,imod
c
      dimension trf(1000,100),thf(100)
c
      data pi/3.141592654/
      data sig/5.67D-08/
c
      ndr=4*ndreg
      npc=ndr+1
      ndt1=0
      ndt2=0
      ic=(nl**2.0+1)/2.0
      iw=ic-(nl-1)/2.0
c
c.....initial condition
c
      do 10 j=1,nrod
      qr(j)=0.0
      do 10 i=1,npc
      tr(j,i)=trst
            if (ql(j).eq.0.0) tr(j,i)=tdst
  10  continue
      do 11 i=1,ndx+1
      th(i)=thst

11  continue
      qr(n)=0.0
c
 100  call interp(tme,hft,time,htrs,ntab)
```

```
            if (tr(ic,npc).lt.tmin) htrs=5600.0
            call interp(tme,tmix,time,tft,ntab)
      call interp(tmep,pdcy,time,fdcy,ntab2)
      call trod
      call thous
c
      qrf=0.0
      do 102 i=1,nrod
      tw=tr(i,npc)
      temp(i)=(sig*tw**4.0d0/qavg)**0.25d0
      qrf=qrf+htrs*area(i)*(tw-tft)
 102  continue
      temp(n)=(sig*th(np1)**4.0d0/qavg)**0.25d0
      qhf=htrs*area(n)*(th(ndx+1)-tft)
      qloss=hloss*area(n)*(th(1)-tenv)
c
      if(ifrad.eq.0) goto 210
c
c.....turn off radiation after quench
            if(htrs.ge.5600.0) then
            qrh=0.0
            do 141 i=1,n
            qr(i)=0.0
 141  continue
            goto 210
      endif
c
            call rads
c
c.....calculate new radiation fluxes qrad
c
      do 201 i=1,n
      qr(i)=(temp(i)**4.0d0 - bs(i))*qavg*emiss(i)/(1.0d0-emiss(i))
 201  continue
      qrh=-qr(n)*area(n)
c
 210  time=time+dt
      ndt1=ndt1+1
      ndt2=ndt2+1
      if(ndt1.eq.nprt1) then
      write(6,*) time,htrs,tr(ic,npc)
      do 301 i=1,nrod
      do 302 j=1,npc
      trf(i,j)=(tr(i,j)-273.14)*9.0/5.0 + 32.0
 302  continue
 301  continue
      do 303 i=1,np1
      thf(i)=(th(i)-273.14)*9.0/5.0 + 32.0
 303  continue
c

c.....3x3 Taverage
      tsum=0.0
      is3=ic-nl-1
      do 402 k=1,3
```

```
      do 401 i=is3,is3+2
      tsum=tsum+trf(i,npc)
 401  continue
      is3=is3+nl
 402  continue
      t33=tsum/9.0
c
c.....5x5 Taverage
      tsum=0.0
      is5=ic-2*nl-2
      do 404 k=1,5
      do 403 i=is5,is5+4
      tsum=tsum+trf(i,npc)
 403  continue
      is5=is5+nl
 404  continue
      t55=tsum/25.0
c
c.....7x7 Taverage
      tsum=0.0
      n7=0
      is7=ic-3*nl-3
      do 406 k=1,7
      do 405 i=is7,is7+6
      if (ql(i).eq.0.0) goto 405
      tsum=tsum+trf(i,npc)
      n7=n7+1
 405  continue
      is7=is7+nl
 406  continue
      t77=tsum/n7
c
c.....Hot-Rods Taverage
      tsum1=0.0
      tsum2=0.0
      ndum=0
      do 407 i=1,nrod
      if (ql(i).eq.0.0) then
      tsum2=tsum2+trf(i,npc)
      ndum=ndum+1
      goto 407
      endif
      tsum1=tsum1+trf(i,npc)
 407  continue
      thot=tsum1/float(nrod-ndum)
      tcold=tsum2/float(ndum)
c
      write(12,601) time,trf(ic,1),trf(ic,npc),trf(22,npc),
     +              trf(1,npc),thf(1),thf(np1),t33,t55,t77
      write(13,701) time,qrh,qrf,qhf,qloss,thot,tcold,thf(np1)
      ndt1=0

           endif
      if(ndt2.eq.nprt2) then
      call print
```

```
      ndt2=0
      endif
c
      if(time.lt.tmax) goto 100
c
      return
c
 601  format(10(1x,F8.2))
 701  format(8(1x,F9.0))
c
      end
c
c*****************************************************************
c
      subroutine rads
c
      implicit double precision (a-h,o-z)
c
      common /vf/ f(1001,1001),area(1001)
      common/heat/q(1001),qrad(1001),qconv(1001),temp(1001),
     +  emiss(1001),bs(1001),qold(1001)
      common/geoint/nrod,n,nl
c
      dimension a(1001,1001),b(1001),c(1001)
c
      do 205 i=1,n
      do 204 j=1,n
 204  a(i,j) =-f(i,j)*(1.0d0-emiss(i))
      a(i,i)=a(i,i)+1.0
 205  continue
      do 206 i=1,n
      b(i)=emiss(i)*temp(i)**4.0d0
 206  continue
c
      call gauss(a,n,b,bs)
c
      return
      end
c
c*****************************************************************
c
      subroutine conv
c
      implicit double precision (a-h,o-z)
c
      common /vf/ f(1001,1001),area(1001)
      common/heat/q(1001),qrad(1001),qconv(1001),temp(1001),

     +  emiss(1001),bs(1001),qold(1001)
      common/heat1/tfad,tenvad,h,hout,hmin,qct,qrt,qt
      common/geoint/nrod,n,nl
      common/temp/told(1001)
      common/converg/alfa
c
      data sig/5.67D-08/
```

```
c
      qct=0.0
      qrt=0.0
      qt=0.0
c
      do 102 i=1,n
      sumbs=0.0d0
      do 101 j=1,n
      sumbs=sumbs+f(i,j)*bs(j)
 101  continue
c
c.....special case: radiation dominated cases
      if (h.lt.hmin) then
      eb=q(i)*(1.0d0-emiss(i))/emiss(i) + bs(i)
      temp(i)=eb**0.25d0
      goto 102
      endif
c
      temp(i)=tfad + (q(i)-bs(i)+sumbs)/h
 102  continue
      c1=(h*tfad+hout*tout)/(h+hout)
      c2=1.0d0/(h+hout)
      temp(n)=c1+c2*(sumbs-bs(n))
c
c.....underrelaxation
      do 103 i=1,n
      temp(i)=(1.0d0-alfa)*told(i) + alfa*temp(i)
 103  continue
c
      do 105 i=1,n
      qconv(i)=h*(temp(i)-tfad)
      qrad(i)=q(i)-qconv(i)
      qrt=qrt+qrad(i)*area(i)
      qt=qt+q(i)*area(i)
      qct=qct+qconv(i)*area(i)
 105  continue
      if (h.lt.hmin) temp(n)=tenvad+qt/(hout*area(n))
c
      return
      end
c
c*********************************************************************
c
       subroutine gauss(a,na,b,c)
c
       implicit double precision (a-h,o-z)
       dimension a(1001,1001),b(1001),c(1001)
c

       k=1
   20  tmp = 1.d0/a(k,k)
       j=k
   30  a(k,j) = a(k,j)*tmp
       if (j.eq.na) goto 40
       j=j+1
```

```
      goto 30
   40  b(k) = b(k)*tmp
      j=k+1
   50  tmp = a(j,k)
      l=k
   60  a(j,l) = a(j,l)-a(k,l)*tmp
      if (l.eq.na) goto 70
      l=l+1
      goto 60
   70  b(j) = b(j)-b(k)*tmp
      if (j.eq.na) goto 80
      j=j+1
      goto 50
   80  if (k.eq.na-1) goto 90
      k=k+1
      goto 20
   90  continue
      c(na) = b(na)/a(na,na)
      i=1
  120  sum = 0.0
      j=na-i+1
  100  sum = sum+a(na-i,j)*c(j)
      if (j.eq.na) goto 110
      j=j+1
      goto 100
  110  c(na-i) = b(na-i)-sum
      if (i.eq.na-1) goto 130
      i=i+1
      goto 120
  130  continue
c
      return
      end
c
c*****************************************************************
c
      subroutine trod
c
      implicit double precision (a-h,o-z)
c
      common/trans1/regsze(4),ql(1000),qr(1000),tr(1000,100),th(100)
      common/trans2/ndreg,ndx,ndr,npc,np1,ntab,ntab2,ifrad,inuc
      common/trans3/dt,tmax,time,tft,s,tenv,hloss,qavg,htrs,trst,
     +              tdst,thst,tmin,fdcy,hgap
      common/trans4/tme(100),hft(100),tmep(100),pdcy(100),tmix(100)
      common/heat/q(1001),qrad(1001),qconv(1001),temp(1001),
     +           emiss(1001),bs(1001),qold(1001)
      common/geoint/nrod,n,nl

           common/geo/vrod(1000)
c
      dimension cd(100),cp(100),t(100),qh(100),ddr(100)
c
      data pi/3.141592654/
c
```

```
      do 201 j=1,nrod
c
      do 10 i=1,npc
      t(i)=tr(j,i)
      qh(i)=0.0
  10  continue
      i1=ndreg+2
      i2=ndreg*2
            do 20 i=i1,i2
      qh(i)=ql(j)*fdcy/float(ndreg-1)
  20  continue
      qvnuc=0.0
      if (inuc.ne.0) qvnuc=fdcy*ql(j)/(vrod(1)+vrod(2)+vrod(3))

c
c.....calculation properties
c
      ireg=1
      jr=1
      do 50 i=1,ndr
      ddr(i)=regsze(ireg)/float(ndreg)
      tn=t(i)
      call prop(tn,ireg,cnd,cpm,inuc)
            if (ql(j).eq.0.0) call prop(tn,4,cnd,cpm,inuc)
            if (i.eq.(ndreg*3+1).and.hgap.ne.0)
     +      cnd=cnd*hgap*ddr(i)/(cnd+hgap*ddr(i))
            cd(i)=cnd
            cp(i)=cpm
      if (jr.eq.ndreg) then
      jr=0
      ireg=ireg+1
      endif
      jr=jr+1
  50  continue
c
c.....calculation conduction in rod
c.....centerline, inner regions, clad surface
c
      r=0.0
c
      dr=ddr(1)
      vol=0.25*pi*dr**2.0
      a=cd(1)*0.5*(t(2)-t(1))
      c=dt/(cp(1)*vol)
      if (inuc.ne.0) qh(1)=qvnuc*vol
      t(1)=t(1)+(qh(1)+2.0*pi*a)*c
c
      r=ddr(1)
      do 101 i=2,ndr

      drm1=ddr(i-1)
      dr=ddr(i)
      vol=pi*(r*(drm1+dr) + (dr**2.0-drm1**2.0)/4.0)
            vol2=pi*(r*drm1-(drm1**2.0)/4.0)
            if (inuc.ne.0) then
```

```
            qh(i)=qvnuc*vol
            if (i.gt.ndreg*3) qh(i)=qvnuc*vol2
            if (i.gt.ndreg*3+1) qh(i)=0.0
      endif
            a=cd(i)*(r+dr/2.0)*(t(i+1)-t(i))/dr
            b=cd(i-1)*(r-drm1/2.0)*(t(i)-t(i-1))/drm1
      c=dt/(cp(i)*vol)
      t(i)=t(i)+(qh(i)+2.0*pi*(a-b))*c
      r=r+dr
 101  continue
c
      vol=pi*(r*dr - 0.25*dr**2.0)
      a=-cd(ndr)*(r-dr/2.0)*(t(npc)-t(npc-1))/dr
      b=r*(qr(j) + htrs*(t(npc)-tft))
      c=dt/(cp(ndr)*vol)
      t(npc)=t(npc)+(qh(npc)+2.0*pi*(a-b))*c
c
      do 151 i=1,npc
      tr(j,i)=t(i)
 151  continue
c
 201  continue
c
      return
      end
c
c*********************************************************************
c
      subroutine thous
c
      implicit double precision (a-h,o-z)
c
      common/trans1/regsze(4),ql(1000),qr(1000),tr(1000,100),th(100)
      common/trans2/ndreg,ndx,ndr,npc,np1,ntab,ntab2,ifrad,inuc
      common/trans3/dt,tmax,time,tft,s,tenv,hloss,qavg,htrs,trst,
     +              tdst,thst,tmin,fdcy,hgap
      common/trans4/tme(100),hft(100),tmep(100),pdcy(100),tmix(100)
      common/heat/q(1001),qrad(1001),qconv(1001),temp(1001),
     +  emiss(1001),bs(1001),qold(1001)
      common/geoint/nrod,n,nl
c
      dimension cd(100),cp(100),t(100)
c
      data pi/3.141592654/
c
      dx=s/float(ndx)
      np1=ndx+1
c
c.....calculation properties

c
      ireg=4
      do 50 i=1,ndx
      tt=th(i)
      call prop(tt,ireg,cnd,cpm,inuc)
```

```
      cd(i)=cnd
      cp(i)=cpm
   50  continue
c
c.....calculation conduction in the housing wall
c
      a=2.0*cd(1)*(th(2)-th(1))/dx
      b=hloss*(th(1)-tenv)
      c=dt/(cp(1)*dx)
      th(1)=th(1)+(a-b)*c
c
      do 101 i=2,ndx
      a=2.0*cd(i)*(th(i+1)-th(i))/dx
      b=2.0*cd(i-1)*(th(i)-th(i-1))/dx
      c=dt/(cp(i)*dx)
      th(i)=th(i)+(a-b)*c
      r=r+dr
  101  continue
c
      a=-2.0*cd(ndx)*(th(np1)-th(np1-1))/dx
      b=htrs*(th(np1)-tft)
      c=dt/(cp(ndx)*dx)
      th(np1)=th(np1)+(a-b-qr(n))*c
c
      return
      end
c
c**********************************************************************
c
      subroutine prop(tk,ireg,cnd,cpm,inuc)
c
      implicit double precision (a-h,o-z)
c
      t=tk-273.14
c
c.....nuclear rod
c
      if (inuc.eq.0) goto 100
            if (ireg.eq.4) goto 110
c
c.....uranium dioxide
            rho=9649.0
      cnd=2.45
      cpm=333.0*rho
      return
c
c.....zircalloy
  110  rho=6560.0
      a=1.461e-2
            b=12.092

          cnd=a*t+b
     cpm=347.0*rho
            return
c
```

```
c.....region 1 and 3 - BN
c
 100  if (ireg.ne.3.and.ireg.ne.1) goto 101
      rho=1910.0
      a=-0.061356
      b=122.734
      cnd=a*t + b
      cpm=1500*rho
      return
c
c.....region 2 - Heater
 101  if (ireg.ne.2) goto 102
      rho=8470.0
            a=4.7742e-10
            b=-1.1151e-6
            c=5.2571e-4
            d=4.0755e-1
            cpm=1000.0*(a*t**3.0+b*t**2.0+c*t+d)*rho
            a=2.8263e-2
            b=17.583

            cnd=a*t+b
      return
c
c.....region 4 - Clad - Inconel 600
c
 102  rho=8270.0
      a=4.7427e-4
            b=4.1430e-1
            cpm=1000.0*(a*t+b)*rho
            a=1.6972e-2
            b=14.599
            cnd=a*t+b
      cnd=15.0
      return
c
      end
c
c
c*************************************************************
c
      subroutine print
c
      implicit double precision (a-h,o-z)
c
      common/heat/q(1001),qrad(1001),qconv(1001),temp(1001),
     +  emiss(1001),bs(1001),qold(1001)
      common/trans3/dt,tmax,time,tft,s,tenv,hloss,qavg,htrs,trst,
     +             tdst,thst,tmin,fdcy,hgap
      common/trans4/tme(100),hft(100),tmep(100),pdcy(100),tmix(100)
      common/printc/tpcv,nprt1,nprt2,imod

common/geoint/nrod,n,nl
c
      data sig/5.67D-08/
```

```
c
c.....print results
      if (imod.eq.0) write(11,900)
      if (imod.eq.1) write(11,904) time
      do 250 i=1,n
      temp(i)=temp(i)/(sig/qavg)**0.25d0
c
c.....conversion to british units
      temp(i)=(temp(i)-273.14)*9.0/5.0 + 32.0
c
 250  continue
c
      k1=1
      k2=k1+nl-1
      do 600 i=1,nl
      write(11,903) (temp(k),k=k1,k2)
      k1=k1+nl
      k2=k2+nl
 600  continue
      write(11,901) temp(n)
      tpcv=(tpcv-273.14)*9.0/5.0 + 32.0
      if (imod.eq.0) write(11,902) tpcv
c
      return
c
 900  format(///,3x,'RESULTS STEADY STATE',
     +       //,3x,'RODS SURFACE TEMPERATURE (F)',//)
 904  format(///,'***********************************************',
     +       /,3x,'RESULTS AT TIME (sec) = ',F7.2,
     +       //,3x,'RODS SURFACE TEMPERATURE (F)',//)
 901  format(/,3x,'HOUSING TEMPERATURE (INSIDE WALL) (F)  = ',F7.2)
 902  format(//,3x,'Rod Surf. Temp. for infinite array at SS (F) = ',
     +       F7.2)
 903  format(20(1x,F7.2))
c
      end
c
c
c**********************************************************************
c
      subroutine vufac(nmx,dd,p,drh)
C
c     the subroutine is based
C     VUFAC   12/06/78 D.R.EVANS
c     and modified by C. Frepoli 3/10/98
c     the symmentry logic (MIRRIM, ISWAP etc.) is deleted
c
      implicit double precision (a-h,o-z)
C
c      DIMENSION AREA(226),R0(225)
      dimension r0(1000)
```

```
      COMMON /VF/ F(1001,1001),area(1001)
      COMMON /RI/ RIJ(1001,1001)
c
      data nf,npt,n,na/1001,200,37,37/
      data pi/3.14159265358979323846/

c
      xlh=p*float(nmx-1)+dd+2.0*drh
c
      nlim=nmx
      n2=nmx*nmx +1
      nl=nmx
      nl=8
      nl1=nmx
      ahs=xlh*4.0
c
      NP=N2-1

      TWOPI=2.*PI

      DO 1700 I=1,NP

      r0(i)=dd/2.0
      AREA(I)=TWOPI*R0(I)

      1700     CONTINUE

      AREA(N2)=ahs
c
      CALL VFAC(F,AREA,AEA,SCALFC,BB,R0,IROW,JCOL,MIRRIM,P,PI,N,
     1NF,NLIM,N2,NA,NSYM,NL,NL1,NPT)

c
       do 998 i=1,n2
       do 997 j=1,n2
       write(9,*) i,j,f(i,j)
  997  continue
       write(9,*) area(i)
  998  continue
c
      return
      END

c
C******      FIJ     12/12/78 D.R.EVANS
       SUBROUTINE FIJ(F,R,P,PI,M,NPT,L,SOURCE,IX,IY,L1,L2,IRC,IA)
      implicit double precision (a-h,o-z)
       DIMENSION F(M,1),R(1),XA(2,100),YA(2,100),RA(2,100)
      COMMON /RI/ RIJ(1001,1001)

INTEGER SOURCE,TARGET,UPPER(14),LOWER(14)

       LOGICAL SKIP

       DATA XA(1,1),YA(1,1)/2*0.D0/
```

```
      DATA SKIP/.FALSE./
      IF(SKIP) GO TO 10
      SKIP=.TRUE.
      RNPT=1.D0/NPT
      DELTA=2.D0*PI*RNPT

      RDELT=1.D0/DELTA

      PIO2=.5D0*PI

      10     CONTINUE

      IF(IRC-2) 12,16,20

      12  CONTINUE

C       ROWS

      IF(IA.EQ.2) GO TO 14

C       ADJACENT ROW

      IXY=IX

      K2=L

      K3=1

      GO TO 24

   14  CONTINUE

C       ROWS BEYOND ADJACENT ROW

      IXY=IY

      IYX=IX
      I3=1

      K2=0

      K3=L
      GO TO 24
   16  CONTINUE
C       HIGHER-NUMBERED COLUMNS
      IF(IA.EQ.2) GO TO 18
C       ADJACENT COLUMN

      K2=1
      GO TO 22
   18  CONTINUE
C       COLUMNS BEYOND ADJACENT COLUMN
      IXY=IX
      IYX=IY
```

```
      I3=L
      K2=0
      K3=1
      GO TO 24
   20 CONTINUE
C       LOWER-NUMBERED COLUMNS
      K2=-1
   22 CONTINUE
      IXY=IY
      K3=L
   24 CONTINUE
C       COMPUTE SHADOWING ROD NUMBERS

      KMI=L2-IXY

      IF(KMI.LT.0) KMI=L1-IXY
      KMIABS=IABS(KMI)
      TARGET=SOURCE+K2+K3*KMI
      I2=K3*ISIGN(1,KMI)
      IF(IA.EQ.2) GO TO 30
C       ADJACENT ROW AND COLUMNS
      K4=KMIABS
      GO TO 40
   30 CONTINUE

C       ROWS AND COLUMNS BEYOND ADJACENT

      K4=KMIABS-1
      UPPER(1)=0
      LOWER(KMIABS)=0
      K5=0
   40 CONTINUE
      DO 70 I=1,K4
      LOWER(I)=SOURCE+I2*I

      IF(IA.EQ.2) GO TO 60

      UPPER(I)=TARGET-I2*(KMIABS-I+1)
      GO TO 70
   60 CONTINUE
      UPPER(I+1)=LOWER(I)+I3
      IF(IYX.EQ.L) UPPER(I+1)=0
      70    CONTINUE

      K=KMIABS+1

C       SET RADII AND COORDINATES OF SOURCE,TARGET, AND ALL POTENTIAL
C       SHADOWING RODS

      R1=R(SOURCE)

      RA(1,1)=R1
      RA(2,K)=R(TARGET)
C     XA(2,1)=0.D0
      XA(2,1)=0.E0
```

```
      YA(2,1)=P
      DO 230 I=1,KMIABS
      FI=I
      PTFI=P*FI

      IP1=I+1

      XA(1,IP1)=PTFI
C     YA(1,IP1)=0.D0
      YA(1,IP1)=0.E0
      XA(2,IP1)=PTFI
      YA(2,IP1)=P
      IF(LOWER(I).EQ.0) GO TO 200
      RA(1,IP1)=R(LOWER(I))
      GO TO 210
  200 CONTINUE
C     RA(1,IP1)=0.D0
      RA(1,IP1)=0.E0

  210 CONTINUE
      IF(UPPER(I).EQ.0) GO TO 220

      RA(2,I)=R(UPPER(I))
      GO TO 230

  220 CONTINUE

C     RA(2,I)=0.D0
      RA(2,I)=0.E0
  230 CONTINUE
      DO 700 K1=L1,L2
      KMI=K1-IXY
      KMIABS=IABS(KMI)
      TARGET=SOURCE+K2+K3*KMI
      K=KMIABS+1
      IF(IA.EQ.2) GO TO 235
      Y1=YA(2,K)
      R2=RA(2,K)
      K4=KMIABS
      GO TO 238
  235 CONTINUE
      IF(R(SOURCE).LE.R(LOWER(1)).AND.
     *  R(LOWER(KMIABS-1)).GE.R(TARGET)) GO TO 700

C     Y1=0.D0

      Y1=0.E0

    R2=R(TARGET)
      K4=KMIABS-1
  238 CONTINUE
      X1=XA(2,K)
      FKMI=KMIABS-1
C     DIAG=FKMI**2+1.D0
      DIAG=FKMI**2+1.E0
```

```
C     RR12=1.D0/(P*DSQRT(DIAG))
      RR12=1.E0/(P* SQRT(DIAG))

      TEMP=P*SQRT((FLOAT(KMIABS))**2+1.)

      RIJ(SOURCE,TARGET)=TEMP-0.5*(R(SOURCE)+R(TARGET))
C     I1=RDELT*(PI-DARCOS((R1+R2)*RR12)-DATAN2(1.D0,FKMI))
      I1=RDELT*(PI-  ACOS((R1+R2)*RR12)- ATAN2(1.E0,FKMI))
  240 CONTINUE
C       COMPUTE VIEW FACTOR
      VIEWFC=0.
      DO 500 IPT=I1,NPT
      XIPT = IPT - 1
      THETA = DELTA * XIPT
C     XV=-R1*DCOS(THETA)
      XV=-R1* COS(THETA)
C     YV=R1*DSIN(THETA)
      YV=R1* SIN(THETA)
C       DETERMINE IF (XV,YV) CAN SEE THE TARGET ROD

      IF(XV*X1+YV*Y1.LE.R1*(R1-R2)) GO TO 500

C       TS IS THE TANGENT TO THE SOURCE ROD AT (XV,YV)
C     TS=DATAN2(-XV,YV)
      TS= ATAN2(-XV,YV)
C       COMPUTE TANGENTS TO TARGET ROD
C       T1 IS THE LOWER TANGENT TO THE TARGET ROD
C       T2 IS THE UPPER TANGENT TO THE TARGET ROD
      X1MXP=X1-XV
      Y1MYP=Y1-YV
      RSQ=X1MXP**2+Y1MYP**2

C     S=DSQRT(RSQ-R2**2)

      S= SQRT(RSQ-R2**2)
C     RRSQ=1.D0/RSQ
      RRSQ=1.E0/RSQ
      SORSQ=S*RRSQ
      R1ORSQ=R2*RRSQ

      A=SORSQ*X1MXP

      B=R1ORSQ*Y1MYP
      C=SORSQ*Y1MYP
      D=R1ORSQ*X1MXP
      XTAMXP=S*(A-B)
      YTAMYP=S*(C+D)

      XTBMXP=S*(A+B)

      YTBMYP=S*(C-D)

C     T2=DATAN2(YTAMYP,XTAMXP)
      T2= ATAN2(YTAMYP,XTAMXP)
C     T1=DATAN2(YTBMYP,XTBMXP)
```

```
      T1= ATAN2(YTBMYP,XTBMXP)

C       COMPUTE TANGENTS THROUGH (XV,YV) TO SHADOWING RODS

C       FIND MINIMUM UPPER SHADOWING AND MAXIMUM LOWER SHADOWING
      DO 300 J=1,2

      DO 300 I=1,K4

      RB=RA(J,I+2-J)
      IF(RB.EQ.0.) GO TO 300
      XB=XA(J,I+2-J)
      YB=YA(J,I+2-J)
      X1MXP=XB-XV
      Y1MYP=YB-YV
      RSQ=X1MXP**2+Y1MYP**2
C     S=DSQRT(RSQ-RB**2)

      S= SQRT(RSQ-RB**2)

      IF(S.EQ.0.) GO TO 260
C     RRSQ=1.D0/RSQ
      RRSQ=1.E0/RSQ
      SORSQ=S*RRSQ
      R1ORSQ=RB*RRSQ
      A=SORSQ*X1MXP
      B=R1ORSQ*Y1MYP
      C=SORSQ*Y1MYP
      D=R1ORSQ*X1MXP

      IF(J.EQ.2) GO TO 250

C       UPPER TANGENTS TO LOWER SHADOWING RODS
      XTAMXP=S*(A-B)
      YTAMYP=S*(C+D)
      TA=DATAN2(YTAMYP,XTAMXP)
c     TA= ATAN2(YTAMYP,XTAMXP)
      T1=DMAX1(TA,T1)
c     T1=AMAX1(TA,T1)
      GO TO 300

  250  CONTINUE
C       LOWER TANGENTS TO UPPER SHADOWING RODS
      XTBMXP=S*(A+B)
      YTBMYP=S*(C-D)
      TB=DATAN2(YTBMYP,XTBMXP)
c     TB= ATAN2(YTBMYP,XTBMXP)
      T2=DMIN1(TB,T2)
c     T2=AMIN1(TB,T2)
      GO TO 300
    260  CONTINUE

      IF(J.EQ.2) GO TO 270

      T1=DMAX1(PIO2,T1)
```

```
c      T1=AMAX1(PIO2,T1)
       GO TO 300
  270  CONTINUE
       T2=DMIN1(0.D0,T2)
c      T2=AMIN1(0.E0,T2)
  300  CONTINUE
       IF (T1 .GE. T2) GO TO 490
       IF (T1 .LT. TS .OR.  T1 .GE. TS + PI) GO TO 320
       PHI1 = T1 - TS
       GO TO 350
  320  CONTINUE
       PHI1 = 0.
       IF (T1 .GE. TS) PHI1 = PI
  350  CONTINUE
       IF (T2 .LT. TS .OR. T2 .GE. TS + PI) GO TO 370

       PHI2 = T2 - TS

       GO TO 380
  370  CONTINUE
       PHI2 = 0.
       IF  (T2 .GE. TS) PHI2 = PI
  380  CONTINUE
C      CONFIG=.5D0*(DCOS(PHI1)-DCOS(PHI2))
       CONFIG=.5E0*( COS(PHI1)- COS(PHI2))
       VIEWFC=VIEWFC+CONFIG
       GO TO 500
  490  CONTINUE
       IF(VIEWFC.NE.0.) GO TO 510
  500  CONTINUE
  510  CONTINUE
       IF(IA.EQ.1) GO TO 550
       IF(K5.EQ.1) GO TO 540
       FSAVE=VIEWFC
       K5=K5+1
       DO 530 I=1,K4
       IF(IYX.EQ.1) GO TO 520
       UPPER(I+1)=LOWER(I)-I3
       RA(2,I+1)=R(UPPER(I+1))
       GO TO 530
  520  CONTINUE
C      RA(2,I+1)=0.D0
       RA(2,I+1)=0.E0

    530  CONTINUE

       GO TO 240
  540  CONTINUE
       VIEWFC=VIEWFC+FSAVE
       K5=0
       DO 545 I=1,K4
       IF(IYX.EQ.L) GO TO 542
       UPPER(I+1)=LOWER(I)+I3
       RA(2,I+1)=R(UPPER(I+1))
       GO TO 545
```

```
  542  CONTINUE
C      RA(2,I+1)=0.D0
       RA(2,I+1)=0.E0
  545  CONTINUE
  550  CONTINUE
       F(SOURCE,TARGET)=VIEWFC*RNPT
  700  CONTINUE
       RETURN
       END
c
C******       PATHLEN 12/14/78 D.R.EVANS

      SUBROUTINE PATHLEN(R,DELTAX,P,N2,L)

      implicit double precision (a-h,o-z)
      DIMENSION F(15),R(1)

      COMMON /RI/ RIJ(1001,1001)

      INTEGER SOURCE
      REAL L1,L2,L3,L4

      DATA F/0.5,0.086740,0.013966,0.001517,0.000424,0.000172,

     1      0.000088,0.000048,0.000034,6*0./
C       COMPUTE PATH LENGTHS FROM RODS TO CANISTER
      DO 100 IX=1,L
      DO 100 IY=1,L
      SOURCE=IY+(IX-1)*L
      HALFR1=0.5*R(SOURCE)
C       PATH OND
      L1=P*FLOAT(IX-1)+DELTAX-HALFR1
C       PATH TWO
      L2=P*FLOAT(L-IX)+DELTAX-HALFR1
C       PATH THREE
      L3=P*FLOAT(IY-1)+DELTAX-HALFR1
C       PATH FOUR

      L4=P*FLOAT(L-IY)+DELTAX-HALFR1

C       PATH LENGTH IS THE VIEW-FACTOR-WEIGHTED MEAN OF FOUR
C       CONTRIBUTIONS
      RIJ(SOURCE,N2)=(L1*F(IX)
     1            +L2*F(L-IX+1)
     2            +L3*F(IY)
     3            +L4*F(L-IY+1)) /
     4            (F(IX)
     5            +F(L-IX+1)
     6            +F(IY)
     7            +F(L-IY+1))
100   CONTINUE

      RETURN

      END
```

```
c
C******      STRING  12/12/78 D.R.EVANS

      SUBROUTINE STRING(F,R,P,PI,M,L,SOURCE,IX,IY)

     implicit double precision (a-h,o-z)
      DIMENSION F(M,1),R(1)
     COMMON /RI/ RIJ(1001,1001)
      DIMENSION TIN(1000,4),THET(1000,4),TEX(1000,2),ALPH(1000,2)
      INTEGER SOURCE,TARGET
      LOGICAL SKIP
      DATA SKIP/.FALSE./,PP/0./
      IF(SKIP) GO TO 10
      SKIP=.TRUE.
C      RPI=1.D0/PI
      RPI=1.E0/PI
C      PIO2=.5D0*PI
      PIO2=.5E0*PI
C      PIO4=.5D0*PIO2
      PIO4=.5E0*PIO2
   10  CONTINUE
      IF(PP.EQ.P) GO TO 20
      PP=P
      PSQ=P**2
C      R13SQ=2.D0*PSQ
      R13SQ=2.E0*PSQ
C      RR13=1.D0/DSQRT(R13SQ)
      RR13=1.E0/ SQRT(R13SQ)
C      RP=1.D0/P

      RP=1.E0/P

   20  CONTINUE

C       COMPUTE TANGENT LENGTHS AND ANGLES FOR CROSSED STRING METHOD

      IF(IX.GT.1.OR.IY.EQ.L) GO TO 145

      J1=SOURCE
      J2=SOURCE+L-2
      DO 140 I=J1,J2
      R1=R(I)
      R2=R(I+1)
      R3=R(I+1+L)
      R4=R(I+L)
      R2MR3=R2-R3

      R4MR3=R4-R3

C      TIN13=DSQRT(R13SQ-(R1+R3)**2)

      TIN13= SQRT(R13SQ-(R1+R3)**2)
C      TIN23=DSQRT(PSQ-(R2+R3)**2)
      TIN23= SQRT(PSQ-(R2+R3)**2)
C      TIN34=DSQRT(PSQ-(R3+R4)**2)
```

```
      TIN34= SQRT(PSQ-(R3+R4)**2)
C     TIN24=DSQRT(R13SQ-(R2+R4)**2)
      TIN24= SQRT(R13SQ-(R2+R4)**2)
      TIN(I,2)=TIN13
      TIN(I+1,3)=TIN23
      TIN(I+L,1)=TIN34
      TIN(I+1,4)=TIN24
C     THET(I,2)=DARSIN(TIN13*RR13)
      THET(I,2)=  ASIN(TIN13*RR13)
C     THET(I+1,3)=DARSIN(TIN23*RP)
      THET(I+1,3)=  ASIN(TIN23*RP)
C     THET(I+L,1)=DARSIN(TIN34*RP)
      THET(I+L,1)=  ASIN(TIN34*RP)
C     THET(I+1,4)=DARSIN(TIN24*RR13)
      THET(I+1,4)=  ASIN(TIN24*RR13)
      IF(R2MR3.EQ.0.) GO TO 100
C     ALPH(I+1,2)=DARCOS(R2MR3*RP)

      ALPH(I+1,2)=  ACOS(R2MR3*RP)

C     TEX(I+1,2)=DSQRT(PSQ-R2MR3**2)
      TEX(I+1,2)= SQRT(PSQ-R2MR3**2)
      GO TO 105
  100 CONTINUE
      ALPH(I+1,2)=PIO2
      TEX(I+1,2)=P
  105 CONTINUE
      IF(R4MR3.EQ.0.) GO TO 110
C     ALPH(I+L,1)=DARCOS(R4MR3*RP)
      ALPH(I+L,1)=  ACOS(R4MR3*RP)
C     TEX(I+L,1)=DSQRT(PSQ-R4MR3**2)
      TEX(I+L,1)= SQRT(PSQ-R4MR3**2)
      GO TO 115
  110 CONTINUE
      ALPH(I+L,1)=PIO2
      TEX(I+L,1)=P
  115 CONTINUE
      IF(I.GT.J1) GO TO 130
      R1MR4=R1-R4
C     TIN14=DSQRT(PSQ-(R1+R4)**2)
      TIN14= SQRT(PSQ-(R1+R4)**2)
      TIN(I,3)=TIN14
C     THET(I,3)=DARSIN(TIN14*RP)
      THET(I,3)=  ASIN(TIN14*RP)
      IF(R1MR4.EQ.0.) GO TO 120

C     ALPH(I,2)=DARCOS(R1MR4*RP)

      ALPH(I,2)=  ACOS(R1MR4*RP)
C     TEX(I,2)=DSQRT(PSQ-R1MR4**2)
      TEX(I,2)= SQRT(PSQ-R1MR4**2)
      GO TO 125
  120 CONTINUE
      ALPH(I,2)=PIO2
      TEX(I,2)=P
```

```
 125  CONTINUE
 130  CONTINUE
      IF(IY.GT.1) GO TO 140
      R1MR2=R1-R2
C     TIN12=DSQRT(PSQ-(R1+R2)**2)
      TIN12= SQRT(PSQ-(R1+R2)**2)
      TIN(I,1)=TIN12
C     THET(I,1)=DARSIN(TIN12*RP)
      THET(I,1)=  ASIN(TIN12*RP)
      IF(R1MR2.EQ.0.) GO TO 135
C     ALPH(I,1)=DARCOS(R1MR2*RP)
      ALPH(I,1)=  ACOS(R1MR2*RP)
C     TEX(I,1)=DSQRT(PSQ-R1MR2**2)
      TEX(I,1)= SQRT(PSQ-R1MR2**2)
      GO TO 140
 135  CONTINUE
      ALPH(I,1)=PIO2
      TEX(I,1)=P

 140  CONTINUE

 145  CONTINUE
C       COMPUTE ADJACENT AND DIAGONAL ROD VIEW FACTORS
C       USING CROSSED STRING METHOD
C       COMPUTE ADJACENT ROD VIEW FACTORS
      R1=R(SOURCE)
      DO 150 I=1,2
      IF(IX.EQ.L.AND.I.EQ.1) GO TO 150
      IF(IY.EQ.L.AND.I.EQ.2) GO TO 150
      TARGET=SOURCE+L**(I-1)
      R2=R(TARGET)
      CROLEN=TIN(SOURCE,2**I-1)+R1*ALPH(SOURCE,I)
         ↵   +R2*(PI-ALPH(SOURCE,I))-(R1+R2)*THET(SOURCE,2**I-1)

      CROMUN=CROLEN-TEX(SOURCE,I)

C     F(SOURCE,TARGET)=.5D0*RPI*CROMUN/R1
      F(SOURCE,TARGET)=.5E0*RPI*CROMUN/R1
      RIJ(SOURCE,TARGET)=P-0.5*(R1+R2)
      IF(IY.NE.IX) GO TO 150

      F(SOURCE,SOURCE+L)=F(SOURCE,TARGET)

      RIJ(SOURCE,SOURCE+L)=RIJ(SOURCE,TARGET)
      GO TO 152
 150  CONTINUE

 152  CONTINUE
      IF(IY.EQ.L) GO TO 190
C       COMPUTE DIAGONAL ROD VIEW FACTORS
      DO 185 I=1,2
      IF(IX.EQ.1.AND.I.EQ.1) GO TO 185
      IF(IX.EQ.L.AND.I.EQ.2) GO TO 185
      MORP1=(-1)**I
      M1ORZ=I-2
```

```
      TARGET=SOURCE+L+MORP1
      R2=R(SOURCE+MORP1)
      R3=R(TARGET)
      R4=R(SOURCE+L)
      TIN12=TIN(SOURCE+M1ORZ,1)
      THET12=THET(SOURCE+M1ORZ,1)
      TIN13=TIN(SOURCE,2**(3-I))
      THET13=THET(SOURCE,2**(3-I))
      TIN14=TIN(SOURCE,3)
      THET14=THET(SOURCE,3)
      TIN23=TIN(SOURCE+MORP1,3)
      THET23=THET(SOURCE+MORP1,3)
      TIN34=TIN(SOURCE+L+M1ORZ,1)
      THET34=THET(SOURCE+L+M1ORZ,1)
      PSI2=PIO2-THET12-THET23
      PSI4=PIO2-THET14-THET34
      IF(PSI2.GT.0.) GO TO 155

      R1MR3=R1-R3
C     ALPH31=DARCOS(R1MR3*RR13)
      ALPH31=  ACOS(R1MR3*RR13)
      PSI312=ALPH31-THET13
      PSI132=PI-ALPH31-THET13
C     TIN12=DSQRT(R13SQ-R1MR3**2)
      TIN12= SQRT(R13SQ-R1MR3**2)
C     TIN23=0.D0
      TIN23=0.E0
C     PSI2=0.D0
      PSI2=0.E0
      GO TO 160
  155 CONTINUE
      PSI312=PIO4+THET12-THET13
      PSI132=PIO4+THET23-THET13
    160 CONTINUE

      IF(PSI4.GT.0.) GO TO 175

      IF(PSI2.LE.0.) GO TO 165
      R1MR3=R1-R3
C     ALPH31=DARCOS(R1MR3*RR13)
      ALPH31=  ACOS(R1MR3*RR13)
      PSI314=ALPH31-THET13
      PSI134=PI-ALPH31-THET13
C     TIN14=DSQRT(R13SQ-R1MR3**2)
      TIN14= SQRT(R13SQ-R1MR3**2)
      GO TO 170

  165 CONTINUE
      PSI314=PSI312
      PSI134=PSI132
      TIN14=TIN12
  170 CONTINUE
C     TIN34=0.D0
      TIN34=0.E0
C     PSI4=0.D0
```

```
      PSI4=0.E0
      GO TO 180
  175 CONTINUE
      PSI314=PIO4+THET14-THET13

      PSI134=PIO4+THET34-THET13

  180 CONTINUE
C     CROLEN=2.D0*TIN13+R1*(PSI312+PSI314)+R3*(PSI132+PSI134)
      CROLEN=2.E0*TIN13+R1*(PSI312+PSI314)+R3*(PSI132+PSI134)
      UNCLEN=TIN12+TIN23+TIN34+TIN14+R2*PSI2+R4*PSI4
      CROMUN=CROLEN-UNCLEN
C     F(SOURCE,TARGET)=.25D0*RPI*CROMUN/R1
      F(SOURCE,TARGET)=.25E0*RPI*CROMUN/R1
      RIJ(SOURCE,TARGET)=SQRT(R13SQ)-0.5*(R1+R3)
  185 CONTINUE
  190 CONTINUE
      RETURN
      END
c
C******      VFAC    12/12/78 D.R.EVANS

      SUBROUTINE VFAC(F,AREA,E,SCALFC,B,R0,IROW,JCOL,MIRRIM,P,PI,N,
         1     M,L,N2,NA,NSYM,NL,NL1,NPT)

     implicit double precision (a-h,o-z)
      DIMENSION F(M,1),AREA(1),E(1),SCALFC(1),B(NA,1),IROW(1),
    1  JCOL(1),MIRRIM(20,1),R0(1)
     COMMON /RI/ RIJ(1001,1001)
      INTEGER ROD,TARGET

      NP=N2-1
      SL=0.25*AREA(N2)

C       SL IS THE DISTANCE BETWEEN OPPOSITE SIDES OF THE CANISTER

      DELTAX=0.5*(SL-P*FLOAT(L-1))

C       DELTAX IS THE DISTANCE FROM THE CENTER OF AN EDGE ROD TO

C       THE ADJACENT FACE OF THE CANISTER

C       CALCULATE THE PATH LENGTH FROM ROD TO CANISTER

      CALL PATHLEN(R0,DELTAX,P,N2,L)

C
C      GENERATE UPPER DIAGONAL PORTION OF VIEW FACTOR MATRIX

      DO 50 IY=1,L

      IYP2=IY+2

      IYP1=IY+1
```

```
      DO 45 IX=1,L

      IYMIX=IY-IX

      IXP2=IX+2

      ROD=IX+L*(IY-1)

C       ZERO OUT MATRIX

      DO 10 KK=ROD,NP
      F(ROD,KK)=0.
      RIJ(ROD,KK)=0.
   10 CONTINUE

C       ADJACENT AND DIAGONAL ROD VIEW FACTORS BY CROSSED STRING

C       METHOD

      CALL STRING(F,R0,P,PI,M,L,ROD,IX,IY)

      IF(IY.EQ.L) GO TO 40

C       MORE-DISTANT VIEW FACTORS BY MODIFIED VIEWPIN METHOD
C       HIGHER-NUMBERED ROWS
C       ADJACENT ROW
      K1=IX-NL
      IF(K1.LE.0) K1=1
      IXM2=IX-2
      IF(IXM2.LT.K1) GO TO 12
      CALL FIJ(F,R0,P,PI,M,NPT,L,ROD,IX,IY,K1,IXM2,1,1)
   12 CONTINUE
      K2=IX+NL
      IF(K2.GT.L) K2=L
      IF(K2.LT.IXP2) GO TO 14

      CALL FIJ(F,R0,P,PI,M,NPT,L,ROD,IX,IY,IXP2,K2,1,1)

   14 CONTINUE
      IF(IYMIX.NE.0) GO TO 20
      DO 15 KK=K1,K2
      IF(KK.LT.IX.OR.KK.EQ.IYP1) GO TO 15
      TARGET=KK+L*IY
      ITARG2=IYP1+(KK-1)*L
      RIJ(ROD,ITARG2)=RIJ(ROD,TARGET)
      F(ROD,ITARG2)=F(ROD,TARGET)
   15 CONTINUE
   20 CONTINUE
      IF(IYP1.GE.L) GO TO 40
C       ROWS BEYOND ADJACENT ROW
      K2=IY+NL1
      IF(K2.GT.L) K2=L

      IF(K2.LT.IYP2) GO TO 24
```

```
      CALL FIJ(F,R0,P,PI,M,NPT,L,ROD,IX,IY,IYP2,K2,1,2)
      IF(IYMIX.NE.0) GO TO 24
      DO 21 KK=IYP2,K2
      TARGET=ROD+(KK-IY)*L
      ITARG2=ROD+KK-IY
      F(ROD,ITARG2)=F(ROD,TARGET)
   21 CONTINUE
   24 CONTINUE
      IF(IX.EQ.1) GO TO 34
C       LOWER-NUMBERED ADJACENT COLUMN
      K2=IY+NL
      IF(K2.GT.L) K2=L

      IF(K2.LT.IYP2) GO TO 40

      CALL FIJ(F,R0,P,PI,M,NPT,L,ROD,IX,IY,IYP2,K2,3,1)
   34 CONTINUE
      IF(IYMIX.EQ.0) GO TO 45
      IF(IX.EQ.L) GO TO 45
C       HIGHER-NUMBERED COLUMNS
C       ADJACENT COLUMN
      CALL FIJ(F,R0,P,PI,M,NPT,L,ROD,IX,IY,IYP2,K2,2,1)
      40 CONTINUE

      IF(IX.EQ.L-1) GO TO 45

C       COLUMNS BEYOND ADJACENT COLUMN
      K2=IX+NL1
      IF(K2.GT.L) K2=L
      IF(K2.LT.IXP2) GO TO 44
      CALL FIJ(F,R0,P,PI,M,NPT,L,ROD,IX,IY,IXP2,K2,2,2)
   44 CONTINUE
   45 CONTINUE

   50 CONTINUE
c
C       FILL VIEW FACTOR MATRIX

      DO 225 I=1,NP
      DO 225 J=I,NP
      RIJ(J,I)=RIJ(I,J)
  225 F(J,I)=F(I,J)*AREA(I)/AREA(J)
      SUMA=1.
      DO 230 I=1,NP
      SUM=1.
      DO 235 J=1,NP
  235 SUM=SUM-F(I,J)
      F(I,N2)=SUM
      RIJ(N2,I)=RIJ(I,N2)

      F(N2,I)=F(I,N2)*AREA(I)/AREA(N2)

  230 SUMA=SUMA-F(N2,I)
      F(N2,N2)=SUMA
      RIJ(N2,N2)=0.25*SL
```

```
c
      RETURN

      END
c
c
c*************************************************
c
      SUBROUTINE INTERP(X,Y,X1,Y1,N)
c
      implicit double precision (a-h,o-z)
c
      dimension x(100),y(100)
c
      DO 100 I=1,n
      I1=I
      IF(X(I1)-X1) 100,100,200
  100 CONTINUE
  200 Y1=Y(I1-1)+((X1-X(I1-1))/(X(I1)-X(I1-1)))*(Y(I1)-Y(I1-1))
      RETURN
      END
```

APPENDIX D1. COBRA-TF LISTINGS

Introduction

Appendix D2 contains an input listing from the two-channel model of COBRA-TF and associated input processing as well as the output for time zero. A full listing of the sub-channel model is not given because the listing is too large because the file is too large, instead only the input file is given here.

Appendix D3 contains the input deck for the sub-channel model.

APPENDIX D2. TWO-CHANNEL MODEL LISTING

```
1********************************* input file listing *********************************
    12345678901234567890123456789012345678901234567890123456789012345678901234567890
  1            0
  2            0          0.0
  3         .001           10           40
  4         1                    **** RBHT Bundle 7x7 Rods   ****
  5    1    1
  6      40.0     1170.       0.0    0.466       124.        0.0    .9999     1.0
  7 air           .0001
  8     2    5
  9     144.8671.74    0 7.22
 10     27.22071.74
 11     32.17918.79
 12     45.04052.95
 13     550.2471.74 7.22    0
 14     3    1
 15     1    3    41.952 1.38  2.0  0.0    0     0 1.0     0   0
 16   16.  0.0
 17     0
 18     4    4    1    0
 19     1    1    2    4.0
 20     1    2                    1
 21     2    1    1   5.75
 22     2    3    4                 1
 23     3    2   22    2.51   10
 24     2     2.51    3     7.72    4     7.72    5     7.72    6     6.85
 25    20     6.85   21     6.85   22     6.85   22     6.85   23     6.85
 26     3    5                    2
 27     4    5                    2
 28     4    1    3    4.0
 29     5    5                    3    4
 30     2
    12345678901234567890123456789012345678901234567890123456789012345678901234567890
 31    50
 32     7    8    1    1    1    1    1    0    0    0
```

```
33  1.2   2   2   3
34  1.2   5   2   3
35  1.2   8   2   3
36  1.2  11   2   3
37  1.2  14   2   3
38  1.2  17   2   3
39  1.2  20   2   3
40  1.2  23   2   3
41   1   8   2   1     1.4    .2952      1.5    1.984
42   2   5   8  11   14   17   20   23
43   3  16.       1   1
44   4  33.       2   1
45   8   3   1   2   2   0   0   0   1
46   1   1   1   2    0.05      16.      1.0    5000.   1
47   3  1.0
48   2   1   1   2    0.05     29.0      1.0    5000.   1
49   4  1.0
50   3   2   0   2    0.05       4.      0.0    5000.   1
51   4  1.0
52   1   3    14.20    14.20      1.0   4           0.     90.0
53   1   2   0   4
54   1   2
55    13.75    521.0   121.75    1563.   157.75    502.0   169.76    502.0
56   2   1   1   2
57   3
58  -1
59    13.75    521.0    169.0     521.
60   9   3
   12345678901234567890123456789012345678901234567890123456789012345678901234567890
61   1 hrod     .374      0.0   4   0
62   1   2.0685  0.0   1   3 .044  1.0   3   2.0545  0.0   3   1  .02  0.0
63   2 tube     .374     .209   1   0
64   3   1.0825  0.0
65   3 wall    14.20     .250   1       0
66   3   1 .250
67   10   3
68    1   17    516.7
69      32.    .1010    8.1400      70.    .1030    8.340
70     212.    .1110    9.090     392.    .1210    10.04
```

```
 71      500.    .1270    10.60     572.    0.131    10.98
 72      752.    .1410    11.93     932.    0.151    12.88
 73     1000.    0.158    13.23    1112.    0.166    13.82
 74     1292.    0.178    14.77    1472.    0.191    15.72
 75     1500.    0.193    15.86    1652.    0.204    16.66
 76     1832.    0.216    17.61    2012.    0.229    18.56
 77     2192.    0.241    19.50
 78    2  14     119.
 79      212.   .16587    67.37     392.   .22014   63.827
 80      572.   .26263    60.28     752.   .29590   56.737
 81      932.   .32194    53.19    1112.   .34233   49.646
 82     1292.   .35829    46.10    1472.   .37078   42.555
 83     1652.   .38056    39.01    1832.   .38822   35.464
 84     2012.   .39421    31.92    2192.   .39891   28.375
 85     2372.   .40259    24.83    2552.   .40546   21.284
 86    3  10     528.8
 87      70.0   .10000   10.083     200.    0.107   11.333
 88      400.   .11400    13.00     600.    0.117   14.833
 89      800.    .120     16.50    1000.    0.125   18.333
 90     1200.    .132     20.00    1400.    0.141   21.833
   12345678901234567890123456789012345678901234567890123456789012345678901234567890
 91     1600.    0.157    23.50    1800.    0.186   25.167
 92   11   1   25
 93    1   5
 94    13.75     0.5   121.75     1.50   157.75     0.5   157.76     0.0
 95    168.0     0.0
 96      0.0      1.     17.5     .921     35.0    .8704     52.5    .8326
 97      70.     .803     87.5    .7755    105.0    .7512    122.5    .7302
 98      140.    .714    157.5    .6973    175.0    .6837    192.5    .6710
 99      220.    .652    255.0    .6332    290.0    .6167    325.0    .6017
100      360.    .588    395.0    .5769    430.0    .5656    465.0    .5562
101      500.    .547    535.0    .5444    570.0    .5304    605.0    .5243
102     1000.    .002
103   13   2   0   2   0   0
104    3   3
105  0.0      0.0  0.1      .801500.      .80
106  0.0      1.0  0.2      1.01500.      1.0
107    1   1   2   1   0     .260     92.05     40.0
108 124.  1.0.9999.0001
```

```
 109
 110    5    5    1    0    0     40.0    1170.0     40.0
 111  124.  1.0.9999.0001
 112
 113   14    5    0    0    0    0    1    2
 114    0
 115    0
 116
 117  500    0    0
 118         .0002         .015          500.          1.0        99999.
 119           5.           1.          800.          800.
 120         -.001         .005          5.0          1.0          200.
    12345678901234567890123456789012345678901234567890123456789012345678901234567890
 121          10.          10.          500.          500.
 122
 123
 124
 125
 126
 127
 128
 129
1
        cobra_tf      date 19980803     time 00:00:00
1                main control parameters are:

                 restart time step . . . . . . . . . . .    0
                 simulation start time . . . . . . . . .      .000
                 outer iteration convergence limit . . .  .0010000
                 maximum number of inner iterations . .   40
                 maximum number of outer iterations  . .   10

   1   1   0   0   0   0   0   0   0   0   0
   2   5   0   0   0   0   0   0   0   0   0
   3   1   0   0   0   0   0   0   0   0   0
   4   4   1   0   0   0   0   0   0   0   0
   7   8   1   1   1   1   1   0   0   0   0
   8   3   1   2   2   0   0   0   1   0   0
   9   3   0   0   0   0   0   0   0   0   0
```

```
  10   3   0   0   0   0   0   0   0   0   0
  11   1  25   0   0   0   0   0   0   0   0
  13   2   0   2   0   0   0   0   0   0   0
  14   5   0   0   0   0   1   2   0   0   0
   0   0   0   0   0   0   0   0   0   0   0
1                                    input summary

                                  **** Test 31504 Bundle Rod 7x7  ****

                                 general information
                                 ******************

0                     initial system operating pressure (psi)  . . .   40.00000
                      initial system steam/water enthalpy   . . . . .1170.00000
                      initial noncondensable gas enthalpy   . . . . . 124.00000
                      initial liquid volume fraction        . . . . .   .00000
                      mass flux for initialization (lb/ft**2-sec) . .   .00000
                      average linear heat rate (kw/ft) . . . . . .     .46600
                      total axial length (inches). . . . . .  174.71997
                      total no. of axial nodes . . . . . .         28

1

                      initial volume fractions of vapor and noncondensable gases

1

 100.00000 percent of the total system volume is initially filled with vapor and/or noncondensable gases. the fraction
 of this gas volume occupied by water vapor and each noncondensable gas is as follows:
 steam         .9999      air     .00010
1

                                    subchannel data

                          nominal        wetted      momentum     momentum      axial variation tables
                subchannel    channel area    perimeter      area         area   continuity momentum   wetted
                  id. no.       (in**2)       (in.)      (bottom)     (top)       area       area    perimeter
                ----------------------------------------------------------------------------------------------
```

1	44.8600	71.740	44.8600	7.2200	0	0	0
2	7.2200	71.740	7.2200	7.2200	0	0	0
3	2.1790	18.790	2.1790	2.1790	0	0	0
4	5.0400	52.950	5.0400	5.0400	0	0	0
5	50.2400	71.740	7.2200	50.2400	0	0	0

0

1 **********

grid spacer data

model selection grid quench front heat transfer to fluid 1
(0=off,1=on) drop breakup at grid spacer 1
grid enhancement of single phase vapor convection 1

grid type 1 material type index, 1
grid length [in] 1.500
grid perimeter [in] 1.984
fraction of channel blocked .295
loss coefficient multiplier 1.400

axial levels containing grid type 1
2 5 8 11 14 17 20 23

grid located in channel	no. of grids in channel	fuel rod - surface index pairs surrounding grid					
3	16.000	1 - 1	0 - 0	0 - 0	0 - 0	0 - 0	0 - 0
4	33.000	2 - 1	0 - 0	0 - 0	0 - 0	0 - 0	0 - 0

0

0 data for lateral momentum convected by axial velocities at section boundries

channel no.	node no.	gap below	gap above	area	node no.	gap below	gap above	area	node no.	gap below	gap above	area	node no.	gap below	gap above	area

0

****

channel thermal connection input data

---

channel no.	fuel rod - surface index pairs						heat slab indices							
3	1 - 1	0 - 0	0 - 0	0 - 0	0 - 0	0 - 0	0	0	0	0	0	0	0	0
4	2 - 1	3 - 1	0 - 0	0 - 0	0 - 0	0 - 0	-1	0	0	0	0	0	0	0

****

0

gap data

gap no.	ik	jk	gap width	gap centroid distance	loss coeff.	frict. flag	gap below	gap above	sign modifier	gaps which face this gap ii side			gaps which face this gap jj side			variation table
1	3	4	1.952	1.380	2.000	.00	0	0	1.000	0	0	0	0	0	0	0

1

channel splitting data - axial level 1 of 4

number of channels	no. of nodes	cell length (nominal)
1	2	.3333

channel	channels above						channels below					
1	2	0	0	0	0	0	1	0	0	0	0	0

1

channel splitting data - axial level 2 of 4

number of channels	no. of nodes	cell length (nominal)
1	1	.4792

channel	channels above						channels below					
2	3	4	0	0	0	0	1	0	0	0	0	0

variable axial noding

node no.	length (ft)	node no.	length (ft)	node no.	length (ft)	node no.	length (ft)	node no.	length (ft)	node no.	length (ft)
2	.4792										

1

channel splitting data - axial level 3 of 4

number of channels	no. of nodes	cell length (nominal)
2	22	.5643

channel	channels above						channels below					
3	5	0	0	0	0	0	2	0	0	0	0	0
4	5	0	0	0	0	0	2	0	0	0	0	0

variable axial noding

node no.	length (ft)	node no.	length (ft)	node no.	length (ft)	node no.	length (ft)	node no.	length (ft)	node no.	length (ft)
2	.2092	3	.6433	4	.6433	5	.6433	6	.5708		
7	.5708	8	.5708	9	.5708	10	.5708	11	.5708		
12	.5708	13	.5708	14	.5708	15	.5708	16	.5708		
17	.5708	18	.5708	19	.5708	20	.5708	21	.5708		

```
              22     .5708        23     .5708
1
                              channel splitting data - axial level   4 of   4

                              number          no. of     cell length
                             of channels        nodes     (nominal)

                                1               3          .3333

      channel          channels above                 channels below
                ----------------------------     ----------------------------
         5       5   0    0    0    0    0       3    4    0    0    0    0

      variable axial noding
      ---------------------
              node   length       node   length       node   length       node   length       node   length
               no.    (ft)         no.    (ft)         no.    (ft)         no.    (ft)         no.    (ft)
              ----   ------       ----   ------       ----   ------       ----   ------       ----   ------
               2     .3333         3     .3333         4     .3333


                              simultaneous solution group information

                   no. of              last cell number in each group
                   groups
                     1                 50
1
   ************************************************************************************************************************************

                                 fuel rod and heat slab model input

                                    no. of fuel rods  =   3              no. of fuel rod surfaces  =   3
                                    no. of heat slabs =   1

   ************************************************************************************************************************************

                                  fuel rod model input
```

fuel rod index	axial location (in.) - (in.)		geometry type	conductor type	radial power factor	axial power profile	renoding flag	minimum node size	rod multiplier
1	13.75 - 162.72		hrod	1	1.000	1	2	.0500	16.000
2	13.75 - 162.72		hrod	1	1.000	1	2	.0500	29.000
3	13.75 - 162.72		tube	2	.000	0	2	.0500	4.000

heat slab model input

heat slab index	channel connection - inside		heated perimeter outside		geometry type	conductor type	slab multiplier
1	4 - 14.20		0 - 14.20		wall	3	1.000

---

conductor geometry description
no. of geometry types = 3

---

type 1 - hrod cylindrical heater rod ----------

rod diameter .3740 (in.)
inside diameter .0000 (in.)
no. of nodes (total) 8
material index (oxide) 0

radial noding information

node no.	material index	radial location	node boundaries (inside)	(outside)	power fraction
1	2	.0484	.0000	.0685	.00000
2	3	.0931	.0685	.1125	1.00000

3	2	.1219	.1125	.1307	.00000
4	2	.1400	.1307	.1488	.00000
5	2	.1582	.1488	.1670	.00000
6	1	.1710	.1670	.1750	.00000
7	1	.1790	.1750	.1830	.00000
8	1	.1870	.1830	.1870	.00000

type 2 - tube tube conductor geometry ----------

outside diameter .3740 (in.)
inside diameter .2090 (in.)
no. of nodes (total) 3
material index (inside) 0
material index (outside) 0

radial noding information

node no.	material index	radial location	node boundaries (inside)	node boundaries (outside)	power fraction
1	1	.1045	.1045	.1251	.00000
2	1	.1472	.1251	.1664	.00000
3	1	.1870	.1664	.1870	.00000

type 3 - wall flat plate conductor geometry ----------

wall perimeter 14.2000 (in.)
wall thickness .2500 (in.)
no. of nodes (total) 3
material index (inside) 0
material index(outside) 0

radial noding information

node no.	material index	radial location	node boundaries (inside)	node boundaries (outside)	power fraction
1	1	.0000	.0000	.0625	.00000
2	1	.1250	.0625	.1875	.00000

3	1	.2500	.1875	.2500	.00000

---

material property tables

---

material type - 1 cold state density = 516.700 (lbm/ft3)

temperature (f)	specific heat (btu/lbm-f)	conductivity (btu/hr-ft-f)
32.0	.10100	8.140
70.0	.10300	8.340
212.0	.11100	9.090
392.0	.12100	10.040
500.0	.12700	10.600
572.0	.13100	10.980
752.0	.14100	11.930
932.0	.15100	12.880
1000.0	.15800	13.230
1112.0	.16600	13.820
212.0	.16587	67.370
392.0	.22014	63.827
572.0	.26263	60.280
752.0	.29590	56.737
932.0	.32194	53.190
1112.0	.34233	49.646
1292.0	.35829	46.100

material type - 2 cold state density = 119.000 (lbm/ft3)

temperature (f)	specific heat (btu/lbm-f)	conductivity (btu/hr-ft-f)
212.0	.16587	67.370
392.0	.22014	63.827
572.0	.26263	60.280
752.0	.29590	56.737
932.0	.32194	53.190

1112.0	.34233	49.646
1292.0	.35829	46.100
1472.0	.37078	42.555
1652.0	.38056	39.010
1832.0	.38822	35.464
70.0	.10000	10.083
200.0	.10700	11.333
400.0	.11400	13.000
600.0	.11700	14.833

material type - 3 cold state density = 528.800 (lbm/ft3)

temperature (f)	specific heat (btu/lbm-f)	conductivity (btu/hr-ft-f)
70.0	.10000	10.083
200.0	.10700	11.333
400.0	.11400	13.000
600.0	.11700	14.833
800.0	.12000	16.500
1000.0	.12500	18.333
1200.0	.13200	20.000
1400.0	.14100	21.833
1600.0	.15700	23.500
1800.0	.18600	25.167

---

axial power profile tables

---

axial profile no. 1 - used by rod nos. = 1 2

rod node no.	axial location (in.)	fluid node no.	axial power factor
1	13.75	5	.5029
2	15.01	5	.5145
3	20.12	6	.5590
4	27.84	7	.6305
5	35.56	8	.7019

6	42.84	9	.7694
7	49.69	10	.8328
8	56.54	11	.8962
9	63.39	12	.9597
10	70.24	13	1.0231
11	77.09	14	1.0865
12	83.94	15	1.1500
13	90.79	16	1.2134
14	97.64	17	1.2768
15	104.49	18	1.3402
16	111.34	19	1.4037
17	118.19	20	1.4671
18	125.04	21	1.4084
19	131.89	22	1.2182
20	138.74	23	1.0279
21	145.59	24	.8376
22	152.44	25	.6474
23	159.29	26	.1930
24	162.72	26	.0000

this table integrates to .9689 over a heated length of 148.97 (in.)

---

power forcing function table

---

transient time (secs)	power factor
.0000	1.0000
17.5000	.9210
35.0000	.8704
52.5000	.8326
70.0000	.8030
87.5000	.7755
105.0000	.7512
122.5000	.7302
140.0000	.7140
157.5000	.6973
175.0000	.6837

192.5000	.6710
220.0000	.6520
255.0000	.6332
290.0000	.6167
325.0000	.6017
360.0000	.5880
395.0000	.5769
430.0000	.5656
465.0000	.5562
500.0000	.5470
535.0000	.5444
570.0000	.5304
605.0000	.5243
1000.0000	.0020

---

1 forcing function tables

0 table 1

time coord.	forcing factor	time coord.	forcing factor	time coord.	forcing factor	time coord.	forcing factor	time coord.	forcing factor
.000	.000	.100	.800	1500.000	.800				

0 table 2

time coord.	forcing factor	time coord.	forcing factor	time coord.	forcing factor	time coord.	forcing factor	time coord.	forcing factor
.000	1.000	.200	1.000	1500.000	1.000				

1 axial and/or injection boundary conditions

boundary type	property specification
1= pressure and enthalpy (axial)	pressure
2= flow and ehthalpy (axial)	mass flow

```
                    3= zero axial flow . . . . . . . . . . . . . . zero
                    4= injected flow and enthalpy  . . . . . . . . injected flow
                    5= pressure sink and enthalpy  . . . . . . . . sink pressure


                                          boundary      specified
                              channel     axial         type          property
                               index      node     (see above)    (see above)     enthalpy

                                 1         1          2              .26         92.05
                                 5         5          1            40.00       1170.00
0

                                    zero crossflow boundary conditions

                                      gap     axial
                                     index    node

                         5     channels will be printed

                                     1    2    3    4    5
0                        3     rods will be printed

                                     1    2    3

0                        1     gaps will be printed

                                     1
0   ***** graphics dump data ***************************************************************************************

         initial run

             maximum number of graphics                (check against dimension of indcmp array --
             dumps  . . . . . . . . . . . . .    500   must not exceed it.)
             normal vessel dump selected
1 trac major edit

    time =  0.000E+00 seconds     delt =  0.000E+00 seconds     time steps =     0   oitno=       0
```

```
    last minimum number of inner iterations was  0 at step     0
    current convergence limits and limitation counts
       delamx      delemx      delrmx      delvmx      delcmx      delpmx
      0.000E+00   0.000E+00   0.000E+00   0.000E+00   0.000E+00   0.000E+00
           0           0           0           0           0           0
    cptime = 0.000E+00
0    channel results     date 19980803  time 00:00:00                           **** Test 31504 Bundle Rod 7x7  ****
*******************************************************************************************************************************
        simulation time =       .00000  seconds          fluid properties for channel    1
node  dist.   pressure       velocity             void fraction              flow rate        flow    heat added     gama
 no.  (ft.)    (psi)         (ft/sec)                                (lbm/s)         reg.       (btu/s)      (lbm/s)
                       liquid  vapor  entr.     liquid  vapor  entr.     liquid    vapor    entr.       liquid    vapor

   3    .67     40.009     .00    .00    .00     .0000 1.0000  .0000     .00000   .00000   .00000   0   .000E+00  .000E+00    .00
   2    .33     40.010     .00    .00    .00     .0000 1.0000  .0000     .00000   .00000   .00000   0   .000E+00  .000E+00    .00
   1    .00     40.010     .00    .00    .00     .0000 1.0000  .0000     .00000   .00000   .00000   0   .000E+00  .000E+00    .00

node  dist.                                 enthalpy                                           density            net
 no.  (ft.)                               (btu/lbm)                                       (lbm/ft3)          entrain
                 ------------------------------------------------------------------------   -------------------------------
                   vapor       hg     vapor-hg    liquid       hf    liq. - hf    mixture       liquid     vapor   mixture

   3    .67       1170.00   1169.77       .23    236.13     236.14      -.01    1169.25      58.29915    .09446    .0945     .000
   2    .33       1170.00   1169.77       .23    236.13     236.14      -.01    1169.25      58.29915    .09446    .0945     .000
   1    .00       1170.00   1169.77       .23    236.13     236.15      -.02    1169.25      58.29915    .09446    .0945     .000

* * * * * * * * * * * * * * * * * * * * * * * * * * * * * * * * * * * * * * * * * * * * * * * * * * * * * * * * * * * * * * * * * * * *

node dist.    mixture    mixture  -- relative velocities --      area   vap./liq.   vap./drop       -------- grid spacers --------
 no.         flow rate  velocity  vap. - liq.  vap. - entr.           interfacial interfacial      grid   temperature   percent
                                                              drag        drag          type       degf      quenched

  3    .67       .00        .00        .00           .00        .0501       .0010       .0010         0           .00        .000
  2    .33       .00        .00        .00           .00        .3115       .0010       .0010         0           .00        .000
  1    .00       .00        .00        .00           .00        .3115       .0010       .0010         0           .00        .000

* * * * * * * * * * * * * * * * * * * * * * * * * * * * * * * * * * * * * * * * * * * * * * * * * * * * * * * * * * * * * * * * * * * *

node dist.    hashl    hascl    hashv    hascv    drop ai  ai source    sent     sdent     qradd     qradv     snkld     gamsd
```

```
  3   .67  347.3965  34.7397   3.4740  34.7397  .1000E-09 .0000E+00 .0000E+00 .0000E+00 .0000E+00 .0000E+00 .0000E+00
.0000E+00
  2   .33  347.3965  34.7397   3.4740  34.7397  .1000E-09 .0000E+00 .0000E+00 .0000E+00 .0000E+00 .0000E+00 .0000E+00
.0000E+00
  1   .00  347.3965  34.7397   3.4740  34.7397  .1000E-09 .0000E+00 .0000E+00 .0000E+00 .0000E+00 .0000E+00 .0000E+00
.0000E+00
0                          ------------------------------- gas volumetric analysis -------------------------------
           hmgas      rmgas   steam    air                                  diam-ld  diam-sd  flow-sd  veloc-sd   gamsd
  3   .67   124.00    .00001  99.990    .010    .000    .000    .000    .000    .0000   .00000 .0000E+00     .00  .0000E+00
  2   .33   124.00    .00001  99.990    .010    .000    .000    .000    .000    .0000   .00000 .0000E+00     .00  .0000E+00
  1   .00   124.00    .00001  99.990    .010    .000    .000    .000    .000    .0000   .00000 .0000E+00     .00  .0000E+00

 ********************************************************************************************************************************************************
0    channel results     date 19980803  time 00:00:00                          **** Test 31504 Bundle Rod 7x7  ****
 ********************************************************************************************************************************************************
        simulation time =       .00000  seconds          fluid properties for channel    2
 node  dist.   pressure        velocity              void fraction                flow rate        flow     heat added      gama
  no.  (ft.)    (psi)          (ft/sec)                                          (lbm/s)          reg.       (btu/s)      (lbm/s)
                      liquid  vapor  entr.     liquid  vapor  entr.     liquid    vapor    entr.        liquid    vapor

   2   1.15     40.009     .00    .00    .00      .0000 1.0000  .0000     .00000   .00000   .00000   0   .000E+00  .000E+00    .00
   1    .67     40.009     .00    .00    .00      .0000 1.0000  .0000     .00000   .00000   .00000   0   .000E+00  .000E+00    .00

 node  dist.                              enthalpy                                        density           net
  no.  (ft.)                             (btu/lbm)                                      (lbm/ft3)         entrain
                 ------------------------------------------------------------------------  ------------------------------
                   vapor       hg      vapor-hg     liquid       hf     liq. - hf     mixture       liquid      vapor    mixture

   2   1.15       1170.00   1169.77        .23     236.13     236.14       -.01     1169.25      58.29915    .09446    .0945     .000
   1    .67       1170.00   1169.77        .23     236.13     236.14       -.01     1169.22      58.29915    .09446    .0945     .000

* * * * * * * * * * * * * * * * * * * * * * * * * * * * * * * * * * * * * * * * * * * * * * * * * * * * * * * * * * * * * * * * * * * * * * * * * * * *

 node dist.    mixture     mixture  -- relative velocities --       area   vap./liq.   vap./drop       -------- grid spacers --------
  no.          flow rate  velocity  vap. - liq.  vap. - entr.           interfacial interfacial      grid   temperature   percent
                                                                          drag        drag          type       degf      quenched

   2   1.15       .00        .00        .00          .00         .0501       .0010       .0010         0         .00        .000
   1    .67       .00        .00        .00          .00         .0501       .0010       .0010         0         .00        .000
```

```
 * * * * * * * * * * * * * * * * * * * * * * * * * * * * * * * * * * * * * * * * * * * * * * * * * * * * * * * * * * * * * * * * * * *

 node dist.    hashl    hascl    hashv    hascv    drop ai  ai source     sent      sdent     qradd     qradv     snkld     gamsd
   2   1.15    80.3732   8.0373    .8037   8.0373  .1000E-09 .0000E+00 .0000E+00 .0000E+00 .0000E+00 .0000E+00 .0000E+00
.0000E+00
   1    .67    80.3732   8.0373    .8037   8.0373  .1000E-09 .0000E+00 .0000E+00 .0000E+00 .0000E+00 .0000E+00 .0000E+00
.0000E+00
0                              -------------------------------- gas volumetric analysis --------------------------------
              hmgas      rmgas   steam    air                                      diam-ld  diam-sd  flow-sd  veloc-sd   gamsd
    2   1.15    124.00    .00001   99.990     .010     .000     .000     .000     .000    .0000   .00000 .0000E+00     .00  .0000E+00
    1    .67    124.00    .00001   99.990     .010     .000     .000     .000     .000    .0000   .00000 .0000E+00     .00  .0000E+00

 *****************************************************************************************************************************
0     channel results     date 19980803  time 00:00:00                          **** Test 31504 Bundle Rod 7x7  ****
 *****************************************************************************************************************************
        simulation time =       .00000  seconds          fluid properties for channel    3
 node  dist.   pressure        velocity              void fraction              flow rate         flow     heat added      gama
  no.  (ft.)    (psi)         (ft/sec)                                  (lbm/s)          reg.      (btu/s)      (lbm/s)
                      liquid  vapor  entr.     liquid  vapor  entr.     liquid     vapor    entr.        liquid    vapor


   23  13.56     40.001     .00    .00    .00      .0000 1.0000  .0000      .00000   .00000   .00000   0   .000E+00  .000E+00    .00
   22  12.99     40.001     .00    .00    .00      .0000 1.0000  .0000      .00000   .00000   .00000   0   .000E+00  .000E+00    .00
   21  12.42     40.002     .00    .00    .00      .0000 1.0000  .0000      .00000   .00000   .00000   0   .000E+00  .000E+00    .00
   20  11.85     40.002     .00    .00    .00      .0000 1.0000  .0000      .00000   .00000   .00000   0   .000E+00  .000E+00    .00
   19  11.28     40.003     .00    .00    .00      .0000 1.0000  .0000      .00000   .00000   .00000   0   .000E+00  .000E+00    .00
   18  10.71     40.003     .00    .00    .00      .0000 1.0000  .0000      .00000   .00000   .00000   0   .000E+00  .000E+00    .00
   17  10.13     40.003     .00    .00    .00      .0000 1.0000  .0000      .00000   .00000   .00000   0   .000E+00  .000E+00    .00
   16   9.56     40.004     .00    .00    .00      .0000 1.0000  .0000      .00000   .00000   .00000   0   .000E+00  .000E+00    .00
   15   8.99     40.004     .00    .00    .00      .0000 1.0000  .0000      .00000   .00000   .00000   0   .000E+00  .000E+00    .00
   14   8.42     40.004     .00    .00    .00      .0000 1.0000  .0000      .00000   .00000   .00000   0   .000E+00  .000E+00    .00
   13   7.85     40.005     .00    .00    .00      .0000 1.0000  .0000      .00000   .00000   .00000   0   .000E+00  .000E+00    .00
   12   7.28     40.005     .00    .00    .00      .0000 1.0000  .0000      .00000   .00000   .00000   0   .000E+00  .000E+00    .00
   11   6.71     40.006     .00    .00    .00      .0000 1.0000  .0000      .00000   .00000   .00000   0   .000E+00  .000E+00    .00
   10   6.14     40.006     .00    .00    .00      .0000 1.0000  .0000      .00000   .00000   .00000   0   .000E+00  .000E+00    .00
    9   5.57     40.006     .00    .00    .00      .0000 1.0000  .0000      .00000   .00000   .00000   0   .000E+00  .000E+00    .00
    8   5.00     40.007     .00    .00    .00      .0000 1.0000  .0000      .00000   .00000   .00000   0   .000E+00  .000E+00    .00
    7   4.43     40.007     .00    .00    .00      .0000 1.0000  .0000      .00000   .00000   .00000   0   .000E+00  .000E+00    .00
    6   3.86     40.007     .00    .00    .00      .0000 1.0000  .0000      .00000   .00000   .00000   0   .000E+00  .000E+00    .00
    5   3.28     40.008     .00    .00    .00      .0000 1.0000  .0000      .00000   .00000   .00000   0   .000E+00  .000E+00    .00
```

4	2.64	40.008	.00	.00	.00	.0000	1.0000	.0000	.00000	.00000	.00000	0	.000E+00	.000E+00	.00
3	2.00	40.009	.00	.00	.00	.0000	1.0000	.0000	.00000	.00000	.00000	0	.000E+00	.000E+00	.00
2	1.36	40.009	.00	.00	.00	.0000	1.0000	.0000	.00000	.00000	.00000	0	.000E+00	.000E+00	.00
1	1.15	40.009	.00	.00	.00	.0000	1.0000	.0000	.00000	.00000	.00000	0	.000E+00	.000E+00	.00

node no.	dist. (ft.)	enthalpy (btu/lbm)						density (lbm/ft3)			net entrain		
		vapor	hg	vapor-hg	liquid	hf	liq. - hf	mixture	liquid	vapor	mixture		
23	13.56	1170.00	1169.77	.23	236.13	236.13	.00	1169.25	58.29915	.09444	.0945	.000	
22	12.99	1170.00	1169.77	.23	236.13	236.13	.00	1169.25	58.29915	.09444	.0945	.000	
21	12.42	1170.00	1169.77	.23	236.13	236.13	.00	1169.25	58.29915	.09444	.0945	.000	
20	11.85	1170.00	1169.77	.23	236.13	236.13	.00	1169.25	58.29915	.09444	.0945	.000	
19	11.28	1170.00	1169.77	.23	236.13	236.13	.00	1169.25	58.29915	.09444	.0945	.000	
18	10.71	1170.00	1169.77	.23	236.13	236.13	.00	1169.25	58.29915	.09444	.0945	.000	
17	10.13	1170.00	1169.77	.23	236.13	236.14	-.01	1169.25	58.29915	.09444	.0945	.000	
16	9.56	1170.00	1169.77	.23	236.13	236.14	-.01	1169.25	58.29915	.09444	.0945	.000	
15	8.99	1170.00	1169.77	.23	236.13	236.14	-.01	1169.25	58.29915	.09444	.0945	.000	
14	8.42	1170.00	1169.77	.23	236.13	236.14	-.01	1169.25	58.29915	.09444	.0945	.000	
13	7.85	1170.00	1169.77	.23	236.13	236.14	-.01	1169.25	58.29915	.09445	.0945	.000	
12	7.28	1170.00	1169.77	.23	236.13	236.14	-.01	1169.25	58.29915	.09445	.0945	.000	
11	6.71	1170.00	1169.77	.23	236.13	236.14	-.01	1169.25	58.29915	.09445	.0945	.000	
10	6.14	1170.00	1169.77	.23	236.13	236.14	-.01	1169.25	58.29915	.09445	.0945	.000	
9	5.57	1170.00	1169.77	.23	236.13	236.14	-.01	1169.25	58.29915	.09445	.0945	.000	
8	5.00	1170.00	1169.77	.23	236.13	236.14	-.01	1169.25	58.29915	.09445	.0945	.000	
7	4.43	1170.00	1169.77	.23	236.13	236.14	-.01	1169.25	58.29915	.09445	.0945	.000	
6	3.86	1170.00	1169.77	.23	236.13	236.14	-.01	1169.25	58.29915	.09445	.0945	.000	
5	3.28	1170.00	1169.77	.23	236.13	236.14	-.01	1169.25	58.29915	.09445	.0945	.000	
4	2.64	1170.00	1169.77	.23	236.13	236.14	-.01	1169.25	58.29915	.09445	.0945	.000	
3	2.00	1170.00	1169.77	.23	236.13	236.14	-.01	1169.25	58.29915	.09445	.0945	.000	
2	1.36	1170.00	1169.77	.23	236.13	236.14	-.01	1169.25	58.29915	.09446	.0945	.000	
1	1.15	1170.00	1169.77	.23	236.13	236.14	-.01	1169.25	58.29915	.09446	.0945	.000	

* *

node no.	dist.	mixture flow rate	mixture velocity	-- relative velocities -- vap. - liq.	vap. - entr.	area interfacial drag	vap./liq. interfacial drag	vap./drop grid type	-------- grid spacers -------- temperature degf	percent quenched

```
 23  13.56      .00       .00       .00         .00       .0151      .0010      .0010       1         .00       .000
 22  12.99      .00       .00       .00         .00       .0151      .0010      .0010       0         .00       .000
 21  12.42      .00       .00       .00         .00       .0151      .0010      .0010       0         .00       .000
 20  11.85      .00       .00       .00         .00       .0151      .0010      .0010       1      502.00       .000
 19  11.28      .00       .00       .00         .00       .0151      .0010      .0010       0         .00       .000
 18  10.71      .00       .00       .00         .00       .0151      .0010      .0010       0         .00       .000
 17  10.13      .00       .00       .00         .00       .0151      .0010      .0010       1     1062.12       .000
 16   9.56      .00       .00       .00         .00       .0151      .0010      .0010       0         .00       .000
 15   8.99      .00       .00       .00         .00       .0151      .0010      .0010       0         .00       .000
 14   8.42      .00       .00       .00         .00       .0151      .0010      .0010       1     1528.70       .000
 13   7.85      .00       .00       .00         .00       .0151      .0010      .0010       0         .00       .000
 12   7.28      .00       .00       .00         .00       .0151      .0010      .0010       0         .00       .000
 11   6.71      .00       .00       .00         .00       .0151      .0010      .0010       1     1330.43       .000
 10   6.14      .00       .00       .00         .00       .0151      .0010      .0010       0         .00       .000
  9   5.57      .00       .00       .00         .00       .0151      .0010      .0010       0         .00       .000
  8   5.00      .00       .00       .00         .00       .0151      .0010      .0010       1     1132.16       .000
  7   4.43      .00       .00       .00         .00       .0151      .0010      .0010       0         .00       .000
  6   3.86      .00       .00       .00         .00       .0151      .0010      .0010       0         .00       .000
  5   3.28      .00       .00       .00         .00       .0151      .0010      .0010       1      933.89       .000
  4   2.64      .00       .00       .00         .00       .0151      .0010      .0010       0         .00       .000
  3   2.00      .00       .00       .00         .00       .0151      .0010      .0010       0         .00       .000
  2   1.36      .00       .00       .00         .00       .0151      .0010      .0010       1      731.43       .000
  1   1.15      .00       .00       .00         .00       .0151      .0010      .0010       0         .00       .000

*******************************************************************

node dist.    hashl    hascl    hashv    hascv    drop ai  ai source    sent     sdent     qradd     qradv     snkld     gamsd
 23  13.56   110.3287  11.0329   1.1033  11.0329  .1000E-09 .0000E+00 .0000E+00 .0000E+00 .0000E+00 .0000E+00 .0000E+00
.0000E+00
 22  12.99   110.3287  11.0329   1.1033  11.0329  .1000E-09 .0000E+00 .0000E+00 .0000E+00 .0000E+00 .0000E+00 .0000E+00
.0000E+00
 21  12.42   110.3287  11.0329   1.1033  11.0329  .1000E-09 .0000E+00 .0000E+00 .0000E+00 .0000E+00 .0000E+00 .0000E+00
.0000E+00
 20  11.85   110.3287  11.0329   1.1033  11.0329  .1000E-09 .0000E+00 .0000E+00 .0000E+00 .0000E+00 .0000E+00 .0000E+00
.0000E+00
 19  11.28   110.3287  11.0329   1.1033  11.0329  .1000E-09 .0000E+00 .0000E+00 .0000E+00 .0000E+00 .0000E+00 .0000E+00
.0000E+00
```

18 10.71 110.3287 11.0329 1.1033 11.0329 .1000E-09 .0000E+00 .0000E+00 .0000E+00 .0000E+00 .0000E+00 .0000E+00
.0000E+00
17 10.13 110.3287 11.0329 1.1033 11.0329 .1000E-09 .0000E+00 .0000E+00 .0000E+00 .0000E+00 .0000E+00 .0000E+00
.0000E+00
16 9.56 110.3287 11.0329 1.1033 11.0329 .1000E-09 .0000E+00 .0000E+00 .0000E+00 .0000E+00 .0000E+00 .0000E+00
.0000E+00
15 8.99 110.3287 11.0329 1.1033 11.0329 .1000E-09 .0000E+00 .0000E+00 .0000E+00 .0000E+00 .0000E+00 .0000E+00
.0000E+00
14 8.42 110.3287 11.0329 1.1033 11.0329 .1000E-09 .0000E+00 .0000E+00 .0000E+00 .0000E+00 .0000E+00 .0000E+00
.0000E+00
13 7.85 110.3287 11.0329 1.1033 11.0329 .1000E-09 .0000E+00 .0000E+00 .0000E+00 .0000E+00 .0000E+00 .0000E+00
.0000E+00
12 7.28 110.3287 11.0329 1.1033 11.0329 .1000E-09 .0000E+00 .0000E+00 .0000E+00 .0000E+00 .0000E+00 .0000E+00
.0000E+00
11 6.71 110.3287 11.0329 1.1033 11.0329 .1000E-09 .0000E+00 .0000E+00 .0000E+00 .0000E+00 .0000E+00 .0000E+00
.0000E+00
10 6.14 110.3287 11.0329 1.1033 11.0329 .1000E-09 .0000E+00 .0000E+00 .0000E+00 .0000E+00 .0000E+00 .0000E+00
.0000E+00
9 5.57 110.3287 11.0329 1.1033 11.0329 .1000E-09 .0000E+00 .0000E+00 .0000E+00 .0000E+00 .0000E+00 .0000E+00
.0000E+00
8 5.00 110.3287 11.0329 1.1033 11.0329 .1000E-09 .0000E+00 .0000E+00 .0000E+00 .0000E+00 .0000E+00 .0000E+00
.0000E+00
7 4.43 110.3287 11.0329 1.1033 11.0329 .1000E-09 .0000E+00 .0000E+00 .0000E+00 .0000E+00 .0000E+00 .0000E+00
.0000E+00
6 3.86 110.3287 11.0329 1.1033 11.0329 .1000E-09 .0000E+00 .0000E+00 .0000E+00 .0000E+00 .0000E+00 .0000E+00
.0000E+00
5 3.28 124.3412 12.4341 1.2434 12.4341 .1000E-09 .0000E+00 .0000E+00 .0000E+00 .0000E+00 .0000E+00 .0000E+00
.0000E+00
4 2.64 124.3412 12.4341 1.2434 12.4341 .1000E-09 .0000E+00 .0000E+00 .0000E+00 .0000E+00 .0000E+00 .0000E+00
.0000E+00
3 2.00 124.3412 12.4341 1.2434 12.4341 .1000E-09 .0000E+00 .0000E+00 .0000E+00 .0000E+00 .0000E+00 .0000E+00
.0000E+00
2 1.36 40.4270 4.0427 .4043 4.0427 .1000E-09 .0000E+00 .0000E+00 .0000E+00 .0000E+00 .0000E+00 .0000E+00
.0000E+00
1 1.15 40.4270 4.0427 .4043 4.0427 .1000E-09 .0000E+00 .0000E+00 .0000E+00 .0000E+00 .0000E+00 .0000E+00
.0000E+00
0 ---------- gas volumetric analysis ----------
hmgas rmgas steam air diam-ld diam-sd flow-sd veloc-sd gamsd
23 13.56 124.00 .00001 99.990 .010 .000 .000 .000 .000 .0000 .00000 .0000E+00 .00 .0000E+00

22	12.99	124.00	.00001	99.990	.010	.000	.000	.000	.000	.0000	.00000	.0000E+00	.00	.0000E+00
21	12.42	124.00	.00001	99.990	.010	.000	.000	.000	.000	.0000	.00000	.0000E+00	.00	.0000E+00
20	11.85	124.00	.00001	99.990	.010	.000	.000	.000	.000	.0000	.00000	.0000E+00	.00	.0000E+00
19	11.28	124.00	.00001	99.990	.010	.000	.000	.000	.000	.0000	.00000	.0000E+00	.00	.0000E+00
18	10.71	124.00	.00001	99.990	.010	.000	.000	.000	.000	.0000	.00000	.0000E+00	.00	.0000E+00
17	10.13	124.00	.00001	99.990	.010	.000	.000	.000	.000	.0000	.00000	.0000E+00	.00	.0000E+00
16	9.56	124.00	.00001	99.990	.010	.000	.000	.000	.000	.0000	.00000	.0000E+00	.00	.0000E+00
15	8.99	124.00	.00001	99.990	.010	.000	.000	.000	.000	.0000	.00000	.0000E+00	.00	.0000E+00
14	8.42	124.00	.00001	99.990	.010	.000	.000	.000	.000	.0000	.00000	.0000E+00	.00	.0000E+00
13	7.85	124.00	.00001	99.990	.010	.000	.000	.000	.000	.0000	.00000	.0000E+00	.00	.0000E+00
12	7.28	124.00	.00001	99.990	.010	.000	.000	.000	.000	.0000	.00000	.0000E+00	.00	.0000E+00
11	6.71	124.00	.00001	99.990	.010	.000	.000	.000	.000	.0000	.00000	.0000E+00	.00	.0000E+00
10	6.14	124.00	.00001	99.990	.010	.000	.000	.000	.000	.0000	.00000	.0000E+00	.00	.0000E+00
9	5.57	124.00	.00001	99.990	.010	.000	.000	.000	.000	.0000	.00000	.0000E+00	.00	.0000E+00
8	5.00	124.00	.00001	99.990	.010	.000	.000	.000	.000	.0000	.00000	.0000E+00	.00	.0000E+00
7	4.43	124.00	.00001	99.990	.010	.000	.000	.000	.000	.0000	.00000	.0000E+00	.00	.0000E+00
6	3.86	124.00	.00001	99.990	.010	.000	.000	.000	.000	.0000	.00000	.0000E+00	.00	.0000E+00
5	3.28	124.00	.00001	99.990	.010	.000	.000	.000	.000	.0000	.00000	.0000E+00	.00	.0000E+00
4	2.64	124.00	.00001	99.990	.010	.000	.000	.000	.000	.0000	.00000	.0000E+00	.00	.0000E+00
3	2.00	124.00	.00001	99.990	.010	.000	.000	.000	.000	.0000	.00000	.0000E+00	.00	.0000E+00
2	1.36	124.00	.00001	99.990	.010	.000	.000	.000	.000	.0000	.00000	.0000E+00	.00	.0000E+00
1	1.15	124.00	.00001	99.990	.010	.000	.000	.000	.000	.0000	.00000	.0000E+00	.00	.0000E+00

****

0 channel results date 19980803 time 00:00:00 **** Test 31504 Bundle Rod 7x7 ****

****

simulation time = .00000 seconds fluid properties for channel 4

node no.	dist. (ft.)	pressure (psi)	velocity (ft/sec)			void fraction			flow rate (lbm/s)			flow reg.	heat added (btu/s)	gama (lbm/s)	
			liquid	vapor	entr.	liquid	vapor	entr.	liquid	vapor	entr.		liquid	vapor	
23	13.56	40.001	.00	.00	.00	.0000	1.0000	.0000	.00000	.00000	.00000	0	.000E+00	.000E+00	.00
22	12.99	40.001	.00	.00	.00	.0000	1.0000	.0000	.00000	.00000	.00000	0	.000E+00	.000E+00	.00
21	12.42	40.002	.00	.00	.00	.0000	1.0000	.0000	.00000	.00000	.00000	0	.000E+00	.000E+00	.00
20	11.85	40.002	.00	.00	.00	.0000	1.0000	.0000	.00000	.00000	.00000	0	.000E+00	.000E+00	.00
19	11.28	40.003	.00	.00	.00	.0000	1.0000	.0000	.00000	.00000	.00000	0	.000E+00	.000E+00	.00
18	10.71	40.003	.00	.00	.00	.0000	1.0000	.0000	.00000	.00000	.00000	0	.000E+00	.000E+00	.00
17	10.13	40.003	.00	.00	.00	.0000	1.0000	.0000	.00000	.00000	.00000	0	.000E+00	.000E+00	.00
16	9.56	40.004	.00	.00	.00	.0000	1.0000	.0000	.00000	.00000	.00000	0	.000E+00	.000E+00	.00

15	8.99	40.004	.00	.00	.00	.0000	1.0000	.0000	.00000	.00000	.00000	0	.000E+00	.000E+00	.00
14	8.42	40.004	.00	.00	.00	.0000	1.0000	.0000	.00000	.00000	.00000	0	.000E+00	.000E+00	.00
13	7.85	40.005	.00	.00	.00	.0000	1.0000	.0000	.00000	.00000	.00000	0	.000E+00	.000E+00	.00
12	7.28	40.005	.00	.00	.00	.0000	1.0000	.0000	.00000	.00000	.00000	0	.000E+00	.000E+00	.00
11	6.71	40.006	.00	.00	.00	.0000	1.0000	.0000	.00000	.00000	.00000	0	.000E+00	.000E+00	.00
10	6.14	40.006	.00	.00	.00	.0000	1.0000	.0000	.00000	.00000	.00000	0	.000E+00	.000E+00	.00
9	5.57	40.006	.00	.00	.00	.0000	1.0000	.0000	.00000	.00000	.00000	0	.000E+00	.000E+00	.00
8	5.00	40.007	.00	.00	.00	.0000	1.0000	.0000	.00000	.00000	.00000	0	.000E+00	.000E+00	.00
7	4.43	40.007	.00	.00	.00	.0000	1.0000	.0000	.00000	.00000	.00000	0	.000E+00	.000E+00	.00
6	3.86	40.007	.00	.00	.00	.0000	1.0000	.0000	.00000	.00000	.00000	0	.000E+00	.000E+00	.00
5	3.28	40.008	.00	.00	.00	.0000	1.0000	.0000	.00000	.00000	.00000	0	.000E+00	.000E+00	.00
4	2.64	40.008	.00	.00	.00	.0000	1.0000	.0000	.00000	.00000	.00000	0	.000E+00	.000E+00	.00
3	2.00	40.009	.00	.00	.00	.0000	1.0000	.0000	.00000	.00000	.00000	0	.000E+00	.000E+00	.00
2	1.36	40.009	.00	.00	.00	.0000	1.0000	.0000	.00000	.00000	.00000	0	.000E+00	.000E+00	.00
1	1.15	40.009	.00	.00	.00	.0000	1.0000	.0000	.00000	.00000	.00000	0	.000E+00	.000E+00	.00

node	dist.	enthalpy (btu/lbm)						density (lbm/ft3)			net entrain
no.	(ft.)	vapor	hg	vapor-hg	liquid	hf	liq. - hf	mixture	liquid	vapor	mixture
23	13.56	1170.00	1169.77	.23	236.13	236.13	.00	1169.25	58.29915	.09444	.0945	.000
22	12.99	1170.00	1169.77	.23	236.13	236.13	.00	1169.25	58.29915	.09444	.0945	.000
21	12.42	1170.00	1169.77	.23	236.13	236.13	.00	1169.25	58.29915	.09444	.0945	.000
20	11.85	1170.00	1169.77	.23	236.13	236.13	.00	1169.25	58.29915	.09444	.0945	.000
19	11.28	1170.00	1169.77	.23	236.13	236.13	.00	1169.25	58.29915	.09444	.0945	.000
18	10.71	1170.00	1169.77	.23	236.13	236.13	.00	1169.25	58.29915	.09444	.0945	.000
17	10.13	1170.00	1169.77	.23	236.13	236.14	-.01	1169.25	58.29915	.09444	.0945	.000
16	9.56	1170.00	1169.77	.23	236.13	236.14	-.01	1169.25	58.29915	.09444	.0945	.000
15	8.99	1170.00	1169.77	.23	236.13	236.14	-.01	1169.25	58.29915	.09444	.0945	.000
14	8.42	1170.00	1169.77	.23	236.13	236.14	-.01	1169.25	58.29915	.09444	.0945	.000
13	7.85	1170.00	1169.77	.23	236.13	236.14	-.01	1169.25	58.29915	.09445	.0945	.000
12	7.28	1170.00	1169.77	.23	236.13	236.14	-.01	1169.25	58.29915	.09445	.0945	.000
11	6.71	1170.00	1169.77	.23	236.13	236.14	-.01	1169.25	58.29915	.09445	.0945	.000
10	6.14	1170.00	1169.77	.23	236.13	236.14	-.01	1169.25	58.29915	.09445	.0945	.000
9	5.57	1170.00	1169.77	.23	236.13	236.14	-.01	1169.25	58.29915	.09445	.0945	.000
8	5.00	1170.00	1169.77	.23	236.13	236.14	-.01	1169.25	58.29915	.09445	.0945	.000
7	4.43	1170.00	1169.77	.23	236.13	236.14	-.01	1169.25	58.29915	.09445	.0945	.000
6	3.86	1170.00	1169.77	.23	236.13	236.14	-.01	1169.25	58.29915	.09445	.0945	.000

5	3.28	1170.00	1169.77	.23	236.13	236.14	-.01	1169.25	58.29915	.09445	.0945	.000
4	2.64	1170.00	1169.77	.23	236.13	236.14	-.01	1169.25	58.29915	.09445	.0945	.000
3	2.00	1170.00	1169.77	.23	236.13	236.14	-.01	1169.25	58.29915	.09445	.0945	.000
2	1.36	1170.00	1169.77	.23	236.13	236.14	-.01	1169.25	58.29915	.09446	.0945	.000
1	1.15	1170.00	1169.77	.23	236.13	236.14	-.01	1169.25	58.29915	.09446	.0945	.000

* *

node no.	dist.	mixture flow rate	mixture velocity	-- relative velocities -- vap. - liq.	vap. - entr.	area interfacial drag	vap./liq. interfacial drag	vap./drop grid type	-------- grid spacers -------- temperature degf	percent quenched
23	13.56	.00	.00	.00	.00	.0350	.0010	.0010	1	.00	.000
22	12.99	.00	.00	.00	.00	.0350	.0010	.0010	0	.00	.000
21	12.42	.00	.00	.00	.00	.0350	.0010	.0010	0	.00	.000
20	11.85	.00	.00	.00	.00	.0350	.0010	.0010	1	502.00	.000
19	11.28	.00	.00	.00	.00	.0350	.0010	.0010	0	.00	.000
18	10.71	.00	.00	.00	.00	.0350	.0010	.0010	0	.00	.000
17	10.13	.00	.00	.00	.00	.0350	.0010	.0010	1	1062.12	.000
16	9.56	.00	.00	.00	.00	.0350	.0010	.0010	0	.00	.000
15	8.99	.00	.00	.00	.00	.0350	.0010	.0010	0	.00	.000
14	8.42	.00	.00	.00	.00	.0350	.0010	.0010	1	1528.70	.000
13	7.85	.00	.00	.00	.00	.0350	.0010	.0010	0	.00	.000
12	7.28	.00	.00	.00	.00	.0350	.0010	.0010	0	.00	.000
11	6.71	.00	.00	.00	.00	.0350	.0010	.0010	1	1330.43	.000
10	6.14	.00	.00	.00	.00	.0350	.0010	.0010	0	.00	.000
9	5.57	.00	.00	.00	.00	.0350	.0010	.0010	0	.00	.000
8	5.00	.00	.00	.00	.00	.0350	.0010	.0010	1	1132.16	.000
7	4.43	.00	.00	.00	.00	.0350	.0010	.0010	0	.00	.000
6	3.86	.00	.00	.00	.00	.0350	.0010	.0010	0	.00	.000
5	3.28	.00	.00	.00	.00	.0350	.0010	.0010	1	933.89	.000
4	2.64	.00	.00	.00	.00	.0350	.0010	.0010	0	.00	.000
3	2.00	.00	.00	.00	.00	.0350	.0010	.0010	0	.00	.000
2	1.36	.00	.00	.00	.00	.0350	.0010	.0010	1	731.43	.000
1	1.15	.00	.00	.00	.00	.0350	.0010	.0010	0	.00	.000

* *

node no.	dist.	hashl	hascl	hashv	hascv	drop ai	ai source	sent	sdent	qradd	qradv	snkld	gamsd

23 13.56 90.5571 9.0557 .9056 9.0557 .1000E-09 .0000E+00 .0000E+00 .0000E+00 .0000E+00 .0000E+00 .0000E+00
.0000E+00
22 12.99 90.5571 9.0557 .9056 9.0557 .1000E-09 .0000E+00 .0000E+00 .0000E+00 .0000E+00 .0000E+00 .0000E+00
.0000E+00
21 12.42 90.5571 9.0557 .9056 9.0557 .1000E-09 .0000E+00 .0000E+00 .0000E+00 .0000E+00 .0000E+00 .0000E+00
.0000E+00
20 11.85 90.5571 9.0557 .9056 9.0557 .1000E-09 .0000E+00 .0000E+00 .0000E+00 .0000E+00 .0000E+00 .0000E+00
.0000E+00
19 11.28 90.5571 9.0557 .9056 9.0557 .1000E-09 .0000E+00 .0000E+00 .0000E+00 .0000E+00 .0000E+00 .0000E+00
.0000E+00
18 10.71 90.5571 9.0557 .9056 9.0557 .1000E-09 .0000E+00 .0000E+00 .0000E+00 .0000E+00 .0000E+00 .0000E+00
.0000E+00
17 10.13 90.5571 9.0557 .9056 9.0557 .1000E-09 .0000E+00 .0000E+00 .0000E+00 .0000E+00 .0000E+00 .0000E+00
.0000E+00
16 9.56 90.5571 9.0557 .9056 9.0557 .1000E-09 .0000E+00 .0000E+00 .0000E+00 .0000E+00 .0000E+00 .0000E+00
.0000E+00
15 8.99 90.5571 9.0557 .9056 9.0557 .1000E-09 .0000E+00 .0000E+00 .0000E+00 .0000E+00 .0000E+00 .0000E+00
.0000E+00
14 8.42 90.5571 9.0557 .9056 9.0557 .1000E-09 .0000E+00 .0000E+00 .0000E+00 .0000E+00 .0000E+00 .0000E+00
.0000E+00
13 7.85 90.5571 9.0557 .9056 9.0557 .1000E-09 .0000E+00 .0000E+00 .0000E+00 .0000E+00 .0000E+00 .0000E+00
.0000E+00
12 7.28 90.5571 9.0557 .9056 9.0557 .1000E-09 .0000E+00 .0000E+00 .0000E+00 .0000E+00 .0000E+00 .0000E+00
.0000E+00
11 6.71 90.5571 9.0557 .9056 9.0557 .1000E-09 .0000E+00 .0000E+00 .0000E+00 .0000E+00 .0000E+00 .0000E+00
.0000E+00
10 6.14 90.5571 9.0557 .9056 9.0557 .1000E-09 .0000E+00 .0000E+00 .0000E+00 .0000E+00 .0000E+00 .0000E+00
.0000E+00
9 5.57 90.5571 9.0557 .9056 9.0557 .1000E-09 .0000E+00 .0000E+00 .0000E+00 .0000E+00 .0000E+00 .0000E+00
.0000E+00
8 5.00 90.5571 9.0557 .9056 9.0557 .1000E-09 .0000E+00 .0000E+00 .0000E+00 .0000E+00 .0000E+00 .0000E+00
.0000E+00
7 4.43 90.5571 9.0557 .9056 9.0557 .1000E-09 .0000E+00 .0000E+00 .0000E+00 .0000E+00 .0000E+00 .0000E+00
.0000E+00
6 3.86 90.5571 9.0557 .9056 9.0557 .1000E-09 .0000E+00 .0000E+00 .0000E+00 .0000E+00 .0000E+00 .0000E+00
.0000E+00
5 3.28 102.0585 10.2059 1.0206 10.2059 .1000E-09 .0000E+00 .0000E+00 .0000E+00 .0000E+00 .0000E+00 .0000E+00
.0000E+00

```
  4  2.64  102.0585  10.2059   1.0206  10.2059  .1000E-09 .0000E+00 .0000E+00 .0000E+00 .0000E+00 .0000E+00 .0000E+00
.0000E+00
  3  2.00  102.0585  10.2059   1.0206  10.2059  .1000E-09 .0000E+00 .0000E+00 .0000E+00 .0000E+00 .0000E+00 .0000E+00
.0000E+00
  2  1.36   33.1822   3.3182    .3318   3.3182  .1000E-09 .0000E+00 .0000E+00 .0000E+00 .0000E+00 .0000E+00 .0000E+00
.0000E+00
  1  1.15   33.1822   3.3182    .3318   3.3182  .1000E-09 .0000E+00 .0000E+00 .0000E+00 .0000E+00 .0000E+00 .0000E+00
.0000E+00
0                      -------------------------------- gas volumetric analysis --------------------------------
          hmgas     rmgas   steam    air                                  diam-ld  diam-sd  flow-sd  veloc-sd   gamsd
  23  13.56   124.00   .00001  99.990   .010    .000    .000    .000    .000   .0000   .00000 .0000E+00    .00  .0000E+00
  22  12.99   124.00   .00001  99.990   .010    .000    .000    .000    .000   .0000   .00000 .0000E+00    .00  .0000E+00
  21  12.42   124.00   .00001  99.990   .010    .000    .000    .000    .000   .0000   .00000 .0000E+00    .00  .0000E+00
  20  11.85   124.00   .00001  99.990   .010    .000    .000    .000    .000   .0000   .00000 .0000E+00    .00  .0000E+00
  19  11.28   124.00   .00001  99.990   .010    .000    .000    .000    .000   .0000   .00000 .0000E+00    .00  .0000E+00
  18  10.71   124.00   .00001  99.990   .010    .000    .000    .000    .000   .0000   .00000 .0000E+00    .00  .0000E+00
  17  10.13   124.00   .00001  99.990   .010    .000    .000    .000    .000   .0000   .00000 .0000E+00    .00  .0000E+00
  16   9.56   124.00   .00001  99.990   .010    .000    .000    .000    .000   .0000   .00000 .0000E+00    .00  .0000E+00
  15   8.99   124.00   .00001  99.990   .010    .000    .000    .000    .000   .0000   .00000 .0000E+00    .00  .0000E+00
  14   8.42   124.00   .00001  99.990   .010    .000    .000    .000    .000   .0000   .00000 .0000E+00    .00  .0000E+00
  13   7.85   124.00   .00001  99.990   .010    .000    .000    .000    .000   .0000   .00000 .0000E+00    .00  .0000E+00
  12   7.28   124.00   .00001  99.990   .010    .000    .000    .000    .000   .0000   .00000 .0000E+00    .00  .0000E+00
  11   6.71   124.00   .00001  99.990   .010    .000    .000    .000    .000   .0000   .00000 .0000E+00    .00  .0000E+00
  10   6.14   124.00   .00001  99.990   .010    .000    .000    .000    .000   .0000   .00000 .0000E+00    .00  .0000E+00
   9   5.57   124.00   .00001  99.990   .010    .000    .000    .000    .000   .0000   .00000 .0000E+00    .00  .0000E+00
   8   5.00   124.00   .00001  99.990   .010    .000    .000    .000    .000   .0000   .00000 .0000E+00    .00  .0000E+00
   7   4.43   124.00   .00001  99.990   .010    .000    .000    .000    .000   .0000   .00000 .0000E+00    .00  .0000E+00
   6   3.86   124.00   .00001  99.990   .010    .000    .000    .000    .000   .0000   .00000 .0000E+00    .00  .0000E+00
   5   3.28   124.00   .00001  99.990   .010    .000    .000    .000    .000   .0000   .00000 .0000E+00    .00  .0000E+00
   4   2.64   124.00   .00001  99.990   .010    .000    .000    .000    .000   .0000   .00000 .0000E+00    .00  .0000E+00
   3   2.00   124.00   .00001  99.990   .010    .000    .000    .000    .000   .0000   .00000 .0000E+00    .00  .0000E+00
   2   1.36   124.00   .00001  99.990   .010    .000    .000    .000    .000   .0000   .00000 .0000E+00    .00  .0000E+00
   1   1.15   124.00   .00001  99.990   .010    .000    .000    .000    .000   .0000   .00000 .0000E+00    .00  .0000E+00

 ************************************************************************************************************************************
0    channel results    date 19980803  time 00:00:00                    **** Test 31504 Bundle Rod 7x7  ****
 ************************************************************************************************************************************
       simulation time =      .00000  seconds         fluid properties for channel    5
node  dist.   pressure        velocity             void fraction              flow rate        flow     heat added      gama
```

no.	(ft.)	(psi)	(ft/sec)						(lbm/s)			reg.	(btu/s)		(lbm/s)	
			liquid	vapor	entr.	liquid	vapor	entr.	liquid	vapor	entr.		liquid	vapor		
4	14.56	40.000	.00	.00	.00	.0000	1.0000	.0000	.00000	.00000	.00000	0	.000E+00	.000E+00	.00	
3	14.23	40.000	.00	.00	.00	.0000	1.0000	.0000	.00000	.00000	.00000	0	.000E+00	.000E+00	.00	
2	13.89	40.001	.00	.00	.00	.0000	1.0000	.0000	.00000	.00000	.00000	0	.000E+00	.000E+00	.00	
1	13.56	40.001	.00	.00	.00	.0000	1.0000	.0000	.00000	.00000	.00000	0	.000E+00	.000E+00	.00	

node	dist.	enthalpy (btu/lbm)						density (lbm/ft3)			net entrain	
no.	(ft.)	vapor	hg	vapor-hg	liquid	hf	liq. - hf	mixture	liquid	vapor	mixture	
4	14.56	1170.00	1169.77	.23	236.13	236.13	.00	1169.25	58.29915	.09443	.0945	.000
3	14.23	1170.00	1169.77	.23	236.13	236.13	.00	1169.25	58.29915	.09444	.0945	.000
2	13.89	1170.00	1169.77	.23	236.13	236.13	.00	1169.25	58.29915	.09444	.0945	.000
1	13.56	1170.00	1169.77	.23	236.13	236.13	.00	1169.29	58.29915	.09444	.0945	.000

* *

node	dist.	mixture	mixture	-- relative velocities --		area	vap./liq.	vap./drop	-------- grid spacers --------		
no.		flow rate	velocity	vap. - liq.	vap. - entr.	interfacial drag	interfacial drag	grid type	temperature degf	percent quenched	
4	14.56	.00	.00	.00	.00	.3489	.0010	.0010	0	.00	.000
3	14.23	.00	.00	.00	.00	.3489	.0010	.0010	0	.00	.000
2	13.89	.00	.00	.00	.00	.3489	.0010	.0010	0	.00	.000
1	13.56	.00	.00	.00	.00	.0501	.0010	.0010	0	.00	.000

* *

node	dist.	hashl	hascl	hashv	hascv	drop ai	ai source	sent	sdent	qradd	qradv	snkld	gamsd
4	14.56	389.0593	38.9059	3.8906	38.9059	.1000E-09	.0000E+00	.0000E+00	.0000E+00	.0000E+00	.0000E+00	.0000E+00	.0000E+00
3	14.23	389.0593	38.9059	3.8906	38.9059	.1000E-09	.0000E+00	.0000E+00	.0000E+00	.0000E+00	.0000E+00	.0000E+00	.0000E+00
2	13.89	389.0593	38.9059	3.8906	38.9059	.1000E-09	.0000E+00	.0000E+00	.0000E+00	.0000E+00	.0000E+00	.0000E+00	.0000E+00

```
  1  13.56   389.0593  38.9059   3.8906  38.9059  .1000E-09 .0000E+00 .0000E+00 .0000E+00 .0000E+00 .0000E+00 .0000E+00
.0000E+00
0                          --------------------------------- gas volumetric analysis ---------------------------------
           hmgas     rmgas   steam    air                                  diam-ld  diam-sd  flow-sd  veloc-sd   gamsd

   4  14.56    124.00    .00001   99.990    .010     .000     .000     .000     .000     .0000    .00000 .0000E+00     .00  .0000E+00
   3  14.23    124.00    .00001   99.990    .010     .000     .000     .000     .000     .0000    .00000 .0000E+00     .00  .0000E+00
   2  13.89    124.00    .00001   99.990    .010     .000     .000     .000     .000     .0000    .00000 .0000E+00     .00  .0000E+00
   1  13.56    124.00    .00001   99.990    .010     .000     .000     .000     .000     .0000    .00000 .0000E+00     .00  .0000E+00

 ********************************************************************************************************************************************
1                        rod results                date    1998  0803  time    00:0  0:00
                                    **** Test 31504 Bundle Rod 7x7  ****

 ********************************************************************************************************************************************

          heater rod number  1                      simulation time =     .00 seconds
          surface no.  1 of  1
          ----------          conducts heat to channels  3  0  0  0  0  0            geometry type =  1
                                and azimuthally to surfaces   1 and   1              no. of radial nodes =  8

 ********************************************************************************************************************************************
  rod      axial      fluid temperatures     surface       heat      heater rod temperatues,
  node     location          (deg-f)          heat flux    transfer          (deg-f)
  no.      (in.)       liquid     vapor     (b/h-ft2)      mode        surface     center
  ----    --------     ------     -----     ---------    --------     -------     ------

   24      162.72         .0         .0     .0000E+00              502.00     502.00      .0000E+00
   23  *   159.29         .0         .0     .0000E+00              502.00     502.00      .0000E+00
   22  *   152.44         .0         .0     .0000E+00              658.35     658.35      .0000E+00
   21  *   145.59         .0         .0     .0000E+00              860.24     860.24      .0000E+00
   20  *   138.74         .0         .0     .0000E+00             1062.12    1062.12       .0000E+00
   19  *   131.89         .0         .0     .0000E+00             1264.00    1264.00       .0000E+00
   18  *   125.04         .0         .0     .0000E+00             1465.89    1465.89       .0000E+00
   17  *   118.19         .0         .0     .0000E+00             1528.70    1528.70       .0000E+00
   16  *   111.34         .0         .0     .0000E+00             1462.61    1462.61       .0000E+00
   15  *   104.49         .0         .0     .0000E+00             1396.52    1396.52       .0000E+00
   14  *    97.64         .0         .0     .0000E+00             1330.43    1330.43       .0000E+00
   13  *    90.79         .0         .0     .0000E+00             1264.34    1264.34       .0000E+00
```

12	*	83.94	.0	.0	.0000E+00	1198.25	1198.25	.0000E+00
11	*	77.09	.0	.0	.0000E+00	1132.16	1132.16	.0000E+00
10	*	70.24	.0	.0	.0000E+00	1066.07	1066.07	.0000E+00
9	*	63.39	.0	.0	.0000E+00	999.98	999.98	.0000E+00
8	*	56.54	.0	.0	.0000E+00	933.89	933.89	.0000E+00
7	*	49.69	.0	.0	.0000E+00	867.80	867.80	.0000E+00
6	*	42.84	.0	.0	.0000E+00	801.71	801.71	.0000E+00
5	*	35.56	.0	.0	.0000E+00	731.43	731.43	.0000E+00
4	*	27.84	.0	.0	.0000E+00	656.94	656.94	.0000E+00
3	*	20.12	.0	.0	.0000E+00	582.46	582.46	.0000E+00
2	*	15.01	.0	.0	.0000E+00	533.11	533.11	.0000E+00
1		13.75	.0	.0	.0000E+00	521.00	521.00	.0000E+00

rod node	axial location	rod temperatures (deg-f) radii in inches							
no.	(in.)	.0484	.0931	.1219	.1400	.1582	.1710	.1790	.1870
23	* 159.29	502.0	502.0	502.0	502.0	502.0	502.0	502.0	502.0
22	* 152.44	658.4	658.4	658.4	658.4	658.4	658.4	658.4	658.4
21	* 145.59	860.2	860.2	860.2	860.2	860.2	860.2	860.2	860.2
20	* 138.74	1062.1	1062.1	1062.1	1062.1	1062.1	1062.1	1062.1	1062.1
19	* 131.89	1264.0	1264.0	1264.0	1264.0	1264.0	1264.0	1264.0	1264.0
18	* 125.04	1465.9	1465.9	1465.9	1465.9	1465.9	1465.9	1465.9	1465.9
17	* 118.19	1528.7	1528.7	1528.7	1528.7	1528.7	1528.7	1528.7	1528.7
16	* 111.34	1462.6	1462.6	1462.6	1462.6	1462.6	1462.6	1462.6	1462.6
15	* 104.49	1396.5	1396.5	1396.5	1396.5	1396.5	1396.5	1396.5	1396.5
14	* 97.64	1330.4	1330.4	1330.4	1330.4	1330.4	1330.4	1330.4	1330.4
13	* 90.79	1264.3	1264.3	1264.3	1264.3	1264.3	1264.3	1264.3	1264.3
12	* 83.94	1198.3	1198.3	1198.3	1198.3	1198.3	1198.3	1198.3	1198.3
11	* 77.09	1132.2	1132.2	1132.2	1132.2	1132.2	1132.2	1132.2	1132.2
10	* 70.24	1066.1	1066.1	1066.1	1066.1	1066.1	1066.1	1066.1	1066.1
9	* 63.39	1000.0	1000.0	1000.0	1000.0	1000.0	1000.0	1000.0	1000.0
8	* 56.54	933.9	933.9	933.9	933.9	933.9	933.9	933.9	933.9
7	* 49.69	867.8	867.8	867.8	867.8	867.8	867.8	867.8	867.8
6	* 42.84	801.7	801.7	801.7	801.7	801.7	801.7	801.7	801.7
5	* 35.56	731.4	731.4	731.4	731.4	731.4	731.4	731.4	731.4

4	*	27.84	656.9	656.9	656.9	656.9	656.9	656.9	656.9	656.9
3	*	20.12	582.5	582.5	582.5	582.5	582.5	582.5	582.5	582.5
2	*	15.01	533.1	533.1	533.1	533.1	533.1	533.1	533.1	533.1

****

heater rod number 2 simulation time = .00 seconds
surface no. 1 of 1
---------- conducts heat to channels 4 0 0 0 0 0 geometry type = 1
and azimuthally to surfaces 1 and 1 no. of radial nodes = 8

****

rod node no.		axial location (in.)	fluid temperatures (deg-f) liquid	vapor	surface heat flux (b/h-ft2)	heat transfer mode	heater rod temperatues, (deg-f) surface	center
24		162.72	.0	.0	.0000E+00	502.00	502.00	.0000E+00
23	*	159.29	.0	.0	.0000E+00	502.00	502.00	.0000E+00
22	*	152.44	.0	.0	.0000E+00	658.35	658.35	.0000E+00
21	*	145.59	.0	.0	.0000E+00	860.24	860.24	.0000E+00
20	*	138.74	.0	.0	.0000E+00	1062.12	1062.12	.0000E+00
19	*	131.89	.0	.0	.0000E+00	1264.00	1264.00	.0000E+00
18	*	125.04	.0	.0	.0000E+00	1465.89	1465.89	.0000E+00
17	*	118.19	.0	.0	.0000E+00	1528.70	1528.70	.0000E+00
16	*	111.34	.0	.0	.0000E+00	1462.61	1462.61	.0000E+00
15	*	104.49	.0	.0	.0000E+00	1396.52	1396.52	.0000E+00
14	*	97.64	.0	.0	.0000E+00	1330.43	1330.43	.0000E+00
13	*	90.79	.0	.0	.0000E+00	1264.34	1264.34	.0000E+00
12	*	83.94	.0	.0	.0000E+00	1198.25	1198.25	.0000E+00
11	*	77.09	.0	.0	.0000E+00	1132.16	1132.16	.0000E+00
10	*	70.24	.0	.0	.0000E+00	1066.07	1066.07	.0000E+00
9	*	63.39	.0	.0	.0000E+00	999.98	999.98	.0000E+00
8	*	56.54	.0	.0	.0000E+00	933.89	933.89	.0000E+00
7	*	49.69	.0	.0	.0000E+00	867.80	867.80	.0000E+00
6	*	42.84	.0	.0	.0000E+00	801.71	801.71	.0000E+00
5	*	35.56	.0	.0	.0000E+00	731.43	731.43	.0000E+00
4	*	27.84	.0	.0	.0000E+00	656.94	656.94	.0000E+00

3	*	20.12	.0	.0	.0000E+00		582.46	582.46	.0000E+00			
2	*	15.01	.0	.0	.0000E+00		533.11	533.11	.0000E+00			
1		13.75	.0	.0	.0000E+00		521.00	521.00	.0000E+00			

rod	axial	rod temperatures (deg-f)									
node	location	radii in inches									
no.	(in.)	.0484	.0931	.1219	.1400	.1582	.1710	.1790	.1870		
23	*	159.29	502.0	502.0	502.0	502.0	502.0	502.0	502.0	502.0	
22	*	152.44	658.4	658.4	658.4	658.4	658.4	658.4	658.4	658.4	
21	*	145.59	860.2	860.2	860.2	860.2	860.2	860.2	860.2	860.2	
20	*	138.74	1062.1	1062.1	1062.1	1062.1	1062.1	1062.1	1062.1	1062.1	
19	*	131.89	1264.0	1264.0	1264.0	1264.0	1264.0	1264.0	1264.0	1264.0	
18	*	125.04	1465.9	1465.9	1465.9	1465.9	1465.9	1465.9	1465.9	1465.9	
17	*	118.19	1528.7	1528.7	1528.7	1528.7	1528.7	1528.7	1528.7	1528.7	
16	*	111.34	1462.6	1462.6	1462.6	1462.6	1462.6	1462.6	1462.6	1462.6	
15	*	104.49	1396.5	1396.5	1396.5	1396.5	1396.5	1396.5	1396.5	1396.5	
14	*	97.64	1330.4	1330.4	1330.4	1330.4	1330.4	1330.4	1330.4	1330.4	
13	*	90.79	1264.3	1264.3	1264.3	1264.3	1264.3	1264.3	1264.3	1264.3	
12	*	83.94	1198.3	1198.3	1198.3	1198.3	1198.3	1198.3	1198.3	1198.3	
11	*	77.09	1132.2	1132.2	1132.2	1132.2	1132.2	1132.2	1132.2	1132.2	
10	*	70.24	1066.1	1066.1	1066.1	1066.1	1066.1	1066.1	1066.1	1066.1	
9	*	63.39	1000.0	1000.0	1000.0	1000.0	1000.0	1000.0	1000.0	1000.0	
8	*	56.54	933.9	933.9	933.9	933.9	933.9	933.9	933.9	933.9	
7	*	49.69	867.8	867.8	867.8	867.8	867.8	867.8	867.8	867.8	
6	*	42.84	801.7	801.7	801.7	801.7	801.7	801.7	801.7	801.7	
5	*	35.56	731.4	731.4	731.4	731.4	731.4	731.4	731.4	731.4	
4	*	27.84	656.9	656.9	656.9	656.9	656.9	656.9	656.9	656.9	
3	*	20.12	582.5	582.5	582.5	582.5	582.5	582.5	582.5	582.5	
2	*	15.01	533.1	533.1	533.1	533.1	533.1	533.1	533.1	533.1	

****

cylindrical tube rod no. 3 simulation time = .00 seconds

surface no. 1 of 1

---------- conducts heat to channels 4 0 0 0 0 0 geometry type = 2

and azimuthally to surfaces 1 and 1 no. of radial nodes = 3

rod node no.		axial location (in.)	outside surface heat flux (b/h-ft2)	outside surface h.t. mode	outside surface **** temperatures (deg-f) **** wall	outside surface vapor	outside surface liquid	inside surface liquid	inside surface vapor	inside surface wall	inside surface h.t. mode	inside surface heat flux (b/h-ftl)
24		162.72	.0000E+00		521.00	.00	.00			521.00		.0000E+00
23	*	159.29	.0000E+00		521.00	.00	.00			521.00		.0000E+00
22	*	152.44	.0000E+00		521.00	.00	.00			521.00		.0000E+00
21	*	145.59	.0000E+00		521.00	.00	.00			521.00		.0000E+00
20	*	138.74	.0000E+00		521.00	.00	.00			521.00		.0000E+00
19	*	131.89	.0000E+00		521.00	.00	.00			521.00		.0000E+00
18	*	125.04	.0000E+00		521.00	.00	.00			521.00		.0000E+00
17	*	118.19	.0000E+00		521.00	.00	.00			521.00		.0000E+00
16	*	111.34	.0000E+00		521.00	.00	.00			521.00		.0000E+00
15	*	104.49	.0000E+00		521.00	.00	.00			521.00		.0000E+00
14	*	97.64	.0000E+00		521.00	.00	.00			521.00		.0000E+00
13	*	90.79	.0000E+00		521.00	.00	.00			521.00		.0000E+00
12	*	83.94	.0000E+00		521.00	.00	.00			521.00		.0000E+00
11	*	77.09	.0000E+00		521.00	.00	.00			521.00		.0000E+00
10	*	70.24	.0000E+00		521.00	.00	.00			521.00		.0000E+00
9	*	63.39	.0000E+00		521.00	.00	.00			521.00		.0000E+00
8	*	56.54	.0000E+00		521.00	.00	.00			521.00		.0000E+00
7	*	49.69	.0000E+00		521.00	.00	.00			521.00		.0000E+00
6	*	42.84	.0000E+00		521.00	.00	.00			521.00		.0000E+00
5	*	35.56	.0000E+00		521.00	.00	.00			521.00		.0000E+00
4	*	27.84	.0000E+00		521.00	.00	.00			521.00		.0000E+00
3	*	20.12	.0000E+00		521.00	.00	.00			521.00		.0000E+00
2	*	15.01	.0000E+00		521.00	.00	.00			521.00		.0000E+00
1		13.75	.0000E+00		521.00	.00	.00			521.00		.0000E+00

1 heat slab results date 1998 0803 time 00:0 0:00

**** Test 31504 Bundle Rod 7x7 ****

heat slab no. 1 (wall) simulation time = .00 seconds
fluid channel on inside surface = 4
fluid channel on outside surface = 0
geometry type = 3
no. of nodes = 3

rod node no.	axial location (in.)	outside surface heat flux (b/h-ft2)	outside surface h.t. mode	outside surface **** temperatures (deg-f) **** wall	outside surface vapor	outside surface liquid	inside surface liquid	inside surface vapor	inside surface wall	inside surface h.t. mode	inside surface heat flux (b/h-ftl)
23	159.29	.0000E+00		521.00		.00	.00	.00	521.00		.0000E+00
22	152.44	.0000E+00		521.00		.00	.00	.00	521.00		.0000E+00
21	145.59	.0000E+00		521.00		.00	.00	.00	521.00		.0000E+00
20	138.74	.0000E+00		521.00		.00	.00	.00	521.00		.0000E+00
19	131.89	.0000E+00		521.00		.00	.00	.00	521.00		.0000E+00
18	125.04	.0000E+00		521.00		.00	.00	.00	521.00		.0000E+00
17	118.19	.0000E+00		521.00		.00	.00	.00	521.00		.0000E+00
16	111.34	.0000E+00		521.00		.00	.00	.00	521.00		.0000E+00
15	104.49	.0000E+00		521.00		.00	.00	.00	521.00		.0000E+00
14	97.64	.0000E+00		521.00		.00	.00	.00	521.00		.0000E+00
13	90.79	.0000E+00		521.00		.00	.00	.00	521.00		.0000E+00
12	83.94	.0000E+00		521.00		.00	.00	.00	521.00		.0000E+00
11	77.09	.0000E+00		521.00		.00	.00	.00	521.00		.0000E+00
10	70.24	.0000E+00		521.00		.00	.00	.00	521.00		.0000E+00
9	63.39	.0000E+00		521.00		.00	.00	.00	521.00		.0000E+00
8	56.54	.0000E+00		521.00		.00	.00	.00	521.00		.0000E+00
7	49.69	.0000E+00		521.00		.00	.00	.00	521.00		.0000E+00
6	42.84	.0000E+00		521.00		.00	.00	.00	521.00		.0000E+00
5	35.56	.0000E+00		521.00		.00	.00	.00	521.00		.0000E+00
4	27.84	.0000E+00		521.00		.00	.00	.00	521.00		.0000E+00
3	20.12	.0000E+00		521.00		.00	.00	.00	521.00		.0000E+00
2	15.01	.0000E+00		521.00		.00	.00	.00	521.00		.0000E+00

1 lateral drift results date 1998 0803 time 00:0 0:00

case 0 **** Test 31504 Bundle Rod 7x7 ****

****

simulation time = .00000 seconds summary for gap 1 connecting channel 3 to channel 4

--- axial --- range (in.)	-------- crossflows (lb/sec) liquid	vapor	entrained	---------- velocities ---------- liquid	vapor	entrained	diff. pii-pjj	pressure ii	pressure jj	void fraction area ii	void fraction area jj	flow
13.8- 16.3	.00	.00	.00	.00	.00	.00	.000	1.0000	1.0000	.034		
16.3- 24.0	.00	.00	.00	.00	.00	.00	.000	1.0000	1.0000	.105		
24.0- 31.7	.00	.00	.00	.00	.00	.00	.000	1.0000	1.0000	.105		
31.7- 39.4	.00	.00	.00	.00	.00	.00	.000	1.0000	1.0000	.105		
39.4- 46.3	.00	.00	.00	.00	.00	.00	.000	1.0000	1.0000	.093		
46.3- 53.1	.00	.00	.00	.00	.00	.00	.000	1.0000	1.0000	.093		
53.1- 60.0	.00	.00	.00	.00	.00	.00	.000	1.0000	1.0000	.093		
60.0- 66.8	.00	.00	.00	.00	.00	.00	.000	1.0000	1.0000	.093		
66.8- 73.7	.00	.00	.00	.00	.00	.00	.000	1.0000	1.0000	.093		
73.7- 80.5	.00	.00	.00	.00	.00	.00	.000	1.0000	1.0000	.093		
80.5- 87.4	.00	.00	.00	.00	.00	.00	.000	1.0000	1.0000	.093		
87.4- 94.2	.00	.00	.00	.00	.00	.00	.000	1.0000	1.0000	.093		
94.2-101.1	.00	.00	.00	.00	.00	.00	.000	1.0000	1.0000	.093		
101.1-107.9	.00	.00	.00	.00	.00	.00	.000	1.0000	1.0000	.093		
107.9-114.8	.00	.00	.00	.00	.00	.00	.000	1.0000	1.0000	.093		
114.8-121.6	.00	.00	.00	.00	.00	.00	.000	1.0000	1.0000	.093		
121.6-128.5	.00	.00	.00	.00	.00	.00	.000	1.0000	1.0000	.093		
128.5-135.3	.00	.00	.00	.00	.00	.00	.000	1.0000	1.0000	.093		
135.3-142.2	.00	.00	.00	.00	.00	.00	.000	1.0000	1.0000	.093		
142.2-149.0	.00	.00	.00	.00	.00	.00	.000	1.0000	1.0000	.093		
149.0-155.9	.00	.00	.00	.00	.00	.00	.000	1.0000	1.0000	.093		
155.9-162.7	.00	.00	.00	.00	.00	.00	.000	1.0000	1.0000	.093		

1 injection boundary conditions date 1998 0803 time 00:0 0:00

case 0 **** Test 31504 Bundle Rod 7x7 ****

****

simulation time = .00000 seconds

```
                        channel   node       wginjt    wlinjt    hginjt    hlinjt
                          no.     no.       lbm/sec   lbm/sec   btu/lbm   btu/lbm

************************************************************************
*                      new time domain reached                         *
*  minimum   maximum    time     long     short   graphics    dump    *
*   time      time     domain    edit     edit     edit               *
*   step      step      end    interval  interval  interval  interval *
*                                                  *
* 2.000E-04 1.500E-02 5.000E+02 5.000E+00 8.000E+02 1.000E+00 8.000E+02 *
************************************************************************

time step ratio      =  1.000E+00

* * * * *  saved graphics data at time     .0000 * * * * * * * * * * *
* * * * *  saved graphics data at time     .9868 * * * * * * * * * * *
* * * * *  saved graphics data at time    1.9918 * * * * * * * * * * *
* * * * *  saved graphics data at time    2.9968 * * * * * * * * * * *
* * * * *  saved graphics data at time    4.0018 * * * * * * * * * * *
```

APPENDIX D3. SUB-CHANNEL MODEL INPUT DECK

```
          0
          0          0.0
        .001           5           40
        1     ****** Sub-Channel Model of RBHT 7x7 Bundle ******
    1    1
      40.0   1169.77       0.0    .46667      124.       0.0     .9999     1.0
air           .0001
    2   18
    1.0681.5875  0.0  0.0    1
   23    1    0
    2.13621.175  0.0  0.0    3
   23    1    0   23    2    0   23    3    0
    3.0681.5875  0.0  0.0    2
   23    2    0   23    4    0
    4.13621.175  0.0  0.0    3
   23    3    0   23    5    0   23    7    0
    5.13621.175  0.0  0.0    4
   23    4    0   23    5    0   23    6    0   23    8    0
    6.0681.5875  0.0  0.0    2
   23    6    0   23    9    0
    7.08741.083  0.0  0.0    2
   23    7    0   23   10    0
    8.08741.083  0.0  0.0    3
   23    8    0   23   10    0   23   11    0
    9.08741.083  0.0  0.0    3
   23    9    0   23   11    0   23   12    0
   10.0275.4339  0.0  0.0    1
   23   12    0
   11.4920 1.01  0.0  0.0    1
    3   13    0
   12.6150 1.01  0.0  0.0    2
    3   13    0    3   14    0
   13.50941.775  0.0  0.0    1
    3   14    0
   14.27242.350  0.0  0.0    2
    3   15    3    3   15    4
   15.34052.938  0.0  0.0    5
    3   15    3    3   15    4    3   16    7    3   16    8    3   16    9
   16.28973.683  0.0  0.0    3
    3   16    7    3   16    8    3   16    9
   175.60710.69  0.0.9026    2
    3    0   15    3    0   16
   186.2803.5001.616  0.0    0
    3   16
    1    1    20.1220.496  0.5  0.0    0    0  1.0    1    3
   1.  0.0
    2    2    30.1220.496  0.5  0.0    0    0  1.0    0    4
   1.  0.0
    3    2    40.1220.496  0.5  0.0    0    0  1.0    1    7
  1.  0.0
    4    3    50.1220.496  0.5  0.0    0    0  1.0    2    8
```

```
1.  0.0
 5   4   50.1220.496  0.5  0.0   0   0  1.0   0   6
1.  0.0
 6   5   60.1220.496  0.5  0.0   0   0  1.0   5   9
1.  0.0
 7   4   70.122.3915  0.5  0.0   0   0  1.0   3  -1
1.  0.0
 8   5   80.122.3915  0.5  0.0   0   0  1.0   4  -1
1.  0.0
 9   6   90.122.3915  0.5  0.0   0   0  1.0   6  -1
1.  0.0
10   7   80.1000.496  0.5  0.5   0   0  1.0   0  11
1.  0.0
11   8   90.1000.496  0.5  0.5   0   0  1.0  10  12
1.  0.0
12   9  100.100.3915  0.5  0.5   0   0  1.0  11  -1
1.  0.0
13  11  120.9920.744  0.0  0.0   0   0  1.0   0  14
1.  0.0
14  12  131.4880.496  0.0  0.0   0   0  1.0  13   0
1.  0.0
15  14  150.1220.744  0.5  0.0   0   0  1.0   0  16
2.  0.0
16  15  160.1220.496  0.5  0.0   0   0  1.0  15   0
3.  0.0
18
 1   2   1   2   2   1   2   4   3   3   5   2
 4   5   2   4   6   4   5   4   3   5   8   7
 6   6   4   6   9   8   7  10   5   8  10   5
 8  11   6   9  11   6   9  12   9  10   8   7
11   9   8  12  12   9
 4   5   1   0
 1   1   2     4.0
17  14  15  16            17
 2   3   2   2.875
14   1   2   3            17
15   4   5   6            17
16   7   8   9  10         17
 3  10  22    2.51   5
 2    2.51   3    7.72   5    7.72   6    6.85  23    6.85
 1  11                   14
 2  11                   14
 3  11                   14
 4  12                   15
 5  12                   15
 6  12                   15
 7  13                   16
 8  13                   16
 9  13                   16
10  13                    16
 4   3   2     4.0
11  18                    1   2   3
12  18                    4   5   6
13  18                    7   8   9  10
 5   1   1     4.0
```

```
 18   18                    11   12   13
 18
235
  7    8    1    1    1    1    1    0    0    0
1.2    2    1    2    3    4    5    6    7    8    9   10
1.2    5    1    2    3    4    5    6    7    8    9   10
1.2    8    1    2    3    4    5    6    7    8    9   10
1.2   11    1    2    3    4    5    6    7    8    9   10
1.2   14    1    2    3    4    5    6    7    8    9   10
1.2   17    1    2    3    4    5    6    7    8    9   10
1.2   20    1    2    3    4    5    6    7    8    9   10
1.2   23    1    2    3    4    5    6    7    8    9   10
  1    8   10    1      1.4    .2952      1.5    1.984
  2    5    8   11   14   17   20   23
  1      0.5    1    1    2    1    3    1
  2      1.0    2    2    3    2    4    1    5    1
  3      0.5    3    3    5    2    6    1
  4      1.0    4    2    5    4    7    1    8    1
  5      1.0    5    3    6    2    8    2    9    1
  6      0.5    6    3    9    2   10    1
  7     0.75    7    2    8    4
  8     0.75    8    3    9    4
  9     0.75    9    3   10    2
 10     0.50   10    3
  8   10    4    3    3   10    6   31    1
  1    1    1    2     0.05       1.      1.0       0.    1   0.
  1 .125
  2    1    1    2     0.05       1.      1.0       0.    1   0.
  1  .25    2  .25
  3    1    1    2     0.05       1.      1.0       0.    1   0.
  1 .125    2  .25    3 .125
  4    1    1    2     0.05       1.      1.0       0.    1   0.
  2  .25    4  .25
  5    1    1    2     0.05       1.      1.0       0.    1   0.
  2  .25    3  .25    5  .25    4  .25
  6    1    1    2     0.05       1.      1.0       0.    1   0.
  3 .125    5  .25    6 .125
  7    1    1    2     0.05       1.      1.0       0.    1   0.
  4  .25    7  .25
  8    1    1    2     0.05       1.      1.0       0.    1   0.
  4  .25    5  .25    8  .25    7  .25
  9    1    1    2     0.05       1.      1.0       0.    1   0.
  5  .25    6  .25    9  .25    8  .25
 10    2    0    2     0.05       1.      0.0       0.    1   0.
  6 .125    9  .25   10 .125
  1    3    0.496     0.496      1.0    7          0.      90.0
  2    3    0.496     0.496      1.0    8          0.      90.0
  3    3    0.496     0.496      1.0    9          0.      90.0
  4    3    0.537     0.287      1.0   10          0.      90.0
  1    9    0    4
  1    2    3    4    5    6    7    8    9
  13.75     822.0    121.75     1600.    157.75     858.0    168.76     858.0
  2    1    0    4
 10
  13.75     372.0    121.75     645.0    157.75     383.0    168.76     383.0
```

```
 3   0   4   4
-1  -2  -3  -4
  13.75    322.0   121.75    482.0   157.75    327.0   168.76    327.0
 1   1  -1  20   0     1.0     1.0     1.0     1.0     1.0
 1   2   4   2   1   2   4   2   1   2   4   2   3   5   9   7
 3   7   9   5

 2   2  -1  20   0     1.0     1.0     1.0     1.0     1.0
 3   5   9   7   2   1   2   4   3   7   9   5   8  12  18  16
 6  10  13  10

 3   3  -1  20   0     1.0     1.0     1.0     1.0     1.0
 6  10  13  10   5   3   7   9   5   9   7   3  11  14  22  19
11  19  22  14

 4   4   2  19   0     1.0     1.0     1.0     1.0     1.0
 8  12  18  16   7   3   5   9   8  16  18  12  17  21  -1  11
14  22  19

 5   5   2  19   0     1.0     1.0     1.0     1.0     1.0
11  14  22  19  10   6  10  13  12  18  16   8  20  25  -2  15
23  26  23

 6   6   3  18   0     1.0     1.0     1.0     1.0     1.0
15  23  26  23  14  11  19  22  14  22  19  11  24  27  -3  24
-3  27

 7   7   4  13   0     1.0     1.0     1.0     1.0     1.0
17  21  -1  16   8  12  18  17  -1  21  20  25  -2

 8   8   4  13   0     1.0     1.0     1.0     1.0     1.0
20  25  -2  19  11  14  22  21  -1  17  24  27  -3

 9   9   5  12   0     1.0     1.0     1.0     1.0     1.0
24  27  -3  23  15  23  26  25  -2  20  28  -4

10  10   6   8   0     1.0     1.0     1.0     1.0     1.0
28  -4  27  24  -3  27  -3  24

-1
  .374      .8    .374    .496
-2
  .374      .8    .100    .496     0.0      0.0      .8    .374

-3
  .374      .8    .100    .496     0.0      0.0      .8    .374

-4
  .374      .8    .100    .496     0.0     .248      .8    .374

-5
  .374      .8    .100    .496     0.0     .248      .8    .374

-6
  .374      .8    .100    .496     0.0     .248      .8    .374
```

```
 9    3
 1 hrod      .374       0.0    4    0
 1    2.0675  0.0    1    3 .045  1.0    3    2.0465  0.0    3    1.0280  0.0
 2 tube      .375      .209    1    0
 3    1 .083  0.0
 3 wall      .496      .250    1    0    0
 3    1 .250
10    3
 1   12     528.8                      Inco
   212.      .111      9.09      392.      .121     10.04
   572.      .131     10.98      752.      .141     11.93
   932.      .151     12.88     1112.      .166     13.82
  1292.      .178     14.77     1472.      .191     15.72
  1652.      .204     16.66     1832.      .216     17.61
  2012.      .229     18.56     2192       .241     19.50
 2   14     119.2                        BN
   212.    .16587     67.37      392.    .22015     63.87
   572.    .26264     60.28      752.    .29590     56.74
   932.    .32194     53.19     1112.    .34233     49.65
  1292.    .35829     46.10     1472.    .37078     42.56
  1652.    .38057     39.01     1832.    .38822     35.47
  2012.    .39421     31.92     2192.    .39891     28.37
  2372.    .40259     24.83     2552.    .40546     21.28
 3   10     528.8                      Mon
    70.      .100    10.083      200.      .107    11.333
   400.      .114    13.000      600.      .117    14.833
   800.      .120    16.500     1000.      .125    18.333
  1200.      .132    20.000     1400.      .141    21.833
  1600.      .157    23.500     1800.      .186    25.167
11    1   25
 1    4
  13.75       .5    121.75       1.5    157.75       .5    157.76       0.0
    0.0       1.      17.5      .921      35.0     .8704      52.5     .8326
    70.      .803      87.5     .7755     105.0     .7512     122.5     .7302
   140.      .714     157.5     .6973     175.0     .6837     192.5     .6710
   220.      .652     255.0     .6332     290.0     .6167     325.0     .6017
   360.      .588     395.0     .5769     430.0     .5656     465.0     .5562
   500.      .547     535.0     .5444     570.0     .5304     605.0     .5243
  1000.      .002
13    2    0    1    0    0
 3    3
0.0       0.0  0.1       1.01500.       1.0
 17    1    2    1    0  .0321610   95.3047      40.0
124.  1.0.9999.0001

 18    4    1    0    0       40. 1169.7685      40.0
124.  1.0.9999.0001

 14    5    0    0    0    0    0    0
  0
  0

300    0    0
     .00001       .00110          0.2          1.0      99000.0
```

```
   .19        50.0       100.0       50.0         0
 .00001      .00200        50.0        1.0     99000.0
  25.0        50.0       100.0        5.0         0
-.00001      .00100       300.0        1.0     99000.0
   5.0         5.0       100.0        5.0         0
  -.001
```